

NASA Contractor Report 178419

7-286

Flight Survey of the 757 Wing Noise Field and Its Effects on Laminar Boundary Layer Transition

Volume III — Extended Data Analysis

**Boeing Commercial Airplane Company
P.O. Box 3707, Seattle, WA 98124**

**Contract NAS1-15325
March 1988**

(NASA-CR-178419) FLIGHT SURVEY OF THE 757
WING NOISE FIELD AND ITS EFFECTS ON LAMINAR
BOUNDARY LAYER TRANSITION. VOLUME 3:
EXTENDED DATA ANALYSIS (Boeing Commercial
Airplane Co.) 286 p

N90-19233

Unclass

CSCL 20A G3/71 0270223

The limitations contained in this legend will be considered void after March 1990. This legend shall be marked on any reproduction of this data in whole or in part.



6 5

7 8

NASA Contractor Report 178419

**Flight Survey of the 757 Wing Noise
Field and Its Effects on Laminar
Boundary Layer Transition**

Volume III — Extended Data Analysis

**Boeing Commercial Airplane Company
P.O. Box 3707, Seattle, WA 98124**

**Contract NAS1-15325
March 1988**



**NATIONAL AERONAUTICS AND SPACE ADMINISTRATION
LANGLEY RESEARCH CENTER**

CONTENTS

	Page
1.0 SUMMARY	1
2.0 INTRODUCTION	3
3.0 SYMBOLS AND ABBREVIATIONS	11
3.1 Acronyms	11
3.2 Mathematical Symbols	11
3.3 Subscripts	12
4.0 NOISE ANALYSIS	13
4.1 Flight Test Data	13
4.1.1 Noise Measurements on Wing Lower Surface With Probe Microphones	13
4.1.1.1 OASPL	13
4.1.1.2 Spectra	13
4.1.1.3 Summary	14
4.1.2 Noise Measurements on Wing Lower Surface Leading Edge With Surface Microphones	14
4.1.2.1 OASPL	14
4.1.2.2 Noise Floors	15
4.1.2.3 Spectra	15
4.1.2.4 Summary	16
4.1.3 Noise Measurements on Wing Upper Surface With Probe Microphones	16
4.1.3.1 OASPL	16
4.1.3.2 Spectra	17
4.1.3.3 Summary	17
4.1.4 Noise Measurements on Wing Upper Surface Leading Edge With Surface Mounted Microphones	18
4.1.4.1 OASPL	18
4.1.4.2 Spectra	19
4.1.4.3 Summary	19
4.1.5 Noise Measurements Near Wing Stagnation Line With Surface Mounted Microphone	20
4.1.5.1 OASPL	20
4.1.5.2 Spectra	20
4.1.5.3 Summary	20
4.1.6 Sideslip Noise Data Comparisons	21
4.1.6.1 Lower Surface Microphones	21
4.1.6.2 Upper Surface Microphones	21
4.1.6.3 Summary	21
4.1.7 Comparison of Present 757 Underwing Data With Underwing Data Measured on 747 Airplane in 1974	22
4.2 Comparison of Predictions Versus Measured Noise Data	119
4.2.1 Description of Prediction Procedures	119
4.2.1.1 Lockheed Procedure	119
4.2.1.2 Boeing Procedures	119
4.2.2 Prediction Flight Conditions	119

PRECEDING PAGE BLANK NOT FILMED

4.2.3	Summary of Prediction Versus Measured Data Comparisons	120
4.2.3.1	Lockheed Prediction Procedure	120
4.2.3.2	Butzel Procedure	121
4.2.3.3	Lu Procedure	121
4.2.4	Details of Prediction Versus Measurement Comparisons	122
4.2.4.1	OASPL	122
4.2.4.2	One-Third Octave Band Spectra	123
4.2.4.3	Fan Tones	124
4.2.5	Conclusions From Prediction Comparisons	125
5.0	BOUNDARY LAYER STABILITY ANALYSIS	171
5.1	Corrections to Measured Flight Pressure Data	171
5.2	Method of Analysis	171
5.3	Results	179
5.4	Recommendation for Revised Transition Data Band	204
5.5	Uncertainty Analysis	210
5.6	Comparison With USS Stability Code	214
5.7	Stability Analysis Conclusions	214
6.0	EFFECT OF NOISE ON BOUNDARY LAYER TRANSITION	223
6.1	Effect of Engine Noise on Extent of Laminar Flow	223
6.2	Comparison of Transition Data With Existing Criteria	231
6.2.1	X-21A Criterion	231
6.2.2	Mangiarotty Criterion	232
6.2.3	Swift and Mungur Criterion	233
6.3	Semiempirical Procedure for Predicting the Onset of Laminar Boundary Layer Transition in the Presence of Intense Sound	244
7.0	CONCLUSIONS AND RECOMMENDATIONS	249
8.0	REFERENCES	251
9.0	APPENDIX: TABULATED PRESSURE DATA	253

FIGURES

Figure	Title	Page
2-1	Microphone Arrays on Wing Upper and Lower Surfaces	5
4-1	Normalized OASPL on Wing Lower Surface, Probe Microphones	23
4-2	Lower Wing Probe Microphones $\frac{1}{3}$ Octave Spectra— $M_{AP} \approx 0.62-0.64$	24
4-3	Lower Wing Probe Microphones $\frac{1}{3}$ Octave Spectra— $M_{AP} \approx 0.70, 0.71$	25
4-4	Lower Wing Probe Microphones $\frac{1}{3}$ Octave Spectra— $M_{AP} \approx 0.75, 0.76$	26
4-5	Lower Wing Probe Microphones $\frac{1}{3}$ Octave Spectra— $M_{AP} \approx 0.78, 0.79$	27
4-6	Lower Wing Probe Microphones $\frac{1}{3}$ Octave Spectra— $M_{AP} \approx 0.80$	28
4-7	Lower Wing Probe Microphones $\frac{1}{3}$ Octave Spectra— $M_{AP} \approx 0.81$	29
4-8	Lower Wing Probe Microphones $\frac{1}{3}$ Octave Spectra— $M_{AP} \approx 0.81$	30
4-9	Lower Wing Probe Microphones $\frac{1}{3}$ Octave Spectra— $M_{AP} \approx 0.82, 0.83$	31
4-10	Microphone 4 Narrow Band Spectra— $M_{AP} \approx 0.62-0.64$	32
4-11	Microphone 8 Narrow Band Spectra— $M_{AP} \approx 0.62-0.64$	33
4-12	Microphone 10 Narrow Band Spectra— $M_{AP} \approx 0.62-0.64$	34
4-13	Microphone 17 Narrow Band Spectra— $M_{AP} \approx 0.62-0.64$	35
4-14	Microphone 4 Narrow Band Spectra— $M_{AP} \approx 0.79-0.80$	36
4-15	Microphone 8 Narrow Band Spectra— $M_{AP} \approx 0.79-0.80$	37
4-16	Microphone 10 Narrow Band Spectra— $M_{AP} \approx 0.79-0.80$	38
4-17	Microphone 17 Narrow Band Spectra— $M_{AP} \approx 0.79-0.80$	39
4-18	Normalized OASPL on Wing Lower Surface Leading Edge Surface Mounted Microphones	40
4-19	Airplane Mach Number Dependence of Microphone 2 OASPL Data With Engine With Bleed Valve Closed	41
4-20	Low Airplane Speed, Low Engine Power $\frac{1}{3}$ Octave Spectra—Lower Wing Leading Edge Microphones	42
4-21	Narrow Band Spectra, Lower Wing Leading Edge Microphones—Low Engine Power, Low Airplane Speed	43
4-22	Lower Wing Leading Edge Microphones $\frac{1}{3}$ Octave Spectra— $M_{AP} \approx 0.62-0.64$	44
4-23	Lower Wing Leading Edge Microphones $\frac{1}{3}$ Octave Spectra— $M_{AP} \approx 0.70-0.71$	45
4-24	Lower Wing Leading Edge Microphones $\frac{1}{3}$ Octave Spectra— $M_{AP} \approx 0.75-0.76$	46
4-25	Lower Wing Leading Edge Microphones $\frac{1}{3}$ Octave Spectra— $M_{AP} \approx 0.78-0.79$	47
4-26	Lower Wing Leading Edge Microphones $\frac{1}{3}$ Octave Spectra— $M_{AP} \approx 0.80$	48
4-27	Lower Wing Leading Edge Microphones $\frac{1}{3}$ Octave Spectra— $M_{AP} \approx 0.81$	49
4-28	Lower Wing Leading Edge Microphones $\frac{1}{3}$ Octave Spectra— $M_{AP} \approx 0.80-0.81$	50
4-29	Lower Wing Leading Edge Microphones $\frac{1}{3}$ Octave Spectra— $M_{AP} \approx 0.82-0.83$	51
4-30	Microphone 2 Narrow Band Spectra— $M_{AP} \approx 0.62-0.64$	52
4-31	Microphone 6 Narrow Band Spectra— $M_{AP} \approx 0.62-0.64$	53
4-32	Microphone 13 Narrow Band Spectra— $M_{AP} \approx 0.62-0.64$	54
4-33	Microphone 15 Narrow Band Spectra— $M_{AP} \approx 0.62-0.64$	55
4-34	Microphone 2 Narrow Band Spectra— $M_{AP} \approx 0.79-0.80$	56
4-35	Microphone 6 Narrow Band Spectra— $M_{AP} \approx 0.79-0.80$	57
4-36	Microphone 13 Narrow Band Spectra— $M_{AP} \approx 0.79-0.80$	58

FIGURES

Figure	Title	Page
4-37	Microphone 15 Narrow Band Spectra— $M_{AP} \approx 0.79-0.80$	59
4-38	Normalized OASPL on Wing Upper Surface Probe Microphone vs. M_{FAN}	60
4-39	Normalized OASPL on Wing Upper Surface Probe Microphone vs. C_L	61
4-40	Normalized OASPL vs. Airplane Mach Number—Upper Surface Probe Microphones ...	62
4-41	Probe Microphones, Upper Surface $\frac{1}{3}$ Octave Spectra Effect of Airplane Mach Number	63
4-42	Probe Microphones, Upper Surface $\frac{1}{3}$ Octave Spectra Effect of Airplane Mach Number	64
4-43	Glove Pressure Distribution Characteristics Summary—WBL 325.	65
4-44	Upper Wing Probe Microphones $\frac{1}{3}$ Octave Spectra— $M_{AP} \approx 0.62-0.64$	66
4-45	Upper Wing Probe Microphones $\frac{1}{3}$ Octave Spectra— $M_{AP} \approx 0.70, 0.71$	67
4-46	Upper Wing Probe Microphones $\frac{1}{3}$ Octave Spectra— $M_{AP} \approx 0.75, 0.76$	68
4-47	Upper Wing Probe Microphones $\frac{1}{3}$ Octave Spectra— $M_{AP} \approx 0.78, 0.79$	69
4-48	Upper Wing Probe Microphones $\frac{1}{3}$ Octave Spectra— $M_{AP} \approx 0.80$	70
4-49	Upper Wing Probe Microphones $\frac{1}{3}$ Octave Spectra— $M_{AP} \approx 0.81$	71
4-50	Upper Wing Probe Microphones $\frac{1}{3}$ Octave Spectra— $M_{AP} \approx 0.80, 0.81$	72
4-51	Upper Wing Probe Microphones $\frac{1}{3}$ Octave Spectra— $M_{AP} \approx 0.82, 0.83$	73
4-52	Microphone 7 Narrow Band Spectra— $M_{AP} \approx 0.62-0.64$	74
4-53	Microphone 9 Narrow Band Spectra— $M_{AP} \approx 0.62-0.64$	75
4-54	Microphone 3 Narrow Band Spectra— $M_{AP} \approx 0.62-0.64$	76
4-55	Microphone 16 Narrow Band Spectra— $M_{AP} \approx 0.62-0.64$	77
4-56	Microphone 7 Narrow Band Spectra— $M_{AP} \approx 0.79-0.80$	78
4-57	Microphone 9 Narrow Band Spectra— $M_{AP} \approx 0.79-0.80$	79
4-58	Microphone 3 Narrow Band Spectra— $M_{AP} \approx 0.79-0.80$	80
4-59	Microphone 16 Narrow Band Spectra— $M_{AP} \approx 0.79-0.80$	81
4-60	Normalized OASPL on Wing Upper Surface Leading Edge Surface Mounted Microphones vs. M_{FAN}	82
4-61	Normalized OASPL on Wing Upper Surface Leading Edge Surface Mounted Microphones vs. C_L	83
4-62	Upper Wing Leading Edge Microphones $\frac{1}{3}$ Octave Spectra— $M_{AP} \approx 0.62-0.64$	84
4-63	Upper Wing Leading Edge Microphones $\frac{1}{3}$ Octave Spectra— $M_{AP} \approx 0.70-0.71$	85
4-64	Upper Wing Leading Edge Microphones $\frac{1}{3}$ Octave Spectra— $M_{AP} \approx 0.75-0.76$	86
4-65	Upper Wing Leading Edge Microphones $\frac{1}{3}$ Octave Spectra— $M_{AP} \approx 0.78-0.79$	87
4-66	Upper Wing Leading Edge Microphones $\frac{1}{3}$ Octave Spectra— $M_{AP} \approx 0.80$	88
4-67	Upper Wing Leading Edge Microphones $\frac{1}{3}$ Octave Spectra— $M_{AP} \approx 0.81$	89
4-68	Upper Wing Leading Edge Microphones $\frac{1}{3}$ Octave Spectra— $M_{AP} \approx 0.80-0.81$	90
4-69	Upper Wing Leading Edge Microphones $\frac{1}{3}$ Octave Spectra— $M_{AP} \approx 0.82-0.83$	91
4-70	Microphone 1 Narrow Band Spectra— $M_{AP} \approx 0.62-0.64$	92
4-71	Microphone 5 Narrow Band Spectra— $M_{AP} \approx 0.62-0.64$	93
4-72	Microphone 11 Narrow Band Spectra— $M_{AP} \approx 0.62-0.64$	94
4-73	Microphone 14 Narrow Band Spectra— $M_{AP} \approx 0.62-0.64$	95
4-74	Microphone 1 Narrow Band Spectra— $M_{AP} \approx 0.79-0.80$	96

FIGURES

Figure	Title	Page
4-75	Microphone 5 Narrow Band Spectra— $M_{AP} \approx 0.79-0.80$	97
4-76	Microphone 11 Narrow Band Spectra— $M_{AP} \approx 0.79-0.80$	98
4-77	Microphone 14 Narrow Band Spectra— $M_{AP} \approx 0.79-0.80$	99
4-78	Normalized OASPL at Wing Stagnation Line Microphone vs. M_{FAN}	100
4-79	Stagnation Point Microphone (Mic 12) $\frac{1}{3}$ Octave Spectra	101
4-80	Stagnation Point Microphone (Mic 12) $\frac{1}{3}$ Octave Spectra (Concluded).....	102
4-81	Microphone 12 Narrow Band Spectra— $M_{AP} \approx 0.62-0.64$	103
4-82	Microphone 12 Narrow Band Spectra— $M_{AP} \approx 0.79-0.80$	104
4-83	Effect of Sideslip on Lower Surface Probe Microphones.....	105
4-84	Effect of Sideslip on Lower Surface Leading Edge Microphones.....	106
4-85	Effect of Sideslip on Upper Surface Probe Microphones.....	107
4-86	Effect of Sideslip on Upper Surface Leading Edge Microphones.....	108
4-87	Effect of Sideslip on $\frac{1}{3}$ Octave Spectra for Lower Wing Microphones	109
4-88	Effect of Sideslip on $\frac{1}{3}$ Octave Spectra for Upper Wing Microphones	110
4-89	Effect of Sideslip on $\frac{1}{3}$ Octave Spectra for Upper Wing Microphones (Continued).....	111
4-90	Effect of Sideslip on $\frac{1}{3}$ Octave Spectra for Upper Wing Microphones (Concluded).....	112
4-91	747 Wing Mounted Microphone Installation.....	113
4-92	Comparison of 747 and 757 Wing Mounted Microphone Noise Data, $\theta \approx 50$ deg.....	114
4-93	Comparison of 747 and 757 Wing Mounted Microphone Noise Data, $\theta \approx 30$ deg.....	115
4-94	Comparison of 747 and 757 Wing Mounted Microphone $\frac{1}{3}$ Octave Spectra Noise Data, $\theta \approx 30$ deg, $M_{AP} \approx 0.80$	116
4-95	Comparison of 747 and 757 Wing Mounted Microphone $\frac{1}{3}$ Octave Spectra Noise Data, $\theta \approx 30$ deg, $M_{AP} \approx 0.60$	117
4-96	Comparison of 747 and 757 Wing Mounted Microphone $\frac{1}{3}$ Octave Spectra Noise Data $\theta \approx 50$ deg, $M_{AP} \approx 0.83$	118
4-97	Measured vs. Predicted Turbine Noise Summary.....	127
4-98	Measured vs. Predicted Shock Noise Summary	128
4-99	Microphone 2 Measured OASPL's vs. Lockheed Procedure Predictions	129
4-100	Microphone 2 Measured OASPL's vs. Lockheed Procedure Predictions Without Convective and Dynamic Amplification Corrections	130
4-101	Microphone 2 Measured OASPL's vs. Boeing-Lu Procedure Predictions for Jet Mixing Noise	131
4-102	Microphone 6 Measured OASPL's vs. Lockheed Procedure Predictions	132
4-103	Microphone 6 Measured OASPL's vs. Lockheed Procedure Predictions Without Convective and Dynamic Amplification Corrections	133
4-104	Microphone 6 Measured OASPL's vs. Boeing Butzel and Lu Procedure Predictions for Jet Shock and Jet Mixing Noise.....	134
4-105	Microphone 13 Measured OASPL's vs. Lockheed Procedure Predictions	135
4-106	Microphone 13 Measured OASPL's vs. Lockheed Procedure Predictions Without Convective and Dynamic Amplification Corrections	136
4-107	Microphone 13 Measured OASPL's vs. Boeing Butzel and Lu Procedure Predictions for Jet Shock and Jet Mixing Noise.....	137

FIGURES

Figure	Title	Page
4-108	Microphone 15 Measured OASPL's vs. Lockheed Procedure Predictions	138
4-109	Microphone 15 Measured OASPL's vs. Lockheed Procedure Predictions Without Convective and Dynamic Amplification Corrections	139
4-110	Microphone 15 Measured OASPL's vs. Boeing Butzel and Lu Procedure Predictions for Jet Shock and Jet Mixing Noise	140
4-111	Microphone 4 Measured OASPL's vs. Lockheed Procedure Predictions	141
4-112	Microphone 4 Measured OASPL's vs. Lockheed Procedure Predictions Without Convective and Dynamic Amplification Corrections	142
4-113	Microphone 4 Measured OASPL's vs. Boeing Butzel and Lu Procedure Predictions for Jet Shock and Jet Mixing Noise	143
4-114	Microphone 8 Measured OASPL's vs. Lockheed Procedure Predictions	144
4-115	Microphone 8 Measured OASPL's vs. Lockheed Procedure Predictions Without Convective and Dynamic Amplification Corrections	145
4-116	Microphone 8 Measured OASPL's vs. Boeing Butzel and Lu Procedure Predictions for Jet Shock and Jet Mixing Noise	146
4-117	Microphone 10 Measured OASPL's vs. Lockheed Procedure Predictions	147
4-118	Microphone 10 Measured OASPL's vs. Lockheed Procedure Predictions Without Convective and Dynamic Amplification Corrections	148
4-119	Microphone 10 Measured OASPL's vs. Boeing Butzel and Lu Procedure Predictions for Jet Shock and Jet Mixing Noise	149
4-120	Microphone 17 Measured OASPL's vs. Lockheed Procedure Predictions	150
4-121	Microphone 17 Measured OASPL's vs. Lockheed Procedure Predictions Without Convective and Dynamic Amplification Corrections	151
4-122	Microphone 17 Measured OASPL's vs. Boeing Butzel and Lu Procedure Predictions for Jet Shock and Jet Mixing Noise	152
4-123	Microphone 2 Measured $\frac{1}{3}$ Octave Spectra vs. Lockheed Procedure Predictions Without Convective and Dynamic Amplification Corrections	153
4-124	Microphone 6 Measured $\frac{1}{3}$ Octave Spectra vs. Lockheed Procedure Predictions Without Convective and Dynamic Amplification Corrections	154
4-125	Microphone 13 Measured $\frac{1}{3}$ Octave Spectra vs. Lockheed Procedure Predictions Without Convective and Dynamic Amplification Corrections	155
4-126	Microphone 15 Measured $\frac{1}{3}$ Octave Spectra vs. Lockheed Procedure Predictions Without Convective and Dynamic Amplification Corrections	156
4-127	Microphone 4 Measured $\frac{1}{3}$ Octave Spectra vs. Lockheed Procedure Predictions Without Convective and Dynamic Amplification Corrections	157
4-128	Microphone 8 Measured $\frac{1}{3}$ Octave Spectra vs. Lockheed Procedure Predictions Without Convective and Dynamic Amplification Corrections	158
4-129	Microphone 10 Measured $\frac{1}{3}$ Octave Spectra vs. Lockheed Procedure Predictions Without Convective and Dynamic Amplification Corrections	159
4-130	Microphone 17 Measured $\frac{1}{3}$ Octave Spectra vs. Lockheed Procedure Predictions Without Convective and Dynamic Amplification	160
4-131	Comparison of Measured $\frac{1}{3}$ Octave Turbine Noise Data at Microphone 10 With Lockheed Procedure Predictions	161
4-132	Microphone 17 Measured $\frac{1}{3}$ Octave Spectra vs. Lockheed Procedure Predictions Without Convective and Dynamic Amplification Corrections	162

FIGURES

Figure	Title	Page
4-133	Microphone 17 Measured $\frac{1}{3}$ Octave Spectra vs. Lockheed Procedure Predictions Without Convective and Dynamic Amplification Corrections	163
4-134	Microphone 10 Measured $\frac{1}{3}$ Octave Spectra vs. Butzel and Lu Predictions, $M_{AP} \approx 0.80$	164
4-135	Microphone 10 Measured $\frac{1}{3}$ Octave Spectra vs. Butzel and Lu Predictions, $M_{AP} \approx 0.60$	165
4-136	Microphone 17 Measured $\frac{1}{3}$ Octave Spectra vs. Butzel and Lu Predictions, $M_{AP} \approx 0.80$	166
4-137	Microphone 17 Measured $\frac{1}{3}$ Octave Spectra vs. Butzel and Lu Predictions, $M_{AP} \approx 0.60$	167
4-138	Comparison of Measured Fan Tone Data With Lockheed Procedure Predictions—Microphone 8	168
4-139	Comparison of Measured Fan Tone Data With Lockheed Procedure Predictions—Microphone 10	169
4-140	Comparison of Measured Fan Tone Data With Lockheed Procedure Predictions—Microphone 17	170
5-1	Effect of Strip-a-Tube Fairing on Static Pressure	173
5-2	Effect of Recessing Strip-a-Tube	174
5-3	Sample Isobar Plot	176
5-4	Typical Stability Analysis Results	177
5-5	N_{TS} vs. N_{CF} Trajectory Curve—Sample Case	178
5-6	757 NLF Glove: Case 1	182
5-7	757 NLF Glove: Case 2	183
5-8	757 NLF Glove: Case 3	184
5-9	757 NLF Glove: Case 4	185
5-10	757 NLF Glove: Case 5	186
5-11	757 NLF Glove: Case 6	187
5-12	757 NLF Glove: Case 7	188
5-13	757 NLF Glove: Case 8	189
5-14	757 NLF Glove: Case 9	190
5-15	757 NLF Glove: Case 10	191
5-16	757 NLF Glove: Case 11	192
5-17	757 NLF Glove: Case 12	193
5-18	757 NLF Glove: Case 13	194
5-19	757 NLF Glove: Case 14	195
5-20	757 NLF Glove: Case 15	196
5-21	757 NLF Glove: Case 16	197
5-22	757 NLF Glove: Case 17	198
5-23	757 NLF Glove: Case 18	199
5-24	757 NLF Glove: Case 19	200
5-25	757 NLF Glove: Case 20	201

FIGURES

Figure	Title	Page
5-26	757 NLF Glove: Case 21	202
5-27	Transition N-Factors for 757 NLF Glove	205
5-28	Transition N-Factors for 757 NLF Glove and F-111 NLF Glove	206
5-29	757 NLF Glove: Upper Surface N-Factor Trajectories	207
5-30	757 NLF Glove: Upper Surface N-Factor Trajectories	208
5-31	Lower Surface N-Factor Trajectories	209
5-32	Uncertainty Analysis of Case 8	212
5-33	Uncertainty Analysis of Case 11	213
5-34	Case 2—Standard Boeing Approach, USS Results	215
5-35	Case 2—Maximum Envelope Approach, USS Results	216
5-36	Case 11—Standard Boeing Approach, USS Results	217
5-37	Case 11—Maximum Envelope Approach, USS Results	218
5-38	Case 13—Standard Boeing Approach, USS Results	219
5-39	Case 13—Maximum Envelope Approach, USS Results	220
5-40	USS Code Results for Standard Boeing Approach Versus Original Analysis Results	221
5-41	Recommended Transition Data Band	222
6-1	Effect of Engine Noise on Extent of Laminar Flow: Case A	225
6-2	Boundary Layer Stability Analysis $M \approx 0.80$, $C_L \approx 0.53$, $\beta \approx 0$ deg	226
6-3	Effect of Engine Noise on Extent of Laminar Flow: Case B	227
6-4	Boundary Layer Stability Analysis $M_\infty \approx 0.70$, $C_L \approx 0.64$, $\beta \approx 0$ deg	228
6-5	Effect of Engine Noise on Extent of Laminar Flow: Case C	229
6-6	Boundary Layer Stability $M_\infty \approx 0.70$, $C_L \approx 0.47$, $\beta \approx +5$ deg	230
6-7	X-21A Acoustic Criterion	235
6-8	Comparison of X-21A and One 757 Flight Data Case	236
6-9	Interpretation of X-21A and 757 Flight Data Comparison	237
6-10	OASPL Distribution and Potential Loss of Laminar Area Due To Engine Noise 757 Lower Surface at Cruise	238
6-11	Amplified Boundary Layer Acoustic Disturbance Growth per Mangiarotty for $M_{AP} = 0.8$ and $M_{AP} = 0.7$	239
6-12	Amplified Boundary Layer Acoustic Disturbance Growth per Mangiarotty for $M_{AP} = 0.7$, $\beta = 5$ deg	240
6-13	One Hz Bandwidth Measured Noise vs. Tollmein-Schlichting Amplification Curves Normalized to Critical SPL per Mungur, $M_{AP} = 0.8$ and 0.7 , $\beta = 0$ deg	241
6-14	One Hz Bandwidth Measured Noise vs. Tollmein-Schlichting Amplification Curves Normalized to Critical SPL per Mungur, $M_{AP} = 0.7$, $\beta = 5$ deg	242
6-15	Tollmien-Schlichting Transition N-Factor vs. Crossflow Transition N-Factor	247
6-16	Illustration of Semiempirical NLF Transition Prediction Procedure	248

TABLES

Table	Title	Page
2-1	Noise-Related Airplane and Engine Data—Flight 1	6
2-2	Noise-Related Airplane and Engine Data—Flight 2	7
2-3	One-Third Octave Band Plot Categories—Flight 1	8
2-4	One-Third Octave Band Plot Categories—Flight 2	9
4-1	Microphone Coordinates	126
5-1	Strip-a-Tube Corrections	175
5-2	Summary of Boundary Layer Stability Results	203
6-1	Comparison of Transition x/c Percentage Predicted by Mangiarotty, Mungur, and Semiempirical Procedures With Measured 757 Data	243

1.0 SUMMARY

A flight test program was completed in June of 1985 using the Boeing 757 flight research aircraft with a NLF glove installed on the right wing just outboard of the engine. The objectives of this program were to measure engine noise levels on the wing and to investigate the effect of engine noise on the extent of laminar flow on the glove. Details of the flight test program and results are discussed in Volume I of this document (ref. 1), and all of the measured data are contained in Volume II (ref. 2). The present volume contains the results of additional engineering analysis of the data.

As part of the additional engineering analysis, an extensive boundary layer stability analysis of the glove data was performed which showed that crossflow disturbances were, in general, much more highly amplified at transition than Tollmien-Schlichting disturbances. For most cases, crossflow N-factors at the measured transition location were between 12 and 18. As a result of this stability analysis, the F-111 transition data band (which can be used as a transition criterion) derived in an earlier study (ref. 3) has been modified.

The stability analysis indicated that the most critical Tollmien-Schlichting disturbances were in the 2500 to 3000 Hz range. The measured noise level ($1/3$ octave) in this frequency range on the glove lower surface varied by 10 to 15 dB from the lowest to the highest engine power setting. However, there was very little change in the extent of laminar flow from the lowest to the highest engine power setting. Since the boundary layer stability analysis indicated that crossflow disturbances are the dominant cause of transition, this small observed effect of variations in engine noise level on the transition location may indicate that engine noise does not have a significant effect on crossflow disturbances. It is possible that for wing designs where Tollmien-Schlichting disturbances are the primary cause of transition that engine noise effects on the extent of laminar flow may be significant.

A limited analysis of the measured noise data was presented in Volume I. Volume III includes the analysis of all of the measured noise data. This extended analysis supported the conclusion reported in Volume I—that engine noise generally dominated the sound measurements on the lower wing surface but wing airflow related sources dominated the upper wing surface noise data. The upper surface wing shock appears to have a strong influence on the upper wing surface noise data. The high fluctuating pressure levels are probably due to boundary layer pressure fluctuations enhanced by the wing shock or sound radiated from the shock boundary layer interaction.

Much of the noise data appears to be contaminated by pressure fluctuations related to uncontrolled factors such as cirrus clouds, wing leading edge vortices that may have been started by the glove/wing interface, and boundary layer disturbances caused by the microphones mounted on the leading edge wing surface. These influences are pointed out when apparent but detailed studies of these influences were not conducted.

Predictions of the lower wing surface noise levels were calculated using a Lockheed procedure (ref. 4) for a number of engine and aerodynamic sources as well as two different Boeing jet mixing noise procedures (refs. 5 and 6) and one Boeing jet shock noise procedure (ref. 5). The general trends of the high engine power noise data for dependence on engine power condition and airplane Mach number were well predicted by the Lockheed jet shock broadband source predictions, when the effects of convective amplification were not included in the calculations. The predicted sound levels were generally approximately 10 dB higher than the measured data, however. The Boeing broadband shock noise predictions gave better level comparisons for microphones near the engine but were approximately 10 dB low for the outboard microphones. It was concluded that jet mixing noise was not evident in the measured data even at the subsonic jet Mach number conditions where the broadband shock noise would no longer be present. The main factor in this conclusion was the lack of an increase in noise levels at given jet exhaust velocity as the airplane speed was reduced. All three of the jet mixing prediction procedures predicted increased jet noise for this situation.

Existing procedures for estimating the effect of noise on the transition point for an airplane wing laminar boundary layer were compared with the 757 results. Three procedures were examined: the X-21 related empirical transition Reynolds number versus acoustic disturbance velocity curve from Reference 7, the Mangiarotty procedure from Reference 8, and the Swift and Mungur T-S amplification procedure from Reference 4. None of the three procedures considered the crossflow disturbance dominance affecting the transition of the 757 glove laminar boundary layer. As a result, a new empirical procedure that utilizes the F-111 and 757 data is proposed. This procedure is presented primarily to stimulate consideration of this type of an approach.

2.0 INTRODUCTION

Application of a laminar flow wing design to commercial transports offers the potential of significant airplane drag reductions. However, a major concern has been whether laminar flow can be sustained in the presence of the noise environment on the wing of a commercial transport with conventional wing-mounted turbofan engines. To investigate this issue, a natural laminar flow (NLF) glove was installed on the right wing of the Boeing 757 flight research airplane just outboard of the engine. A series of flight tests was conducted in June of 1985 in which noise levels were measured on the wing and glove, and pressures and the extent of laminar flow were measured on the glove. Details of the flight test program and results are discussed in Volume I of this report (ref. 1). Tabulations and plots of all of the measured data are contained in Volume II (ref. 2). The present volume contains the results of additional engineering analysis of the data.

Only a small part of the measured noise data was examined in the analysis of Volume I. All of the measured data has been analyzed in Volume III. The conclusions of Volume I regarding the dominance of engine noise for the lower wing microphones and airflow noise for the upper wing microphones are supported by the analysis of the complete data set. For convenience in examining the acoustic data, the tabulated noise-related airplane data, engine data, and data categories from Volume I are reproduced as Tables 2-1, 2-2, 2-3, and 2-4 in this volume. Also the figure showing the microphone placement positions on the upper and lower wing surfaces is reproduced as Figure 2-1 in this volume.

To help understand the engine noise sources that were responsible for the measured 757 lower wing noise characteristics, predictions of engine and airframe noise components were calculated using existing procedures. The major procedure used was a nearfield engine noise and airframe noise method developed by Lockheed (ref. 4). Noise generation was predicted for engine sources including the fan, compressor, turbine, and jet and for airframe sources including the wing boundary layer and wing trailing edge. In addition, two Boeing procedures were used to predict jet noise.

A major part of the additional engineering analysis consisted of a stability analysis of 21 flight test data cases. The objective of this analysis was to determine the relative importance of crossflow (C-F) and Tollmien-Schlichting (T-S) disturbances in causing transition, and to provide additional data for use in calibrating transition methods based on linear stability theory. The stability results were also used to help interpret the measured effect of noise on the extent of laminar flow on the glove.

Another part of the additional engineering analysis consisted of comparing the 757 glove results with previous wind tunnel and flight test results pertaining to the effect of noise on boundary layer transition. The 757 NLF glove test is the first flight test data for a configuration with wing-mounted engines. However, the X-21 program (ref. 9), which was a flight test of a configuration with aft-mounted engines, did find a trend of decreasing extent of laminar flow with increasing engine noise levels. Therefore, it is useful to compare the results from that program with the 757 test data. There are also several sets of wind tunnel test data that were compared to the 757 results.

The 757 NLF glove data allows an evaluation of the validity of current methods for predicting the effect of noise on the extent of laminar flow. Two of those methods were evaluated in the present study. They were those of Mangiarotty (ref. 8) and Swift and Mungur (ref. 4). Both methods assume that the sound wave generates a T-S disturbance at the leading edge of the wing, which grows until transition takes place. The frequency dependent T-S amplifications calculated from stability theory are applied to the acoustic velocity that is calculated assuming a plane wave. Both procedures require the experimental determination of a transfer function to determine the resulting flow disturbance velocity and a transition criterion. Although both methods are similar there are detail differences. The effect of crossflow on the disturbance growth or transition criterion is not considered in either method. As a result, both methods predicted a much greater extent of laminar boundary layer than was observed when a condition resulting in low T-S disturbance amplification and high crossflow disturbance amplification was flown.

The need to include a consideration of crossflow disturbance growth when evaluating laminar boundary stability is satisfied for *background* disturbance levels (normal atmospheric turbulence and smooth airfoil) using the experimentally derived F-111/757 T-S N-factor versus crossflow N-factor criterion band. A method is suggested that uses the F-111/757 N-factor data to evaluate the influence of noise as well. The method assumes that noise does not influence the growth of crossflow disturbances directly. However, the crossflow disturbance growth rate does determine the level of the T-S amplified acoustic disturbance at which transition is predicted.

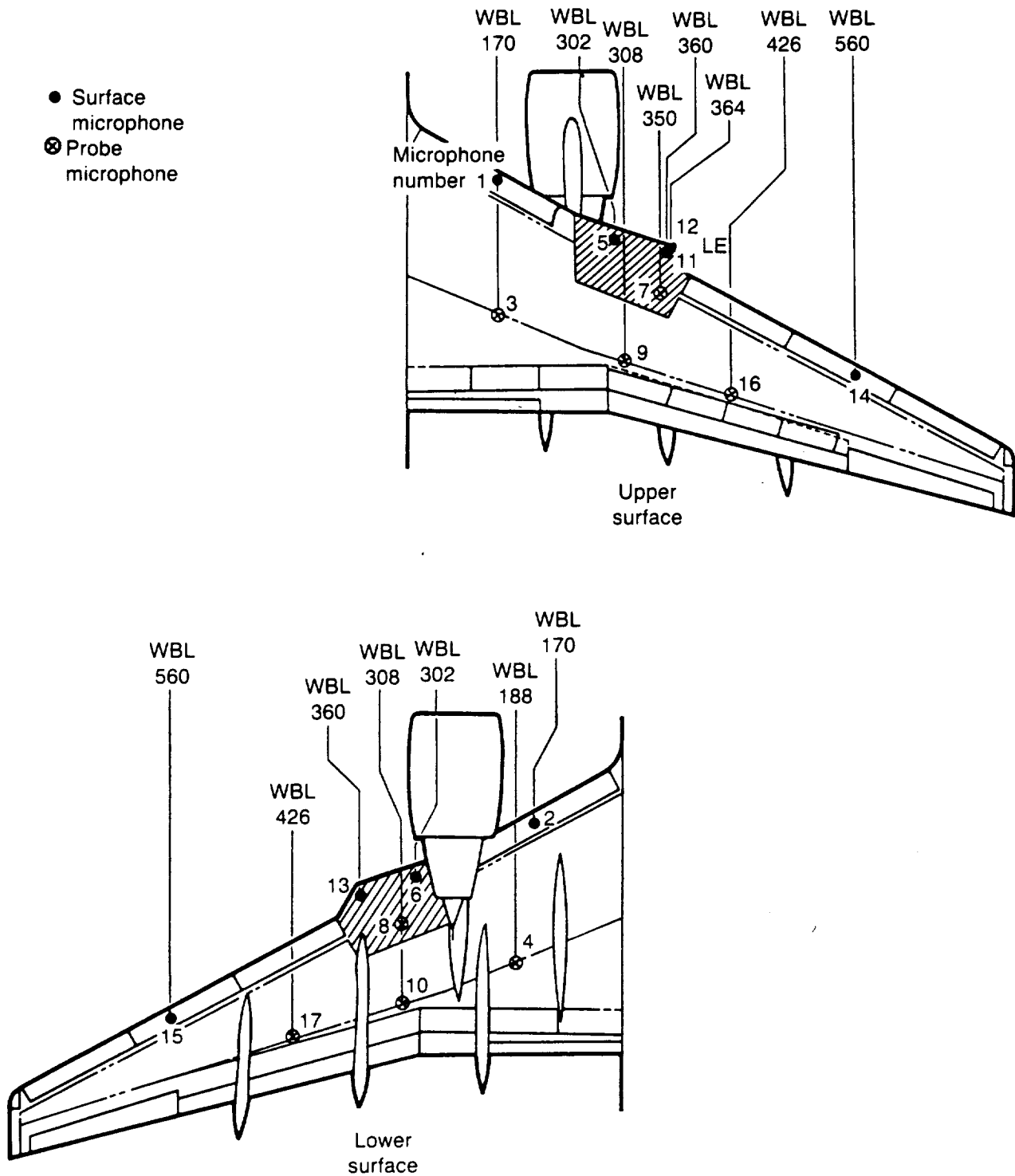


Figure 2-1. Microphone Arrays on Wing Upper and Lower Surfaces

Table 2-1. Noise-Related Airplane and Engine Data — Flight 1

Cond. no.	Airplane Mach no.	Pressure altitude, ft	C _L	Sideslip, deg	N _{1C} , r/min (left eng)	N _{1C} , r/min (right eng)	N ₁ , r/min (right eng)	Mach no. (fan exhaust)
005	0.81	38 952	0.52	-0.2	4366	4010	3644	1.23
006.1	0.79	39 008	0.54	5.8	4388	4382	3971	1.28
001	0.82	38 950	0.49	-0.3	4348	4175	3800	1.27
002	0.81	39 012	0.50	5.4	4359	4353	3974	1.29
109	0.79	38 957	0.53	-0.7	4391	3810	3461	1.17
006.2	0.80	38 926	0.51	-6.4	4369	4348	3962	1.28
035	0.81	39 952	0.53	-0.3	4359	4017	3633	1.23
036	0.78	39 957	0.56	-0.4	4394	3908	3519	1.18
013	0.80	40 948	0.55	0.2	4129	4366	3934	1.28
014	0.81	40 946	0.54	0	4222	4220	3823	1.27
015	0.81	40 946	0.54	-0.2	4367	4115	3733	1.25
016	0.80	41 002	0.56	6.3	4383	4245	3848	1.26
017	0.80	40 878	0.55	-7.1	4374	4366	3986	1.28

Compressor bleed closed for all conditions

Table 2-2. Noise-Related Airplane and Engine Data — Flight 2

Cond. no.	Airplane Mach no.	Pressure altitude, ft	C _L	Sideslip, deg	N _{1C} , r/min (left eng)	N _{1C} , r/min (right eng)	N ₁ , r/min (right eng)	Mach no. (fan exhaust)
201	0.80	30 011	0.35	-0.6	4161	3227	3109	1.06o
202	0.79	30 080	0.36	3.2	4174	3240	3114	1.05o
203	0.79	30 075	0.36	-4.0	4179	3294	3167	1.07o
204	0.81	34 001	0.42	-0.2	4300	3424	3224	1.10o
205	0.79	34 008	0.43	3.9	4317	3437	3230	1.09o
206	0.80	34 000	0.42	-3.9	4304	3481	3274	1.11o
207	0.81	36 000	0.45	0	4359	3585	3333	1.17o
210	0.80	36 998	0.48	-0.3	4376	3660	3380	1.14c
211	0.80	37 994	0.50	-0.2	4361	3850	3538	1.19c
212	0.79	37 988	0.51	3.9	4382	3867	3545	1.18c
213	0.80	37 927	0.50	-3.7	4361	3796	3485	1.17c
214	0.81	38 987	0.52	-0.1	4365	3954	3614	1.21c
215	0.82	38 988	0.50	-0.1	4346	4042	3701	1.24c
216	0.83	38 986	0.48	0	4331	4327	3971	1.30c
218	0.70	37 007	0.62	-0.6	4437	3582	3265	1.05o
217	0.71	37 007	0.60	-0.5	4350	3557	3248	1.06c
219.1	0.64	35 020	0.67	0.7	2491	4493	4121	1.19c
220.1	0.62	35 009	0.71	-0.8	4502	2928	2683	0.86o
221	0.63	35 007	0.68	-0.6	4500	2315	2123	0.76o
222	0.81	38 991	0.50	0.1	4365	3903	3571	1.20c
248	0.82	38 990	0.48	0.2	4344	4023	3692	1.24c
249	0.78	38 993	0.53	0	4393	3717	3391	1.14o
250	0.75	38 999	0.57	0	4438	3723	3382	1.12o
251	0.76	38 997	0.56	0.2	3623	4426	4023	1.26c
252	0.75	38 994	0.57	-0.4	3977	4007	3638	1.19c
223	0.80	40 483	0.53	-0.2	4004	4340	3934	1.28c
224	0.80	40 482	0.54	-0.4	4081	4102	3714	1.24c
225	0.80	40 483	0.54	-0.7	4373	3793	3437	1.18o
226	0.79	40 426	0.55	4.8	4383	3965	3587	1.20c
227	0.80	40 449	0.54	-4.0	4373	3993	3617	1.21c
228	0.79	41 296	0.57	-0.5	4395	2645	2384	0.94o
229	0.75	40 793	0.61	-0.4	4442	3330	2994	1.04o
231	0.70	39 015	0.64	0.7	3575	4508	4059	1.23c
232	0.70	39 008	0.65	0	3993	4019	3618	1.15c
233	0.70	39 005	0.65	-0.3	4518	3631	3270	1.06o
234	0.70	39 042	0.64	6.8	4512	3786	3412	1.09c
235	0.71	38 954	0.62	-6.7	4505	3816	3443	1.11c
236	0.71	38 920	0.63	-0.8	4510	2602	2349	0.85o
237	0.71	39 005	0.62	-0.5	4506	3280	2962	0.99o
239	0.80	38 000	0.46	-0.5	4376	3557	3271	1.12o
240	0.80	38 003	0.46	3.9	4382	3673	3377	1.14o
241	0.80	40 971	0.53	0	4373	4034	3653	1.23c
242	0.83	40 968	0.49	0.3	4338	4321	3930	1.30c
243	0.82	38 976	0.46	0.2	3700	4345	3985	1.29c
244	0.82	38 972	0.45	-0.3	4085	4116	3776	1.26c
245	0.82	38 974	0.45	-0.3	4351	3865	3542	1.20c
246	0.82	38 989	0.46	4.0	3895	4355	3987	1.29c
247	0.81	38 548	0.45	-0.7	4364	2501	2293	0.93o
238	0.69	36 497	0.53	-0.7	4501	1097	1001	0.70o

o — Bleed vave open

c — Bleed valve closed

Table 2-3. One-Third Octave Band Plot Categories—Flight 1

	Cond. no.	Airplane Mach no.	Altitude (10 ³ ft)	Right engine N _{1C} (r/rim)	Sideslip, (deg)
Category 1 Zero sideslip	001	0.82	39	4175	0
	005	0.81	39	4010	0
	035	0.81	40	4019	0
	036	0.78	40	3908	0
	109	0.79	39	3810	0
Category 2 Positive sideslip	002	0.81	39	4353	5.4
	006.1	0.79	39	4382	5.8
	016	0.80	41	4245	6.3
Category 3 Negative sideslip	006.2	0.80	39	4348	-6.4
	017	0.80	41	4366	-7.1
Category 6 Engine power variation	013	0.80	41	4366	0
	014	0.81	41	4221	0
	015	0.81	41	4115	0

Table 2-4. One-Third Octave Band Plot Categories—Flight 2 (Continued)

	Cond. no.	Mach no.	Altitude (10 ³ ft)	Right engine N _{1C}	Sideslip, deg	
Category 1 Altitude variation— no sideslip	201	0.80	30	3227	0	
	204	0.81	34	3424	0	
	207	0.81	36	3585	0	
	210	0.80	37	3660	0	
	211	0.80	38	3850	0	
	239	0.80	38	3557	0	
	214	0.81	39	3954	0	
	241	0.80	41	4034	0	
Category 2 Positive sideslip	202	0.79	30	3240	3.2	
	205	0.79	34	3437	3.9	
	212	0.79	38	3867	3.9	
Category 3 Negative sideslip	203	0.79	30	3294	-4.0	
	206	0.80	34	3481	-3.9	
	213	0.80	38	3796	-3.7	
Category 4 Bleed valve check	217	0.71	37	3557	0	
	218	0.70	37	3582	0	
Category 5 Engine power variation M _{AP} = 0.63	219	0.64	35	4493	0	Narrowband analyzed
	220	0.62	35	2928	0	
	221	0.63	35	2315	0	
Category 6 Engine power variation M _{AP} = 0.8	223	0.80	40.5	4340	0	Narrowband analyzed
	224	0.80	40.5	4102	0	
	225	0.80	40.5	3793	0	
	228	0.79	41.3	2645	0	
Category 7 Engine power variation M _{AP} = 0.7	231	0.70	39	4508	0	
	232	0.70	39	4019	0	
	233	0.70	39	3631	0	
	237	0.71	39	3280	0	
	236	0.71	39	2602	0	
	238	0.69	36.5	1097	0	

Table 2-4. One-Third Octave Band Plot Categories—Flight 2 (Concluded)

	Cond. no.	Mach no.	Altitude (10 ³ ft)	Right engine N _{1C}	Sideslip, deg	
Category 8 Engine power variation M _{AP} = 0.82	243	0.82	39	4345	0	
	244	0.82	39	4116	0	
	245	0.82	39	3865	0	
	247	0.81	38.5	2501	0	
Category 9 Sideslip variation M _{AP} = 0.8	224	0.80	40.5	4102	0	
	225	0.80	40.5	3793	0	
	226	0.79	40.5	3965	4.8	
	227	0.80	40.5	3993	-4.0	
Category 10 Sideslip variation M _{AP} = 0.7	232	0.70	39	4019	0	
	233	0.70	39	3631	0	
	234	0.70	38	3786	6.8	
	235	0.71	39	3816	-6.7	
Category 11 Other sideslip data	240	0.80	38	3673	3.9	
	246	0.82	39	4355	4.0	
Category 12 Other zero sideslip	242	0.83	43	4321	0	
	249	0.78	39	3717	0	
	250	0.75	39	3723	0	
	251	0.76	39	4426	0	
	252	0.75	39	4007	0	
	229	0.75	40.5	3330	0	
	215	0.82	39	4042	0	
	216	0.83	39	4331	0	
	248	0.82	39	4023	0	
	222	0.81	39	3903	0	

3.0 SYMBOLS AND ABBREVIATIONS

3.1 ACRONYMS

C-F	Crossflow
LE	Leading edge
NLF	Natural laminar flow
OASPL	Overall sound pressure level
SPL	Sound pressure level = $20 \log \frac{P_{rms}}{0.0002 \text{ dynes/cm}^2}$
TS	Tollmien-Schlichting
WBL	Wing buttock line

3.2 MATHEMATICAL SYMBOLS

A	Disturbance amplitude
A _o	Disturbance amplitude at neutral stability point
c	Chord
C _L	Airplane lift coefficient
C _p	Pressure coefficient
C _{pN}	Pressure coefficient based on component of velocity normal to leading edge
$\ln A/A_o$	Disturbance amplification factor
M	Mach number
M _{AP}	Airplane Mach number
M _{FAN}	Fan jet exhaust Mach number
N	Disturbance amplification factor
N ₁	Engine fan r/min
N _{1C}	N ₁ corrected to standard day temperature (59° F)
N _{CF}	Crossflow amplification factor
N _{TS}	Tollmien-Schlichting amplification factor
P	Pressure
P ₄₀	Reference pressure—ambient pressure at 40,000-ft altitude on standard day
Re _C	Reynolds number based on chord

s	Arc length along surface from leading edge
s/c	Normalized arc length along surface from leading edge
x	Distance from leading edge along airfoil chord
x/c	Normalized distance from leading edge along airfoil chord
z	Airfoil ordinate
α	Airplane angle of attack
$\alpha_{r_s}^*$	Spanwise component of wave number vector
β	Airplane sideslip angle (positive nose left)
γ	Ratio of specific heats
Λ	Sweep angle
ψ	Angle of disturbance wave number vector with respect to local potential flow velocity direction
ρ	Density
ω^*	Dimensional disturbance frequency

3.3 SUBSCRIPTS

amb	Ambient
E2	Engine No. 2 (on glove side)
max	Maximum
tr	Transition
∞	Undisturbed reference condition
i	Incident

4.0 NOISE ANALYSIS

4.1 FLIGHT TEST DATA

This section contains the results of the analysis of all of the flight test noise data. Included are the noise measurements on both the upper and the lower surface with both surface microphones and probe microphones. Also included are sideslip noise data comparisons and a comparison of the data from this test with those measured on a 747 airplane in 1974.

4.1.1 Noise Measurements on Wing Lower Surface With Probe Microphones

4.1.1.1 OASPL

Figure 4-1 shows plots of normalized OASPL versus fan exhaust jet Mach number (M_{Fan}) for the underwing probe microphones. All of the data is for the zero sideslip airplane condition. Flight Mach numbers from 0.62 to 0.83 are included. The plots show essentially the same features as those plotted in Volume I, which included only a limited selection of the measured data. All of the lower wing probe microphones show noise levels increasing with increasing engine power. Since, at a given airplane Mach number, the airplane flight parameters were held nearly constant as engine power was increased, the increasing noise levels are attributed to engine generated noise. The engine noise measured by microphones 4 and 10 shows very little flight Mach number dependence. A dependence on flight Mach number is seen at microphone 8 for high engine power conditions and microphone 17 for low engine power conditions. Changing flight speed can change measured engine noise in two ways. First, the measured radiation angle will be changed because of the receiver motion and second, engine noise sources can be affected by the airplane motion. For example, changes in the jet shear layer turbulence will modify jet noise generation and sound propagation through the shear layer.

4.1.1.2 Spectra

One-third octave spectra grouped by flight Mach number, are shown in Figures 4-2 to 4-9. Figures 4-10 to 4-13 are narrow band spectra for the lower flight Mach numbers, $M_{AP} \approx 0.6$, and Figures 4-14 to 4-17 are narrow band spectra for the higher flight Mach number, $M_{AP} \approx 0.8$. For $M_{AP} \approx 0.6$, microphones 8, 10, and 17 (figs. 4-11, 4-12, and 4-13) clearly show the presence of turbomachinery tones. As M_{Fan} increases, the turbomachinery tones become somewhat masked by broadband noise as seen for the highest engine power condition for $M_{AP} = 0.6$ and $M_{AP} = 0.8$ in Figures 4-14 to 4-17. The analysis in Section 4.2 suggests that the broadband noise at the higher engine power conditions is generated by the interaction of jet turbulence with shocks contained within the jet flow when the fan or primary jet is supersonic.

Except for the highest engine power conditions, the microphone 4 spectra are dominated by engine bleed flow noise, as discussed in Volume I. The microphone 4 narrow band spectra, for the engine conditions for which bleed flow noise dominates, have a somewhat periodic shape (figs. 4-10 and 4-14). This shape suggests constructive/destructive interference of noise reflected from the wing surface with noise radiating directly to the probe microphone. Destructive interference occurs at frequencies related by

$$f_{(n+1)} - f_n = 2f_1$$

where f_1 is the lowest frequency for which destructive interference occurs and is inversely proportional to the propagation time difference of the direct and reflected signal. The *valleys* in the narrow band spectra occur at frequency intervals of approximately 2400 Hz. The above equation would therefore predict the first valley to occur at 1200 Hz, which appears to be the case. The $M_{AP} = 0.6$ data for microphone 8 (fig. 4-11) also shows some of the peak/valley characteristic seen for microphone 4. When engine noise dominates the spectrum, as for microphones 10 and 17 for low airplane speeds (figs. 4-12 and 4-13) and all the lower wing probe microphones at the higher airplane speeds (figs. 4-14 to 4-17), the narrow band spectra do not show evidence of wing reflection interference effects. This implies a time coherence for the bleed flow noise, which is larger than that of the engine noise. All data analysis used 32-sec averaging time. In any case, the microphone 4 data indicates that the probe microphones are responding to sound both radiated directly to the microphone and reflected from the wing surface to the microphone. If the reflected sound is not coherent with the direct radiation, it adds approximately 3 dB to the direct radiation levels at all frequencies. Therefore, subtracting 3 dB from the probe microphones other than microphone 4 should give a good approximation to the sound levels radiated directly from the engine.

4.1.1.3 Summary

The following summarizes the analysis of the lower wing probe microphone data:

1. The dependence of the noise levels on engine power condition indicates that the engine generated noise was the dominant source of pressure fluctuations measured by the lower wing probe microphones.
2. Turbomachinery tones were strongly evident at lower engine power conditions but jet shock broadband noise dominated at high engine power.
3. Microphone 4 was dominated by engine bleed valve noise for all except the higher engine power conditions.
4. The probe microphones were affected by sound reflected from the wing surface as well as sound radiated directly from the engine to the microphones.
5. Subtraction of 3 dB to remove the effect of wing reflection is appropriate for all probe microphones except microphone 4.

4.1.2 Noise Measurements on Wing Lower Surface Leading Edge With Surface Microphones

4.1.2.1 OASPL

Figure 4-18 show plots of normalized OASPL versus M_{Fan} for the underwing leading edge surface mounted microphones. It is believed that engine bleed valve noise contributed to the OASPL for much of the microphone 2 data. The circled points are those for which the bleed valve was open. If these points are ignored, an airplane Mach number dependence is seen for microphone 2 with the OASPL levels increasing with a 60-log airplane Mach number relationship (fig. 4-19). (The contribution of the airplane electrical interference 400-Hz tone has been removed from the OASPL data.) The 60-log airplane Mach number dependence suggests that airflow noise such as boundary layer noise is a primary source for this microphone. Noise generated by airflow separation behind the microphone fairing may also be important.

The microphone 6 data in Figure 4-18 shows very little airplane Mach number dependence except for some *outlying* points. The outlier point at M_{Fan} equal to 0.70 is identified as being due to nacelle spillage. As pointed out in Volume 1, the airplane was in a slight dive with the engine windmilling for this condition. As a result, turbulent airflow from the engine nacelle was impinging on the microphone causing a high reading. The outlier point for condition 247 at $M_{Fan} = 0.93$ is shown as affected by cirrus clouds. Other conditions that were measured in the presence of cirrus clouds are consistent with the main data trend. However, considering for example conditions 223, 224, and 225, it was found that their OASPLs and spectra were consistent with the data trend at microphone 6 but showed high levels at microphone 13 and to some degree at microphone 15. Since the cirrus clouds experienced were somewhat scattered, it appears that they were not impinging on all microphones simultaneously. There are other outlier points such as those for condition 204 and 245 for microphone 6 for which no explanation is evident. It is possible that light cirrus clouds were present but not noted when condition 245 was measured. However, the hot film data for conditions 204 showed no evidence of cirrus clouds.

Except for the outlier points, the microphone 6 data shows an engine power dependence similar to that seen for the aft underwing probe microphones. As for the aft probe microphones, this engine power dependence is felt to indicate a dominance of engine noise.

The OASPL data for microphones 13 and 15 both seem to show an airplane Mach number dependence. Microphone 13 also shows a great deal of irregularity particularly at the higher airplane Mach numbers and engine power conditions. Most of this irregularity is attributable to cirrus clouds as indicated. The data points for conditions 228 and 218 do not follow the data trends for their respective airplane Mach numbers, but no explanation for their behavior is known.

4.1.2.2 Noise Floors

Figure 4-20 compares the lower engine power ($M_{Fan} = 0.76$), lowest flight Mach number ($M_{AP} = 0.63$) $\frac{1}{3}$ octave spectral data from each of the lower wing leading edge microphones to attempt to identify possible nonengine noise floors. The corresponding narrow band spectra are shown in Figure 4-21. The primary features of the data from microphone 2 are attributed to the airplane electrical system interference and to the engine bleed. Microphones 6 and 13 show a significant tone from the engine fan. Also the narrow band spectra show a broadband peak with an unidentified tone near 4000 Hz for both microphones 6 and 13. The frequency of this tone could not be related to the turbomachinery blade counts and therefore it does not appear to be due to engine noise. Another broadband peak is seen at 2500 Hz for microphone 13. Microphone 15 is seen to be influenced by the airplane electrical system interference. The narrow band spectrum of microphone 15 shows a moderate broadband peak near 4000 Hz, but the unidentified tone noted for microphones 6 and 13 near 4000 Hz is not present. The lowest level noise characteristics measured by the four microphones were therefore quite different. The noise floors appear to be set by different sources including engine bleed valve noise, engine fan noise, non-engine tone noise, airplane electrical interference, and other unidentified broadband sources.

4.1.2.3 Spectra

The $\frac{1}{3}$ octave band spectra for the lower wing leading edge microphones are shown in Figures 4-22 through 4-29. They are grouped by airplane Mach number. Those conditions for which cirrus clouds were observed are indicated. The narrow band spectra for flight Mach number ≈ 0.6 and 0.8 are shown in Figures 4-30 through 4-37. Tones from the airplane electrical system, engine fan, and turbine are indicated on the narrow band spectra. As reported in Volume I, tones which were not relatable to engine turbomachinery were also observed.

4.1.2.4 Summary

The following summarizes the analysis of the lower wing leading edge surface mounted microphone data:

1. Microphone 2 appears to be affected by engine bleed valve noise at the lower engine power conditions for which the bleed valve is open. When the bleed valve is closed, microphone 2 appears to be dominated by airflow noise.
2. When present, cirrus clouds caused high microphone readings.
3. The main trend of the microphone 6 data is increasing noise level with increasing engine power indicating engine noise dominance.
4. The data from microphone 13 is in many cases affected by cirrus cloud contamination.
5. The sources contributing to the noise floors of the lower wing leading edge microphones were not completely identifiable. However, the effects of engine bleed noise, nonengine tones, and airplane electrical interference were observed.

4.1.3 Noise Measurement on Wing Upper Surface With Probe Microphones

4.1.3.1 OASPL

Plots of normalized OASPL versus M_{Fan} for the wing upper surface probe microphones are shown in Figure 4-38. The clear dependence of noise on engine power through M_{Fan} seen for the lower wing microphones is not apparent. Although there does appear to be an airplane Mach number dependence the trend is not consistent. For example, the $M_{AP} = 0.6-0.7$ data showed levels lower than for the other flight Mach numbers at microphone 9 but showed the highest levels at microphone 7. For given flight Mach numbers, some cases show relatively constant noise levels as engine power is changed while others show variability to as much as 15 dB. The data of Figure 4-38 is replotted as a function of airplane lift coefficient (C_L) in Figure 4-39. Although the data appears less scattered than the M_{Fan} plots of Figure 4-38 when a given airplane Mach number range is considered, the dependence on C_L and airplane Mach number is still complex. Figure 4-40 plots normalized OASPL versus airplane Mach number. A somewhat similar behavior is seen for all of the microphones with the noise levels first increasing with airplane Mach number and then rapidly decreasing. The 60% chord microphones (Mics 3, 9, and 16) all show the rapid decrease occurring for airplane Mach number in the range of 0.8. The 30% chord microphone (Mic 7) however shows the falloff occurring at a lower airplane Mach number ($M_{AP} \approx 0.7$). The $1/3$ octave spectra shown in Figures 4-41 and 4-42 indicate that the peak noise levels seen in Figure 4-40 are associated with a large increase in low frequency noise. Figure 4-43 shows predicted wing pressure distributions for the glove midspan for various airplane Mach numbers and C_L s. For the highest C_L , a shock is expected near the leading edge ($x/c \approx 10\%$) at $M_{AP} = 0.7$. As the airplane Mach number is increased to $M_{AP} = 0.8$ the shock moves aft to approximately 50% chord. It is therefore possible that the behavior seen in Figure 4-40 is relatable to the wing shock. The noise at a given microphone may be increasing as the shock approaches it from the leading edge as the airplane Mach number is increased. The rapid decrease in noise level then seems to occur as the shock moves behind the microphone. Microphone 7 therefore experiences maximum noise levels at a lower airplane Mach number because it is closer to the leading edge. The high noise levels observed may be due to boundary layer turbulence directly or sound generated by the shock wave interacting with the turbulent boundary layer. The increased thickness of the boundary layer behind the shock may be sufficient to cause high levels of boundary layer pressure fluctuations at the elevated probe microphone as the shock gets closer and stronger with increasing airplane Mach number.

For airplane Mach numbers in the range of 0.6 the wing airflow is subsonic. Since there is no evidence of engine noise at the upper wing probe microphones and no shocks are present for $M_{AP} = 0.6$,

the noise levels at this flight condition may represent a *floor* due to airflow over the microphones or some other nonengine source of sound. It is therefore interesting to compare the noise levels at $M_{AP} \approx 0.6$ for the upper and corresponding lower wing microphones. The OASPL levels measured at the lowest engine power conditions (excluding the engine windmill condition for which nacelle spillage occurred) for the lower wing probe microphones are indicated in Figure 4-40. It is seen that the lower wing microphones measured less noise than the corresponding upper wing microphones at $M_{AP} \approx 0.6$. In fact, the lowest levels measured at the upper wing probe microphones occurred at the highest airplane Mach numbers. It may be that the upper wing probes were more affected by turbulent boundary layer pressure fluctuations than those on the lower wing. The thinner boundary layer at $M_{AP} = 0.8$ compared with that at $M_{AP} = 0.6$ may explain the lower noise levels at $M_{AP} = 0.8$ after the shock has moved past the microphone. However, based on the flat plate relationship, $\delta \propto U^{-1/5}$, one would only expect a 6% boundary layer thickness reduction going from $M_{AP} = 0.6$ to $M_{AP} = 0.8$. It may be that a downstream noise source, at the trailing edge for example, is responsible for the noise floor at $M_{AP} = 0.6$ on the upper wing, but for some reason is not as important for the lower wing. The very low levels at $M_{AP} = 0.8$ on the upper wing may be due to the wing shock. When the shock moves behind the microphone, it may *block* the microphone from receiving sound from the trailing edge.

4.1.3.2 Spectra

One-third octave spectra, normalized to an altitude of 40,000 ft, are shown in Figures 4-44 to 4-51. The data is grouped by airplane Mach number. The spectrum shape for microphone 7 for $M_{AP} = 0.7$, (fig. 4-45) at which the OASPL was a maximum, shows a peak near 3,000 Hz and a smaller peak near 400 Hz. The $M_{AP} = 0.8$ spectra for the other upper wing aft probe microphones (fig. 4-48) peak at frequencies of 400 Hz or lower. As was shown in Figure 4-41 and 4-42, the low frequency noise is related to the presence of the shock in front of the microphone. Narrow band spectra plots for airplane Mach numbers of approximately 0.6 and 0.8 are shown in Figures 4-52 to 4-59. The large low frequency peak for the 60% chord microphones at $M_{AP} = 0.8$ (figs. 4-57 to 4-59) corresponds to the low frequency noise seen in the 1/3 octave results associated with the presence of wing shocks.

4.1.3.3 Summary

1. The upper wing probe microphones do not show engine noise influence, as indicated by the lack of M_{Fan} dependence.
2. Maximum noise levels appear to be related to the wing shock, but it is not clear if they are due to noise generated by the shock boundary layer interaction or boundary layer pressure fluctuations enhanced by the shock.
3. The shock related *noise* appears to be low frequency (≈ 400 Hz) dominated.
4. The noise measured by a microphone appears to drop off rapidly as the shock moves downstream of the microphone. In fact, the minimum noise levels were measured at the highest airplane Mach numbers when the shock is farthest aft. This may indicate that trailing edge noise may be important, second to the wing shock. The shock could *block* the microphones from trailing edge noise when it is between them and the wing trailing edge.
5. At low airplane Mach numbers ($M_{AP} \approx 0.6$) the upperwing probe microphones show higher noise levels than the corresponding lower wing microphones. If trailing edge generated noise is the dominant noise source for the upper wing at this M_{AP} , it appears it is less intense at the lower wing microphones.

4.1.4 Noise Measurements on Wing Upper Surface Leading Edge With Surface Mounted Microphones

4.1.4.1 OASPL

Plots of normalized OASPL versus M_{Fan} are shown in Figure 4-60 for the upper wing leading edge (5% chord) surface mounted microphones. As was the case for the upper wing probe microphones a M_{Fan} dependence, which would indicate engine noise dominance, is not clearly evident. The microphone 1 data covers a very narrow OASPL range of the order of 4 dB with the primary dependence appearing to be airplane Mach number. The other microphones show a more complex behavior.

When plotted versus airplane lift coefficient, the microphone 5 data (fig. 4-61) shows a better correlation than for M_{Fan} , especially if the data influenced by nacelle spillage and cirrus clouds is eliminated. The data point for condition 242 has a gain recording error of 12-18 dB based on the recorded gains for other similar conditions. For the higher Mach number conditions ($M_{AP} \geq 0.7$) the boundary layer on the upper glove surface was found to be laminar back to 20% to 30% chord. The high noise levels measured by microphone 5 therefore suggest that the microphone or the microphone ramp was causing the local boundary layer to become turbulent near the microphone. It is not known why the noise level appears initially to decrease as C_L increases. The airplane Mach number decreases for the higher C_L s so that a M_{AP} dependence is possibly influencing the data to some degree. It does appear that there may be a tendency for the noise to decrease with increasing C_L until $C_L \approx 0.62$ however. For $C_L \geq 0.62$, the noise level begins to increase with C_L . For these points, the hot film data indicated that the laminar boundary layer transition point was very close to the glove leading edge. The increased noise level is probably related to this transition. It is interesting to note that the $1/3$ octave spectrum shape for the low Mach number/high C_L points at microphone 5 (fig. 4-62) is quite different from the higher Mach number cases (fig. 4-63 for example). It appears that the boundary layer transition resulted in lower frequency noise than that due to the microphone tripping the local laminar boundary layer.

The data from microphone 11 is quite complicated whether plotted versus M_{Fan} or airplane C_L . It was found that the upper wing boundary layer at the outboard edge of the glove near microphone 11 transitioned forward of 15% chord (which was the location of the most forward hot film transducer in this region) for all flight conditions. The static pressure distribution measured in this region showed a strong adverse gradient near the 5% chord location. Microphone 11 was mounted slightly outboard (WBL = 360) of the region where these aerodynamic measurements were made (WBL = 355) and may have been influenced by transitioning boundary layer flow. It is also possible that vortices associated with the rapid sweep change at the outboard edge of the glove were causing pressure fluctuations at the microphone. There seems to be a trend of noise increasing with airplane C_L for this microphone that could indicate increased vorticity as angle of attack is increased. As was observed for microphone 5, the high C_L points occur at low M_{AP} values. The low M_{AP} spectra (fig. 4-62) appear to show relatively more low frequency noise than at higher airplane Mach numbers (fig. 4-64). At high airplane Mach numbers, the microphone 11 OASPLs show a great deal of scatter. Despite the scatter in the corresponding OASPLs the $1/3$ octave spectra for microphone 11 at the higher airplane Mach numbers show shapes very similar to those of microphones 1 and 5.

The normalized OASPL versus M_{Fan} and C_L plots for microphone 14 are similar to those of microphone 5 except that the levels for microphone 14 are 12 to 14 dB lower. The microphone 14 data is also approximately 15 dB lower than that of microphone 1. The reason for the relatively low levels at microphone 14 is not known. Assuming that microphones 1, 5, and 14 are all responding primarily to airflow turbulence pressure fluctuations, the low microphone 14 level implies lower turbulence levels. The similarity of the parametric dependence of microphone 14 with that of microphone 5 is interesting since microphone 5 is located on the NLF glove whereas microphone 14 is located on the wing surface. It has been speculated that the leading edge of the wing may be laminar even on the nonglove region. While this would explain the parametric similarity of microphones 5 and 14, the level difference remains. Since the microphone installation itself is probably disturbing the flow, as mentioned above,

detailed differences in these installations and the local boundary layer characteristics may be important. The *magic bond* potting used to fare the microphones to the wing surface was handworked with minimal precision. Perhaps the resulting fairing differences were important.

4.1.4.2 Spectra

The normalized $1/3$ octave spectra are shown in Figures 4-62 to 4-69 grouped by airplane Mach number. It is believed that the pressure fluctuations measured by these microphones were primarily due to boundary layer pressure fluctuations. Therefore, the rms voltages measured by the hot films at 5% and 7.5% chord near microphone 5 are also noted. While they indicate the state of the boundary layer over the smooth section of the glove, local flow effects such as separation over the microphone fairing would not be indicated by the hot film transducers. Generally, hot film rms voltages less than 15 mv indicate laminar flow, values of the order of 100 mv indicate transitional flow and intermediate values usually are representative of turbulent flow. Most cases for which rms values greater than 30 mv were measured at the 5% chord hot film also show increased noise measured at microphone 5. For $M_{AP} \approx 0.6$ (fig. 4-62) a low frequency peak was observed at microphone 5 while the 5% chord hot film measured approximately 30 mv. Cirrus clouds are seen to result in high microphone levels and hot film levels in Figures 4-65 and 4-66. In some cases, high rms levels were observed at the 5% hot film but no corresponding increase was observed at microphone 5. In most of these cases, high noise levels were observed at another microphone. These were probably cirrus cloud influences as well since the clouds were variable and could be intercepted by one section of the wing while not present at another.

Narrow band spectra for $M_{AP} \approx 0.6$ and $M_{AP} \approx 0.8$ are shown in Figures 4-70 to 4-77. No engine turbomachinery tones are identifiable in these figures, consistent with the contention that engine noise was not significant for the upper wing microphones. The low frequency ($f \leq 500$ Hz) peak related to boundary layer transition near microphone 5 on the NLF glove at $M_{AP} = 0.6$ is clearly seen in Figure 4-71.

4.1.4.3 Summary

1. The upper wing surface leading edge microphones did not show a clear M_{Fan} dependence indicative of engine noise dominance as seen for the lower wing microphones.
2. Airflow noise sources such as boundary layer pressure fluctuations, cirrus clouds, and wing vortices are believed to dominate the upper wing leading edge microphones.
3. Transition of the laminar boundary layer to turbulent flow near the leading edge of the NLF glove at low airplane Mach number was seen to result in an increase of low frequency broadband noise at microphone 5 in particular and microphone 11 to a lesser degree.
4. Microphone 11 OASPL showed more scatter than the other leading edge microphones although its $1/3$ octave spectrum shape remained relatively constant. Aerodynamic disturbances such as boundary layer pressure fluctuations enhanced because of the adverse pressure gradient near this microphone and vortices emanating from the rapid sweep change at the outboard edge of the glove may be responsible for this variability.
5. The noise levels measured at the most outboard microphone were of the order of 15 dB lower than the inboard leading edge microphones. Since the spectra from this microphone are similar in shape to the spectra of the inboard microphones, it is believed that boundary layer pressure fluctuations dominate this microphone as well. If this is the case, the low OASPL levels imply lower boundary layer turbulence levels. It is not clear why the outboard region of the wing leading edge would have appreciably different boundary layer characteristics compared to inboard. It is speculated that microphone fairing differences may give rise to different local boundary layers although it would seem that the fairing variations would not be large enough to account for 15 dB.

4.1.5 Noise Measurements Near Wing Stagnation Line With Surface Mounted Microphone

4.1.5.1 OASPL

The normalized OASPL versus M_{Fan} data for microphone 12, which was positioned on the approximate stagnation line of the glove, is shown in Figure 4-78. There appears to be a difference in the behavior of the lower airplane Mach number data compared with the higher Mach number data. The $M_{AP} \geq 0.78$ data shows increasing noise with M_{Fan} indicating engine noise dominance. The lower airplane Mach number data however is more complex. At the lower M_{Fan} points the $M_{AP} = 0.62$ and $M_{AP} = 0.75$ data show the highest levels. The $M_{AP} = 0.7$ data, although intermediate to the $M_{AP} = 0.6$ and 0.75 cases, shows noise levels that appear more consistent with the high airplane speeds. With the exception of the $M_{AP} = 0.7$ data, the high noise levels observed for the low airplane Mach numbers may be explained in terms of higher airplane angle of attack associated with the lower flight speeds.

4.1.5.2 SPECTRA

The angle-of-attack values are tabulated on the $1/3$ octave spectrum plots shown in Figures 4-79 and 4-80. The $1/3$ octave spectra show a spectrum shape difference for the low and high flight speed data as well. The lower flight Mach number spectra appear to peak at higher frequencies, whereas the higher flight Mach number data tends to peak in the range of 1 KHz as engine power is increased. Notwithstanding the $M_{AP} = 0.7$ data, it may be argued that the lower flight speed data is dominated by turbulent pressure fluctuations associated with the higher angles of attack. At the higher airplane Mach numbers, this noise is reduced because of the associated lower angle of attack and the engine noise dominates. As was discussed in Volume I, the leading edge microphone will be somewhat shielded from noise sources located behind the engine such as in jet flow. This could explain the low engine noise levels measured by this microphone compared to microphone 13 located nearby but on the lower wing surface.

Narrow band spectra for $M_{AP} \approx 0.6$ and 0.8 are shown in Figures 4-81 and 4-82. Generally, the spectra indicate broadband noise dominance. The $M_{AP} \approx 0.6$ data shows a very low frequency tone that is not apparent in the $1/3$ octave data and is therefore at a frequency less than 45 Hz. The source of this tone is not known. A tone at approximately 5.7 KHz was observed for the $M_{AP} = 0.8$ data. Since its frequency was independent of engine power conditions, it does not appear to be engine noise related.

4.1.5.3 Summary

1. Pressure fluctuations associated with boundary layer turbulence tend to dominate microphone 12 at lower flight speeds for which the airplane angle of attack is relatively high.
2. At higher airplane Mach numbers and associated lower airplane angles of attack, engine noise is observed as the engine power is increased.
3. When engine noise is dominating microphone 12 the levels are of the order of 15 dB lower than those observed at microphone 13, which is close to microphone 12 but on the underside of the wing.
4. It is probable that the wing partially shields microphone 12 for the dominant engine noise sources that are probably located in the jet flow behind the engine.

4.1.6 Sideslip Noise Data Comparisons

4.1.6.1 Lower Surface Microphones

To investigate the effect of wing sweep angle on the laminar boundary layer transition, tests were conducted with varying amounts of airplane sideslip. Both positive and negative sideslip angles ranging from +7 deg to -7 deg were tested. The effect of sideslip on the OASPL noise levels measured on the lower wing are shown in Figures 4-83 and 4-84. Except for microphones 2 and 13, noise levels tended to be highest with negative sideslip. The aft probe microphones (fig. 4-83) show the same trend of increasing noise with increasing engine power for the nonzero as for the zero sideslip conditions. The slight noise increase with negative sideslip for those microphones may result from an effective change of directivity angle and propagation distance for the microphone relative to the jet exhaust noise source. The jet exhaust flow direction will not change directly with sideslip because of the freestream flow. It is also possible that noise generation within the jet flow changes with sideslip because of the changed mixing with the freestream air.

The lower wing leading edge microphones (fig. 4-84) show a somewhat different behavior compared to the aft probe microphones. Microphone 6 showed a small noise increase for negative sideslip as was seen for the aft microphones except for the two lowest engine power negative sideslip points. These points showed a relatively large noise increase. The reason for this large increase is not known. Because of the proximity of microphone 6 to the engine, it may be susceptible to nacelle spillage or possible jet turbulence impingement, which could be more severe with negative sideslip than with positive sideslip.

Microphone 13 shows highest noise levels with positive sideslip. This may result from disturbances related to the rapid sweep change at the outboard edge of the glove. Streamlines from this area would tend to pass closer to microphone 13 with positive sideslip. The data at microphone 15 again shows the highest levels for negative sideslip. Because of its distance from the engine, microphone 15 is probably not strongly dominated by engine noise even at the high power conditions. Airflow changes over the microphone occurring with changes in sideslip may therefore be expected to result in changes in boundary layer pressure fluctuations. However, it is not clear whether positive or negative sideslip should lead to higher noise levels.

4.1.6.2 Upper Surface Microphones

The upper wing microphones (figs. 4-85 and 4-86) generally were more strongly affected by sideslip changes than those on the lower wing except for the two microphones closest to the fuselage (mics 1 and 3). This is consistent with the belief that the pressure fluctuations measured by the upper wing microphones were due to airflow related noise sources. The small changes at microphones 1 and 3 probably indicate that the aerodynamic changes on this section of the wing were smaller than at the outboard sections.

One-third octave spectra showing the effect of sideslip for selected microphones are shown in Figures 4-87 to 4-90. Generally, the noise changes are broadband.

4.1.6.3 Summary

1. The probe microphones on the lower wing surface showed a slight broadband noise increase with negative sideslip compared to zero or positive sideslip. The change may result from the change in radiation directivity angle from the jet flow noise sources resulting from the relative microphone position change associated with the sideslip.
2. The lower wing leading edge microphones showed a more varied behavior with sideslip than the lower wing aft probe microphones. It is possible that effects such as airflow separation from the nacelle, jet flow impingement, leading edge vortices, and boundary layer turbulence are affecting the leading edge microphones but have little effect on the aft probes.

3. The upper wing microphones showed much stronger effects of sideslip than those on the lower wing. This seems consistent with the belief that the pressure fluctuations measured by the upper wing are due primarily to airflow sources (turbulence or turbulence generated acoustic waves).

4.1.7 Comparison of Present 757 Underwing Data With Underwing Data Measured on a 747 Airplane in 1974

Noise measurements made by Boeing on the wing of a 747 in 1974 were used for laminar flow wing noise assessment in reference 8. Comparison of the 747 data with the present 757 data was used to help verify both the 757 data and the previous assessment.

Figure 4-91 is a schematic showing the microphone placement for the 747 test. A fairing approximately 17-ft long was mounted on the lower wing surface, outboard of engine number four, at approximately WBL 944. Eight 1/4-in B&K microphones were mounted into the fairing so that the microphones were flush with the fairing surface.

Figure 4-92 compares normalized OASPL data from microphone F04 from the 747 test with data from microphones 8 and 17 from the 757 test. All three microphones were at a geometric angle from the engine axis (with origin at center of fan nozzle) of approximately 50 deg. The sideline distance for the 747 data was intermediate between the sideline distances for the two 757 microphones. Figure 4-93 compares 747 and 757 OASPL data for a geometric angle of approximately 30 deg for about the same normalized sideline distance. Microphones 8 and 17 from the 757 test were probe microphones. Because of reflection from the wing, the probe microphone OASPLs may be 0 to 3 dB lower than what would be measured by surface microphones. Since measurement points were not precisely duplicated for the two tests, it cannot be determined if the differences seen in Figures 4-92 and 4-93 represent noise source differences or measurement location differences. The results seem reasonably consistent, however.

Comparison of 1/3 octave band spectra for the 747 and 757 tests are shown in Figures 4-94 to 4-96. As for the OASPL comparisons, the 747 data seems reasonably consistent with the 757 results.

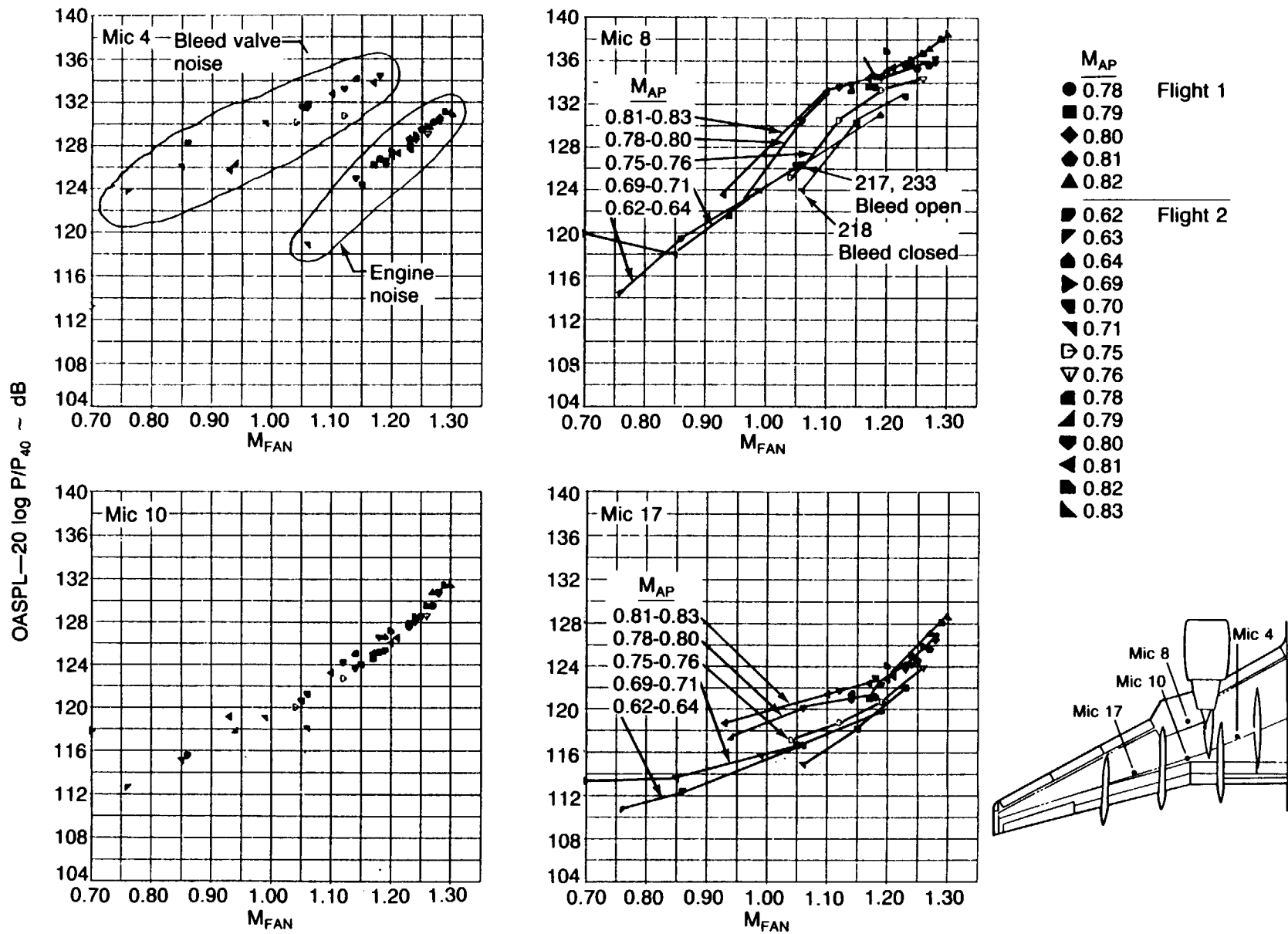


Figure 4-1. Normalized OASPL on Wing Lower Surface, Probe Microphones

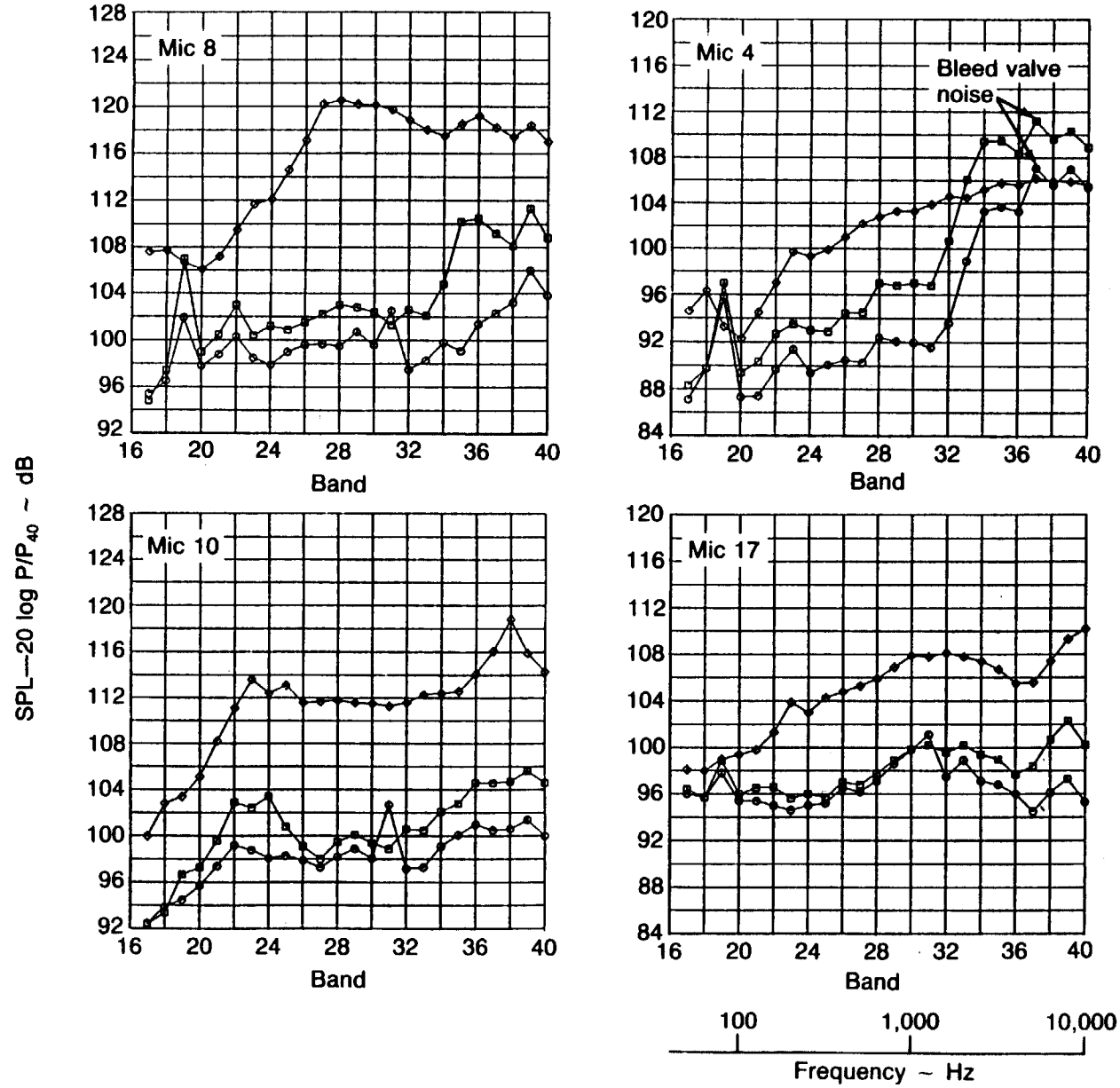


Figure 4-2. Lower Wing Probe Microphones 1/3 Octave Spectra— $M_{AP} \approx 0.62-0.64$

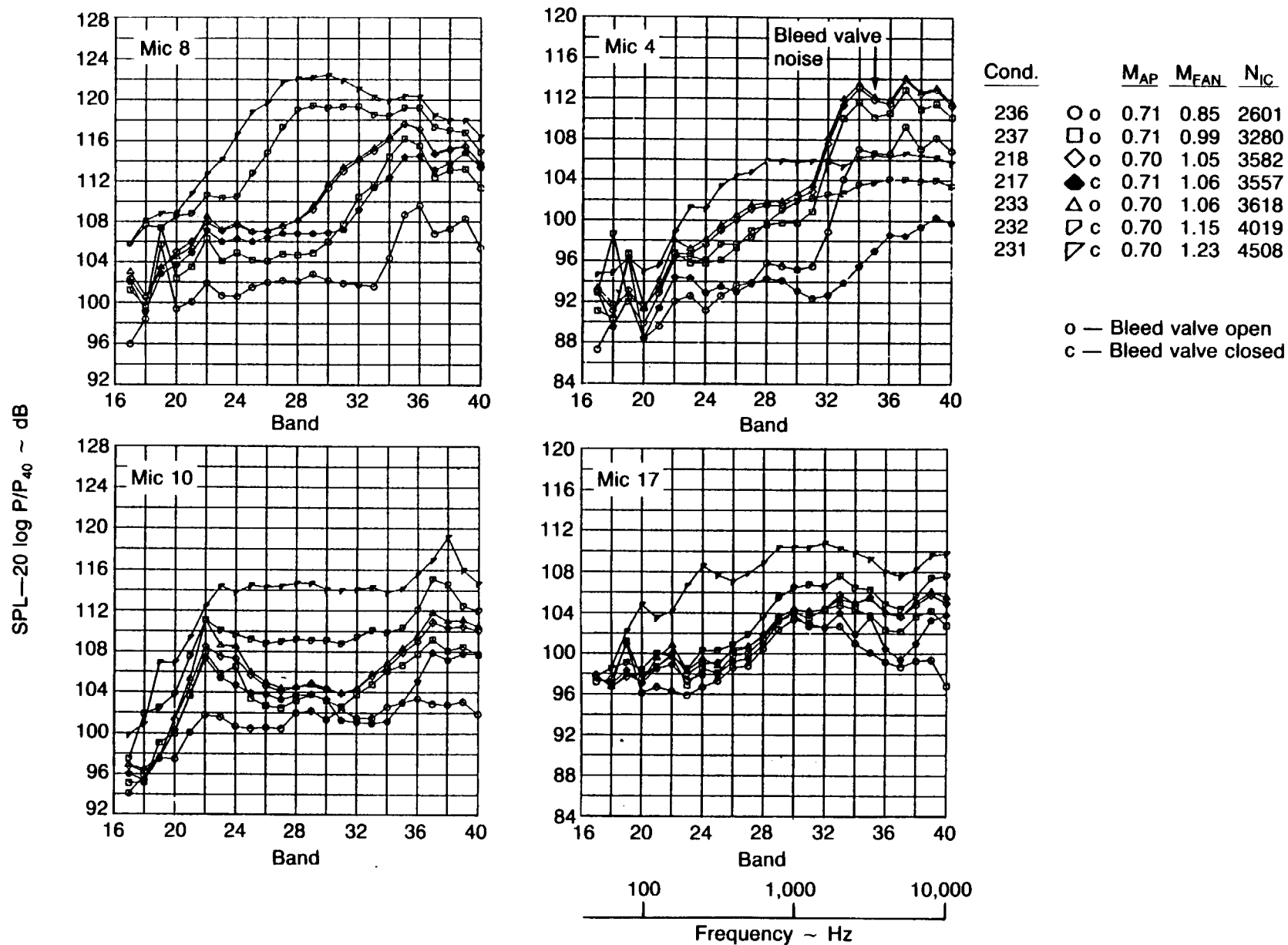


Figure 4-3. Lower Wing Probe Microphones 1/3 Octave Spectra— $M_{AP} \approx 0.70, 0.71$

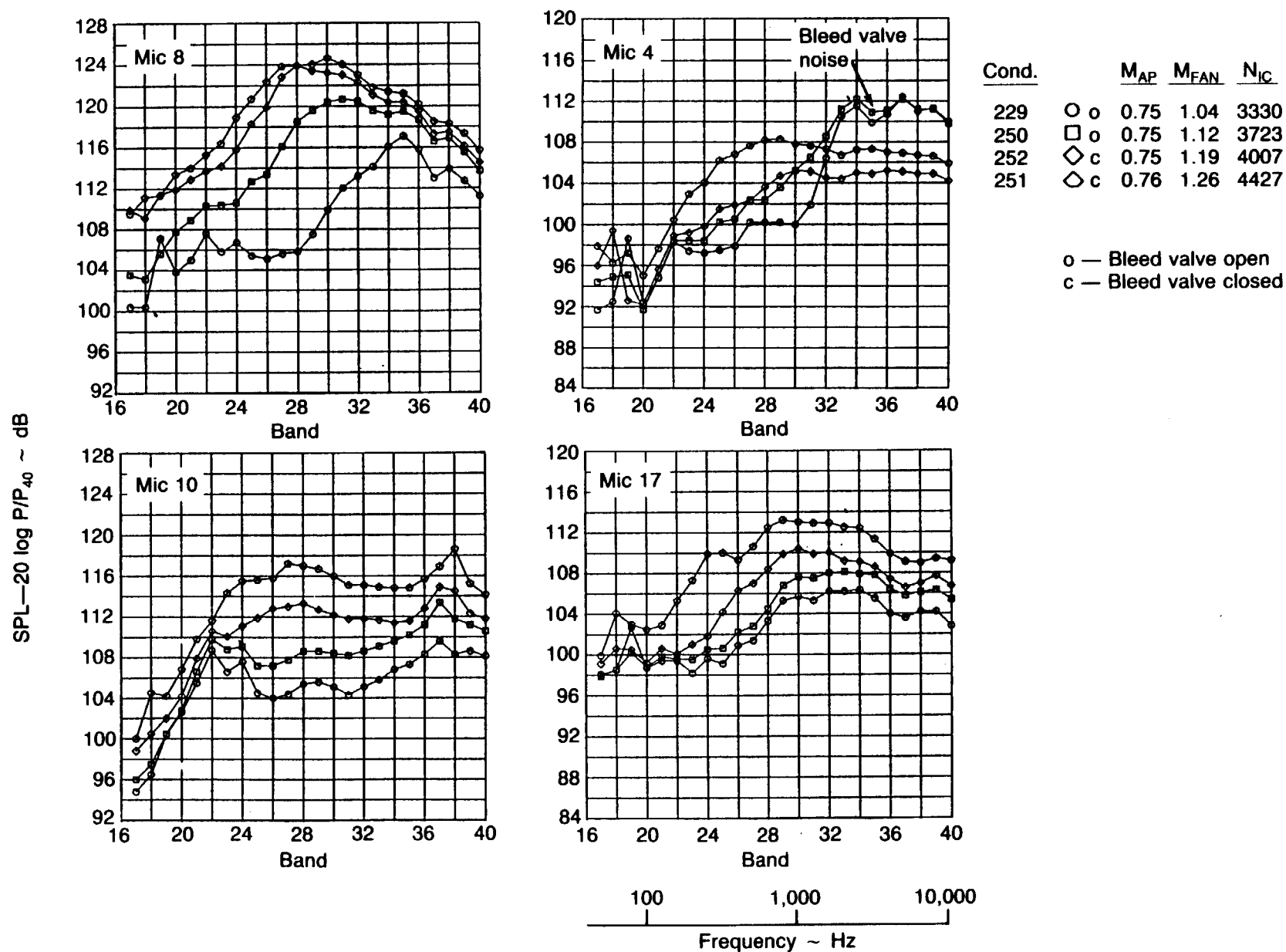


Figure 4-4. Lower Wing Probe Microphones 1/3 Octave Spectra— $M_{AP} \approx 0.75, 0.76$

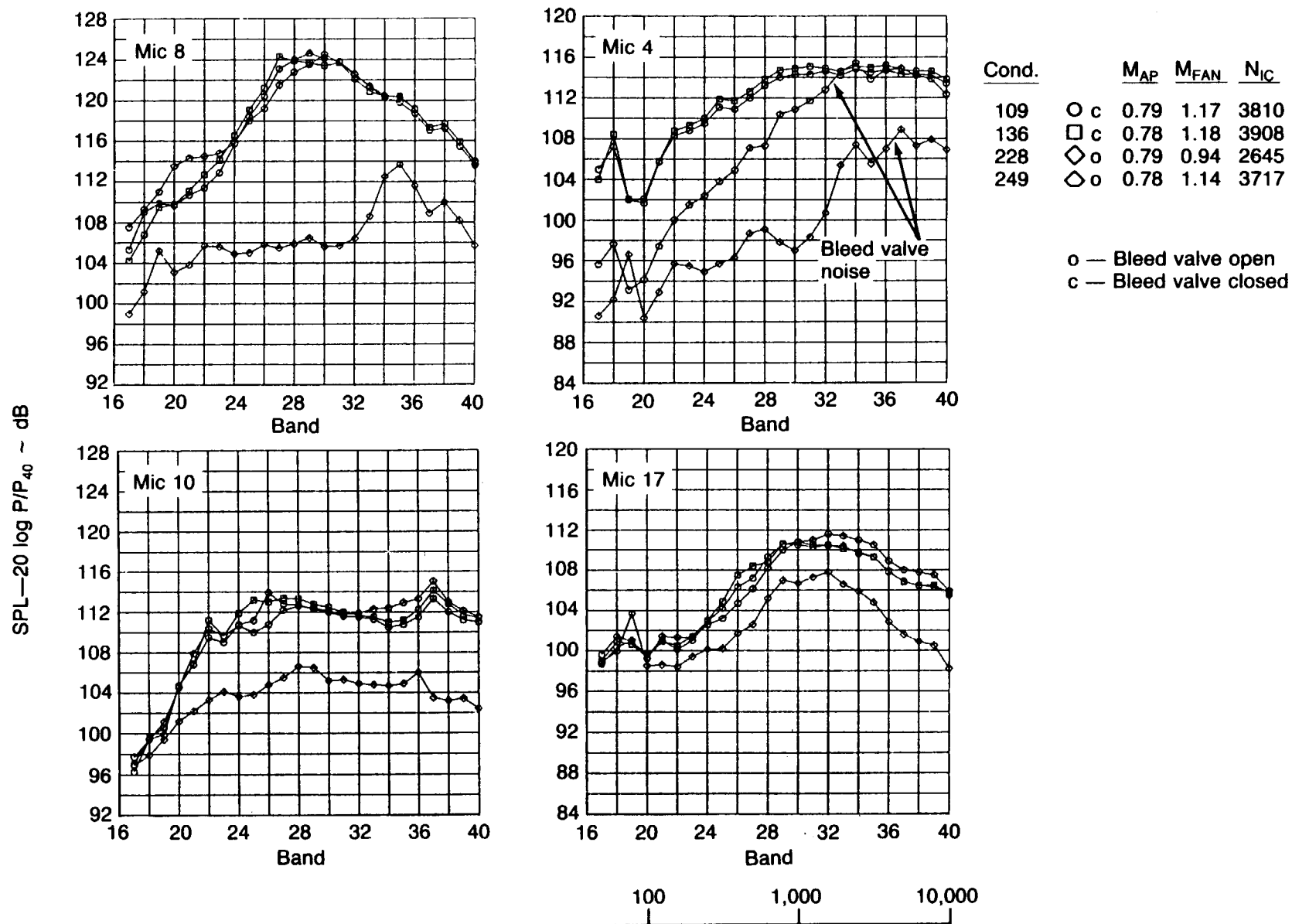


Figure 4-5. Lower Wing Probe Microphones 1/3 Octave Spectra— $M_{AP} \approx 0.78, 0.79$

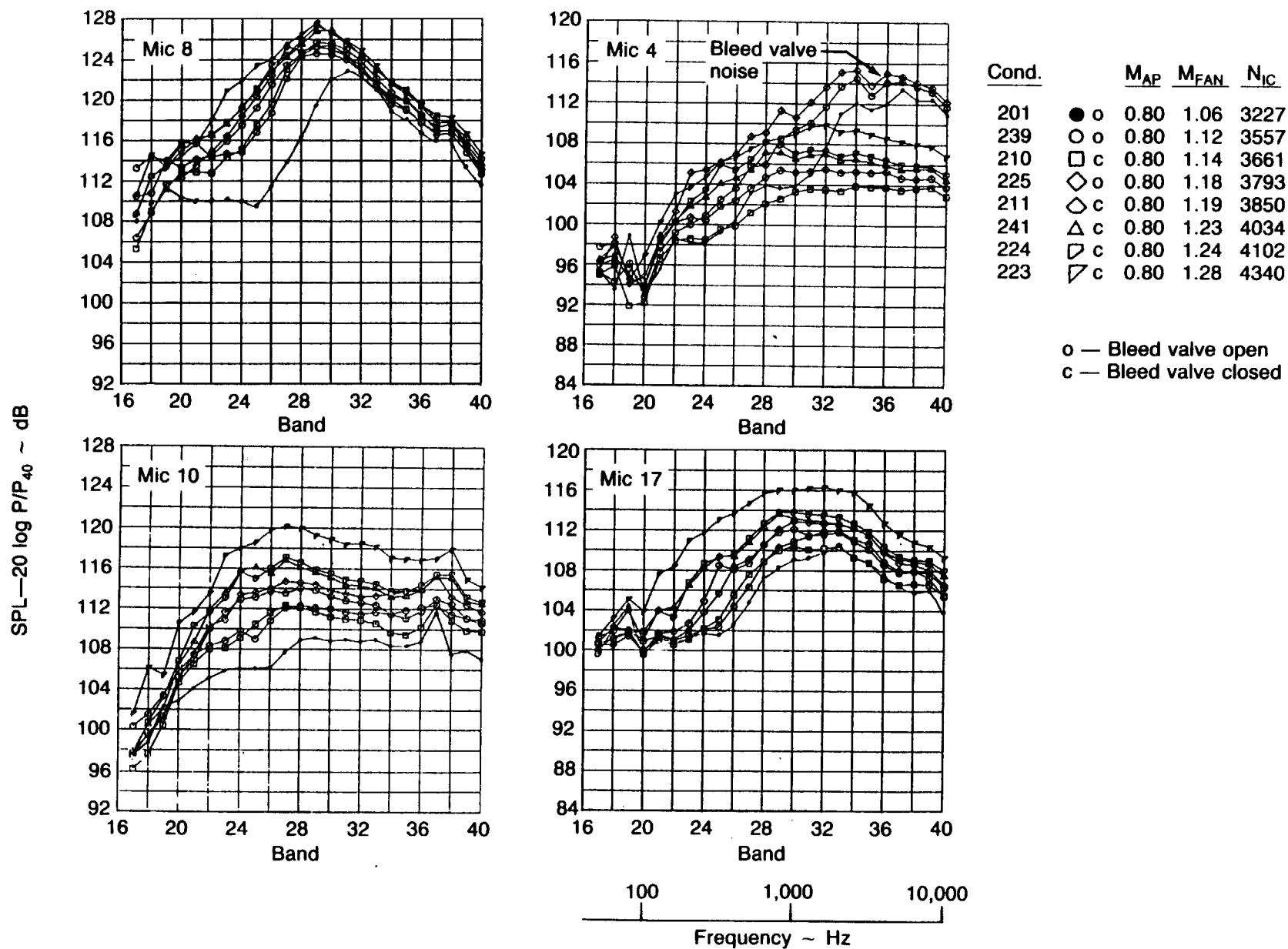


Figure 4-6. Lower Wing Probe Microphones $\frac{1}{3}$ Octave Spectra— $M_{AP} \approx 0.80$

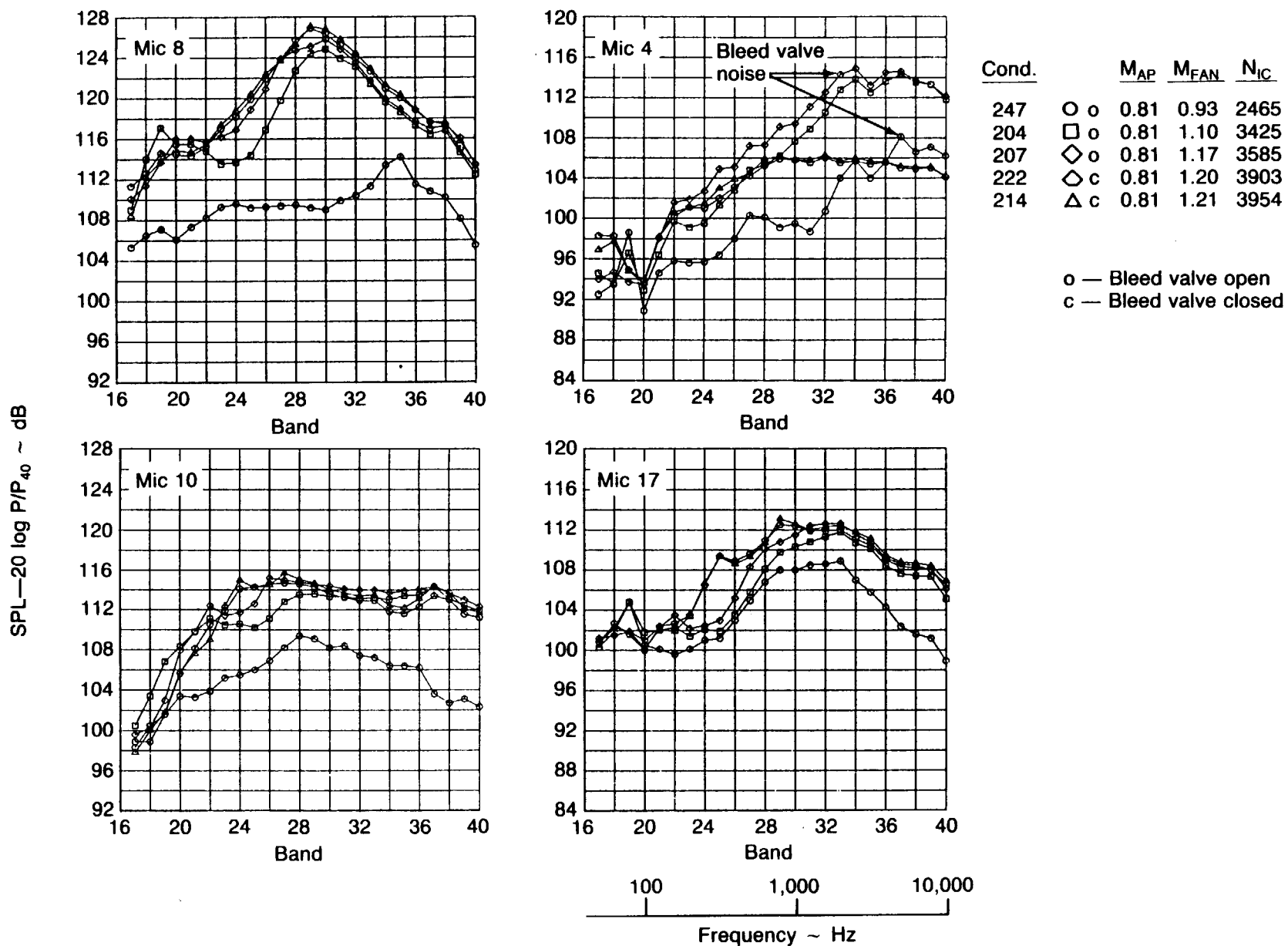


Figure 4-7. Lower Wing Probe Microphones $1/3$ Octave Spectra— $M_{AP} \approx 0.81$

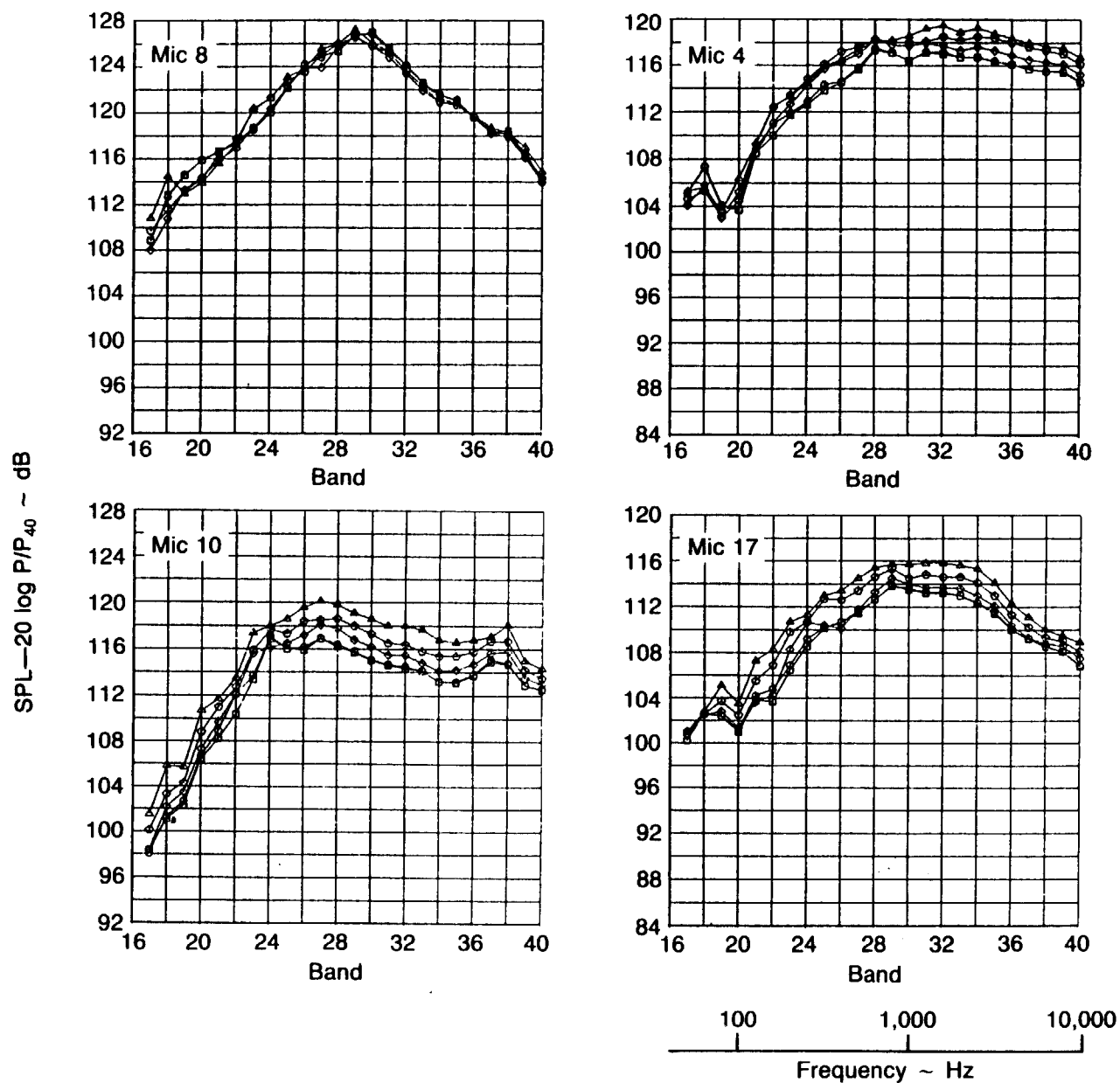


Figure 4-8. Lower Wing Probe Microphones $1/3$ Octave Spectra— $M_{AP} = 0.81$

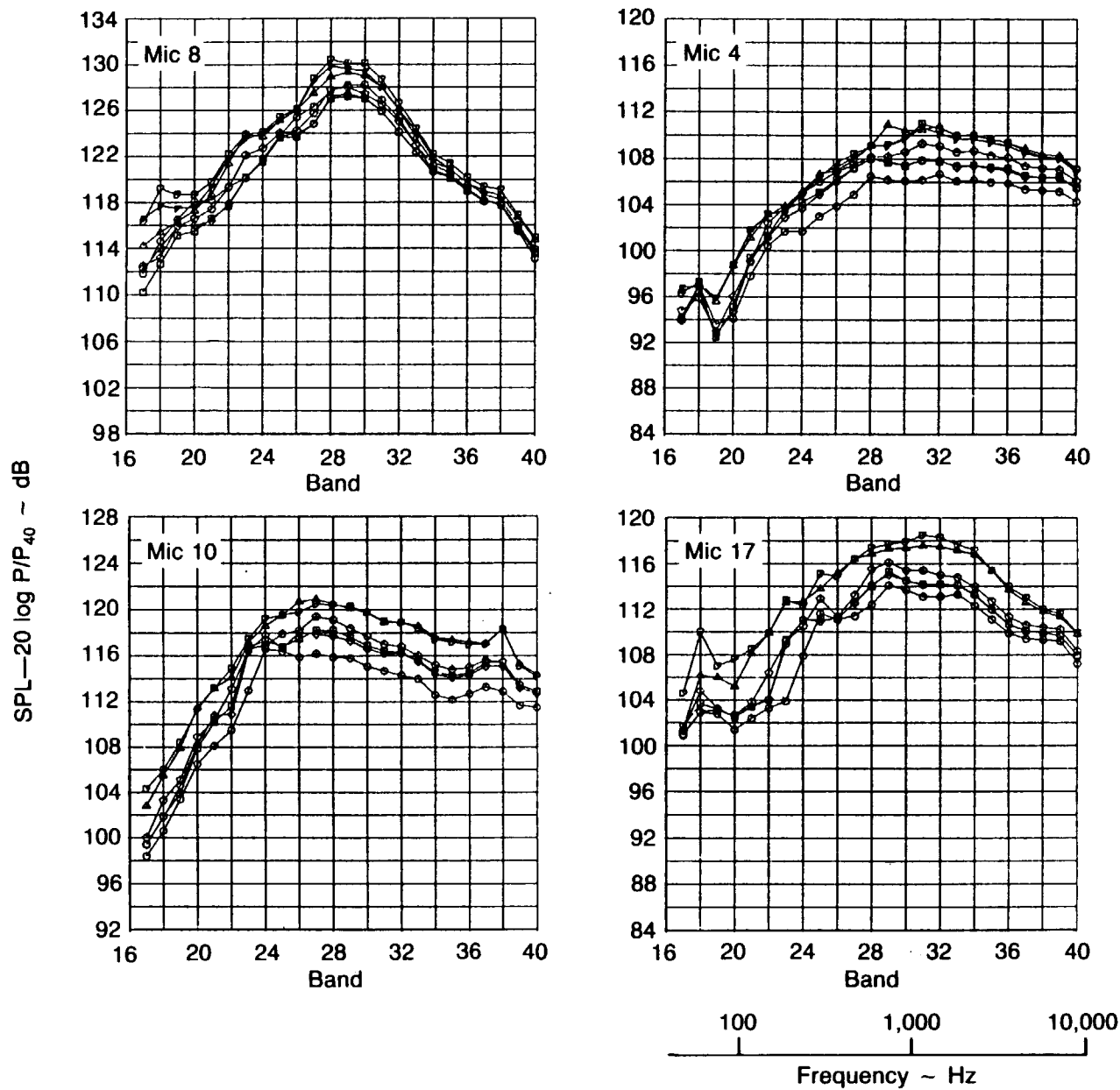


Figure 4-9. Lower Wing Probe Microphones 1/3 Octave Spectra— $M_{AP} \approx 0.82, 0.83$

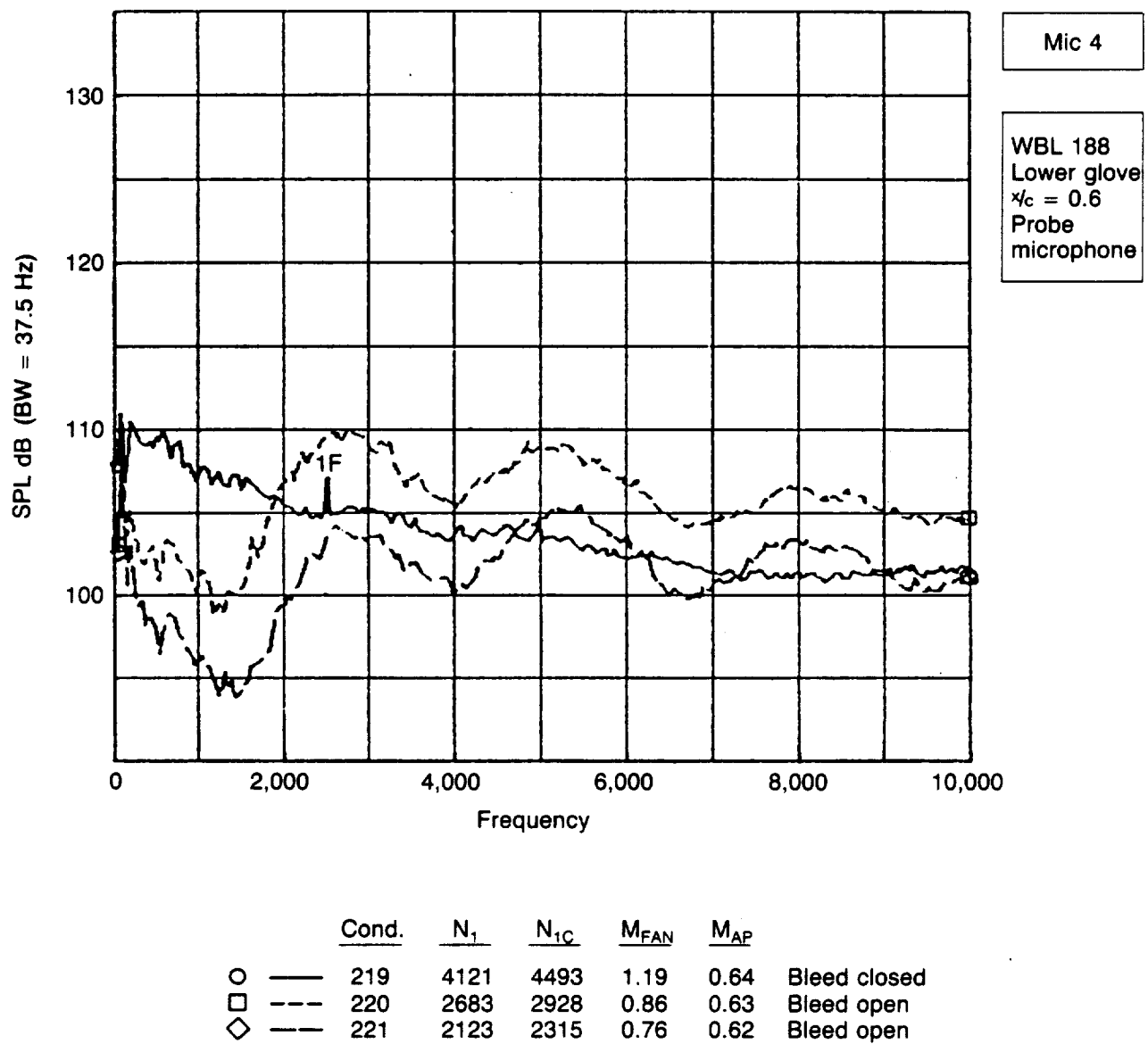


Figure 4-10. Microphone 4 Narrow Band Spectra— $M_{AP} \approx 0.62-0.64$

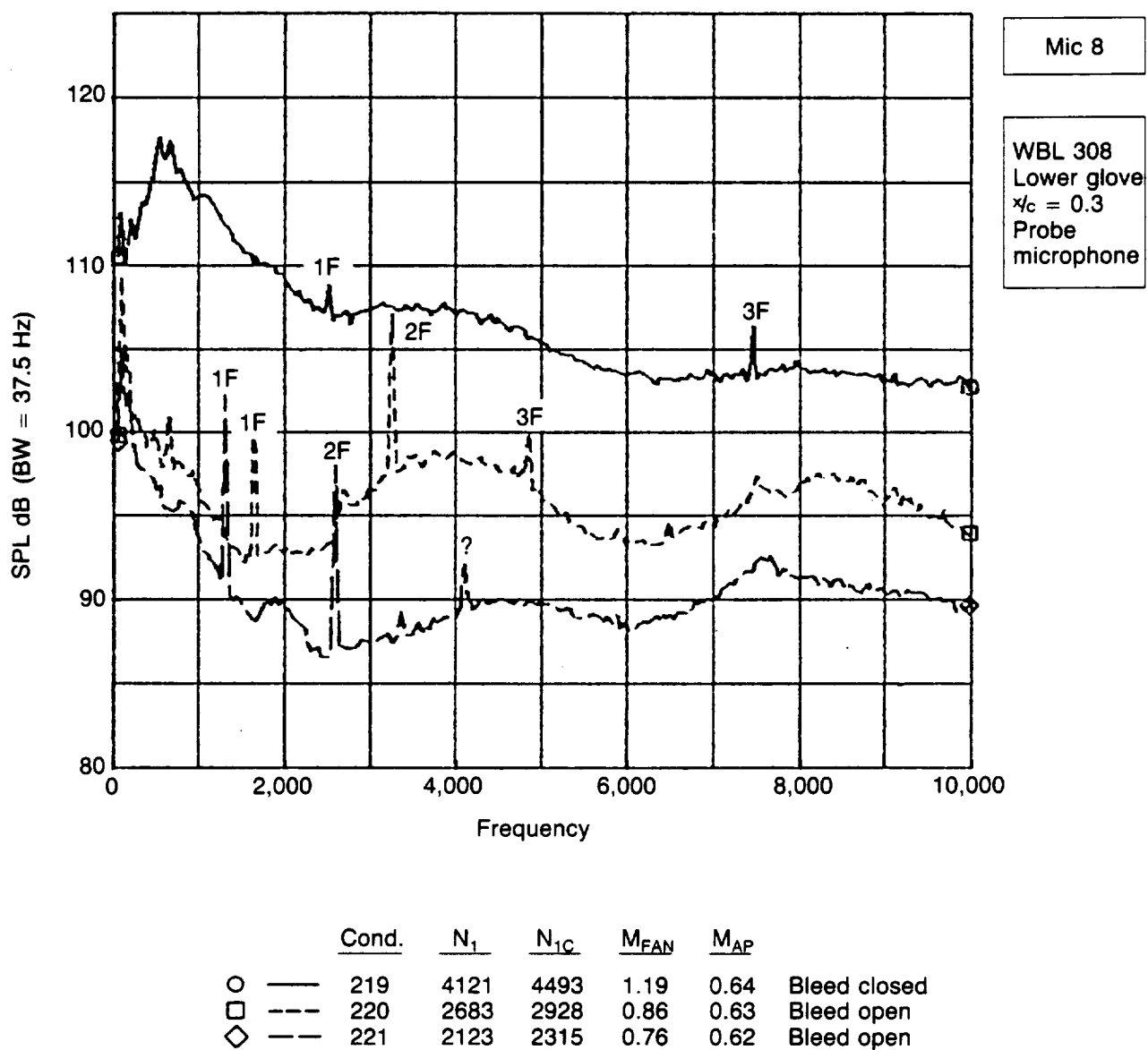
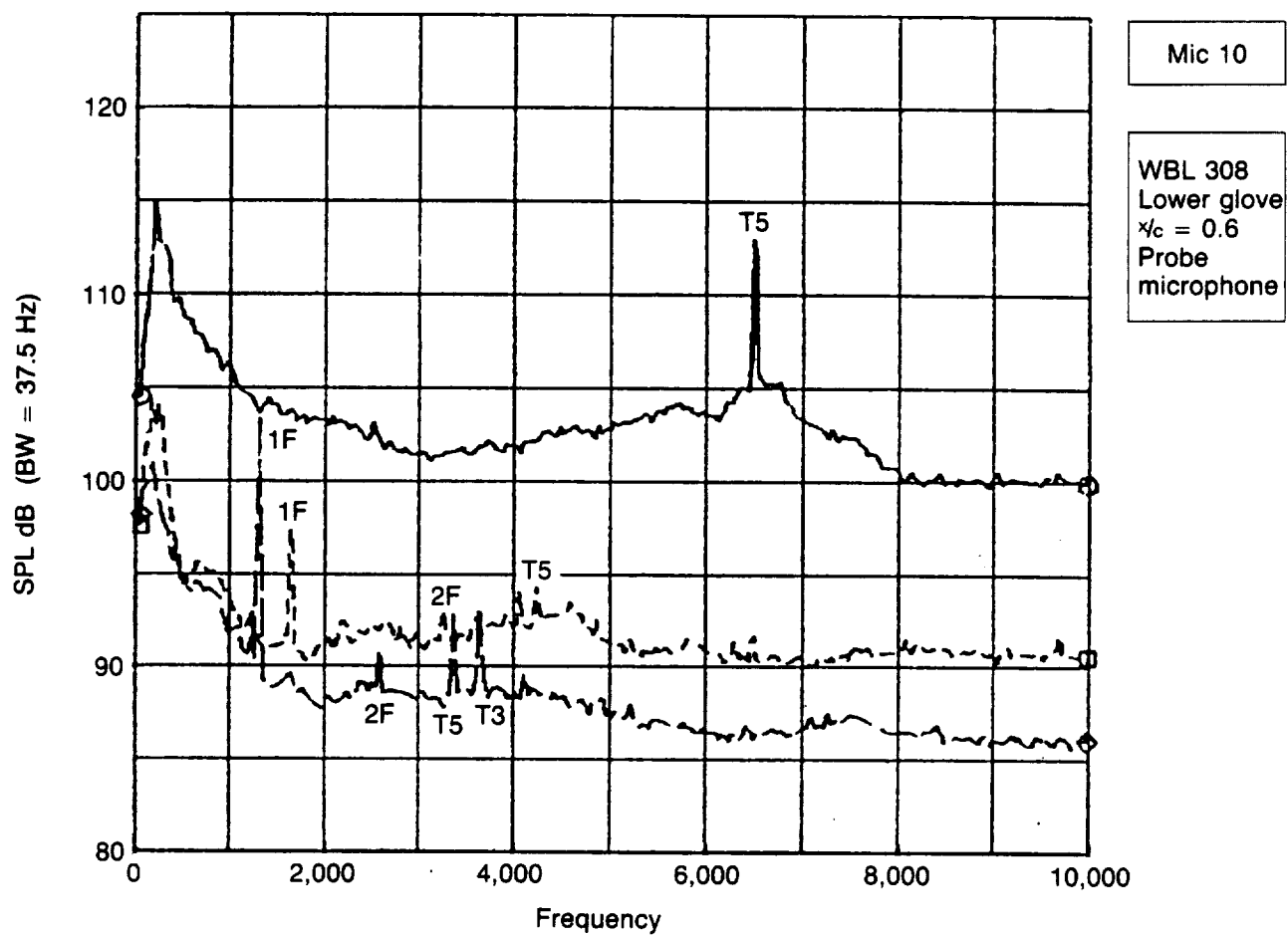


Figure 4-11. Microphone 8 Narrow Band Spectra— $M_{AP} \approx 0.62-0.64$



		Cond.	N_1	N_{1C}	M_{FAN}	M_{AP}	
○	—	219	4121	4493	1.19	0.64	Bleed closed
□	---	220	2683	2928	0.86	0.63	Bleed open
◇	---	221	2123	2315	0.76	0.62	Bleed open

Figure 4-12. Microphone 10 Narrow Band Spectra— $M_{AP} \approx 0.62-0.64$

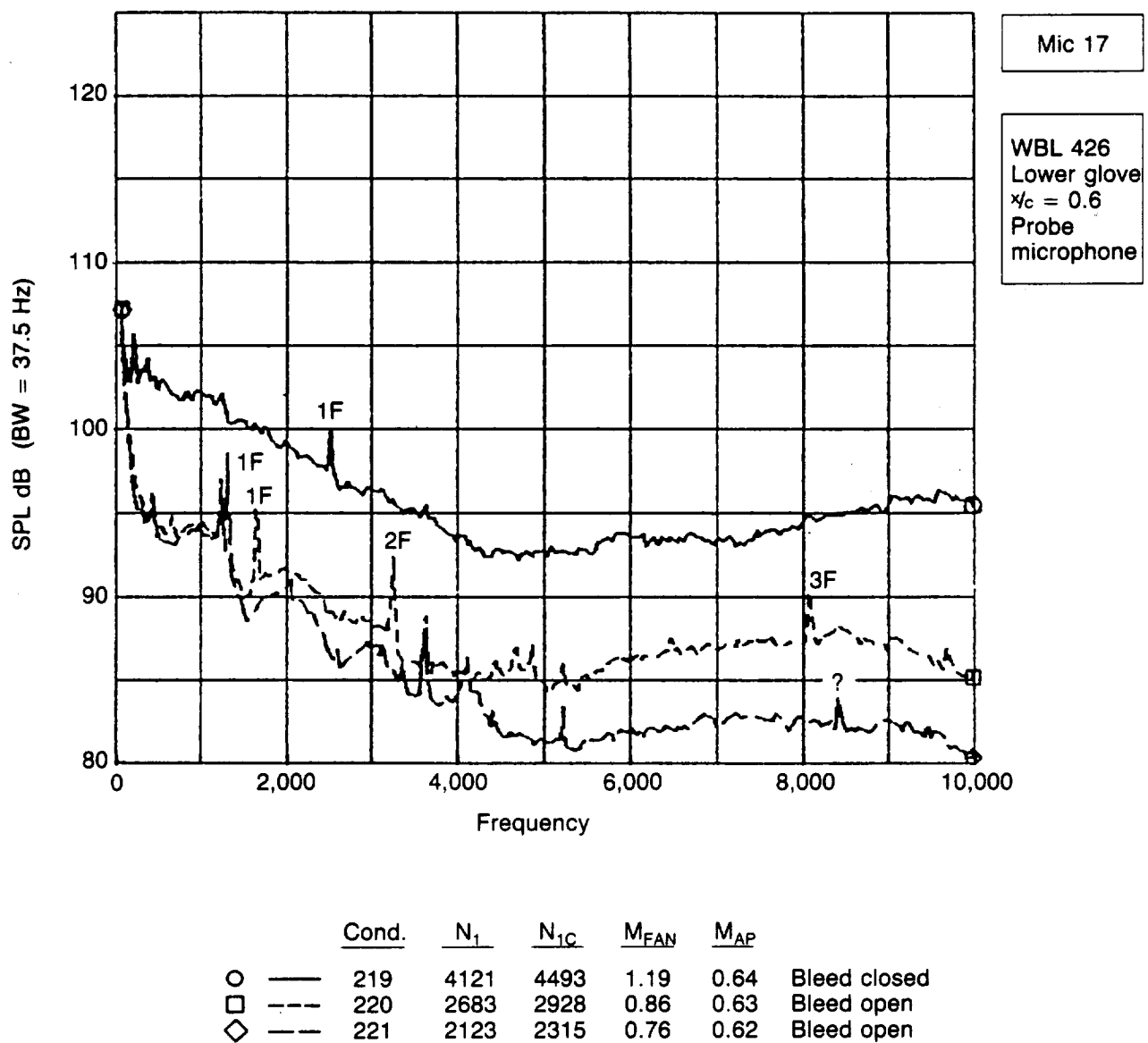


Figure 4-13. Microphone 17 Narrow Band Spectra— $M_{AP} = 0.62-0.64$

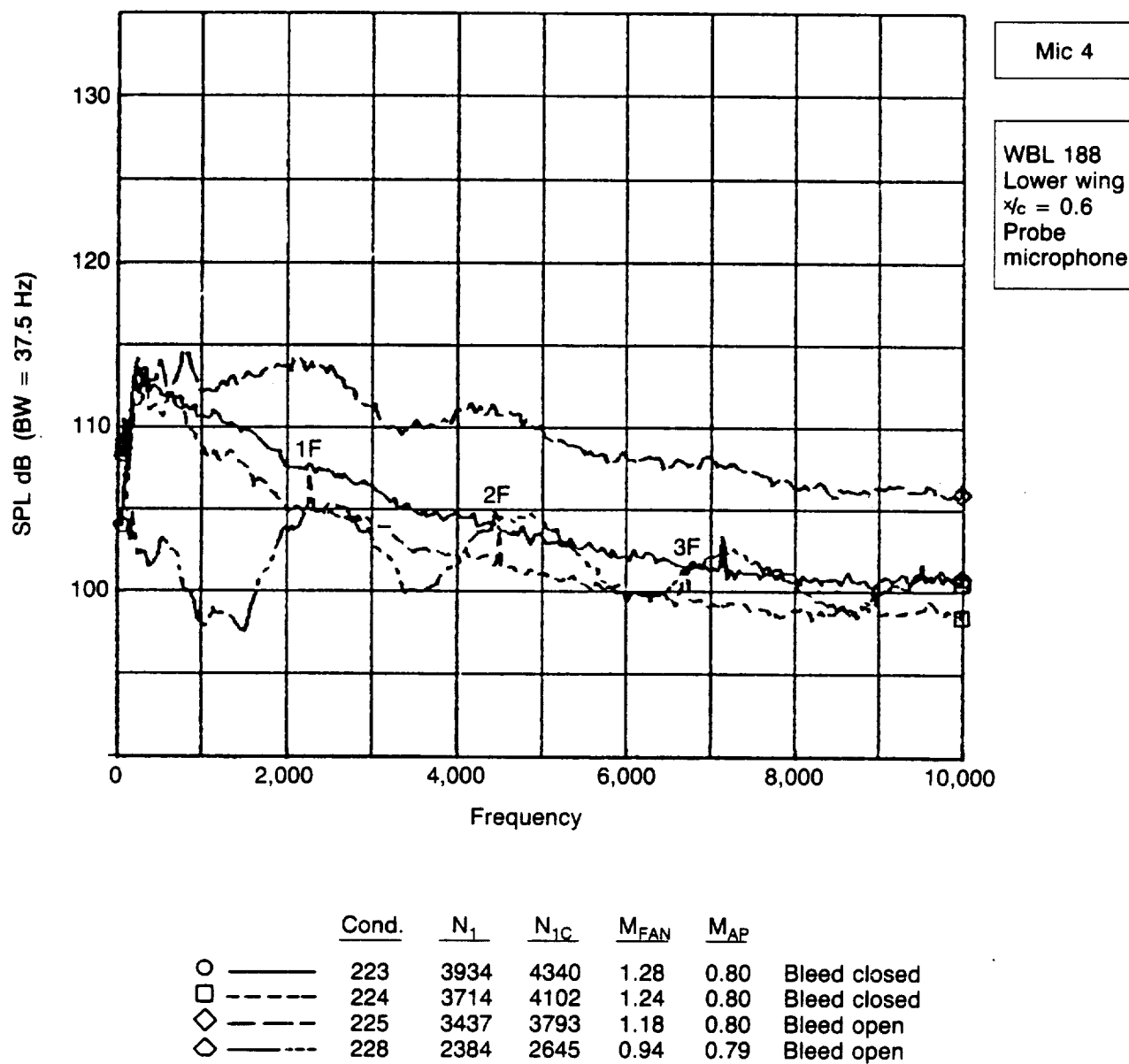


Figure 4-14. Microphone 4 Narrow Band Spectra— $M_{AP} \approx 0.79-0.80$

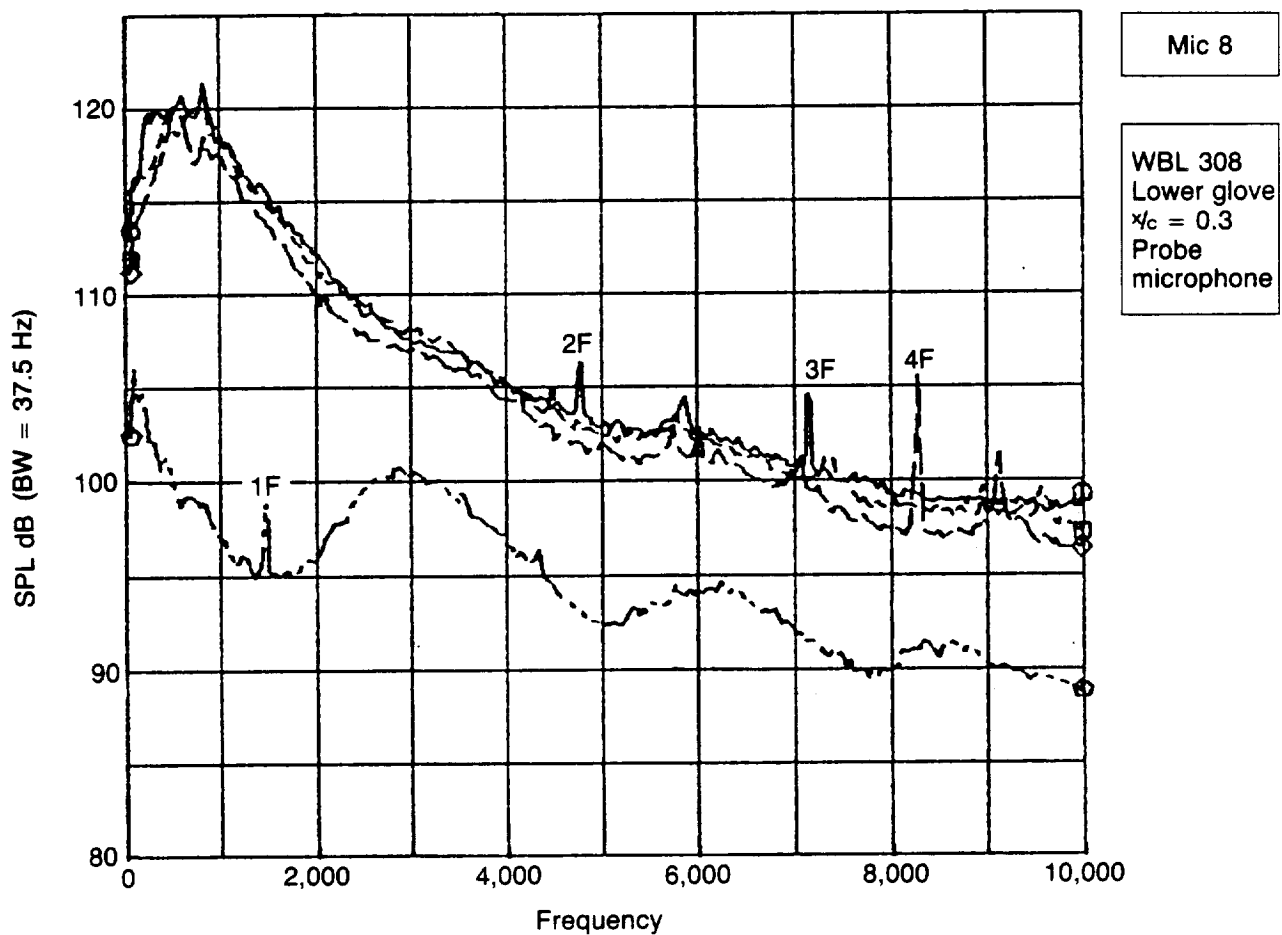


Figure 4-15. Microphone 8 Narrow Band Spectra— $M_{AP} = 0.79-0.80$

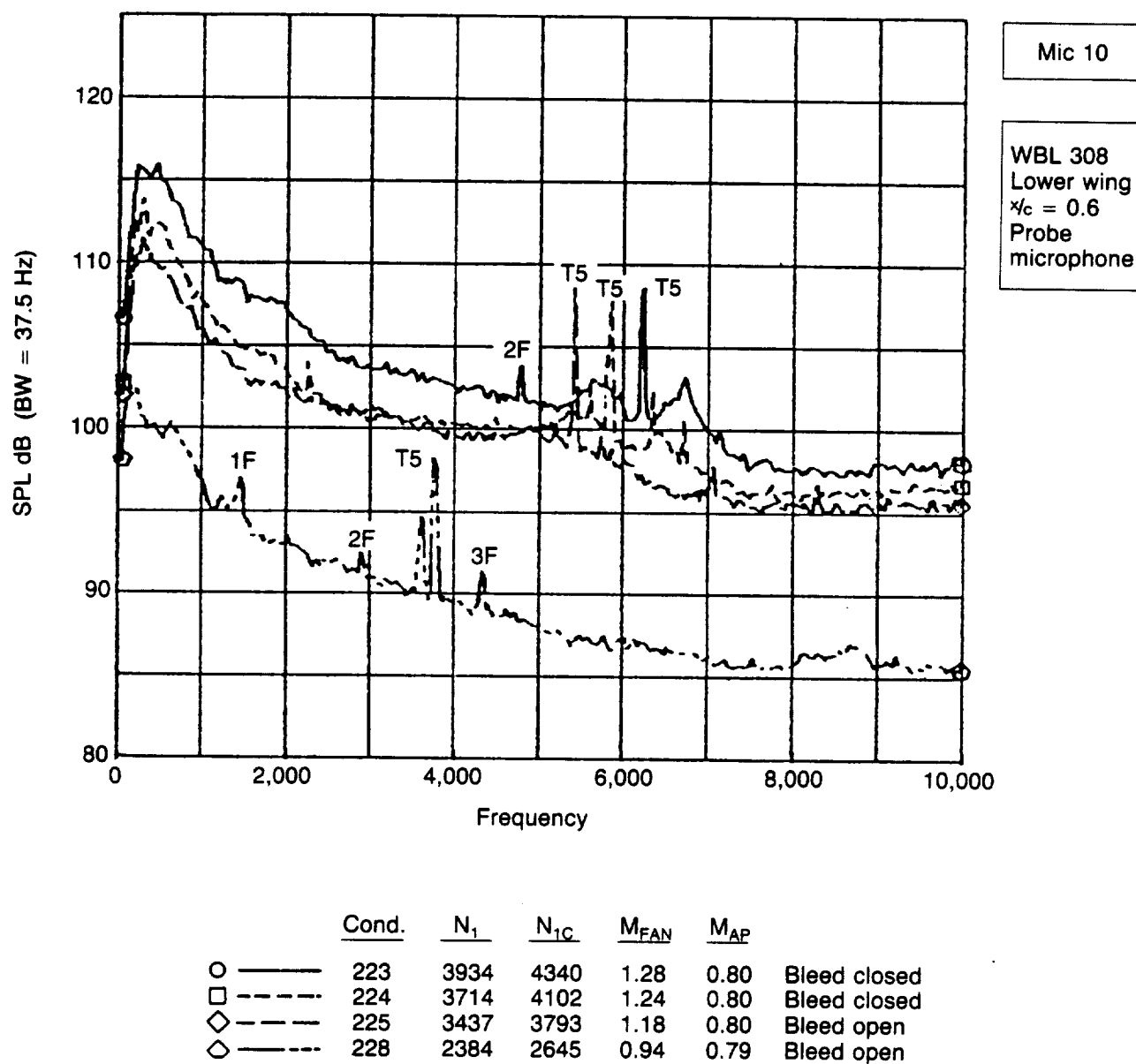


Figure 4-16. Microphone 10 Narrow Band Spectra— $M_{AP} \approx 0.79-0.80$

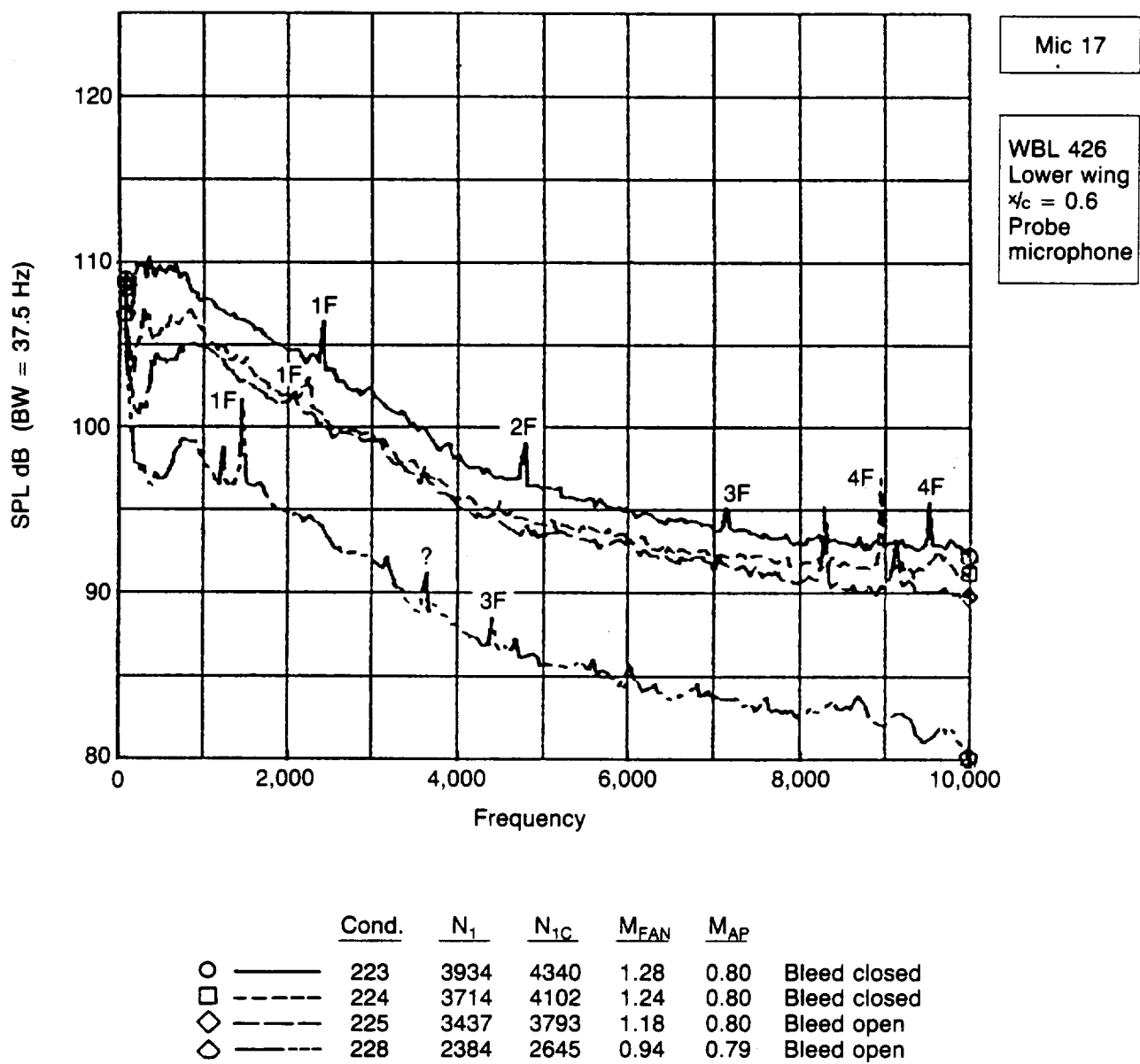


Figure 4-17. Microphone 17 Narrow Band Spectra— $M_{AP} \approx 0.79-0.80$

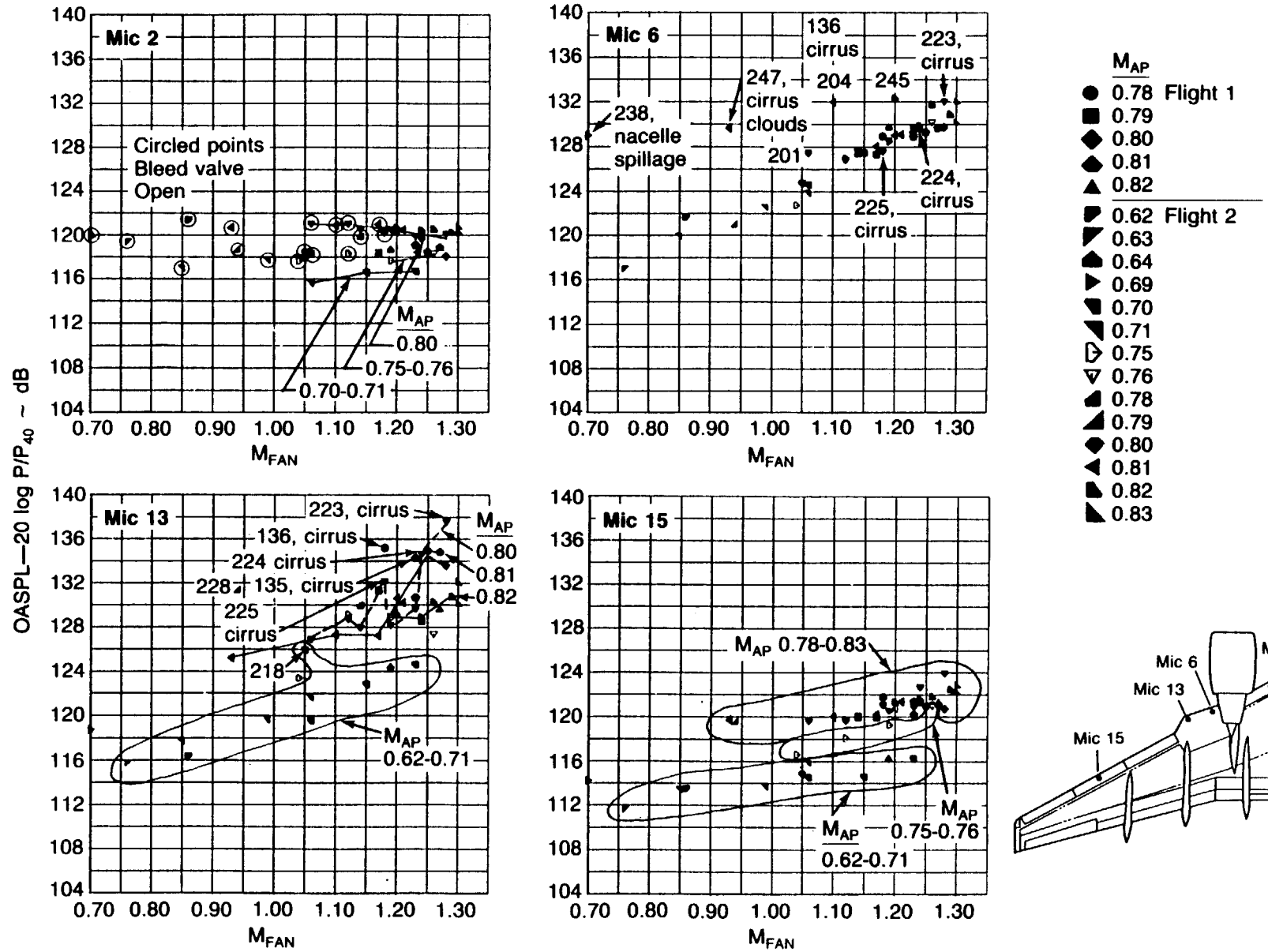


Figure 4-18. Normalized OASPL on Wing Lower Surface Leading Edge Surface Mounted Microphones

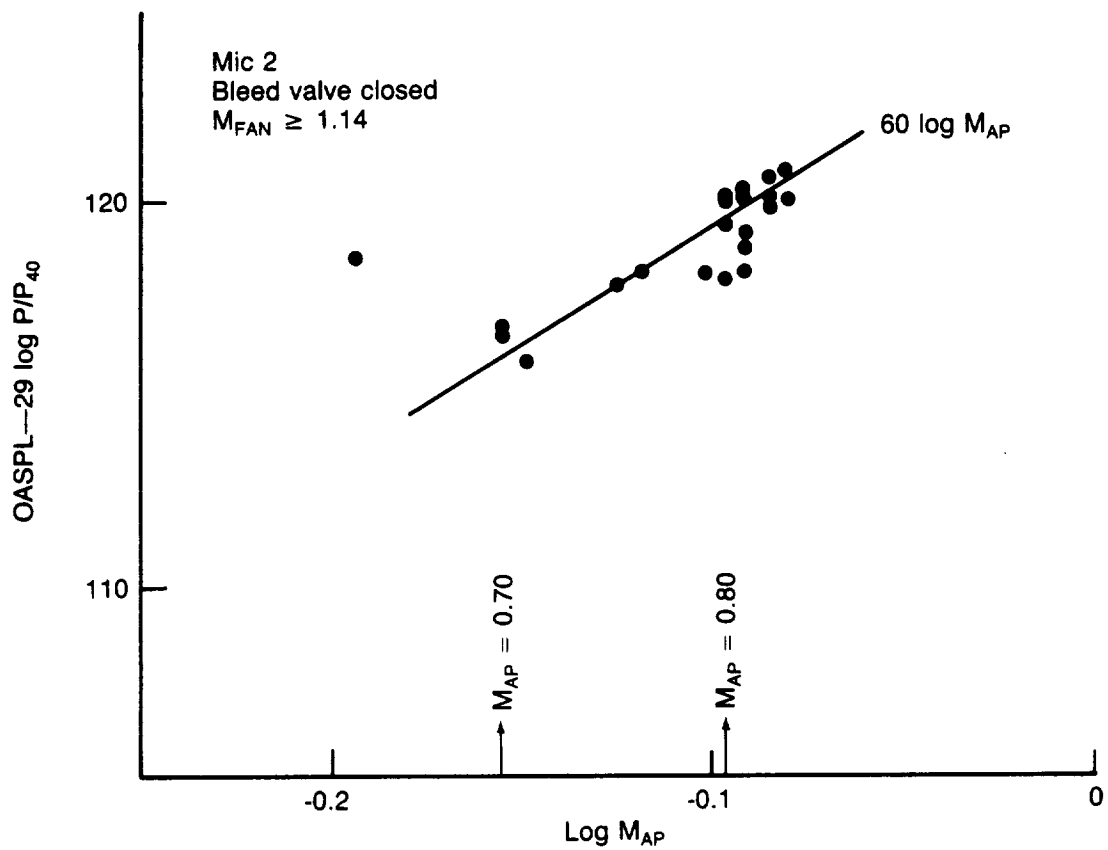


Figure 4-19. Airplane Mach Number Dependence of Microphone 2 OASPL Data With Engine With Bleed Valve Closed

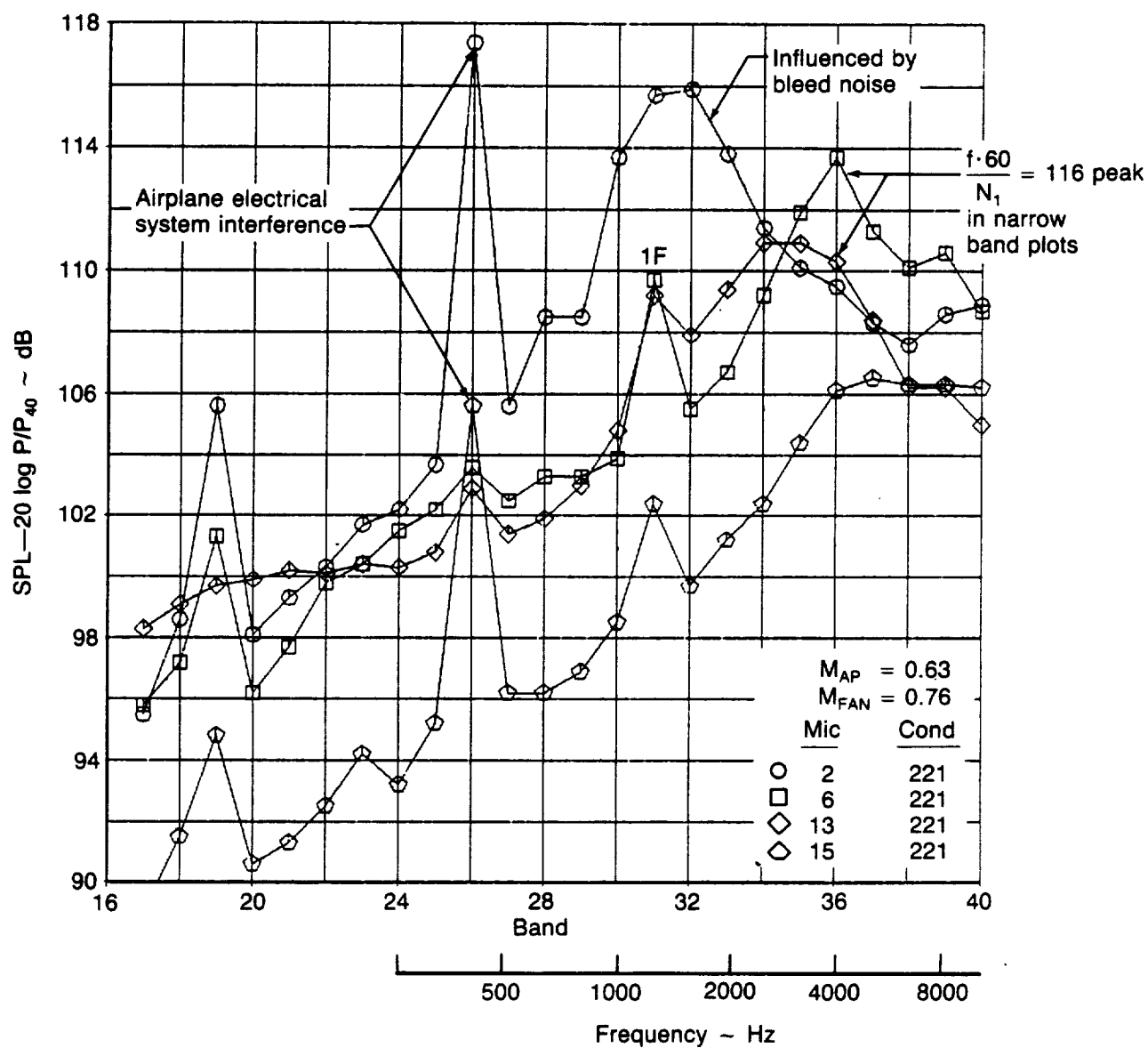


Figure 4-20. Low Airplane Speed, Low Engine Power $1/3$ Octave Spectra—Lower Wing Leading Edge Microphones

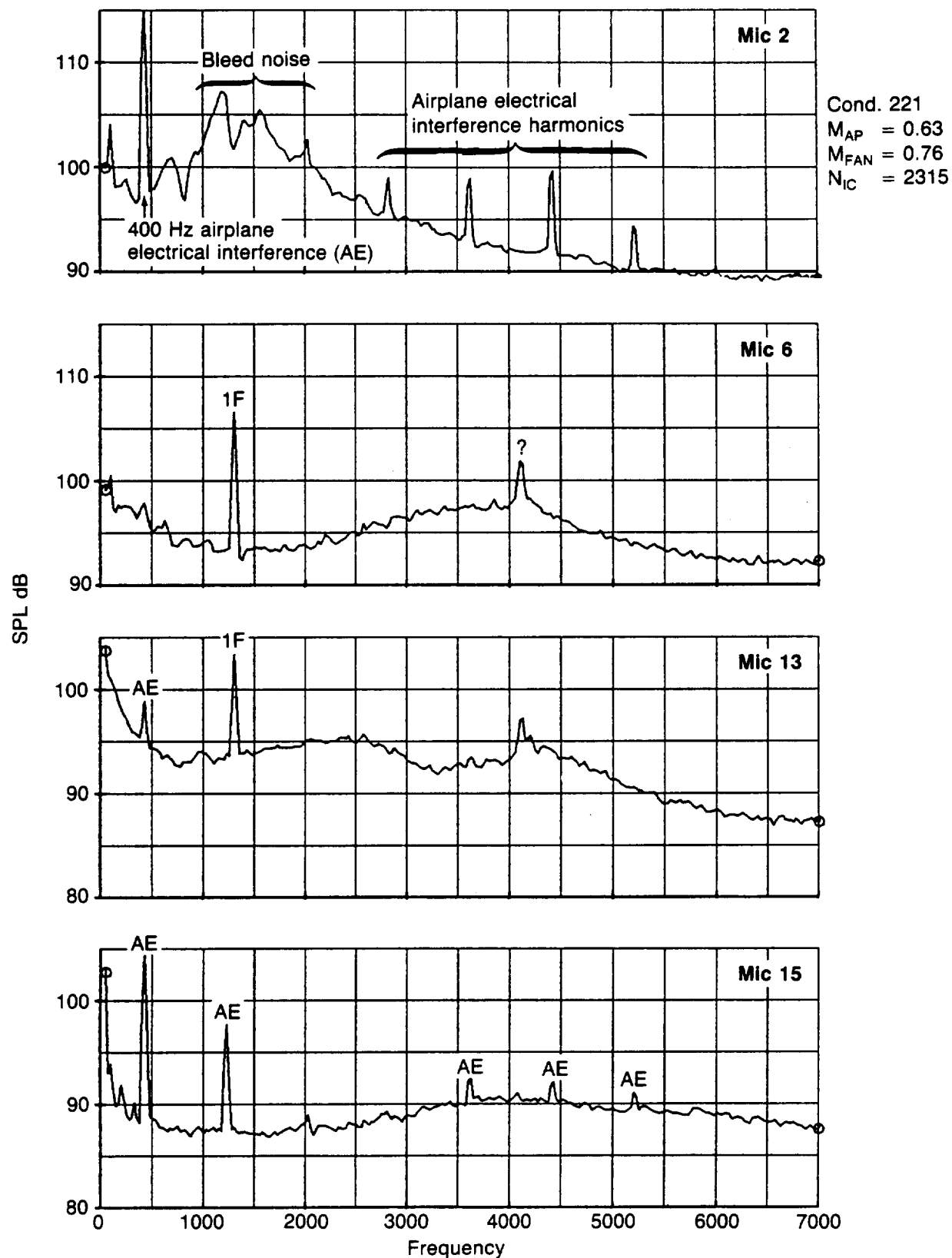


Figure 4-21. Narrow Band Spectra, Lower Wing Leading Edge Microphones—Low Engine Power, Low Airplane Speed

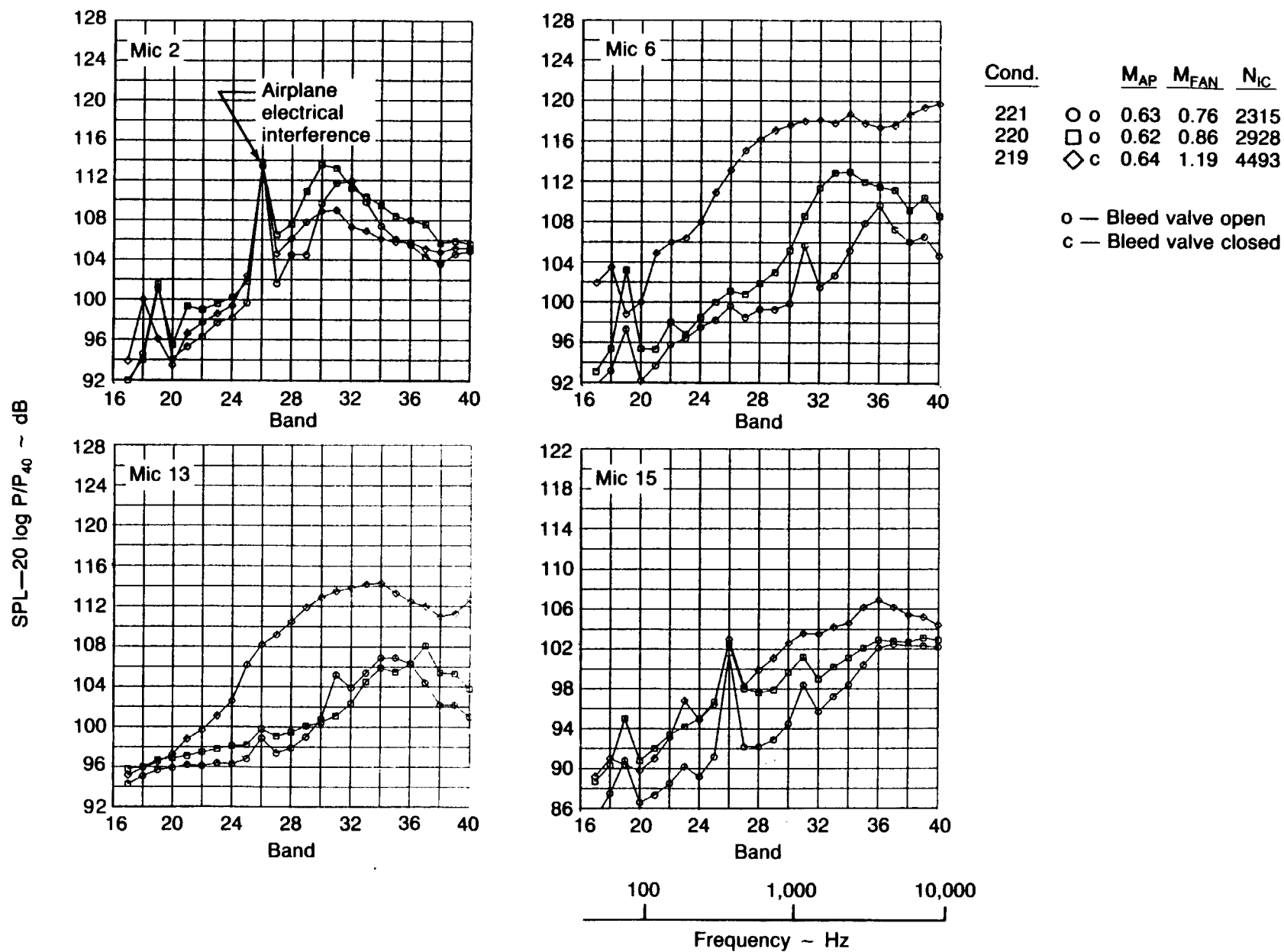


Figure 4-22. Lower Wing Leading Edge Microphones $1/3$ Octave Spectra— $M_{AP} \approx 0.62-0.64$

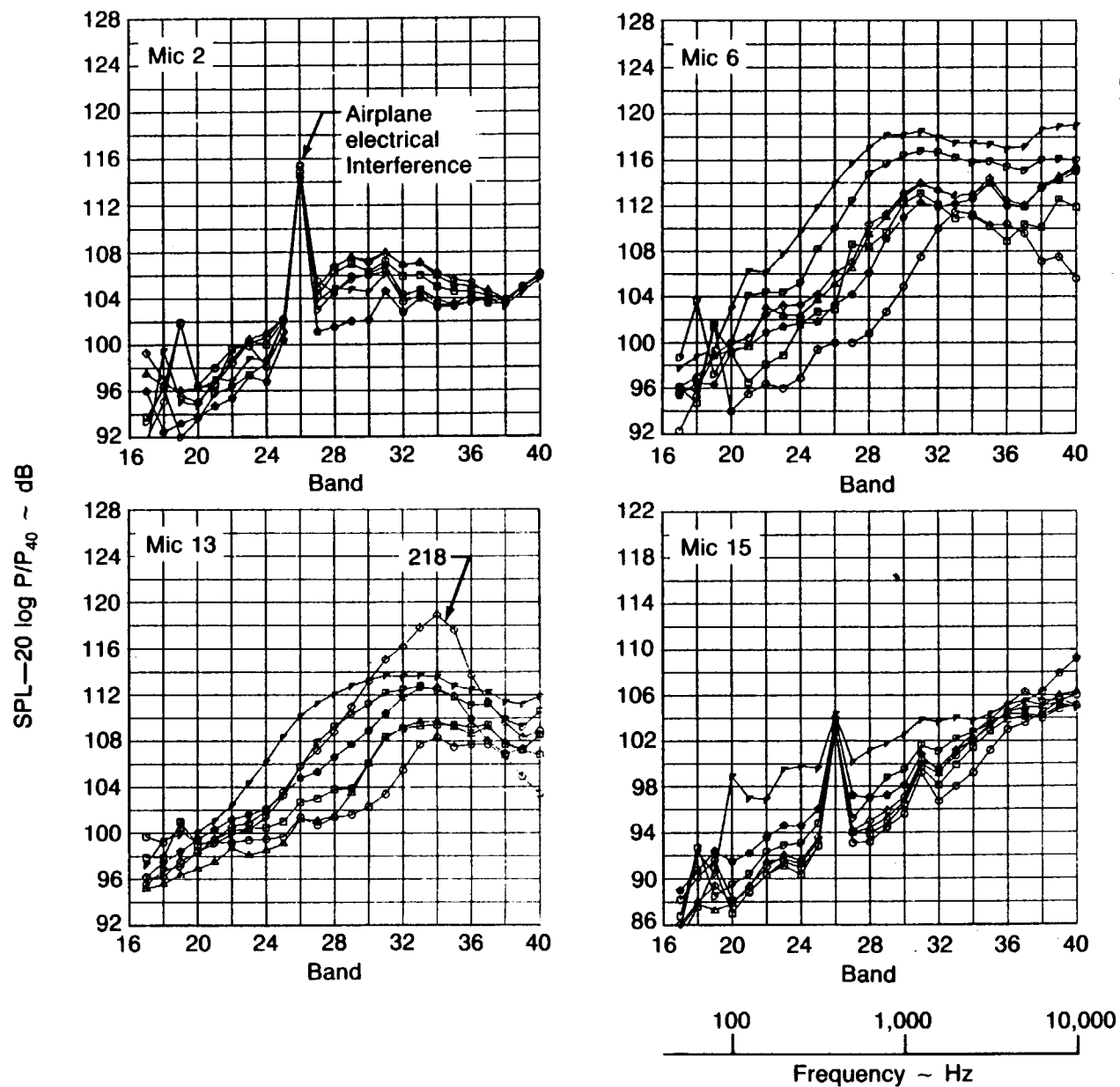


Figure 4-23. Lower Wing Leading Edge Microphones 1/3 Octave Spectra—M_{AP} ≈ 0.70-0.71

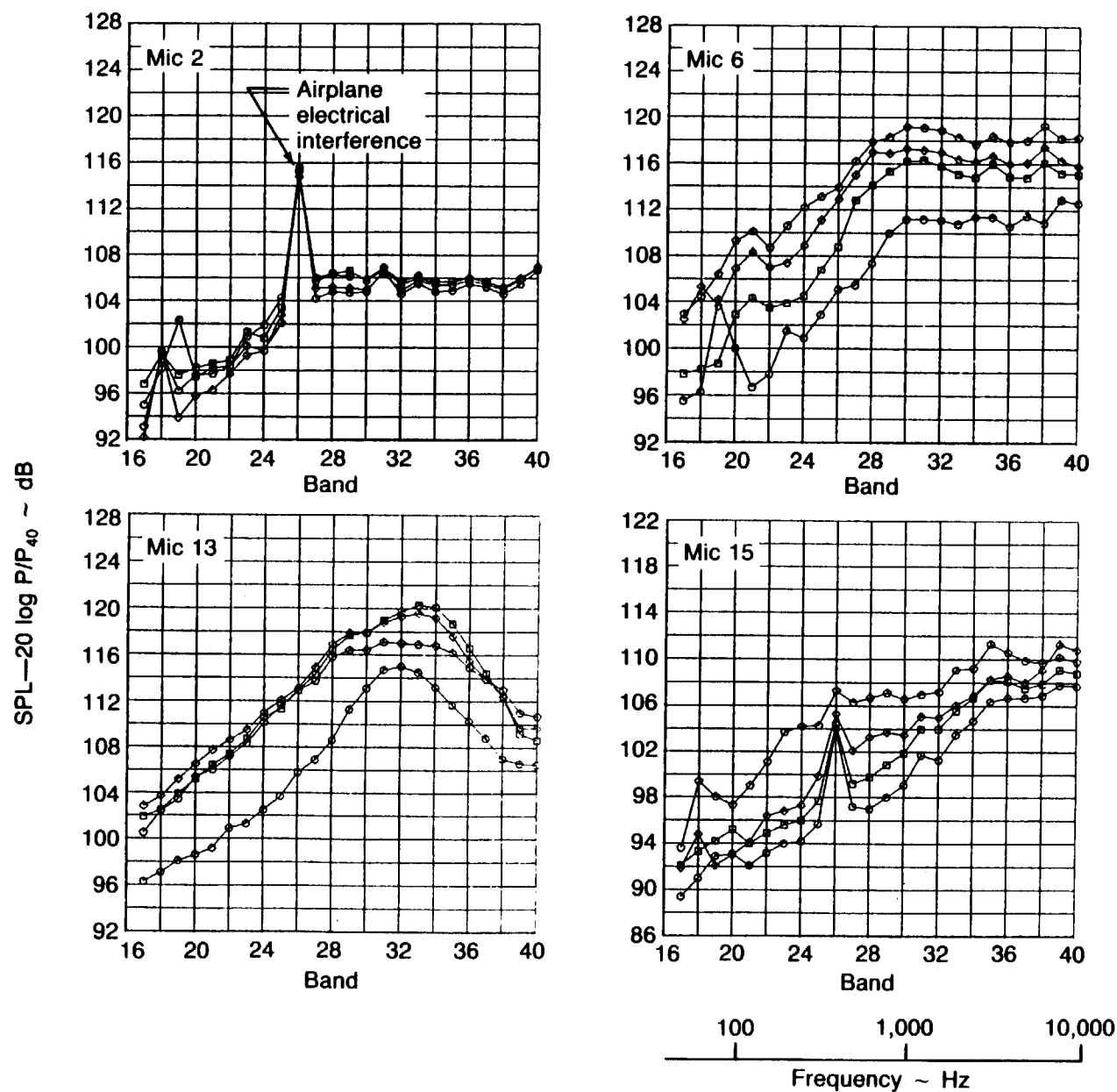


Figure 4-24. Lower Wing Leading Edge Microphones $\frac{1}{3}$ Octave Spectra— $M_{AP} \approx 0.75-0.76$

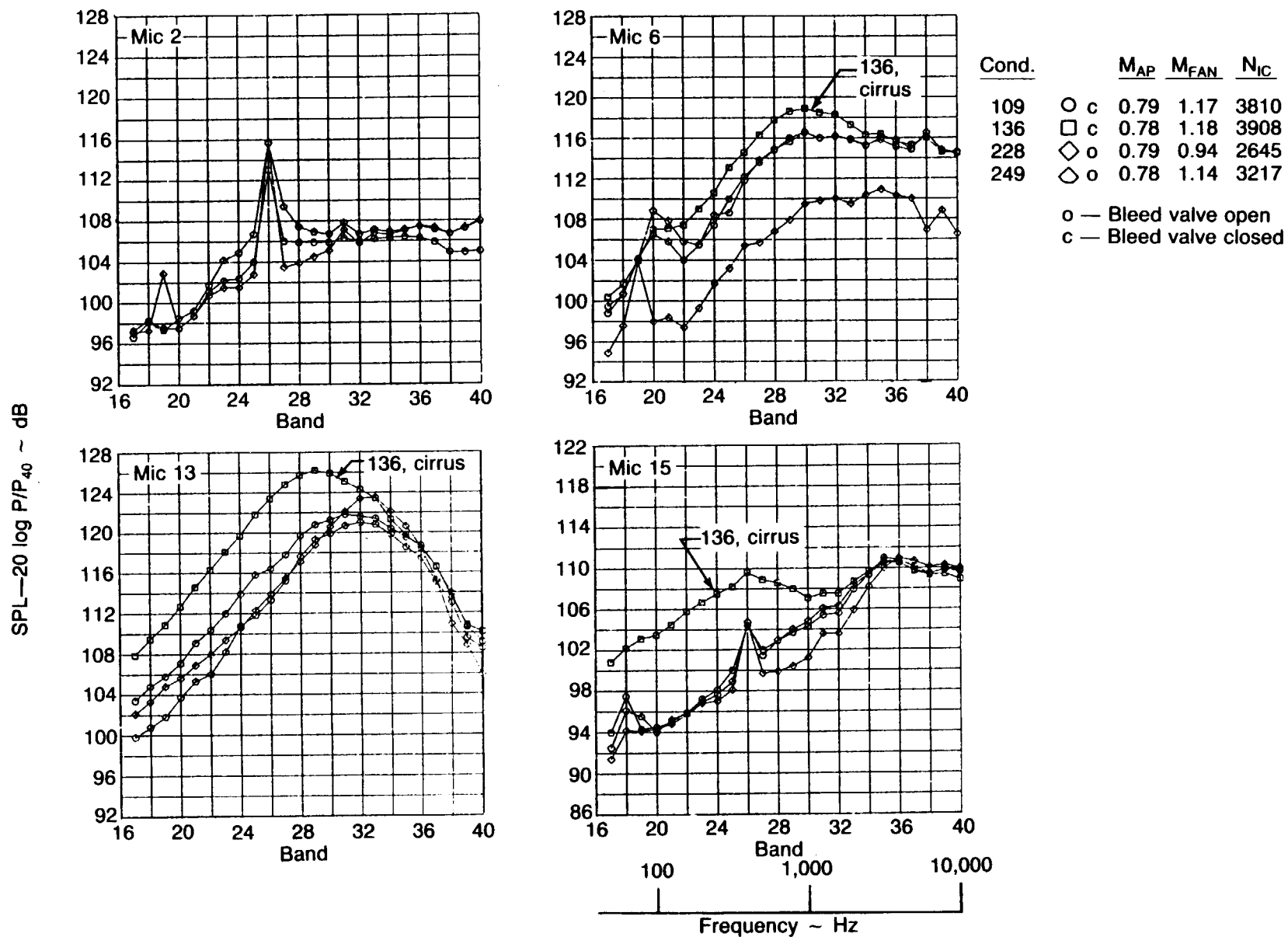


Figure 4-25. Lower Wing Leading Edge Microphones $1/3$ Octave Spectra— $M_{AP} = 0.78-0.79$

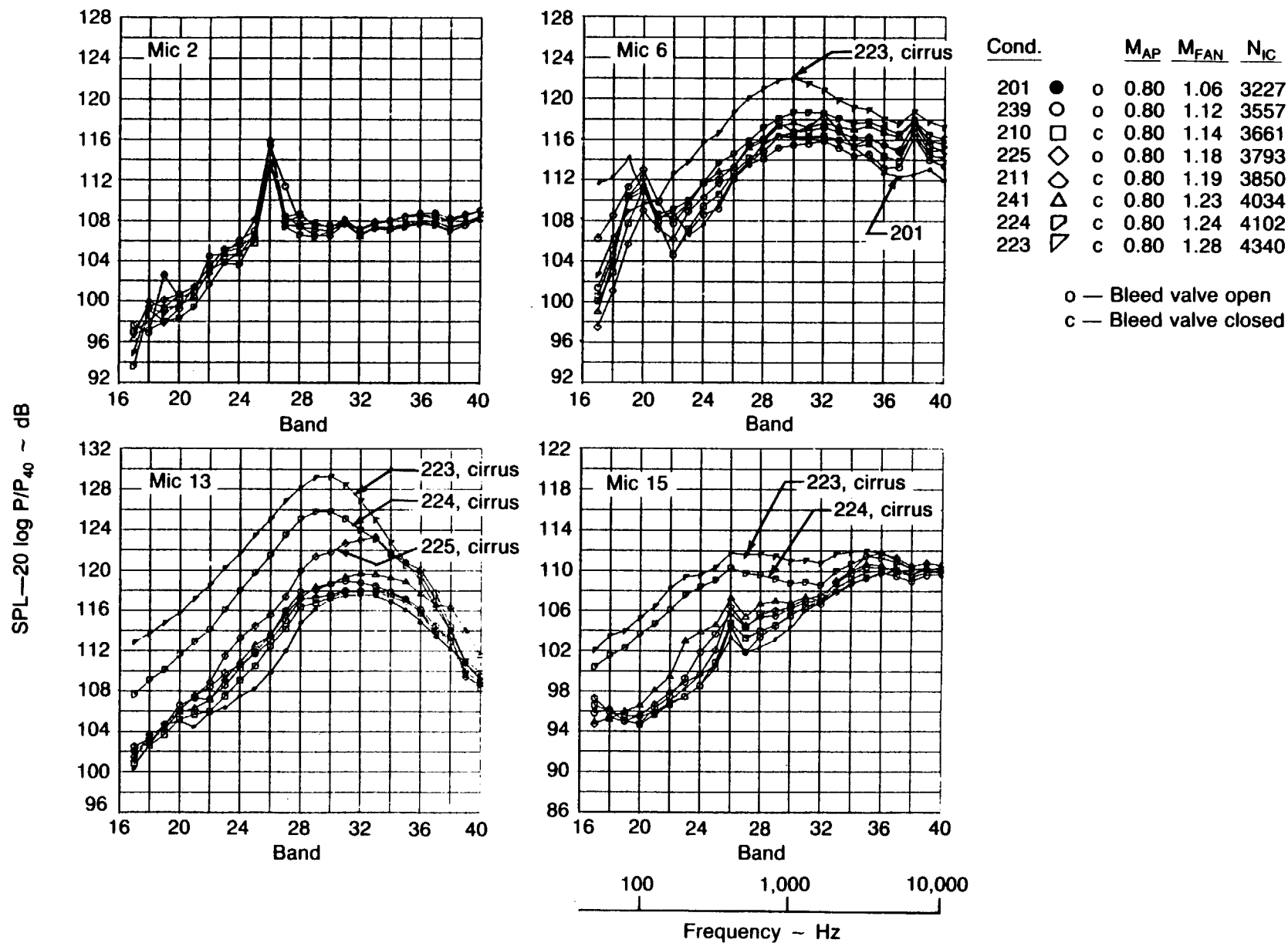
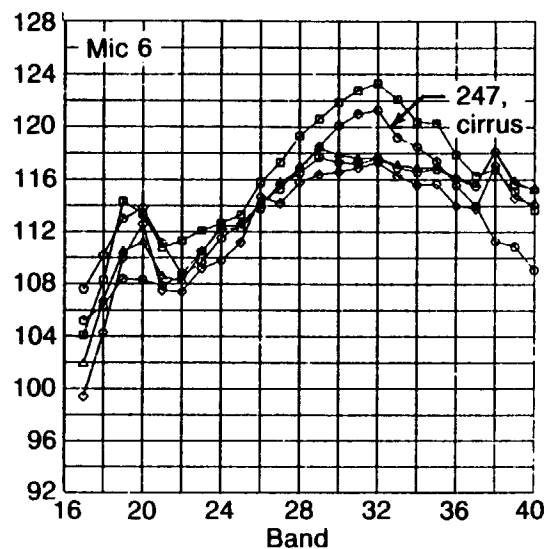
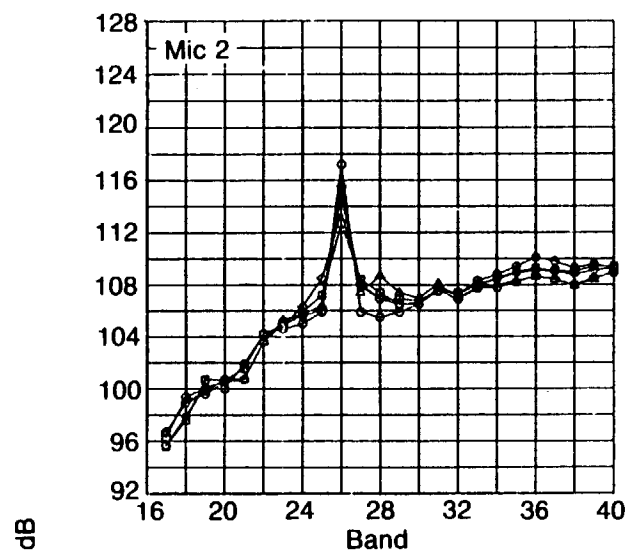


Figure 4-26. Lower Wing Leading Edge Microphones 1/3 Octave Spectra— $M_{AP} \approx 0.80$



Cond.		M_{AP}	M_{FAN}	N_{IC}
247	○ c	0.81	0.93	2465
204	□ c	0.81	1.10	3425
207	◇ c	0.81	1.17	3585
222	◊ c	0.81	1.20	3903
214	△ c	0.81	1.21	3954

c — Bleed valve closed

SPL—20 log P/P₄₀ ~ dB

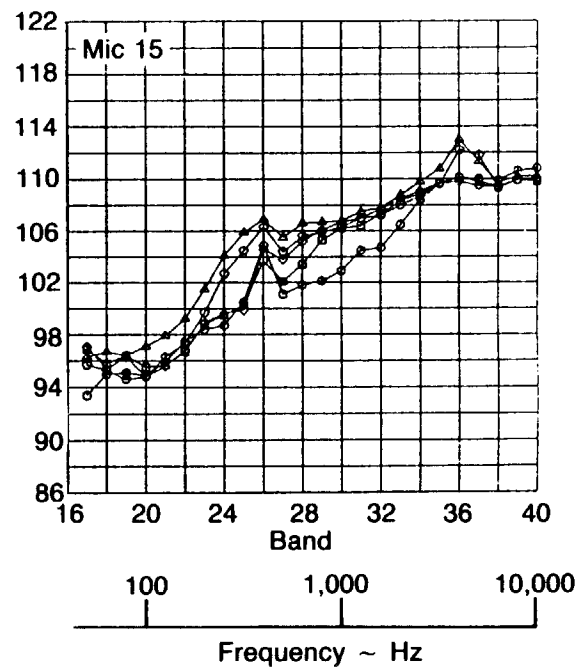
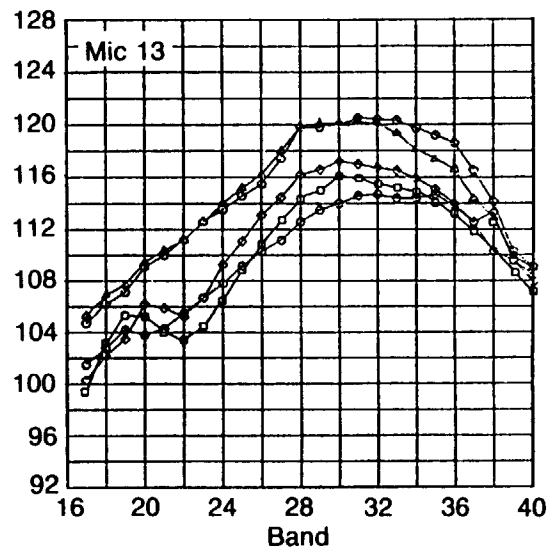


Figure 4-27. Lower Wing Leading Edge Microphones $1/3$ Octave Spectra— $M_{AP} \approx 0.81$

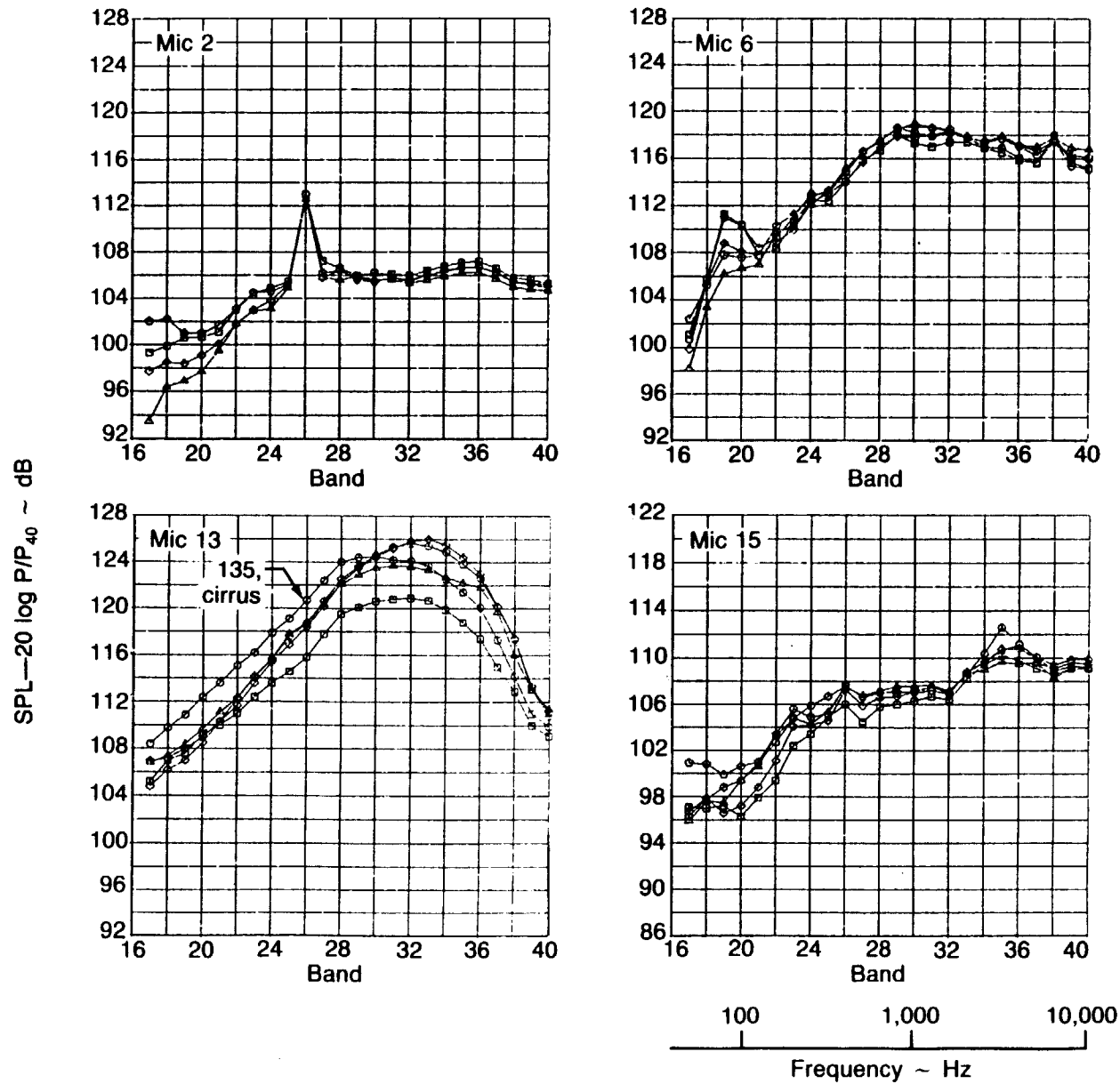


Figure 4-28. Lower Wing Leading Edge Microphones 1/3 Octave Spectra— $M_{AP} = 0.80-0.81$

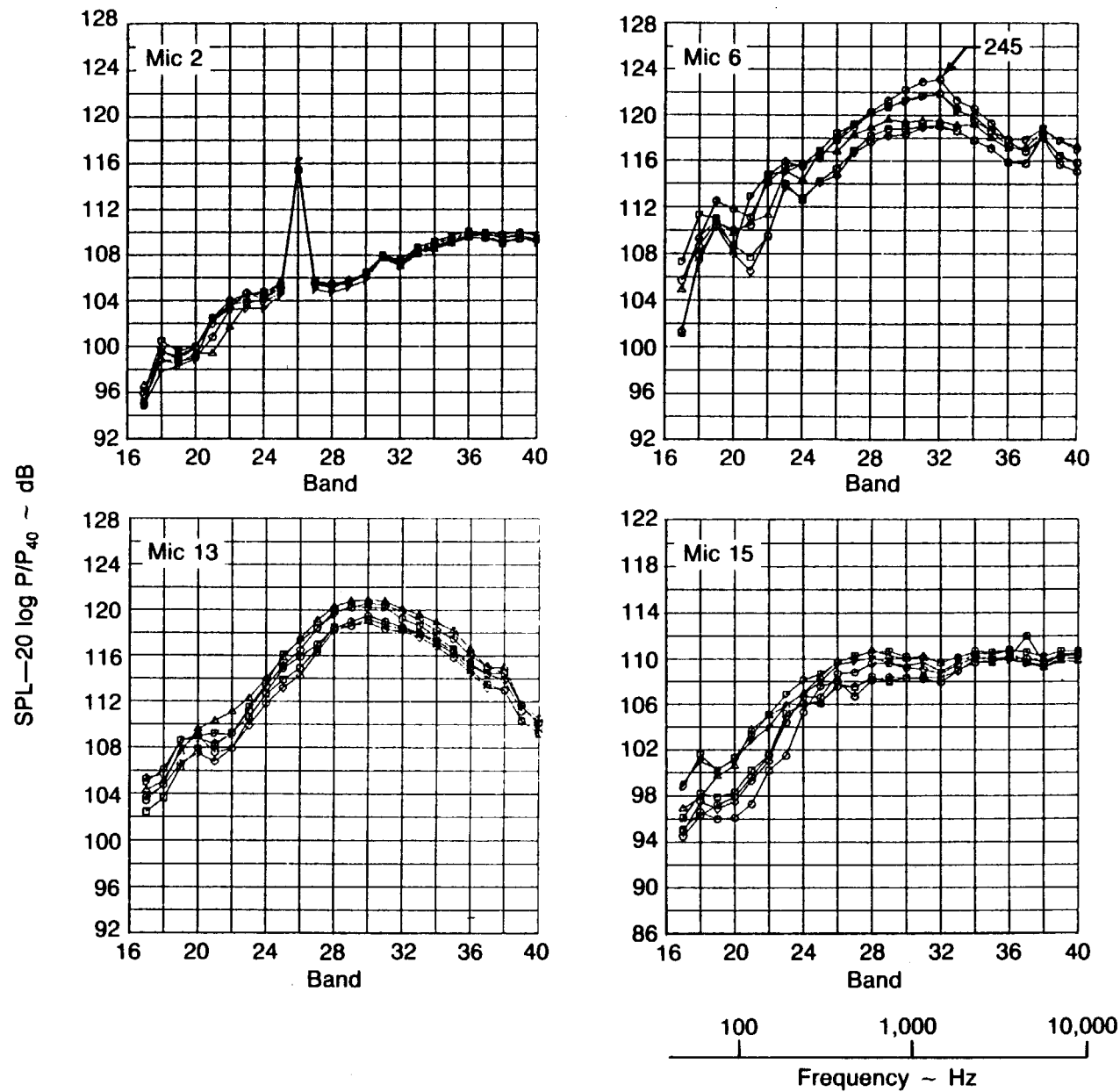


Figure 4-29. Lower Wing Leading Edge Microphones 1/3 Octave Spectra—M_{AP} ≈ 0.82-0.83

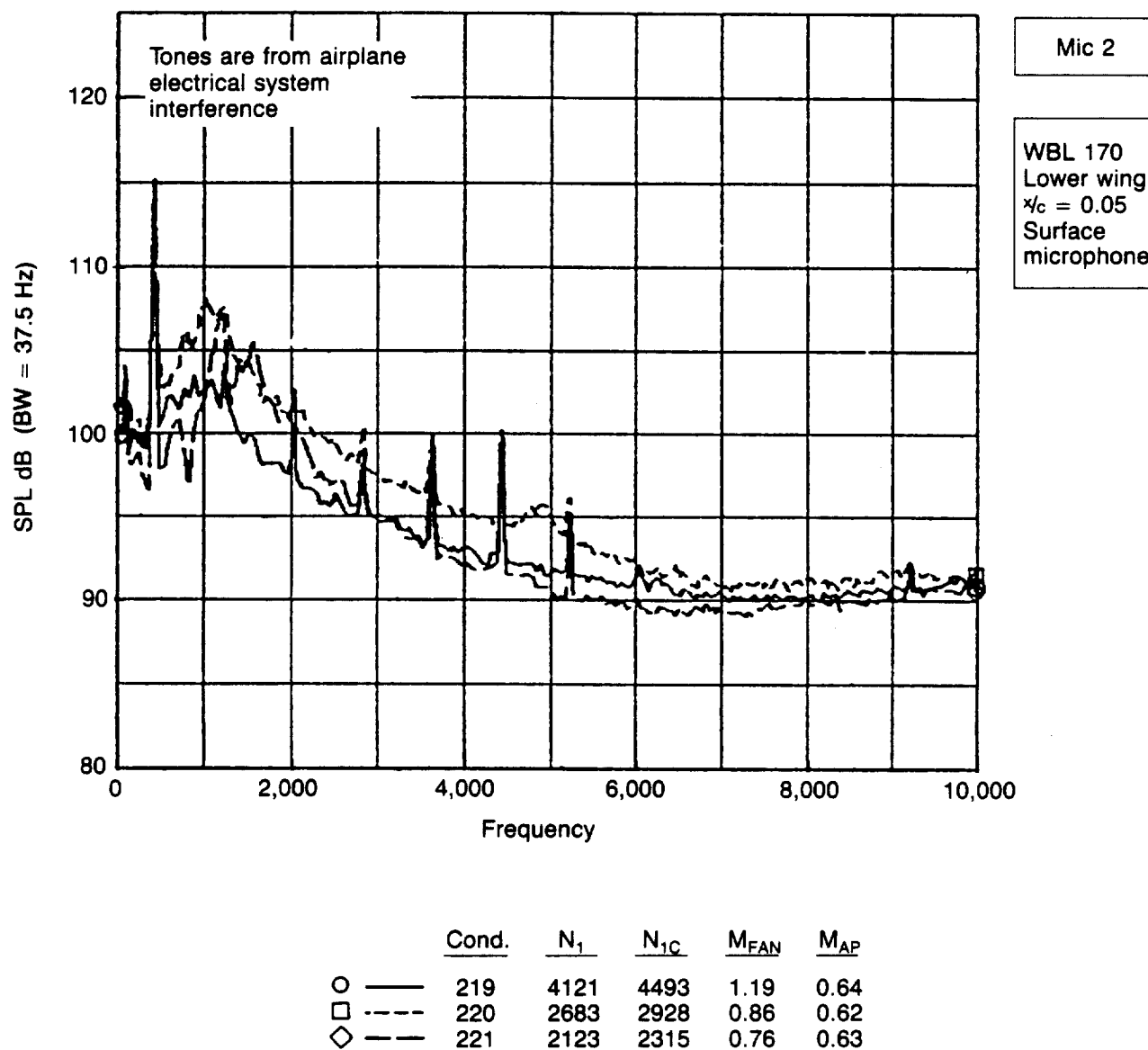


Figure 4-30. Microphone 2 Narrow Band Spectra— $M_{AP} = 0.62-0.64$

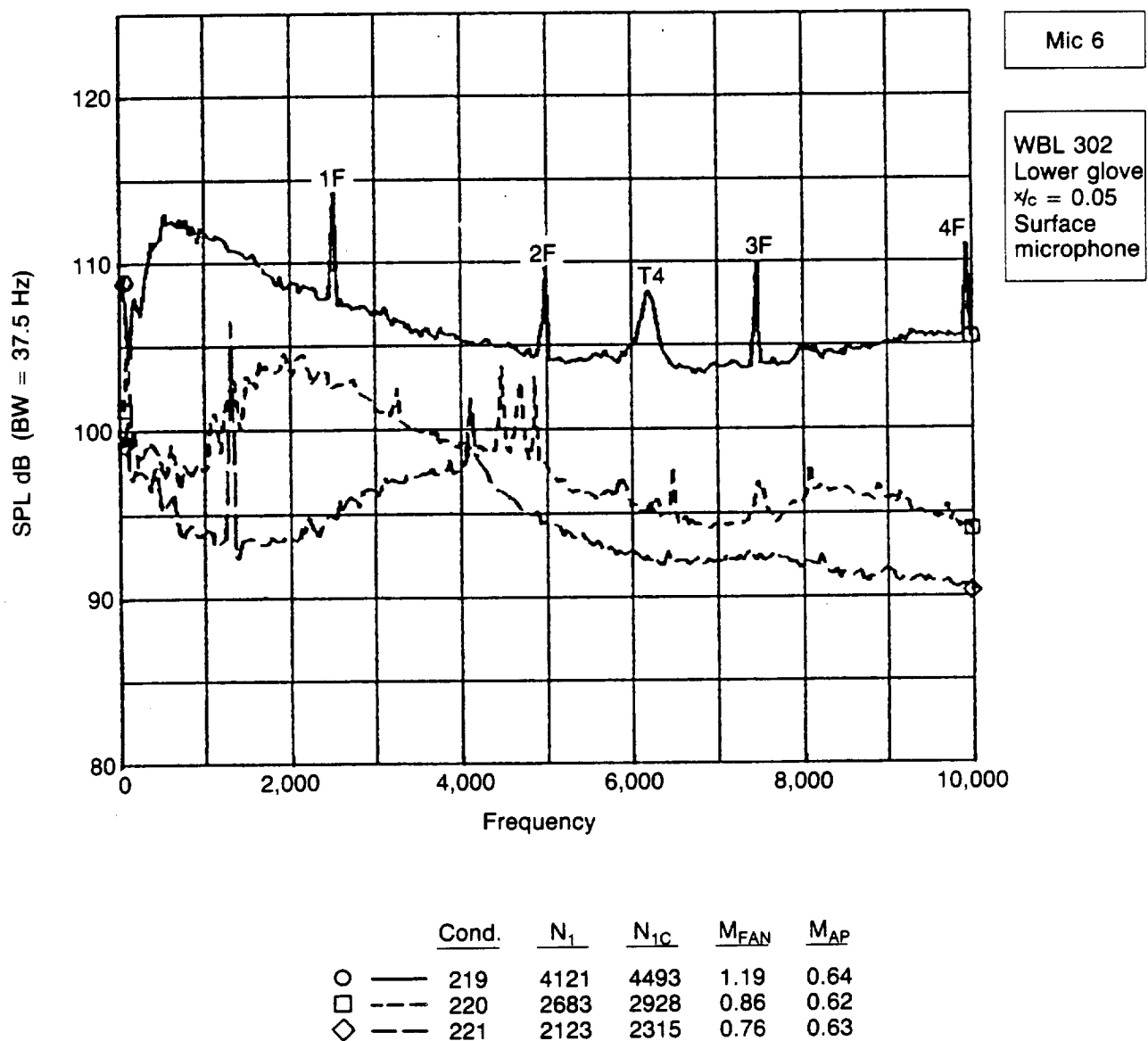


Figure 4-31. Microphone 6 Narrow Band Spectra— $M_{AP} \approx 0.62$ – 0.64

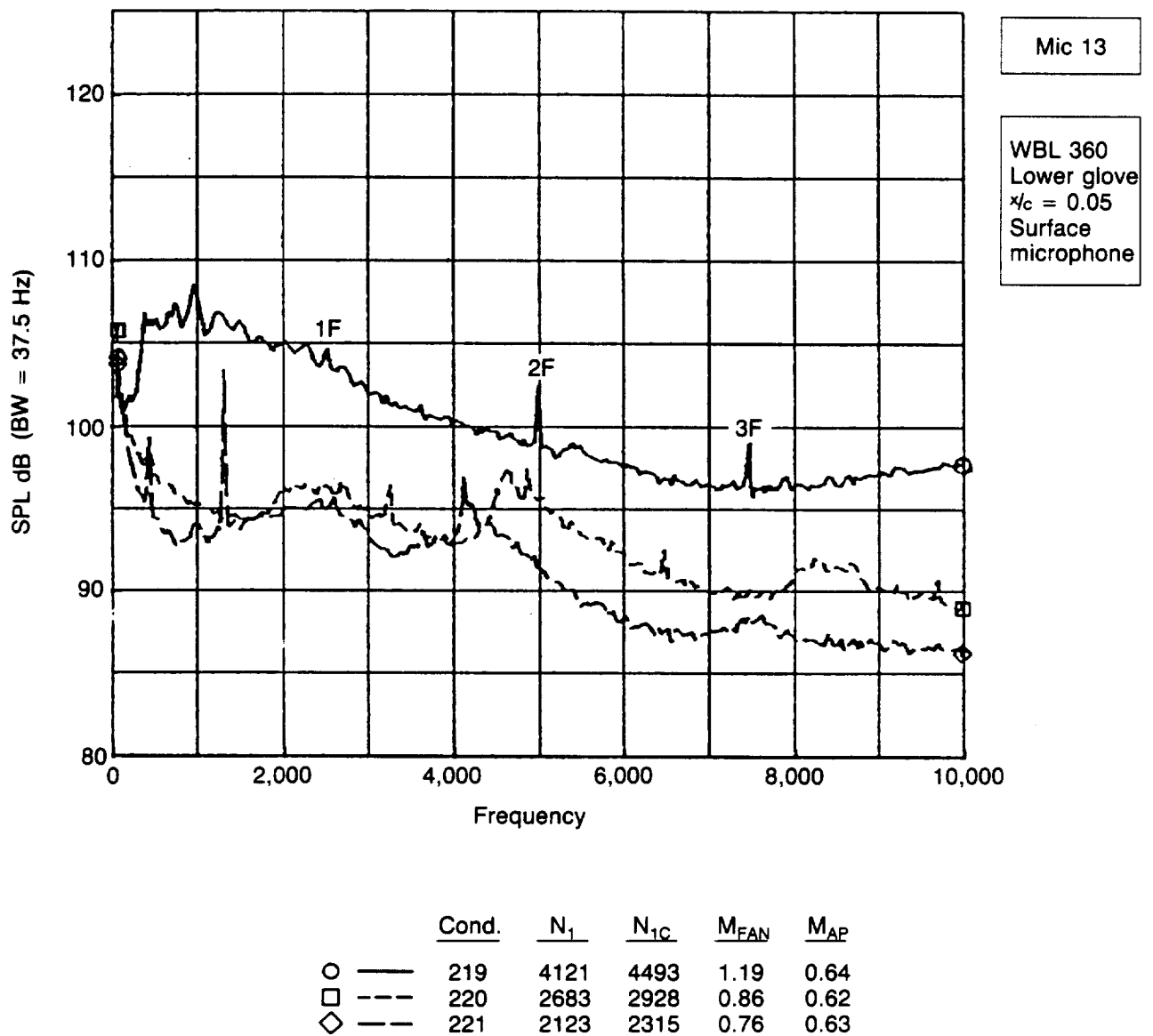


Figure 4-32. Microphone 13 Narrow Band Spectra— $M_{AP} \approx 0.62-0.64$

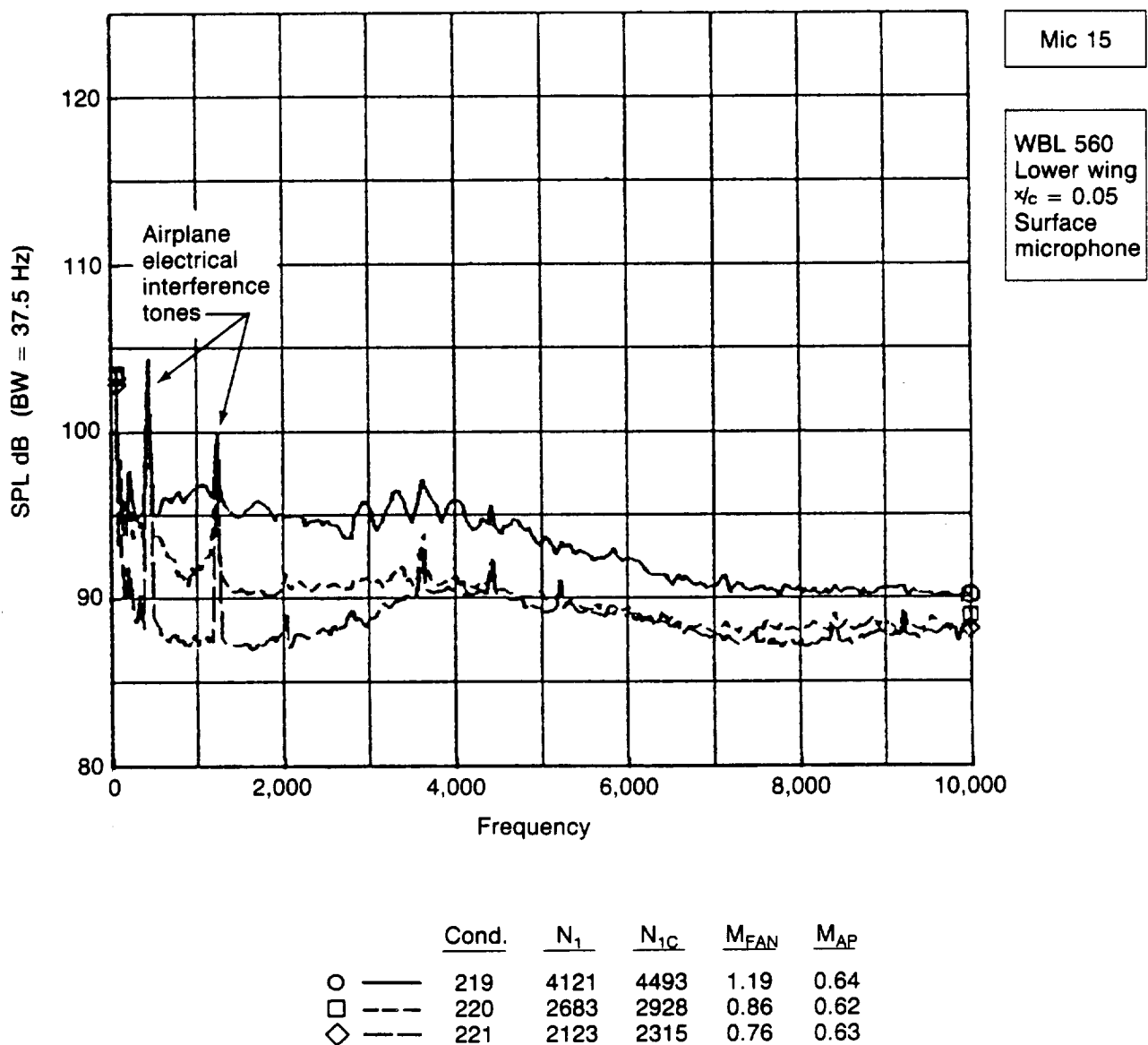


Figure 4-33. Microphone 15 Narrow Band Spectra— $M_{AP} \approx 0.62-0.64$

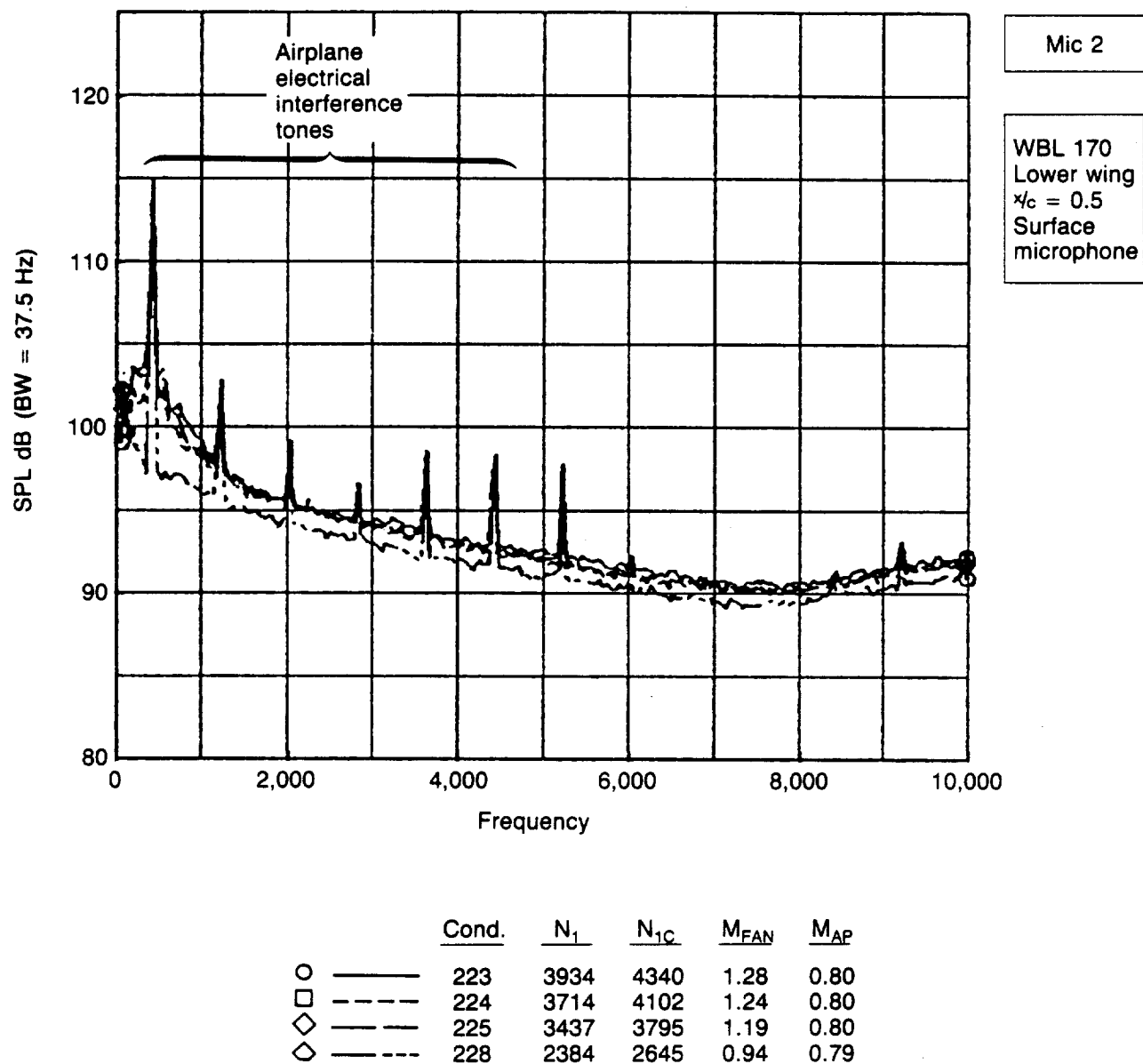
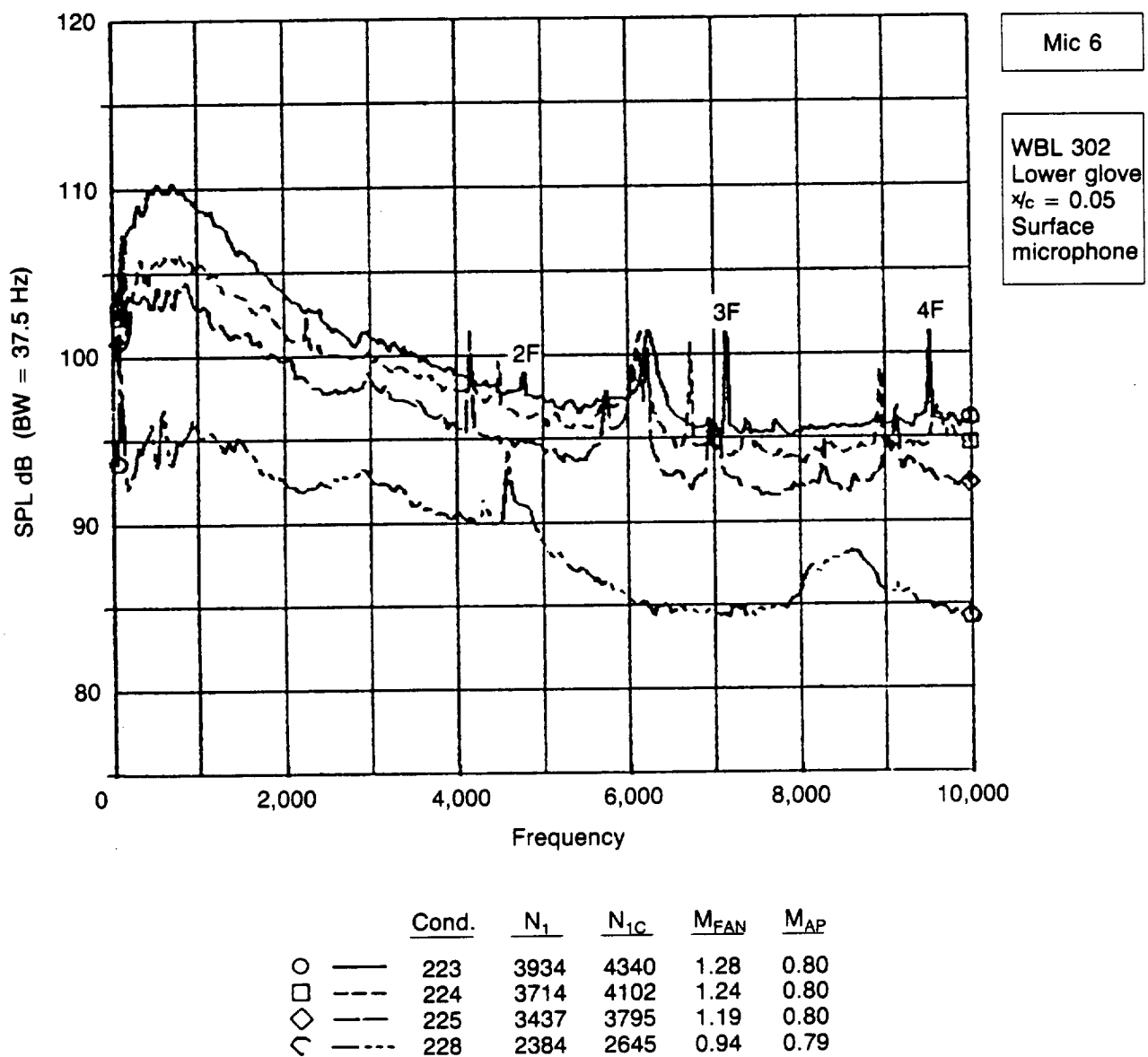
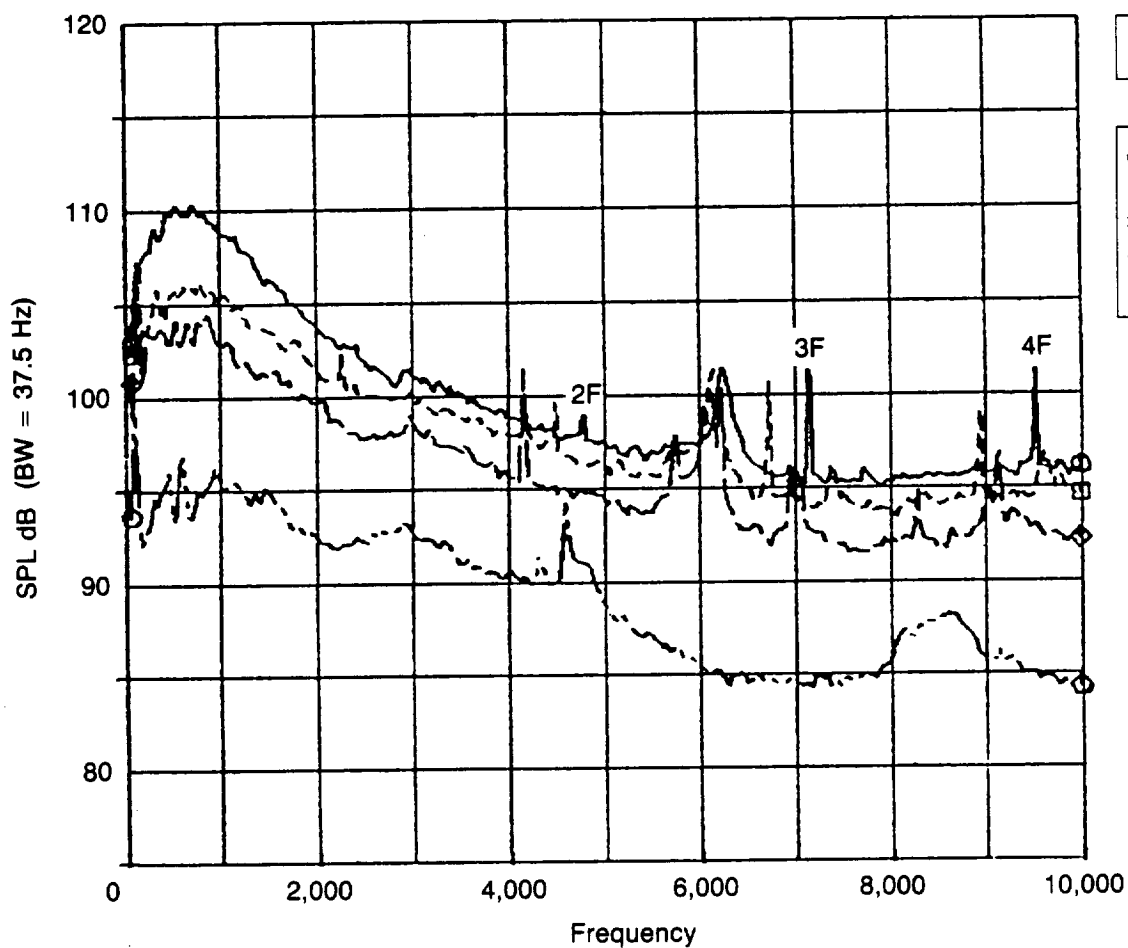


Figure 4-34. Microphone 2 Narrow Band Spectra— $M_{AP} \approx 0.79-0.80$



WBL 302
Lower glove
 $\chi_c = 0.05$
Surface
microphone



		Cond.	N_1	N_{1C}	M_{FAN}	M_{AP}
○	—	223	3934	4340	1.28	0.80
□	---	224	3714	4102	1.24	0.80
◇	-.-	225	3437	3795	1.19	0.80
∨	----	228	2384	2645	0.94	0.79

Figure 4-35. Microphone 6 Narrow Band Spectra— $M_{AP} \approx 0.79-0.80$

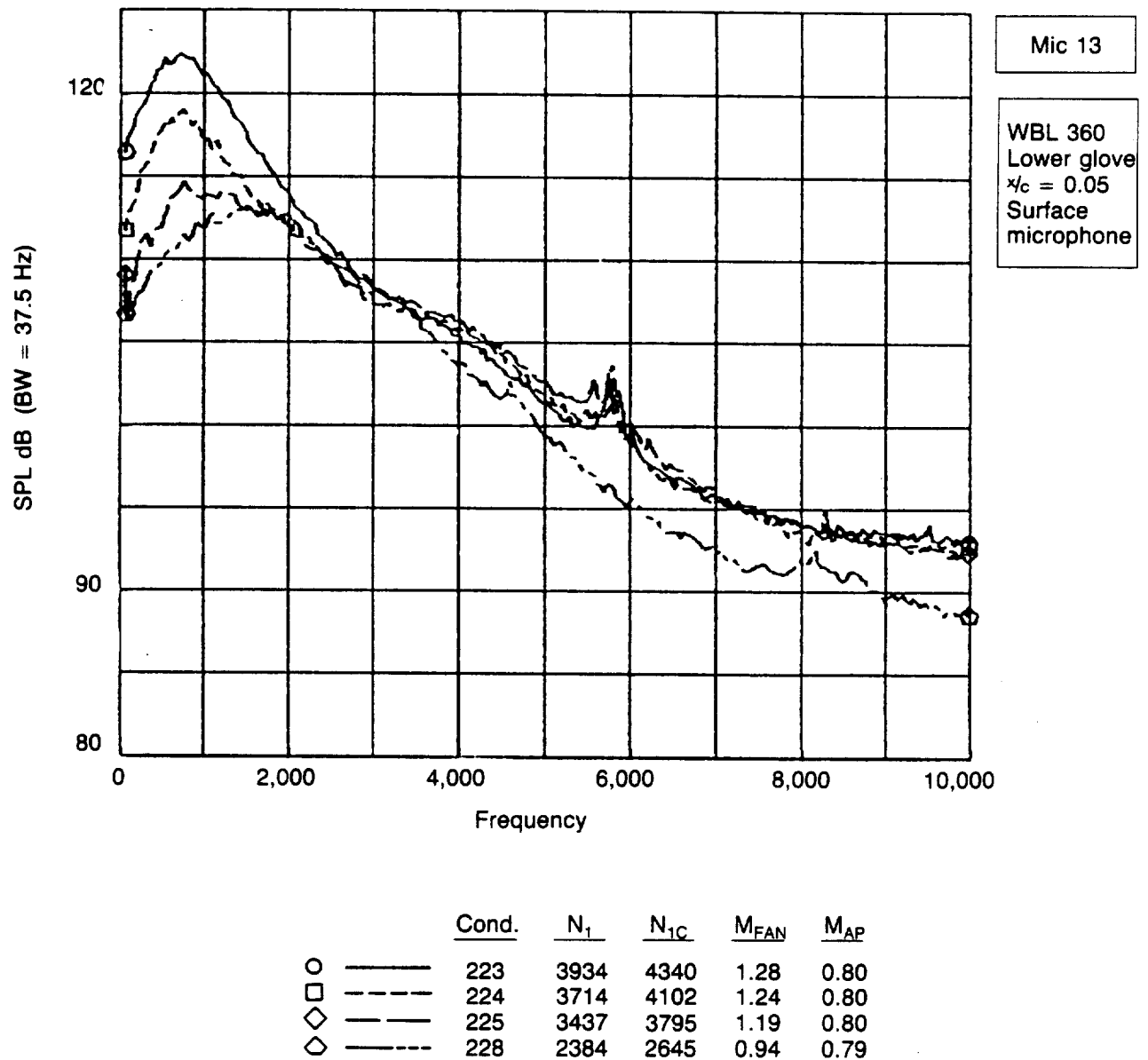


Figure 4-36. Microphone 13 Narrow Band Spectra— $M_{AP} \approx 0.79-0.80$

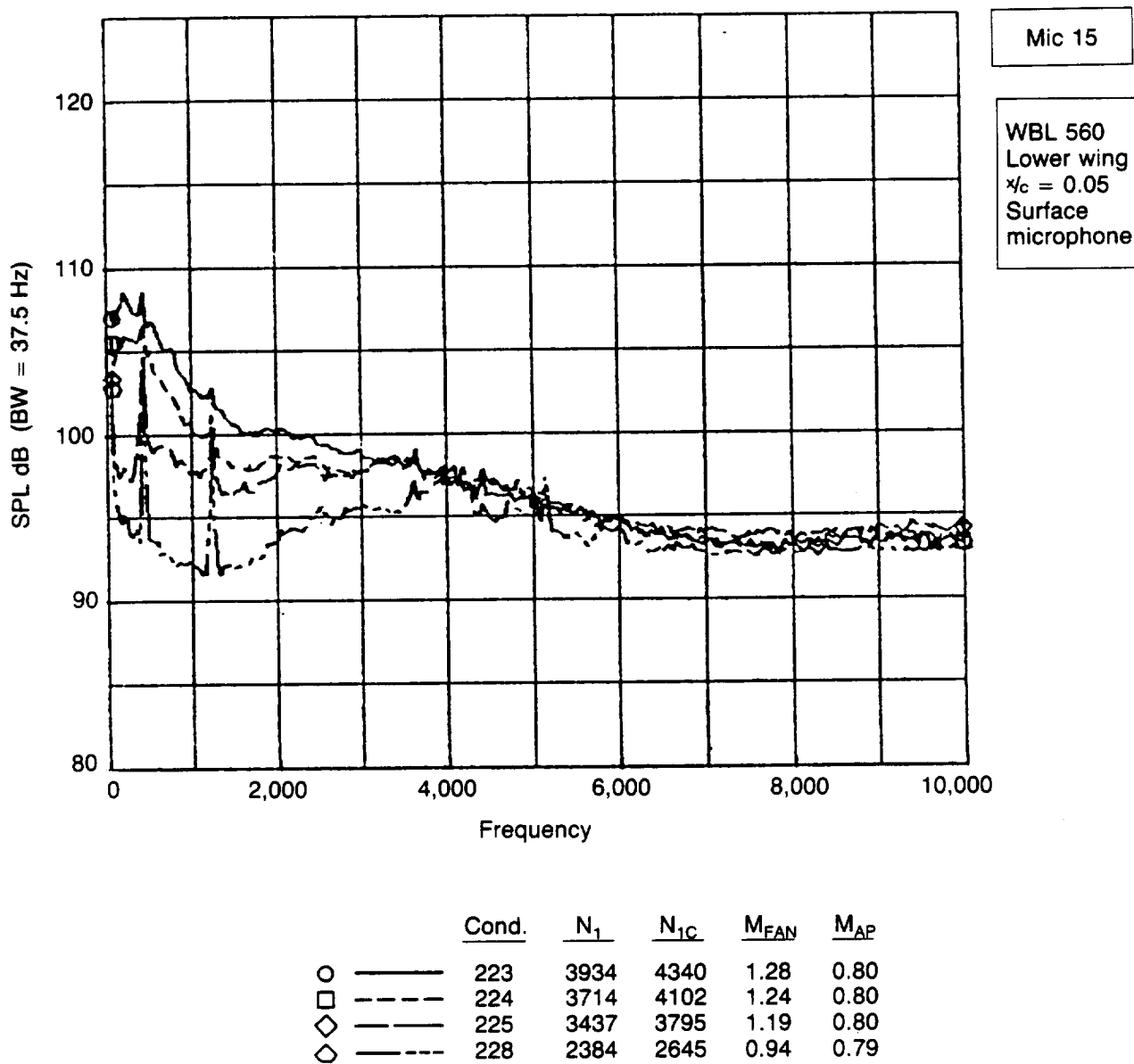
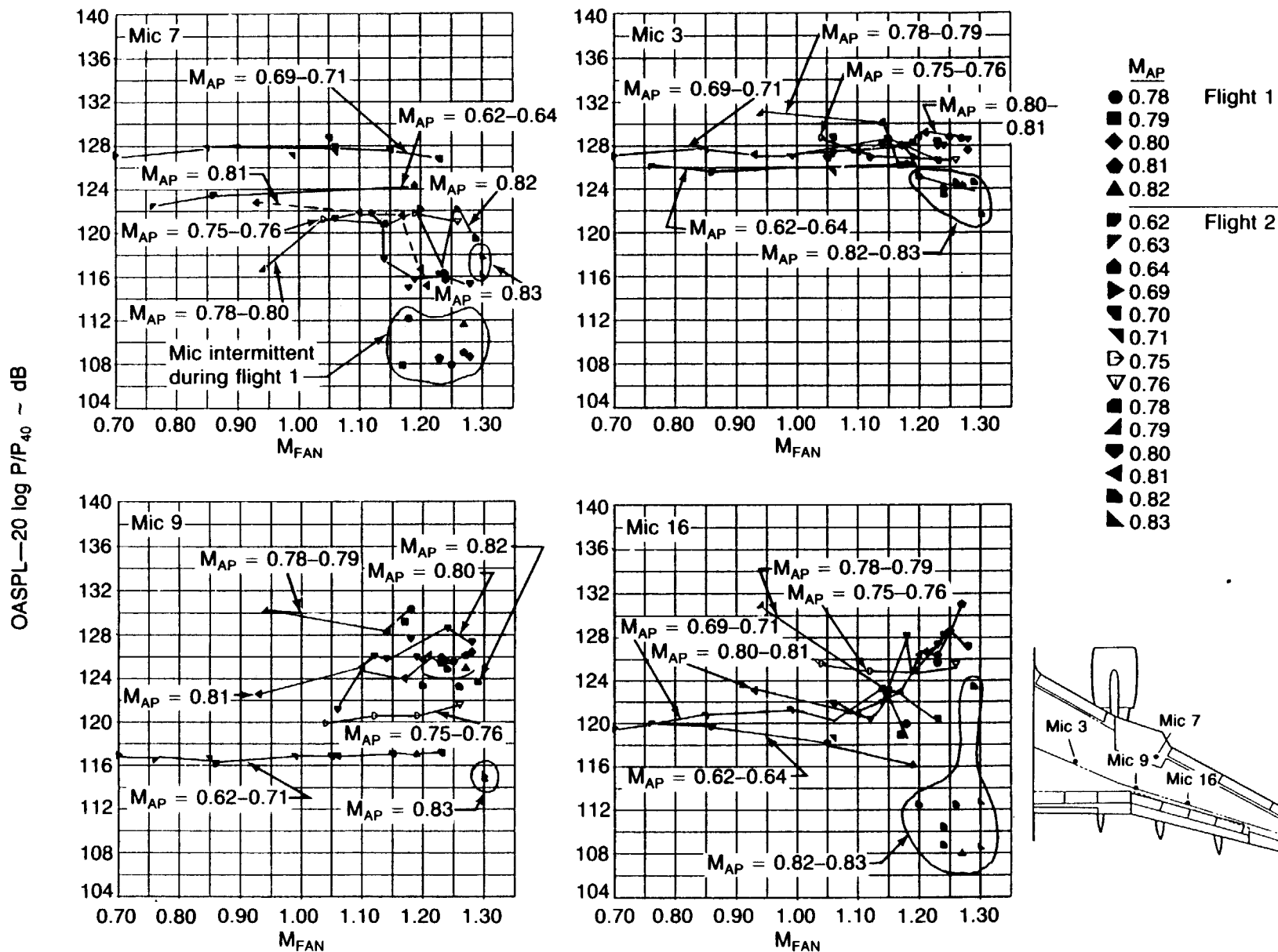


Figure 4-37. Microphone 15 Narrow Band Spectra— $M_{AP} \approx 0.79-0.80$



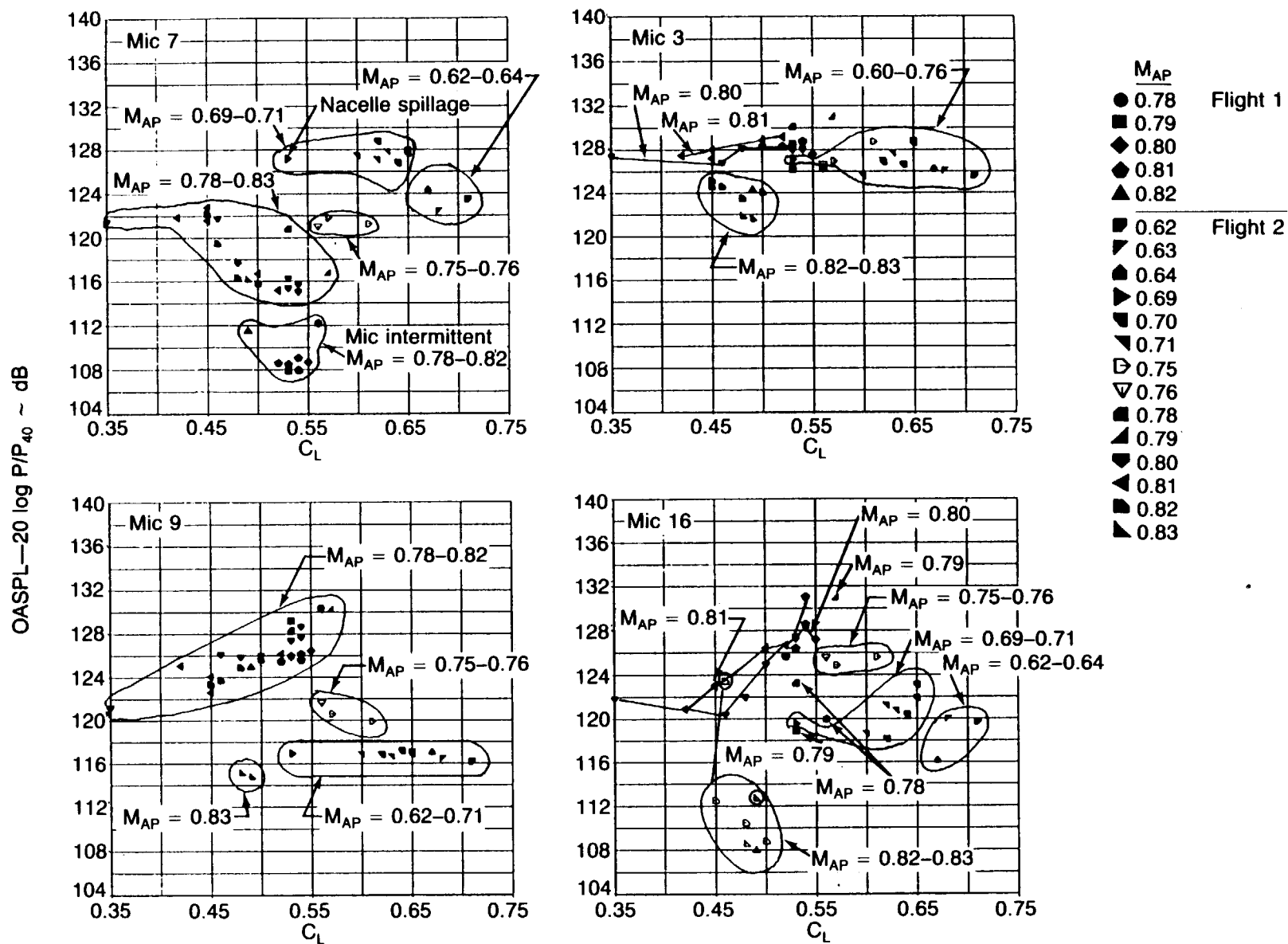


Figure 4-39. Normalized OASPL on Wing Upper Surface Probe Microphone vs. C_L

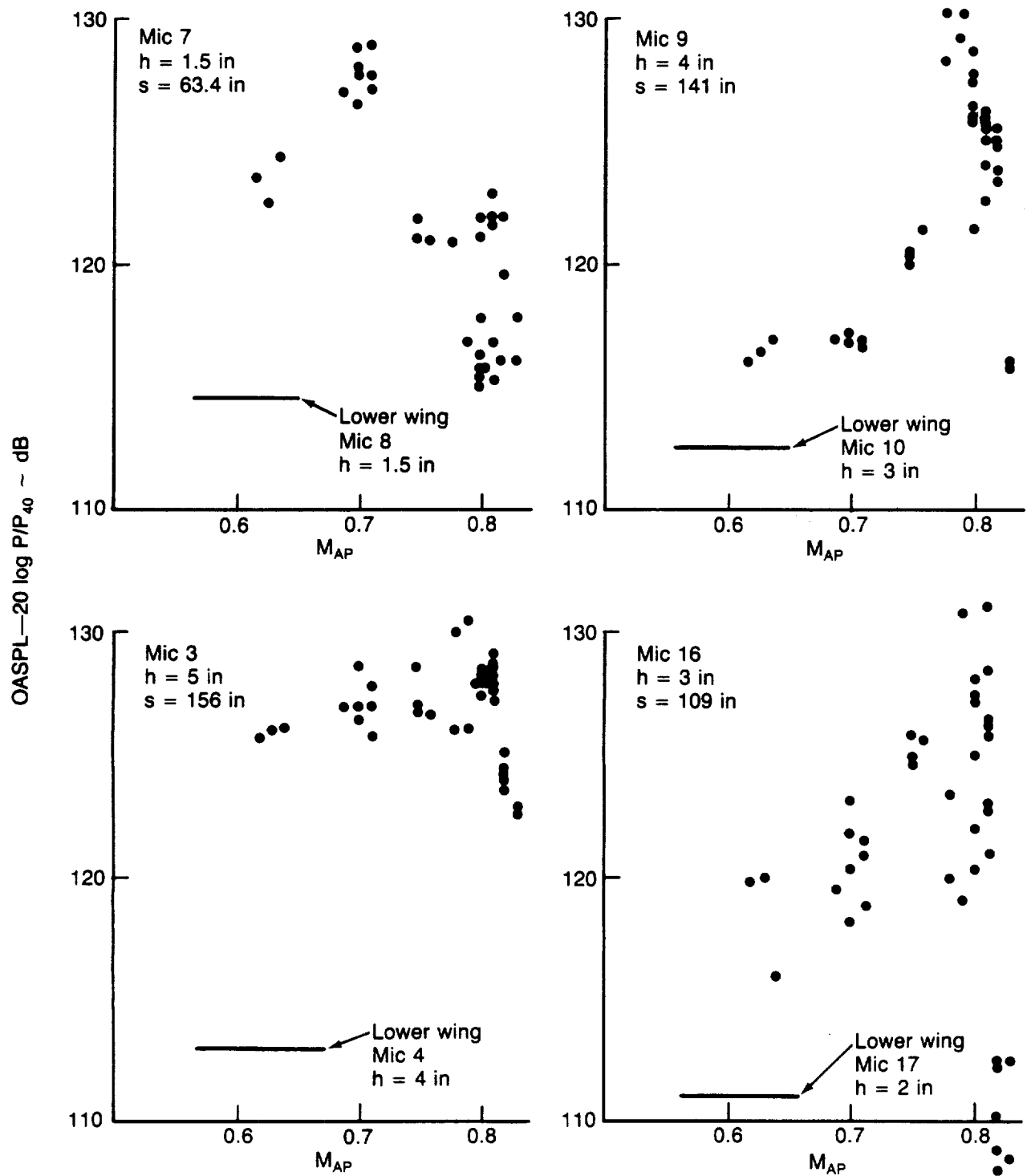


Figure 4-40. Normalized OASPL vs. Airplane Mach Number—Upper Surface Probe Microphones

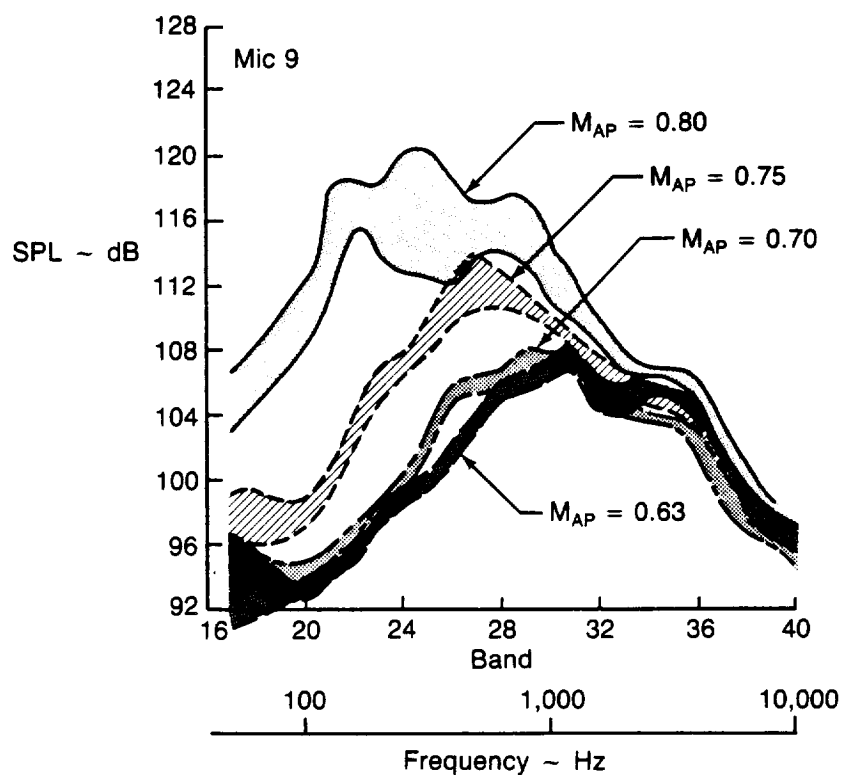
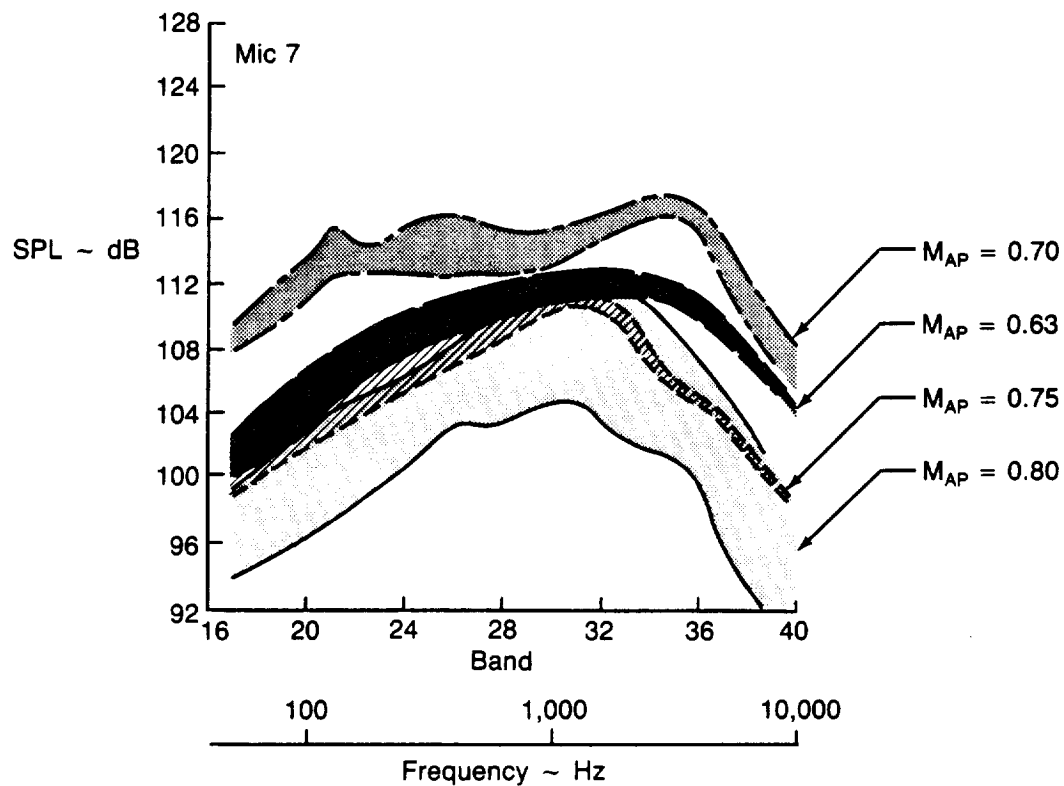


Figure 4-41. Probe Microphones, Upper Surface $1/3$ Octave Spectra Effect of Airplane Mach Number

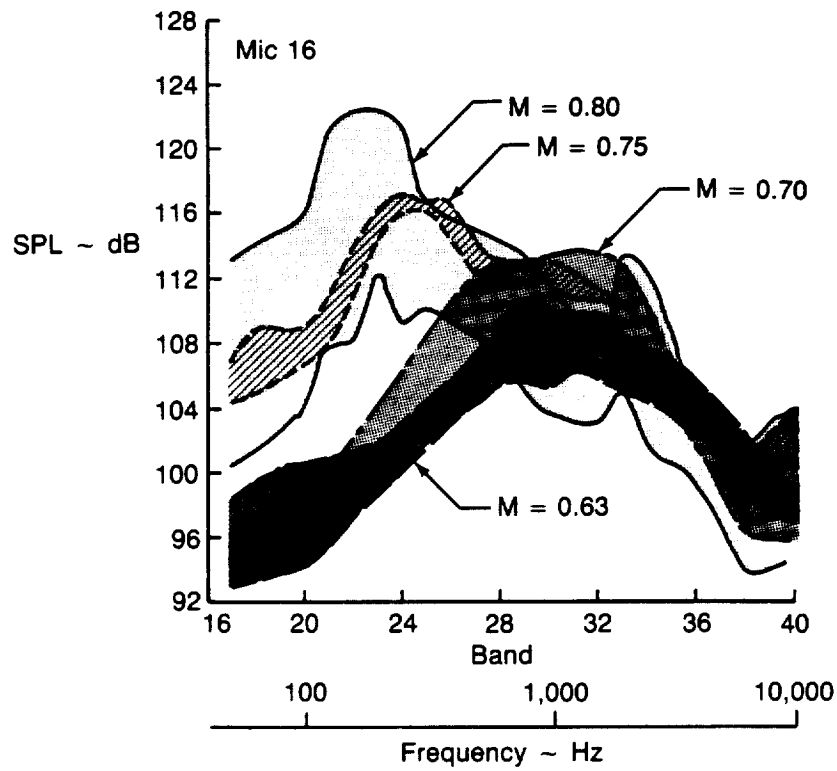
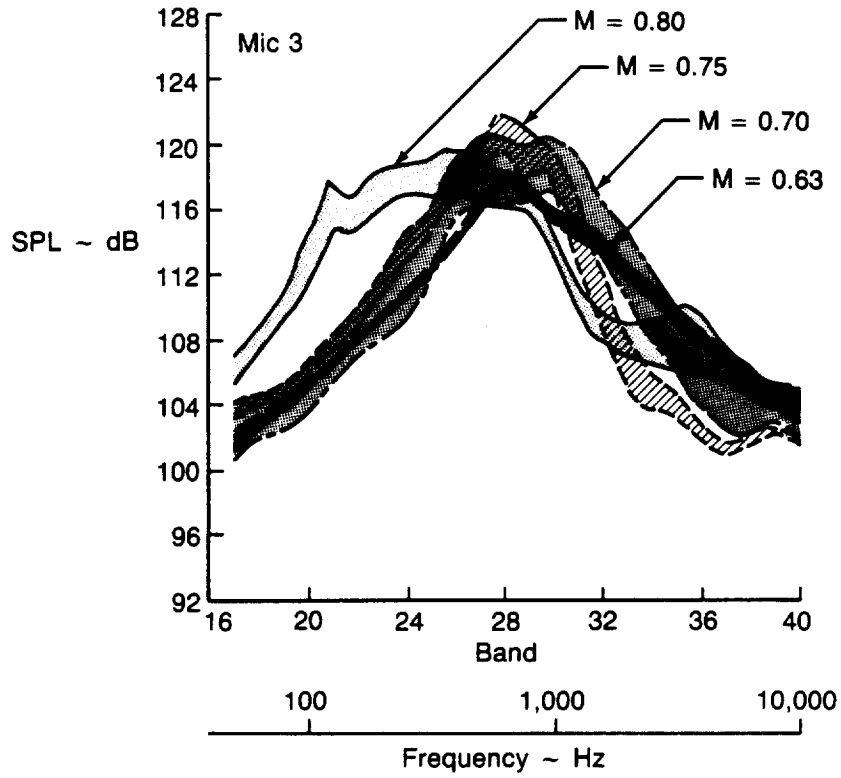


Figure 4-42. Probe Microphones, Upper Surface 1/3 Octave Spectra Effect of Airplane Mach Number

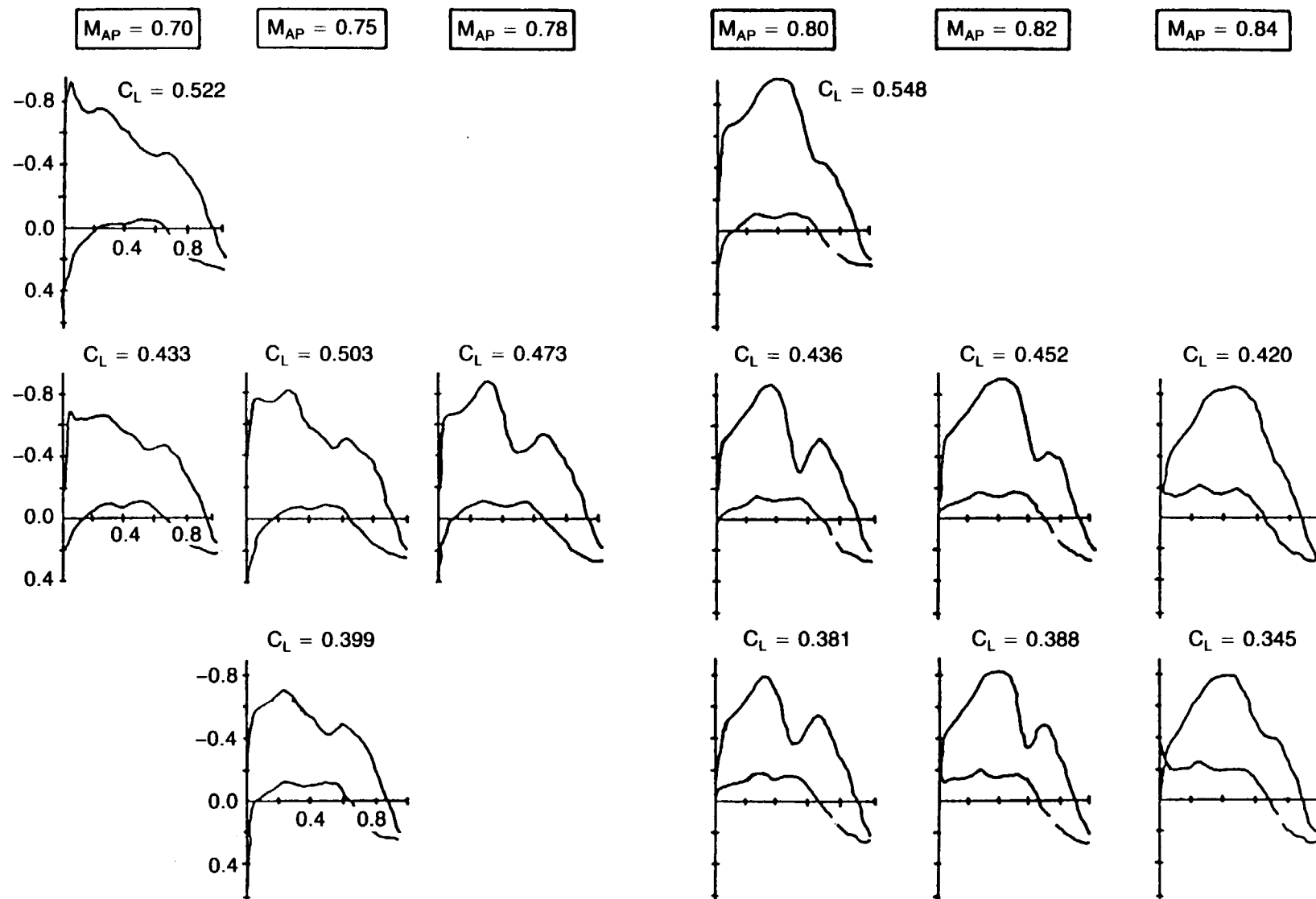


Figure 4-43. Glove Pressure Distribution Characteristics Summary—WBL 325

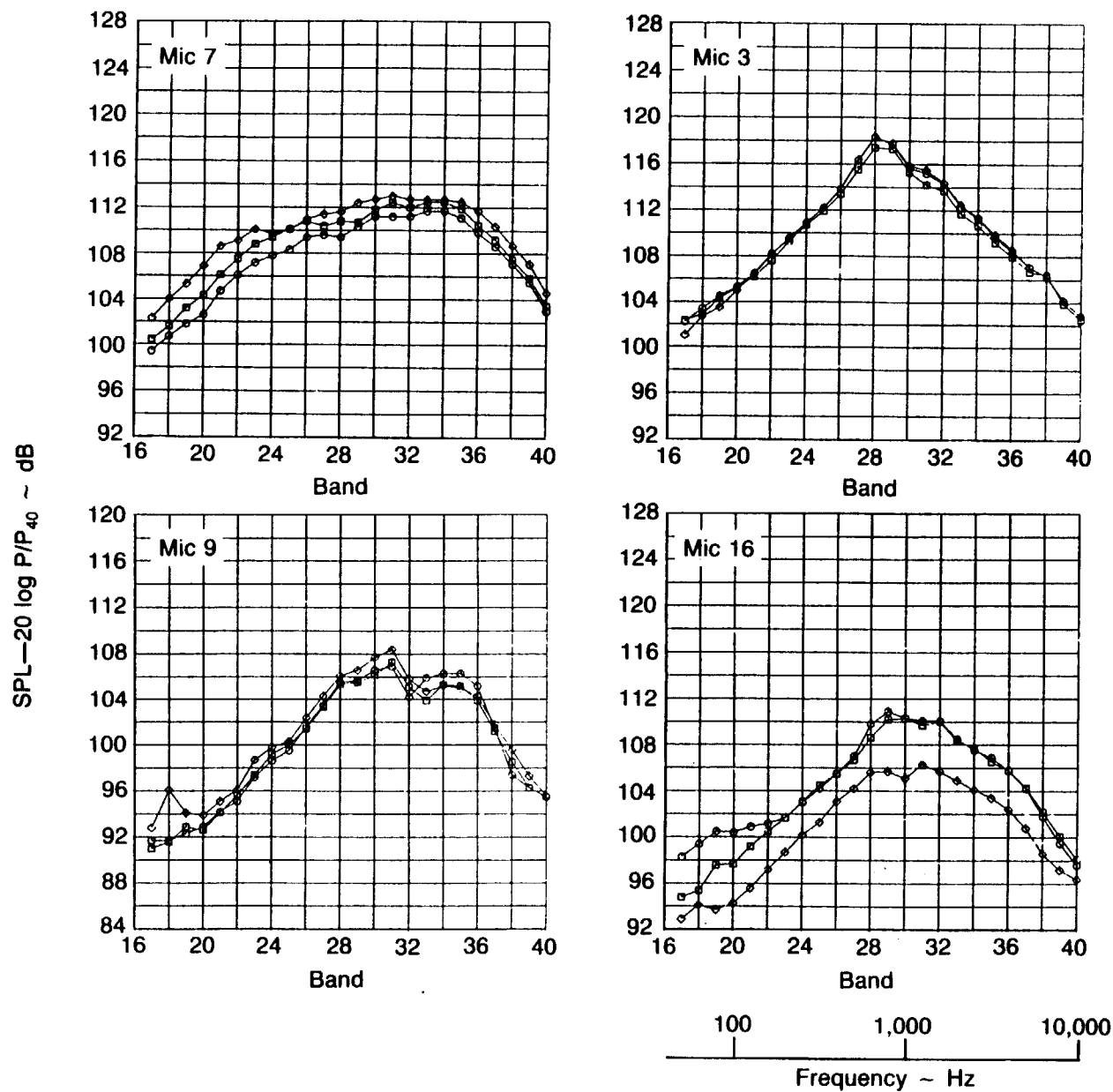


Figure 4-44. Upper Wing Probe Microphones $1/3$ Octave Spectra— $M_{AP} \approx 0.62$ – 0.64

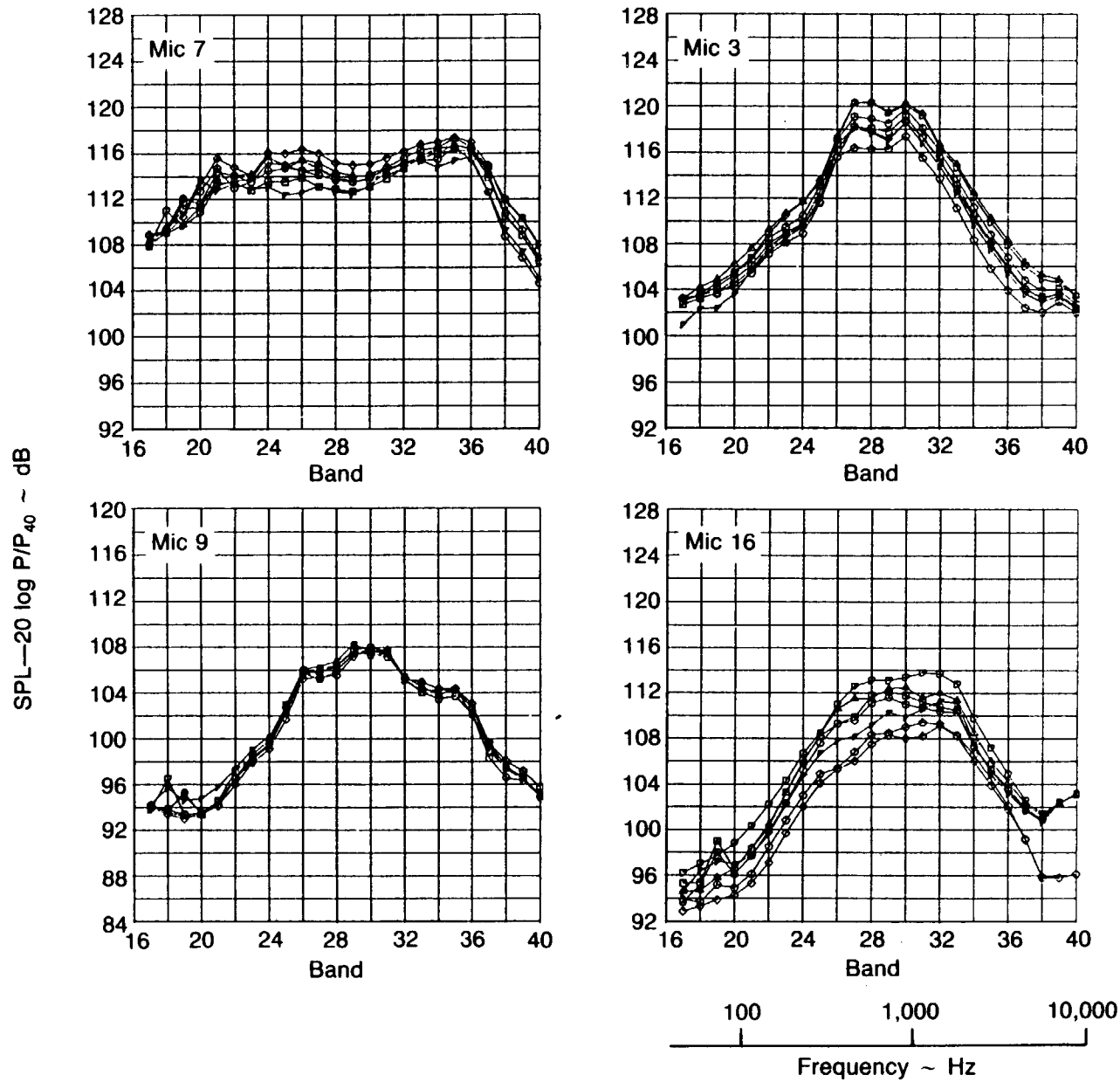


Figure 4-45. Upper Wing Probe Microphones 1/3 Octave Spectra— $M_{AP} \approx 0.70, 0.71$

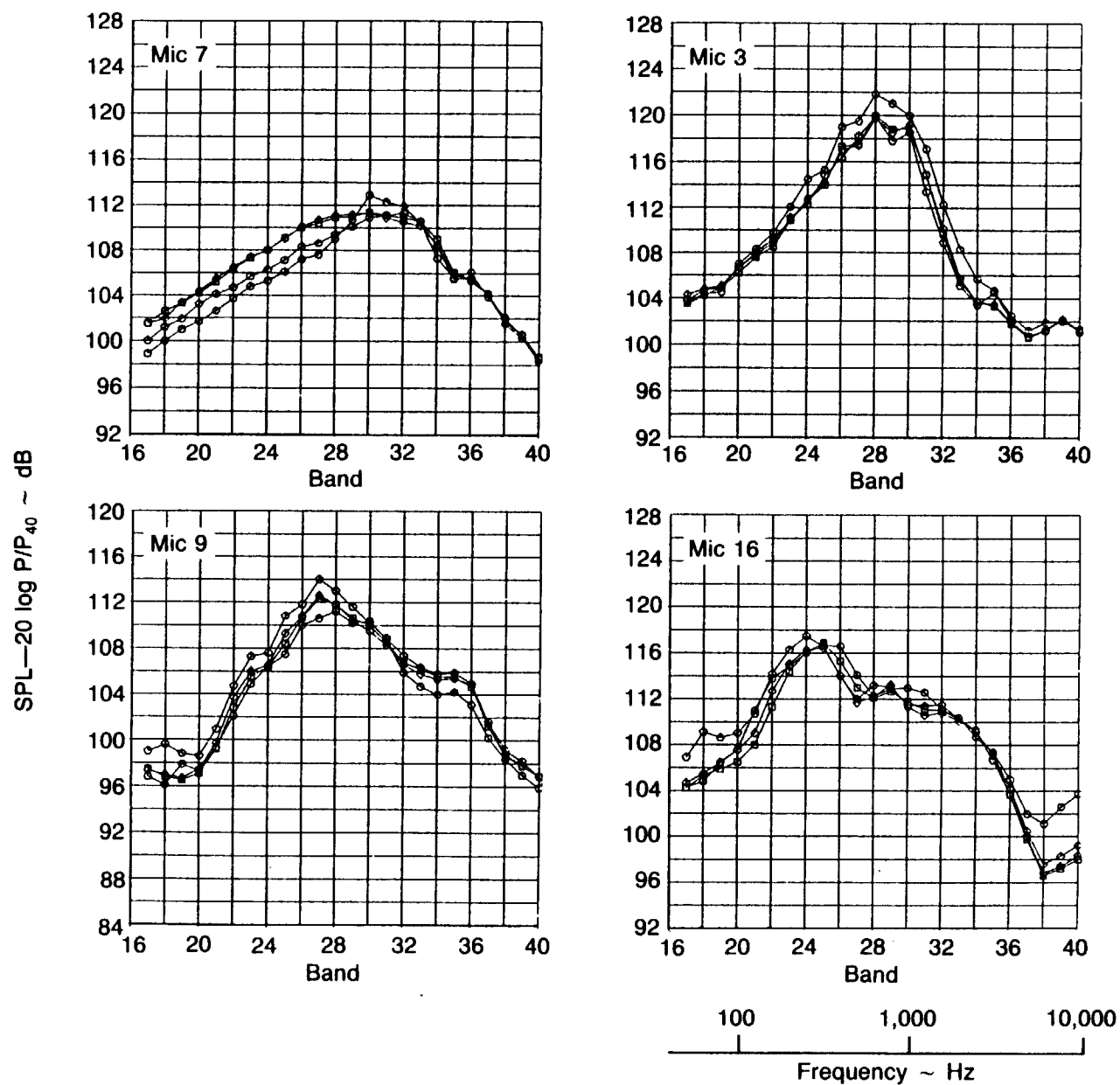


Figure 4-46. Upper Wing Probe Microphones $1/3$ Octave Spectra— $M_{AP} \approx 0.75, 0.76$

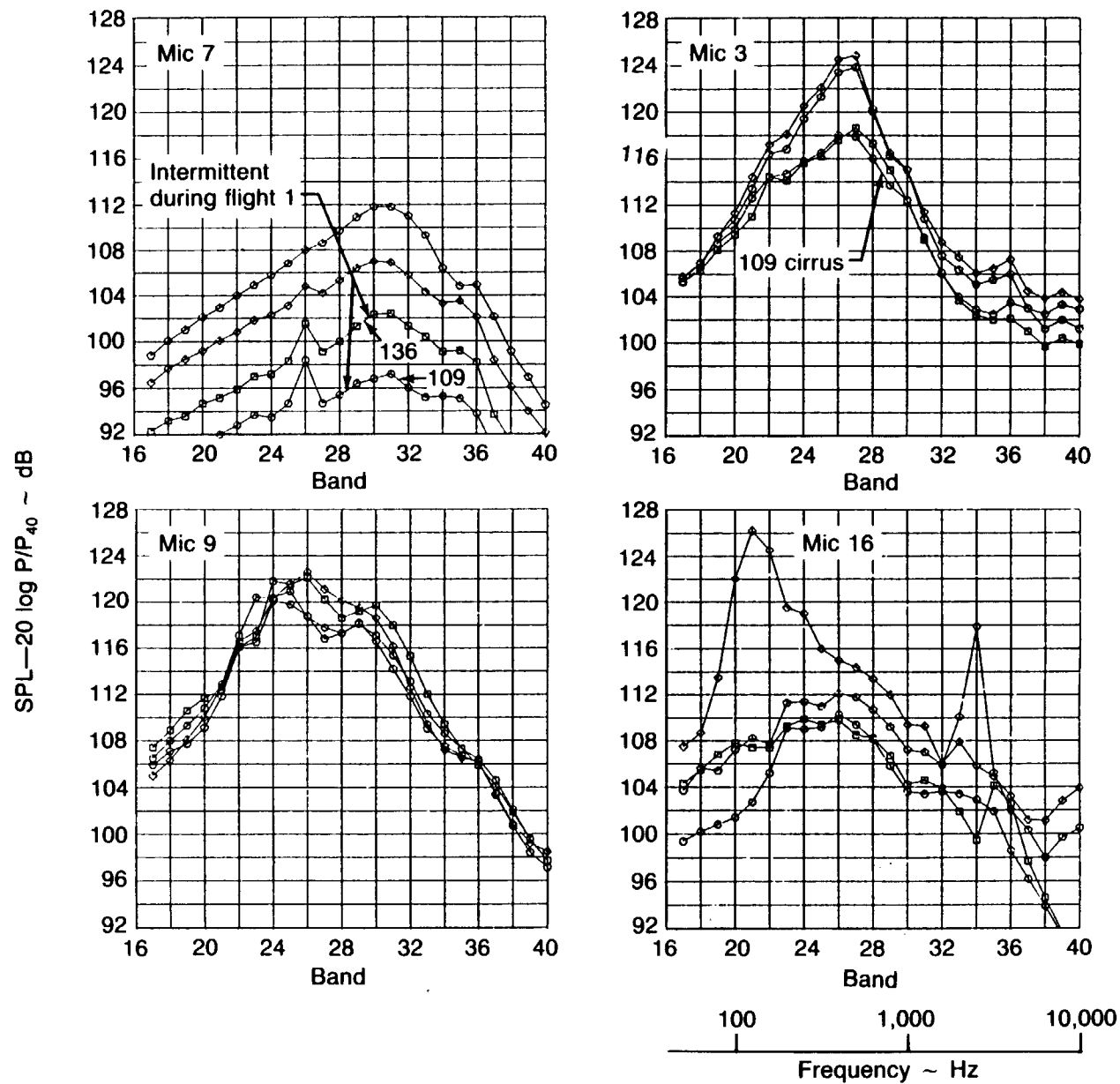


Figure 4-47. Upper Wing Probe Microphones $1/3$ Octave Spectra— $M_{AP} \approx 0.78, 0.79$

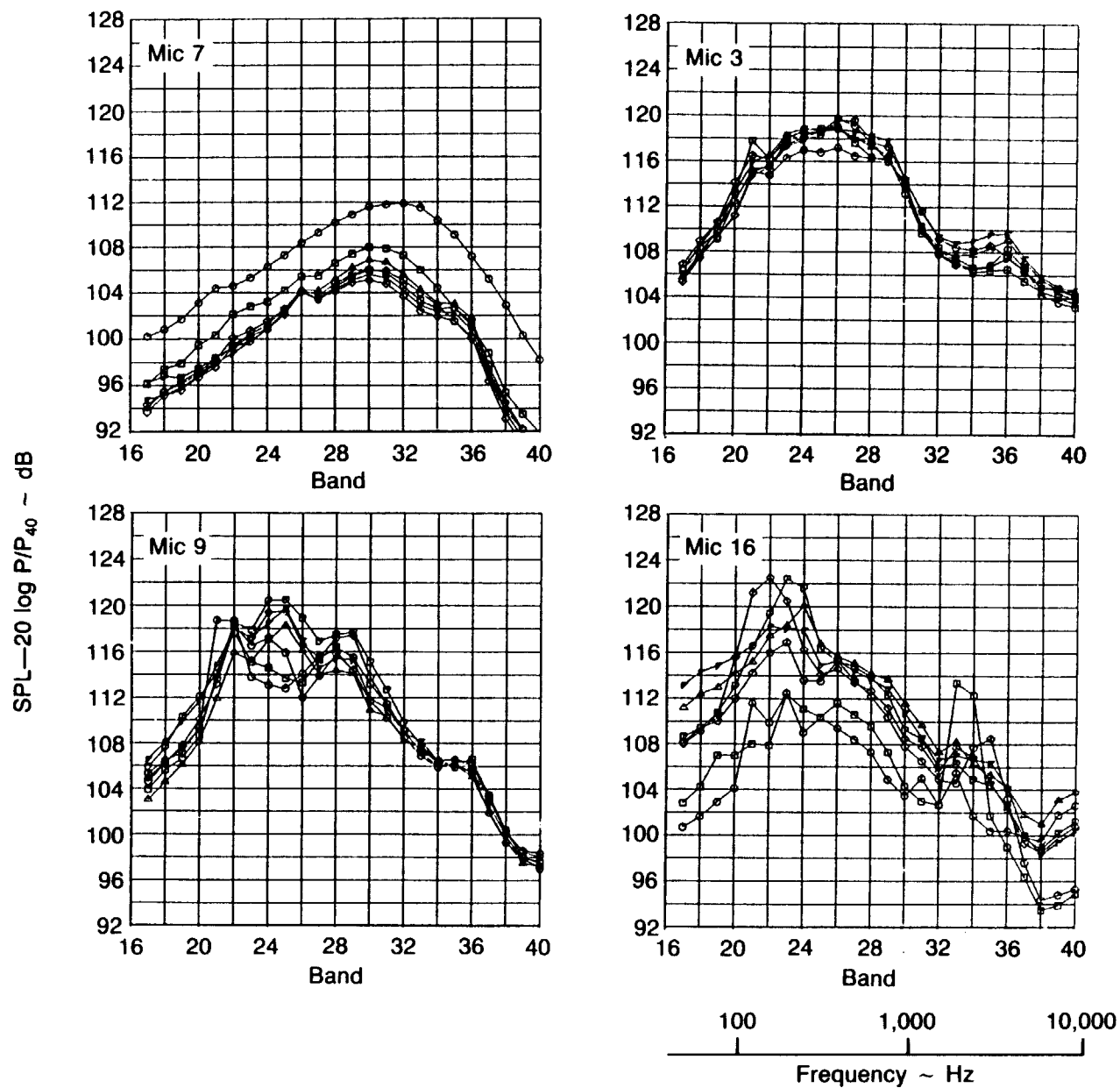


Figure 4-48. Upper Wing Probe Microphones $1/3$ Octave Spectra— $M_{AP} \approx 0.80$

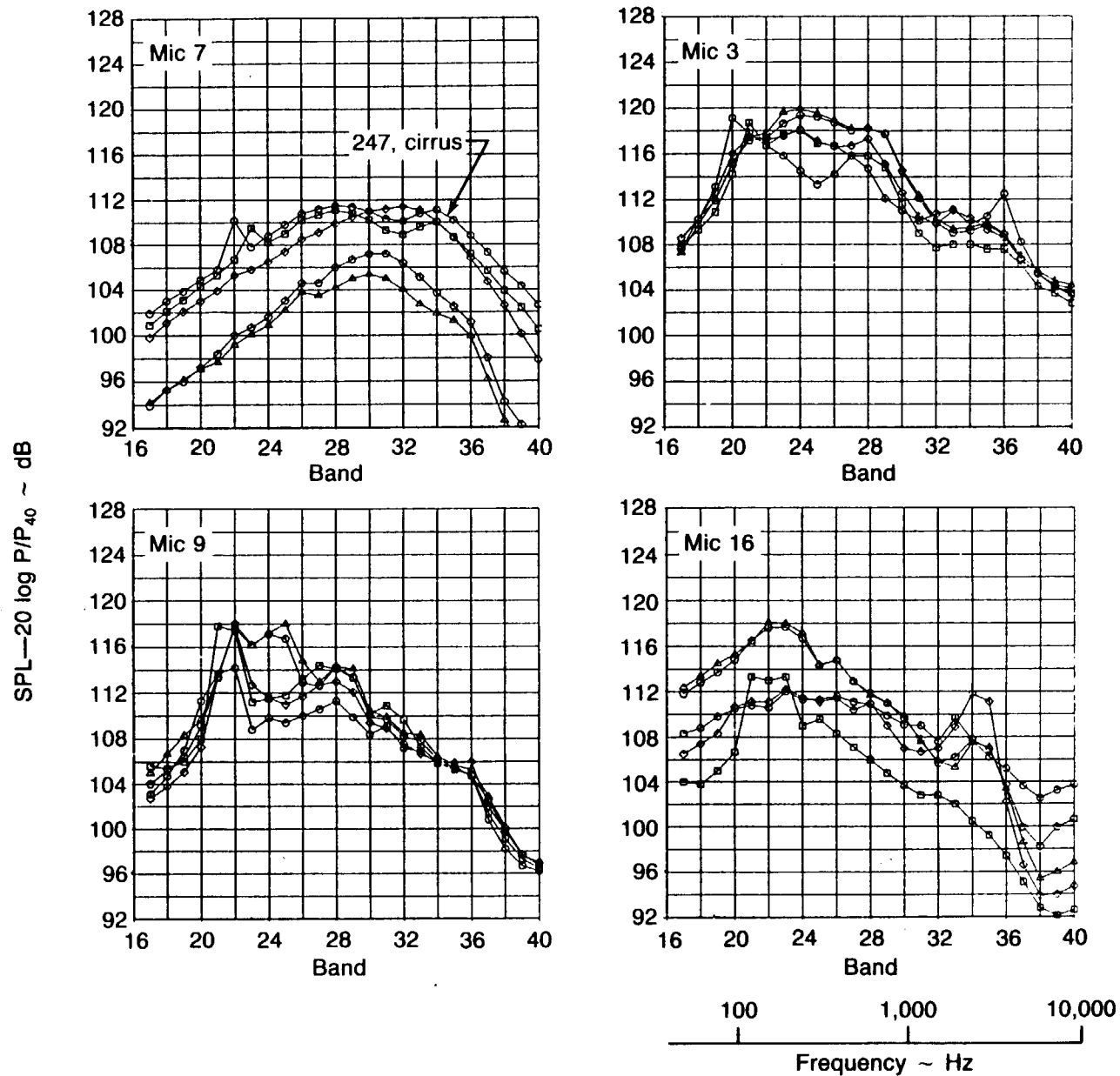


Figure 4-49. Upper Wing Probe Microphones $1/3$ Octave Spectra— $M_{AP} \approx 0.81$

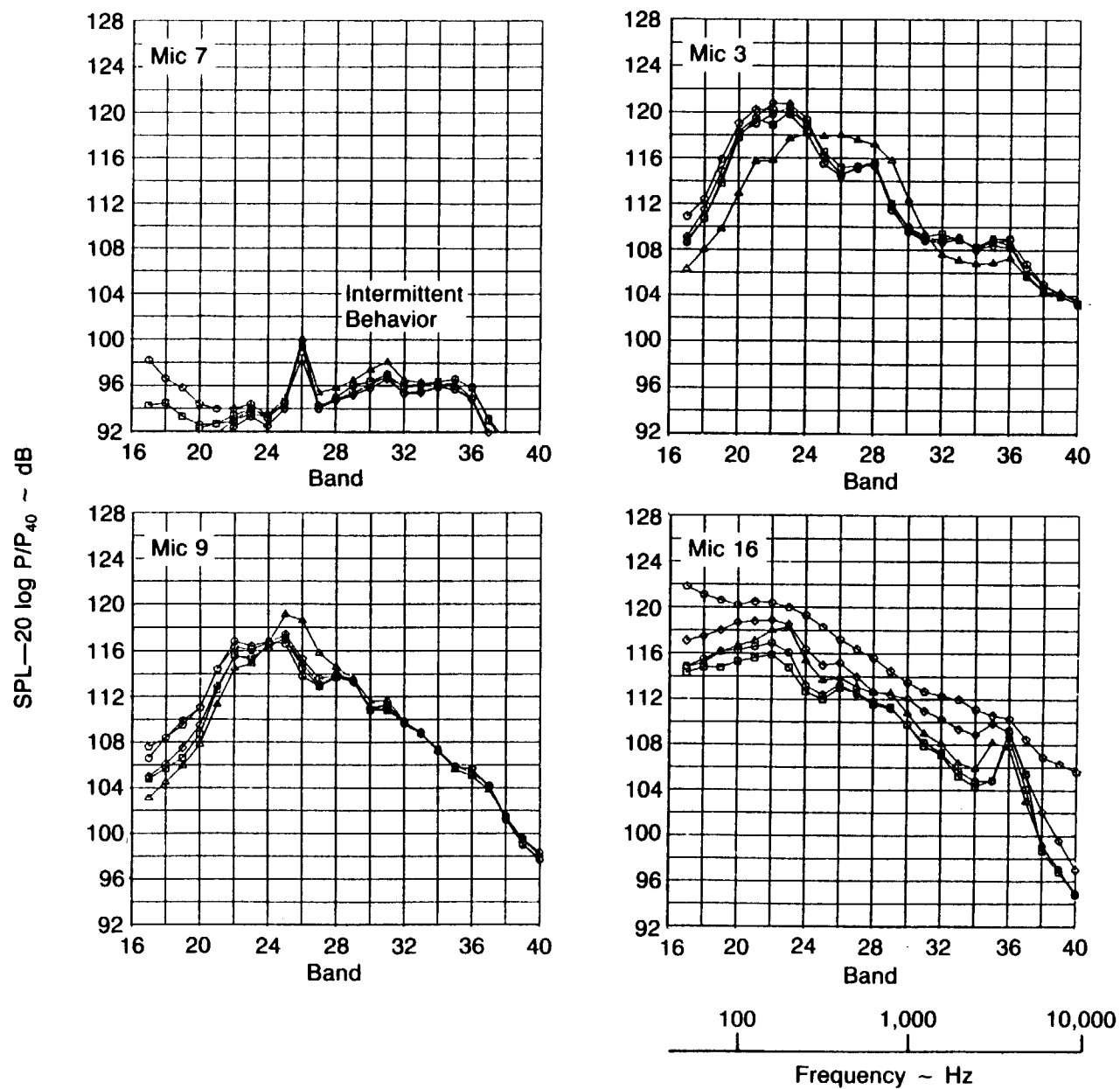


Figure 4-50. Upper Wing Probe Microphones $\frac{1}{3}$ Octave Spectra— $M_{AP} \approx 0.80, 0.81$

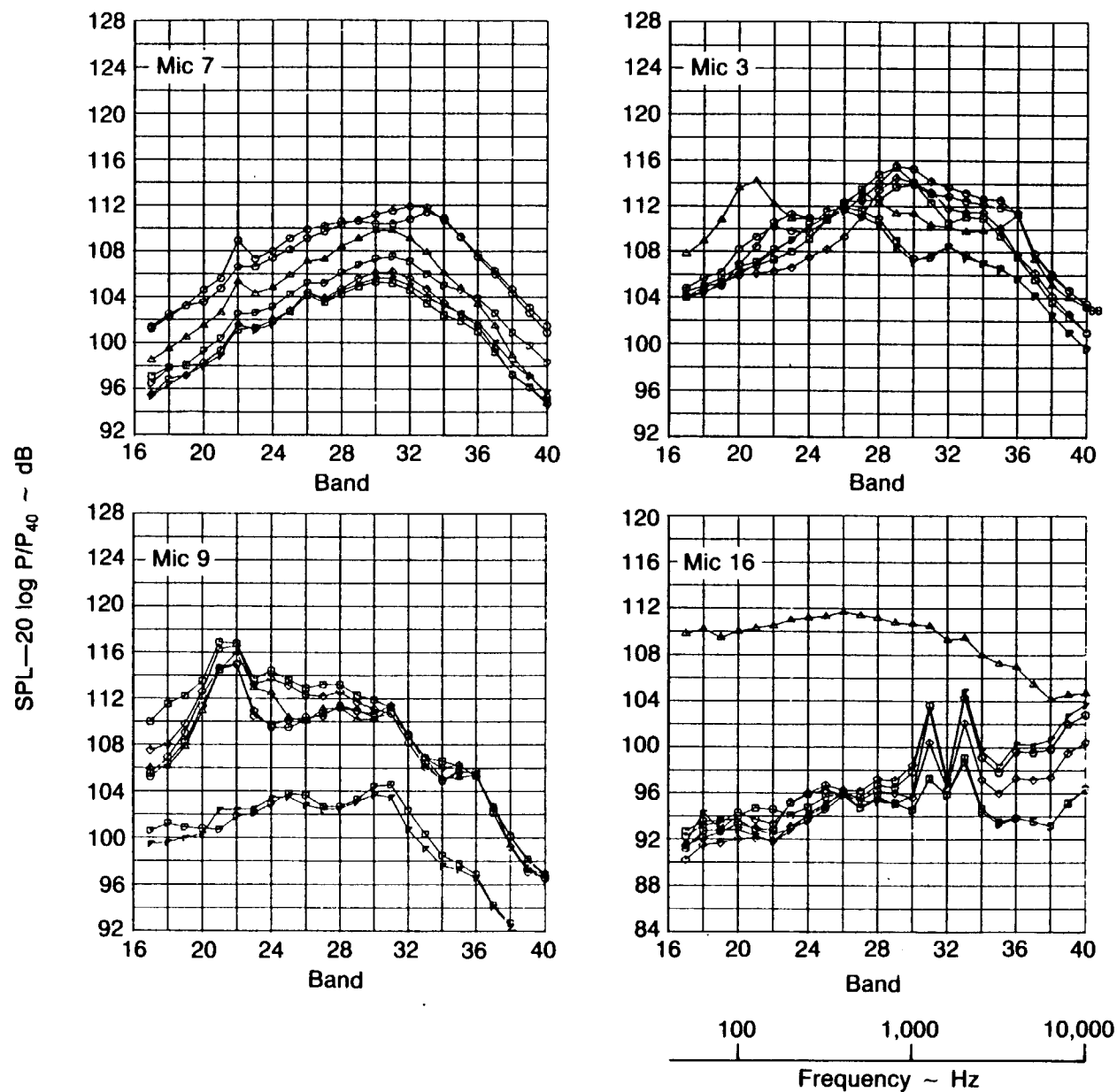


Figure 4-51. Upper Wing Probe Microphones $1/3$ Octave Spectra— $M_{AP} \approx 0.82, 0.83$

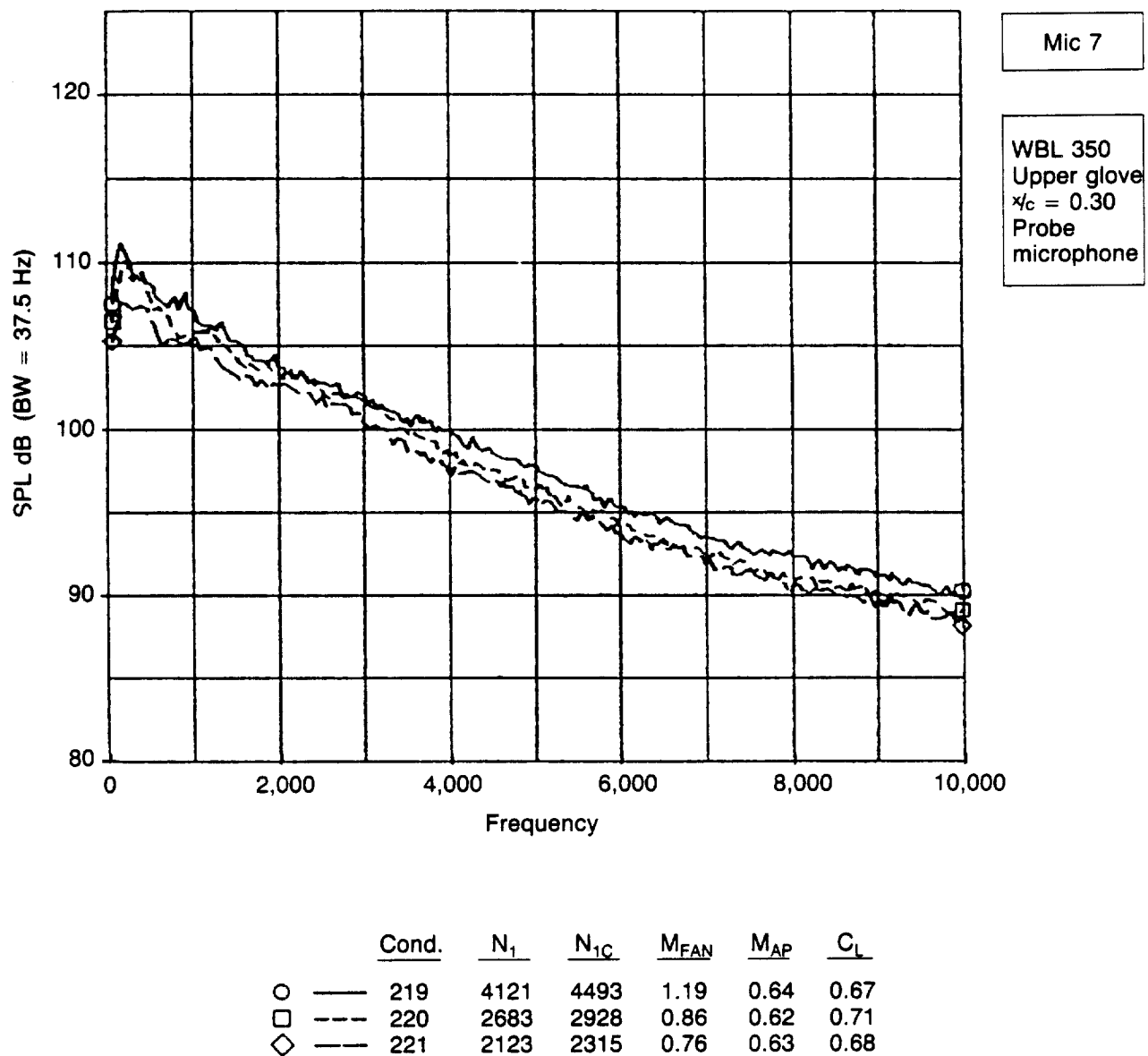
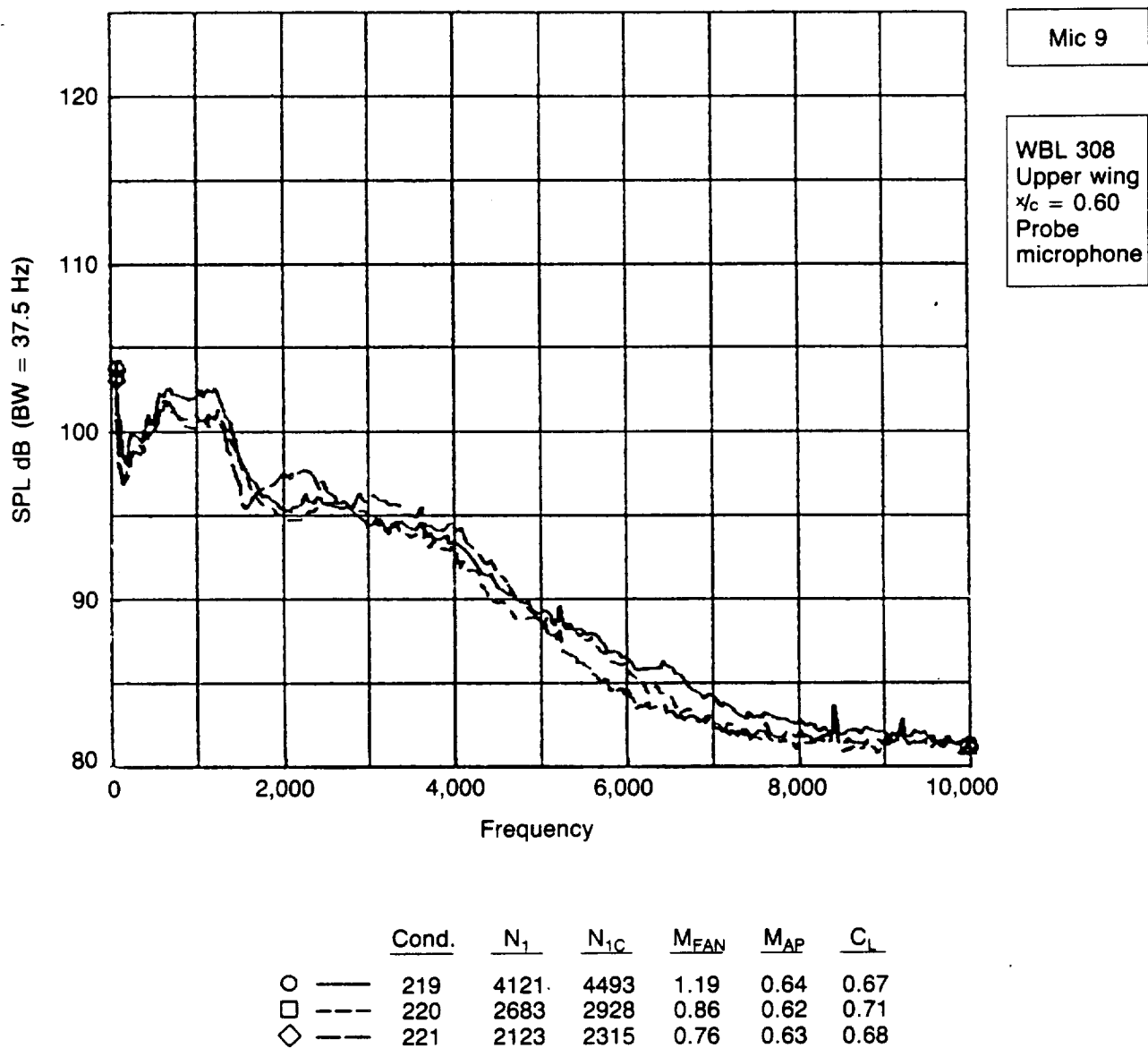


Figure 4-52. Microphone 7 Narrow Band Spectra— $M_{AP} \approx 0.62-0.64$



WBL 308
Upper wing
 $x/c = 0.60$
Probe
microphone

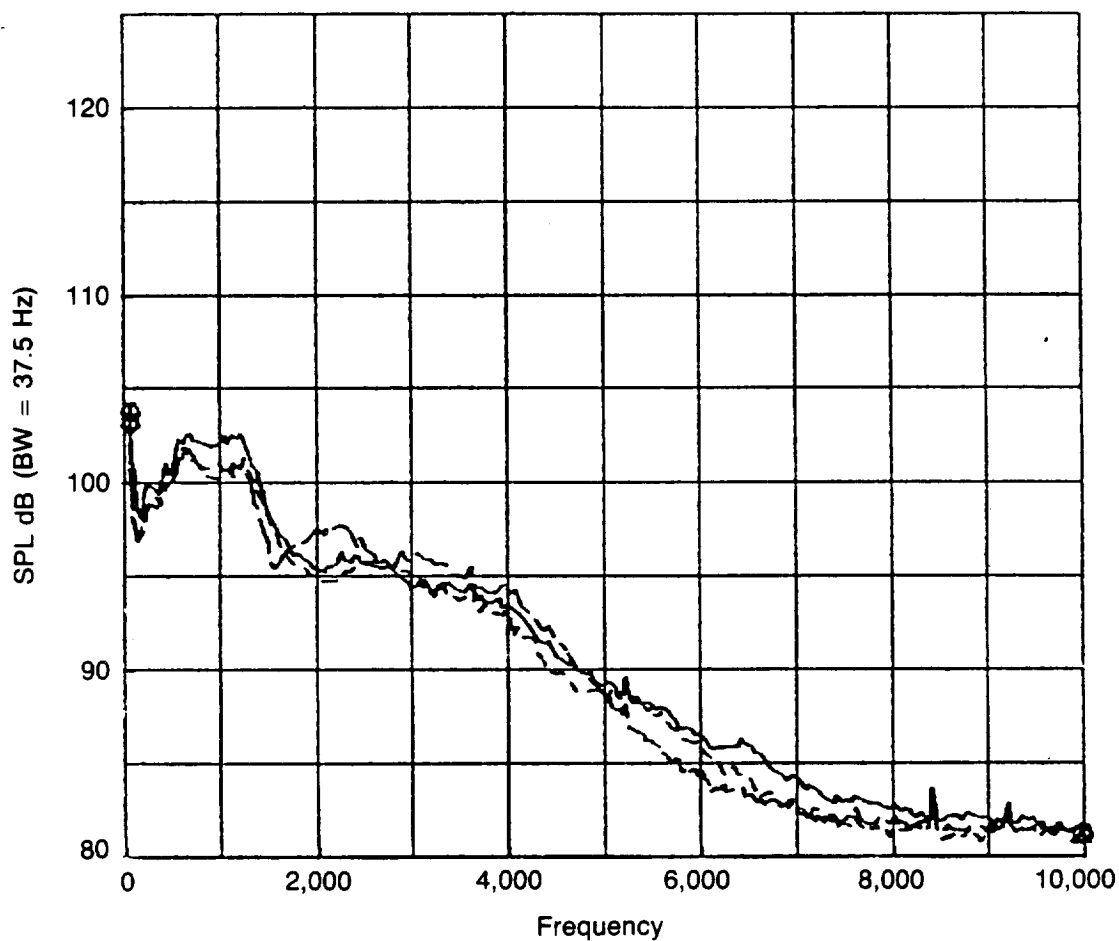


Figure 4-53. Microphone 9 Narrow Band Spectra— $M_{AP} \approx 0.62-0.64$

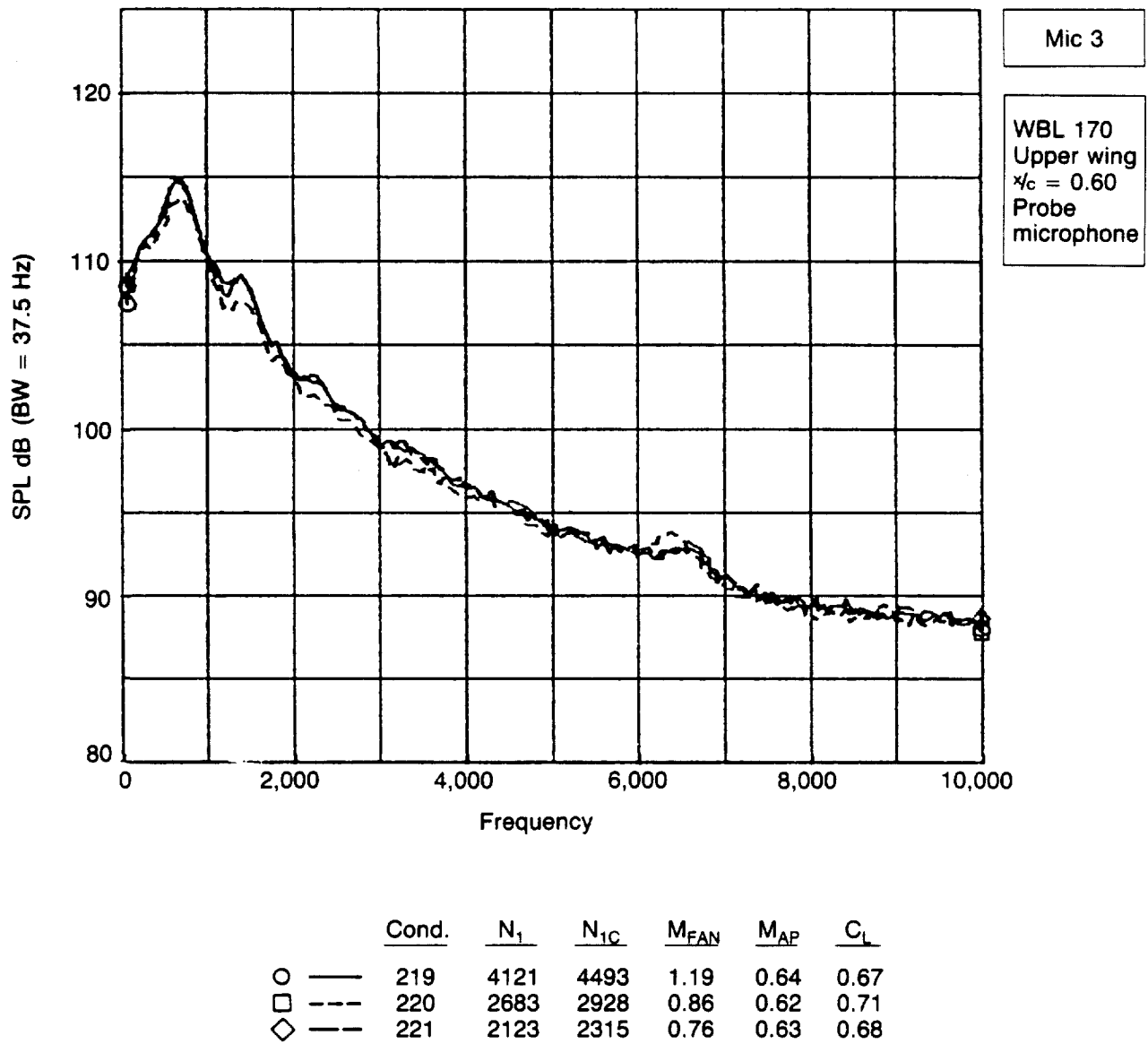
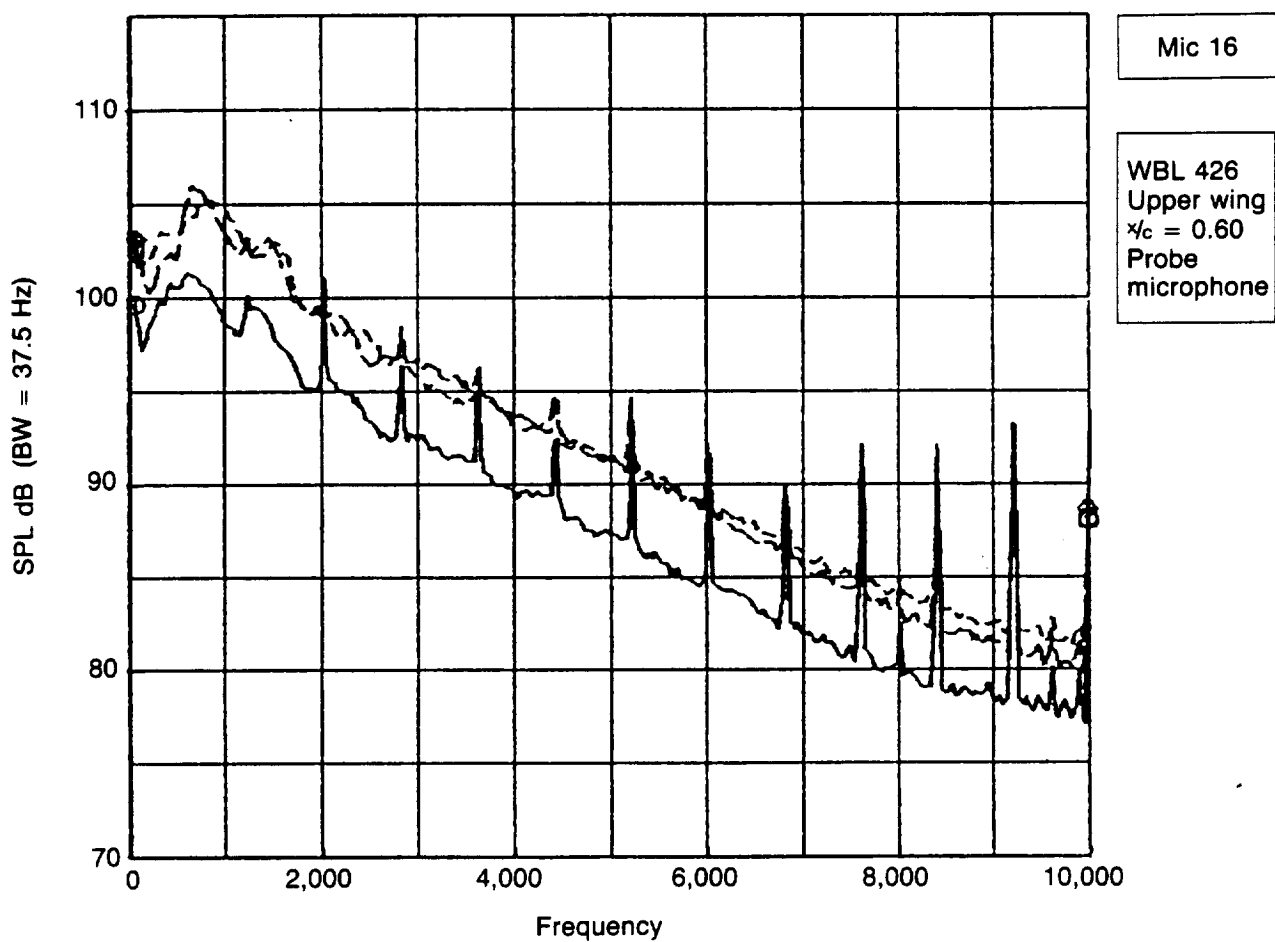


Figure 4-54. Microphone 3 Narrow Band Spectra— $M_{AP} = 0.62-0.64$



	Cond.	N_1	N_{1C}	M_{FAN}	M_{AP}	C_L
○ —	219	4121	4493	1.19	0.64	0.67
□ ---	220	2683	2928	0.86	0.62	0.71
◇ -.-	221	2123	2315	0.76	0.63	0.68

Figure 4-55. Microphone 16 Narrow Band Spectra— $M_{AP} \approx 0.62-0.64$

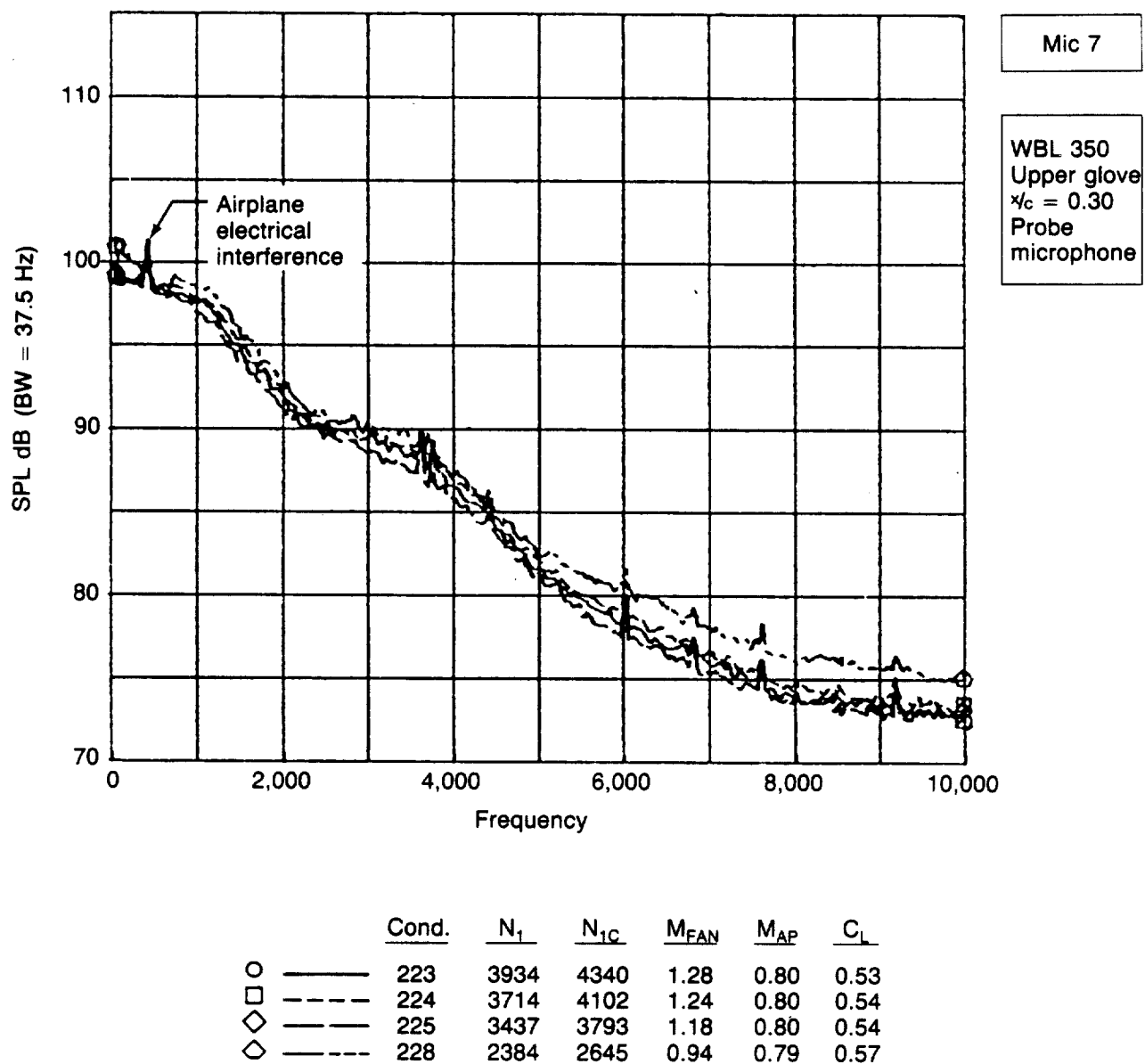


Figure 4-56. Microphone 7 Narrow Band Spectra— $M_{AP} \approx 0.79-0.80$

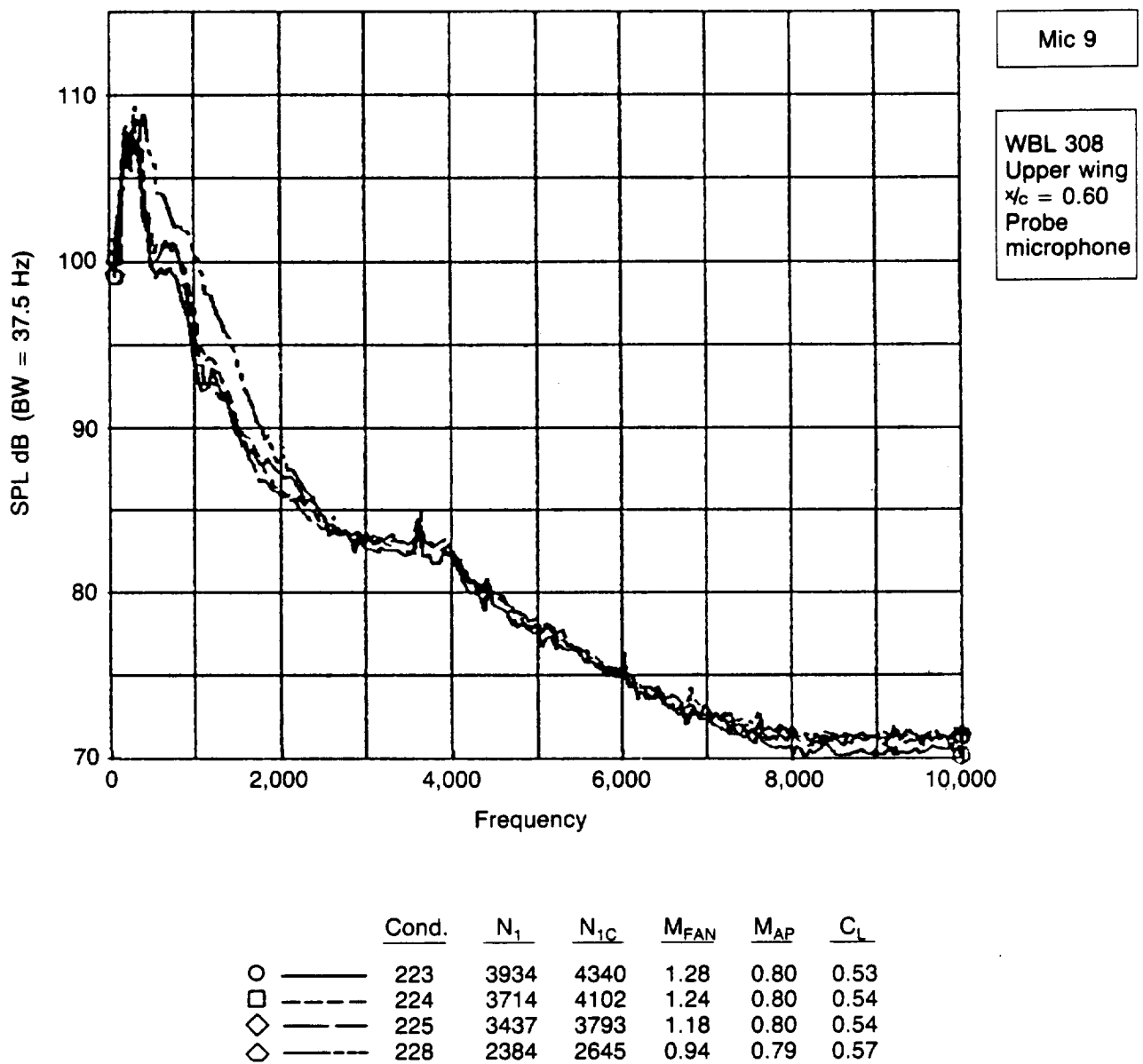


Figure 4-57. Microphone 9 Narrow Band Spectra— $M_{AP} = 0.79-0.80$

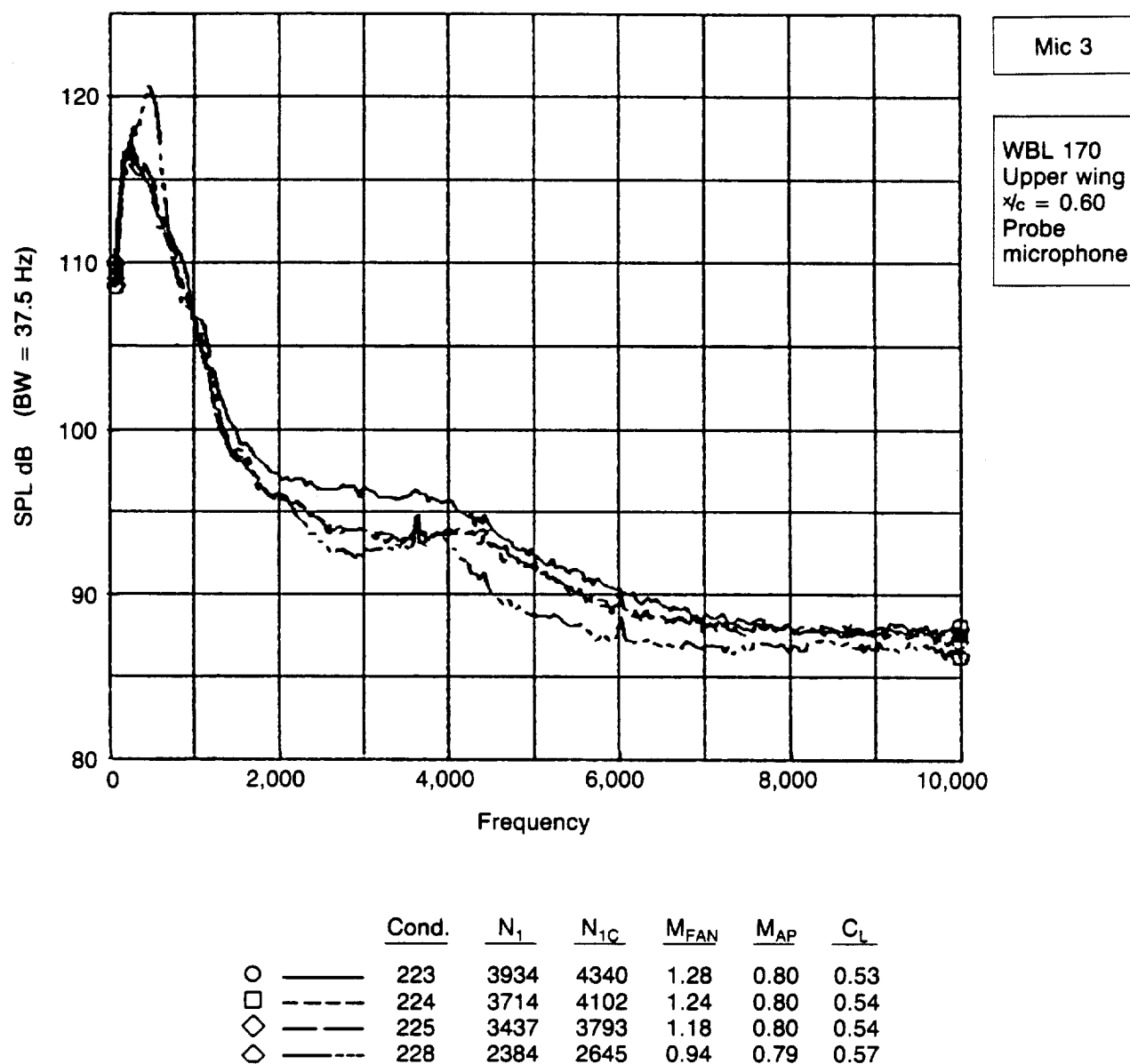


Figure 4-58. Microphone 3 Narrow Band Spectra— $M_{AP} \approx 0.79-0.80$

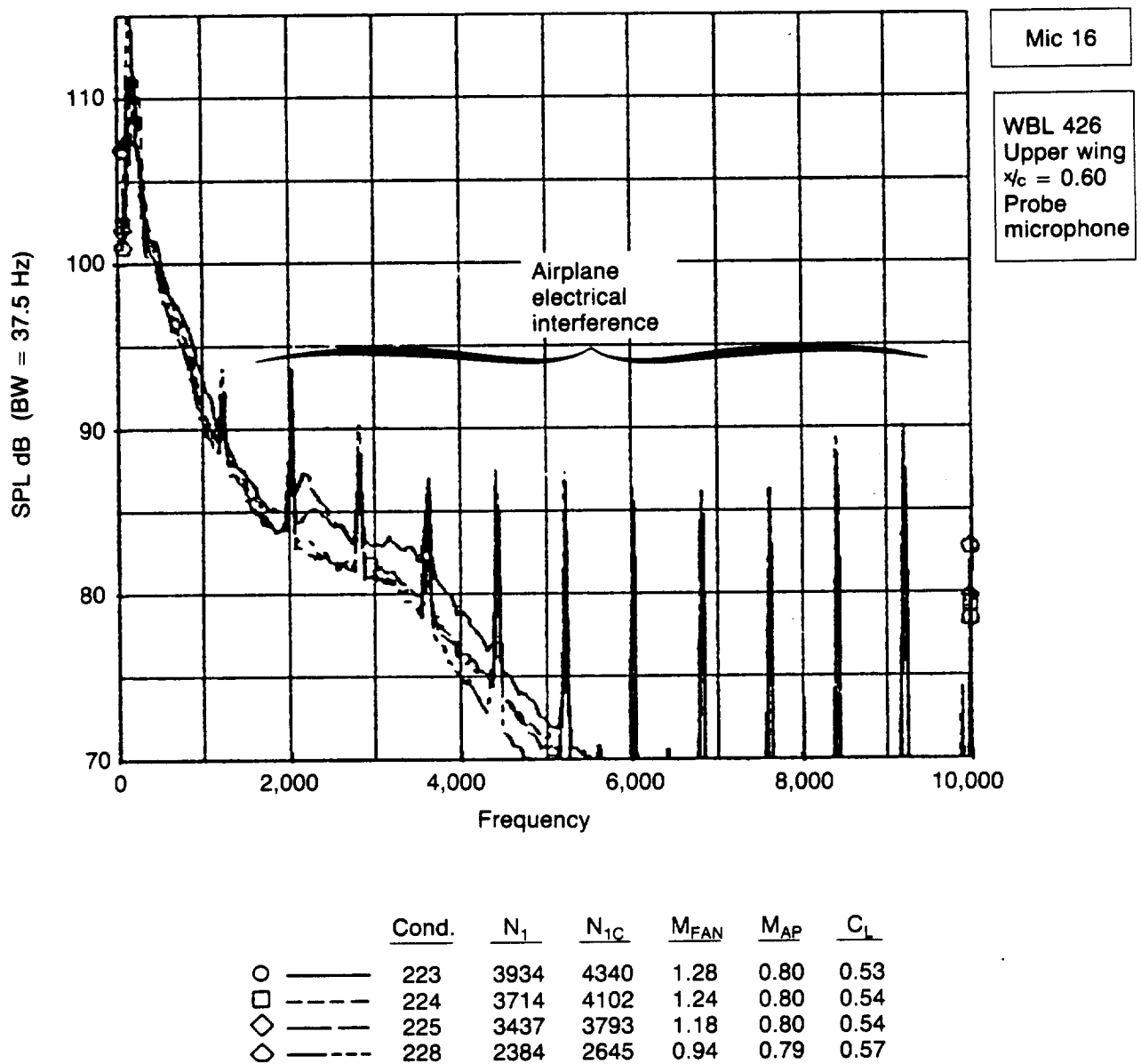


Figure 4-59. Microphone 16 Narrow Band Spectra— $M_{AP} \approx 0.79-0.80$

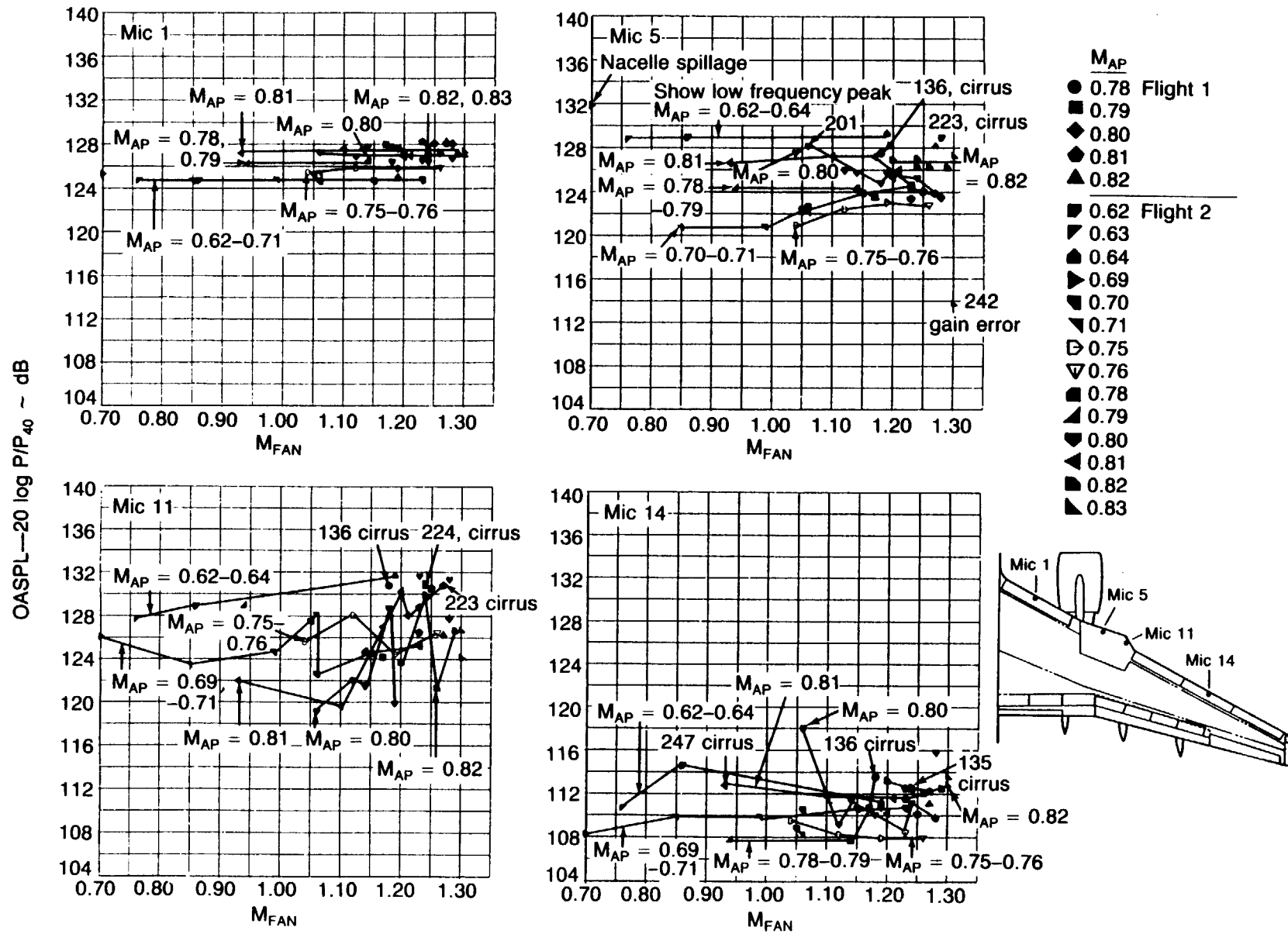


Figure 4-60. Normalized OASPL on Wing Upper Surface Leading Edge Surface Mounted Microphones vs. M_{FAN}

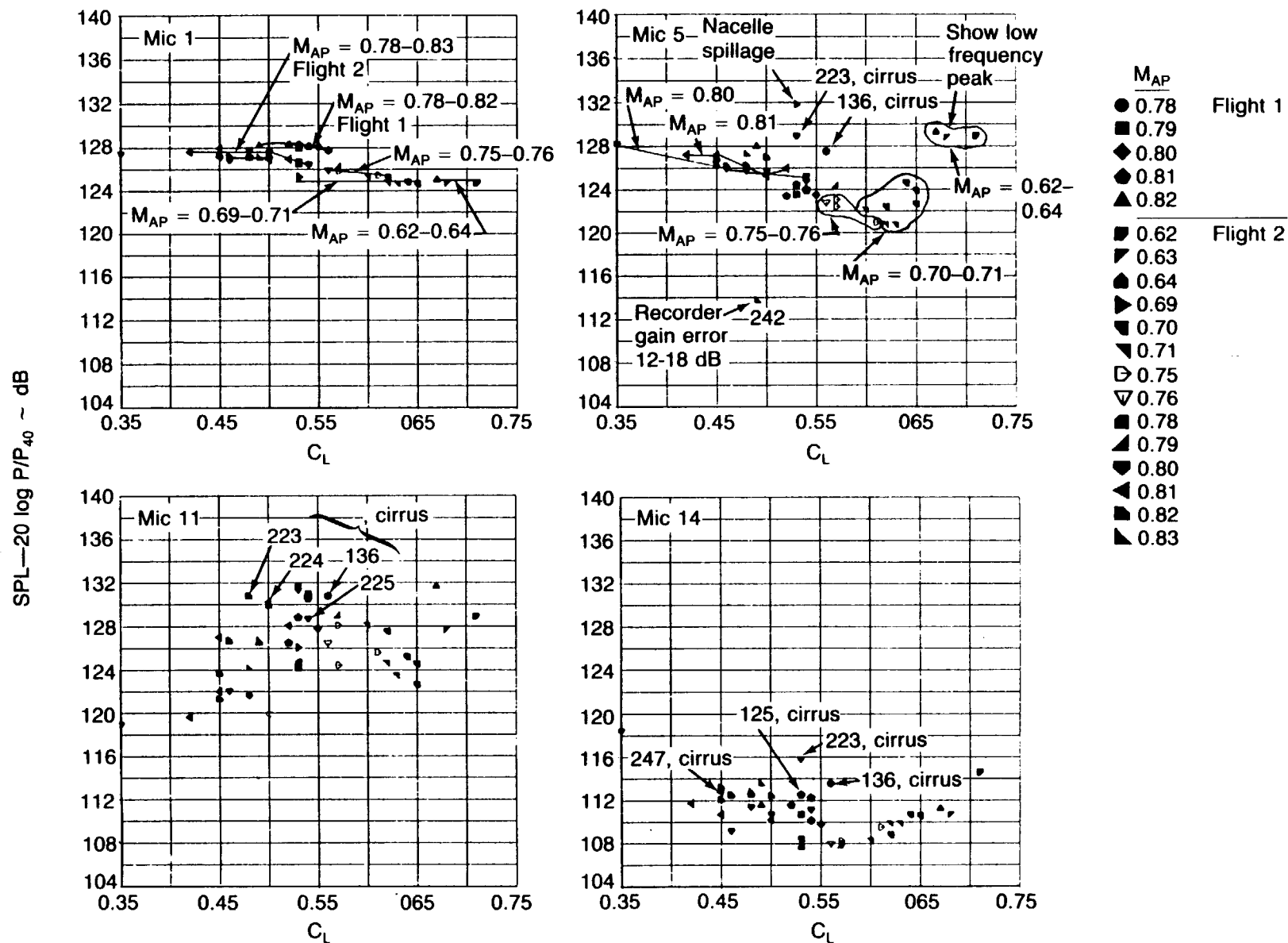


Figure 4-61. Normalized OASPL on Wing Upper Surface Leading Edge Surface Mounted Microphones vs. C_L

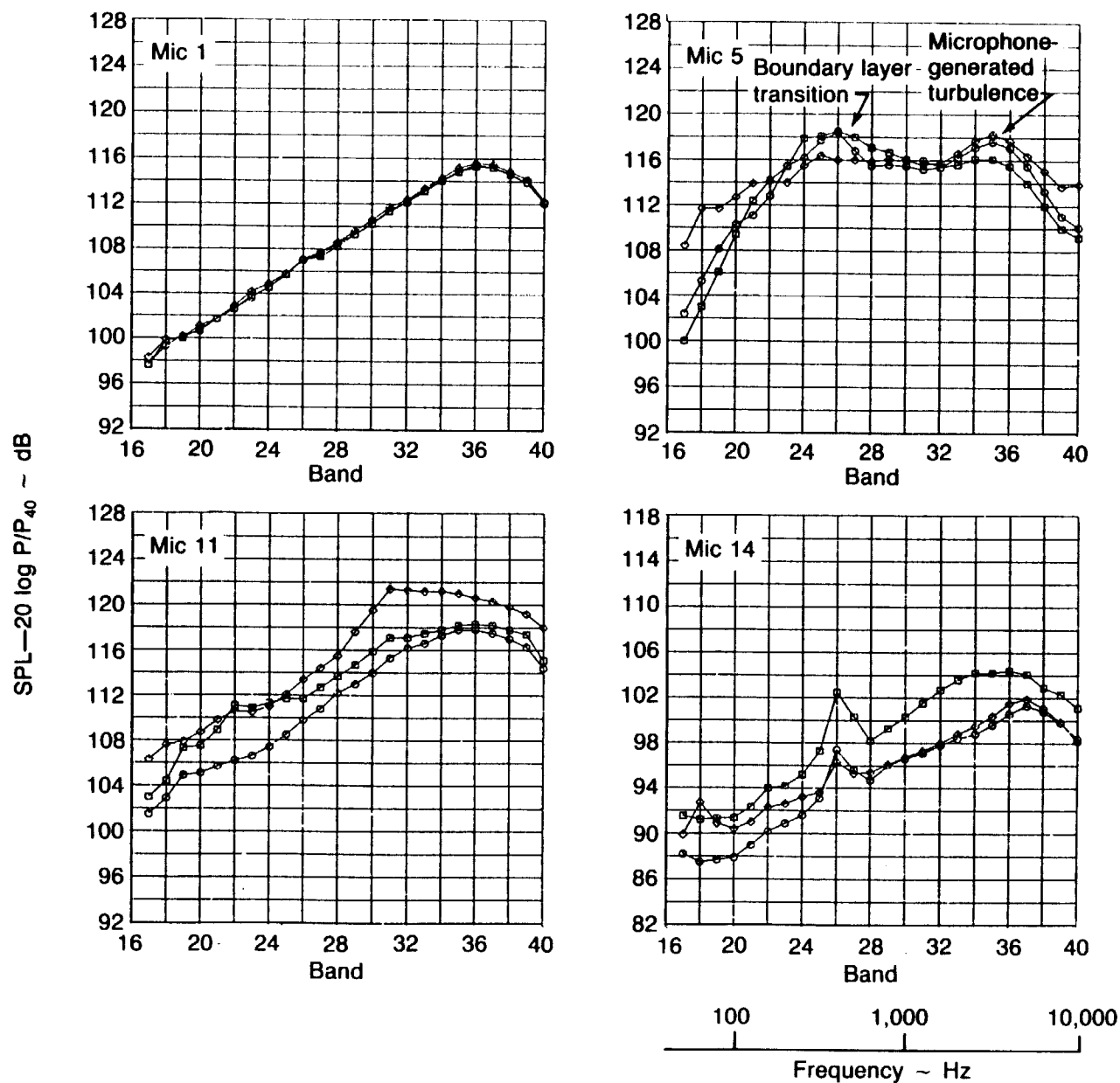
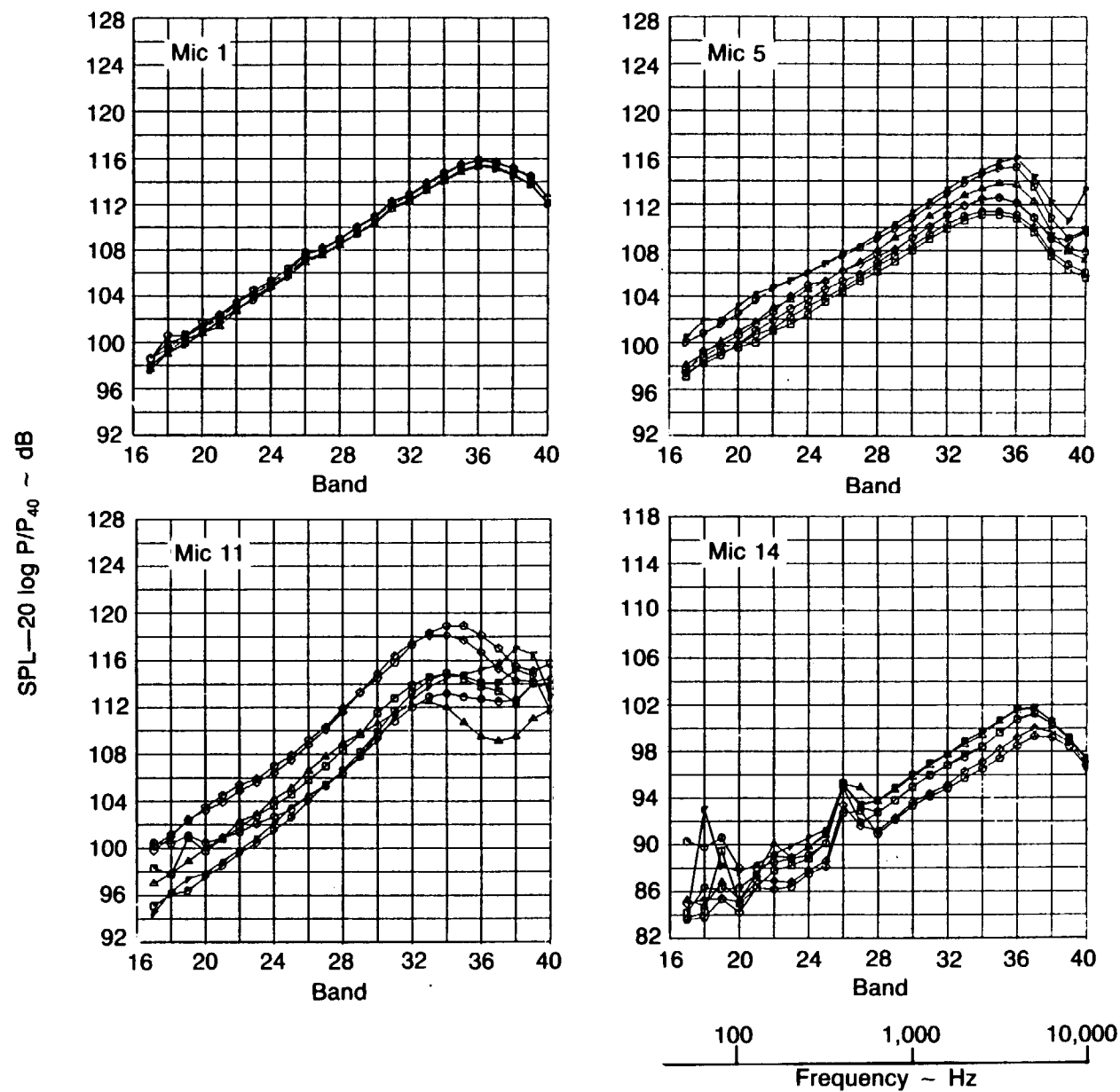


Figure 4-62. Upper Wing Leading Edge Microphones $1/3$ Octave Spectra— $M_{AP} \approx 0.62-0.64$

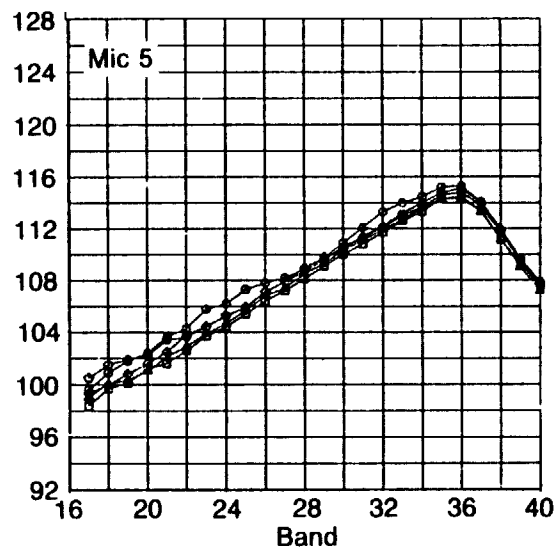
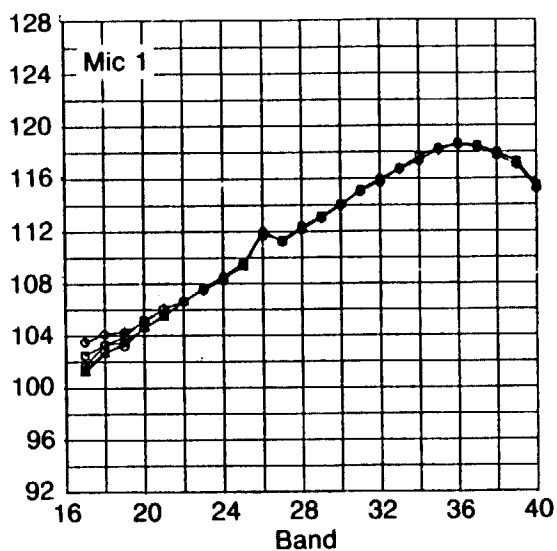


Cond.	M _{AP}	M _{FAN}	C _L
236 ○	0.71	0.85	0.62
237 □	0.71	0.99	0.63
218 ◇	0.70	1.05	0.62
217 ◇	0.71	1.06	0.60
233 △	0.70	1.06	0.65
232 ▽	0.70	1.15	0.65
231 ▽	0.70	1.23	0.64

Hot Film rms
Voltage ~ V

Cond.	x/c	
	5%	7.5%
236	0.006	0.089
237	0.005	0.087
218	0.006	0.030
217	0.010	0.034
233	0.006	0.033
232	0.006	0.034
231	0.005	0.038

Figure 4-63. Upper Wing Leading Edge Microphones 1/3 Octave Spectra— $M_{AP} \approx 0.70-0.71$



Cond.		M_{AP}	M_{FAN}	C_L
135	○	0.81	1.23	0.53
105	□	0.81	1.23	0.52
115	◇	0.81	1.25	0.54
114	◇	0.81	1.27	0.54
113	△	0.80	1.28	0.55

Hot Film rms
Voltage ~ V

Cond.	x/c	
	5%	7.5%
135	0.039	0.076
105	0.006	0.008
115	0.006	0.008
114	0.006	0.008
113	0.006	0.008

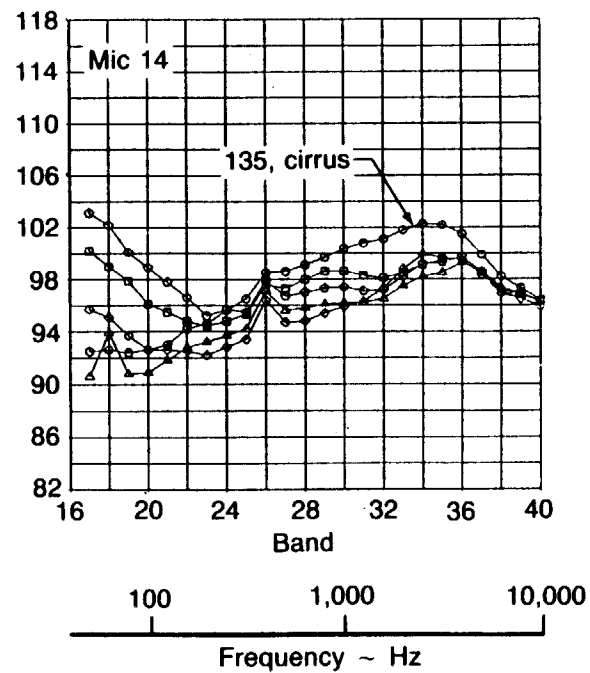
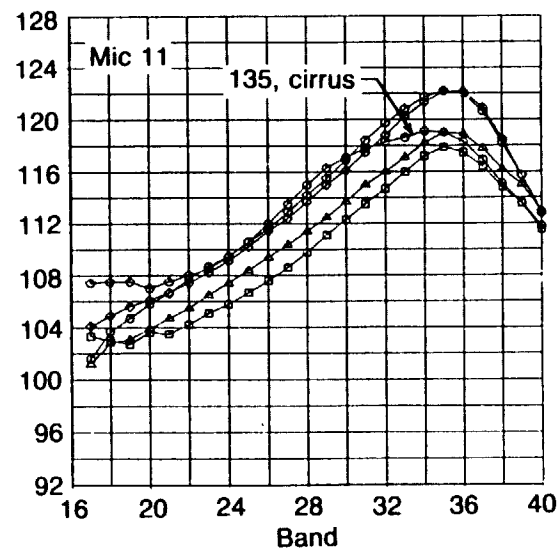
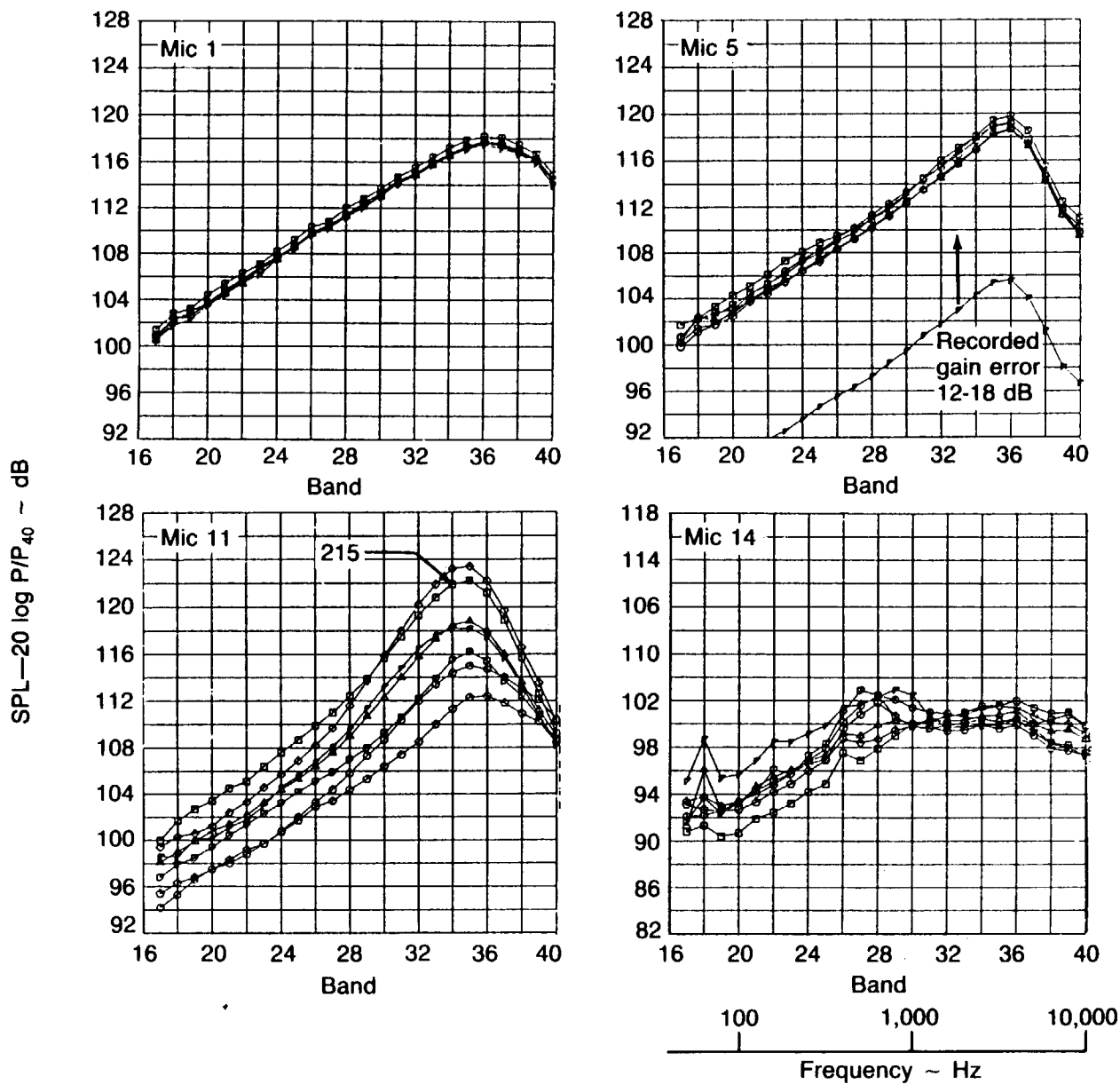


Figure 4-68. Upper Wing Leading Edge Microphones $1/3$ Octave Spectra— $M_{AP} \approx 0.80-0.81$

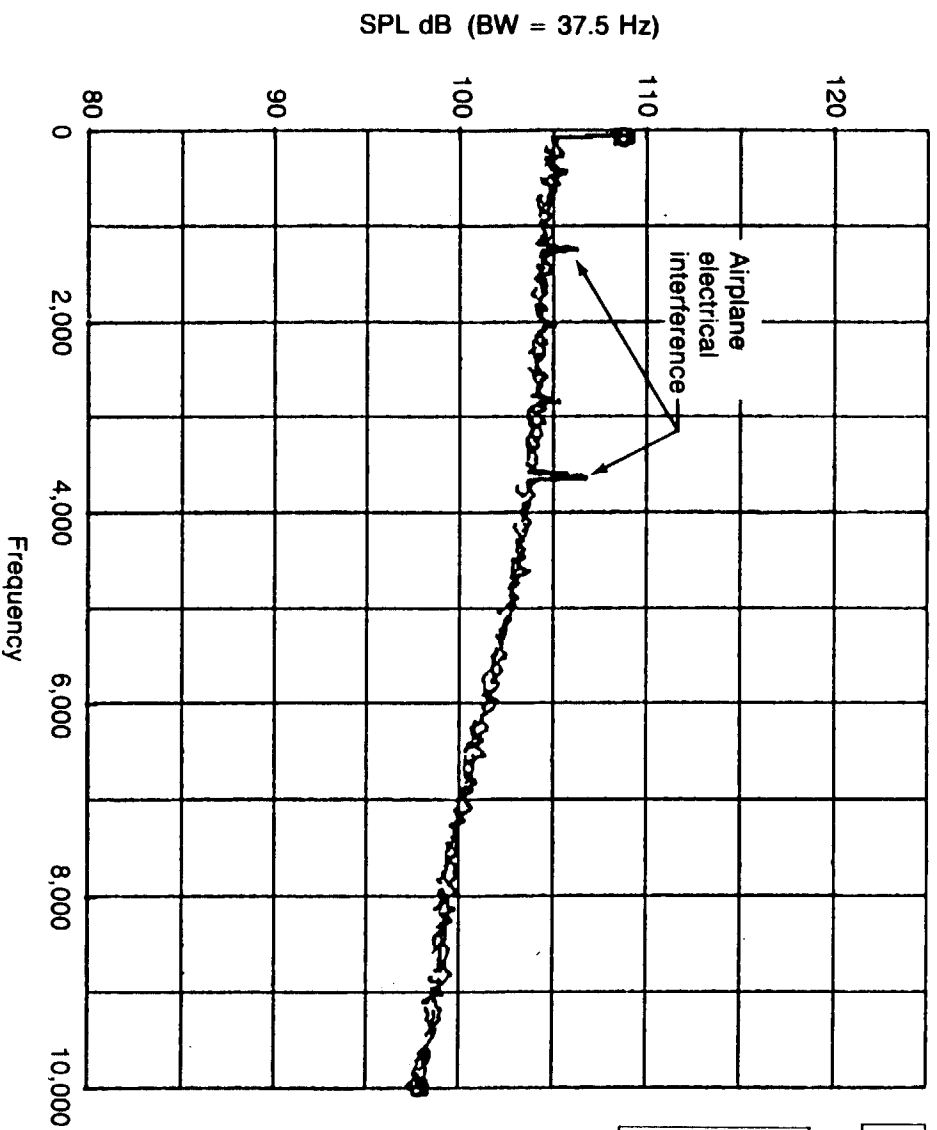


Cond.		M_{AP}	M_{FAN}	C_L
245	○	0.82	1.20	0.45
215	□	0.82	1.24	0.50
248	◇	0.82	1.24	0.48
244	◊	0.82	1.26	0.45
243	△	0.82	1.29	0.46
216	▽	0.83	1.30	0.48
242	◃	0.83	1.30	0.49

Hot Film rms
Voltage ~ V

Cond.	x/c	
	5%	7.5%
245	0.006	0.010
215	0.032	0.061
248	0.005	0.008
244	0.006	0.008
243	0.006	0.008
216	0.005	0.008
242	0.006	0.008

Figure 4-69. Upper Wing Leading Edge Microphones $\frac{1}{3}$ Octave Spectra— $M_{AP} \approx 0.82-0.83$



	Cond.	N_1	N_{1C}	M_{EAN}	M_{AP}	C_L
○	219	4121	4493	1.19	0.64	0.67
□	220	2683	2928	0.86	0.62	0.71
◇	221	2123	2315	0.76	0.62	0.68

Figure 4-70. Microphone 1 Narrow Band Spectra— $M_{AP} \approx 0.62$ —0.64

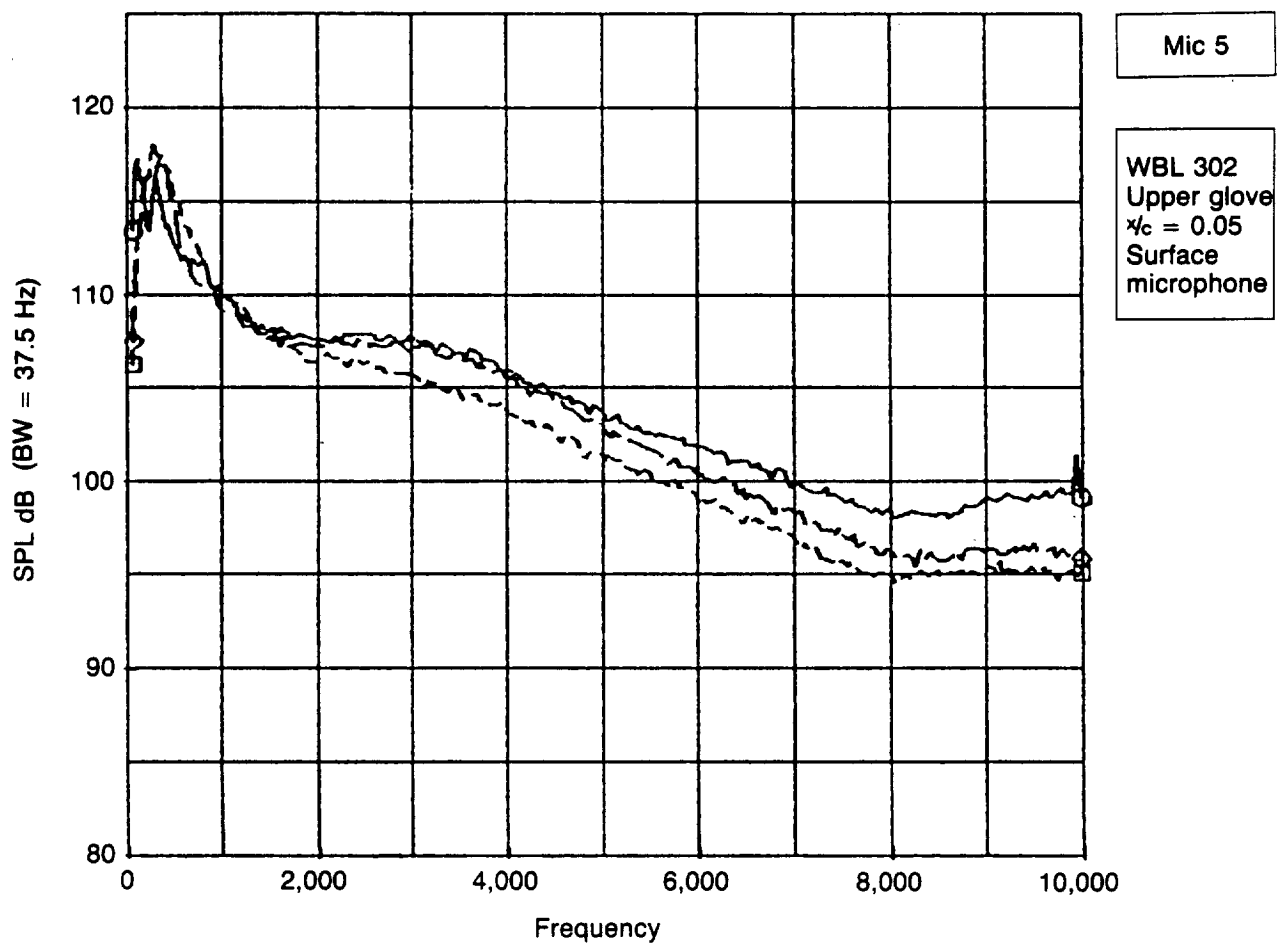


Figure 4-71. Microphone 5 Narrow Band Spectra— $M_{AP} = 0.62$ — 0.64

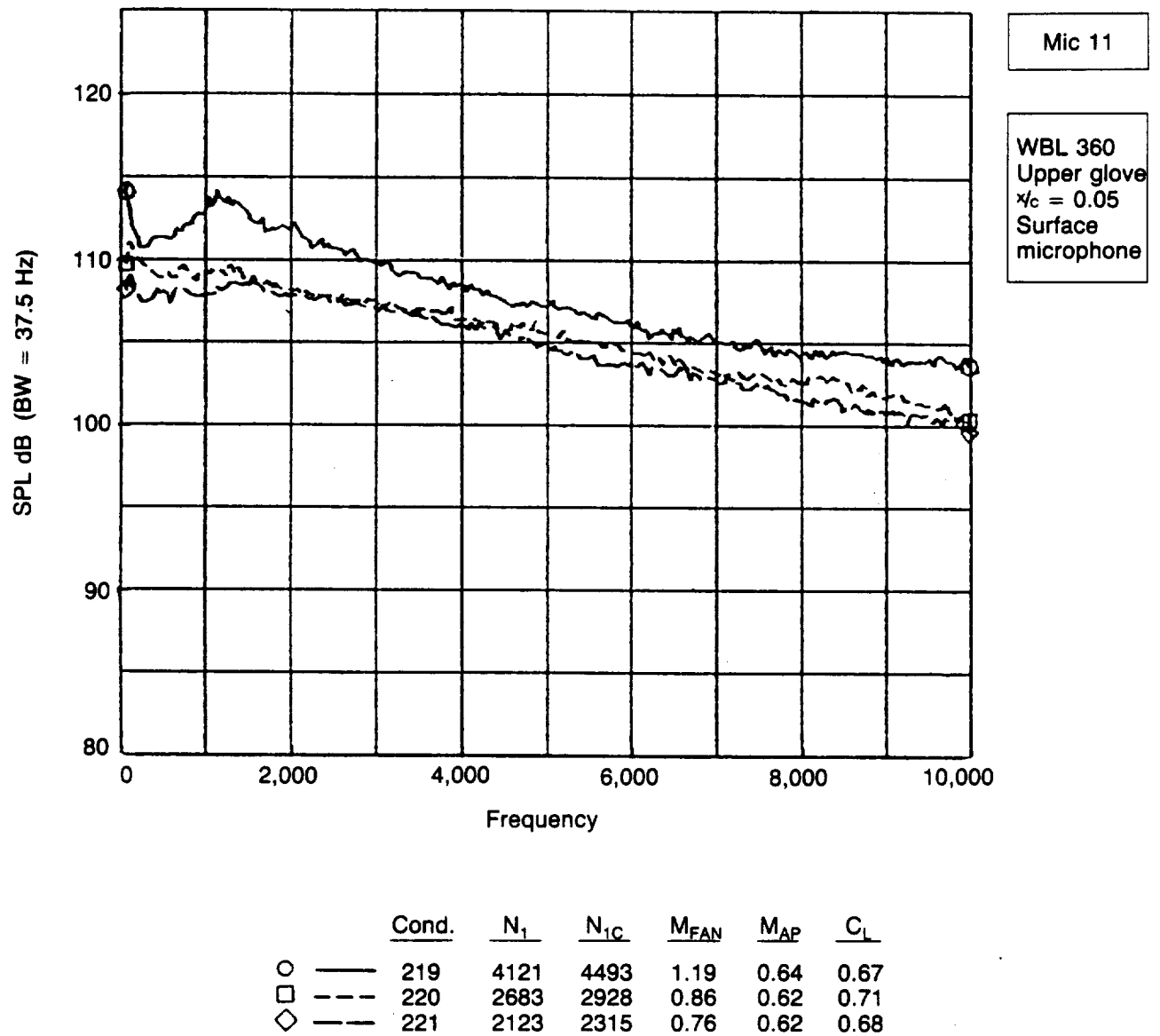


Figure 4-72. Microphone 11 Narrow Band Spectra— $M_{AP} \approx 0.62$ — 0.64

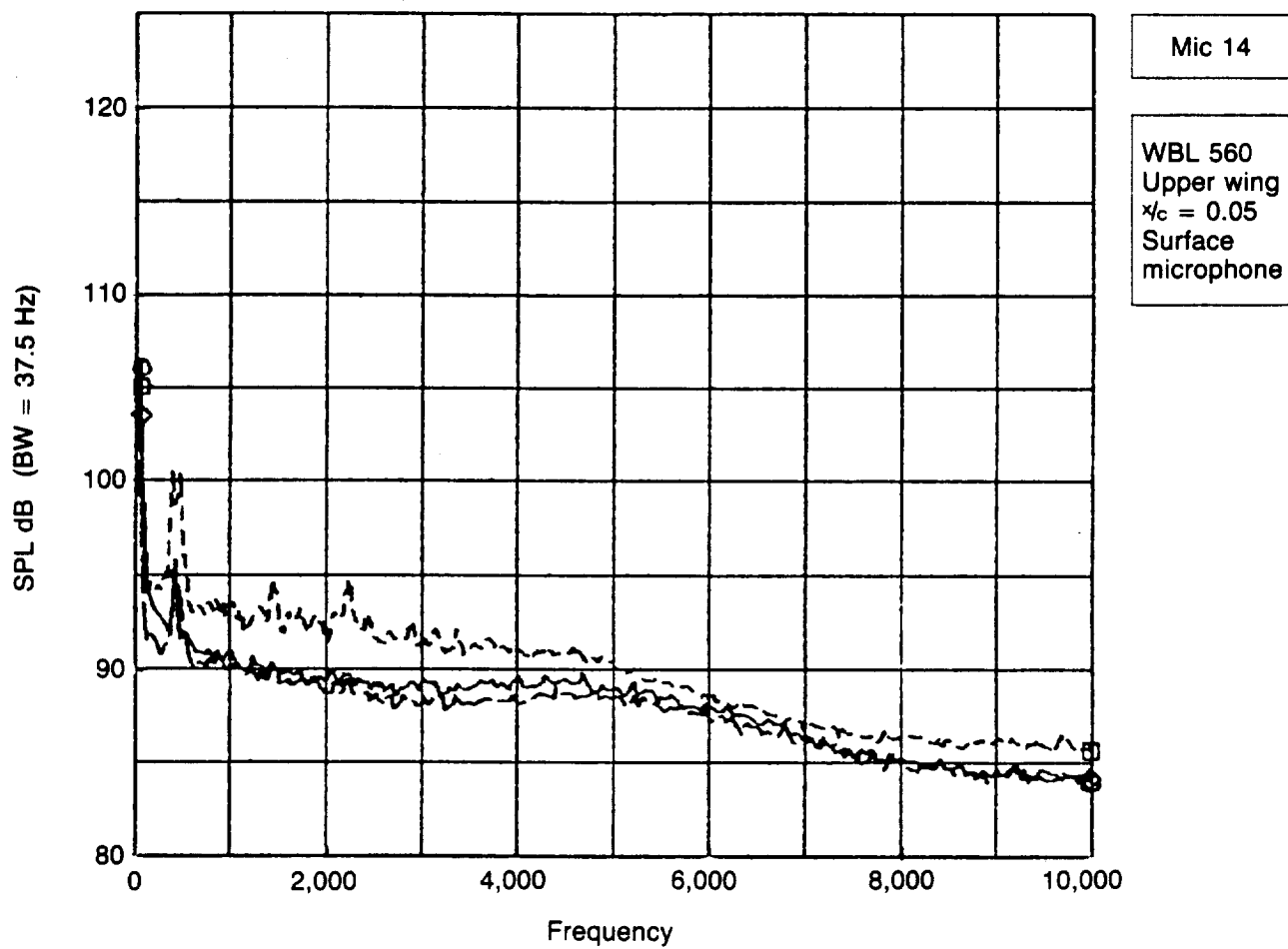


Figure 4-73. Microphone 14 Narrow Band Spectra— $M_{AP} \approx 0.62-0.64$

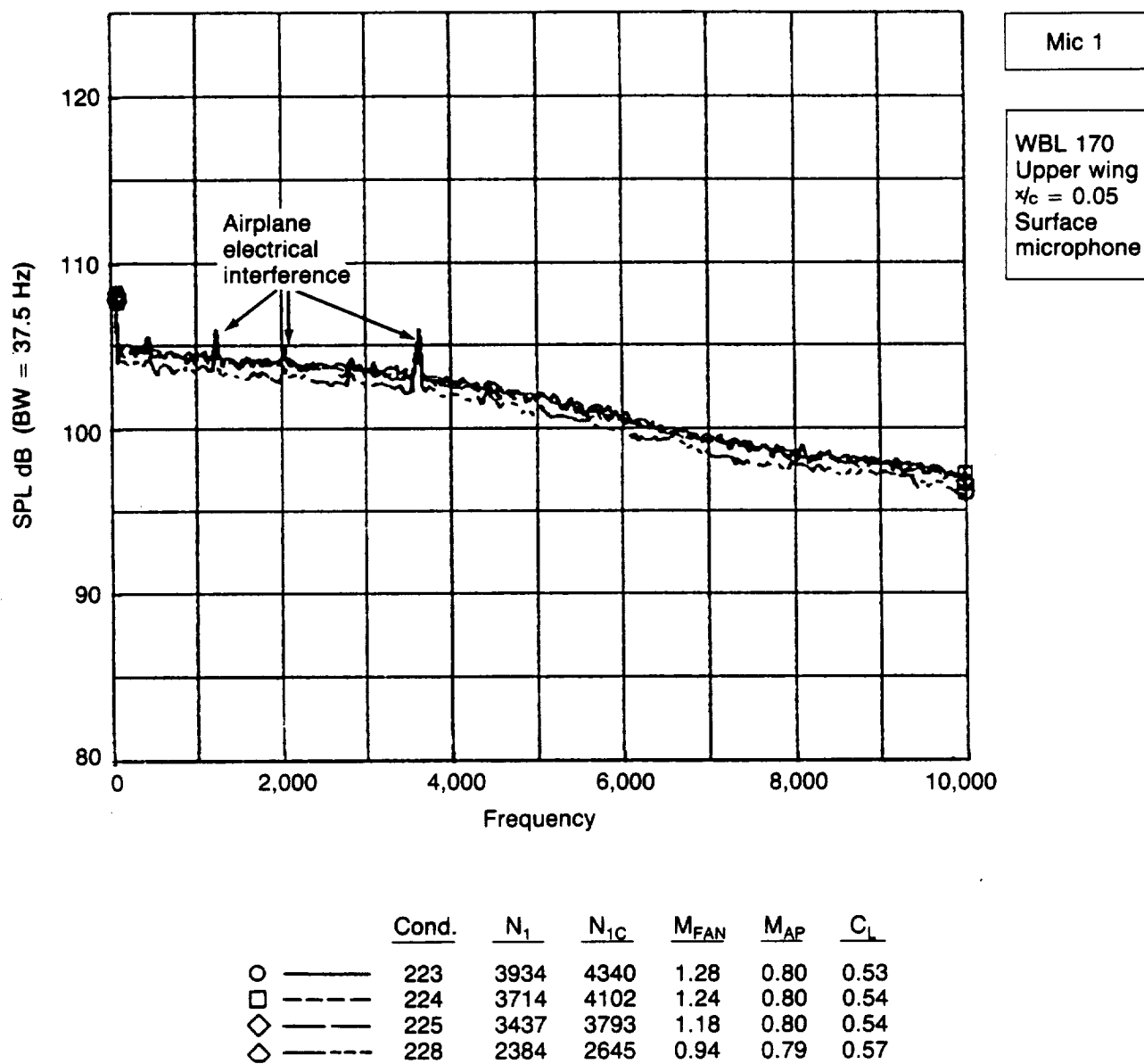
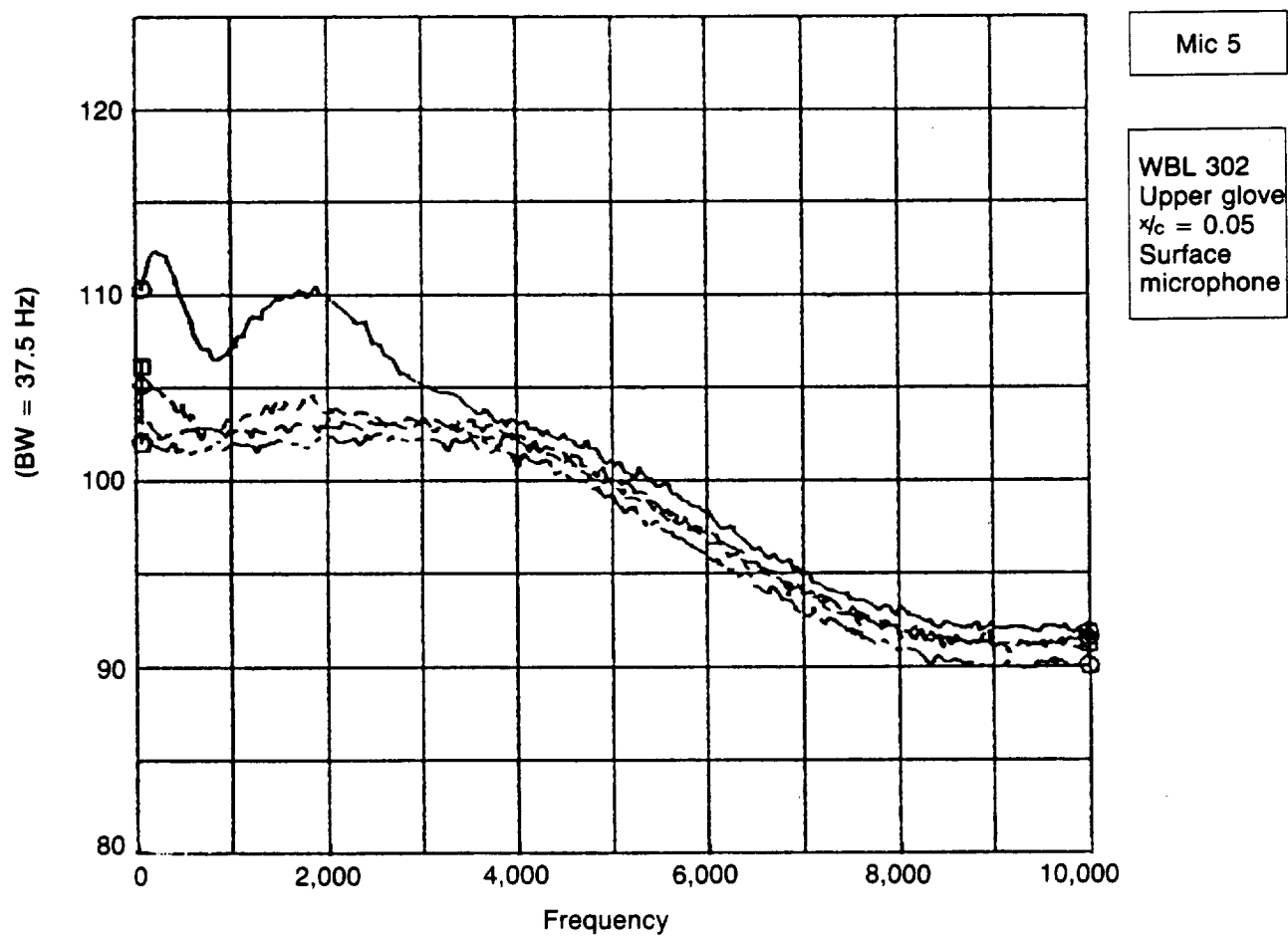
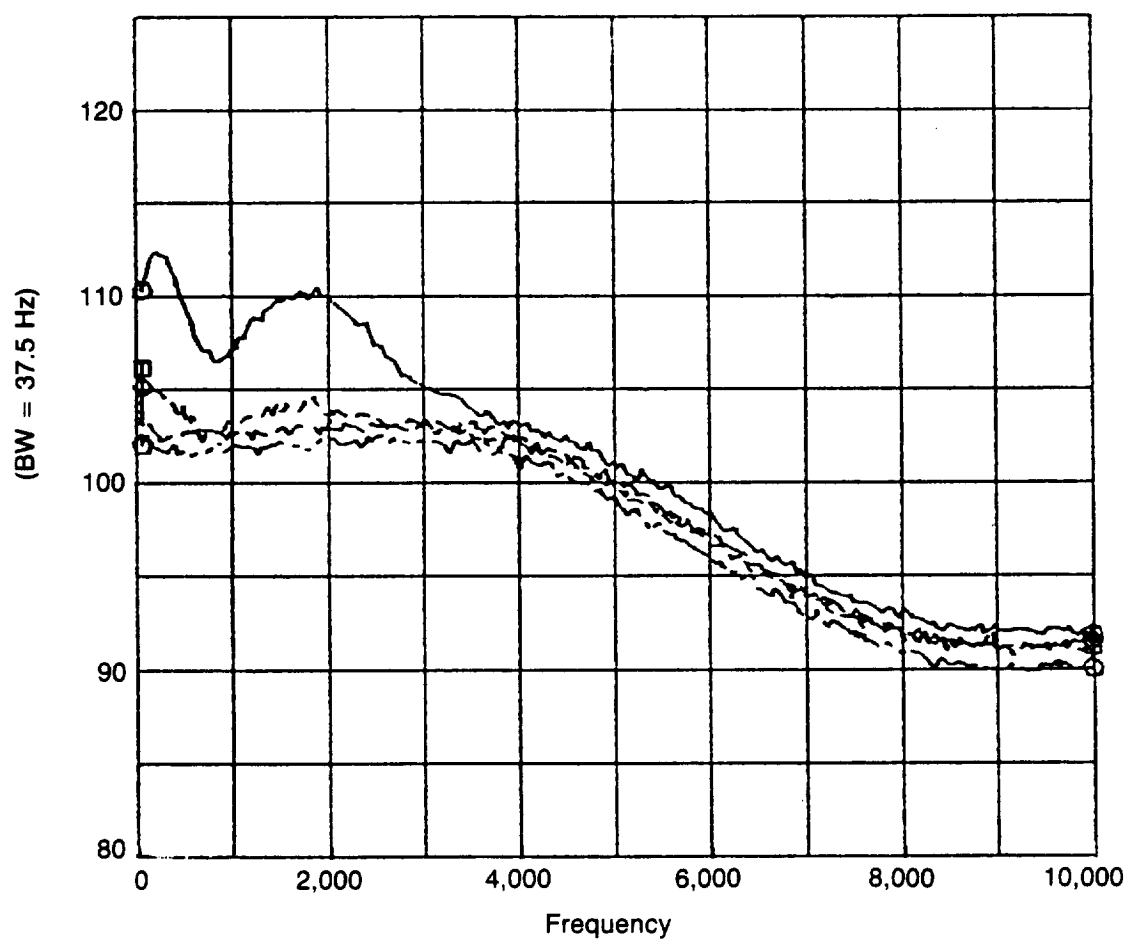


Figure 4-74. Microphone 1 Narrow Band Spectra— $M_{AP} \approx 0.79-0.80$



WBL 302
Upper glove
 $\chi_c = 0.05$
Surface
microphone



		Cond.	N_1	N_{1C}	M_{FAN}	M_{AP}	C_L
○	—	223	3934	4340	1.28	0.80	0.53
□	----	224	3714	4102	1.24	0.80	0.54
◇	—	225	3437	3793	1.18	0.80	0.54
◇	----	228	2384	2645	0.94	0.79	0.57

Figure 4-75. Microphone 5 Narrow Band Spectra— $M_{AP} \approx 0.79$ — 0.80

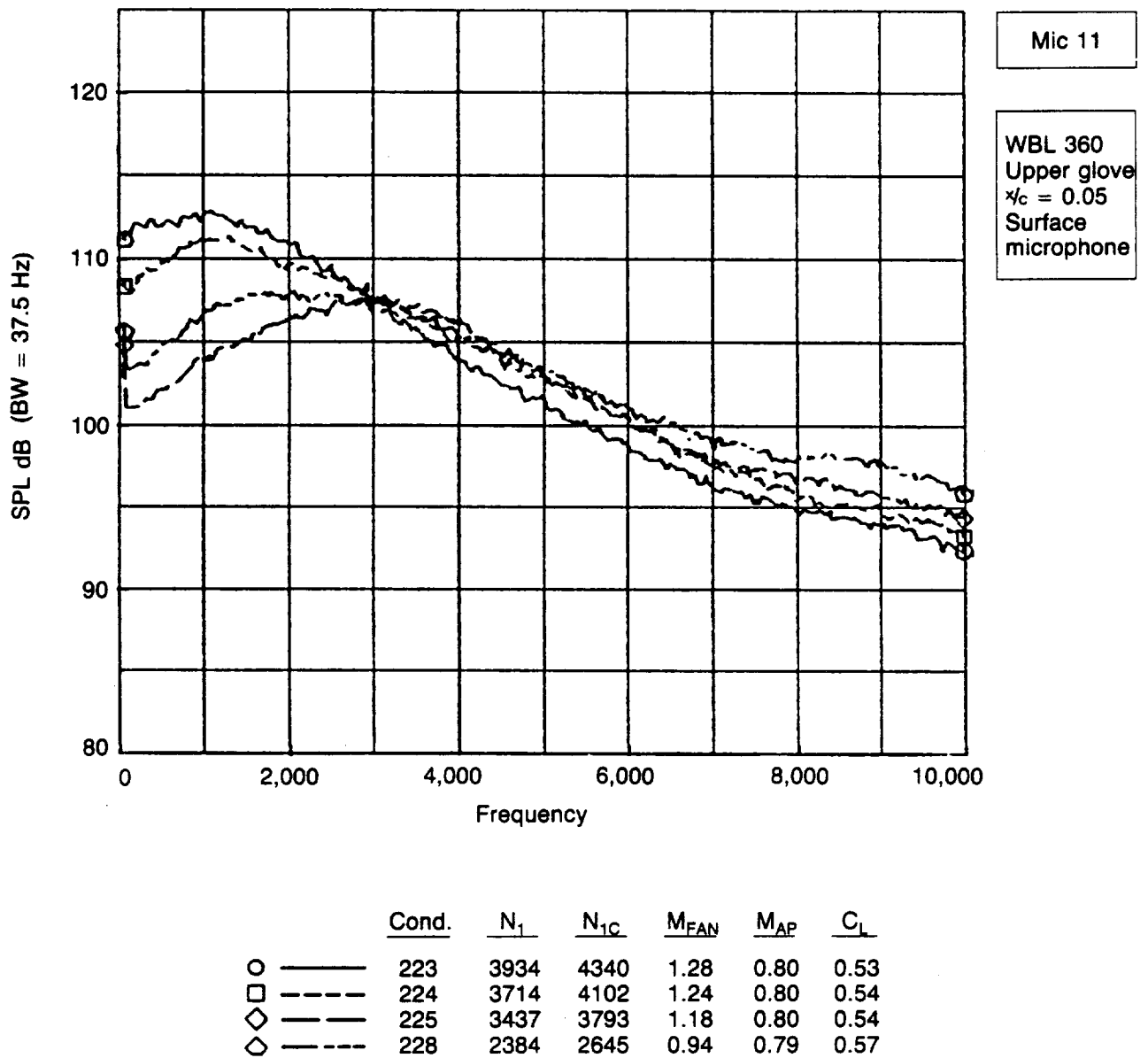
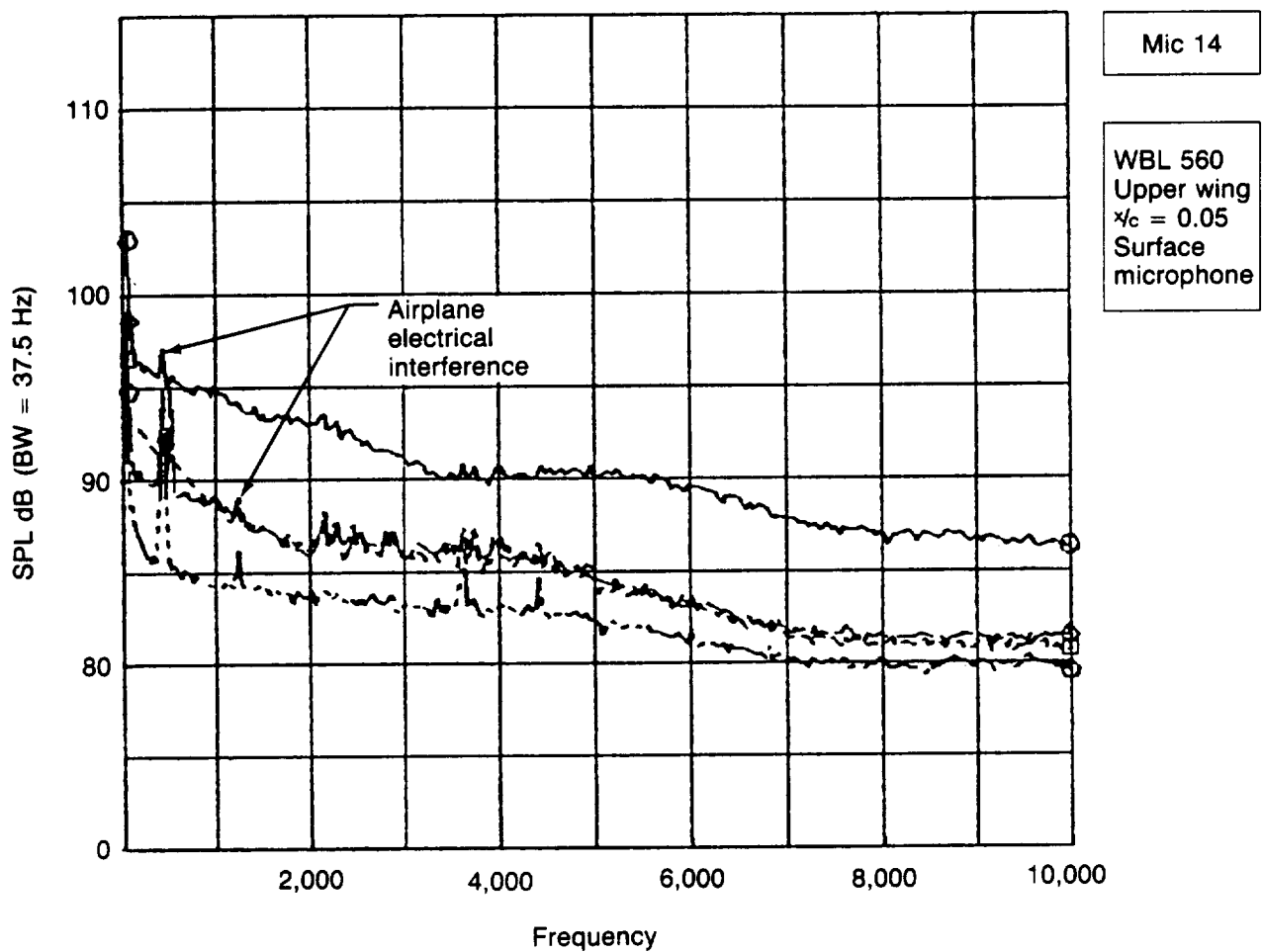


Figure 4-76. Microphone 11 Narrow Band Spectra— $M_{AP} \approx 0.79$ — 0.80



	Cond.	N_1	N_{1C}	M_{FAN}	M_{AP}	C_L
○ ———	223	3934	4340	1.28	0.80	0.53
□ - - - -	224	3714	4102	1.24	0.80	0.54
◇ ———	225	3437	3793	1.18	0.80	0.54
◇ - - - -	228	2384	2645	0.94	0.79	0.57

Figure 4-77. Microphone 14 Narrow Band Spectra— $M_{AP} = 0.79-0.80$

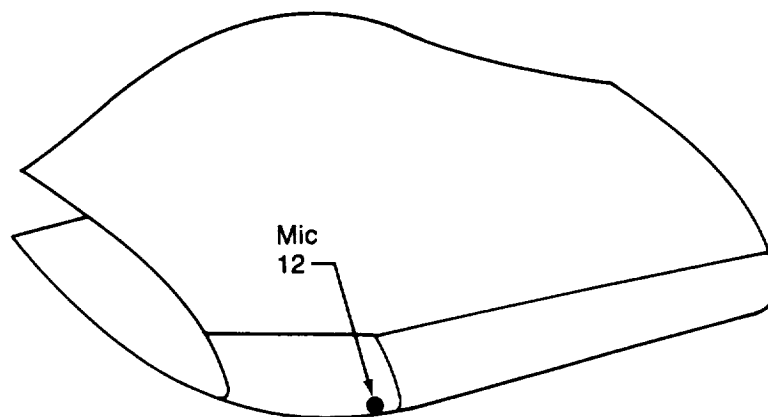
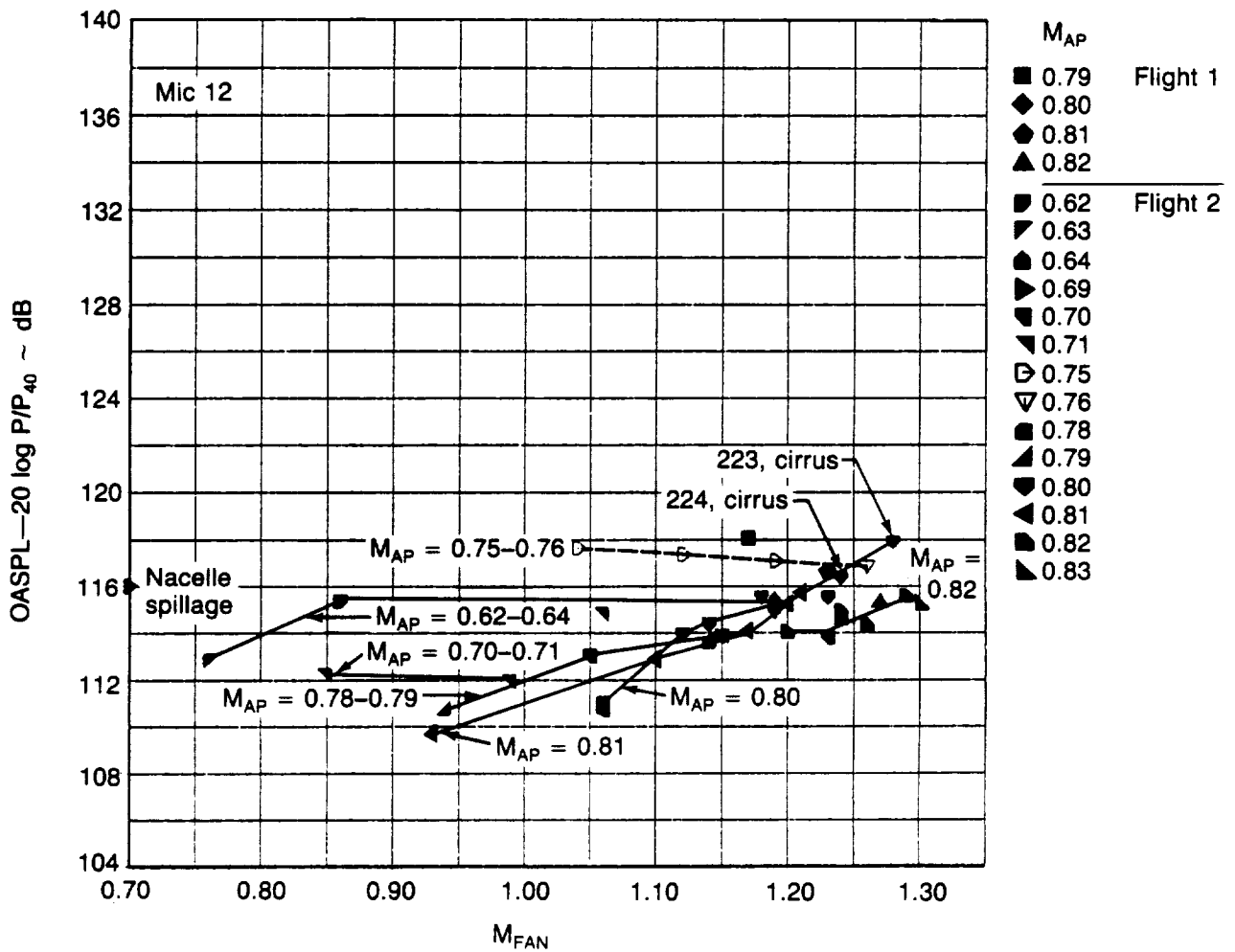
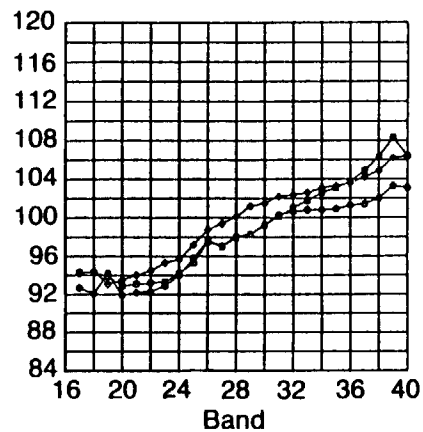
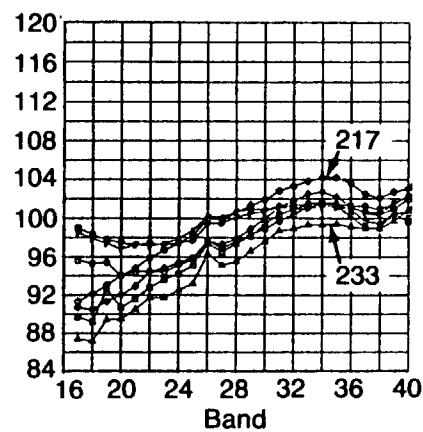


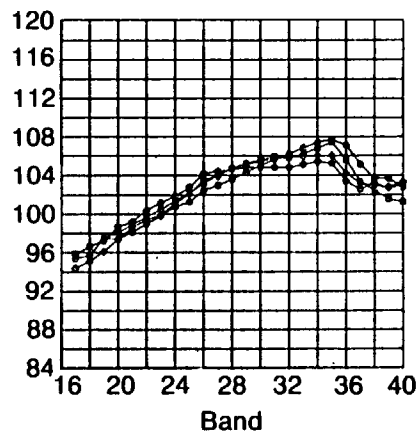
Figure 4-78. Normalized OASPL at Wing Stagnation Line Microphone vs. M_{FAN}

SPL—20 log P/P₄₀ ~ dB

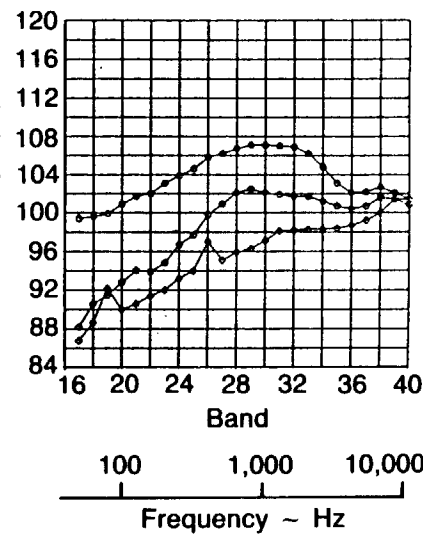
Cond.		M_{AP}	M_{FAN}	C_L
221	○	0.63	0.76	0.68
220	□	0.62	0.86	0.71
219	◇	0.64	1.19	0.67
α_B (deg)				
221		5.40		
220		5.64		
219		5.28		



Cond.		M_{AP}	M_{FAN}	C_L
236	○	0.71	0.85	0.62
237	□	0.71	0.99	0.63
218	◇	0.70	1.05	0.62
217	◇	0.71	1.06	0.60
233	△	0.70	1.06	0.65
232	▽	0.70	1.15	0.65
231	▽	0.70	1.23	0.64
α_B (deg)				
236		4.47		
237		4.39		
218		4.38		
217		4.18		
233		4.65		
232		4.59		
231		4.58		

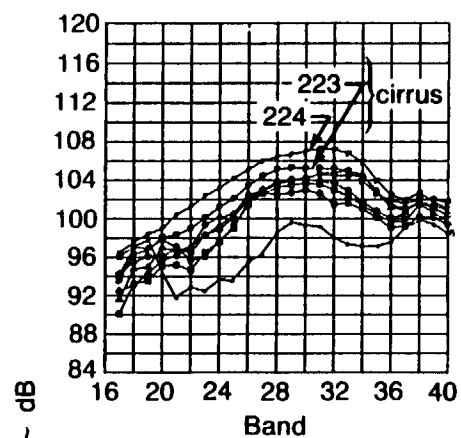


Cond.		M_{AP}	M_{FAN}	C_L
229	○	0.75	1.04	0.61
250	□	0.75	1.12	0.57
252	◇	0.75	1.19	0.57
251	◇	0.76	1.26	0.56
α_B (deg)				
229		3.86		
250		3.63		
252		3.52		
251		3.51		



Cond.		M_{AP}	M_{FAN}	C_L
109	○	0.79	1.17	0.53
228	◇	0.79	0.94	0.57
249	◇	0.78	1.14	0.53
α_B (deg)				
109		3.03		
228		3.36		
249		3.04		

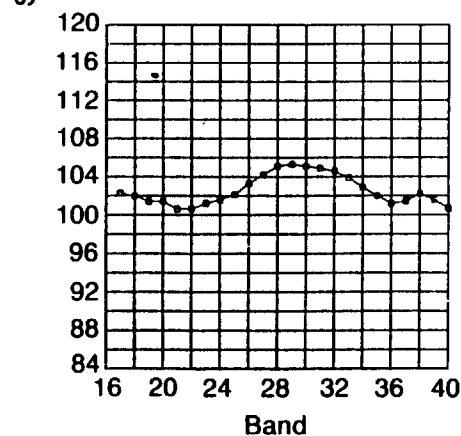
Figure 4-79. Stagnation Point Microphone (Mic 12) $1/3$ Octave Spectra



Cond.		M_{AP}	M_{FAN}	C_L
201	●	0.80	1.06	0.35
239	○	0.80	1.12	0.46
210	□	0.80	1.14	0.48
225	◇	0.80	1.18	0.54
211	◊	0.80	1.19	0.50
241	△	0.80	1.23	0.53
224	▽	0.80	1.24	0.54
223	▽	0.80	1.28	0.53

α_B (deg)

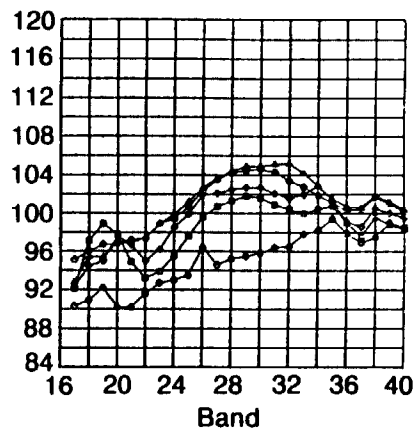
201	1.72
239	2.41
210	2.61
225	2.92
211	2.67
241	2.92
224	3.05
223	2.94



Cond.		M_{AP}	M_{FAN}	C_L
105	□	0.81	1.23	0.52

α_B (deg)

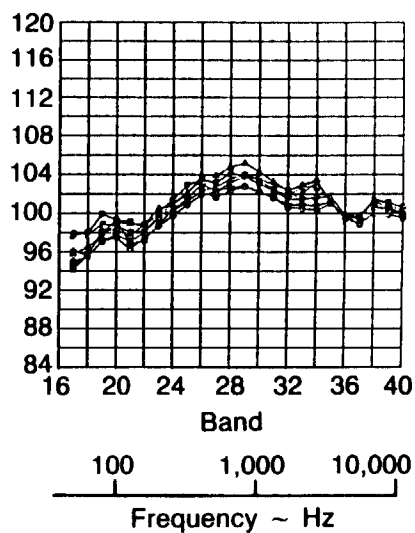
105	2.76
-----	------



Cond.		M_{AP}	M_{FAN}	C_L
247	○	0.81	0.93	0.45
204	□	0.81	1.10	0.42
207	◇	0.81	1.17	0.45
222	◊	0.81	1.20	0.50
214	△	0.81	1.21	0.52

α_B (deg)

247	2.30
204	2.15
207	2.31
222	2.68
214	2.82



Cond.		M_{AP}	M_{FAN}	C_L
245	○	0.82	1.20	0.45
215	□	0.82	1.24	0.50
248	◇	0.82	1.24	0.48
244	◊	0.82	1.26	0.45
243	△	0.82	1.29	0.46
216	▽	0.83	1.30	0.48
242	▽	0.83	1.30	0.49

α_B (deg)

245	2.18
215	2.55
248	2.39
244	2.19
243	2.25
216	2.04
242	2.45

Figure 4-80. Stagnation Point Microphone (Mic 12) $1/3$ Octave Spectra (Concluded)

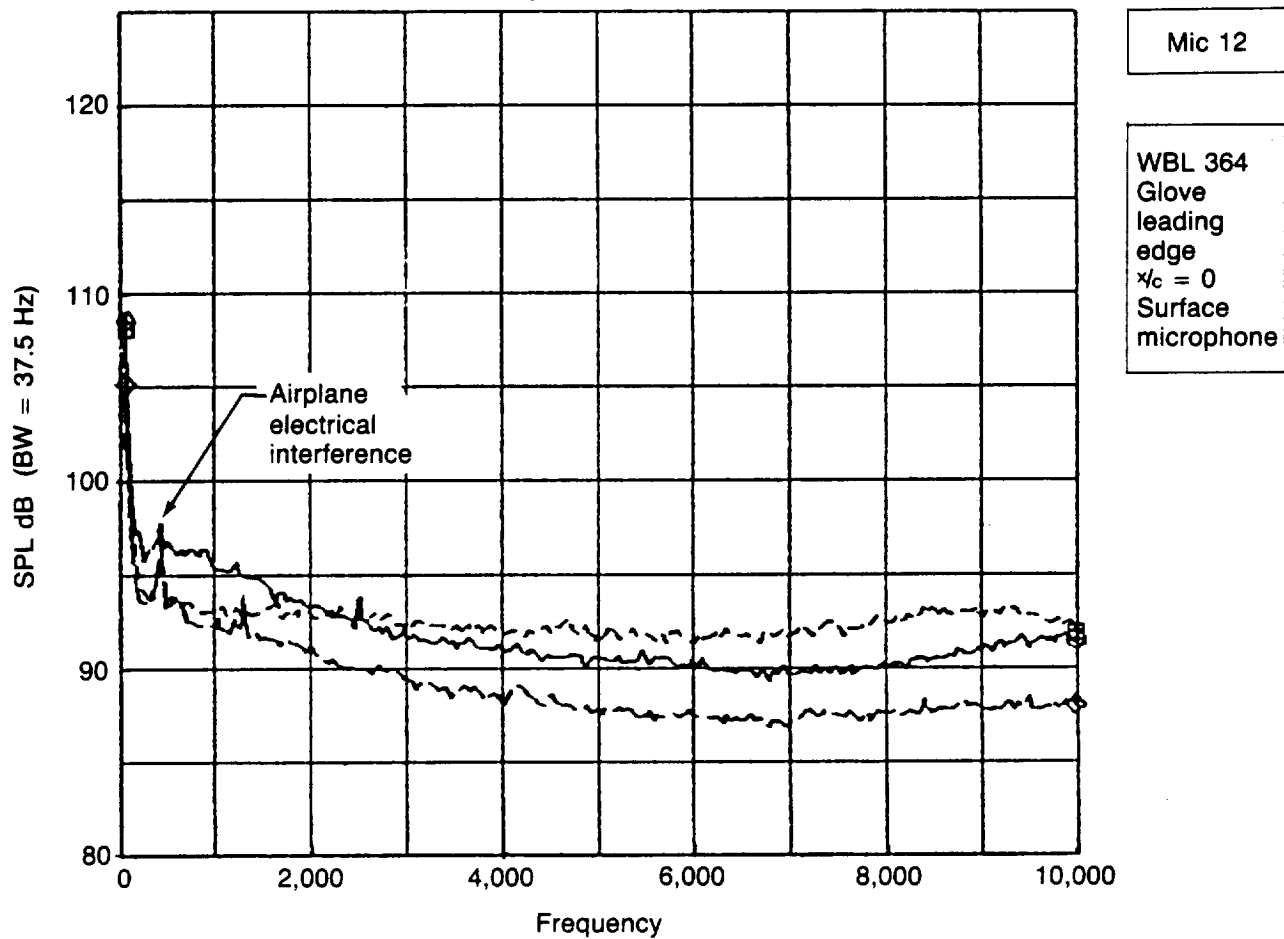
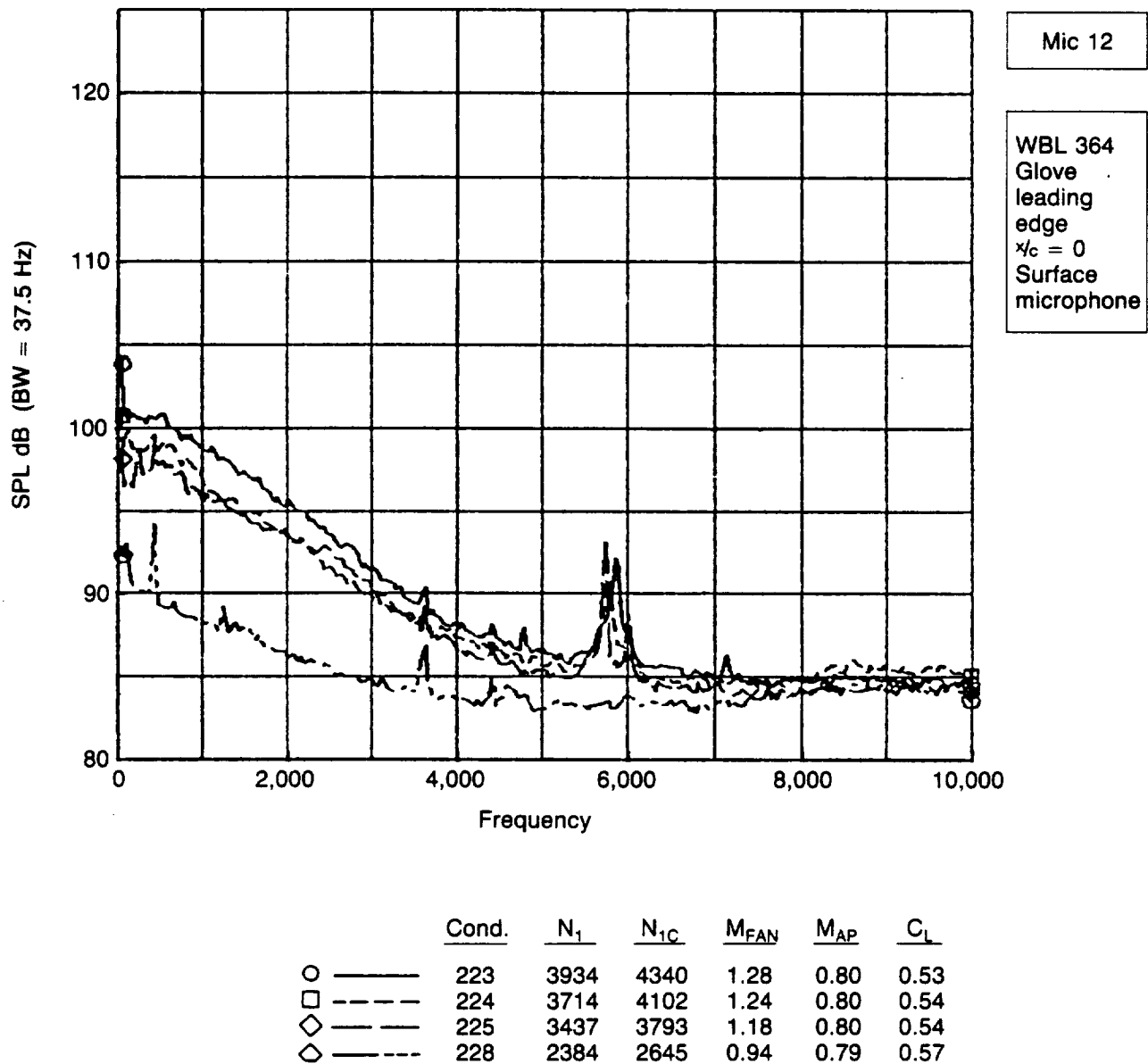


Figure 4-81. Microphone 12 Narrow Band Spectra— $M_{AP} = 0.62-0.64$



WBL 364
Glove
leading
edge
 $x/c = 0$
Surface
microphone

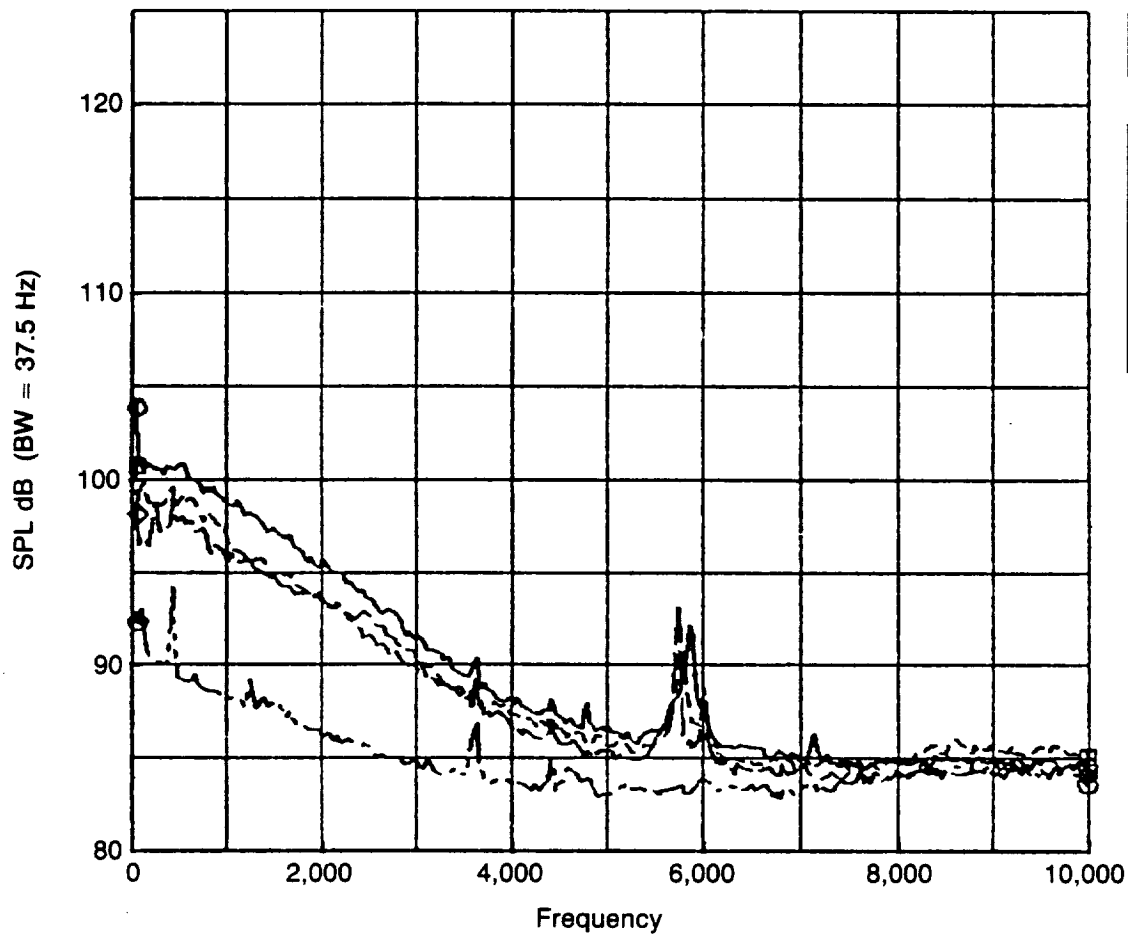
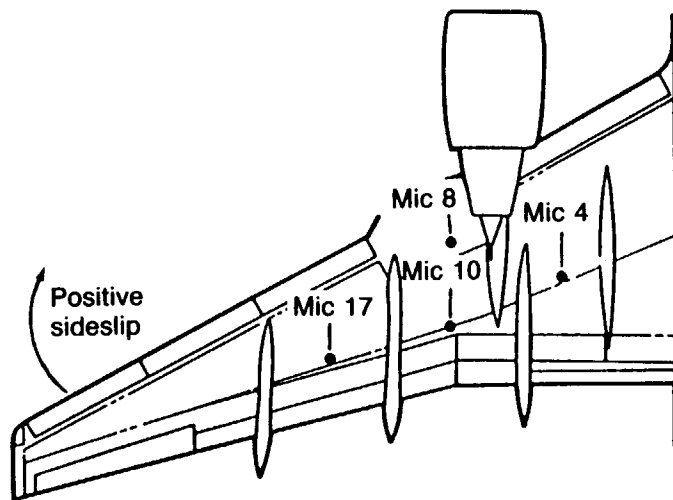


Figure 4-82. Microphone 12 Narrow Band Spectra— $M_{AP} \approx 0.79-0.80$



	M_{AP}	β (deg)
○	0.80	6
◇	0.80	4
◊	0.79	5
△	0.70	7
□	0.80	-6.5
▽	0.80	-4
▽	0.71	-7
x	0.80	0

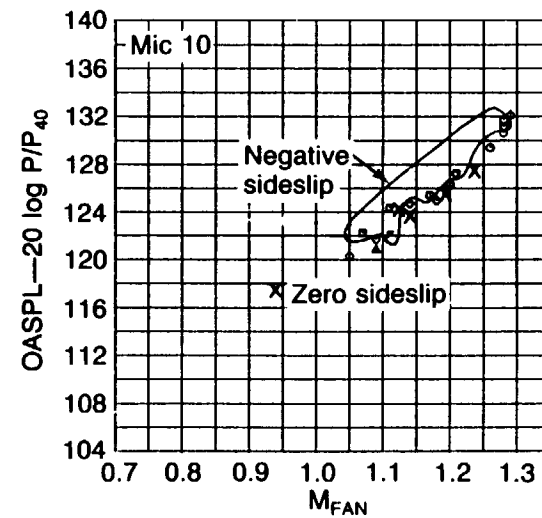
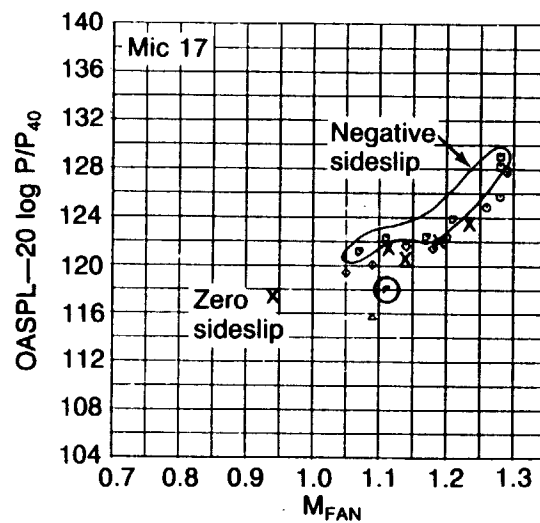
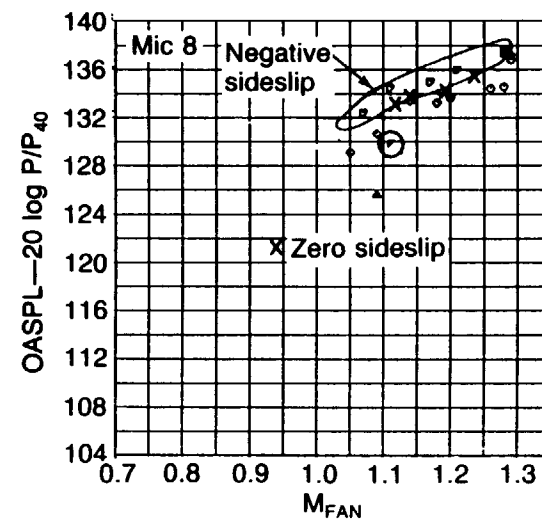
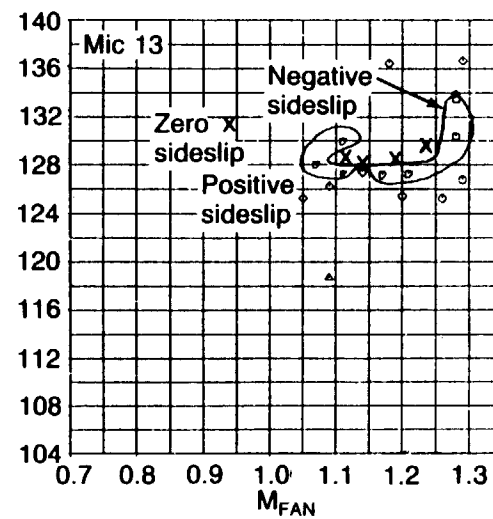
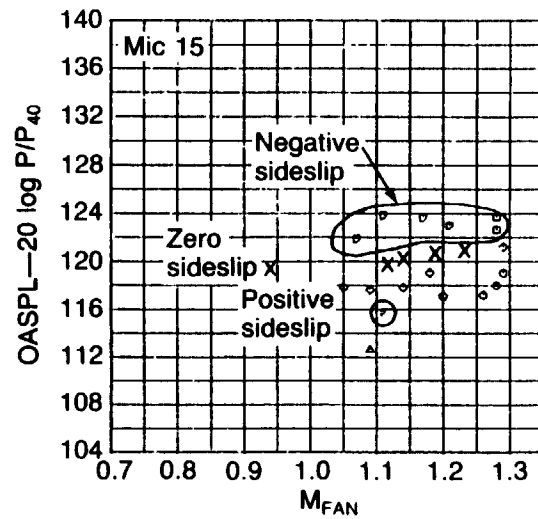
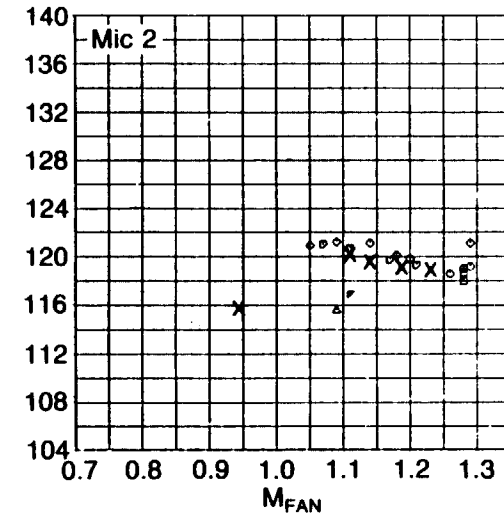
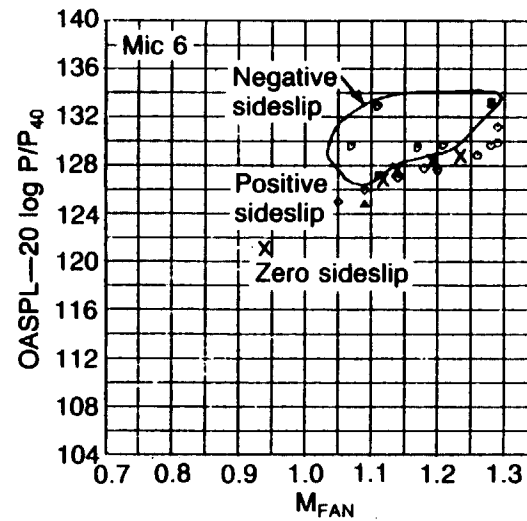
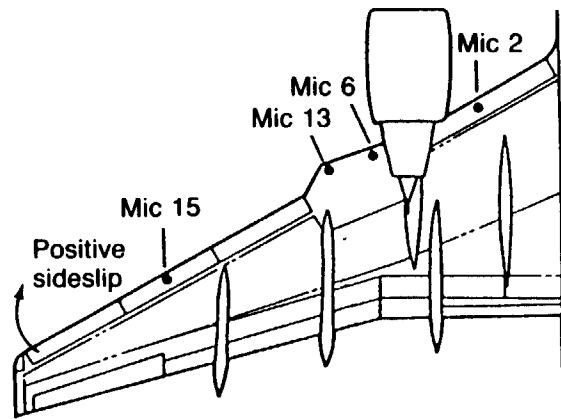
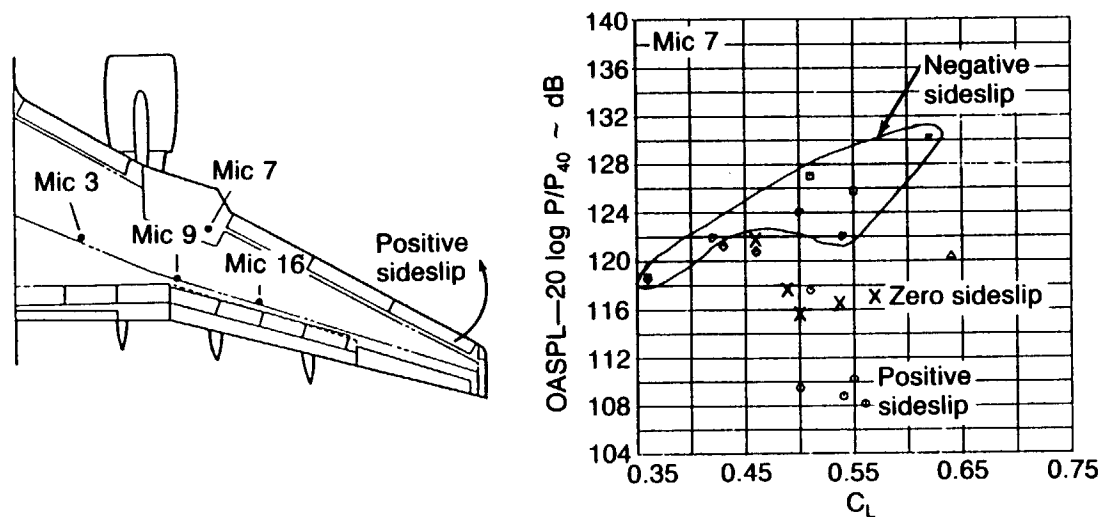


Figure 4-83. Effect of Sideslip on Lower Surface Probe Microphones



	M_{AP}	β (deg)
○	0.80	6
◇	0.80	4
◊	0.79	5
△	0.70	7
□	0.80	-6.5
▤	0.80	-4
▥	0.71	-7
x	0.80	0

Figure 4-84. Effect of Sideslip on Lower Surface Leading Edge Microphones



M_{AP}	β (deg)
○ 0.80	6
◇ 0.80	4
◊ 0.79	5
△ 0.70	7
□ 0.80	-6.5
▤ 0.80	-4
▥ 0.71	-7
x 0.80	0

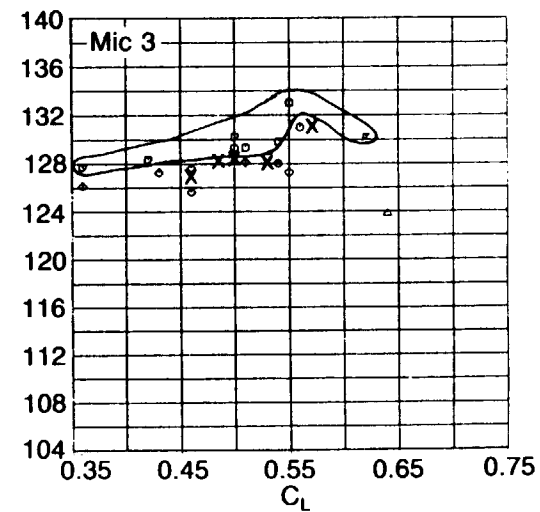
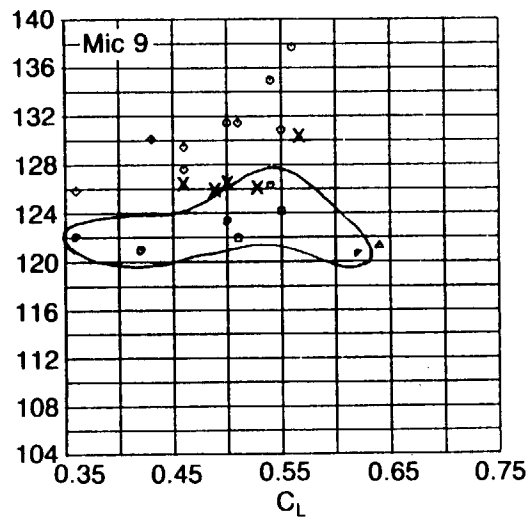
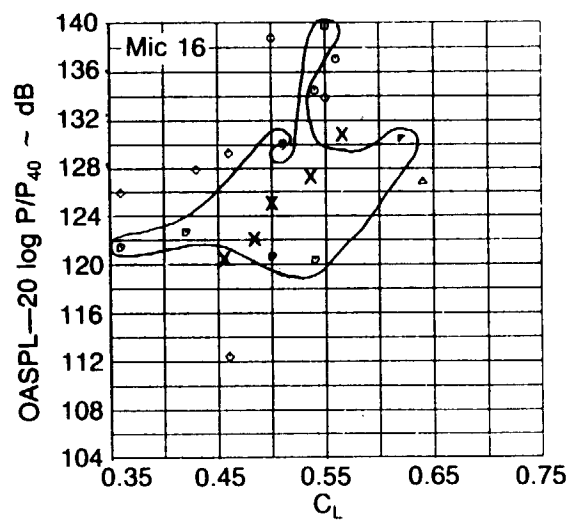
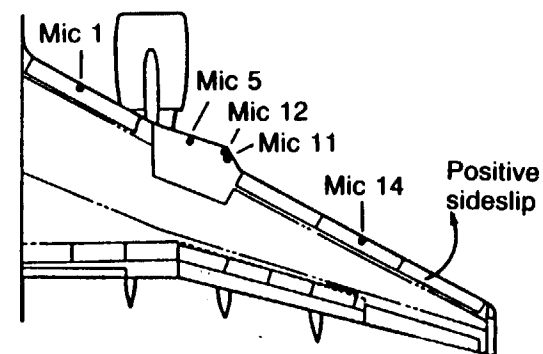
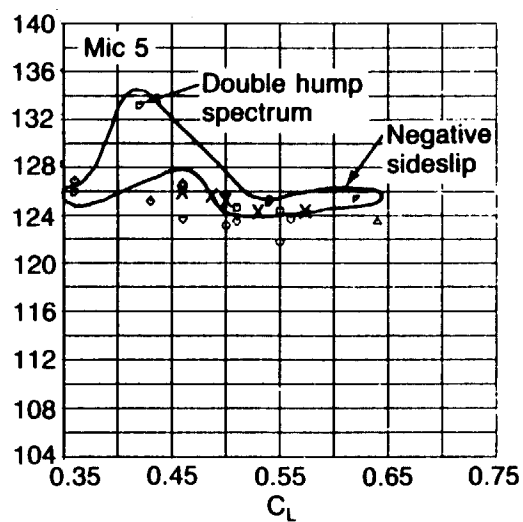
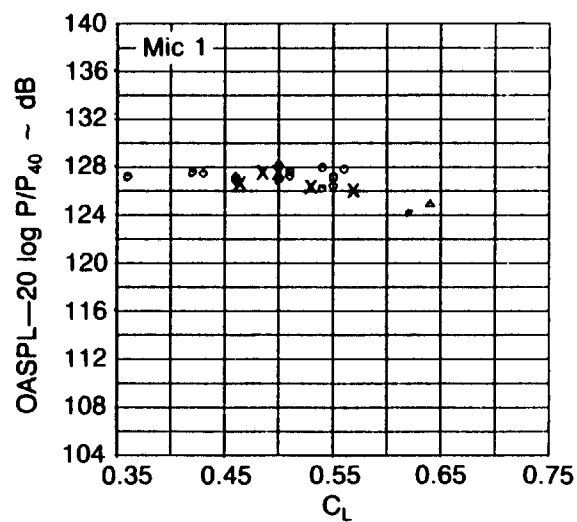


Figure 4-85. Effect of Sideslip on Upper Surface Probe Microphones



M_{AP}	β (deg)
○ 0.80	6
◇ 0.80	4
△ 0.79	5
△ 0.70	7
□ 0.80	-6.5
▤ 0.80	-4
▥ 0.71	-7
x 0.80	0

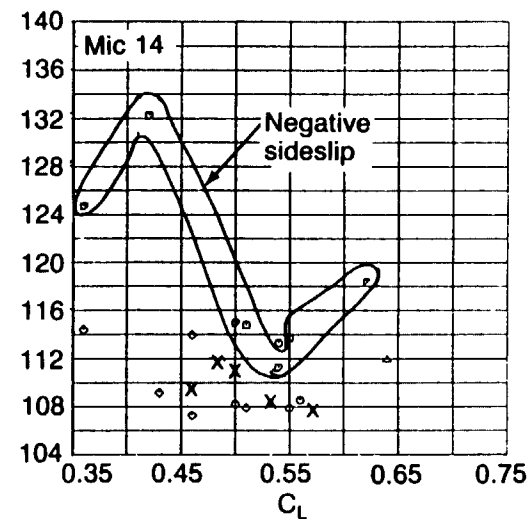
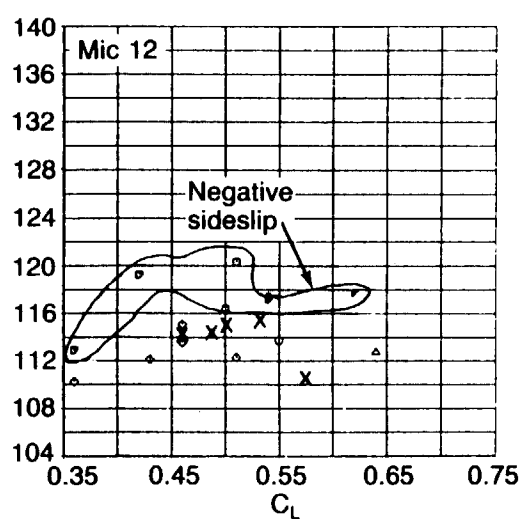
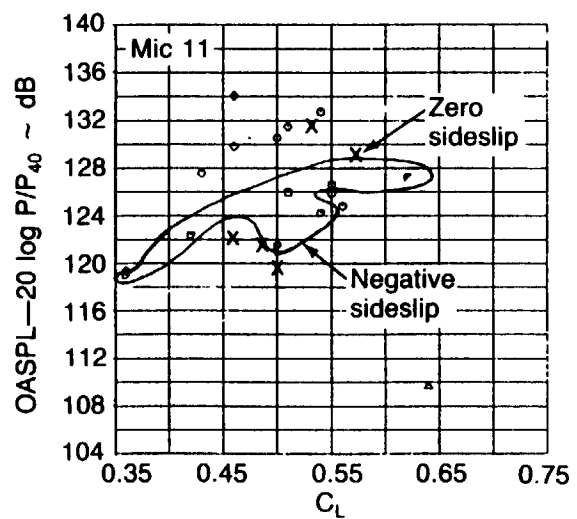


Figure 4-86. Effect of Sideslip on Upper Surface Leading Edge Microphones

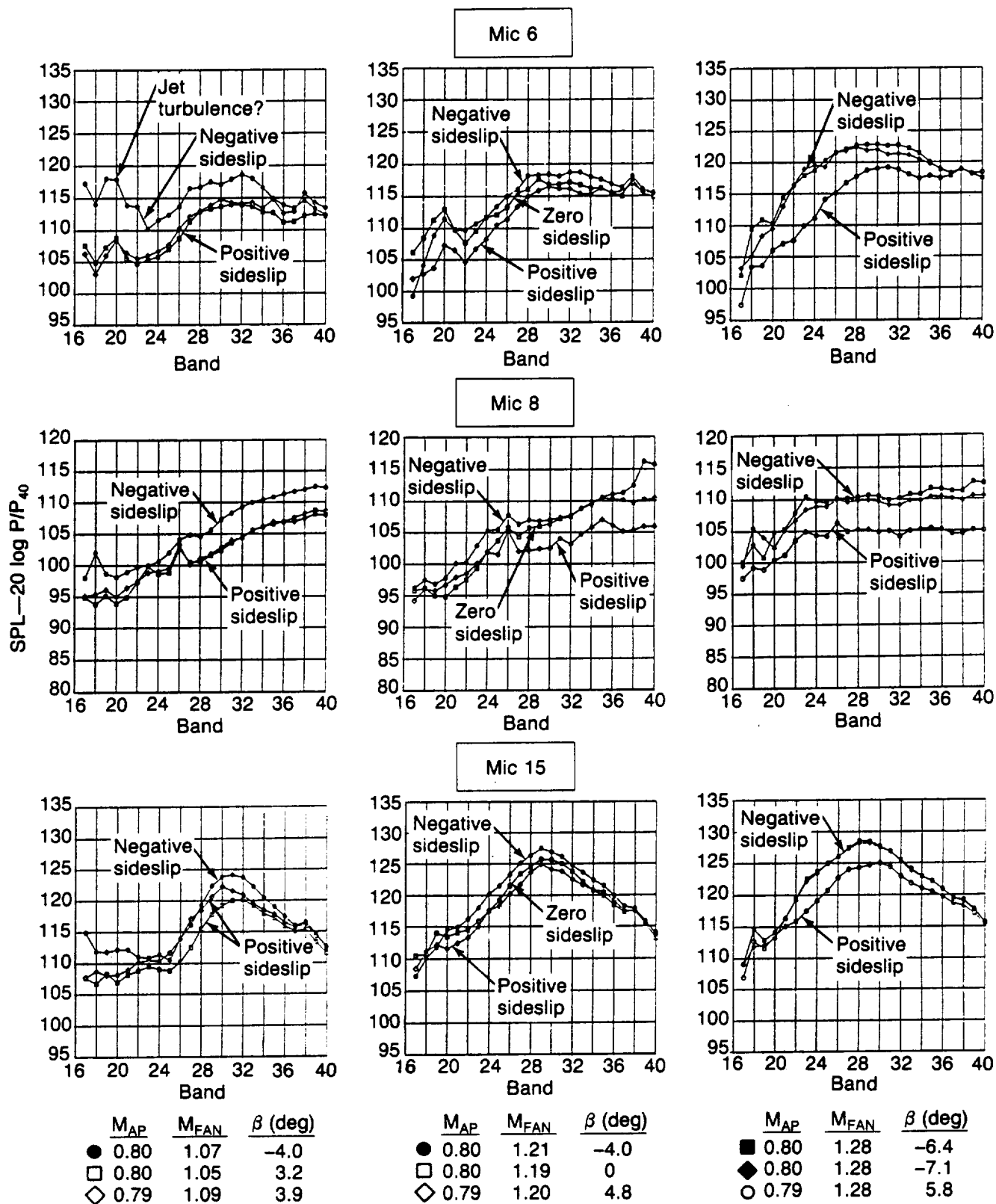
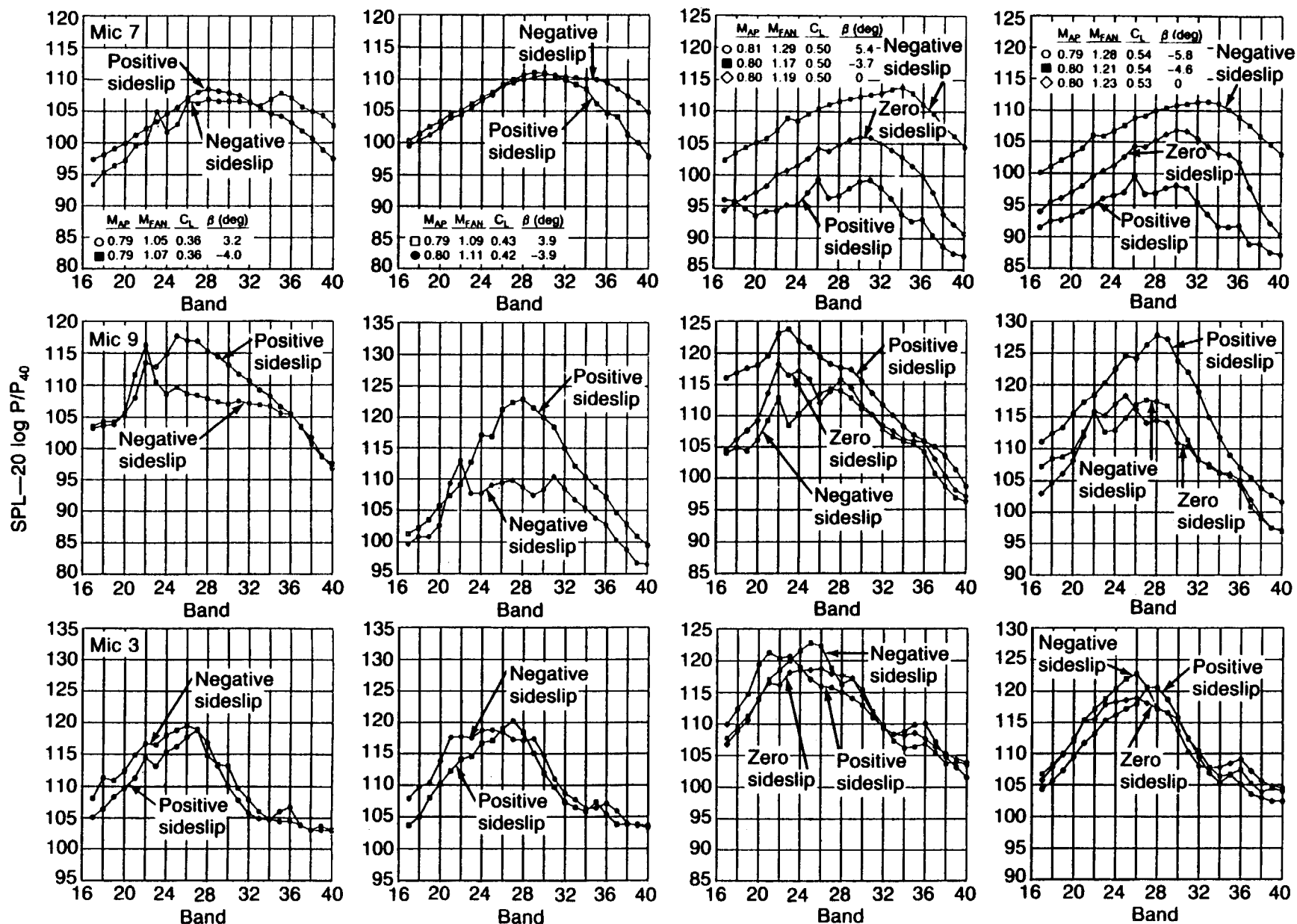


Figure 4-87. Effect of Sideslip on $1/3$ Octave Spectra for Lower Wing Microphones

Figure 4-88. Effect of Sideslip on $1/3$ Octave Spectra for Upper Wing Microphones

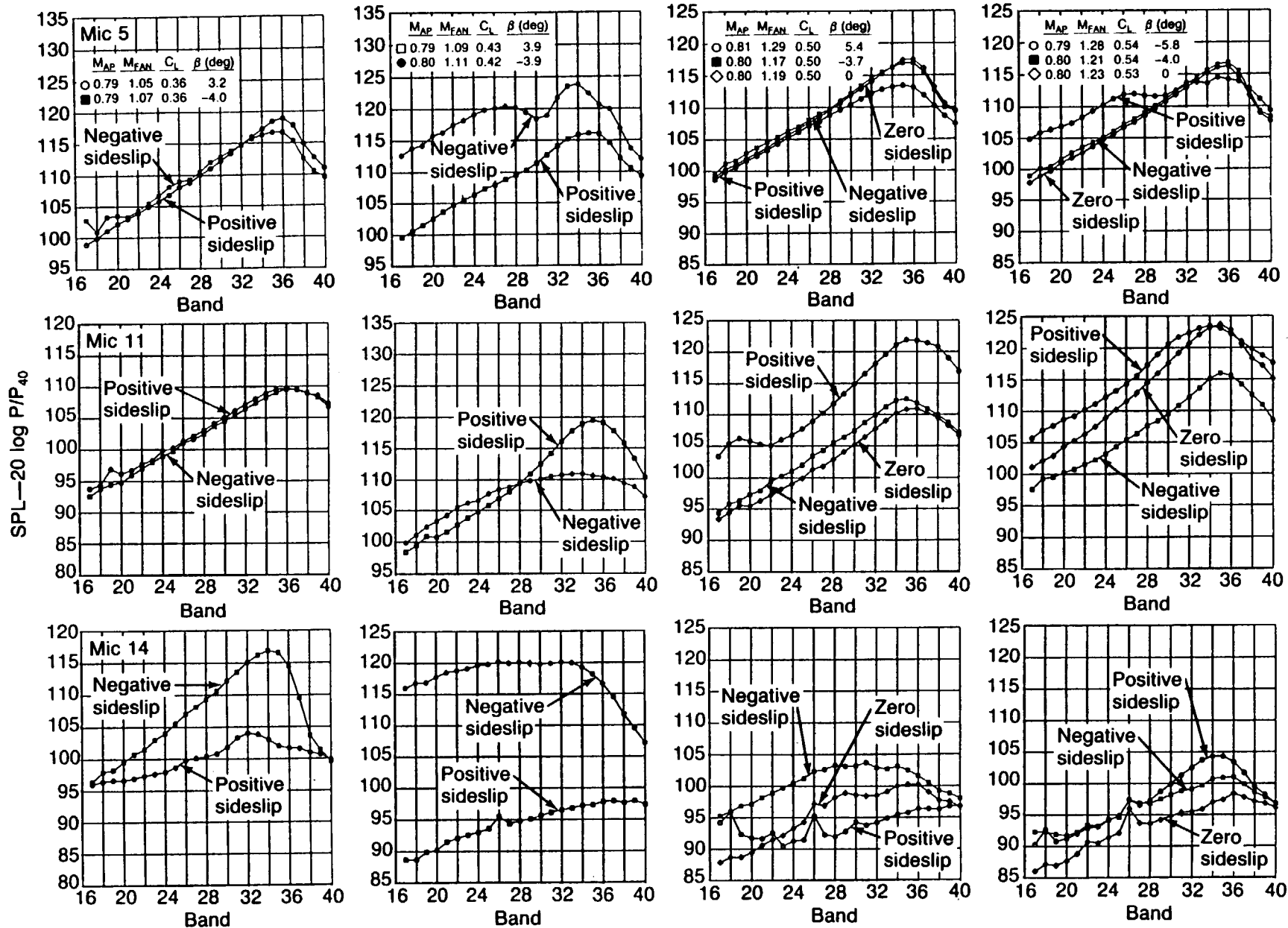
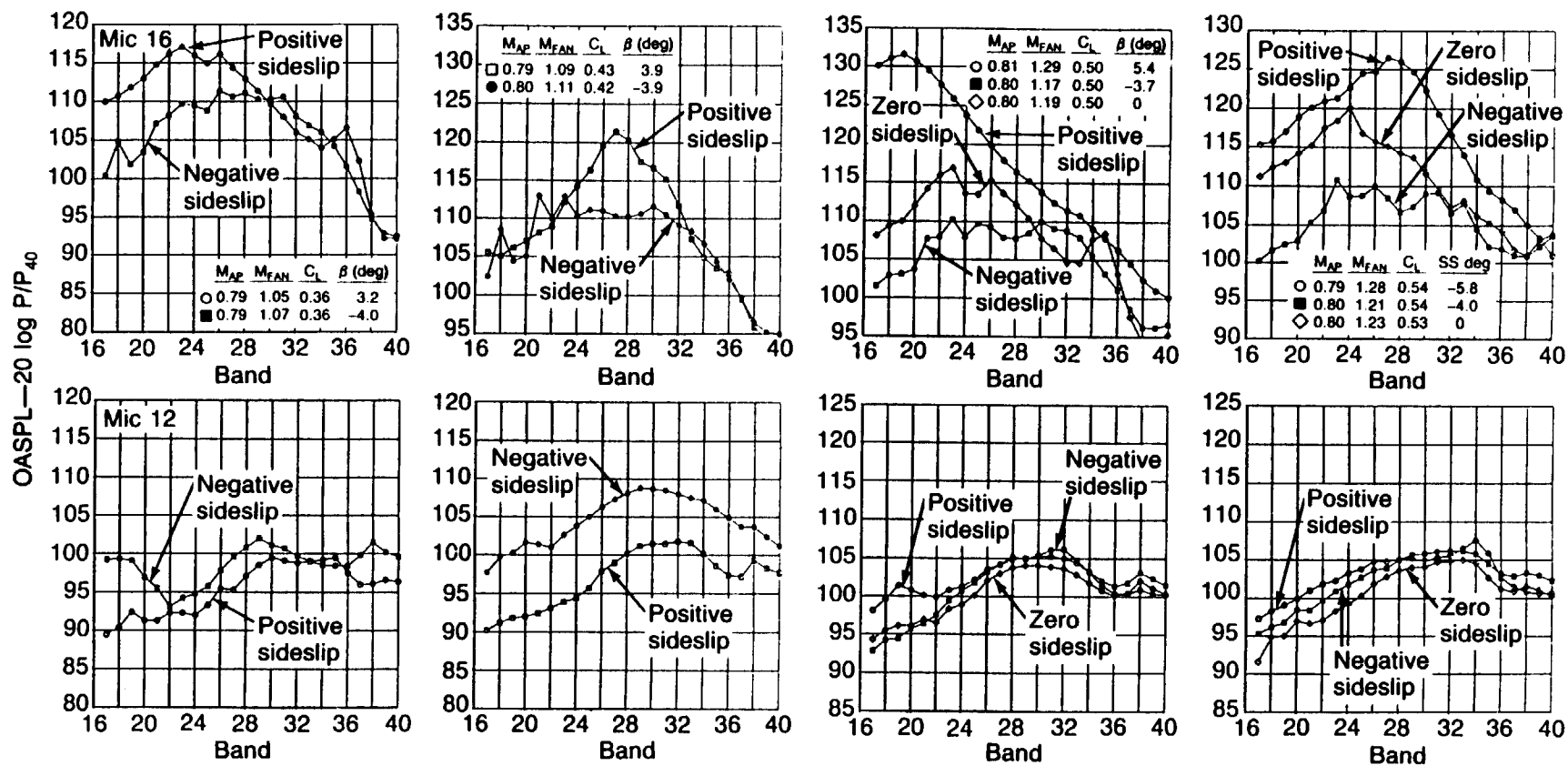


Figure 4-89. Effect of Sideslip on $1/3$ Octave Spectra for Upper Wing Microphones (Continued)

Figure 4-90. Effect of Sideslip on $1/3$ Octave Spectra for Upper Wing Microphones (Concluded)

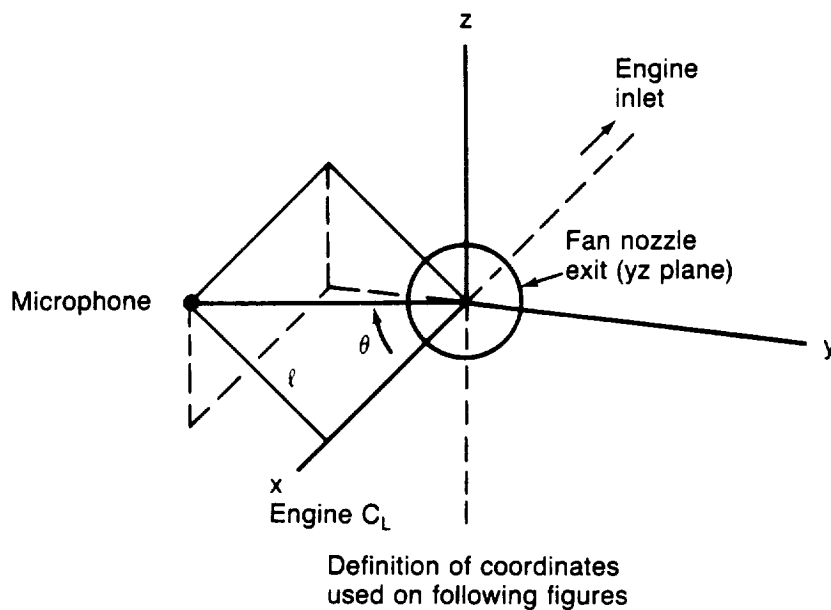
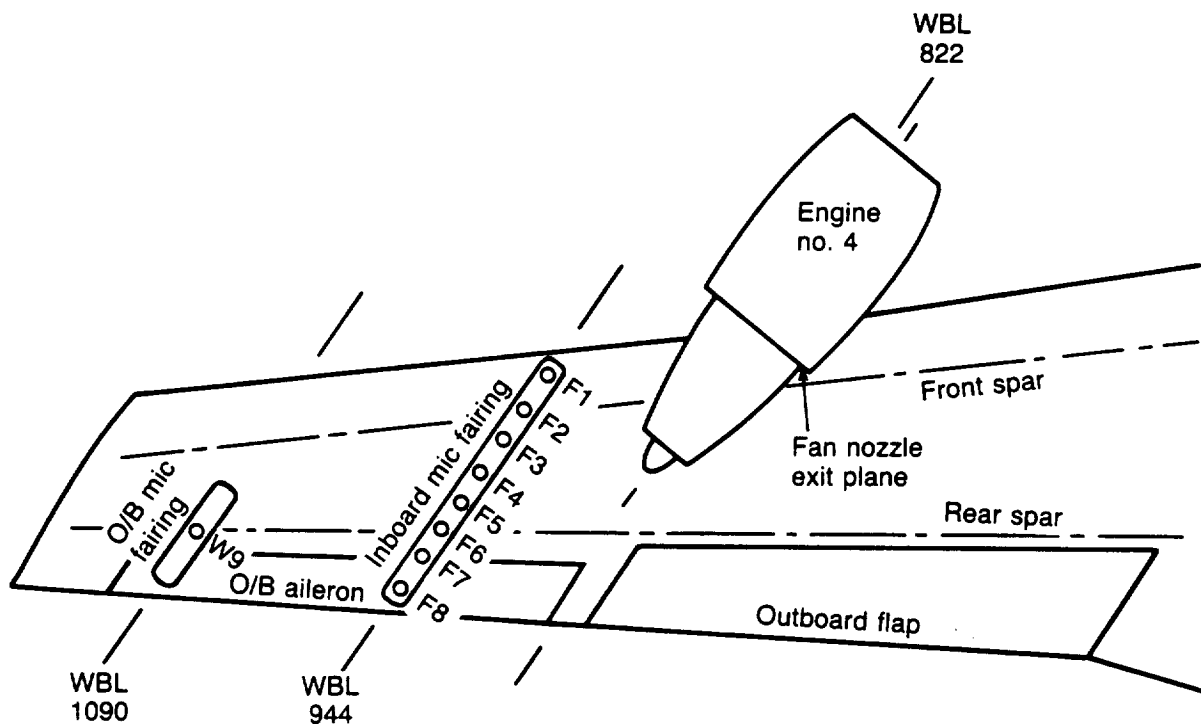
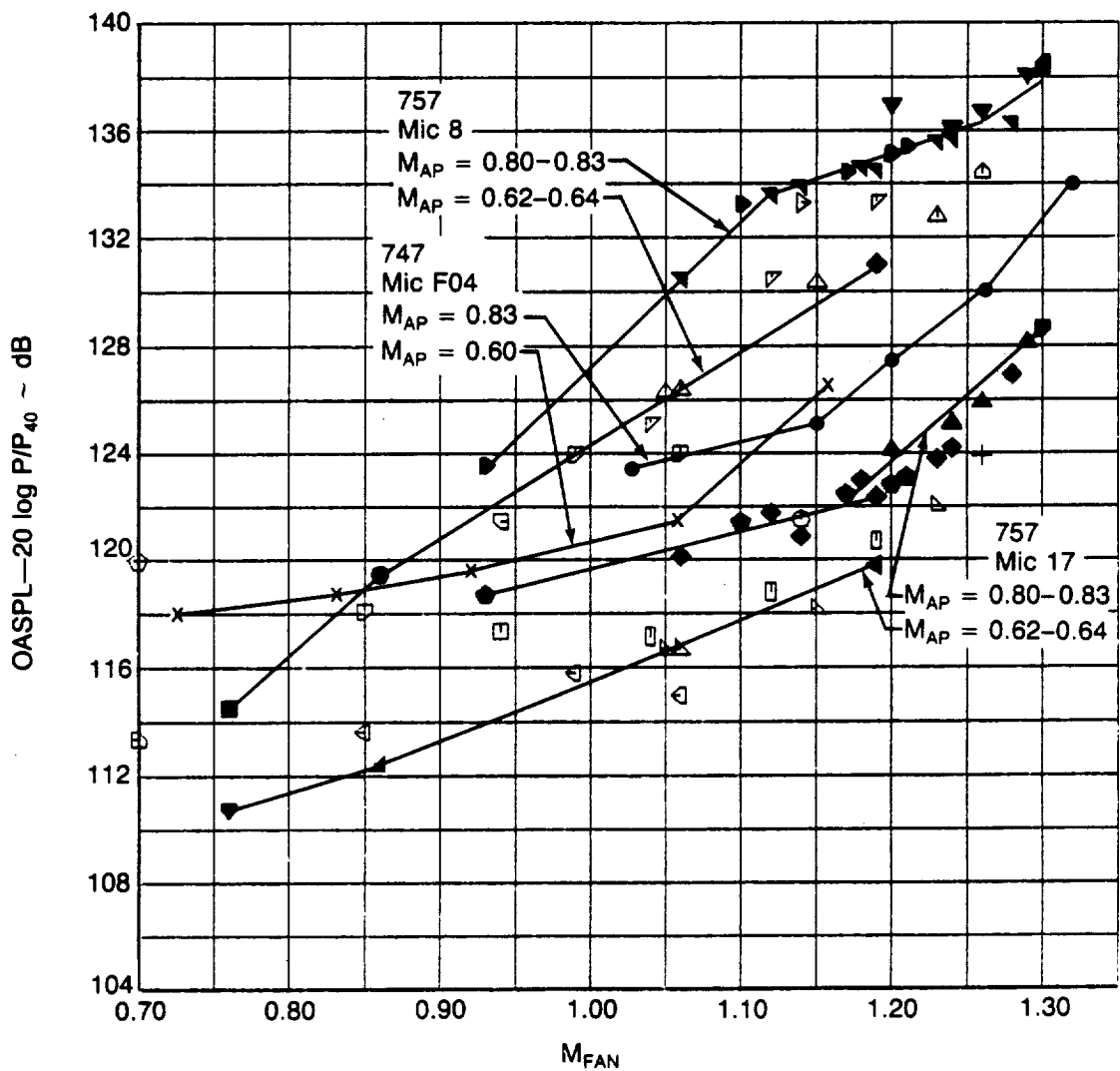


Figure 4-91. 747 Wing Mounted Microphone Installation



757

747

Mic 8

Mic17

Mic F04

$\theta = 52 \text{ deg}$
 $x = 61 \text{ in}$
 $\ell = 6.5 \text{ ft}$
 $\ell/D = 0.94$

$\theta = 50 \text{ deg}$
 $x = 109 \text{ in}$
 $\ell = 15.3 \text{ ft}$
 $\ell/D = 2.2$

$\theta = 50.8 \text{ deg}$
 $x = 91 \text{ in}$
 $\ell = 10.2 \text{ ft}$
 $\ell/D = 1.45$

Figure 4-92. Comparison of 747 and 757 Wing Mounted Microphone Noise Data, $\theta = 50 \text{ deg}$

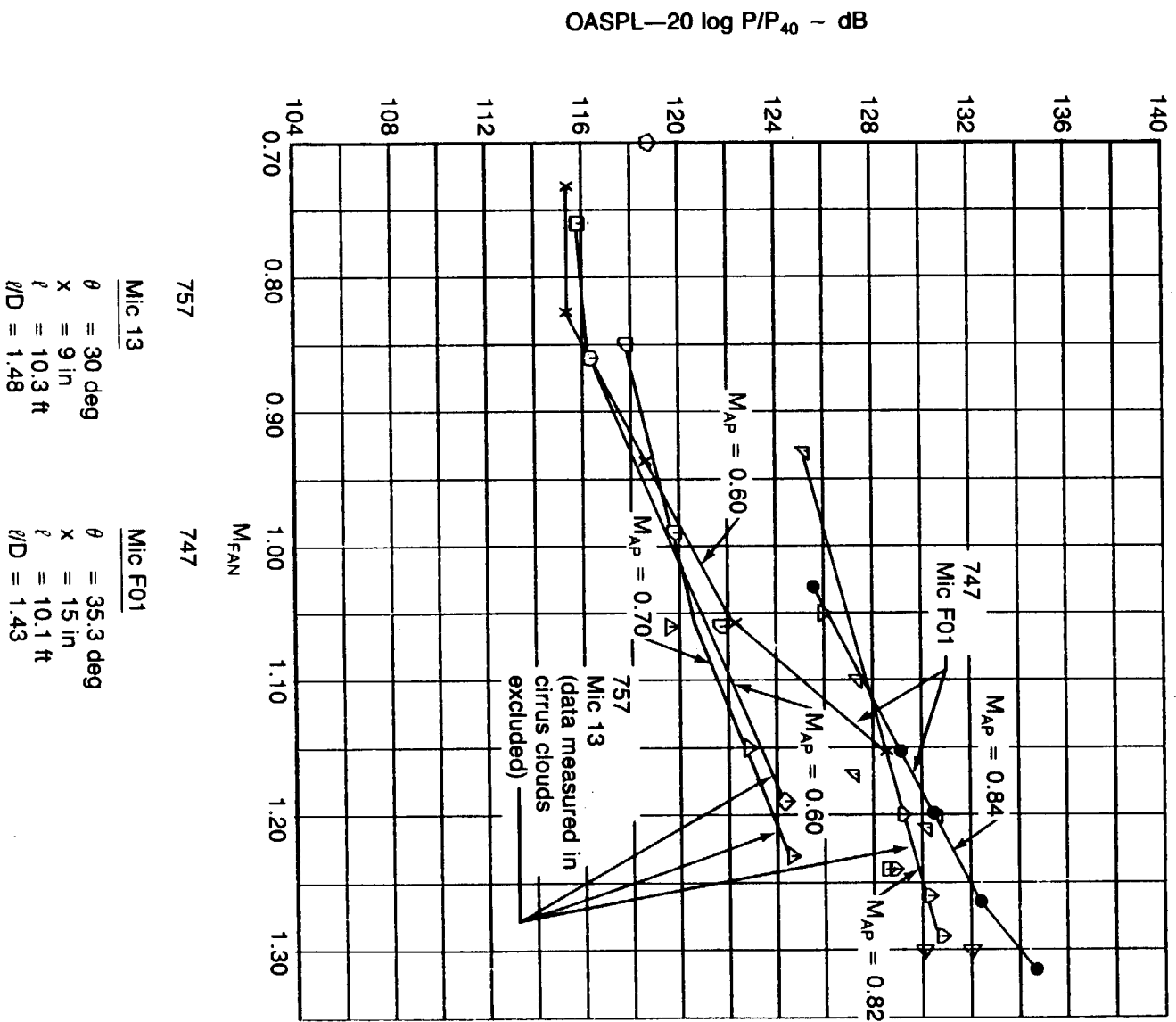
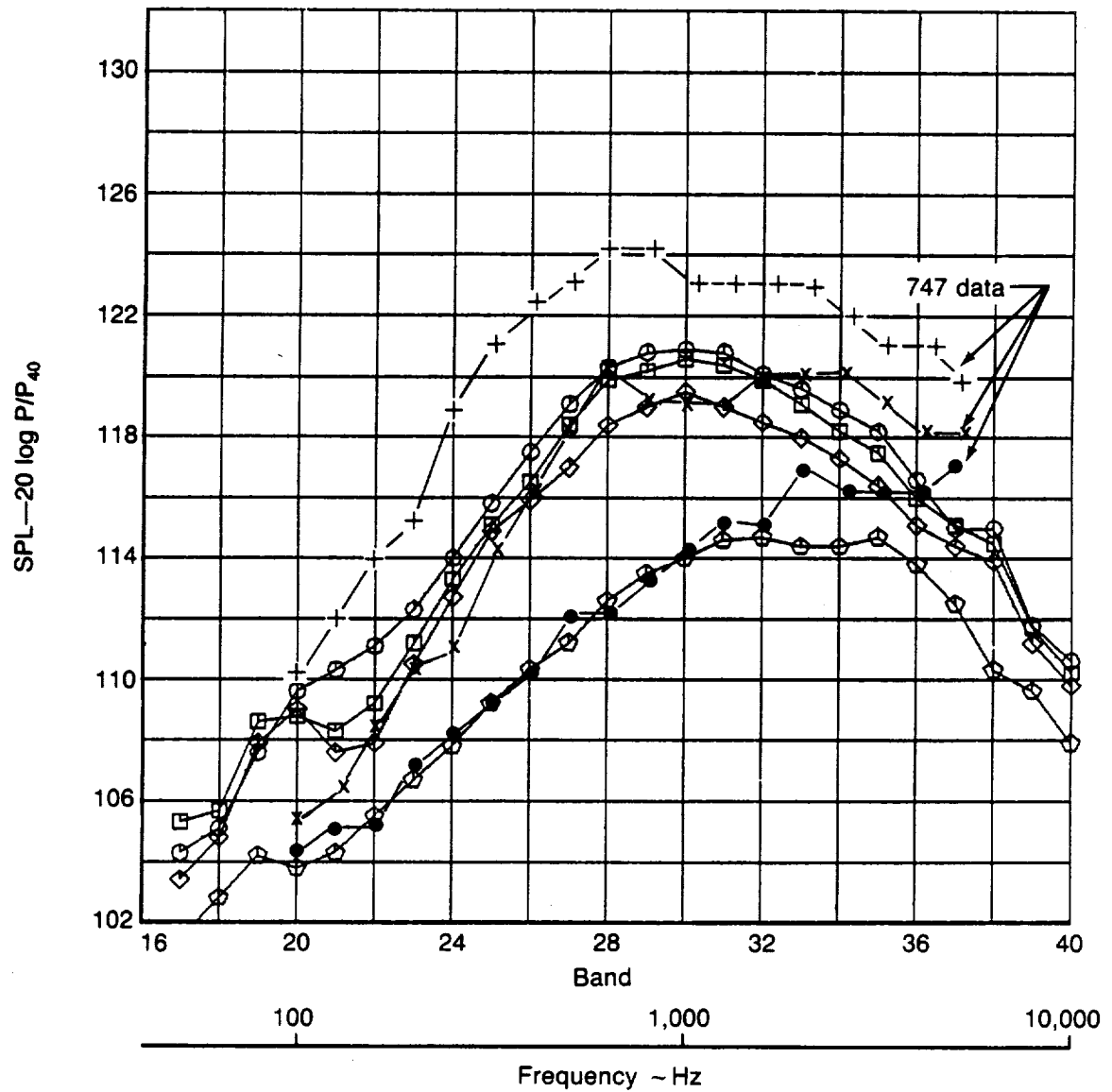


Figure 4.93. Comparison of 747 and 757 Wing Mounted Microphone Noise Data, $\theta = 30 \text{ deg}$



757

Mic 13

$\theta = 30$ deg

$x = 9$ in

$\ell = 10.3$ ft

$\ell/D = 1.48$

M_{FAN}

○

1.29

M_{AP}

○

0.82

□

1.26

○

0.82

◇

1.20

○

0.82

◇

0.92

○

0.81

747

Mic F01

$\theta = 35.3$ deg

$x = 15$ in

$\ell = 10.1$ ft

$\ell/D = 1.43$

$M_{AP} = 0.83$

M_{FAN}

●—●

1.03

○

0.83

x—x

1.20

○

0.83

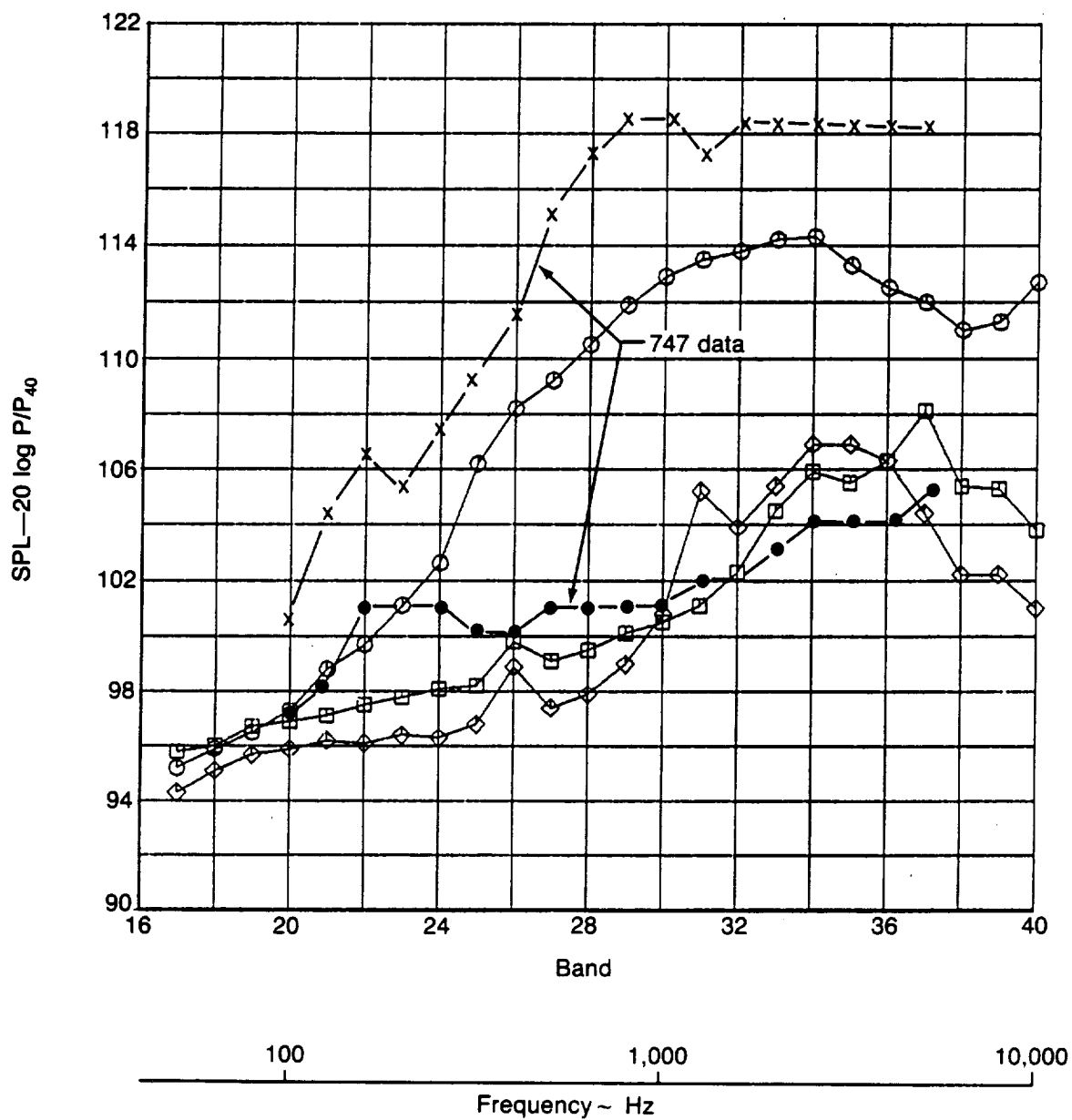
+—+

1.32

○

0.83

Figure 4.94. Comparison of 747 and 757 Wing Mounted Microphone 1/3 Octave Spectra Noise Data, $\theta = 30$ deg, $M_{AP} = 0.80$



757
Mic 13

$\theta = 30 \text{ deg}$
 $x = 9 \text{ in}$
 $l = 10.3 \text{ ft}$
 $l/D = 1.48$

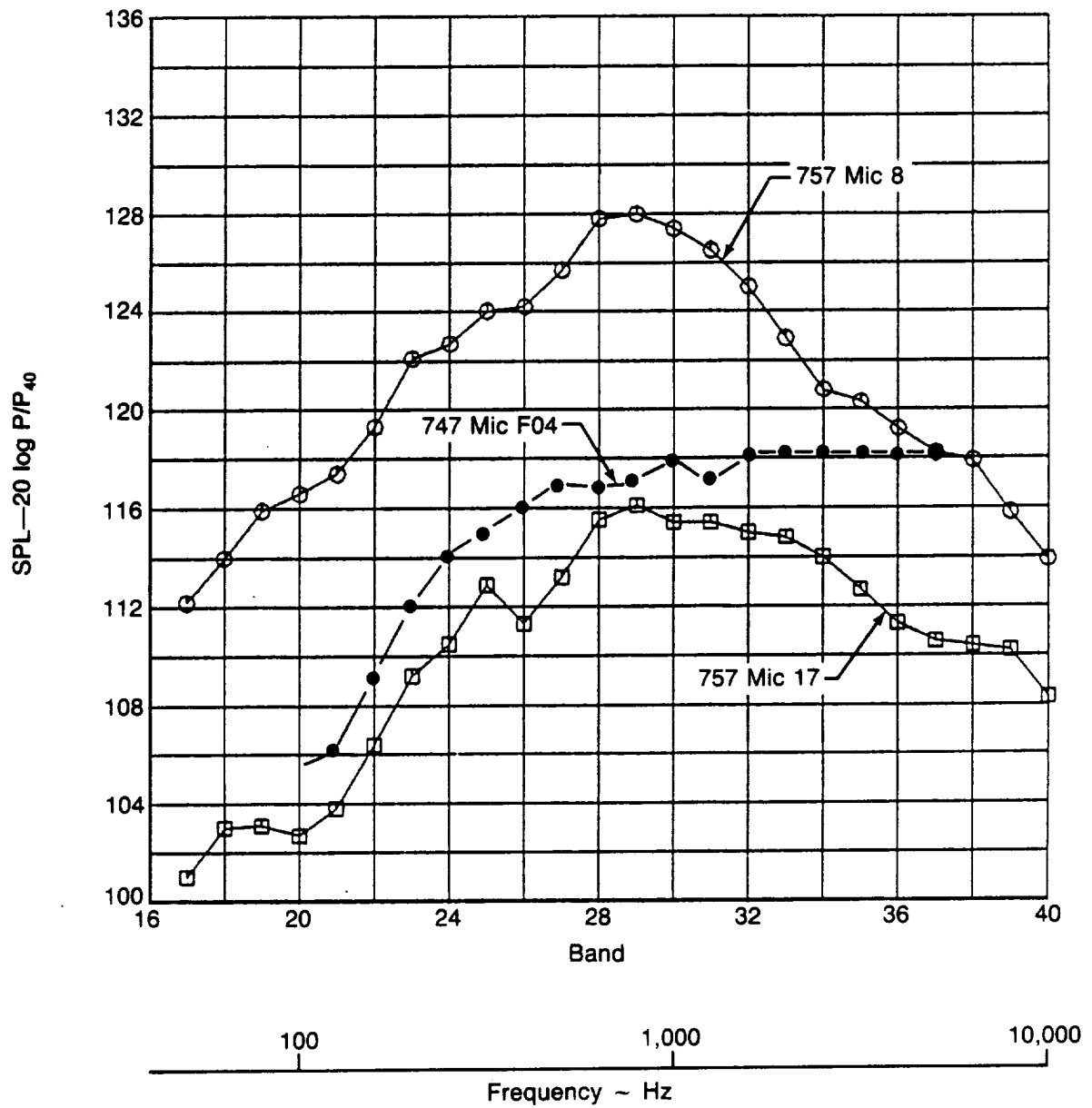
	M_{FAN}	M_{AP}
\circ	1.19	0.64
\square	0.86	0.62
\diamond	0.76	0.63

747
Mic F01

$\theta = 35.3 \text{ deg}$
 $x = 15 \text{ in}$
 $l = 10.1 \text{ ft}$
 $l/D = 1.43$
 $M_{AP} = 0.60$

	M_{FAN}	M_{AP}
\bullet	0.73	0.60
$x-x$	1.16	0.60

Figure 4-95. Comparison of 747 and 757 Wing Mounted Microphone 1/3 Octave Spectra Noise Data, $\theta = 30 \text{ deg}$, $M_{AP} \approx 0.60$



757 Mic 8	747 Mic F04	757 Mic 17
$\theta = 52 \text{ deg}$	$\theta = 50.8 \text{ deg}$	$\theta = 50 \text{ deg}$
$x = 61 \text{ in}$	$x = 91 \text{ in}$	$x = 109 \text{ in}$
$\ell = 6.5 \text{ ft}$	$\ell = 10.2 \text{ ft}$	$\ell = 15.3 \text{ ft}$
$\ell/D = 0.94$	$\ell/D = 1.45$	$\ell/D = 2.2$
$M_{FAN} = 1.26$	$M_{FAN} = 1.27$	$M_{FAN} = 1.26$
$M_{AP} = 0.82$	$M_{AP} = 0.83$	$M_{AP} = 0.82$

Figure 4-96. Comparison of 747 and 757 Wing Mounted Microphone 1/3 Octave Spectra Noise Data $\theta = 50 \text{ deg}$, $M_{AP} \approx 0.83$

4.2 COMPARISON OF PREDICTIONS VERSUS MEASURED NOISE DATA

4.2.1 Description of Prediction Procedures

Predictions of the noise measured by the microphones mounted on the lower wing were made using three different procedures. The following is a brief description of these procedures.

4.2.1.1 Lockheed Procedure

Reference 1 describes nearfield engine noise and airframe noise prediction methods incorporated into a computer program by the Lockheed-Georgia Company under contract to NASA. The user's guide to the computer program is contained in Reference 10. The noise sources predicted are as follows:

Engine Noise

- Inlet fan
- Inlet low pressure compressor
- Aft fan
- Turbine
- Jet mixing
- Jet shock broadband
- Jet shock tone

Airframe Noise

- Boundary layer radiated noise
- Trailing edge noise

A magnetic tape of the Fortran code was received from NASA and run on the Boeing CDC6600 computer.

4.2.1.2 Boeing Procedures

Two Boeing prediction procedures were used for comparison with the 757 lower wing microphone results. The *Butzel* prediction methodology is described in Reference 5. This procedure provides predictions for jet noise and jet shock broadband noise only. The Butzel procedures are essentially empirical and are based on YC14 data and the 747 data discussed in Section 4.1.7. The *Lu* procedure only predicts jet mixing noise. No shock effects are included. The procedure is based on relatively low speed ($M \leq 0.3$) wind tunnel data, which is then *extrapolated* to higher airplane speeds. A description of the procedure is contained in Reference 6.

4.2.2 Prediction Flight Conditions

Predictions were calculated for the following conditions:

$M_{AP} = 0.8$
Altitude = 40,000 ft
Engine r/min (NIC)

4321
4096
3806
3505
3103
2845
2303

$M_{AP} = 0.6$
Altitude = 35,000 ft
Engine r/min (NIC)

4659
4428
4021
3547
2770
2148

The Lockheed procedure was used for predictions at all lower wing microphones. For the Butzel and Lu procedures, predictions were only made for the microphones outboard of the engine. This was felt sufficient to evaluate these procedures since they do not predict any fan or turbine noise sources. Table 4-1 shows the microphone geometric parameters that are used by the prediction procedures for the lower wing microphone locations.

The engine parameters needed for the engine noise component predictions were read directly from or estimated from parameters calculated by the PW 2037 engine cycle computer program. Flow areas were estimated from an engine drawing when internal flow Mach numbers needed to be calculated. N_{1C} and fan nozzle pressure ratio were measured during the flight test. Comparison of the N_{1C} versus M_{Fan} curve determined from the flight data with that determined from the engine cycle calculations show the deck to be within about 3% of M_{Fan} . This difference would cause approximately 1.5 dB error in the jet noise calculations at $M_{AP} = 0.8$.

4.2.3 Summary of Prediction Versus Measured Data Comparisons

The following is a brief overview of the noise prediction/flight data comparisons. Details of the comparisons are given in later sections.

4.2.3.1 Lockheed Prediction Procedure:

1. Aft Fan Noise

- Not predicted as a dominant component.
- Higher than inlet fan for all lower wing measurement points
- Fan tone predictions ± 10 dB relative to measured data if convective amplification used, -5 to $+15$ dB if convective amplification not used.

2. Turbine Noise

- Turbine tone predictions were high by 20 dB or more at leading edge microphones when convective amplification was used. When convective amplification was not used, tone predictions were 20 dB lower than those with convective amplification at leading edge microphones (fig. 4-97).
- Maximum turbine noise level measured at microphone 10. Prediction with convective amplification modeled this microphone measurement well. Prediction without convective amplification was 5 dB high at this microphone (fig. 4-97).

3. Jet Noise

- Prediction procedure would not give jet mixing noise prediction for microphones close to the engine (microphones 2, 4, 6, 8, and 10). Also an intermediate engine power condition failed for $M_{AP} = 0.6$.
- Although it can't be stated with certainty, jet predictions are probably high. A noise increase of 5 to 10 dB is predicted at intermediate subsonic fan jet exhaust conditions when the airplane Mach number is reduced from $M = 0.8$ to $M = 0.6$ at constant fan jet Mach numbers. Since this increase is not observed in the 757 data, it is concluded that jet noise is not the dominant broadband noise source as predicted in this power setting range.

4. Shock Noise (Broadband)

- Broadband shock noise appears to be the dominant noise source for the lower wing at supersonic fan exhaust jet Mach numbers.
- Predictions for leading edge microphones are 10 to 40 dB high when convective amplification is applied and 5 to 10 dB high without convective amplification (fig. 4-98).
- Predictions for aft microphones are 0 to 10 dB high with convective amplification and 5 to 10 dB high without (fig. 4-98).

5. Shock Noise (Tone)

- Generally, shock screech was not evident in measured data so this component was not predicted. (Preliminary predictions showed very high levels.)

6. Trailing Edge Noise

- Predicted to be dominant noise source at aft microphones and an important contributor at leading edge microphones for $M_{AP} = 0.8$ when convective amplification is applied. This is not supported by the data. Removing convective amplification lowered prediction by 20 to 30 dB.

7. Boundary Layer Radiated Noise

- Turbulent boundary layer radiated noise predicted for wing surface radiation. Predicted levels more than 40 dB less than measured overall noise levels. Therefore, this noise source is not considered important.

4.2.3.2 Butzel Procedure

1. Shock Noise (Broadband)

- Uses mixed jet parameters for shock noise predictions. When $M_{Fan\ Jet}$ is slightly above 1, $M_{Mixed\ Jet} \leq 1$, and no shock noise is predicted. This is probably incorrect.
- For higher $M_{Fan\ Jet}$ values, predictions compare well with data for microphones near engine, but were approximately 10 dB low for outboard microphones 15 and 17 (fig. 4-98).

2. Jet Noise

- Predictions were 10 to 15 dB lower than Lockheed procedure predictions.
- Predictions still probably high.

4.2.3.3 Lu Procedure

1. Jet Noise

- Predictions 20 to 30 dB lower than Butzel predictions and 30 to 45 dB lower than Lockheed.
- Predictions more than 30 dB below measured data.

4.2.4 Details of Prediction Versus Measurement Comparisons

4.2.4.1 OASPL

Figures 4-99 to 4-122 compare predicted versus measured OASPL data for all of the lower wing microphones. The plots are grouped by microphone number with three plots shown for each microphone. The first shows measured data versus the Lockheed procedure predictions with convective amplification applied. The second shows measured data versus Lockheed predictions without convective amplification applied. The third shows measured data versus the Butzel and Lu predictions.

Use of the convective amplification correction in the Lockheed predictions resulted in large overpredictions for the leading edge microphones in particular. In Figure 4-98, it is seen that the broadband shock noise is overpredicted by 10 to 40 dB depending on microphone position. The wing trailing edge noise prediction is also high because of the convective amplification and the forward radiation angle of all microphones for this source. As a result, it was decided to modify the Lockheed prediction computer program so that convective and dynamic amplification would not be applied. The resulting predictions show significantly better agreement with the measured data.

For the supersonic fan exhaust Mach numbers the broadband shock noise is predicted to be the dominant noise source at all microphones. While the Lockheed predictions for the broadband shock noise still are of the order of 10 dB higher than the measured data, the trend with M_{Fan} in the supersonic region seems correctly predicted. Removing the convective amplification correction results in nearly the same broadband shock noise predicted for airplane Mach numbers of 0.6 and 0.8 at a given M_{Fan} . The measured data also shows a relative insensitivity to airplane Mach number at the higher M_{Fan} . The broadband shock noise prediction drops off very fast as M_{Fan} approaches 1.

For those microphones for which the Lockheed procedure gave jet noise predictions (Mics 13, 15, and 17), jet noise was predicted to dominate for the high subsonic M_{Fan} conditions with turbomachinery noise dominating at the low M_{Fan} s (figs. 4-106, 4-109, and 4-121).

Examining Figures 4-109 and 4-121, the jet noise for $M_{AP} = 0.6$ is predicted to be approximately 7 to 10 dB higher than for $M_{AP} = 0.8$. This results in a predicted increase in OASPL of 5 to 7 dB for the high subsonic M_{Fan} s going from $M_{AP} = 0.8$ to $M_{AP} = 0.6$. This increase was not observed in the measured data. In fact, for microphones 15 and 17 the noise levels showed a reduction of approximately 5 dB going from $M_{AP} = 0.8$ to $M_{AP} = 0.6$ (figs. 4-18 and 4-1). An increase in jet noise for this airplane Mach number change was also predicted by the Butzel and Lu procedures and is due to the increase in relative jet velocity ($V_{jet} - V_{airplane}$). The fact that the measured noise did not increase with decreasing airplane Mach number at a constant fan jet Mach number leads to the conclusion that jet mixing noise was not a dominant source in any power setting range. This also implies that the Lockheed procedure jet noise predictions for microphones 13, 15, and 17 are high.

The Lockheed procedure predicts significant levels of turbomachinery noise with turbine and inlet fan noise being most important for the leading edge microphones and turbine noise being most important for the aft microphones. These sources are examined in more detail below. The trailing edge noise source generally is predicted to be insignificant when convective amplification is not included. Also, the noise radiated by the wing boundary layer was predicted to be well below (30 to 70 dB) the measured data.

The Butzel procedure gives predictions for jet shock broadband noise and jet mixing noise. The shock broadband noise predictions were within 5 dB of the measured data for the high supersonic fan jet Mach numbers for the microphones closer to the engine (mics 4, 6, 8, and 10). The predictions were low by 5 to 10 dB for the microphones farther from the engine (mics 13, 15, and 17). The procedure uses the mixed jet Mach number for the shock noise prediction that results in no shock noise for some cases for which the fan jet is supersonic and the core jet is subsonic. This is probably incorrect. Since the PW 2037 is not a mixed flow engine, shocks will exist in the fan jet for these cases. The Butzel procedure jet noise

predictions are of the order of 10 dB lower than the Lockheed jet predictions at microphones 13, 15, and 17. However, the predicted jet noise for $M_{AP} = 0.6$ generally is close to the measured data. Again, because a noise increase was not measured when the airplane speed was reduced at a constant fan jet exhaust Mach number, it appears that the Butzel procedure jet noise predictions are too high.

The Lu jet noise predictions generally are well below the measured data. These predictions otherwise show trends similar to the Lockheed and the Butzel procedures. The Lu jet noise procedure is based on low speed wind tunnel data ($M_{Tunnel} \approx 0.3$) that is extrapolated for the $M_{AP} = 0.6$ and $M_{AP} = 0.8$ conditions. Since jet noise does not appear to contribute to the 757 data, the procedure cannot be further evaluated.

4.2.4.2 One-Third Octave Band Spectra

Figures 4-123 to 4-130 are comparisons of the Lockheed procedure predicted $1/3$ octave spectra with measured data for the lower wing microphones. Generally, predictions are shown for all of the noise sources that significantly contribute to the OASPL at the given microphone position. The jet mixing noise prediction is only shown for microphones 13, 15, and 17. The Lockheed computer program would not provide jet mixing noise predictions for the microphones closer to the engine. The predictions shown are for a high engine power condition, $N_{IC} = 4321$ r/min, at an airplane Mach of 0.8, and an altitude of 40,000 ft. Generally, the measured data are shown for a range of engine power conditions below and slightly above that for the predictions. Each figure also shows the geometric angles of the microphone relative to the center of the primary nozzle, fan nozzle, and inlet respectively (see figures on table 4-1). Also, the calculated radiation angles for noise sources located at these locations are shown. The radiation angle differs from the geometric angle because of the airplane motion. The radiation angles for inlet noise sources are seen to be to the aft (≤ 90 deg) for all of the microphone positions. For noise sources located at the primary nozzle (or aft of the primary nozzle), the radiation angles are all forward (≥ 90 deg) except for microphones 10 and 17. For noise sources located at the fan nozzle, the radiation angles vary from aft ($\theta_{min} = 41$ deg) to forward ($\theta_{max} = 157$ deg).

The most striking feature of the predicted spectra are the high levels for the fan jet shock broadband noise component. At the high engine power condition for which the prediction was made, the fan jet Mach number is 1.26. The corresponding primary jet Mach number is 1.15. The relative values of the fan jet and primary jet shock broadband noise vary with microphone position but the fan shock noise is always dominant. Microphone 13 (fig. 4-125) is the only location for which the measured data was near to the level of the predicted shock broadband noise. However, it is believed that this data is contaminated because of the presence of cirrus clouds during measurement. As stated in volume I, it is not clear how the cirrus clouds contaminate the microphone signal, although it is believed that either impact noise from the ice crystals or increased boundary layer turbulence may be involved. Generally, the shock broadband noise prediction shows a more distinct spectrum peak than seen in the measured data. The predicted peak usually occurs at frequencies higher than 1 KHz, which was also the case for the measured data.

The Lockheed procedure predicted jet mixing noise (shown only for microphones 13, 15, and 17 in Figures 4-125, 4-126, and 4-130) would peak in the frequency range of 400 Hz. Except for the data contaminated by cirrus clouds, the predicted jet noise is 5 to 10 dB higher than the measured data in this frequency range (see fig. 4-130 for microphone 17 in particular).

The turbomachinery noise predictions are best evaluated with narrow band data. However, some observations from the $1/3$ octave plots are possible. The predicted inlet noise spectrum shape appears to be combination tone noise dominated for the high engine power case shown. Also, the peak levels of the predicted inlet noise are near to or greater than the measured data at the inlet noise predicted peak frequency for microphones 2, 4, 6, and 15. Combination tone noise was not observed in the narrow band spectra of the measured data. The prediction of combination tone noise is therefore high. The turbine noise is most clearly seen in the measured data at microphone 10 (fig. 4-129). At $M_{AP} = 0.8$, the radiation angle to microphone 10 for sources at the primary nozzle is 66 deg from the aft engine axis. As seen

in Figure 4-129, the predicted turbine component peak $\frac{1}{3}$ octave level for $M_{Fan} = 1.26$ is about 3 dB below the measured peak for $M_{Fan} = 1.24$. This is considered good agreement since contribution from other noise sources such as shock broadband noise would bring the total predicted level in the turbine frequency range up if these sources were added to the turbine component. Referring to Figure 4-131, it is seen that the prediction for turbine noise shows very little drop off as engine power is reduced. The plot in Figure 4-131 compares measured $\frac{1}{3}$ octave SPLs from the $\frac{1}{3}$ octave in which the 5th stage turbine tone is located versus predicted turbine component peak $\frac{1}{3}$ octave levels. As for the predicted turbine OASPL in Figure 4-118, the turbine tone $\frac{1}{3}$ octave SPL shows a small change over the entire engine power range. The measured data on the other hand shows a strong power setting dependence. At the lowest power conditions for which data was measured, the measurements are approximately 10 dB below the predictions. The slow variation of the predicted turbine noise with engine power setting appearing in Figure 4-118 to correspond well with the measured data is therefore misleading.

Figures 4-132 and 4-133 are comparisons of Lockheed procedure predictions with measured $\frac{1}{3}$ octave spectra for an airplane Mach number of 0.6 at microphone 17. Microphone 17 is shown because the Lockheed procedure gave jet noise predictions for this microphone position. For $M_{Fan} = 1.15$, shown in Figure 4-132, the predicted jet mixing noise and fan jet shock noise overpredict the measured data by more than 10 dB. For $M_{Fan} = 0.81$, shown in Figure 4-133, the turbine tone noise prediction is at least 4 dB high. The jet noise prediction peak is within 3 dB of the measured data for this M_{Fan} , but it is not clear that jet noise actually contributes significantly to the measured data. As discussed previously, if jet noise were an important contributor at the subsonic M_{Fan} s, reducing the airplane Mach number from $M_{AP} = 0.8$ to $M_{AP} = 0.6$ at constant M_{Fan} would result in a noise increase. Since this was not observed, it was concluded that jet noise was not significant. The source of the measured low to midfrequency broadband noise that dominates the $\frac{1}{3}$ octave spectra for $M_{Fan} = 0.76$ and $M_{Fan} = 0.86$ in Figure 4-133 is not known. Since the levels are relatively low (≈ 100 dB), it is quite possible that we are no longer observing engine noise at all. Airflow generated noise sources such as boundary layer turbulence pressure fluctuations, turbulence on the transducer, or some other undetermined source may be dominating.

One-third octave spectrum predictions for jet mixing and jet shock noise using the Butzel procedure and for jet mixing noise using the Lu procedure are shown in Figures 4-134 to 4-137. Compared to the Lockheed procedure, the Butzel shock noise spectra peak at much lower frequencies. At microphone 17, the Butzel procedure jet noise predictions peak at significantly higher frequencies than the Lu or the Lockheed predictions. The Lu procedure jet predictions are seen to be well below the measured data. Both procedures predict jet noise to increase going from $M_{AP} = 0.8$ to $M_{AP} = 0.6$, as was the case for the Lockheed procedure.

4.2.4.3 Fan Tones

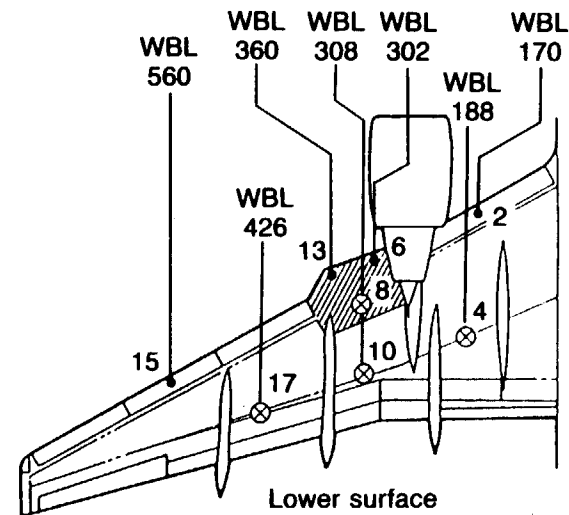
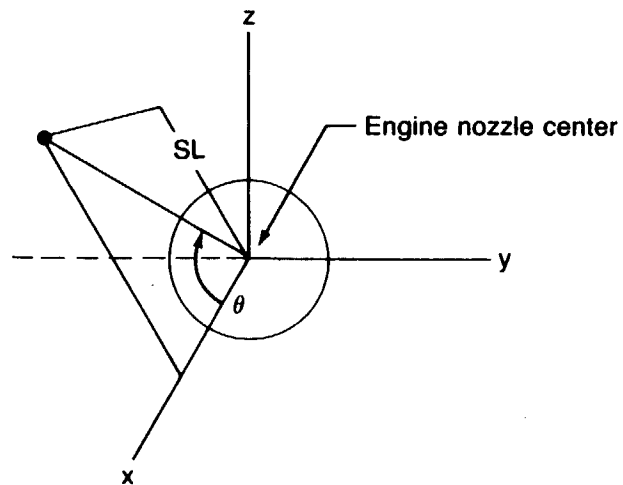
The narrow band spectra shown in Figures 4-10 to 4-17 and Figures 4-30 to 4-37 show the presence of fan tone harmonics. This data was used to compare measured fan tone levels with the Lockheed procedure predictions. Comparison plots for microphones 8, 10, and 17 are shown in Figures 4-138 to 4-140. The prediction curves were obtained from the $\frac{1}{3}$ octave band aft fan component predictions. The broadband noise SPL was estimated from the $\frac{1}{3}$ octave prediction and logarithmically subtracted from the predicted SPL of the $\frac{1}{3}$ octave containing the tone. Comparisons are shown for the fan fundamental and the fan second harmonic. It is seen that the fan blade passing frequency tone is underpredicted at all three microphones with the disagreement increasing as engine power is decreased. The predictions for the second harmonic however appear quite good for microphones 10 and 17. Some significant disagreement is seen for low engine power at microphone 8. The fan tone prediction includes a prediction of the attenuation effect of the acoustic lining in the fan duct. No effort to evaluate the hardwall prediction and acoustic lining effect separately was made.

4.2.5 Conclusions From Prediction Comparisons

1. Use of convective amplification in the Lockheed predictions resulted in large overpredictions for the leading edge microphones in particular.
2. Broadband shock noise is predicted to be the dominant noise source at all microphones for the supersonic fan exhaust Mach number engine conditions. Lockheed broadband shock noise predicted data trends such as OASPL curve shape dependence on M_{Fan} and relative insensitivity to airplane Mach number (when convective amplification is not applied) showed agreement with measured data. However, predicted levels were of the order of 10 dB high.
3. Lockheed and Butzel jet mixing noise predictions are probably high. At subsonic M_{Fan} conditions both procedures predict a substantial noise increase going from $M_{AP} \approx 0.6$ to $M_{AP} \approx 0.8$ because of the *relative velocity* dependence of jet mixing noise. The measured data on the other hand showed a decrease in noise or no change when the airplane speed was reduced. It is therefore concluded that jet mixing noise was not an important noise source in the 757 data.
4. Turbomachinery noise generally was not well predicted by the Lockheed program. No attempt was made to separate the effects of acoustic lining in the predictions or measurements from the source level predictions.

Table 4-1. Microphone Coordinates

	Microphone Number							
	2	4	6	8	10	13	17	15
X distance from fan exit plane, ft	-2.4	11.0	3.7	8.2	15.0	5.9	18.4	15.9
X distance from primary exit plane, ft	-8.6	4.8	-2.5	2.0	8.8	-0.4	12.2	9.7
X distance from inlet plane, ft	8.7	22.1	14.8	19.3	26.1	16.9	29.5	27.0
$SL = (Y^2 + Z^2)^{1/2}$, ft	7.8	6.6	6.0	6.5	6.5	10.2	15.3	26.3
θ primary nozzle, deg	138	54	113	73	37	92	51	70
θ fan nozzle, deg	107	31	58	38	23	60	40	59
θ inlet, deg	42	17	22	19	14	31	27	44



$M_{AP} = 0.80$
 $N_{IC} = 4321$
 $M_{FAN} = 1.26$

M—Measured narrow band data level for turbine tone.
 If < sign, then tone not above broadband data

L—Lockheed procedure 1/3 octave turbine prediction. (At most 3 dB above tone level)

() No convective amplification applied to Lockheed prediction procedure

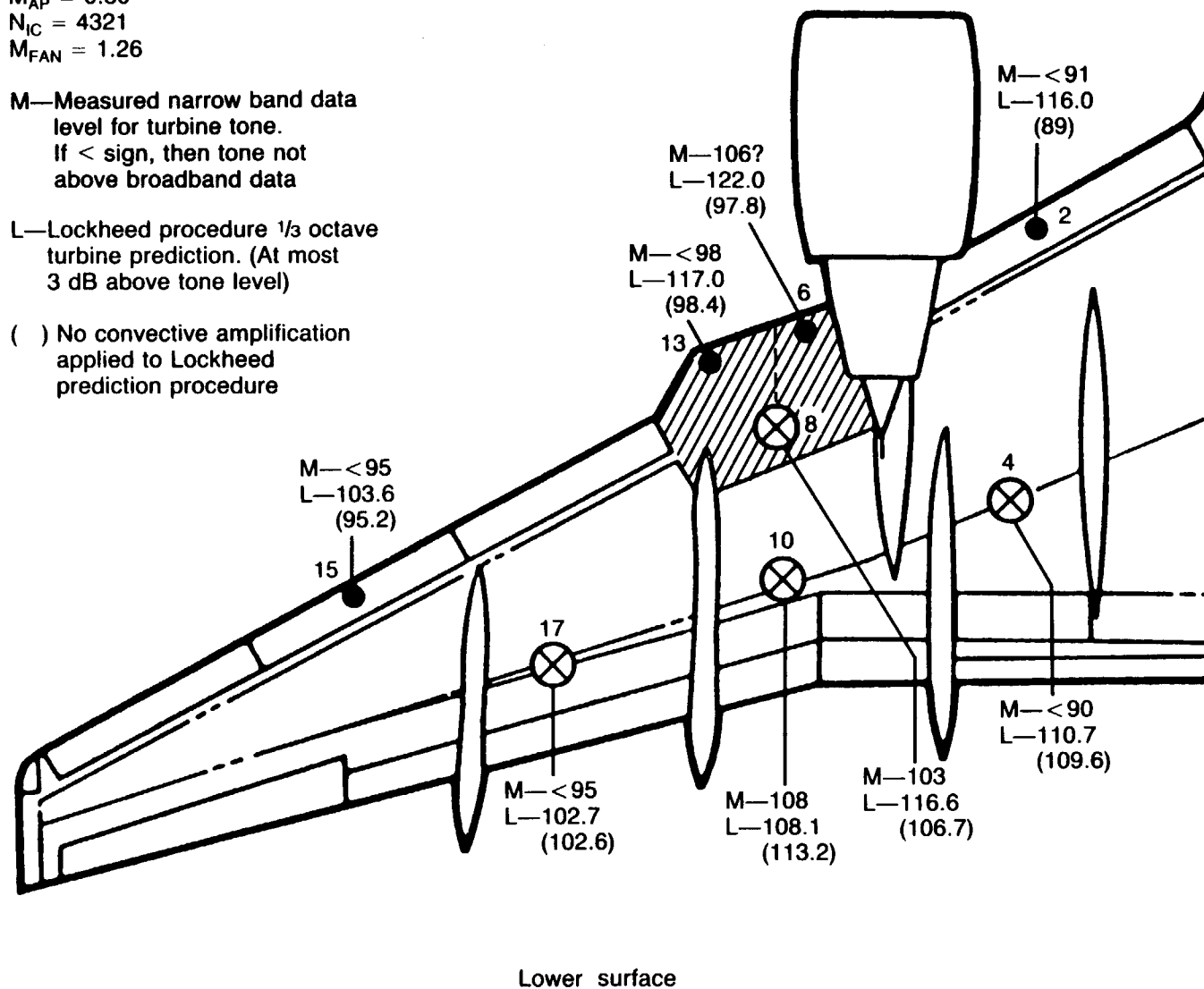


Figure 4-97. Measured vs. Predicted Turbine Noise Summary

$M_{AP} = 0.80$
 $N_{IC} = 4321$
 $M_{FAN} = 1.26$

M—Measured OASPL
 L—Lockheed shock broadband prediction
 () No convective amplification
 and no dynamic amplification
 applied to Lockheed
 prediction procedure
 B—Butzel shock prediction

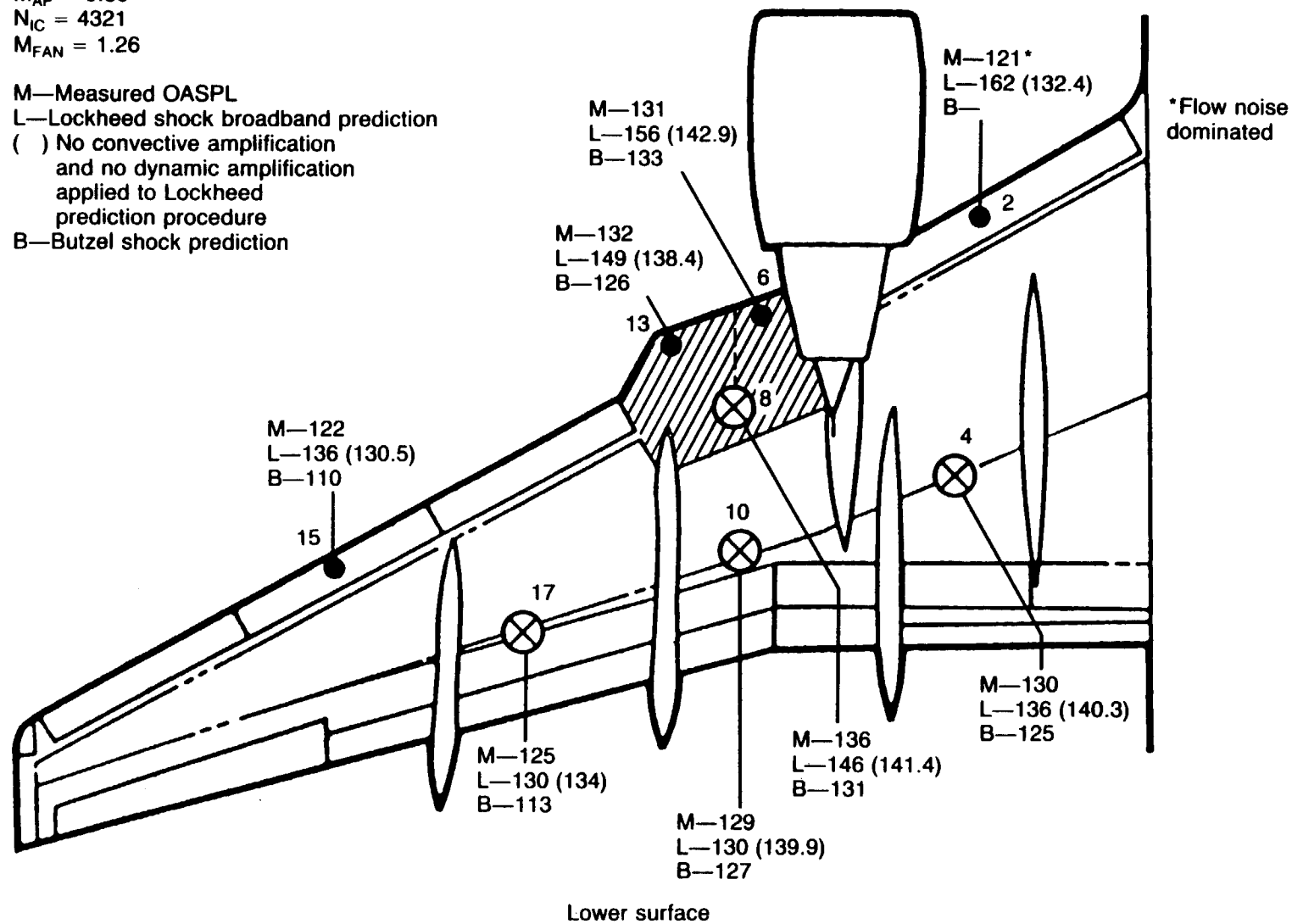
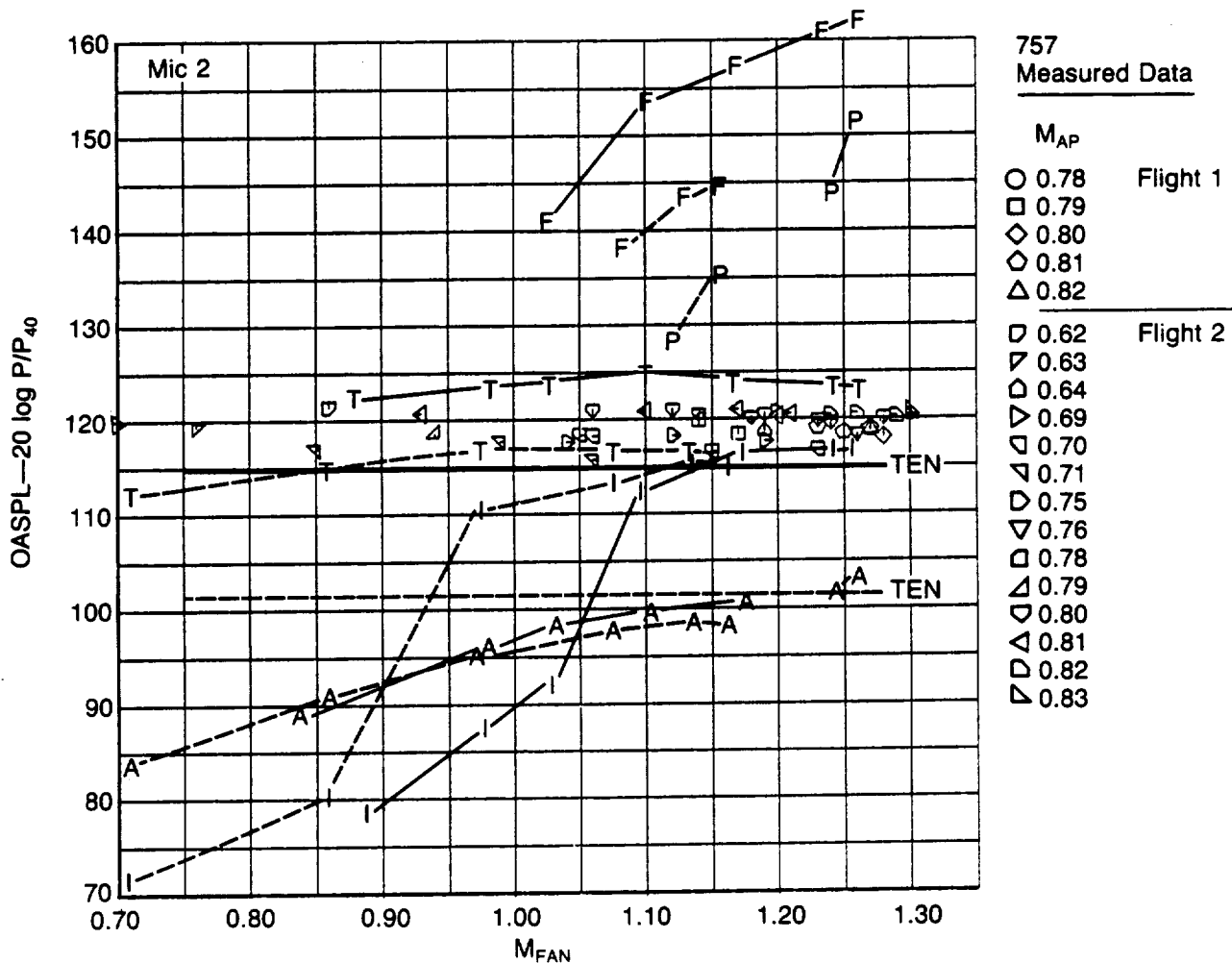


Figure 4-98. Measured vs. Predicted Shock Noise Summary



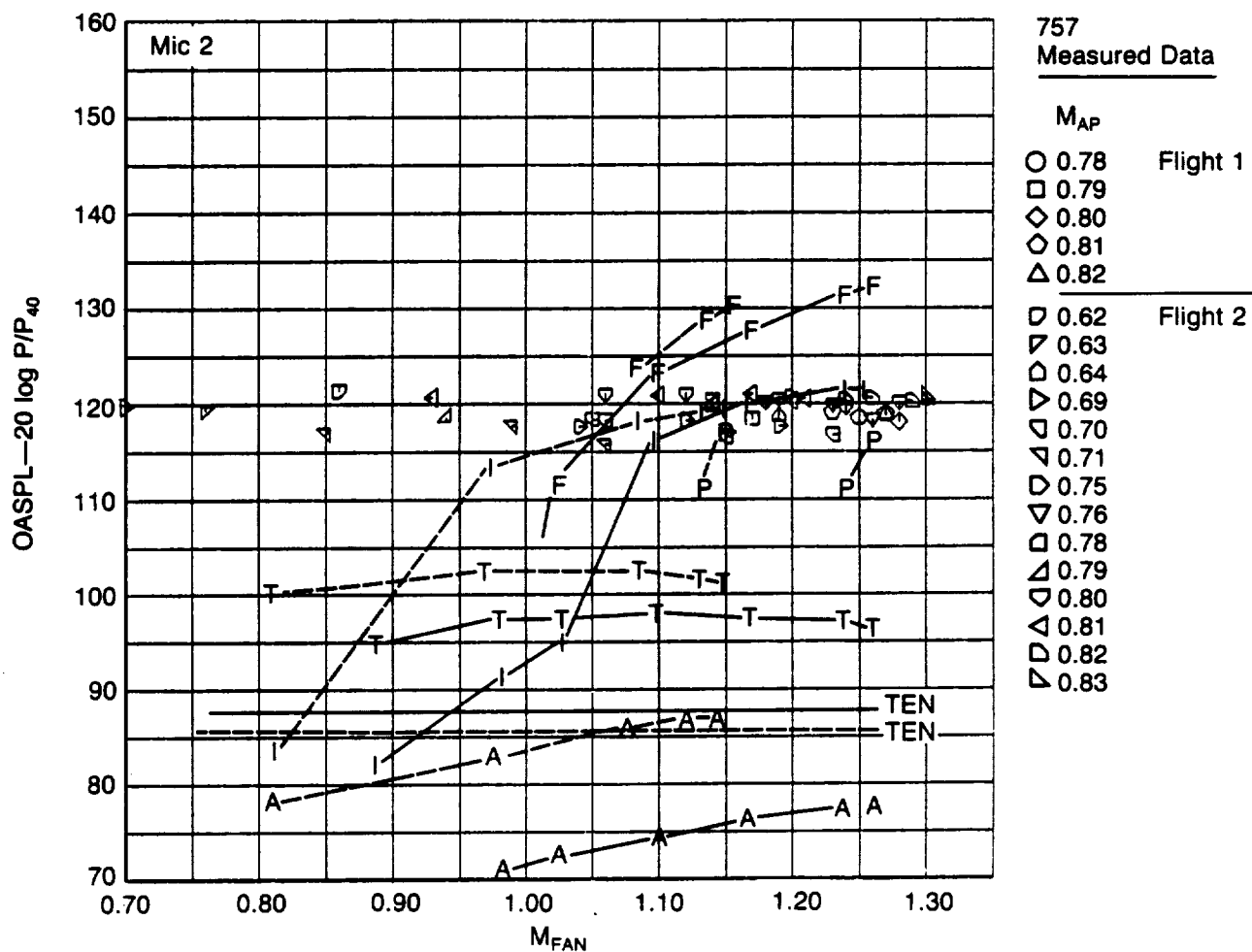
Lockheed
procedure
predictions

Note: Predictions include
"convective amplification"
and "dynamic amplification"
corrections

— $M_{AP} = 0.80$ TBLN = 60.4 dB
- - - $M_{AP} = 0.60$ TBLN = 60.3 dB

F — Fan jet shock broadband
P — Primary jet shock broadband
T — Turbine
A — Aft radiated fan
I — Inlet radiated fan
J — Jet mixing (not predicted)
TEN — Trailing edge
TBLN — Turbulent boundary layer

Figure 4-99. Microphone 2 Measured OASPL's vs. Lockheed Procedure Predictions



Lockheed
procedure
predictions

Note: Predictions do not include
"convective amplification"
and "dynamic amplification"
corrections

— M_{AP} = 0.80 TBLN = 51.5 dB
--- M_{AP} = 0.60 TBLN = 54.1 dB

F — Fan jet shock broadband
P — Primary jet shock broadband
T — Turbine
A — Aft radiated fan
I — Inlet radiated fan
J — Jet mixing (not predicted)
TEN — Trailing edge
TBLN — Turbulent boundary layer

Figure 4-100. Microphone 2 Measured OASPL's vs. Lockheed Procedure Predictions Without Convective and Dynamic Amplification Corrections

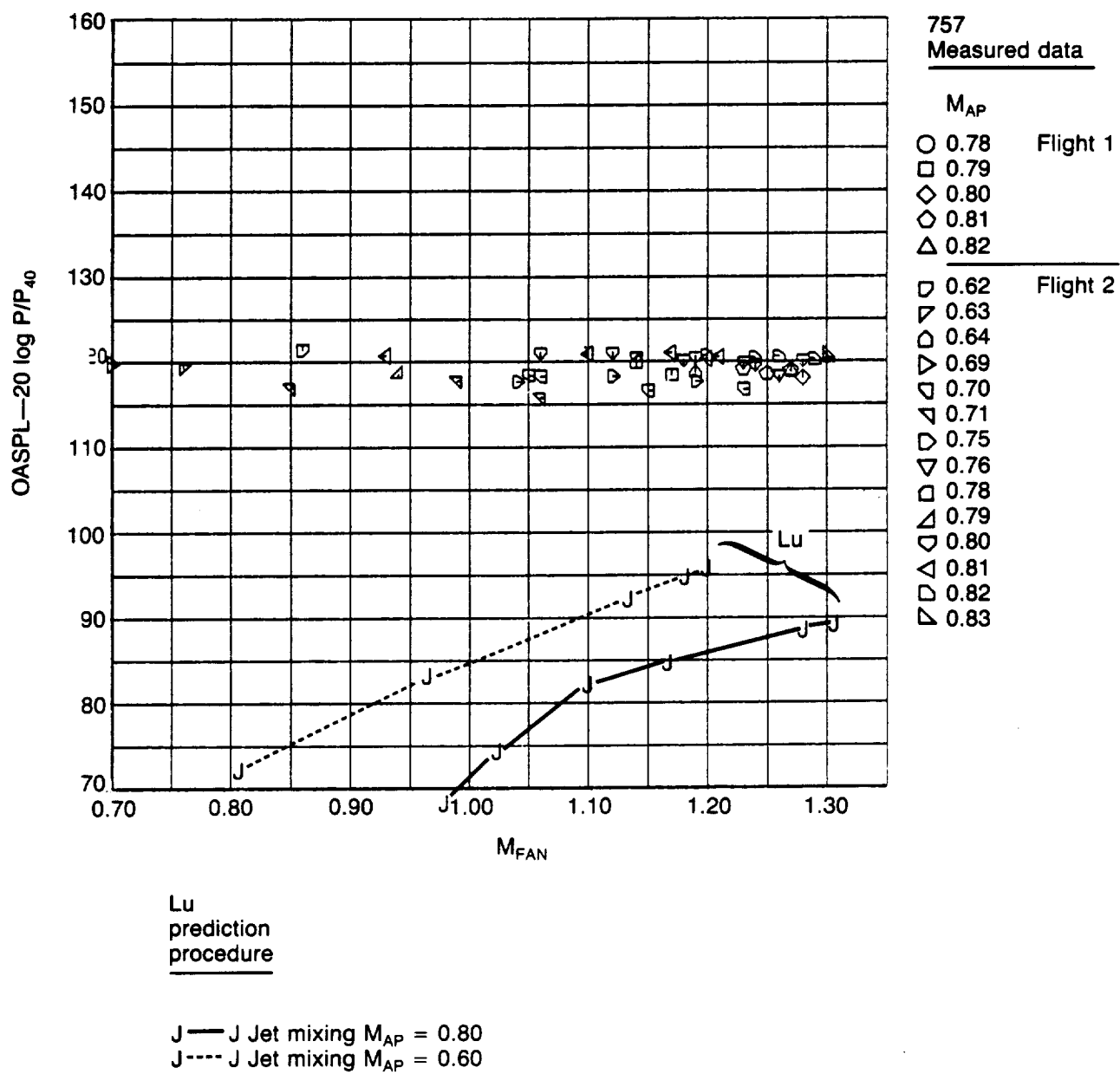


Figure 4-101. Microphone 2 Measured OASPL's vs. Boeing-Lu Procedure Predictions for Jet Mixing Noise

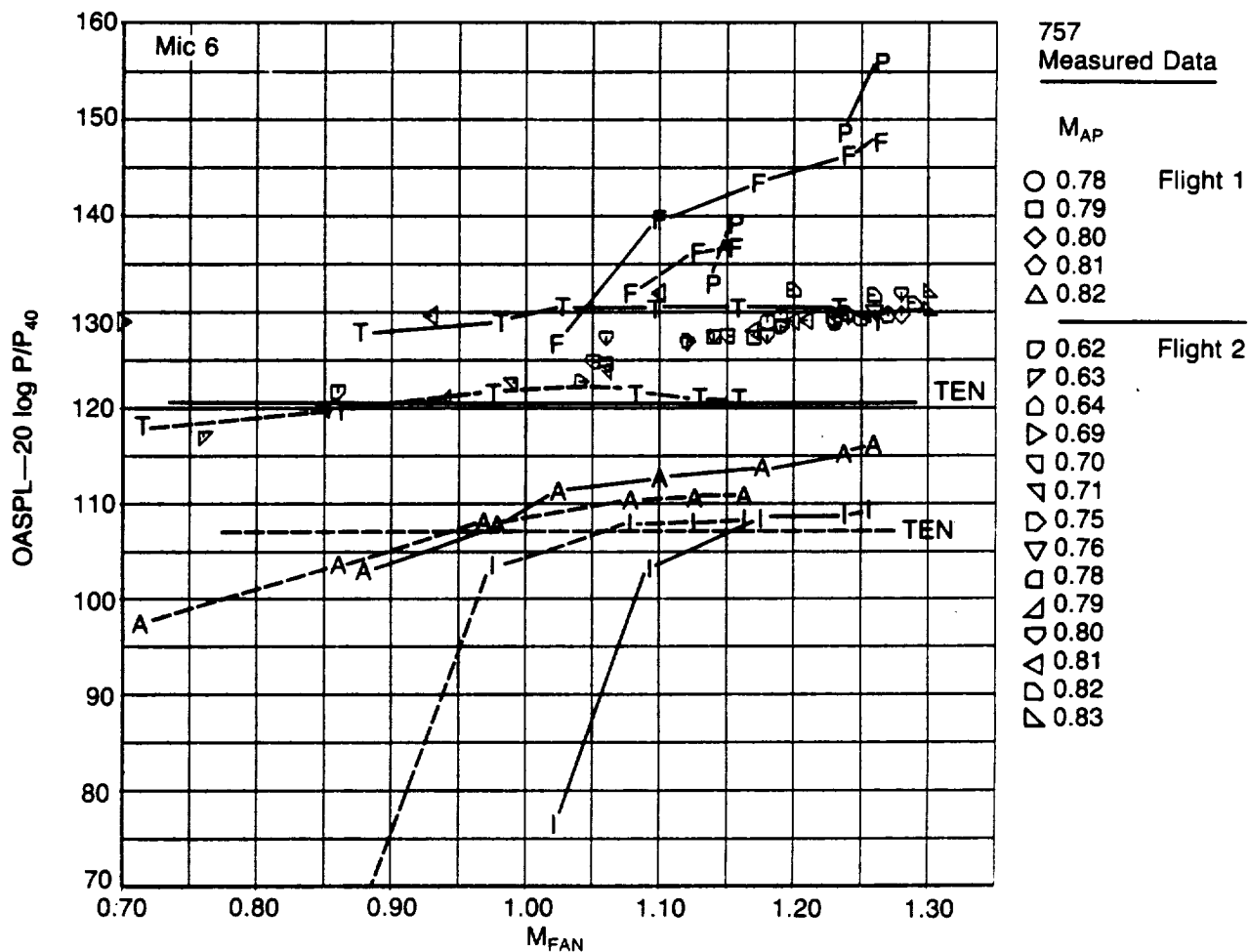


Figure 4-102. Microphone 6 Measured OASPL's vs. Lockheed Procedure Predictions

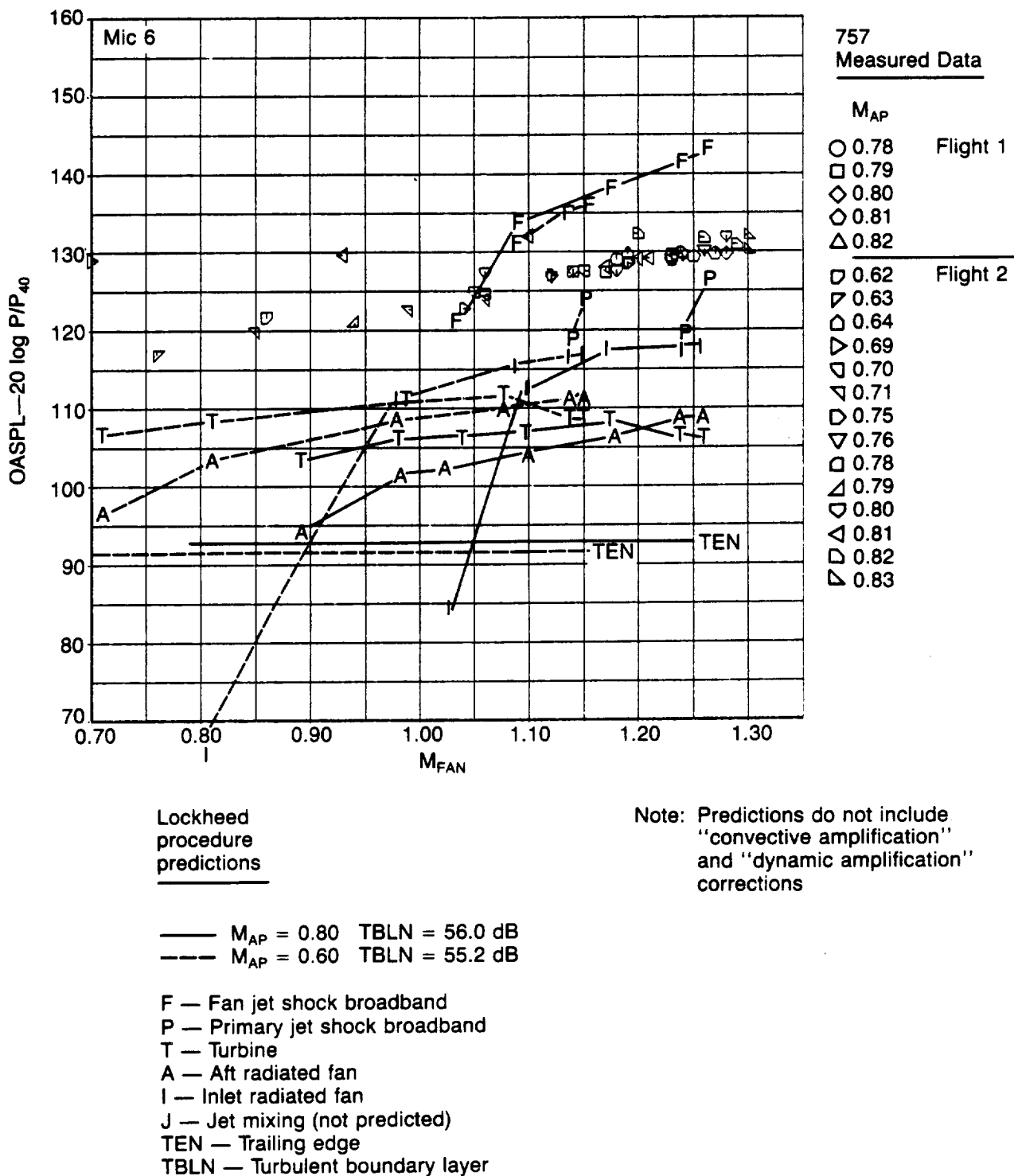


Figure 4-103. Microphone 6 Measured OASPL's vs. Lockheed Procedure Predictions Without Convective and Dynamic Amplification Corrections

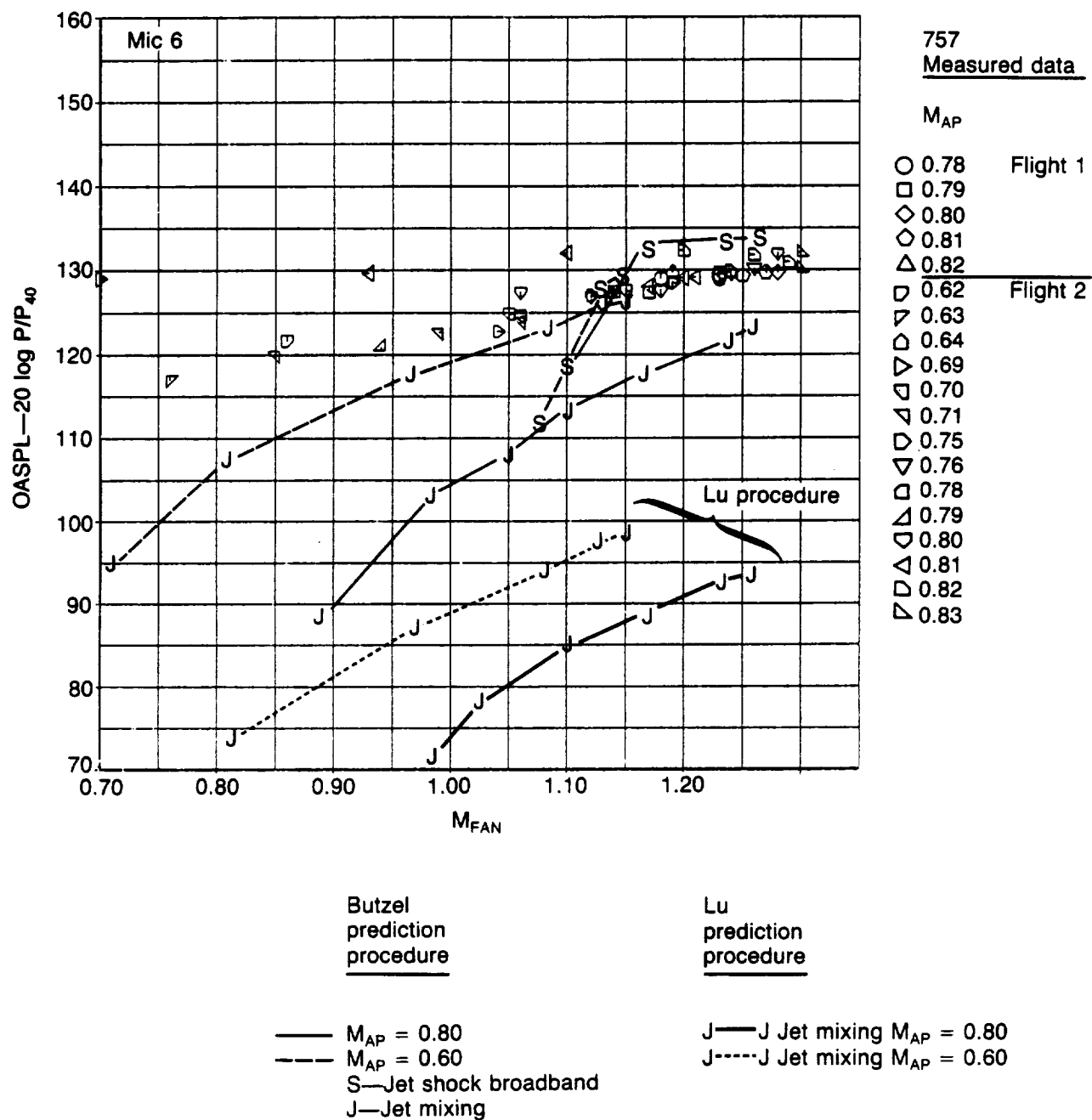


Figure 4-104. Microphone 6 Measured OASPL's vs. Boeing Butzel and Lu Procedure Predictions for Jet Shock and Jet Mixing Noise.

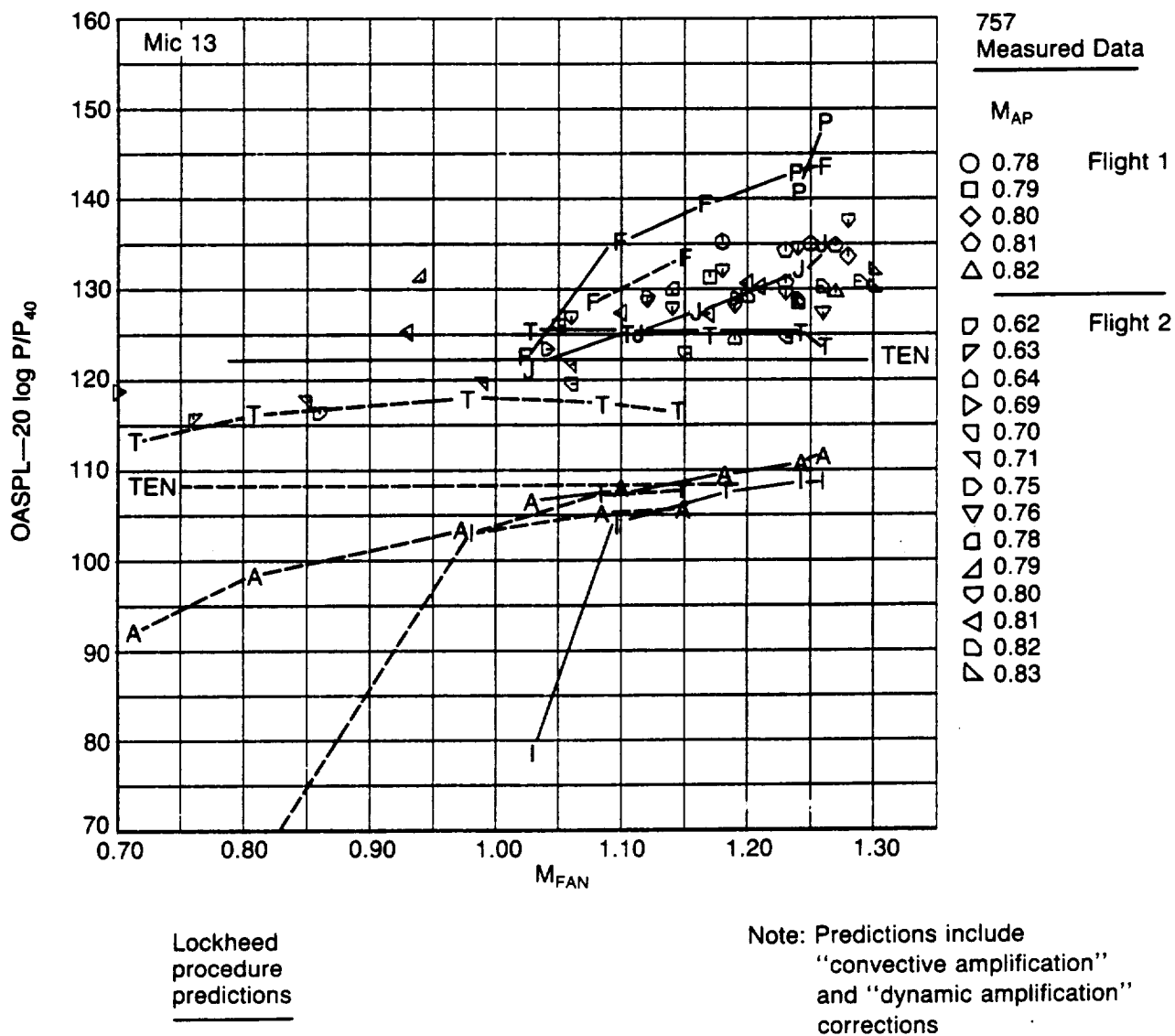


Figure 4-105. Microphone 13 Measured OASPL's vs. Lockheed Procedure Predictions

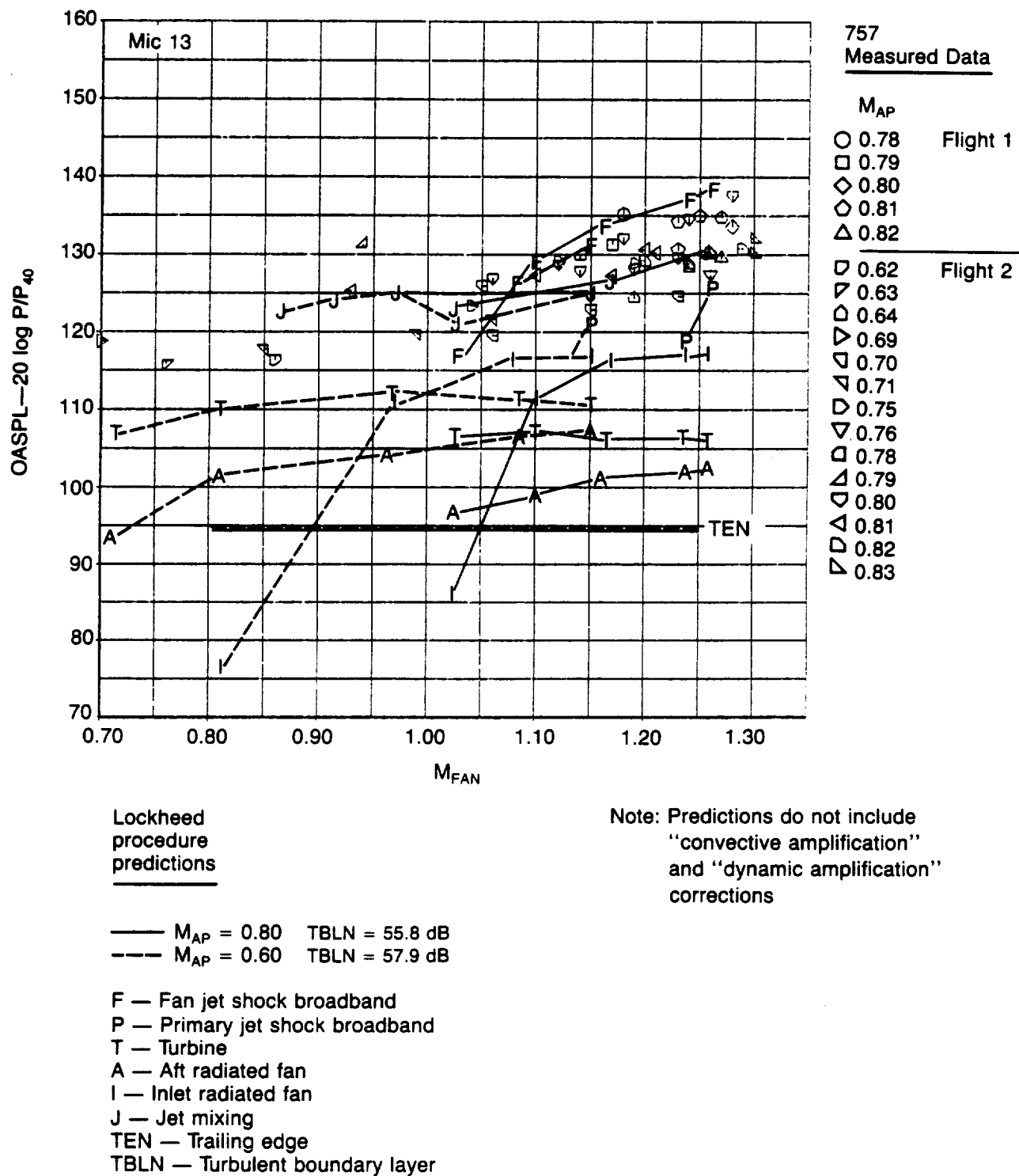


Figure 4-106. Microphone 13 Measured OASPL's vs. Lockheed Procedure Predictions Without Convective and Dynamic Amplification Corrections

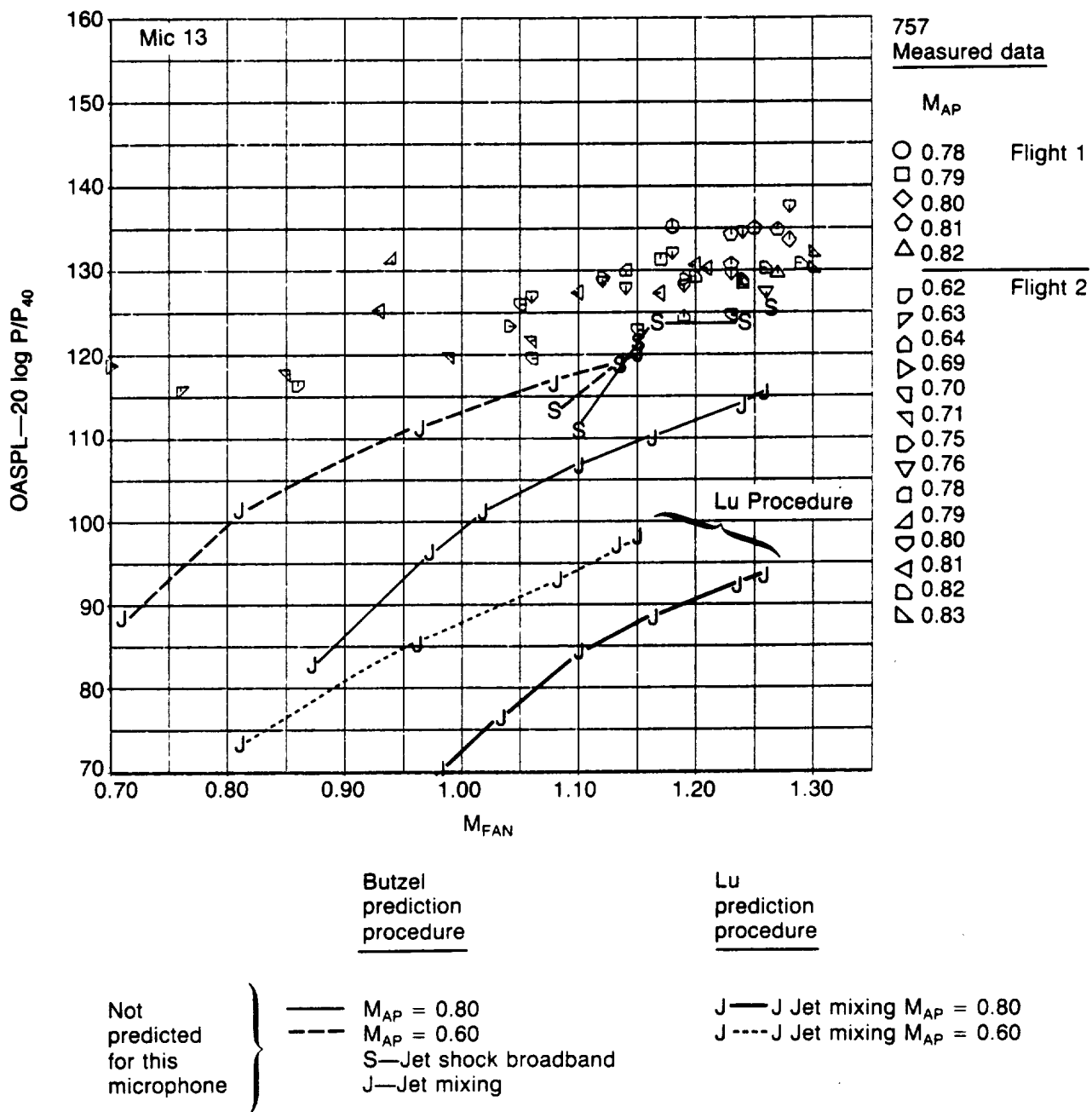
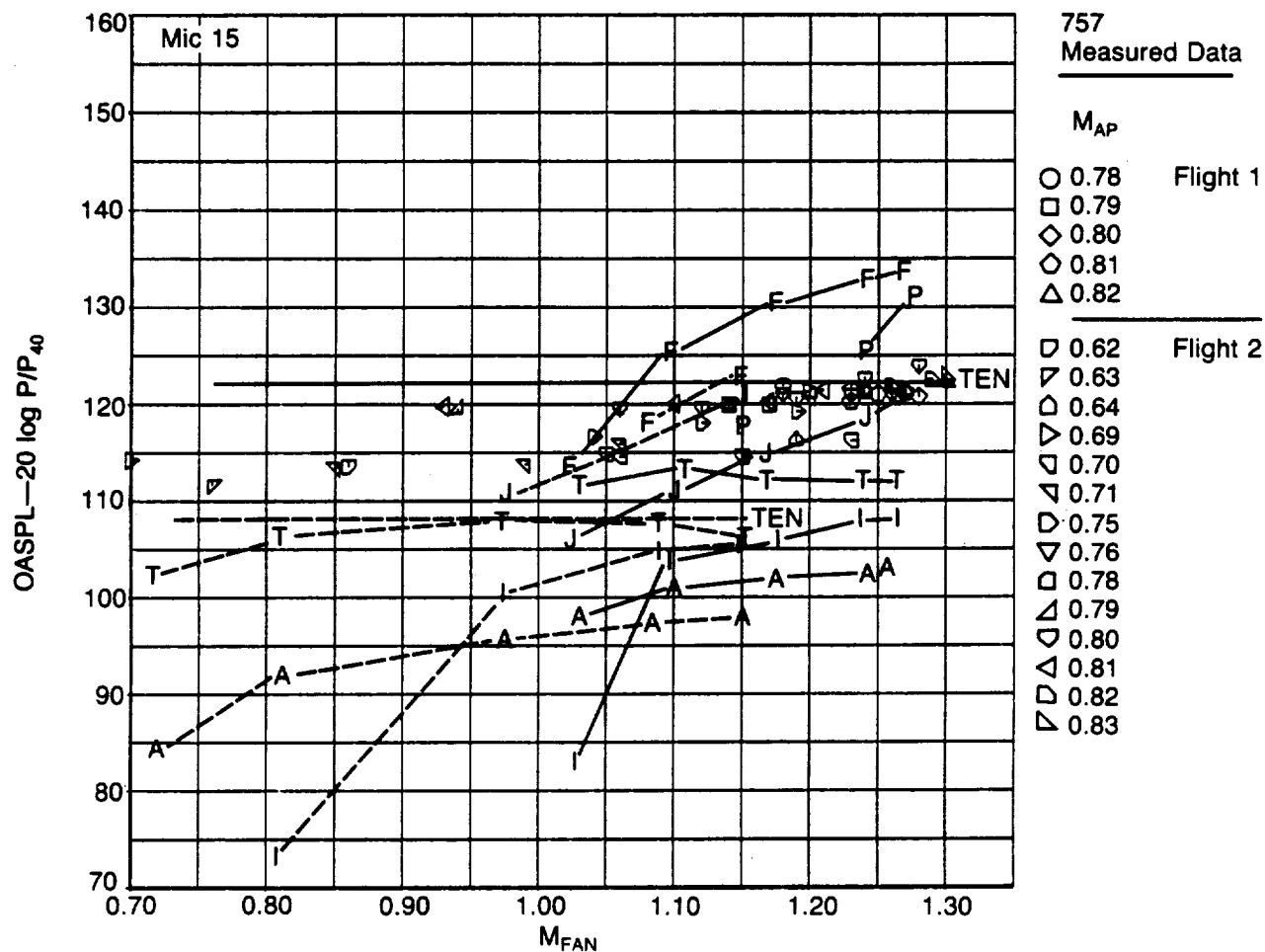


Figure 4-107. Microphone 13 Measured OASPL's vs. Boeing Butzel and Lu Procedure Predictions for Jet Shock and Jet Mixing Noise.



Lockheed
procedure
predictions

— M_{AP} = 0.80 TBLN = 63.3 dB
 --- M_{AP} = 0.60 TBLN = 59.7 dB

F — Fan jet shock broadband
 P — Primary jet shock broadband
 T — Turbine
 A — Aft radiated fan
 I — Inlet radiated fan
 J — Jet mixing
 TEN — Trailing edge
 TBLN — Turbulent boundary layer

Note: Predictions include
 "convective amplification"
 and "dynamic amplification"
 corrections

Figure 4-108. Microphone 15 Measured OASPL's vs. Lockheed Procedure Predictions

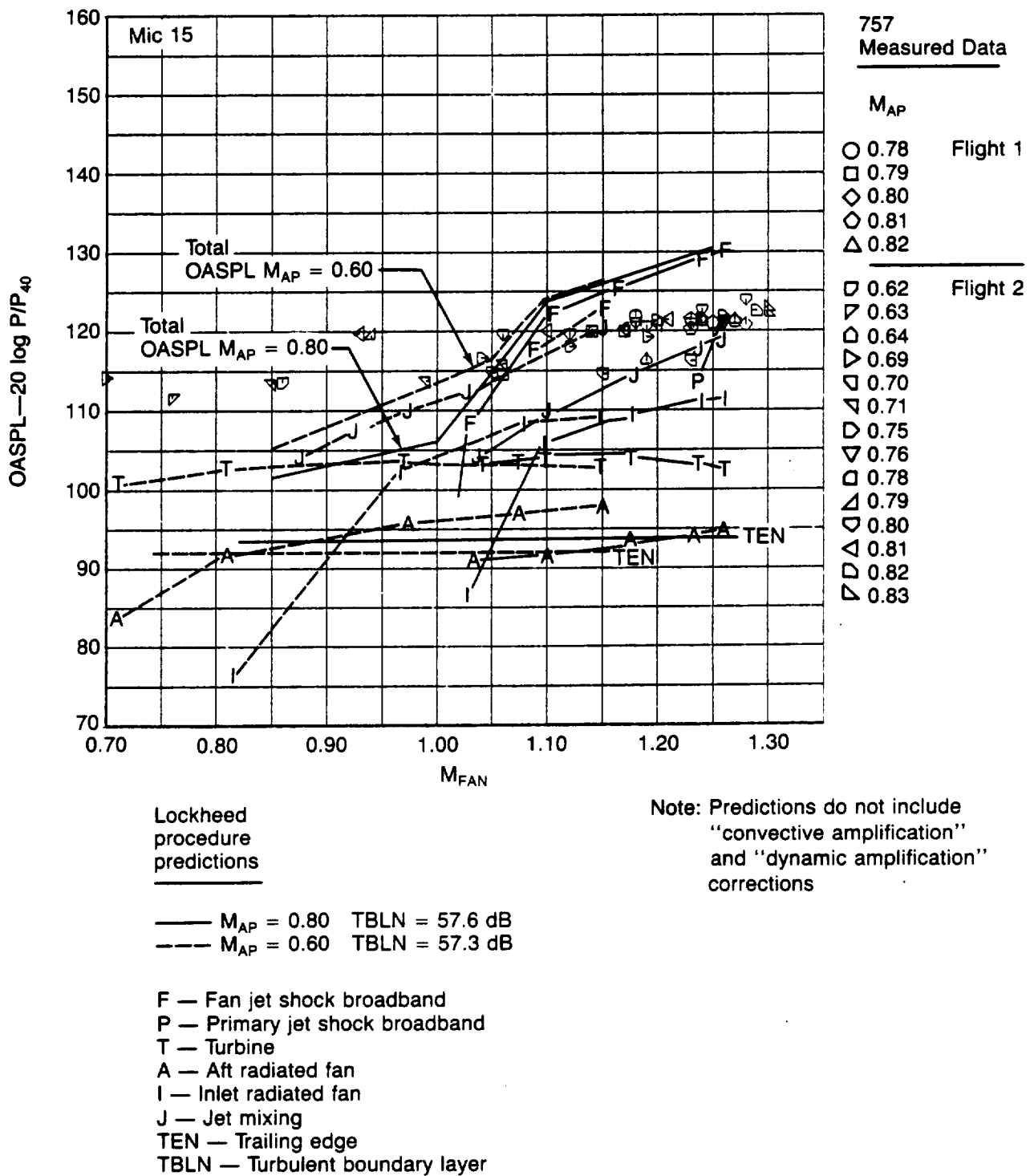


Figure 4-109. Microphone 15 Measured OASPL's vs. Lockheed Procedure Predictions Without Convective and Dynamic Amplification Corrections

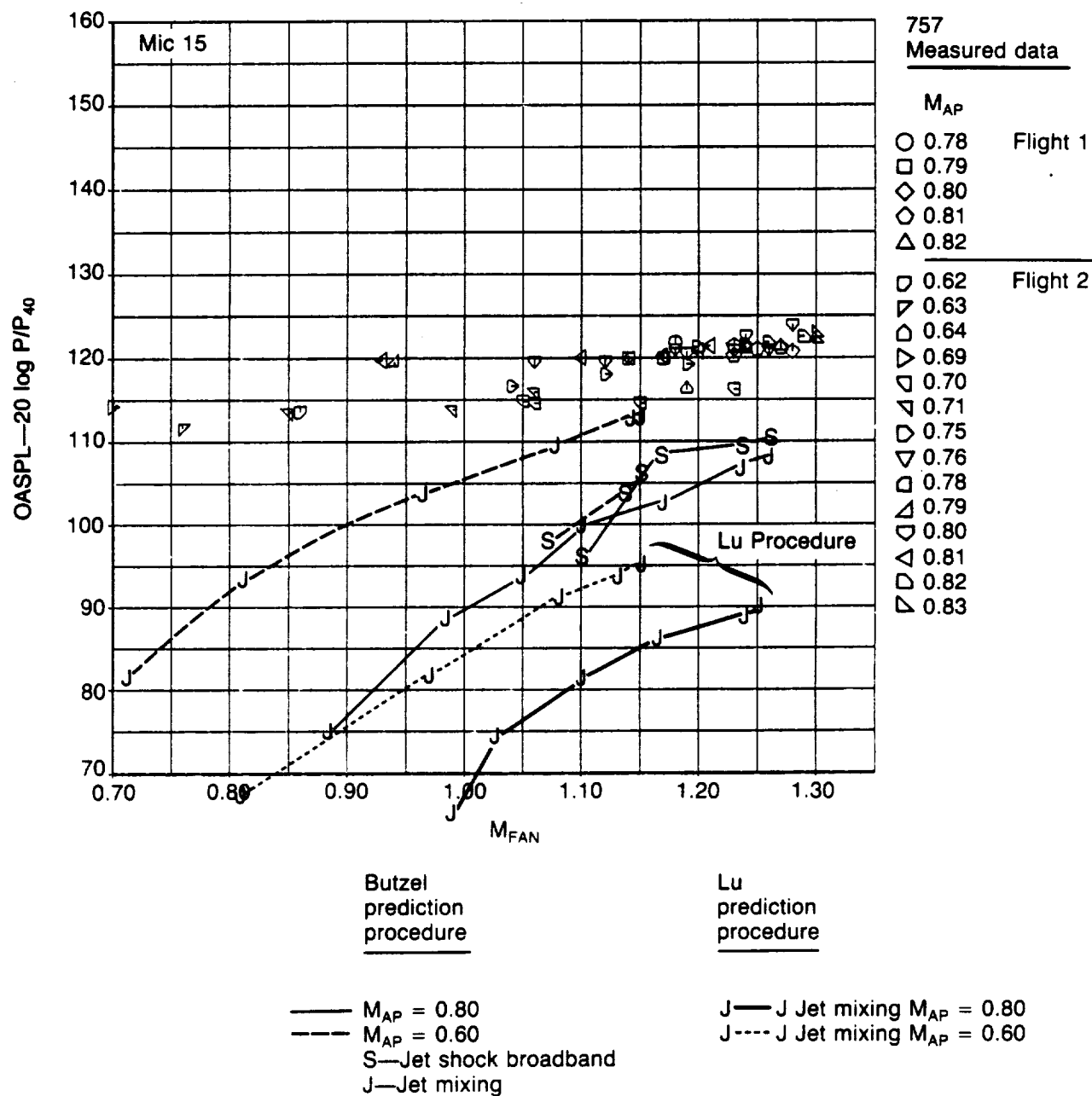
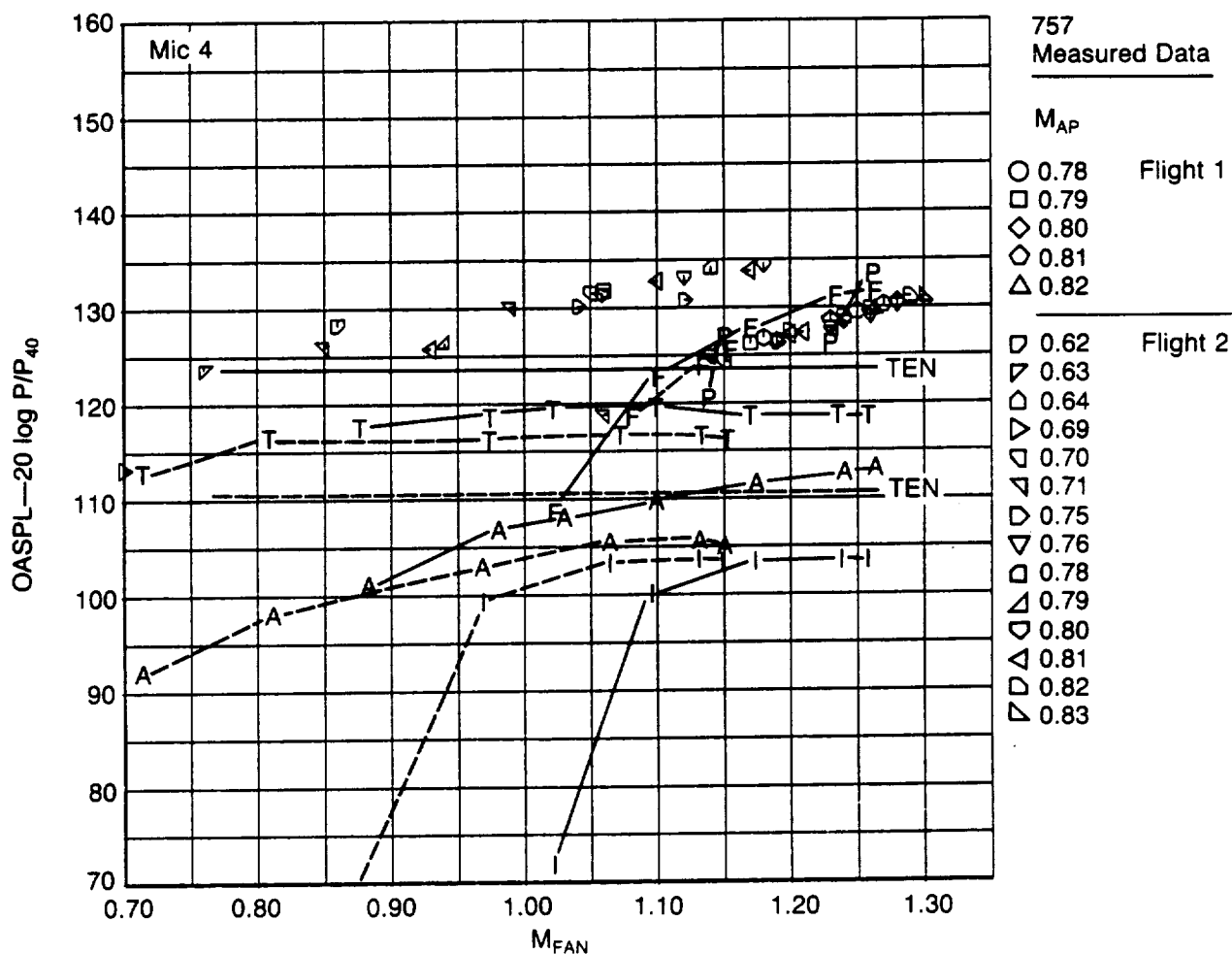
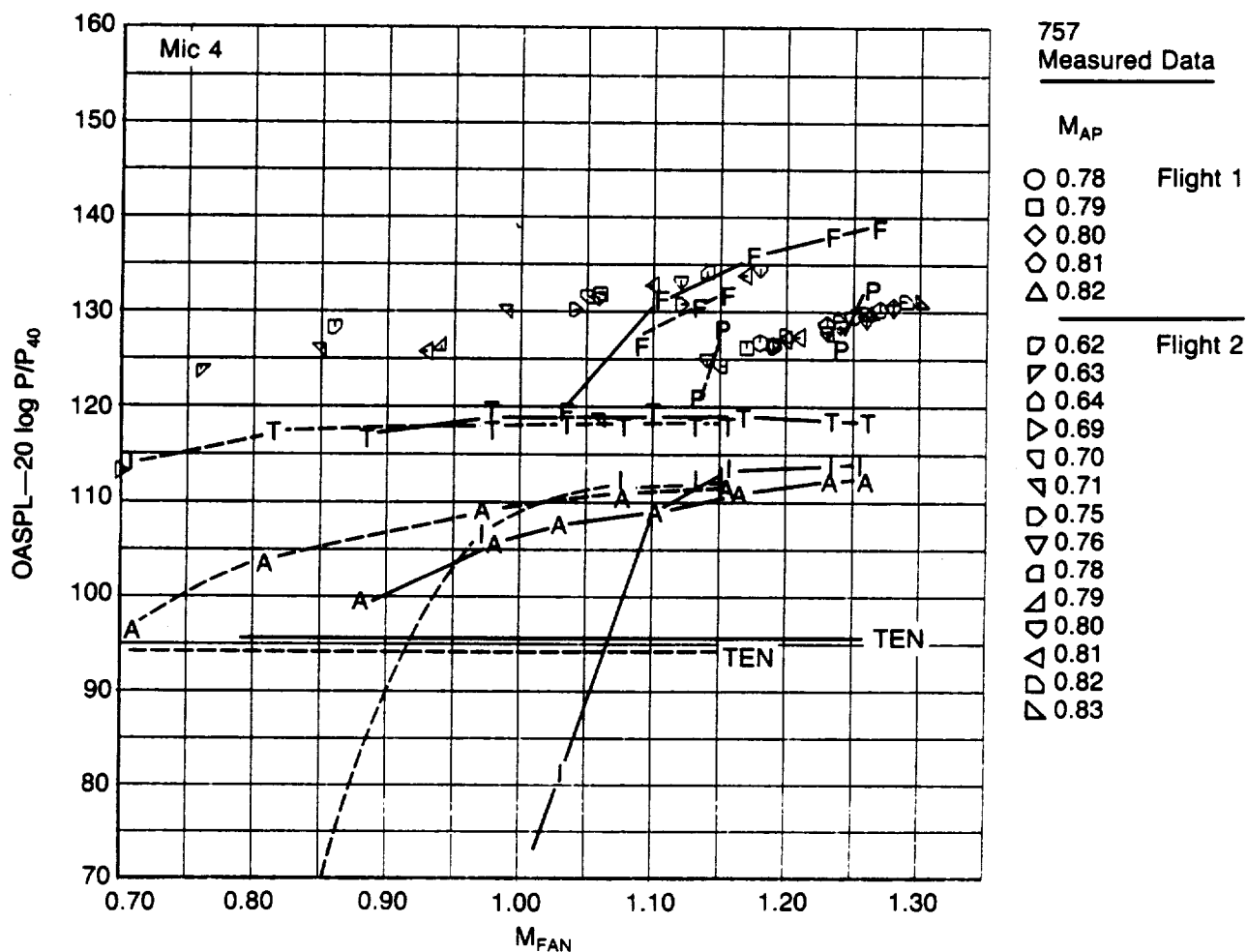


Figure 4-110. Microphone 15 Measured OASPL's vs. Boeing Butzel and Lu Procedure Predictions for Jet Shock and Jet Mixing Noise.



Note: Predictions include "convective amplification" and "dynamic amplification" corrections

Figure 4-111. Microphone 4 Measured OASPL's vs. Lockheed Procedure Predictions



Lockheed
procedure
predictions

Note: Predictions do not include
"convective amplification"
and "dynamic amplification"
corrections

— $M_{AP} = 0.80$ TBLN = 76.8 dB
 --- $M_{AP} = 0.60$ TBLN = 67.8 dB

F — Fan jet shock broadband
 P — Primary jet shock broadband
 T — Turbine
 A — Aft radiated fan
 I — Inlet radiated fan
 J — Jet mixing (not predicted)
 TEN — Trailing edge
 TBLN — Turbulent boundary layer

Figure 4-112. Microphone 4 Measured OASPL's vs. Lockheed Procedure Predictions Without Convective and Dynamic Amplification Corrections

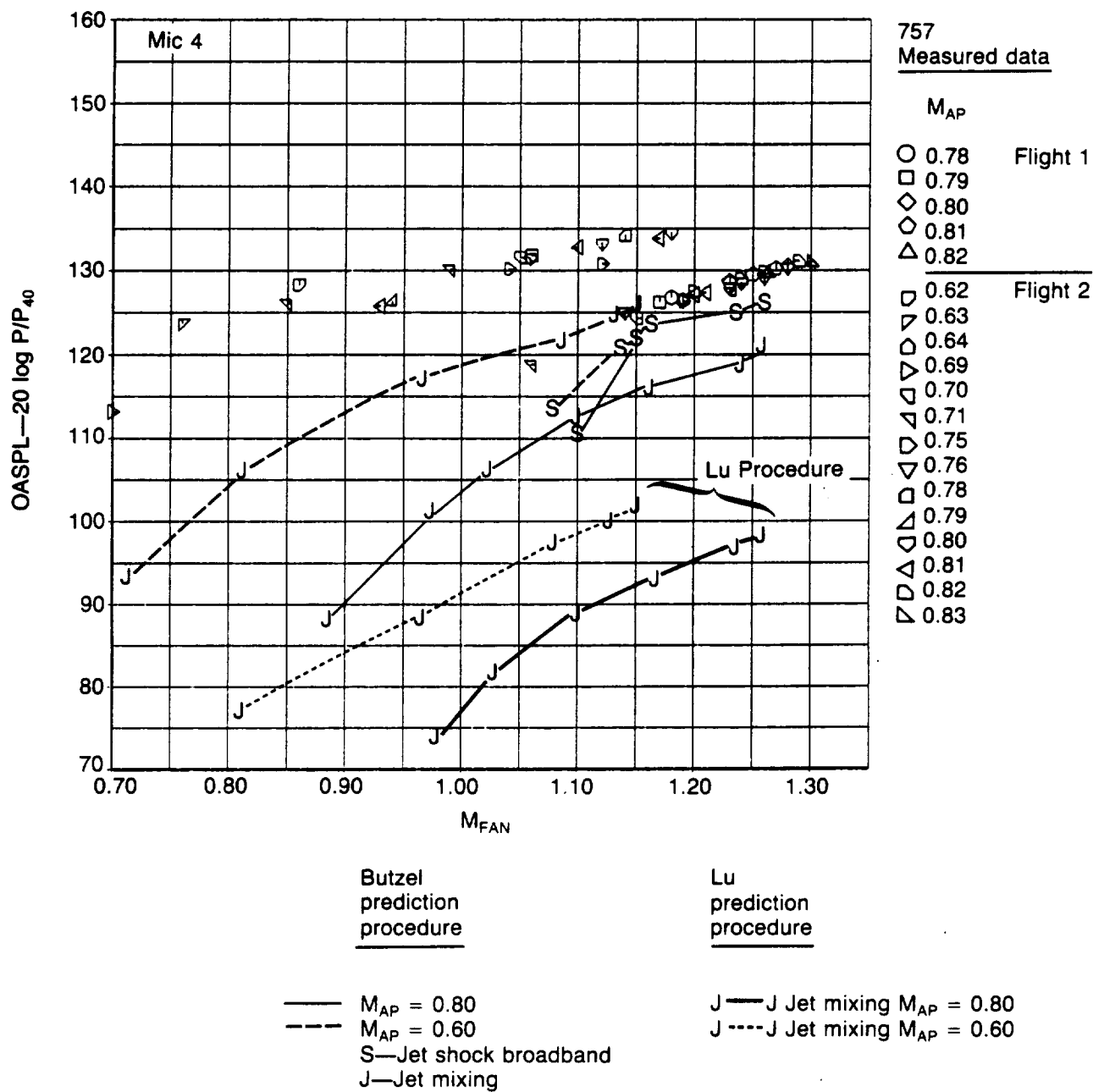
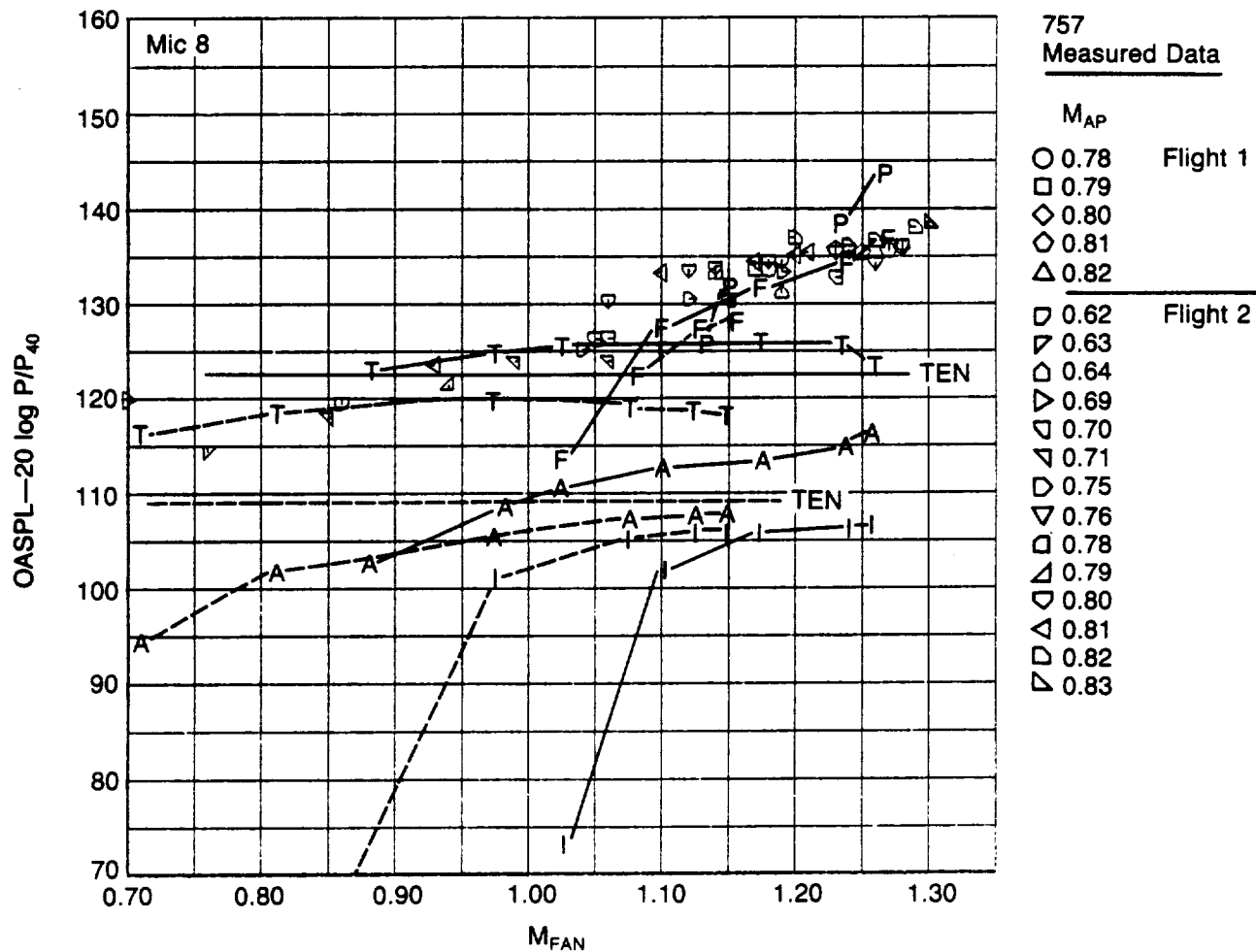


Figure 4-113. Microphone 4 Measured OASPL's vs. Boeing Butzel and Lu Procedure Predictions for Jet Shock and Jet Mixing Noise.



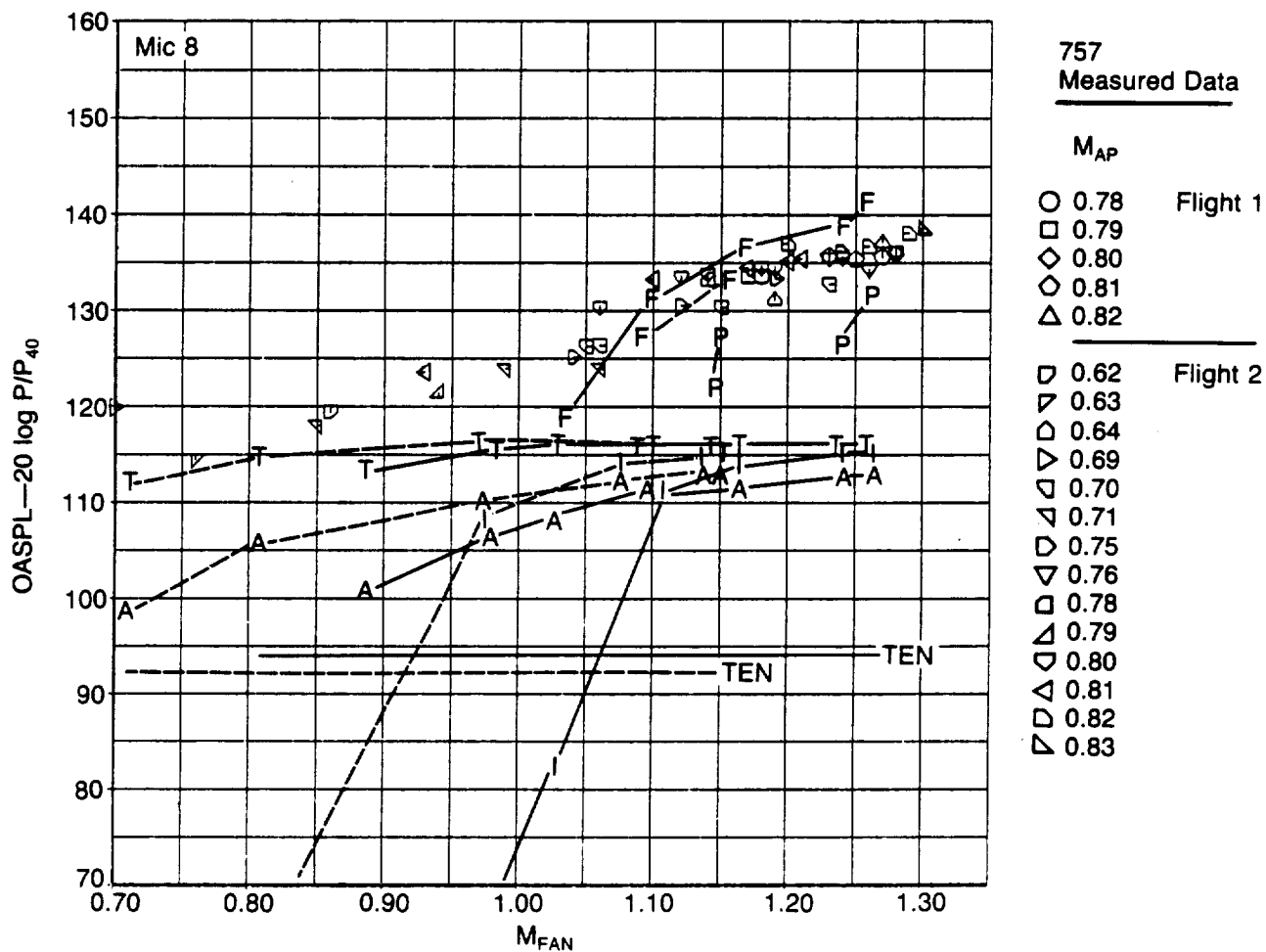
Lockheed
procedure
predictions

Note: Predictions include
"convective amplification"
and "dynamic amplification"
corrections

— $M_{AP} = 0.80$ TBLN = 82.7 dB
- - - $M_{AP} = 0.60$ TBLN = 81.5 dB

F — Fan jet shock broadband
P — Primary jet shock broadband
T — Turbine
A — Aft radiated fan
I — Inlet radiated fan
J — Jet mixing (not predicted)
TEN — Trailing edge
TBLN — Turbulent boundary layer

Figure 4-114. Microphone 8 Measured OASPL's vs. Lockheed Procedure Predictions



Note: Predictions do not include "convective amplification" and "dynamic amplification" corrections

Figure 4-115. Microphone 8 Measured OASPL's vs. Lockheed Procedure Predictions Without Convective and Dynamic Amplification Corrections

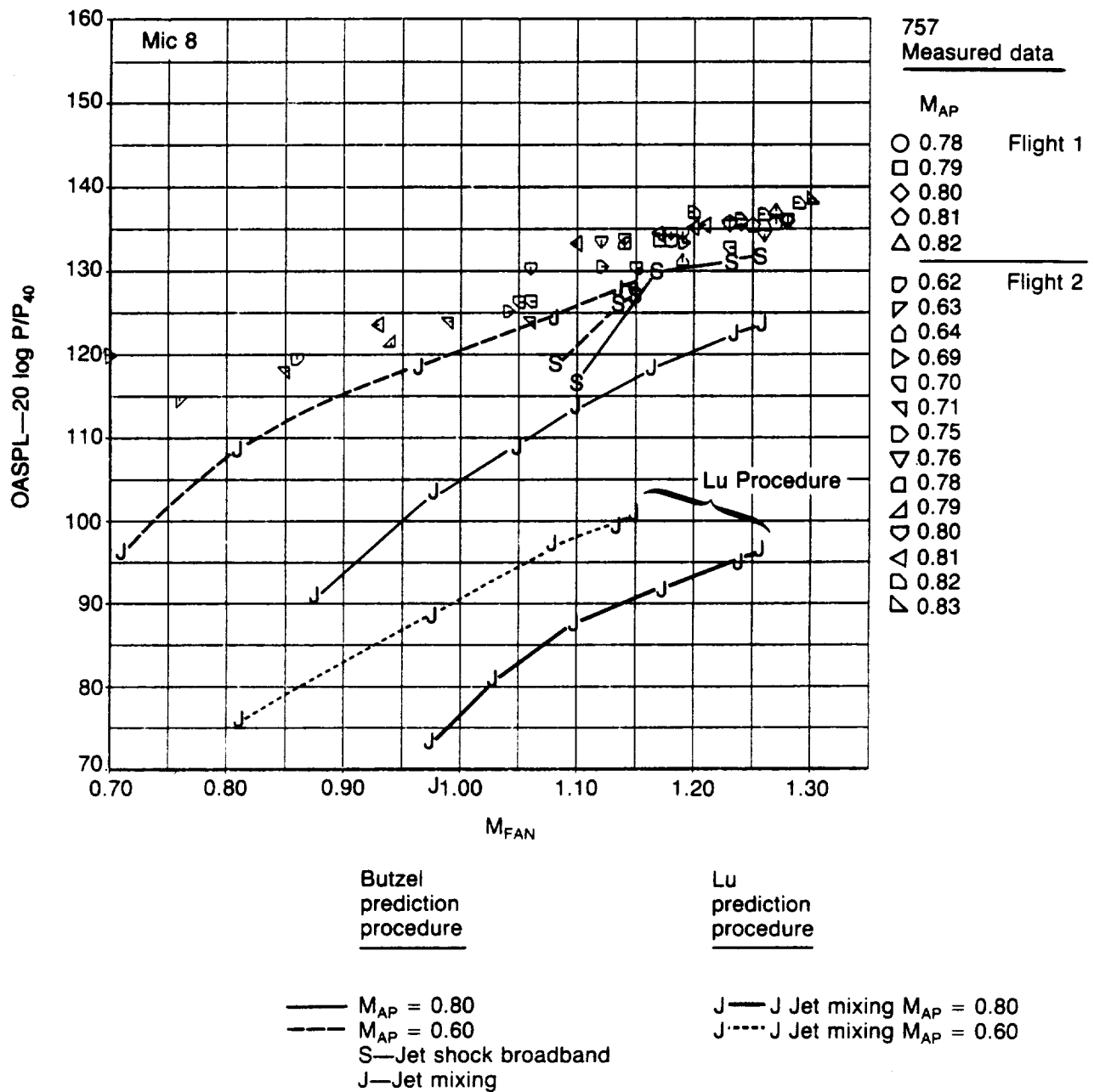
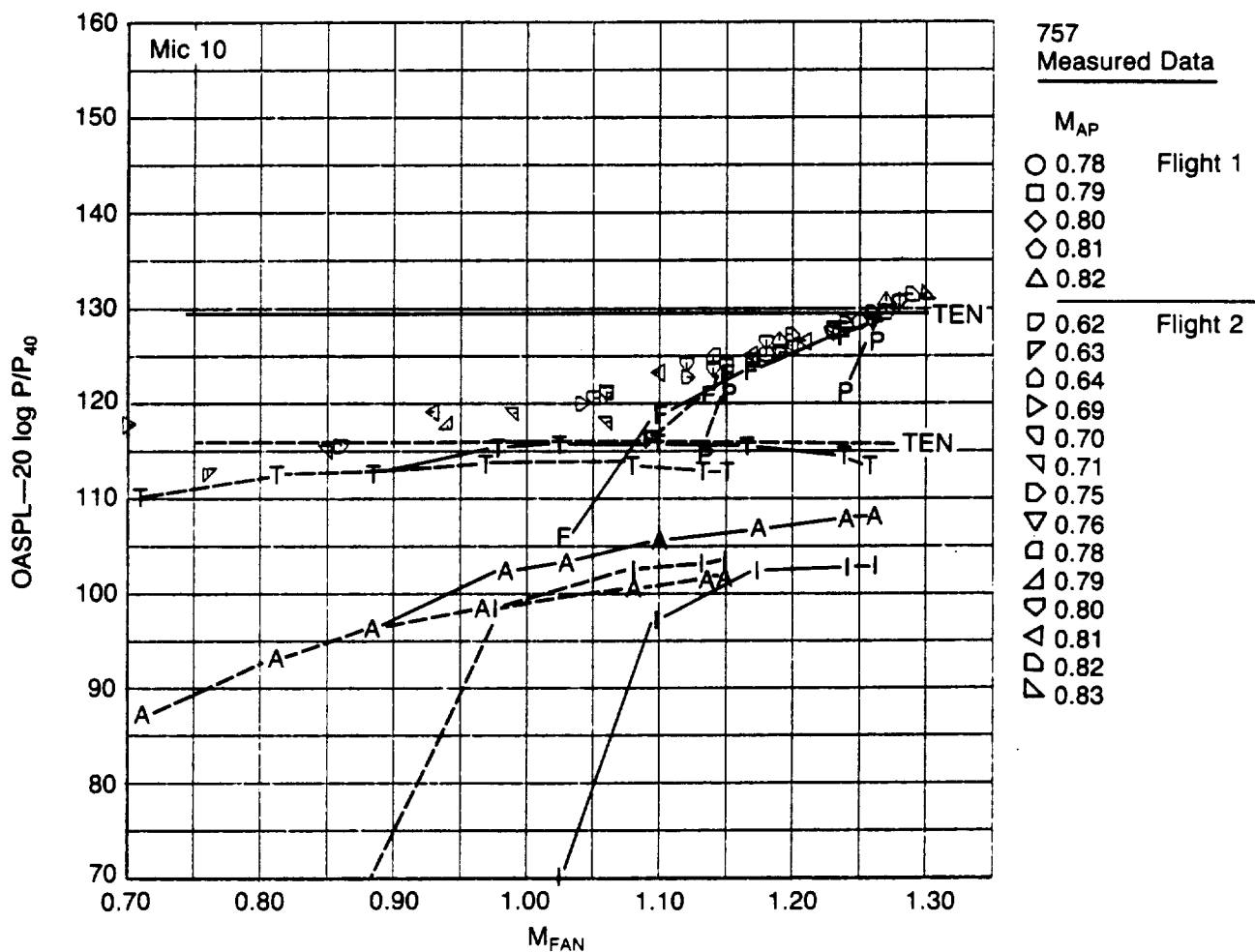


Figure 4-116. Microphone 8 Measured OASPL's vs. Boeing Butzel and Lu Procedure Predictions for Jet Shock and Jet Mixing Noise.



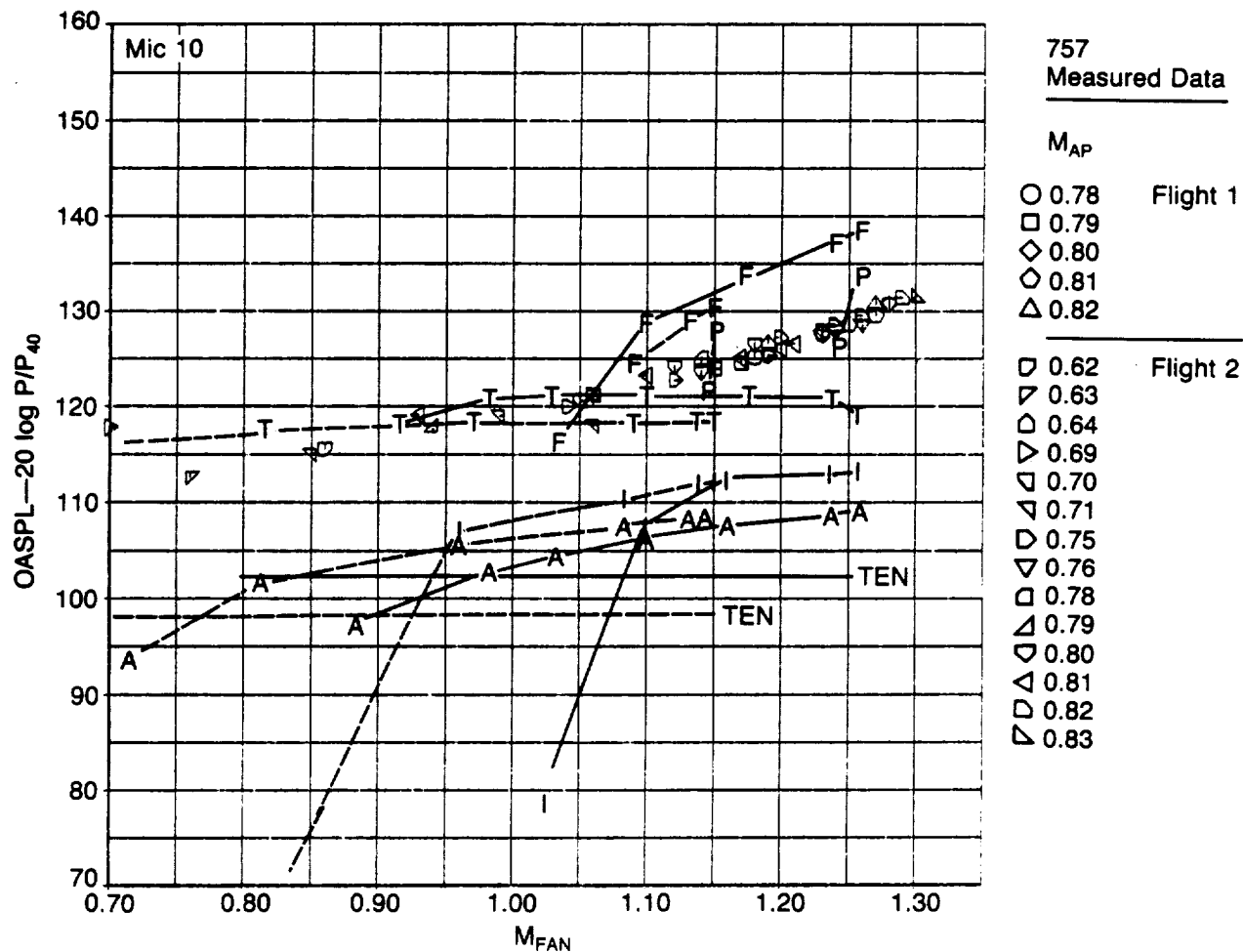
Lockheed
procedure
predictions

Note: Predictions include
"convective amplification"
and "dynamic amplification"
corrections

— M_{AP} = 0.80 TBLN = 78.9 dB
- - - M_{AP} = 0.60 TBLN = 71.3 dB

F — Fan jet shock broadband
P — Primary jet shock broadband
T — Turbine
A — Aft radiated fan
I — Inlet radiated fan
J — Jet mixing (not predicted)
TEN — Trailing edge
TBLN — Turbulent boundary layer

Figure 4-117. Microphone 10 Measured OASPL's vs. Lockheed Procedure Predictions



Note: Predictions do not include "convective amplification" and "dynamic amplification" corrections

Figure 4-118. Microphone 10 Measured OASPL's vs. Lockheed Procedure Predictions Without Convective and Dynamic Amplification Corrections

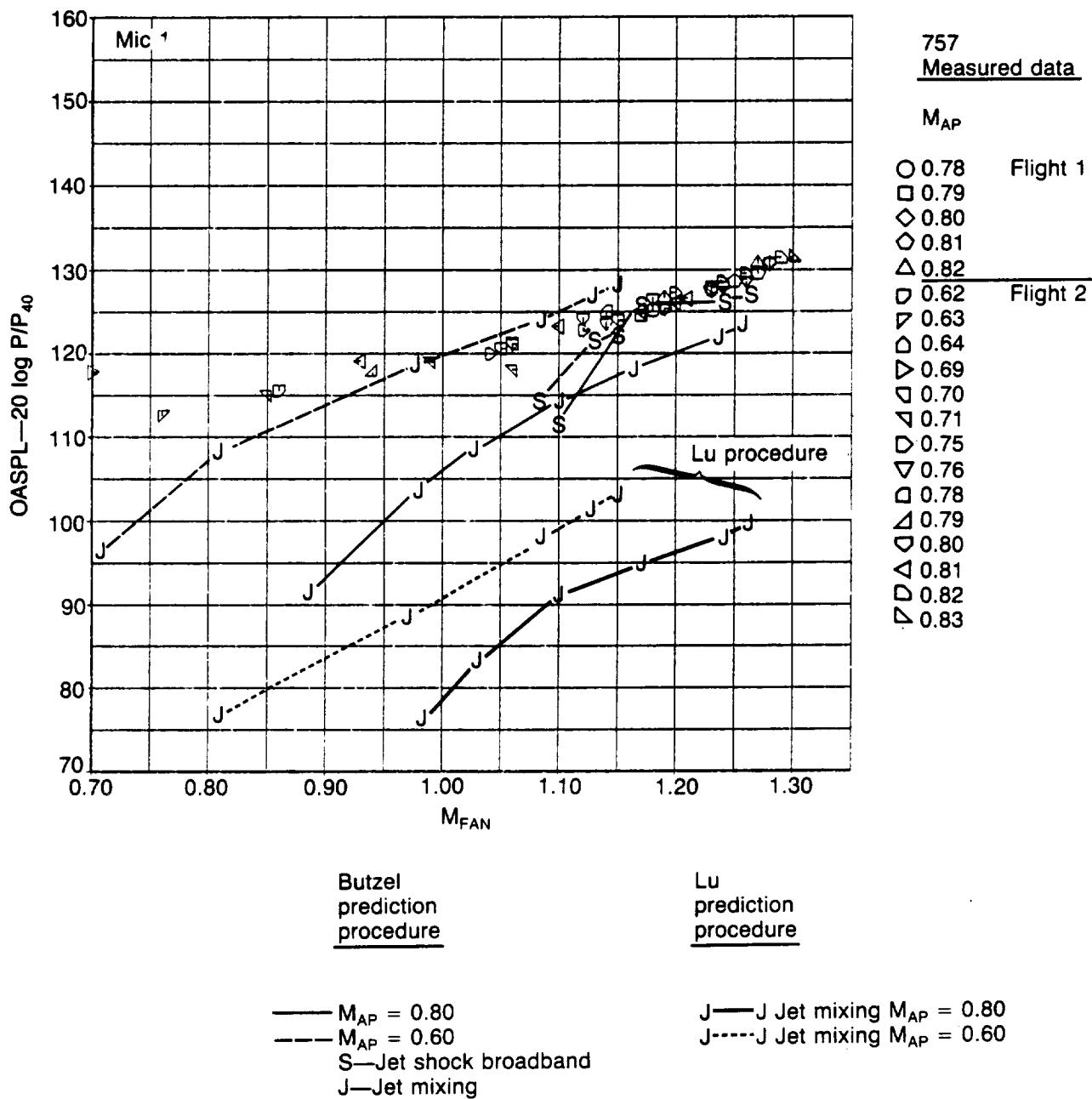


Figure 4-119. Microphone 10 Measured OASPL's vs. Boeing Butzel and Lu Procedure Predictions for Jet Shock and Jet Mixing Noise.

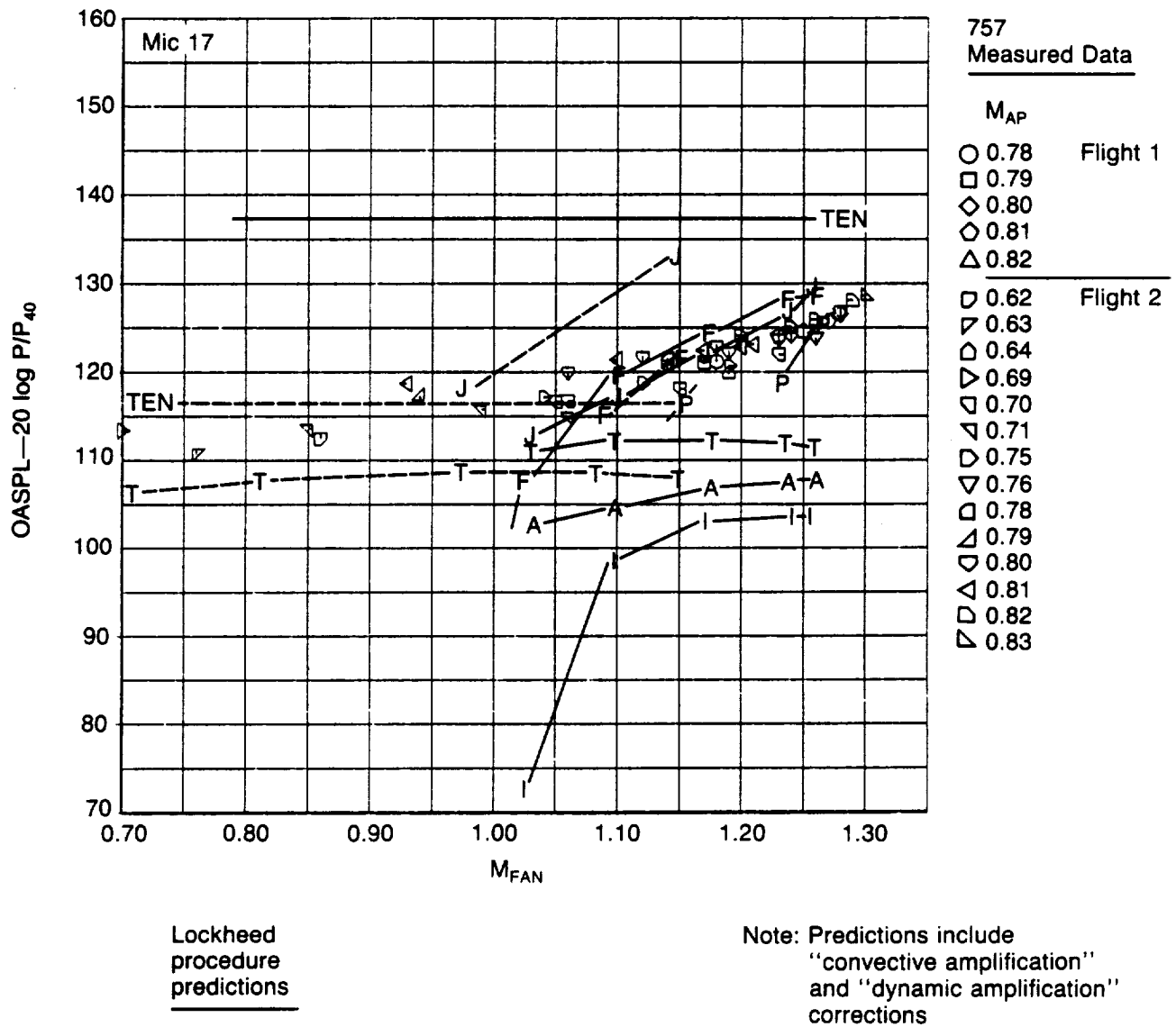


Figure 4-120. Microphone 17 Measured OASPL's vs. Lockheed Procedure Predictions

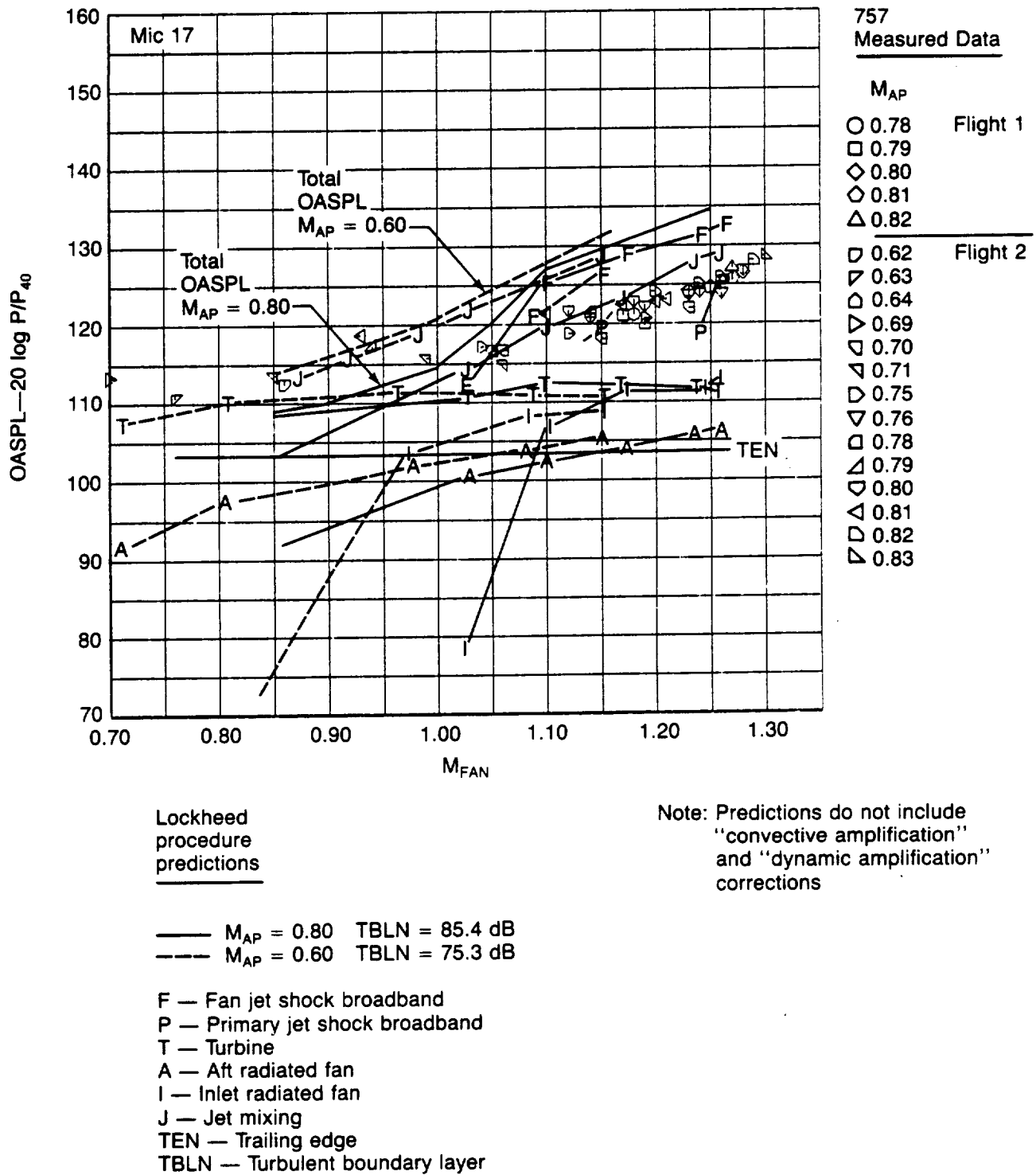


Figure 4-121. Microphone 17 Measured OASPL's vs. Lockheed Procedure Predictions Without Convective and Dynamic Amplification Corrections

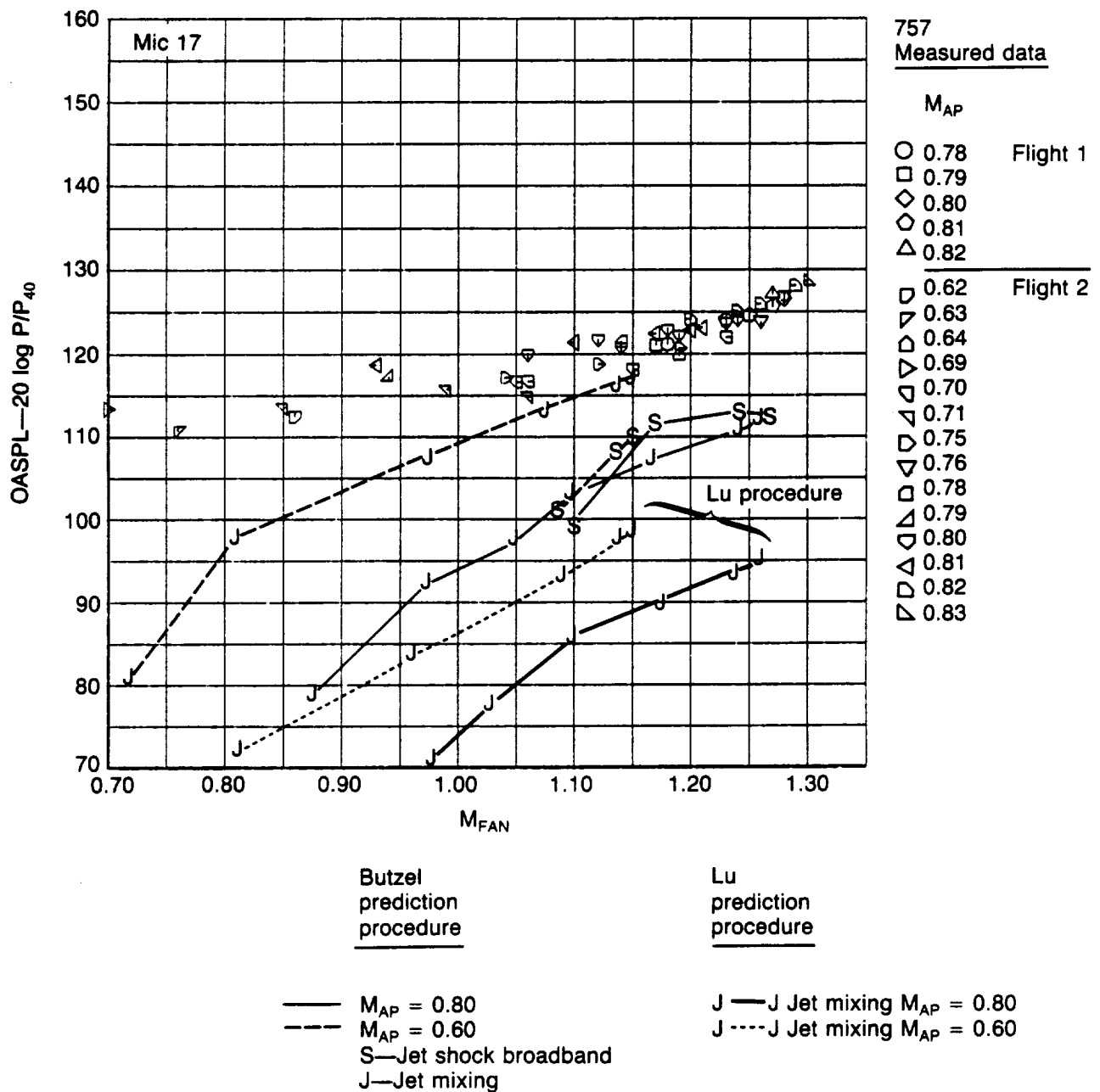
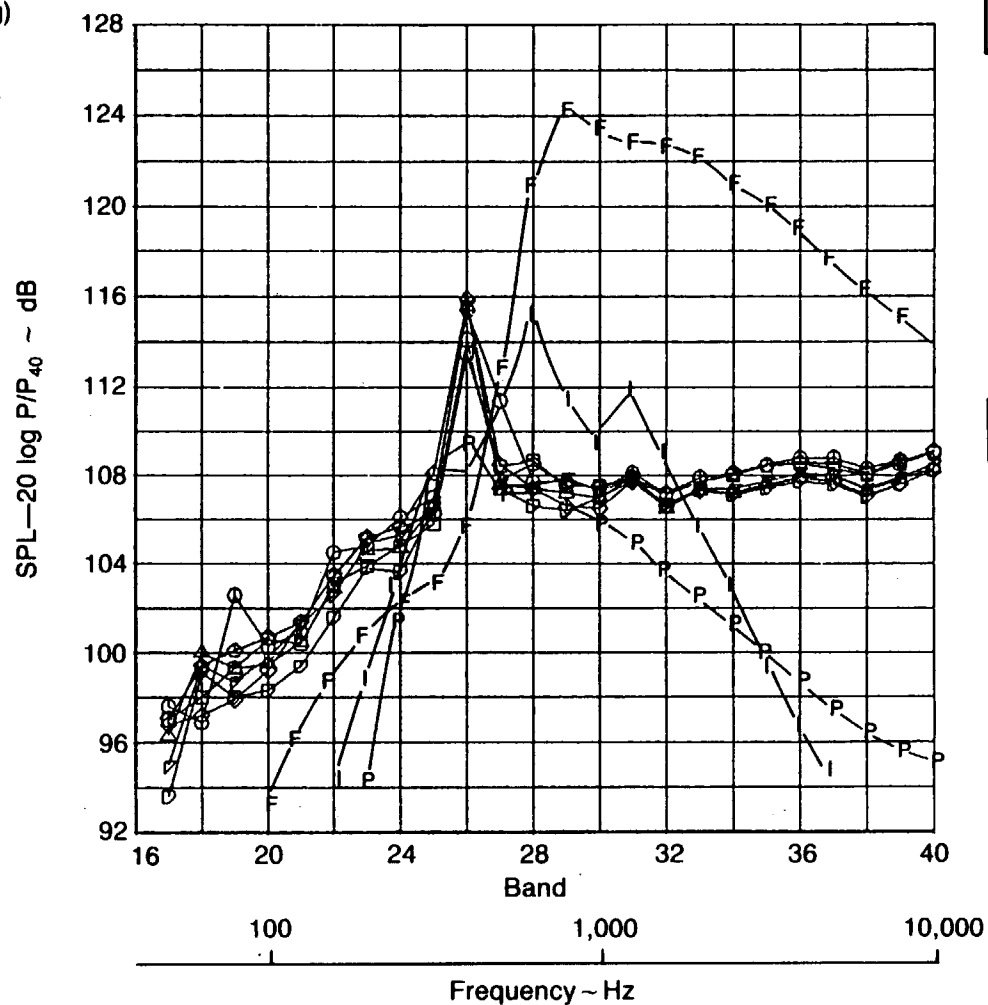


Figure 4-122. Microphone 17 Measured OASPL's vs. Boeing Butzel and Lu Procedure Predictions for Jet Shock and Jet Mixing Noise.

Mic 2

	Geom (deg)	Radiation (deg)
θ_p	138	170
θ_F	107	157
θ_i	42	74



Lockheed Procedure Predictions—
No Convective and Dynamic
Amplification Corrections

F—Fan jet shock broadband

P—Primary jet shock broadband

I—Inlet fan

$M_{AP} = 0.80$

$M_{FAN} = 1.26$

$N_{IC} = 4321$

757 Measured Data

Cond.		M_{AP}	M_{FAN}	N_{IC}
239	○ o	0.80	1.12	3557
210	□ c	0.80	1.14	3661
225	◇ o	0.80	1.18	3793
211	◇ c	0.80	1.19	3850
241	△ c	0.80	1.23	4034
224	▽ c	0.80	1.24	4102
223	▽ c	0.80	1.28	4340
201	● o	0.80	1.06	3227

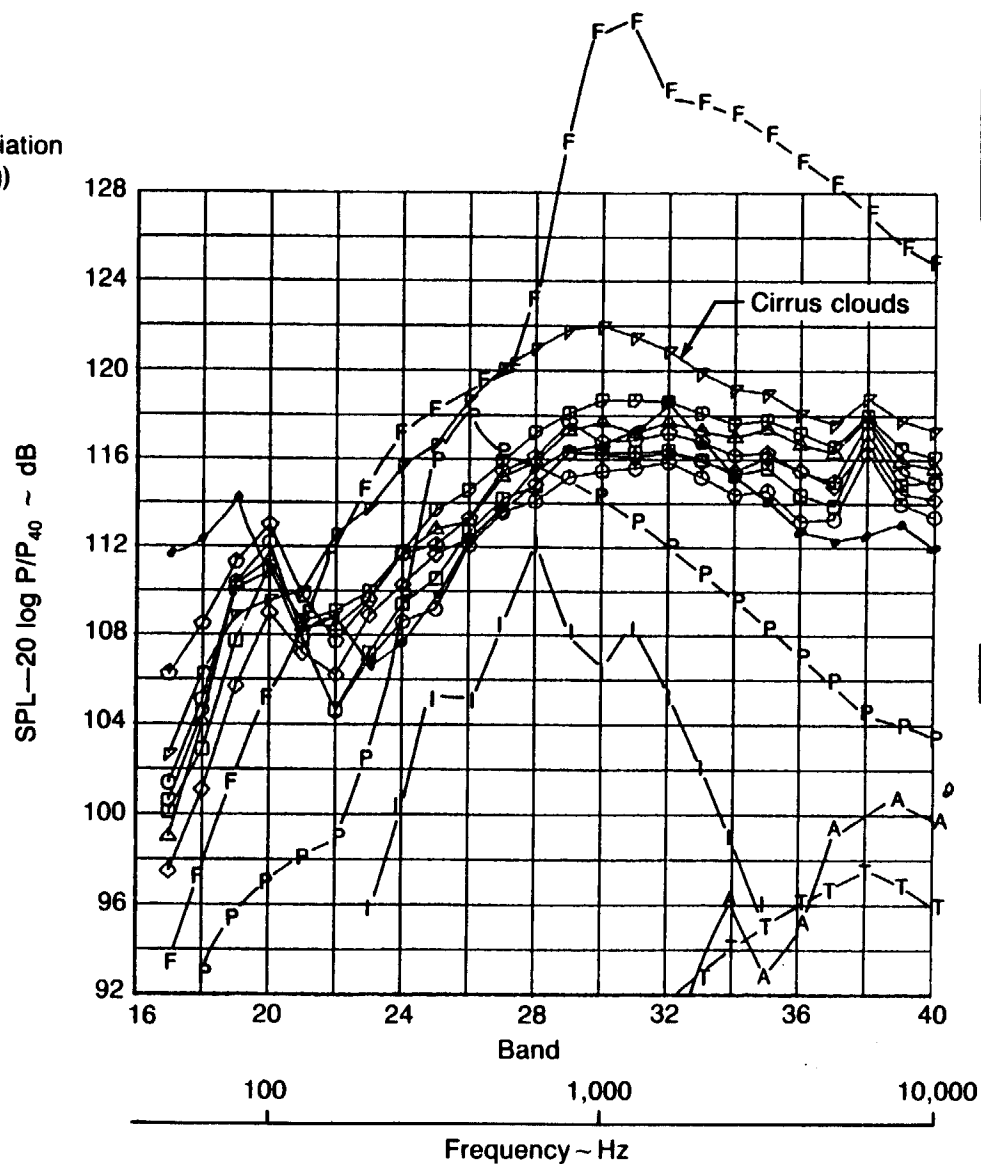
o — Bleed valve open

c — Bleed valve closed

Figure 4-123. Microphone 2 Measured 1/3 Octave Spectra vs. Lockheed Procedure Predictions
Without Convective and Dynamic Amplification Corrections

Mic 6

	Geom (deg)	Radiation (deg)
θ_P	113	160
θ_F	58	100
θ_I	22	40



Lockheed Procedure Predictions—
No Convective and Dynamic
Amplification Corrections

F—Fan jet shock broadband
P—Primary jet shock broadband
I—Inlet fan
A—Aft radiated fan
T—Turbine

$$M_{AP} = 0.80$$

$$M_{FAN} = 1.26$$

$$N_{IC} = 4321$$

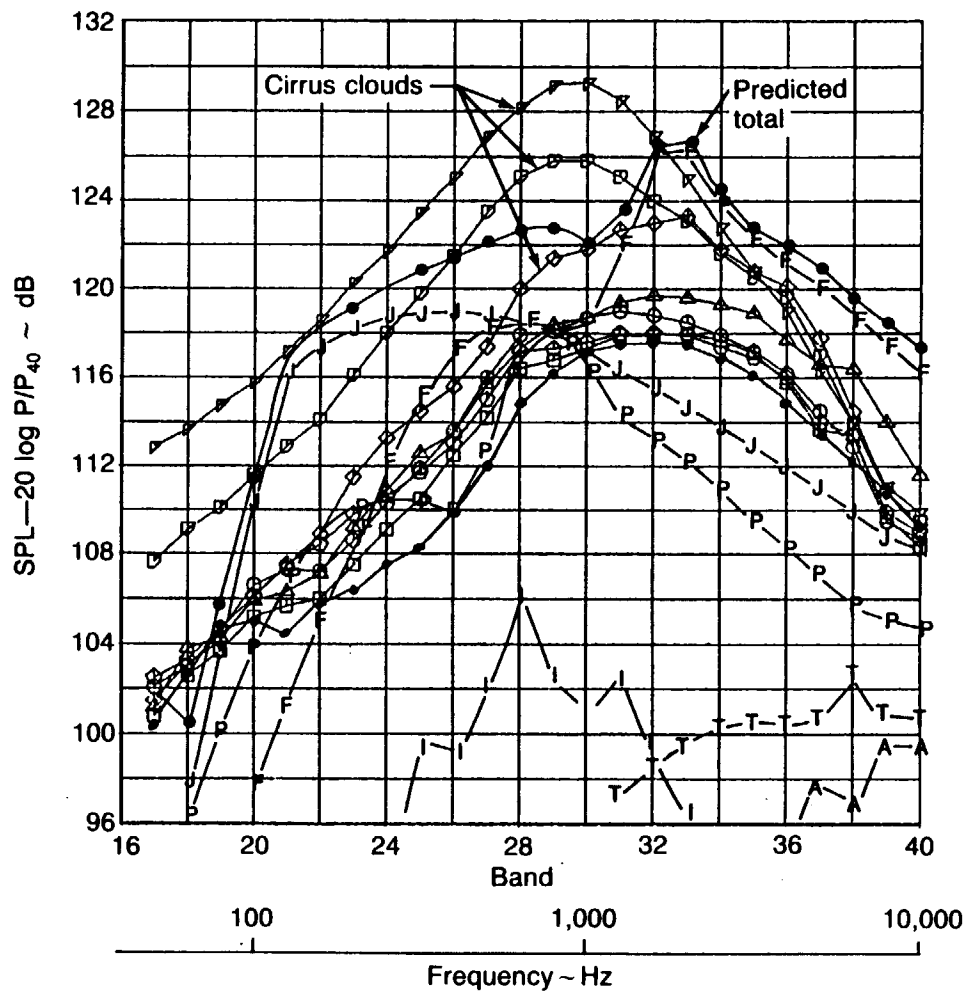
757 Measured Data

Cond.		M_{AP}	M_{FAN}	N_{IC}
239	○ o	0.80	1.12	3557
210	□ c	0.80	1.14	3661
225	◇ o	0.80	1.18	3793
211	◇ c	0.80	1.19	3850
241	△ c	0.80	1.23	4034
224	▽ c	0.80	1.24	4102
228	▽ c	0.80	1.28	4340
201	● o	0.80	1.06	3227

Figure 4-124. Microphone 6 Measured 1/3 Octave Spectra vs. Lockheed Procedure Predictions Without Convective and Dynamic Amplification Corrections

Mic 13

	Geom (deg)	Radiation (deg)
θ_P	92	145
θ_F	60	105
θ_I	31	55



Lockheed Procedure Predictions—
No Convective and Dynamic
Amplification Corrections

$$M_{AP} = 0.80$$

$$M_{FAN} = 1.26$$

$$N_{IC} = 4321$$

●—Total

F—Fan jet shock broadband

P—Primary jet shock broadband

J—Jet mixing

T—Turbine

A—Aft fan

I—Inlet fan

757 Measured Data

Cond.		M_{AP}	M_{FAN}	N_{IC}
239	○ o	0.80	1.12	3557
210	□ c	0.80	1.14	3661
225	◇ o	0.80	1.18	3793
211	◇ c	0.80	1.19	3850
241	△ c	0.80	1.23	4034
224	▽ c	0.80	1.24	4102
223	▽ c	0.80	1.28	4340
201	● o	0.80	1.06	3227

Figure 4-125. Microphone 13 Measured 1/3 Octave Spectra vs. Lockheed Procedure Predictions
Without Convective and Dynamic Amplification Corrections

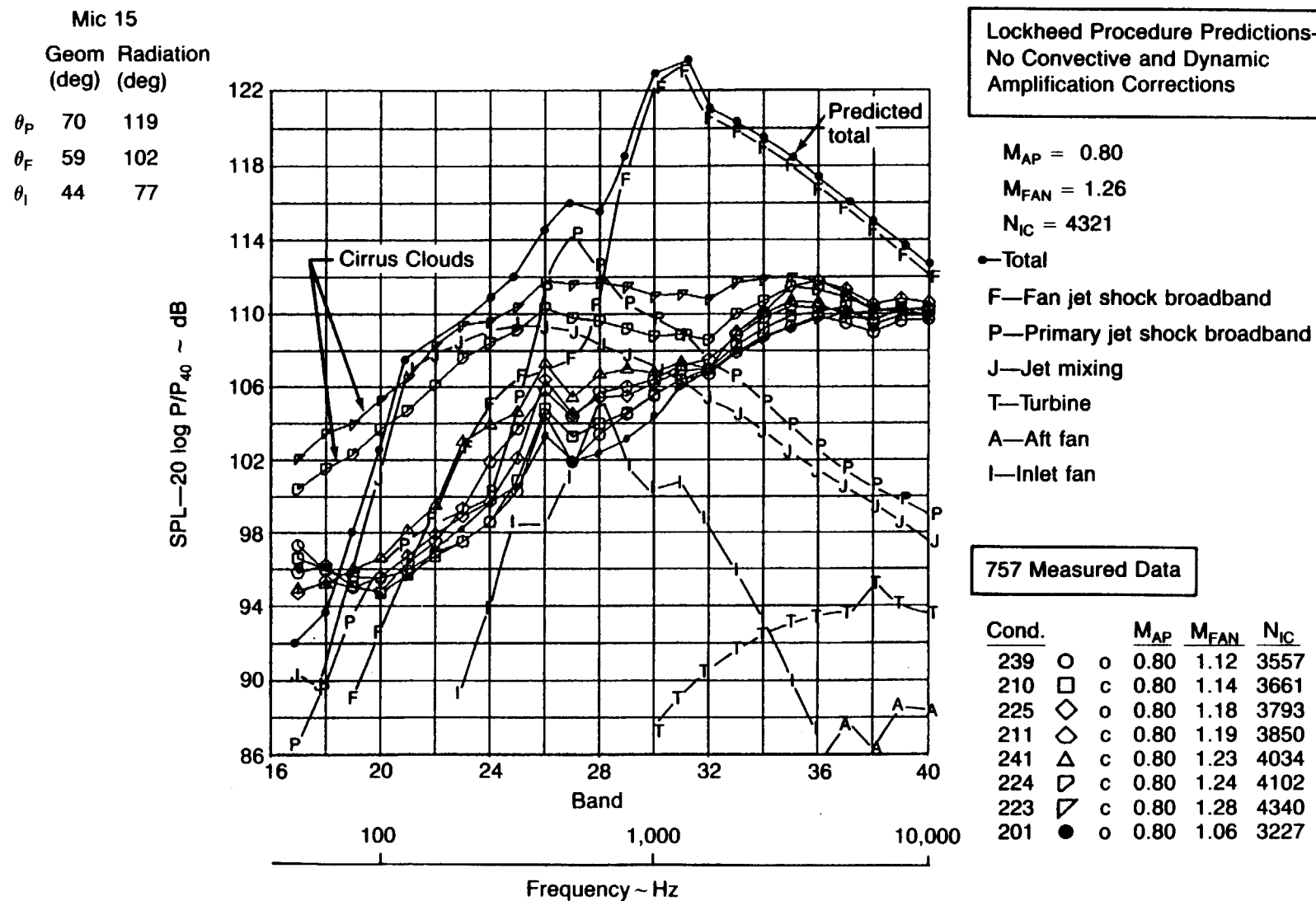
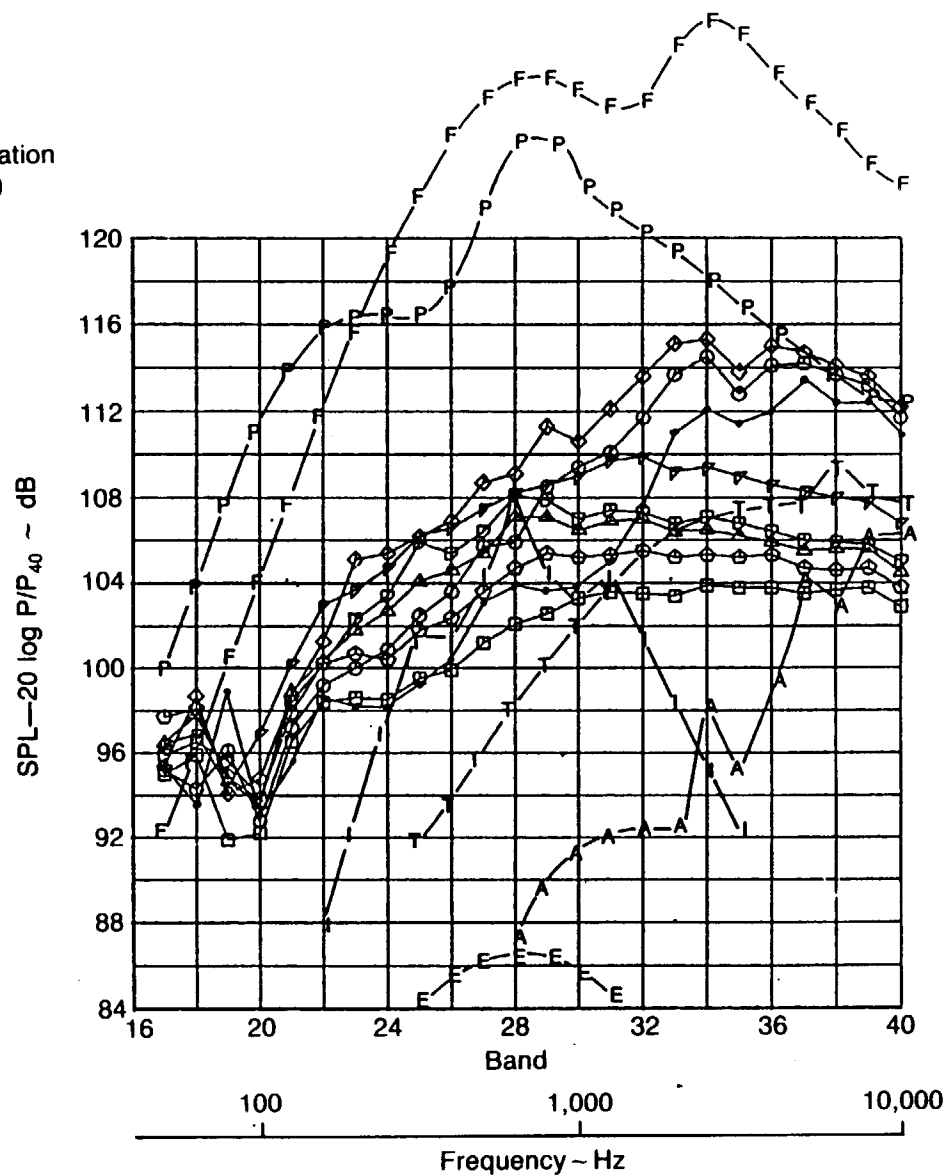


Figure 4-126. Microphone 15 Measured 1/3 Octave Spectra vs. Lockheed Procedure Predictions Without Convective and Dynamic Amplification Corrections

Mic 4
Geom Radiation
(deg) (deg)
 θ_P 54 95
 θ_F 31 55
 θ_I 17 30



Lockheed Procedure Predictions—
No Convective and Dynamic
Amplification Corrections

$$M_{AP} = 0.80$$

$$M_{FAN} = 1.26$$

$$N_{IC} = 4321$$

F—Fan jet shock broadband

P—Primary jet shock broadband

T—Turbine

I—Inlet fan

A—Aft fan

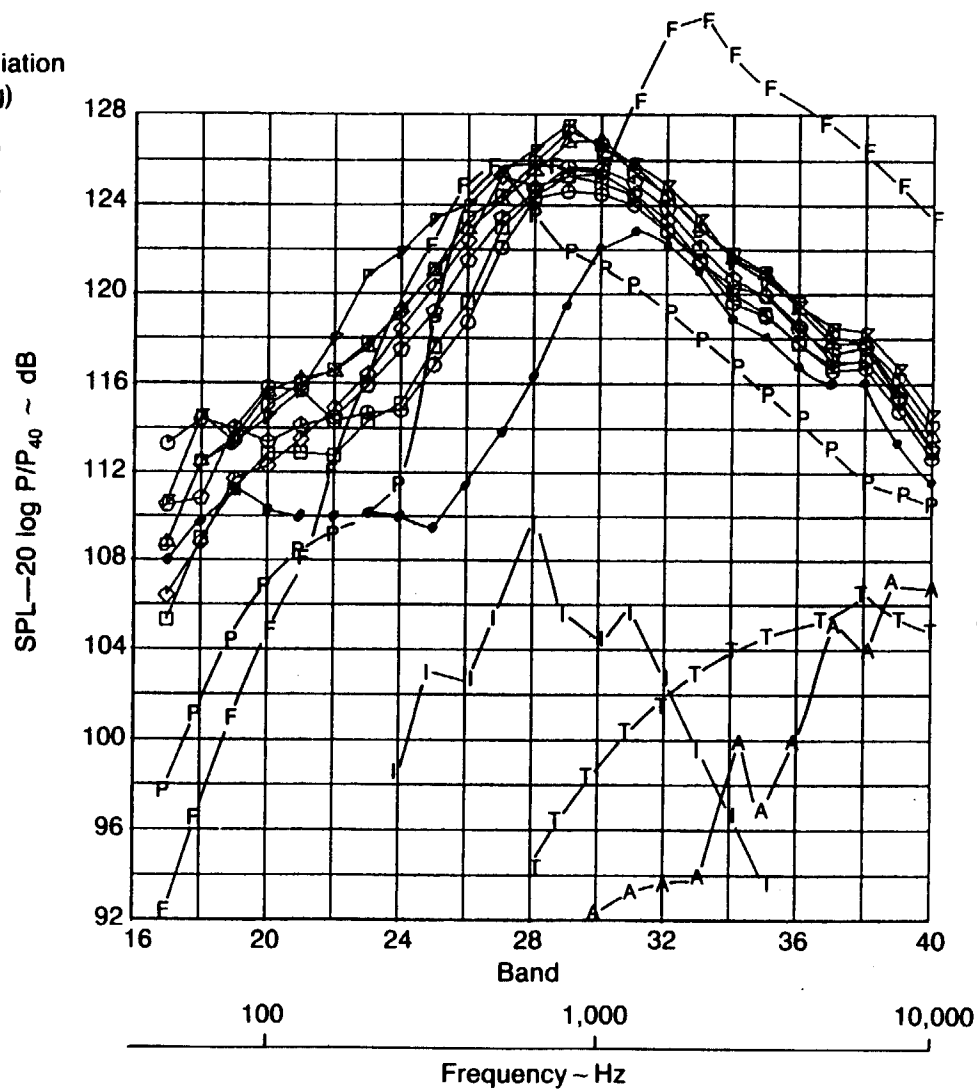
E—Trailing edge

757 Measured Data

Cond.		M_{AP}	M_{FAN}	N_{IC}
239	○ o	0.80	1.12	3557
210	□ c	0.80	1.14	3661
225	◇ o	0.80	1.18	3793
211	◇ c	0.80	1.19	3850
241	△ c	0.80	1.23	4034
224	▽ c	0.80	1.24	4102
223	▽ c	0.80	1.28	4340
201	● o	0.80	1.06	3227

Figure 4-127. Microphone 4 Measured 1/3 Octave Spectra vs. Lockheed Procedure Predictions Without Convective and Dynamic Amplification Corrections

Mic 8		
	Geom (deg)	Radiation (deg)
θ_P	73	123
θ_F	38	68
θ_I	19	34



Lockheed Procedure Predictions—
No Convective and Dynamic
Amplification Corrections

$$M_{AP} = 0.80$$

$$M_{FAN} = 1.26$$

$$N_{IC} = 4321$$

F—Fan jet shock broadband

P—Primary jet shock broadband

T—Turbine

I—Inlet fan

A—Aft fan

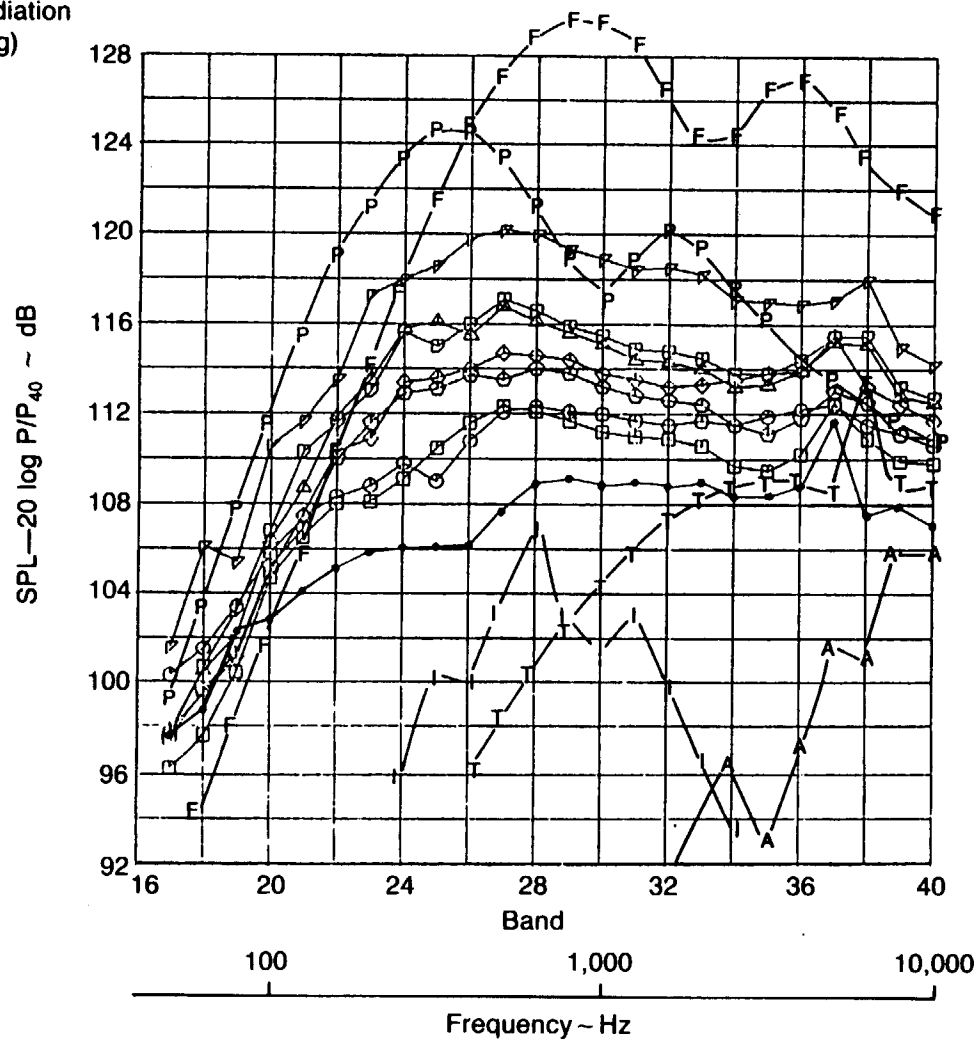
757 Measured Data

Cond.			M_{AP}	M_{FAN}	N_{IC}
239	○	o	0.80	1.12	3557
210	□	c	0.80	1.14	3661
225	◇	o	0.80	1.18	3793
211	◇	c	0.80	1.19	3850
241	△	c	0.80	1.23	4034
224	▽	c	0.80	1.24	4102
223	▽	c	0.80	1.28	4340
201	●	o	0.80	1.06	3227

Figure 4-128. Microphone 8 Measured 1/3 Octave Spectra vs. Lockheed Procedure Predictions Without Convective and Dynamic Amplification Corrections

Mic 10

	Geom (deg)	Radiation (deg)
θ_P	37	66
θ_F	23	41
θ_I	14	25



Lockheed Procedure Predictions—
No Convective and Dynamic
Amplification Corrections

$M_{AP} = 0.80$

$M_{FAN} = 1.26$

$N_{IC} = 4321$

F—Fan jet shock broadband

P—Primary jet shock broadband

T—Turbine

I—Inlet fan

A—Aft fan

757 Measured Data

Cond.			M_{AP}	M_{FAN}	N_{IC}
239	○	o	0.80	1.12	3557
210	□	c	0.80	1.14	3661
225	◇	o	0.80	1.18	3793
211	◇	c	0.80	1.19	3850
241	△	c	0.80	1.23	4034
224	▽	c	0.80	1.24	4102
223	▽	c	0.80	1.28	4340
201	●	o	0.80	1.06	3227

Figure 4-129. Microphone 10 Measured 1/3 Octave Spectra vs. Lockheed Procedure Predictions Without Convective and Dynamic Amplification Corrections

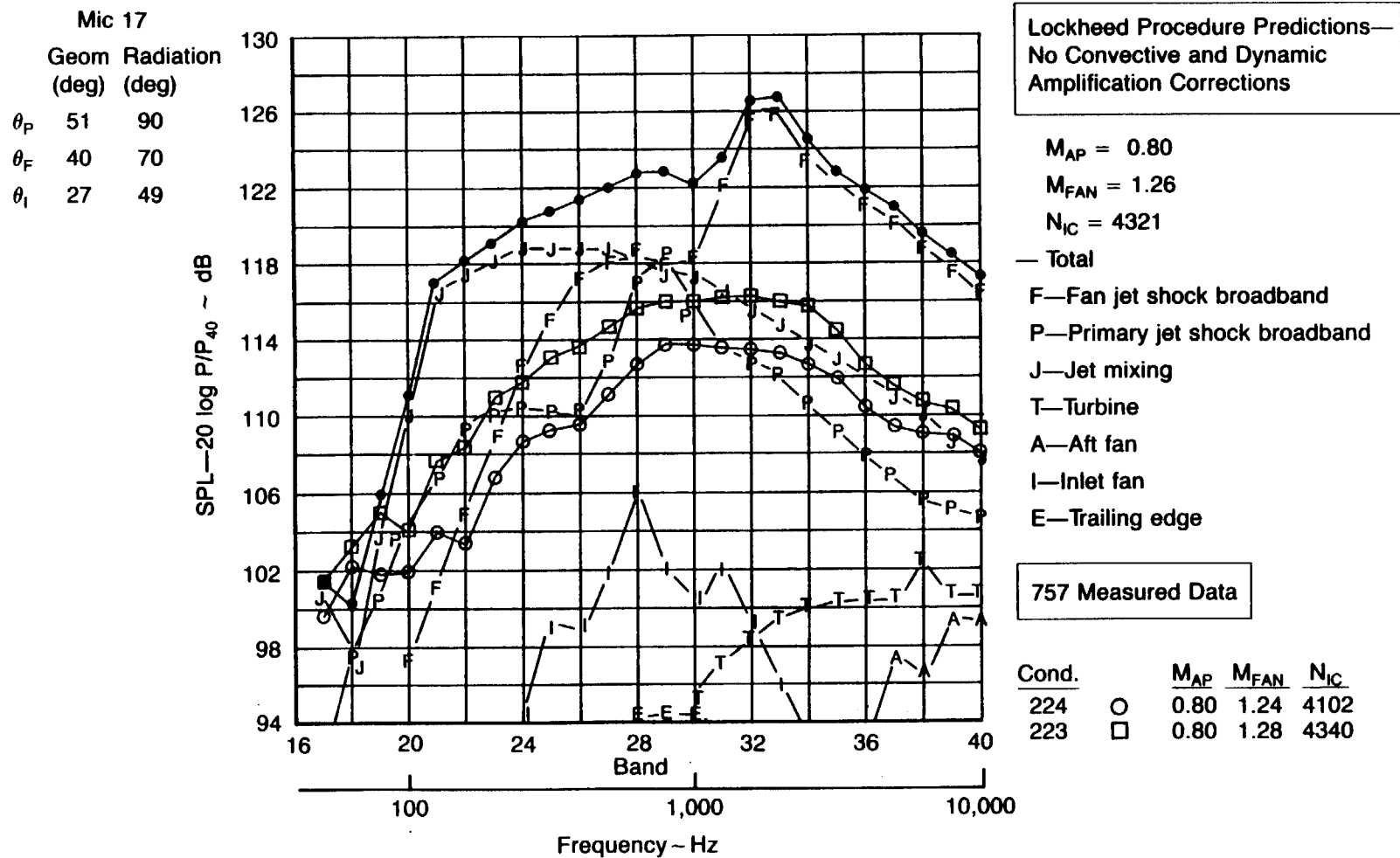
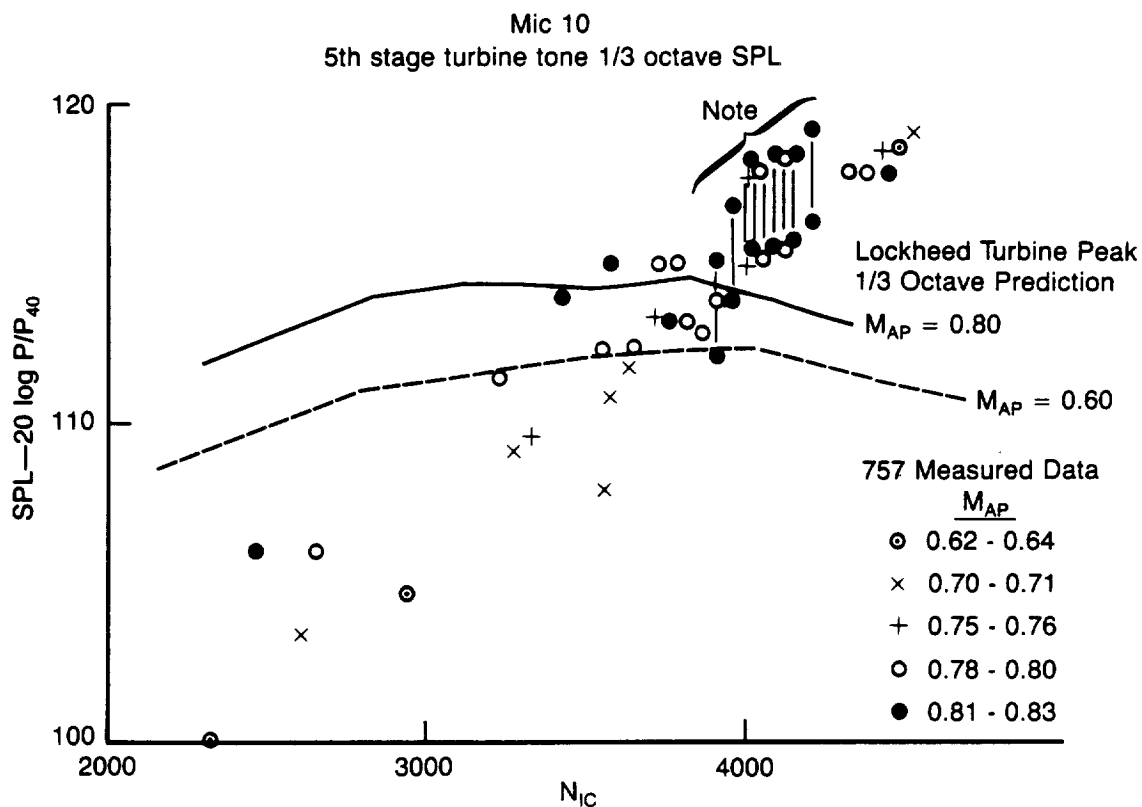
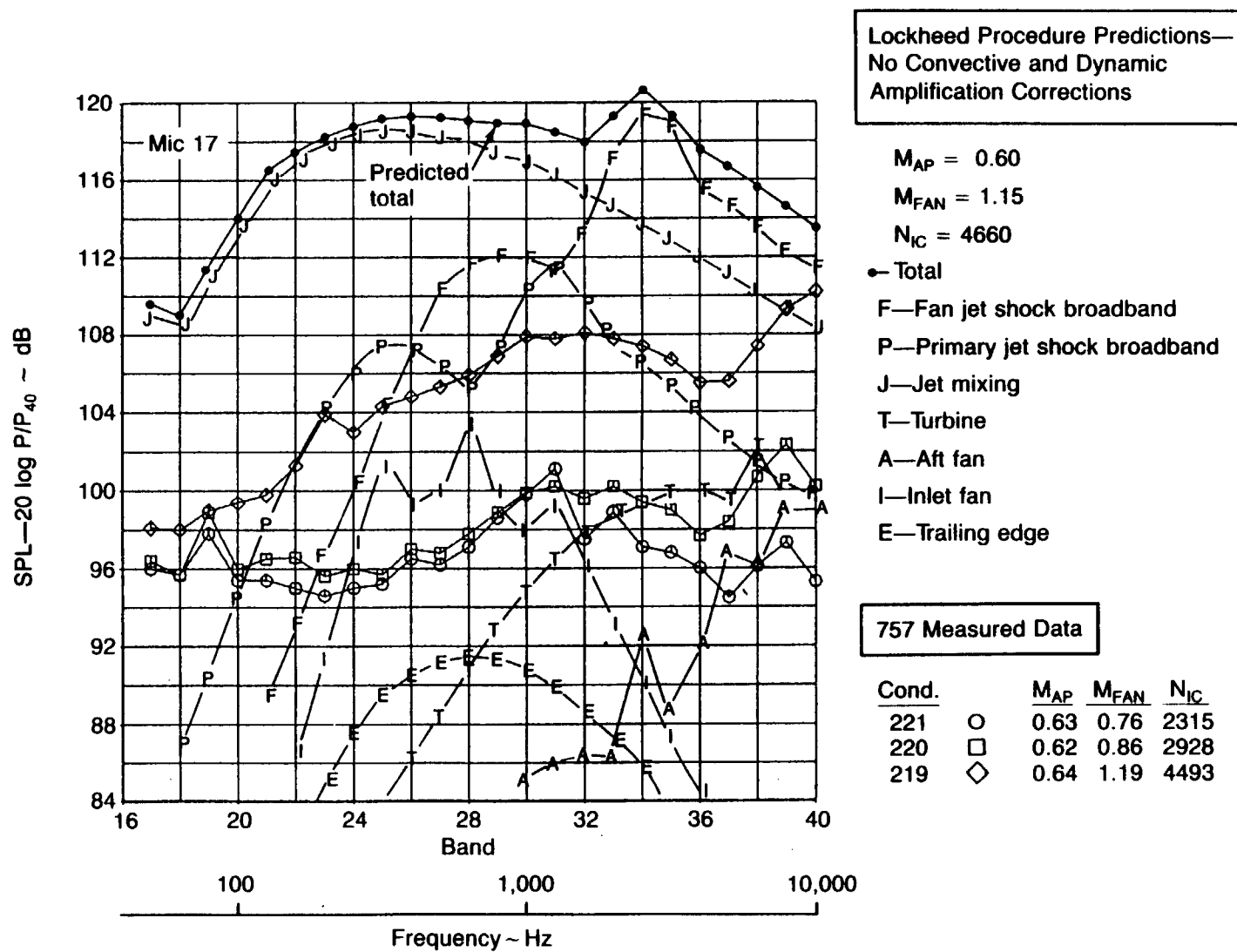


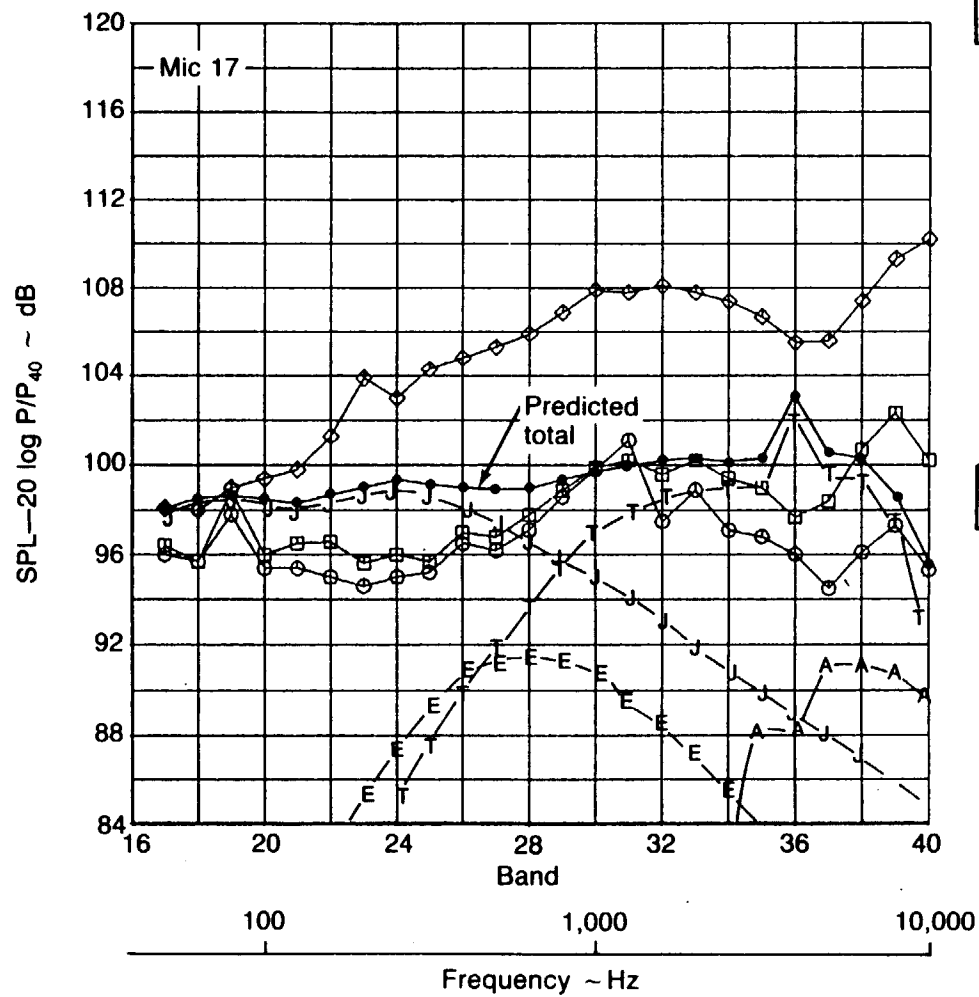
Figure 4-130. Microphone 17 Measured 1/3 Octave Spectra vs. Lockheed Procedure Predictions Without Convective and Dynamic Amplification



Note: Turbine tone near 1/3 octave band edge. High SPL level is log sum of two 1/3 octave bands that are affected by turbine tone. Low SPL is SPL of band in which tone is calculated to fall. True tone level is between these levels

Figure 4-131. Comparison of Measured 1/3 Octave Turbine Noise Data at Microphone 10 With Lockheed Procedure Predictions





Lockheed Procedure Predictions—
No Convective and Dynamic
Amplification Corrections

$$M_{AP} = 0.60$$

$$M_{FAN} = 0.81$$

$$N_{IC} = 2770$$

● Total

J—Jet mixing

T—Turbine

A—Aft fan

E—Trailing edge

757 Measured Data

Cond.		M_{AP}	M_{FAN}	N_{IC}
221	○	0.63	0.76	2315
220	□	0.62	0.86	2928
219	◇	0.64	1.19	4493

Figure 4-133. Microphone 17 Measured 1/3 Octave Spectra vs. Lockheed Procedure Predictions Without Convective and Dynamic Amplification Corrections

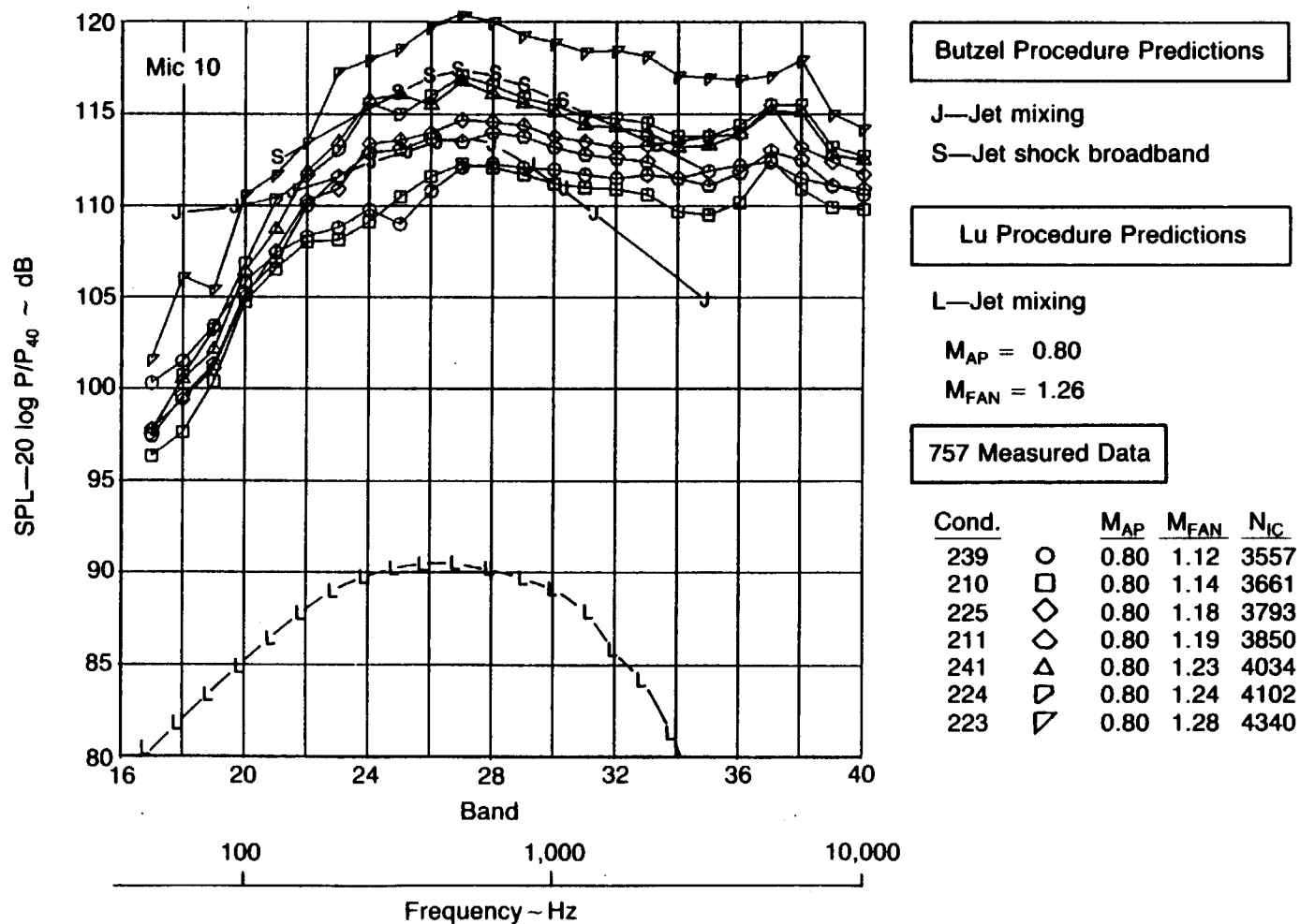


Figure 4-134. Microphone 10 Measured $1/3$ Octave Spectra vs. Butzel and Lu Predictions,
 $M_{AP} = 0.80$

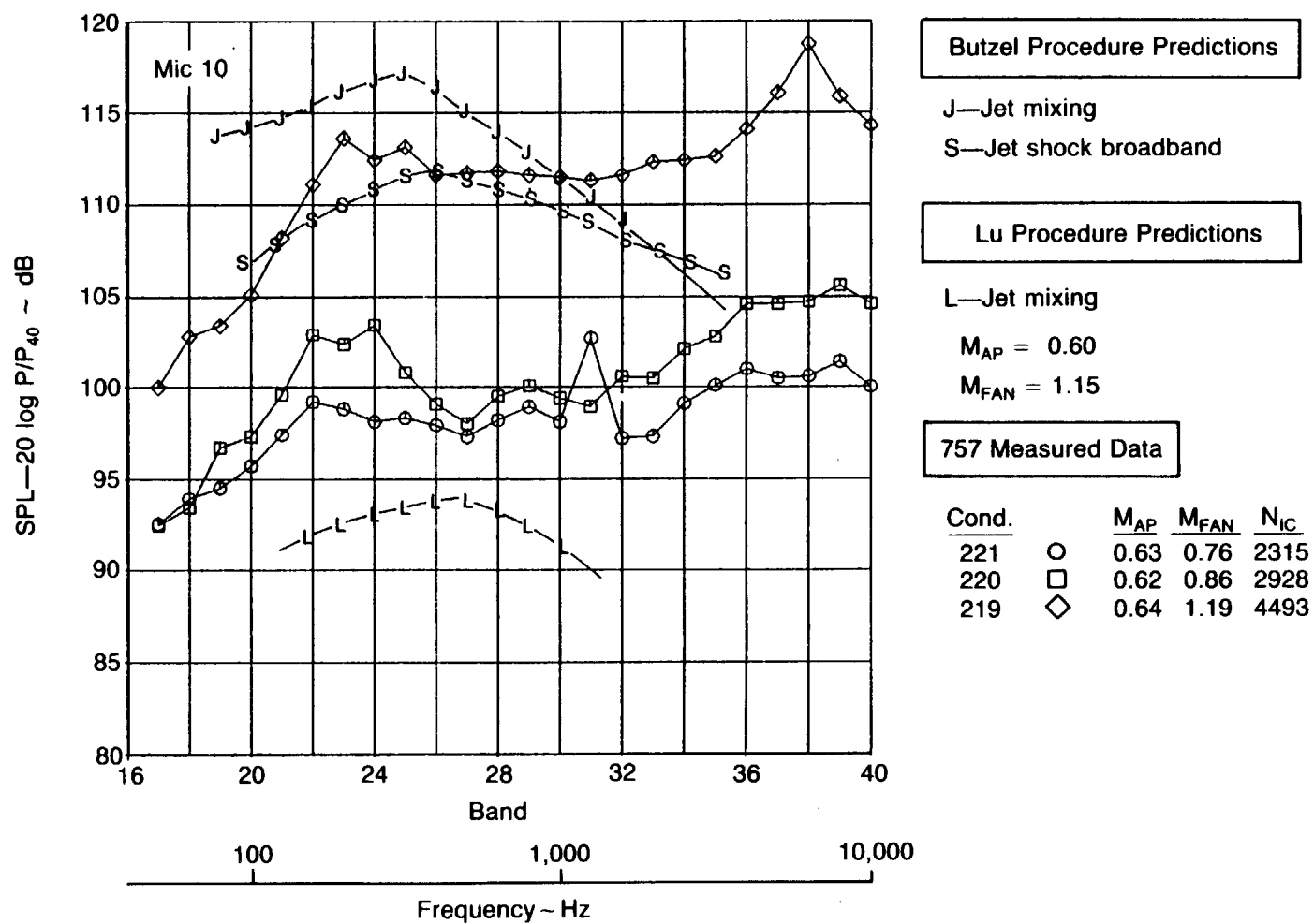


Figure 4-135. Microphone 10 Measured $1/3$ Octave Spectra vs. Butzel and Lu Predictions, $M_{AP} \approx 0.60$

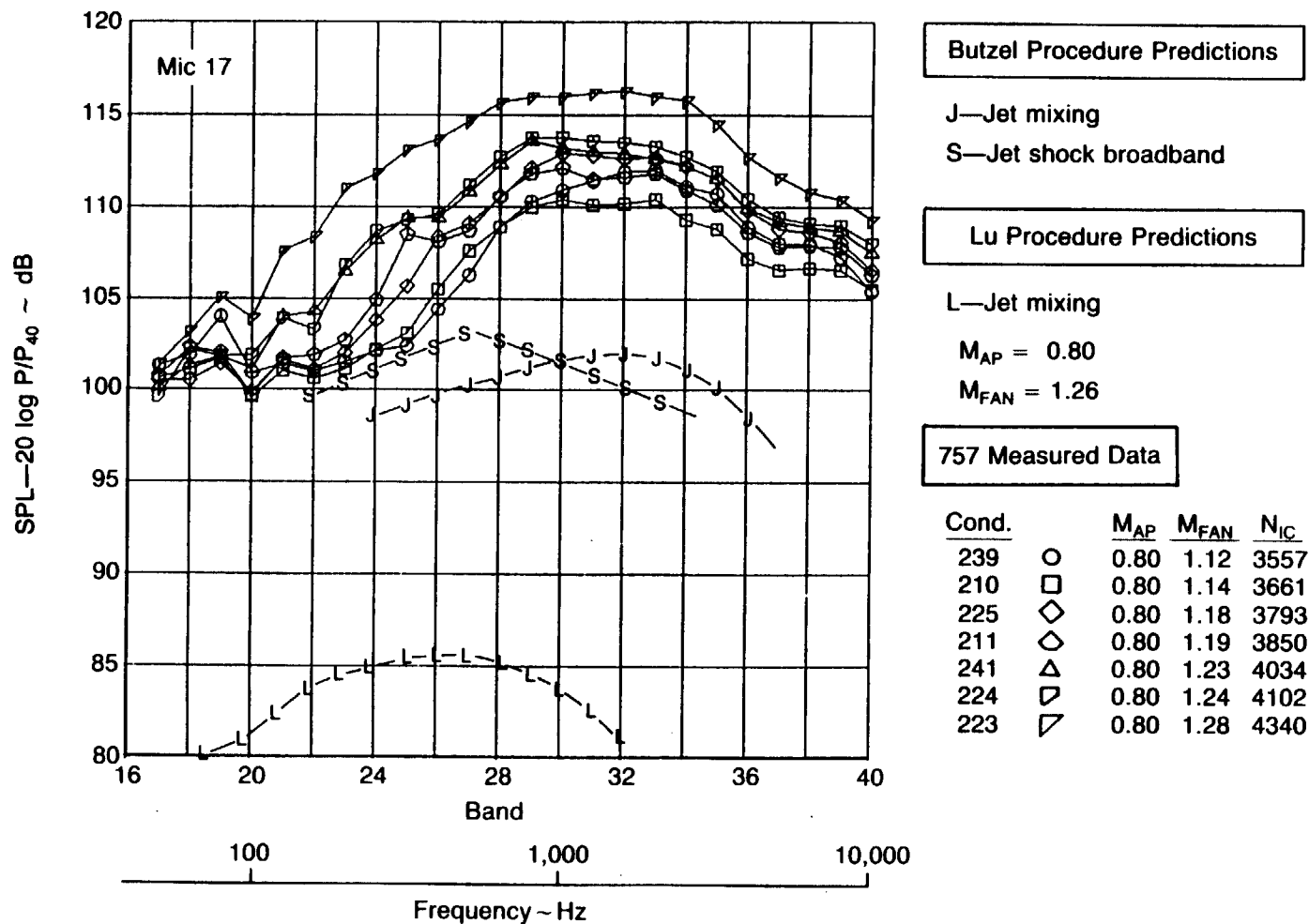


Figure 4-136. Microphone 17 Measured $1/3$ Octave Spectra vs. Butzel and Lu Predictions, $M_{AP} \approx 0.80$

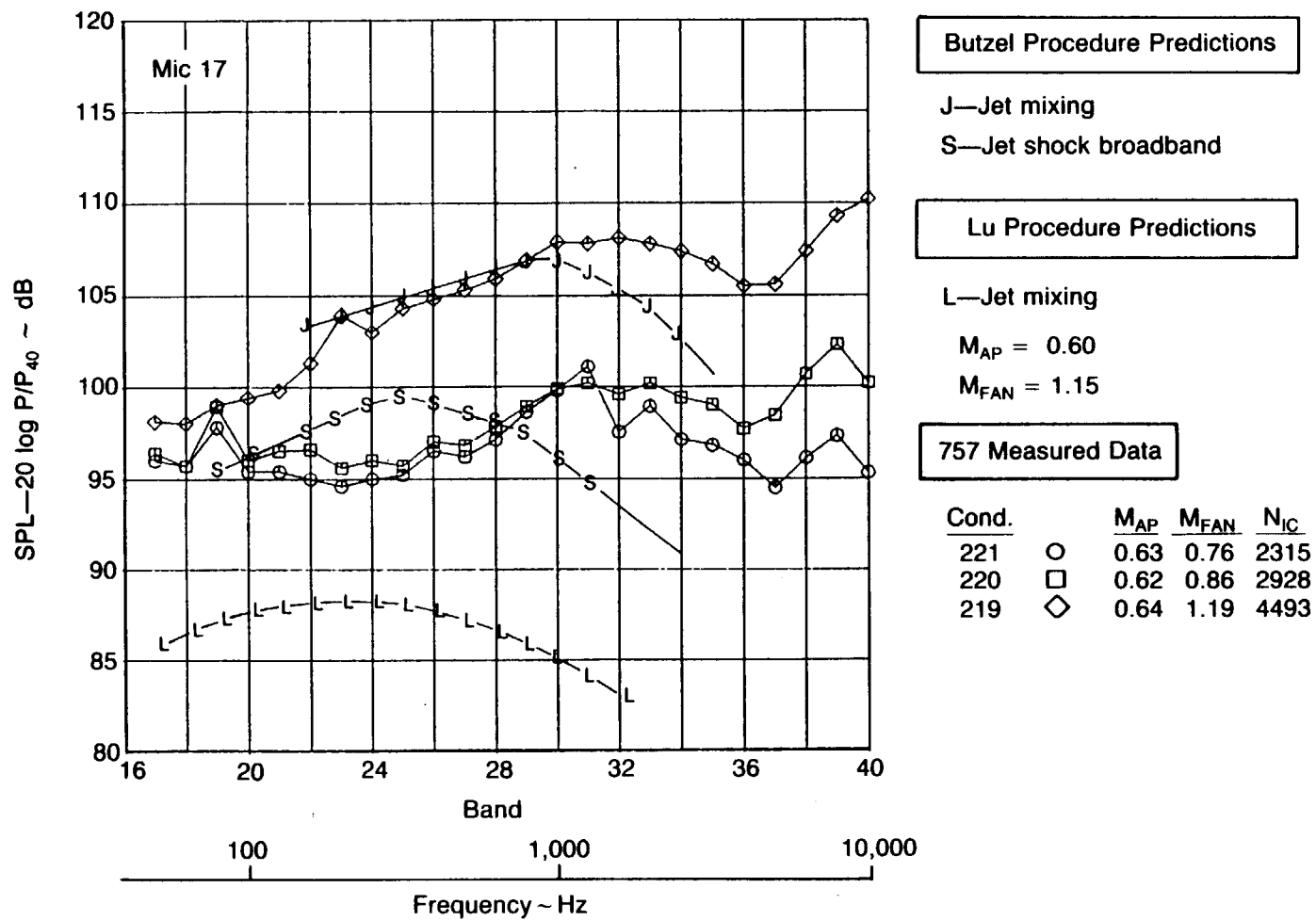


Figure 4-137. Microphone 17 Measured $1/3$ Octave Spectra vs. Butzel and Lu Predictions, $M_{AP} \approx 0.60$

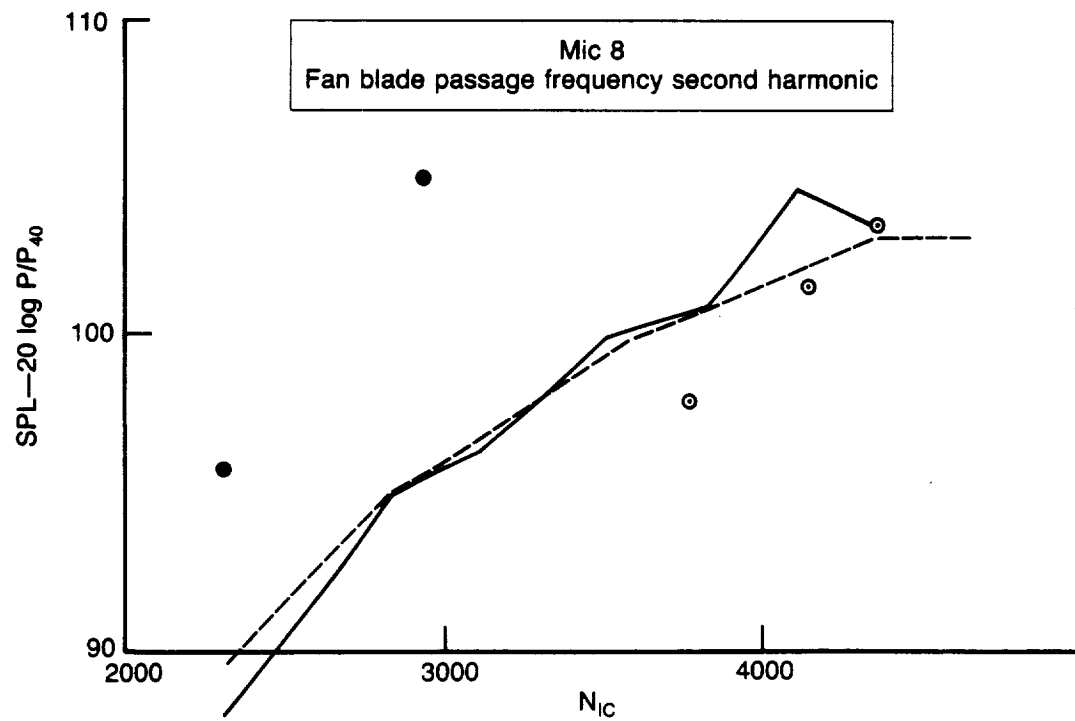
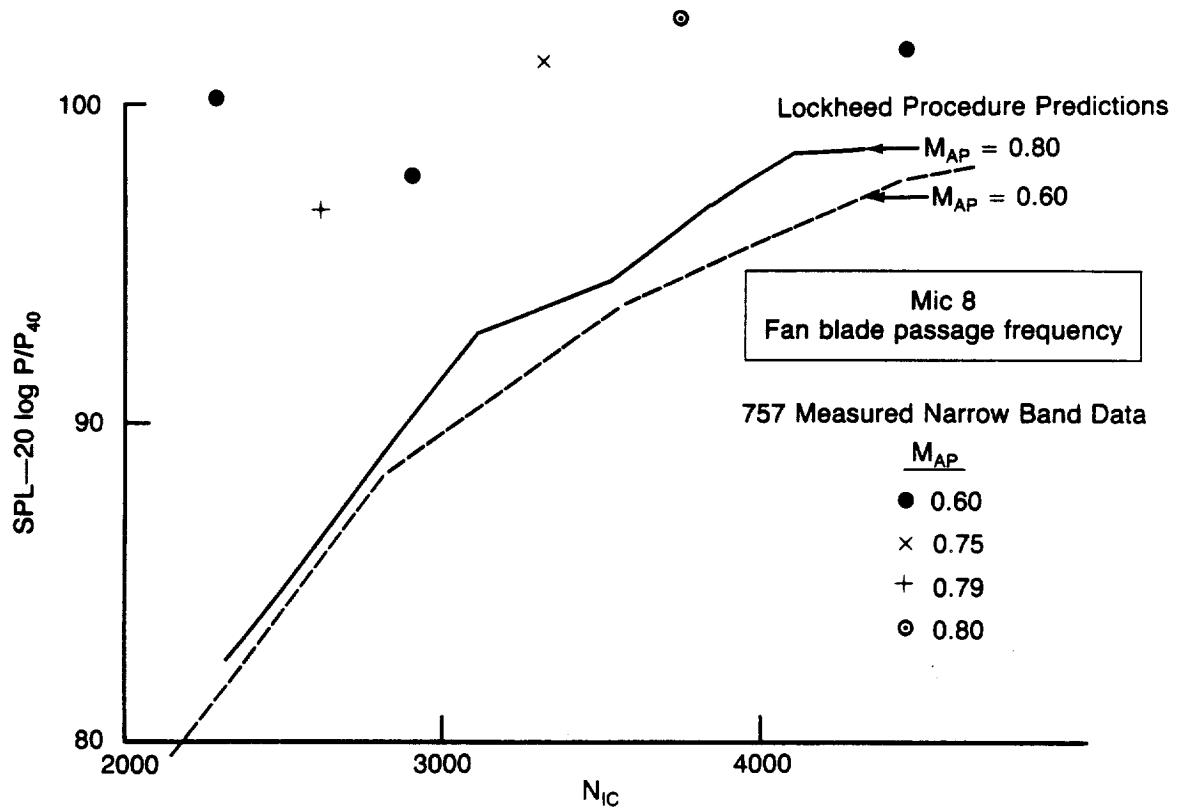


Figure 4-138. Comparison of Measured Fan Tone Data With Lockheed Procedure Predictions—Microphone 8

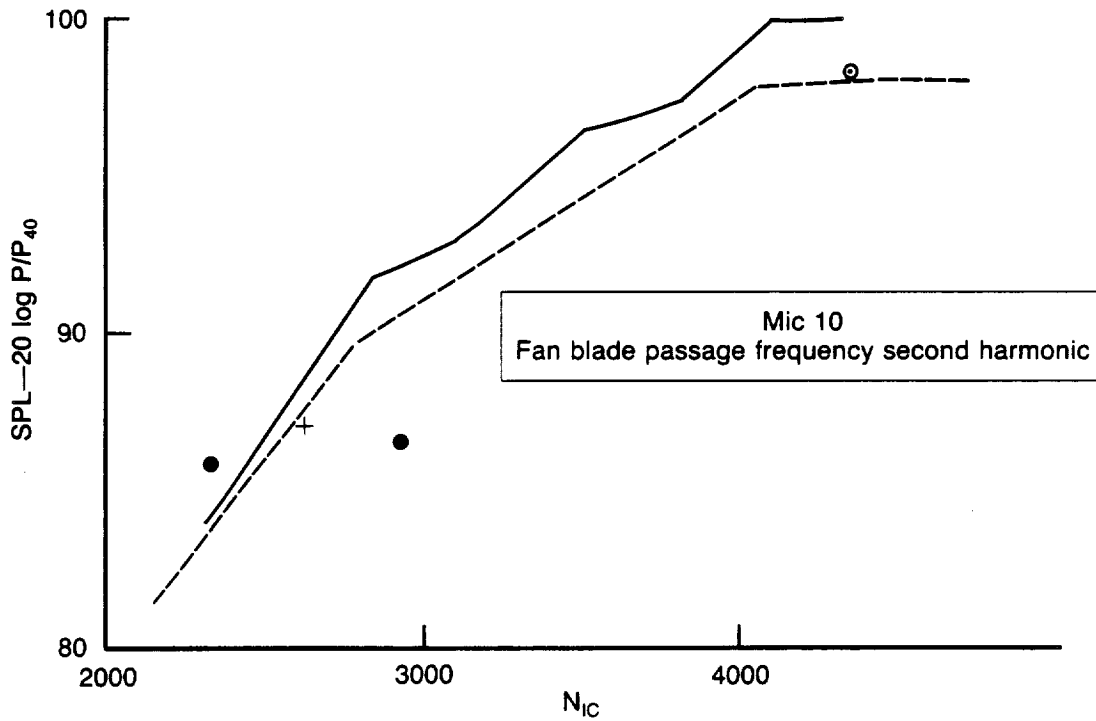
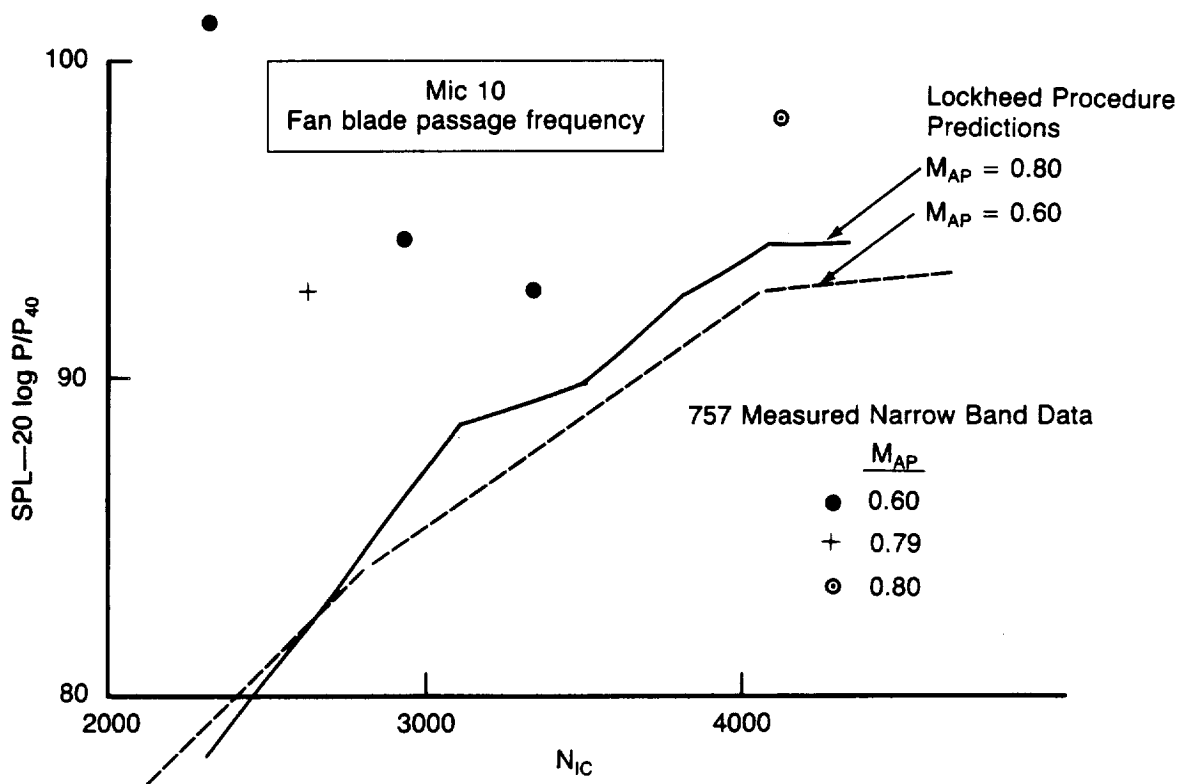


Figure 4-139. Comparison of Measured Fan Tone Data With Lockheed Procedure Predictions—Microphone 10

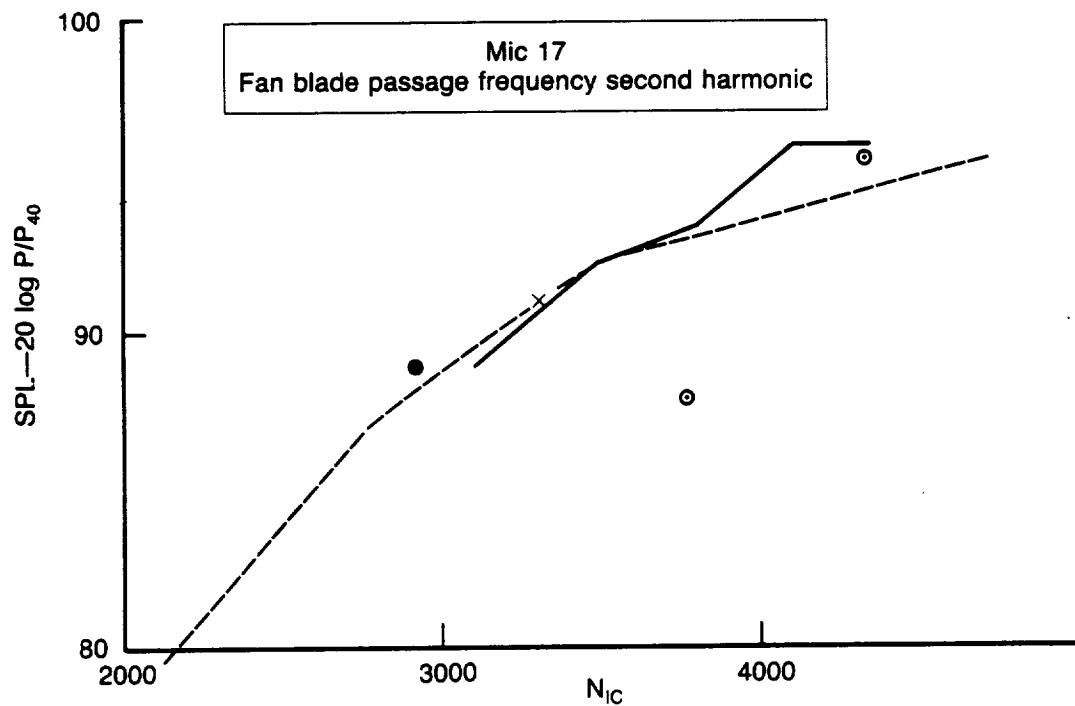
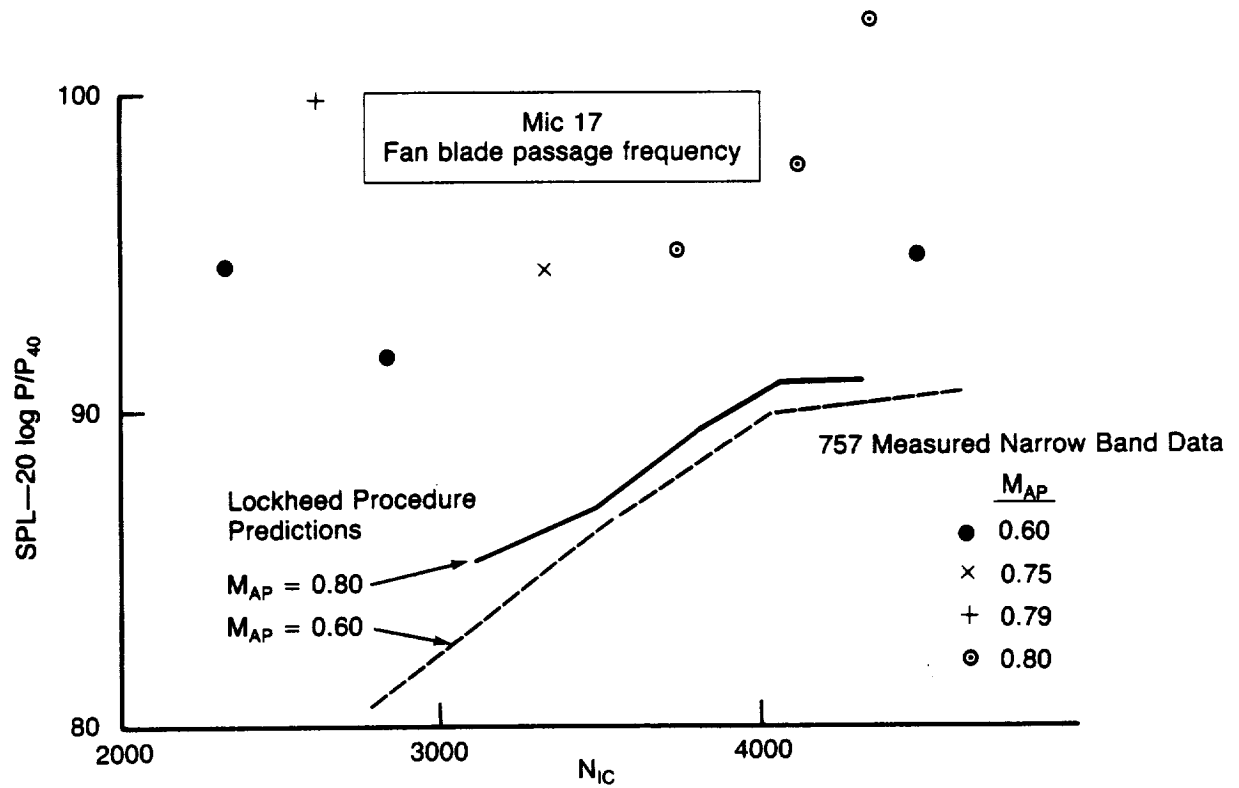


Figure 4-140. Comparison of Measured Fan Tone Data With Lockheed Procedure Predictions—Microphone 17

5.0 BOUNDARY LAYER STABILITY ANALYSIS

The major *aerodynamics* task in the extended engineering analysis of the 757 NLF glove flight data was the boundary layer stability analysis at 21 different flight conditions. The objective of this stability analysis was to compute crossflow (C-F) and Tollmien-Schlichting (T-S) disturbance amplification factors (N-factors) at transition. These results add to the data base from which the boundary layer stability methods are calibrated to allow estimation of the location of transition from laminar to turbulent flow. The flight data used for this analysis consisted of the pressure data, hot film data, and flight conditions.

5.1 CORRECTION TO MEASURED FLIGHT PRESSURE DATA

Static pressure belts (strip-a-tube) were used to acquire pressure data at both the inboard and outboard glove locations. Separate strip-a-tubes were installed on the glove's upper and lower surface, as discussed in detail in Section 6.2.1 of Volume I. Because the strip-a-tube was not wrapped continuously from the upper surface around to the lower surface (to avoid tripping the attachment line flow), its presence produced a change in the airfoil contour at the forward end of the strip-a-tube that affected the measured pressures, primarily at the first two pressure ports. An attempt was made to correct the pressure data at these two ports for this strip-a-tube interference effect prior to using it in the stability analysis. The approach is described below.

At the inboard glove pressure measurement station, for which data was taken on Flights 1 and 2, the results of a wind tunnel test conducted specifically to determine the strip-a-tube interference effect were used to correct the measured flight data at Ports 1 and 2. These wind tunnel results were discussed previously in Section 6.2 of Volume II, and are shown in Figure 5-1. The key part of this approach was to compute the local Mach number on the glove at the location of Port 1 and Port 2 and use the wind-tunnel-derived pressure correction for the closest available Mach number.

The wind tunnel test referred to above was performed after the completion of the flight test. During the flight test, another step was taken to determine the magnitude of the strip-a-tube correction. For Flight 4 pressures were measured only at the outboard glove station. On the glove upper surface, the most forward part of the strip-a-tube (3-tube width, as shown in Figure 6-3 in Volume I) was recessed into the surface so that it was essentially flush. The expectation was that this would result in a pressure measurement very close to that which exists on the undisturbed glove surface for Port 1, at the expense of a possible increased effect at the Port 2 location. By comparing the pressure measurements for Flights 4 and 3 at the same flight condition, the effect of recessing the strip-a-tube can be seen. The measured results are shown in Figure 5-2. For a given condition, the most accurate measured pressures would consist of the Port 1 pressure from Flight 4 and the Port 2 pressure from Flight 3. Aft of Port 2, the pressures from both flights are essentially the same. This is the approach that was used to obtain the outboard corrected pressure data used in the stability analysis. At those conditions for which there was no good pressure data from Flight 3 (as discussed in Section 6.2 of Volume II), Flight 4 data was used for all of the ports without any corrections. Table 5-1 summarizes all of the strip-a-tube corrections made.

5.2 METHOD OF ANALYSIS

For each flight condition for which a boundary layer stability analysis was performed, it was necessary to estimate the isobar pattern on the glove from the measured pressure data. Using results obtained from the Boeing transonic analysis code, A488G, as a guide, isobars were faired between the measured pressures at the inboard and outboard glove locations. Figure 5-3 shows a sample plot of the faired isobars as well as the A488G isobars used for guidance.

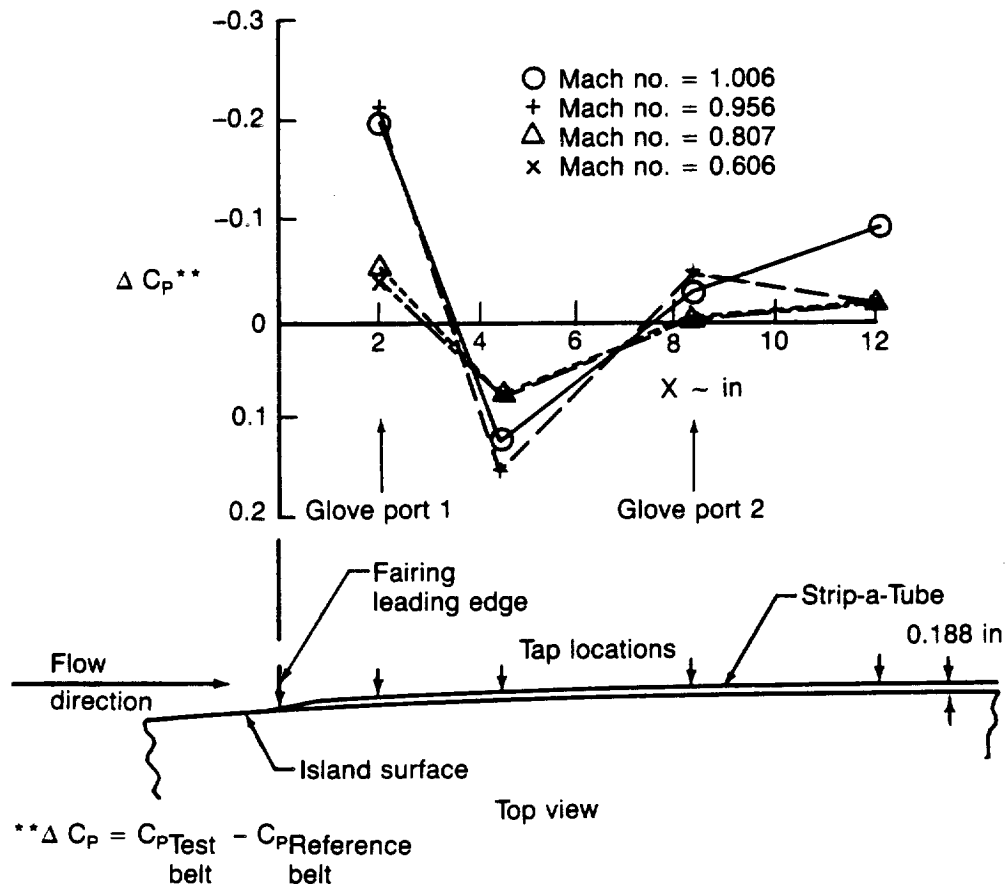
The next step was to use the isobar plot to determine the pressure distribution at the chosen analysis station. In most cases WBL 308.5 was chosen, since the greatest extent of laminar flow usually was achieved at that location. However, WBL 325 was used in some cases. These data along with the corresponding flight conditions, were then used as input to a Boeing laminar boundary layer code (A552), which computes compressible boundary layer parameters on infinite swept wings. The isobar sweep at the chosen spanwise analysis station was used to determine the sweep angle input to A552. In most cases, there was a region of fairly low isobar sweep ahead of 10% chord, with higher isobar sweep aft of that location. To account for this effect, two separate A552 analyses were made. The first used the average sweep angle for the low sweep region and extended only to the end of that region. The second used the average sweep angle for the high sweep region and extended from the leading edge to the end of the glove. Boundary layer data from the two solutions were then patched together using the low sweep results in the forward region and the high sweep results in the aft region. The primary outputs from A552 are the boundary layer velocity profiles parallel and perpendicular to the local potential flow streamline and the boundary layer temperature profile.

The A552 output data served as input to the stability analysis program, which is a modified version of a code developed by L. M. Mack (ref. 11). This program solves the boundary layer stability equations for three dimensional, linearized, parallel flow, assuming a perfect gas. It can calculate either the temporal or spatial stability. In the present study, spatial stability was chosen.

For each chosen flight condition the T-S and C-F instabilities were analyzed. T-S disturbances were followed downstream keeping wave angle and frequency fixed, with the wave angle corresponding closely to that which results in the highest N-factor envelope at transition. To define the envelope, a range of frequencies was analyzed for each case. The C-F disturbances were followed downstream keeping the frequency fixed at zero and letting the wave angle vary in accordance with the irrotationality condition, as proposed by Mack (ref. 12). This results in a constant spanwise component of the wave number (constant α_s^*) as the disturbance propagates downstream. The crossflow disturbance envelope is defined by analyzing a series of disturbances having a range of spanwise wave number components. Zero frequency was chosen because, for swept wings, frequencies near zero typically give rise to the highest amplitude ratio crossflow disturbances when the irrotationality condition is followed (ref. 12). The final results of the stability analysis consisted of boundary layer disturbance growth curves, as defined by the amplification factor (N-factor), which is the natural logarithm of the ratio of the disturbance amplitude, A , at any point to its amplitude, A_0 , at the neutral stability point (fig. 5-4 shows an example).

To see the interaction between the C-F and T-S instabilities, a trajectory curve was plotted on the N_{TS} versus N_{CF} plane. This result was then superimposed on the transition data band, previously established by test results from a NLF glove on an F-111 aircraft (ref. 3), as shown in Figure 5-5. The resulting data point at the middle of the transition uncertainty band is the primary result of the analysis, and can be added to the F-111 transition data base, resulting in a refinement of the method calibration. The transition uncertainty band for a given case usually is defined by the location of the last laminar hot film and the location of the first turbulent hot film. However, for those cases where one of the hot films gave a *transitional* indication, the uncertainty band is arbitrarily shown as $\pm 1\%$ about this location.

Results



Installation

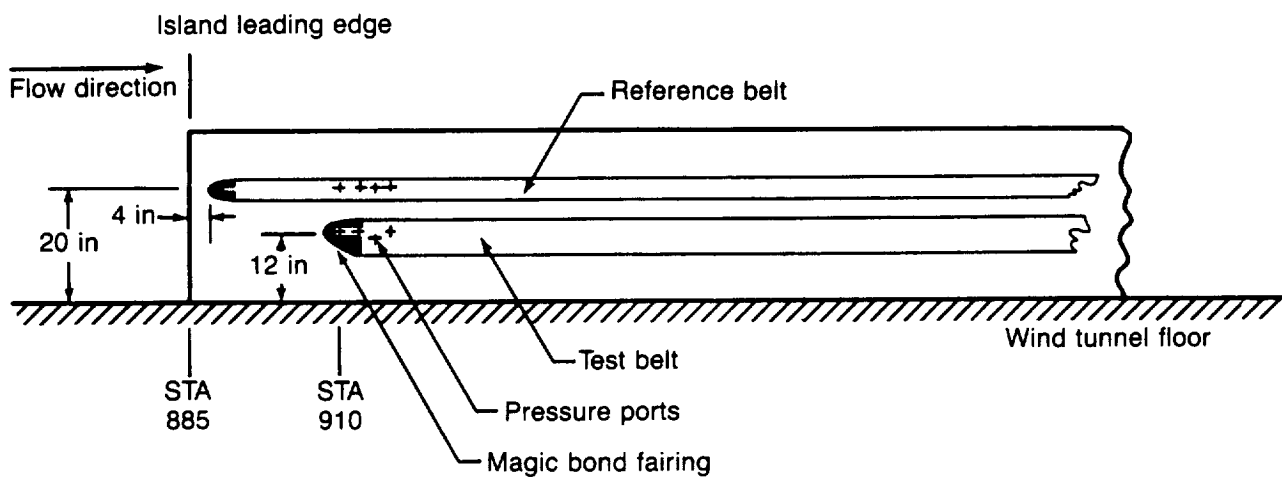


Figure 5-1. Effect of Strip-a-Tube Fairing on Static Pressures

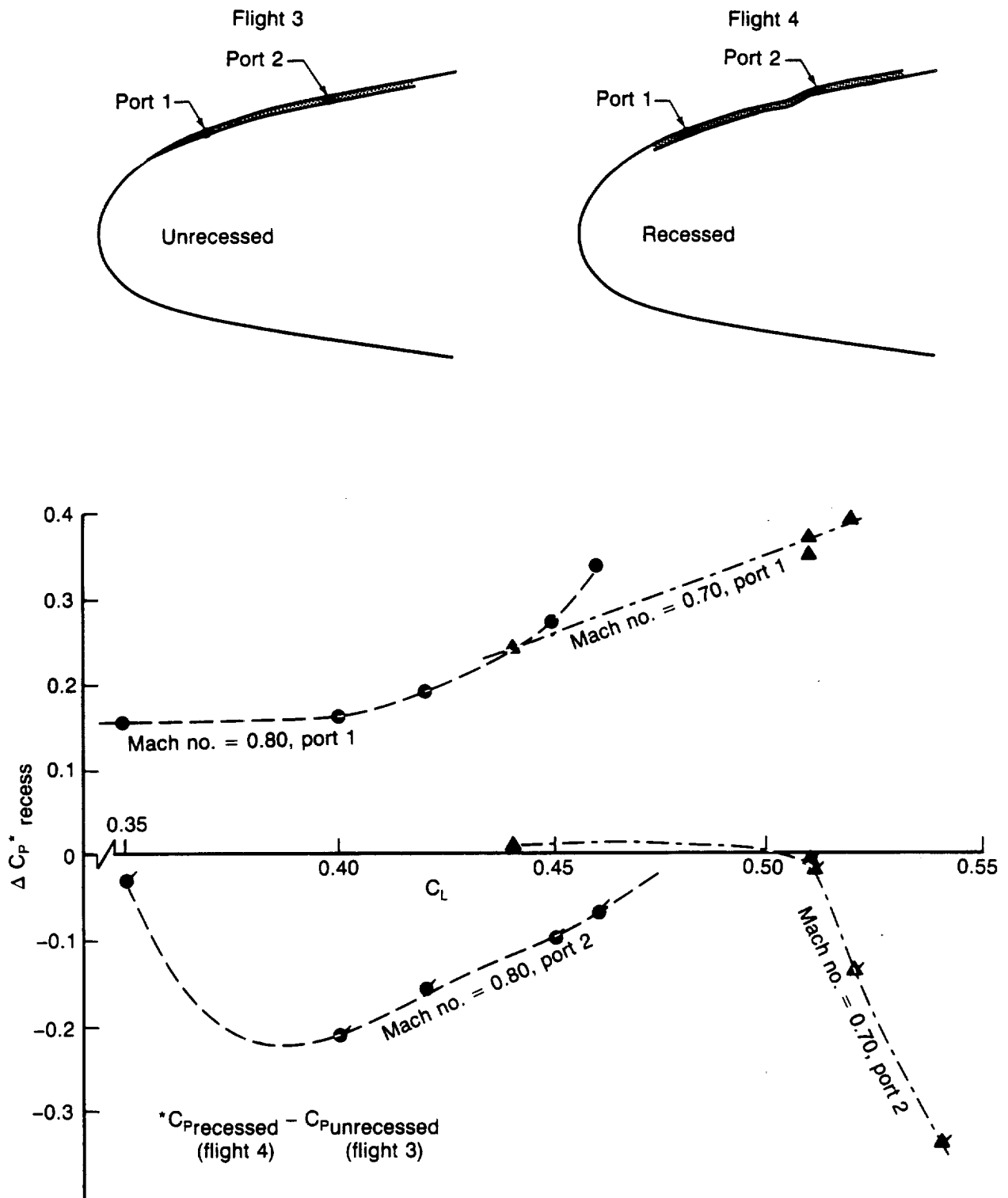


Figure 5-2. Effect of Recessing Strip-a-Tube

Table 5-1. Strip-a-Tube Corrections

Case	Inboard station (WBL 296)		Outboard station (WBL 353)	
	ΔC_{P_1}	ΔC_{P_2}	ΔC_{P_1}	ΔC_{P_2}
1	0.200	0.030	0	—
2	0.050	0.002	0.050	0
3	0.200	0.030	0	—
4	0.170	0.025	0.130	0.025
5	0.050	0.002	0.130	0.003
6	0.040	0.003	0	—
7	0.005	0.005	—	0.005
8	0.030	0.003	—	0.003
9	0.200	0.030	0	—
10	0.174	0.030	0.280	0.025
11	0.177	0.025	0	—
12	0.160	0.030	0	—
13	0.200	0.030	0	—
14	0.040	0.002	0	—
15	0.210	0.030	0	—
16	0.050	0.003	0	—
17	0.168	0.030	0.360	0.030
18	0.050	0.005	0.360	0.005
19	0.192	0.030	0	—
20	0.050	0.002	0	—
21	0.040	0.003	0	0.070

— No adequate correction available
 ΔC_{P_1} , ΔC_{P_2} C_P corrections at pressure ports 1 and 2

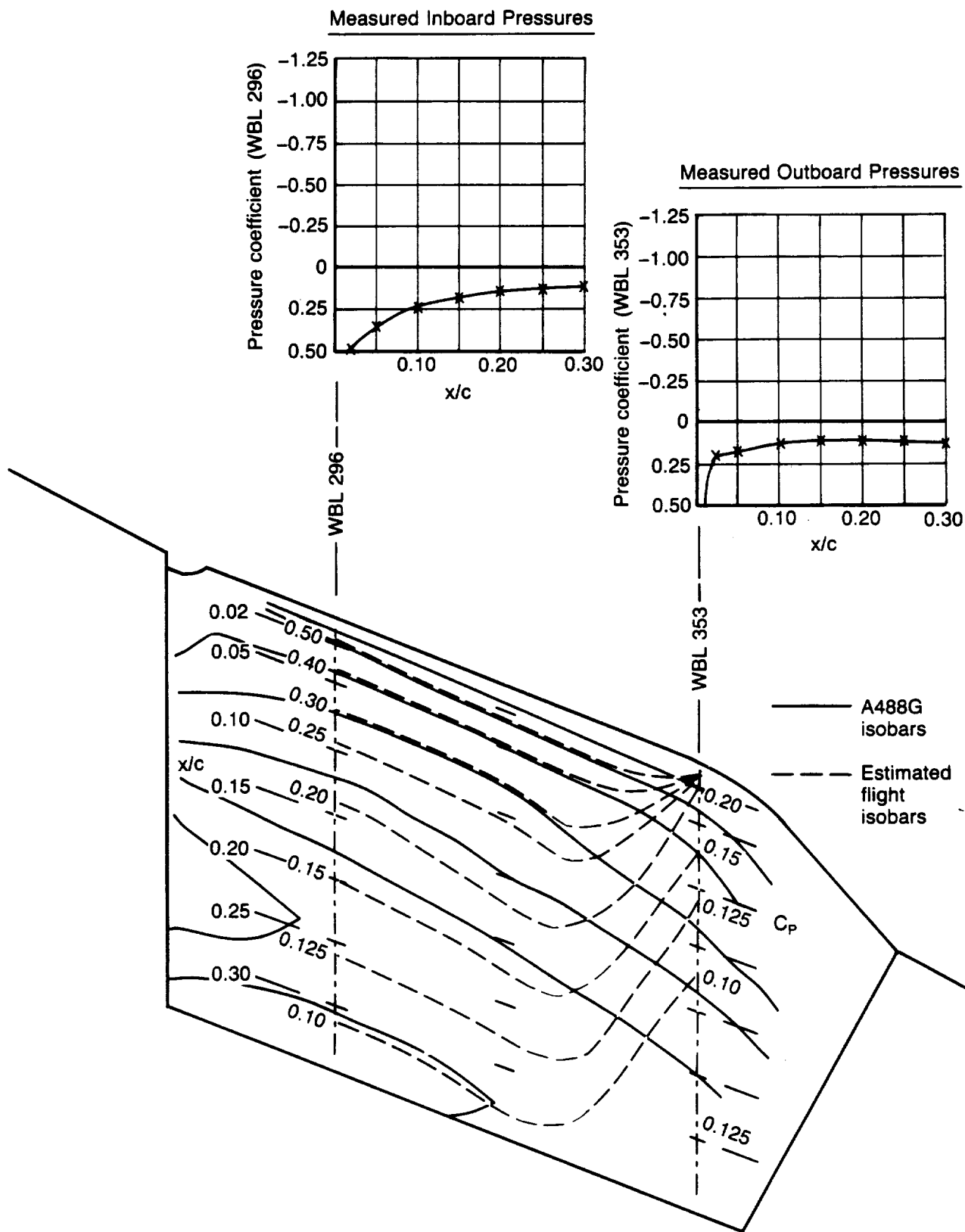


Figure 5-3. Sample Isobar Plot

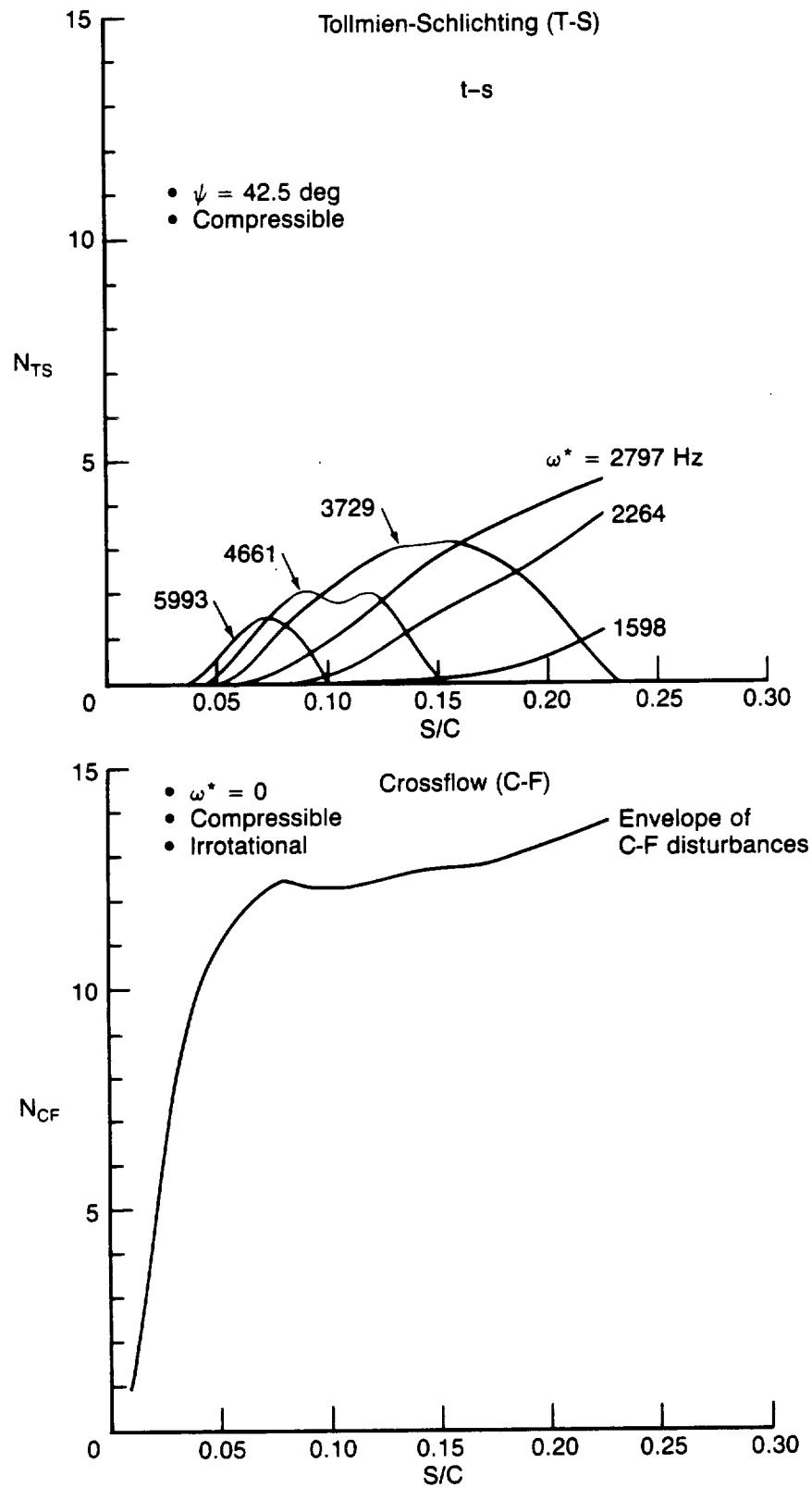


Figure 5-4. Typical Stability Analysis Results

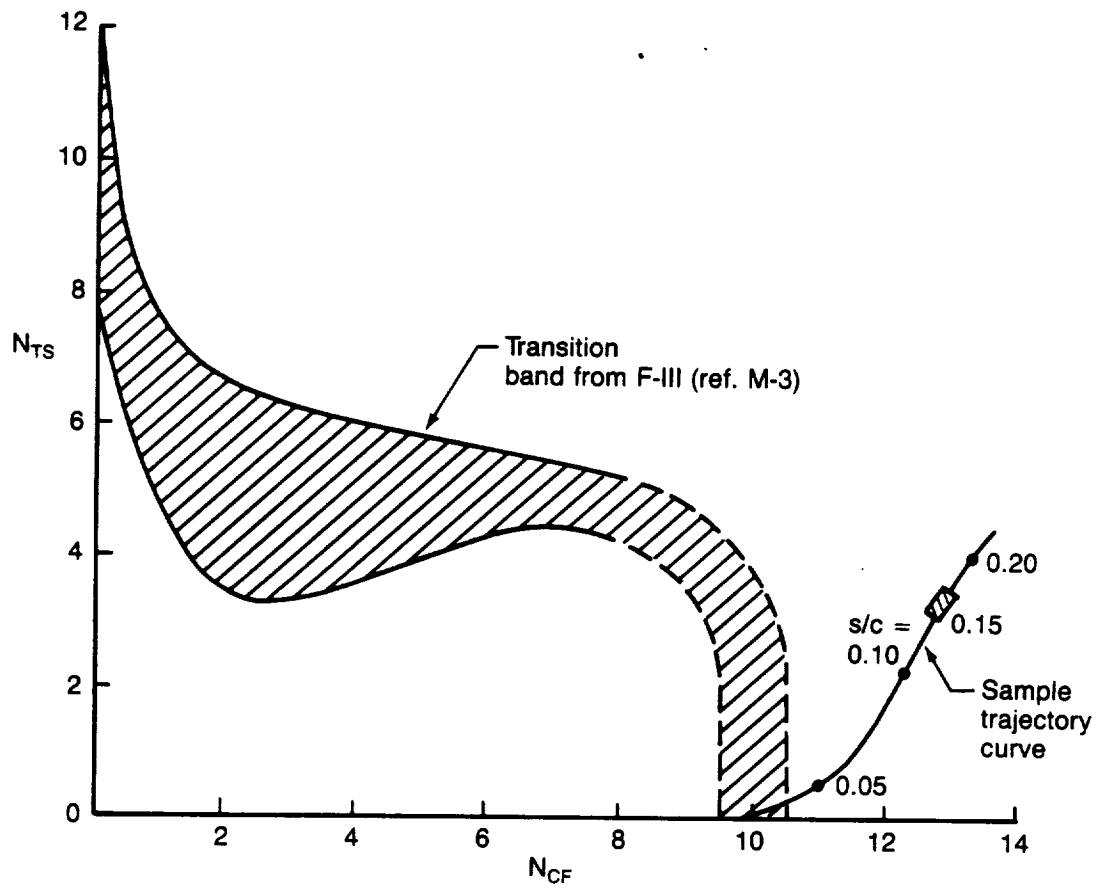


Figure 5-5. N_{TS} vs. N_{CF} Trajectory Curve—Sample Case

5.3 RESULTS

From the accumulated flight test data, 21 cases were chosen for the present study. Each of these cases was subjected to a thorough stability analysis. In the following section, a case-by-case discussion is presented, along with summary plots of the results. The C_{pN} versus s/c plots for each case correspond to the pressure coefficients based on the velocity normal to the lower of the two sweep angles analyzed. The Appendix contains tabulations of the pressure distributions for each case at both of the analyzed sweep angles.

Case 1:

This case was for the upper surface at WBL 308.5. The isobar sweeps fell into three regions: an average of 22 deg sweep from the leading edge to 7% chord, an average of 32 deg between 8% and 17% chord, and an average of 28 deg from 18% to 30% chord. The flight conditions were near those of the glove design condition. Laminar flow extended to about 29% chord (s/c), with an NTS of 0.8 and NCF of 12.4. Figure 5-6 summarizes the input data and results for this case.

Case 2:

This case was for the lower surface at WBL 308.5. The analysis sweep angles were set to 22 deg from the leading edge to 7% chord and 32 deg from 8% to 25% chord. The flight conditions were identical to those of Case 1. The transition occurred at about 18% chord (s/c) with an NTS of 2.7 and NCF of 12.1. Figure 5-7 summarizes this case.

Case 3:

This case is summarized in Figure 5-8. It was a high Mach, intermediate C_L case for the upper surface at WBL 308.5. The analysis sweep angles were set to 20 deg from leading edge to 10% chord and 30 deg from 11% to 30% chord. Transition occurred at about 30% chord (s/c) with an NTS of 1.5 and NCF of 14.6.

Case 4:

This case was for the upper surface at WBL 308.5. The analysis sweep angles were set to 16.50 deg from leading edge to 9% chord and 27.5 deg from 10% to 30% chord. The flight conditions were cruise Mach, low altitude, low C_L , and high positive sideslip. Transition occurred at about 25% chord (s/c) with an NTS of 1.8 and NCF of 12.1. Figure 5-9 summarizes this case.

Case 5:

This case was for the lower surface at WBL 308.5. The analysis sweep angles were set to 14.5 deg from leading edge to 10% chord and 38.5 deg from 11% to 25% chord. The flight conditions were identical to those of Case 4. Transition occurred at about 20% chord (s/c) with an NTS of 3.5 and NCF of 6.7. Figure 5-10 summarizes this case.

Case 6:

This case was for the lower surface at WBL 325. The analysis sweep angles were set to 21.6 deg from leading edge to 7% chord and 37.6 deg from 8% to 25% chord. The flight Mach number was about 0.7, and the C_L was 0.647. Transition occurred at about 16% chord (s/c) with an NTS of 0.7 and NCF of 13.9. Figure 5-11 summarizes this case.

Case 7:

This was a low Mach, high positive sideslip case for the lower surface at WBL 325. The analysis sweep angles were set to 16 deg from leading edge to 9% chord and 20 deg from 10% to 30% chord. Transition occurred at about 26% chord (s/c) with zero NTS and NCF of 12.2. Figure 5-12 summarizes this case.

Case 8:

This case was for the lower surface at WBL 325. In the analysis, a single sweep angle of 25 deg was used for the entire glove. This was an intermediate Mach number case ($M = .75$). Transition occurred at about 20% chord (s/c) with an NTS of 3.0 and NCF of 17.8. Figure 5-13 summarizes this case.

Case 9:

This case was for the upper surface at WBL 308.5. The analysis sweep angles were set to 19.8 deg from the leading edge to 7% chord and 42.8 deg from 8% to 25% chord. The flight conditions were identical to those of Case 8. Transition occurred at about 19% chord (s/c) with an NTS of 3.2 and NCF of 4.6. Figure 5-14 summarizes this case.

Case 10:

This was a cruise Mach, intermediate C_L case for the upper surface at WBL 308.5. The analysis sweep angles were set to 19.4 deg from leading edge to 9% chord and 32.4 deg from 10% to 30% chord. Transition occurred at about 24% chord (s/c) with an NTS of 0.1 and NCF of 14.2. Figure 5-15 summarizes this case.

Case 11:

This was another cruise Mach, intermediate C_L case for the upper surface at WBL 308.5. The analysis sweep angles were set to 19.9 deg from leading edge to 7% chord and 32.9 deg from 8% to 30% chord. Transition occurred at about 28% chord (s/c) with an NTS of 0.9 and NCF of 17.8. Figure 5-16 summarizes this case.

Case 12:

This was a high Mach, intermediate C_L case for the upper surface at WBL 308.5. The analysis sweep angles were set to 21.9 deg from leading edge to 8% chord and 27.9 deg from 9% to 30% chord. Transition occurred at about 29% chord (s/c) with an NTS of 0.9 and NCF of 17.9. Figure 5-17 summarizes this case.

Case 13:

This was a design flight condition case with high positive sideslip for the upper surface at WBL 308.5. The analysis sweep angles were set to 16 deg from leading edge to 5% chord and 30 deg from 6% to 30% chord. Transition occurred at about 26% chord (s/c) with zero NTS and NCF of 7.1. Figure 5-18 summarizes this case.

Case 14:

This case was for the lower surface at WBL 308.5. The analysis sweep angles were set to 20 deg from leading edge to 8% chord and 27.5 deg from 9% to 30% chord. Flight conditions were identical to those of Case 13. Transition occurred at about 24% chord (s/c) with an NTS of 1.2 and NCF of 15.8. Figure 5-19 summarizes this case.

Case 15:

This was a design flight condition case with high negative sideslip for the upper surface at WBL 308.5. The analysis sweep angles were set to 20.1 deg from leading edge to 8% chord and 38.1 deg from 9% to 30% chord. Transition occurred at about 29% chord (s/c) with an NTS of 1.1 and NCF of 14.3. Figure 5-20 summarizes this case.

Case 16:

This case was for the lower surface at WBL 325. The analysis sweep angles were set to 31.1 deg from leading edge to 8% chord and 41.6 deg from 9% to 25% chord. Flight conditions were identical to those of Case 15. Transition occurred at about 16% chord (s/c) with an NTS of 3.1 and NCF of 12.8. Figure 5-21 summarizes this case.

Case 17:

This was a cruise Mach, intermediate C_L case for the upper surface at WBL 308.5, similar to Case 10. The analysis sweep angles were set to 18.4 deg from leading edge to 8% chord and 30.9 deg from 9% to 30% chord. Transition occurred at about 29% chord (s/c) with an NTS of 1.5 and NCF of 13.7. Figure 5-22 summarizes this case.

Case 18:

This case was for the lower surface at WBL 308.5. The analysis sweep angles were set to 22.9 deg from leading edge to 9% chord and 35.9 deg from 10% to 30% chord. Flight conditions were identical to those of Case 17. Transition occurred at about 21% chord (s/c) with an NTS of 3.9 and NCF of 9.9. Figure 5-23 summarizes this case.

Case 19:

This was a cruise Mach, intermediate C_L case for the upper surface at WBL 308.5. The analysis sweep angles were set to 17.8 deg from leading edge to 9% chord and 32.3 deg from 10% to 30% chord. Transition occurred at about 28% chord (s/c) with an NTS of 0.5 and NCF of 13.4. Figure 5-24 summarizes this case.

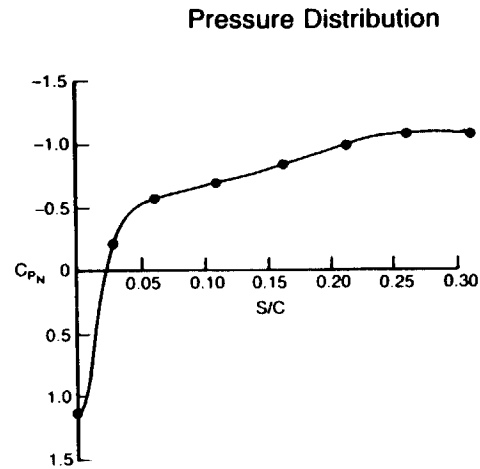
Case 20:

This case was for the lower surface at WBL 308.5. The analysis sweep angles were set to 23.8 deg from leading edge to 8% chord and 28.8 deg from 9% to 25% chord. Flight conditions were identical to those of Case 19. Transition occurred at about 21% chord (s/c) with an NTS of 3.3 and NCF of 13.6. Figure 5-25 summarizes this case.

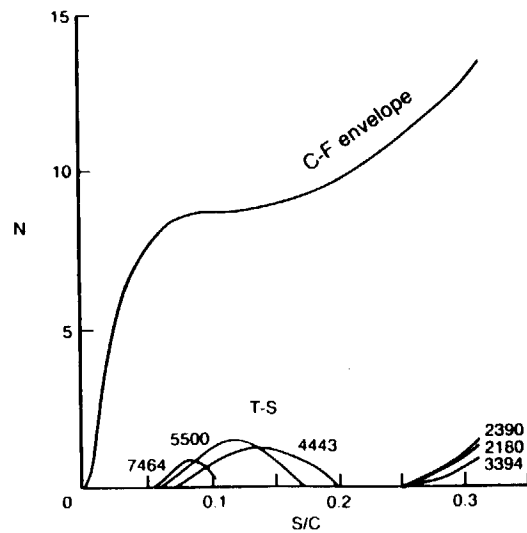
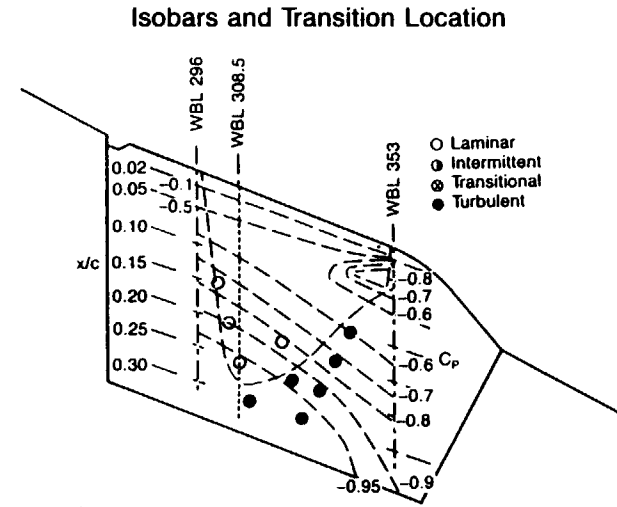
Case 21:

This case was for the lower surface at WBL 325. The analysis sweep angles were set to 14.2 deg from leading edge to 9% chord and 21.7 deg from 10% to 30% chord. Flight conditions were low Mach number, low altitude, and high sideslip. Transition occurred at about 26% chord (s/c) with an NTS of 2.1 and NCF of 7.2. Figure 5-26 summarizes this case.

The results for all 21 cases are summarized in Table 5-2. In Figure 5-27 the N-factors at transition are shown for each case, together with the F-111 transition N-factor data band. The bands shown for each case represent the uncertainty in the measured transition location for each case, as explained earlier.



- Upper surface; WBL 308.5
- Flight 3, cond. 16 (outbd C_p)
- Flight 2, cond. 223 (inbd C_p)
- $M_\infty = 0.804$, alt = 40,483 ft
- $Re_C = 25.5 \times 10^6$
- $C_L = 0.534$



Crossflow

- Compressible
- Irrotational
- $\omega^* = 0$
- $\Lambda = 22$ deg (0 to 0.07 x/c)
- $\Lambda = 32$ deg (0.08 to 0.17 x/c)
- $\Lambda = 28$ deg (0.18 to 0.30 x/c)

Tollmien-Schlichting

- Compressible
- $\psi = 35$ deg

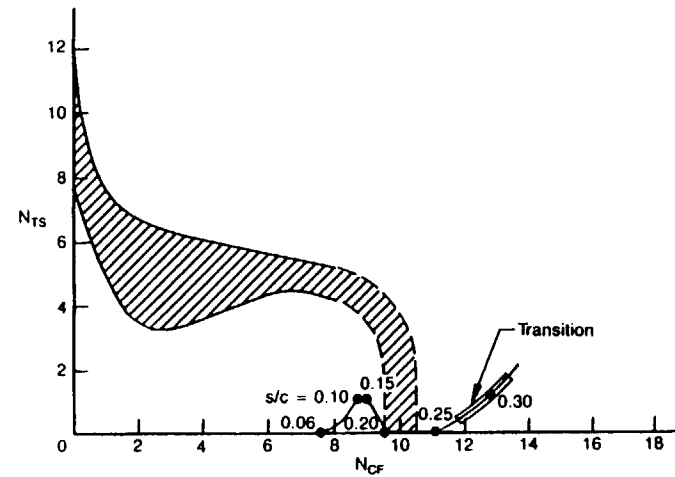
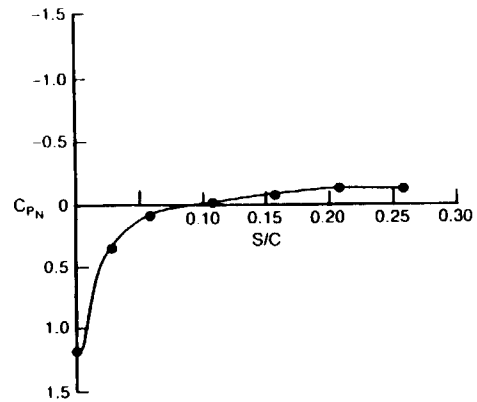


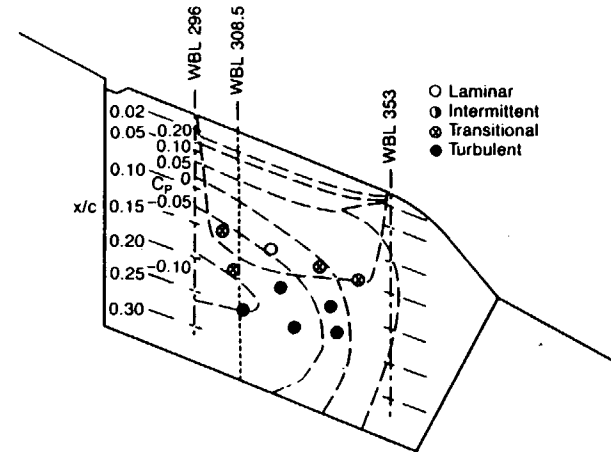
Figure 5-6. 757 NLF Glove: Case 1

Pressure Distribution

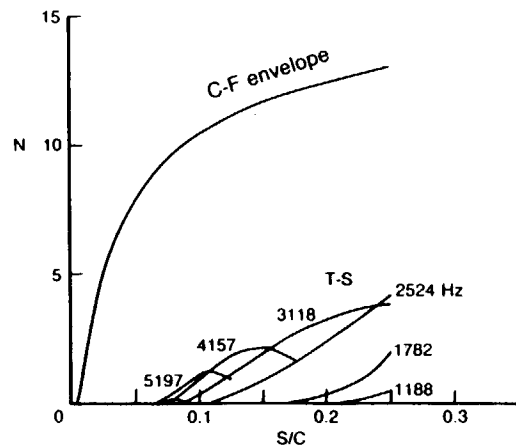


- Lower surface; WBL 308.5
- Flight 3, cond. 16 (outbd C_P)
- Flight 2, cond. 223 (inbd C_P)
- $M_\infty = 0.804$, alt = 40,483 ft
- $Re_C = 25.5 \times 10^6$
- $C_L = 0.537$

Isobars and Transition Location



Boundary Layer Stability



Crossflow

- Compressible
- Irrotational
- $\omega^* = 0$
- $\Lambda = 22$ deg (0 to 0.07 x/c)
- $\Lambda = 32$ deg (0.08 to 0.25 x/c)

Tollmien-Schlichting

- Compressible
- $\psi = 35$ deg

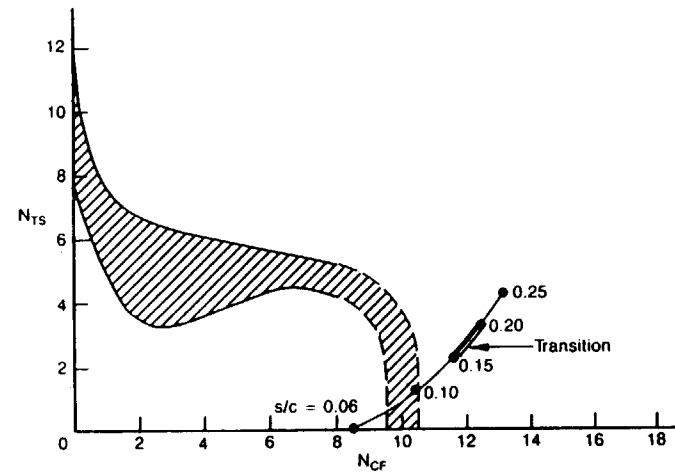
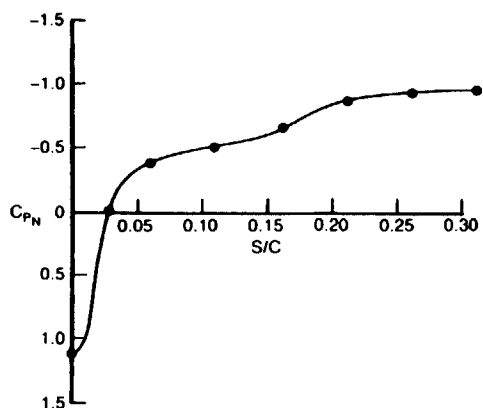


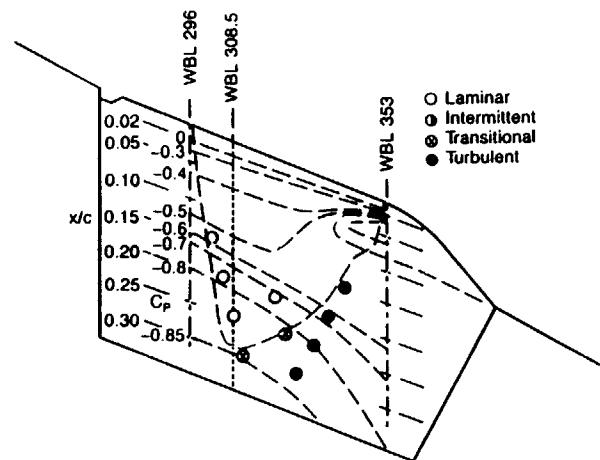
Figure 5-7. 757 NLF Glove: Case 2

Pressure Distribution

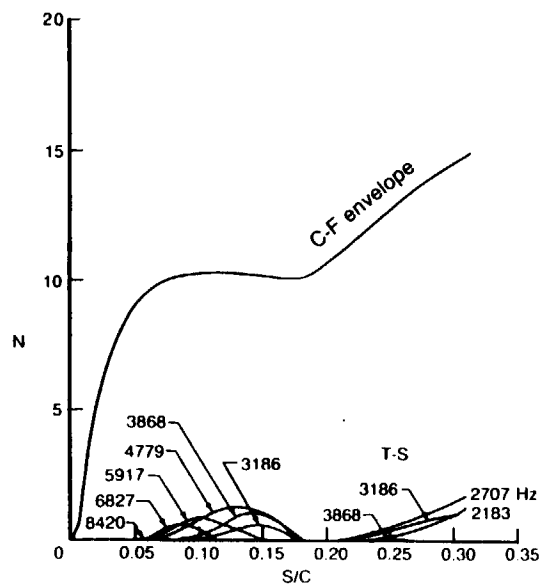


- Upper surface; WBL 308.5
- Flight 2, cond. 242 (inbd C_p)
- Flight 3, cond. 30 (outbd C_p)
- $M_\infty = 0.825$, alt = 40,761 ft
- $Re_C = 25.90 \times 10^6$
- $C_L = 0.49$
- $\beta = 3.3$ deg

Isobars and Transition Location



Boundary Layer Stability



Crossflow

- Compressible
- Irrotational
- $\omega^* = 0$
- $\Lambda = 20$ deg (0 to 0.10 x/c)
- $\Lambda = 30$ deg (0.11 to 0.30 x/c)

Tollmien-Schlichting

- Compressible
- $\psi = 50$ deg

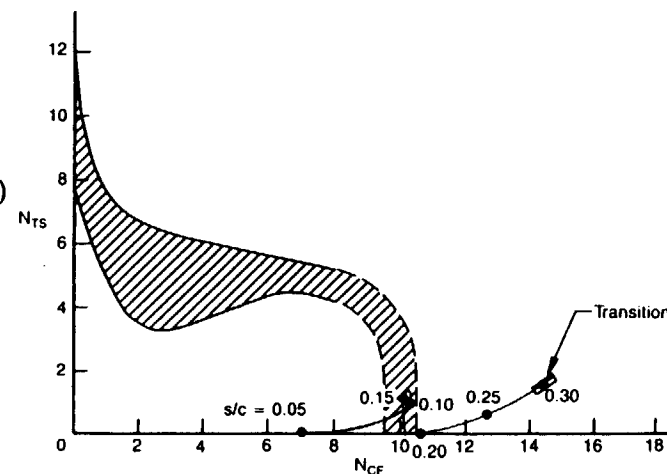
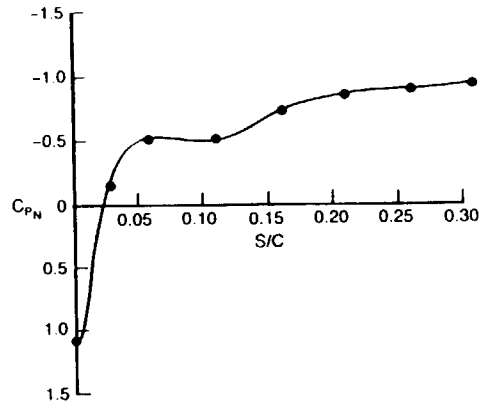


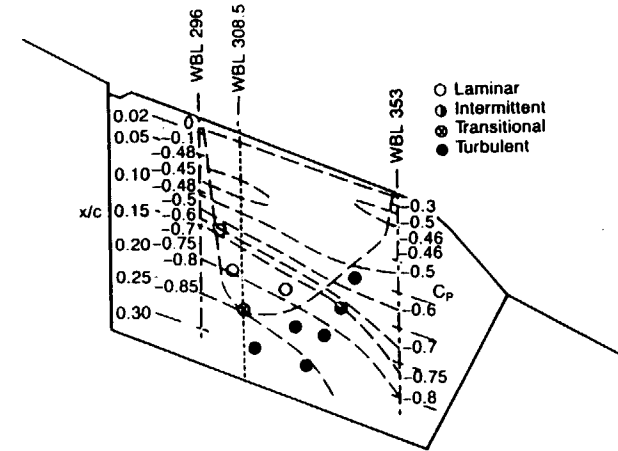
Figure 5-8. 757 NLF Glove: Case 3

Pressure Distribution

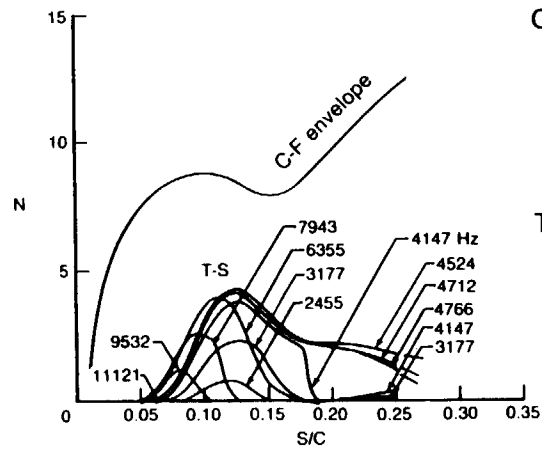


- Upper surface; WBL 308.5
- Flight 2, cond. 202 (inbd C_p)
- Flight 3, cond. 4 (outbd C_p)
- $M_\infty = 0.793$, alt = 30,080 ft
- $Re_C = 38.3 \times 10^6$
- $C_L = 0.359$

Isobars and Transition Location



Boundary Layer Stability



Crossflow

- Compressible
- Irrotational
- $\omega^* = 0$
- $\Lambda = 16.5$ deg (0 to 0.09 x/c)
- $\Lambda = 27.5$ deg (0.10 to 0.25 x/c)

Tollmien-Schlichting

- Compressible
- $\psi = 50$ deg

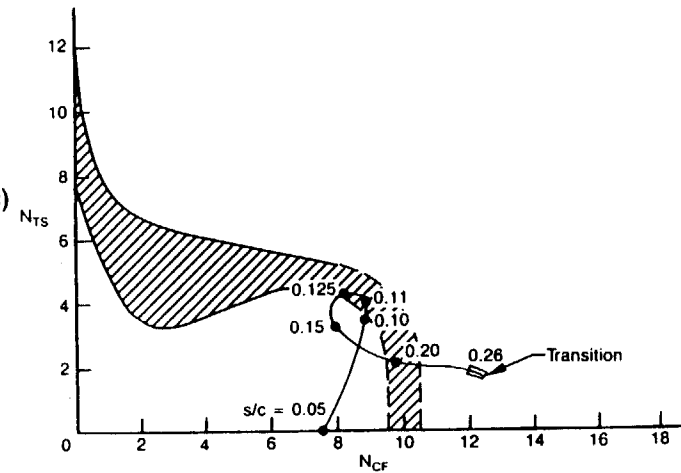
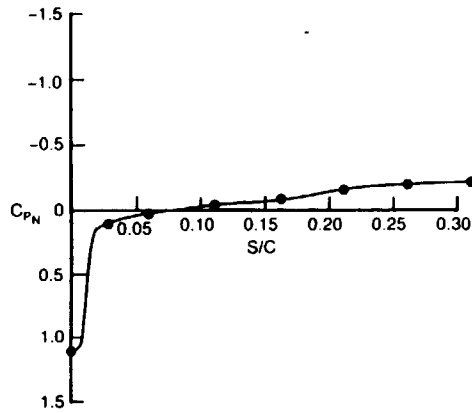


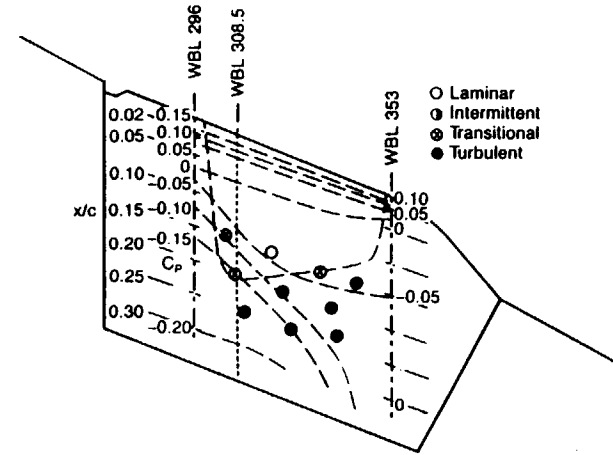
Figure 5-9. 757 NLF Glove: Case 4

Pressure Distribution

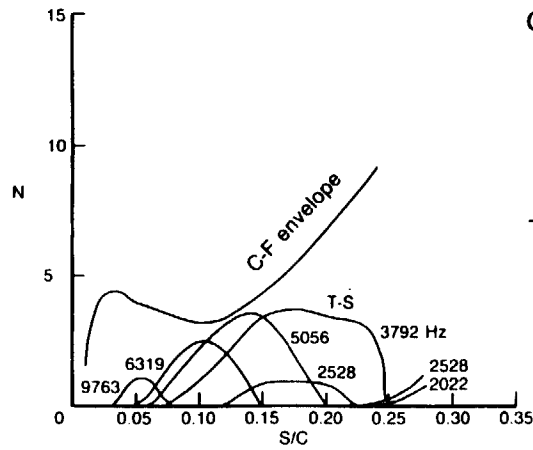


- Lower surface; WBL 308.5
- Flight 2, cond. 202 (inbd C_p)
- Flight 3, cond. 4 (outbd C_p)
- $M_\infty = 0.793$, alt = 30,080 ft
- $Re_C = 38.35 \times 10^6$
- $C_L = 0.359$

Isobars and Transition Location



Boundary Layer Stability



Crossflow

- Compressible
- Irrotational
- $\omega^* = 0$
- $\Lambda = 14.5$ deg (0 to 0.10 x/c)
- $\Lambda = 38.5$ deg (0.11 to 0.30 x/c)

Tollmien-Schlichting

- Compressible
- $\psi = 30$ deg

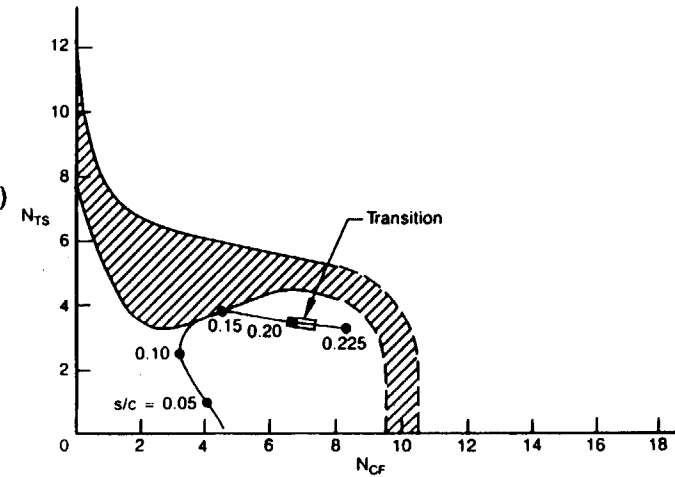
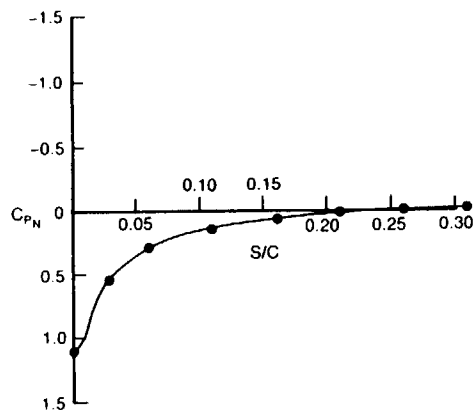


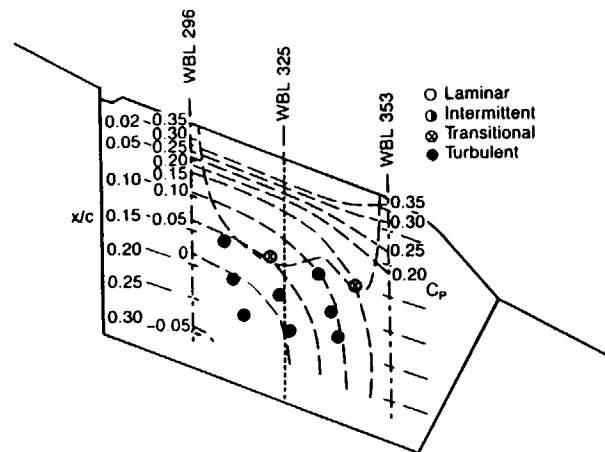
Figure 5-10. 757 NLF Glove: Case 5

Pressure Distribution

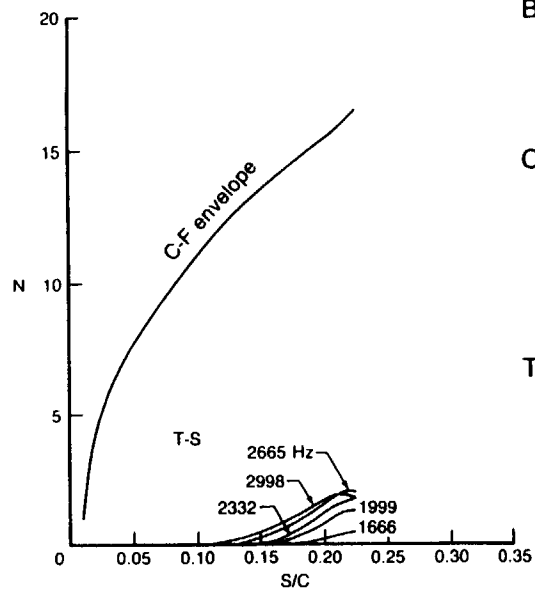


- Lower surface; WBL 325
- Flight 2, cond. 232 (inbd C_P)
- Flight 3, cond. 22 (outbd C_P)
- $M_\infty = 0.697$, alt = 39,009 ft
- $Re_C = 23.14 \times 10^6$
- $C_L = 0.647$

Isobars and Transition Location



Boundary Layer Stability



Crossflow

- Compressible
- Irrotational
- $\omega^* = 0$
- $\Lambda = 21.6$ deg (0 to 0.07 x/c)
- $\Lambda = 37.6$ deg (0.08 to 0.25 x/c)

Tollmien-Schlichting

- Compressible
- $\psi = 20$ deg

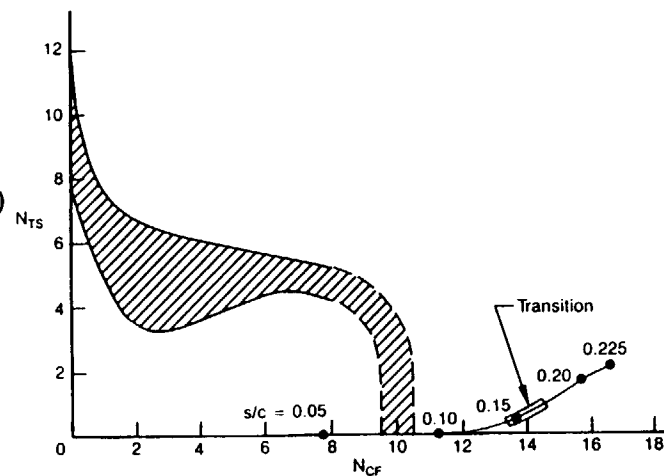
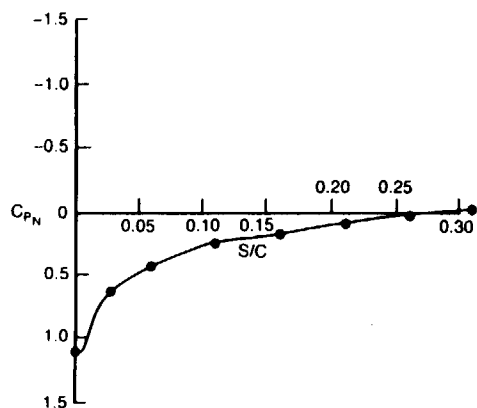


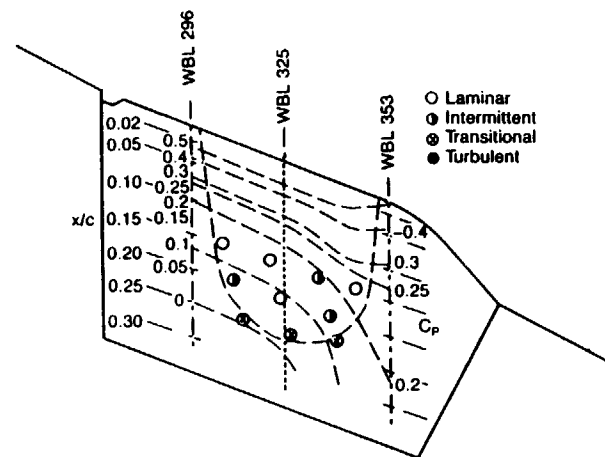
Figure 5-11. 757 NLF Glove: Case 6

Pressure Distribution

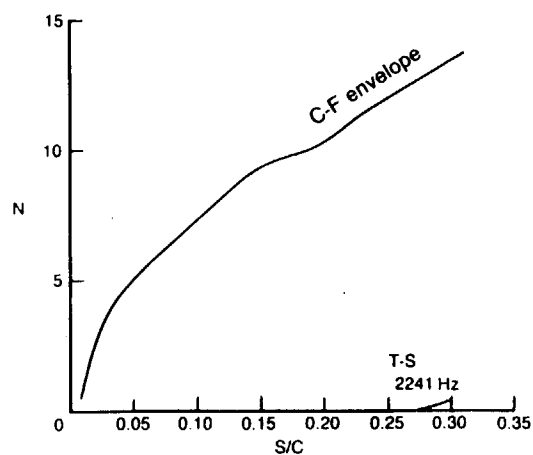


- Lower surface; WBL 325
- Flight 2, cond. 234 (inbd C_p)
- Flight 3, cond. 24 (outbd C_p)
- $M_\infty = 0.699$, alt = 39,042 ft
- $Re_C = 23.17 \times 10^6$
- $C_L = 0.644$
- $\beta = 6.8$ deg

Isobars and Transition Location



Boundary Layer Stability



Crossflow

- Compressible
- Irrotational
- $\omega^* = 0$
- $\Lambda = 16$ deg (0 to 0.09 x/c)
- $\Lambda = 20$ deg (0.10 to 0.30 x/c)

Tollmien-Schlichting

- Compressible
- $\psi = 20$ deg

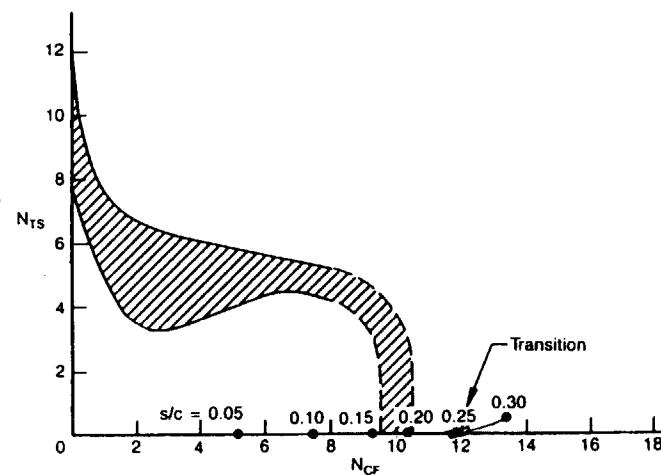
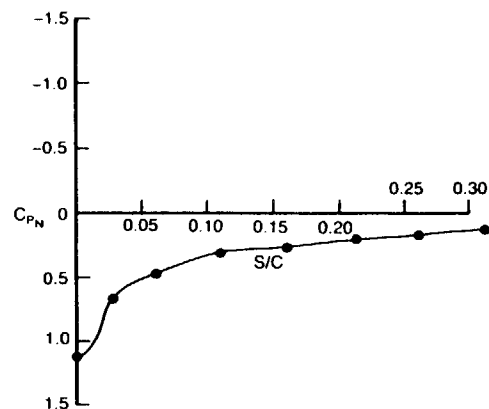


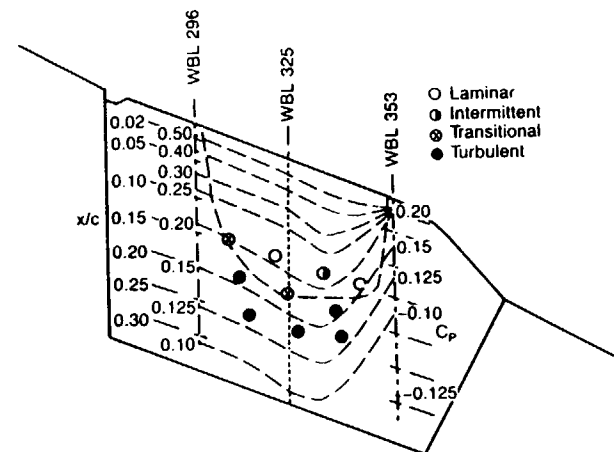
Figure 5-12. 757 NLF Glove: Case 7

Pressure Distribution

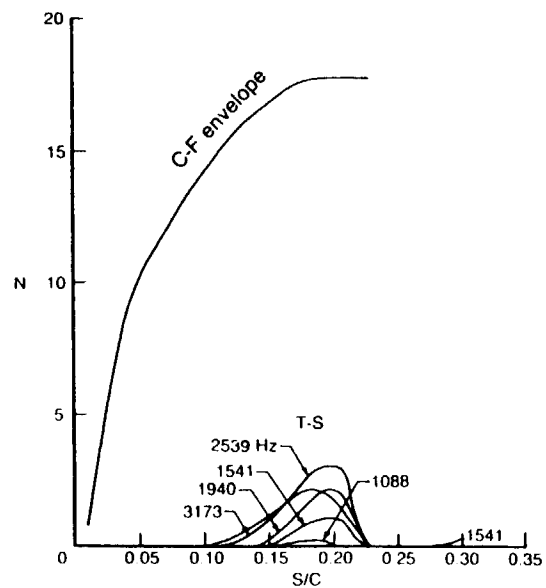


- Lower surface; WBL 325
- Flight 2, cond. 252 (inbd C_P)
- Flight 3, cond. 29 (outbd C_P)
- $M_\infty = 0.753$, alt = 38,994 ft
- $Re_C = 25.01 \times 10^6$
- $C_L = 0.569$

Isobars and Transition Location



Boundary Layer Stability



Crossflow

- Compressible
- Irrotational
- $\omega^* = 0$
- $\Lambda = 25$ deg (0 to 0.30 x/c)

Tollmien-Schlichting

- Compressible
- $\psi = 30$ deg

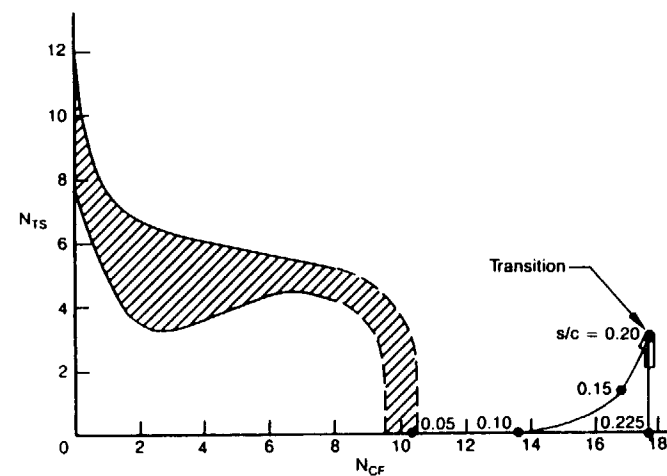
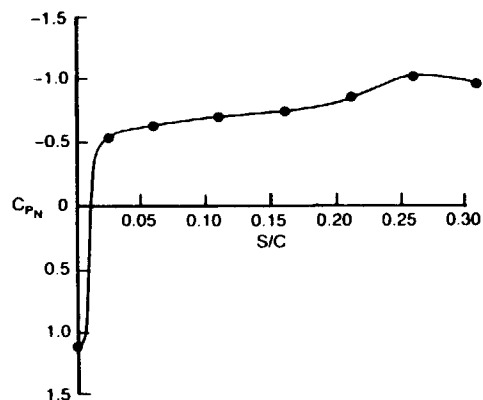


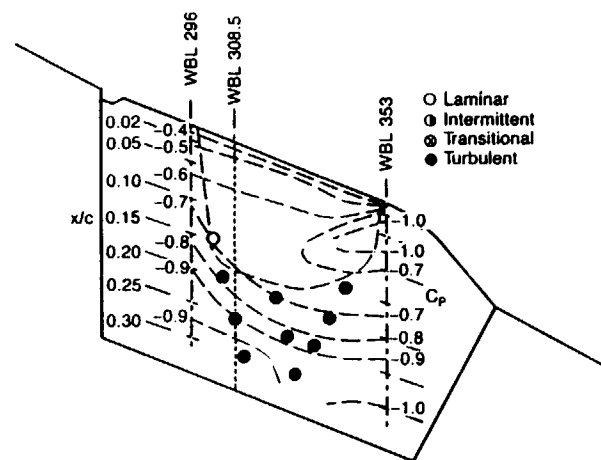
Figure 5-13. 757 NLF Glove: Case 8

Pressure Distribution

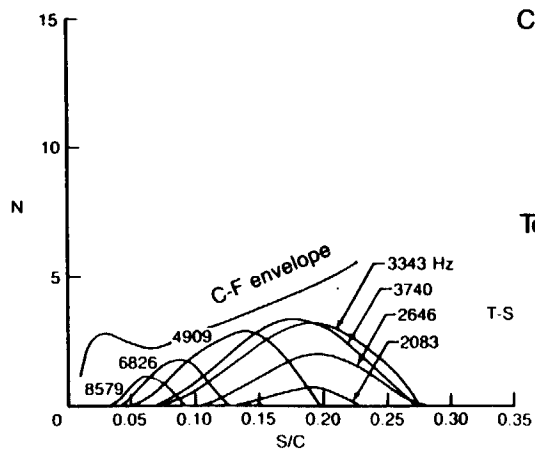


- Upper surface; WBL 308.5
- Flight 2, cond. 252 (inbd C_P)
- Flight 3, cond. 29 (outbd C_P)
- $M_\infty = 0.753$, alt = 38,994 ft
- $Re_C = 25.69 \times 10^6$
- $C_L = 0.569$

Isobars and Transition Location



Boundary Layer Stability



Crossflow

- Compressible
- Irrotational
- $\omega^* = 0$
- $\Lambda = 19.8$ deg (0 to 0.07 x/c)
- $\Lambda = 42.8$ deg (0.08 to 0.25 x/c)

Tollmien-Schlichting

- Compressible
- $\psi = 42.5$ deg

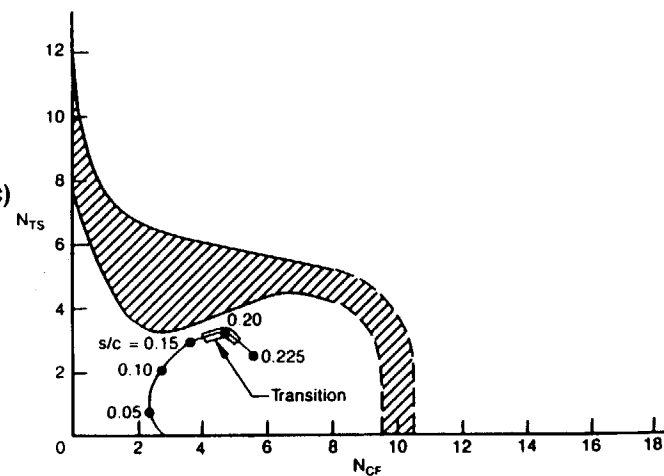
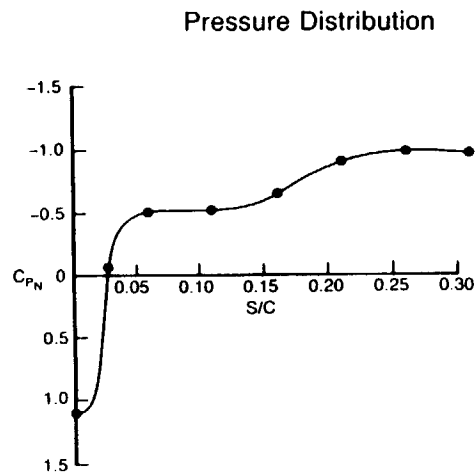
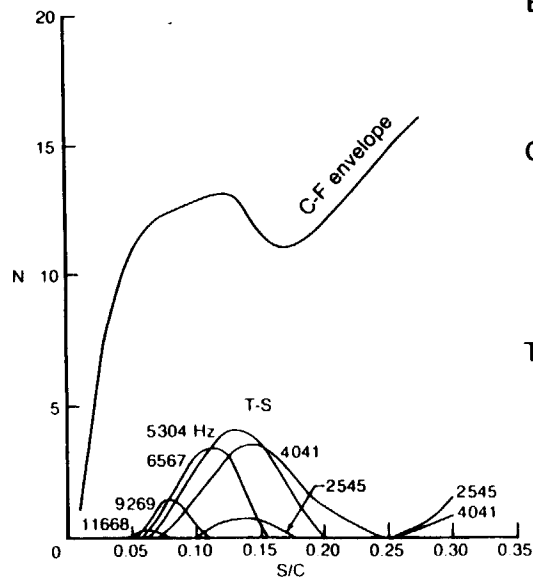
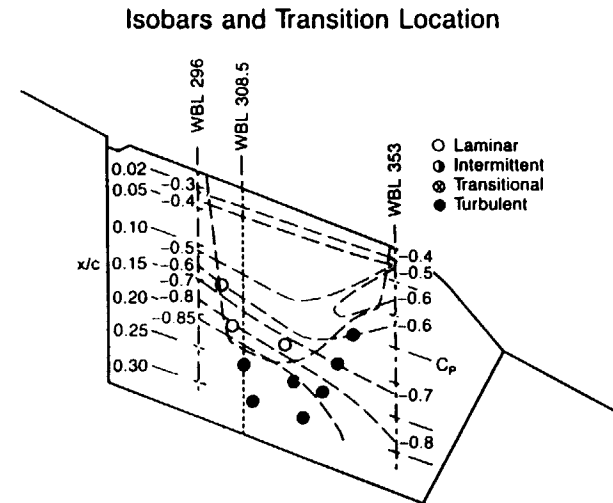


Figure 5-14. 757 NLF Glove: Case 9



- Upper surface; WBL 308.5
- Flight 2, cond. 207 (inbd C_p)
- Flight 3, cond. 12 (outbd C_p)
- $M_\infty = 0.809$, alt = 36,000 ft
- $Re_C = 31.64 \times 10^6$
- $C_L = 0.450$



Boundary Layer Stability

Crossflow

- Compressible
- Irrotational
- $\omega^* = 0$
- $\Lambda = 19.4$ deg (0 to 0.09 x/c)
- $\Lambda = 32.4$ deg (0.10 to 0.30 x/c)

Tollmien-Schlichting

- Compressible
- $\psi = 42.5$ deg

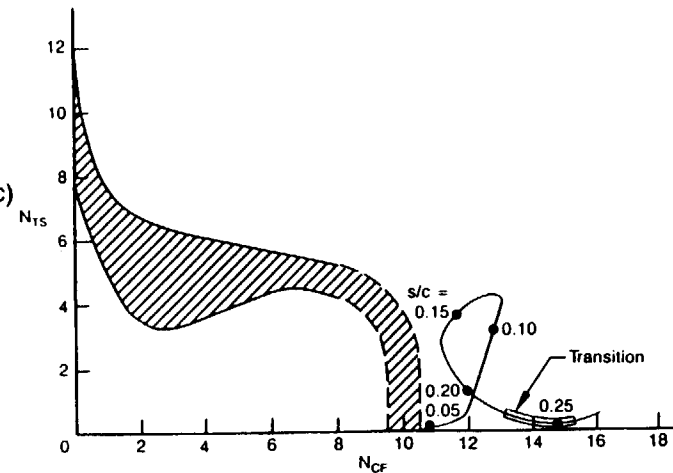
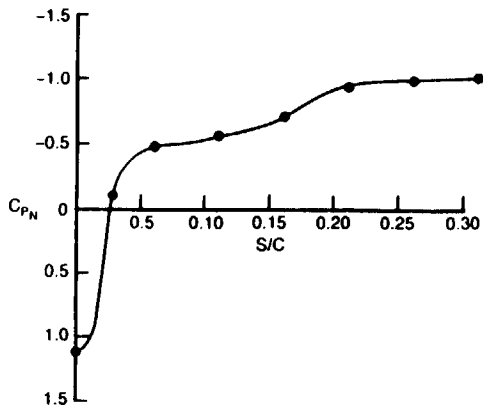


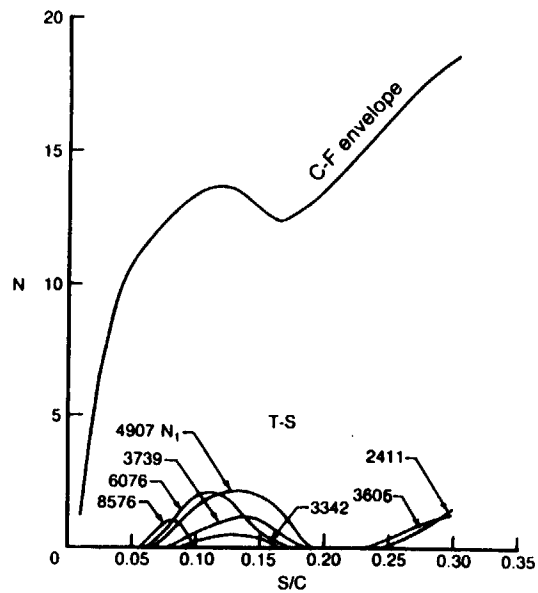
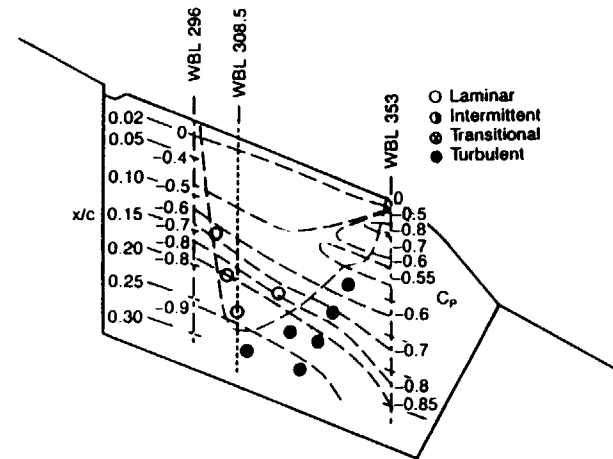
Figure 5-15. 757 NLF Glove: Case 10

Pressure Distribution



- Upper surface; WBL 308.5
- Flight 2, cond. 210 (inbd C_P)
- Flight 3, cond. 13 (outbd C_P)
- $M_\infty = 0.801$, alt = 36,998 ft
- $Re_C = 30.0 \times 10^6$
- $C_L = 0.480$

Isobars and Transition Location



Boundary Layer Stability

Crossflow

- Compressible
- Irrotational
- $\omega^* = 0$
- $\Lambda = 19.9$ deg (0 to 0.07 x/c)
- $\Lambda = 32.9$ deg (0.08 to 0.30 x/c)

Tollmien-Schlichting

- Compressible
- $\psi = 42.5$ deg

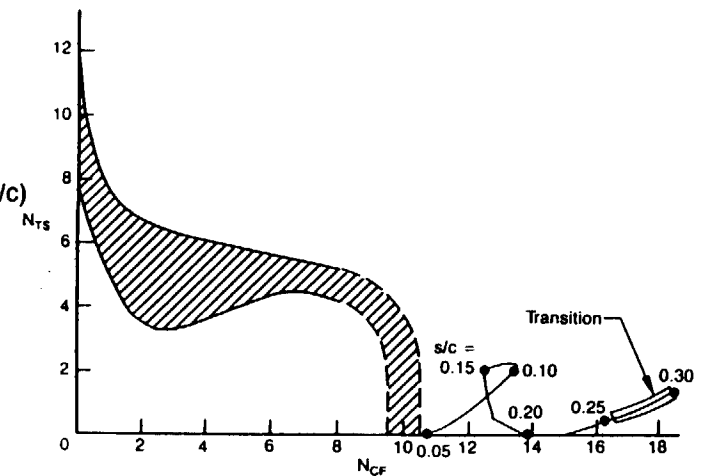
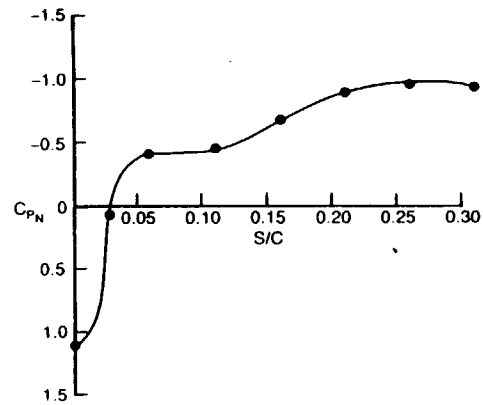


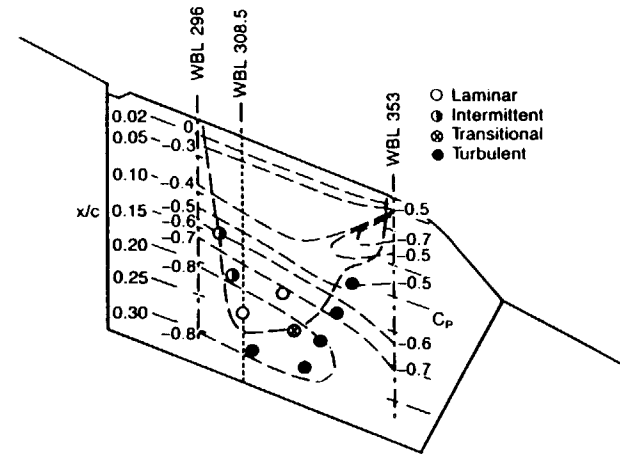
Figure 5-16. 757 NLF Glove: Case 11

Pressure Distribution

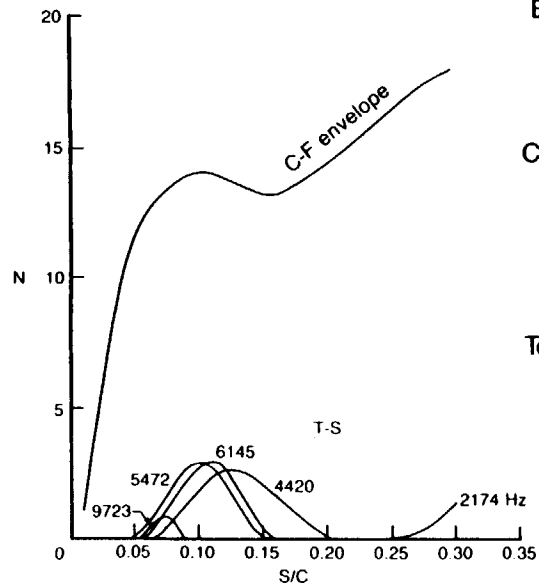


- Upper surface; WBL 308.5
- Flight 2, cond. 216 (inbd C_P)
- Flight 3, cond. 15 (outbd C_P)
- $M_\infty = 0.832$, alt = 38,986 ft
- $Re_C = 28.39 \times 10^6$
- $C_L = 0.478$

Isobars and Transition Location



Boundary Layer Stability



Crossflow

- Compressible
- Irrotational
- $\omega^* = 0$
- $\Lambda = 21.9$ deg (0 to 0.08 x/c)
- $\Lambda = 27.9$ deg (0.09 to 0.30 x/c)

Tollmien-Schlichting

- Compressible
- $\psi = 42.5$ deg

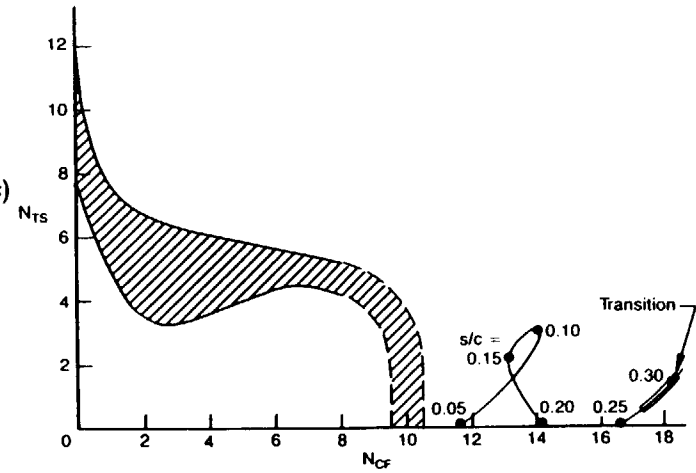
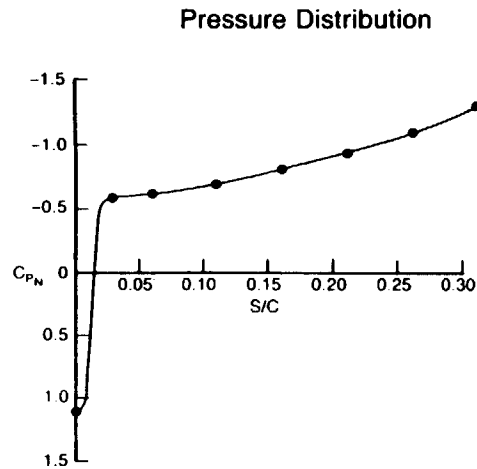
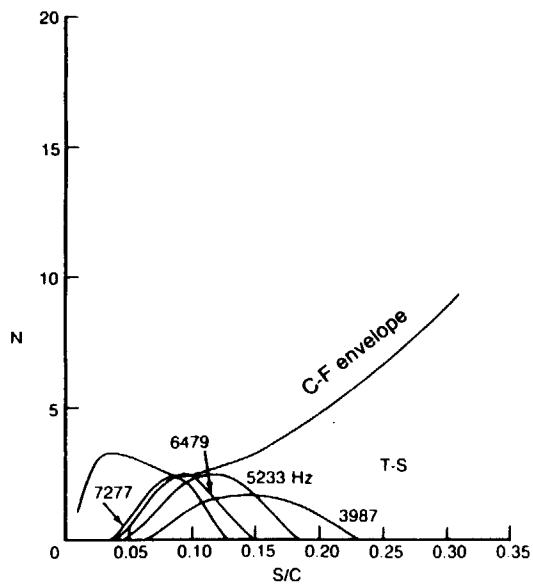
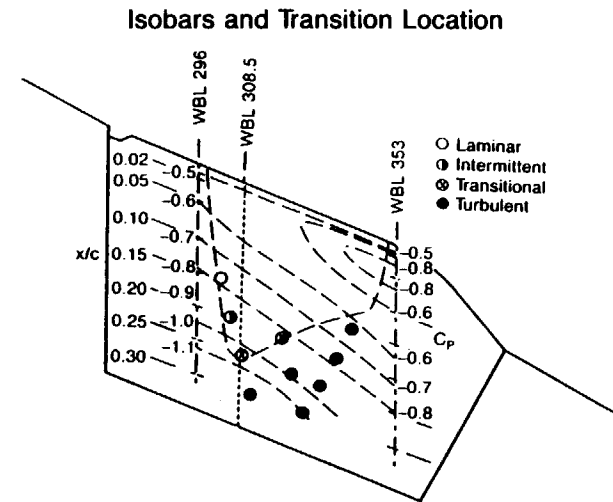


Figure 5-17. 757 NLF Glove: Case 12



- Upper surface; WBL 308.5
- Flight 2, cond. 226 (inboard C_p)
- Flight 3, cond. 19 (outboard C_p)
- $M_\infty = 0.792$, alt = 40,426 ft
- $Re_C = 25.16 \times 10^6$
- $C_L = 0.545$
- $\beta = 4.8$ deg



Crossflow

- Compressible
- Irrotational
- $\omega^* = 0$
- $\Lambda = 16$ deg (0 to 0.05 x/c)
- $\Lambda = 30$ deg (0.06 to 0.30 x/c)

Tollmien-Schlichting

- Compressible
- $\psi = 42.5$ deg

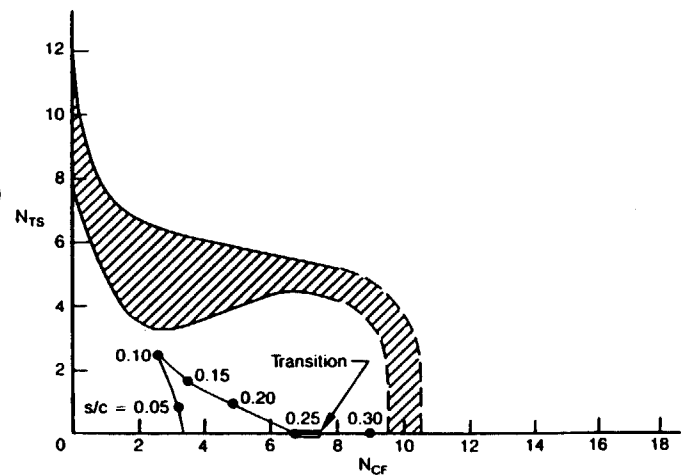
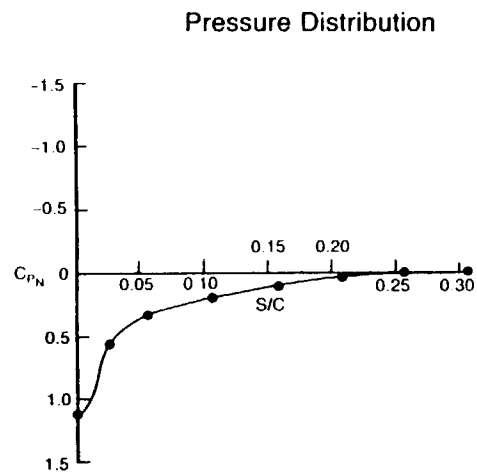
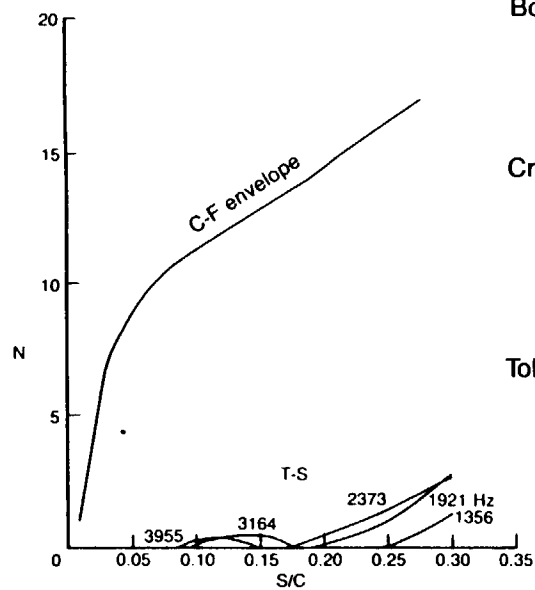
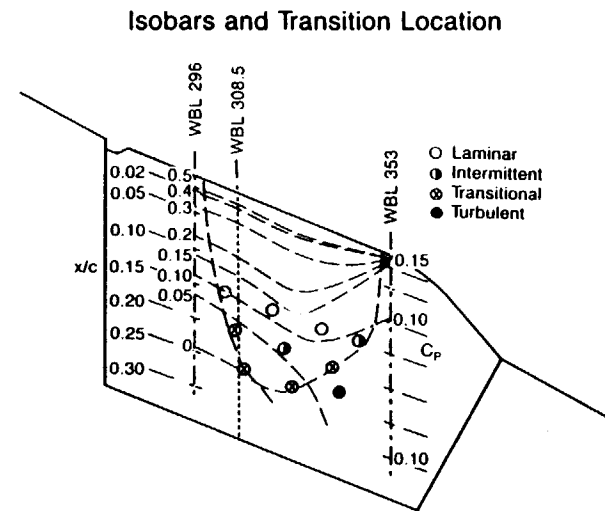


Figure 5-18. 757 NLF Glove; Case 13



- Lower surface; WBL 308.5
- Flight 2, cond. 226 (inbd C_p)
- Flight 3, cond. 19 (outbd C_p)
- $M_\infty = 0.792$, alt = 40,426 ft
- $Re_C = 25.15 \times 10^6$
- $C_L = 0.545$
- $\beta = 4.8$ deg



Crossflow

- Compressible
- Irrotational
- $\omega^* = 0$
- $\Lambda = 20$ deg (0 to 0.08 x/c)
- $\Lambda = 27.5$ deg (0.09 to 0.30 x/c)

Tollmien-Schlichting

- Compressible
- $\psi = 42.5$ deg

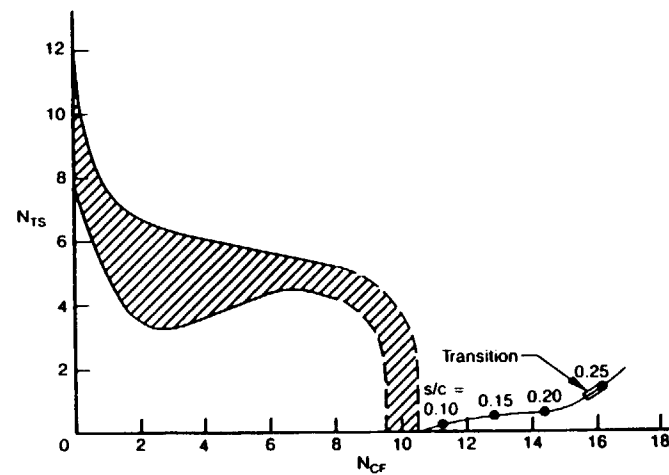
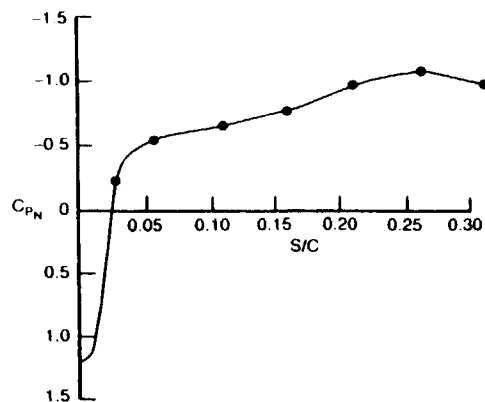


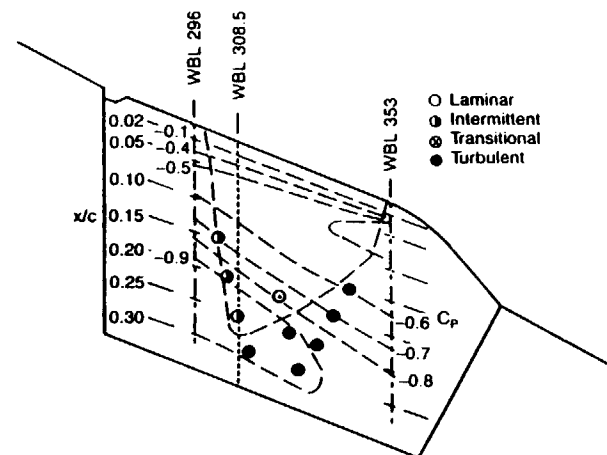
Figure 5-19. 757 NLF Glove: Case 14

Pressure Distribution

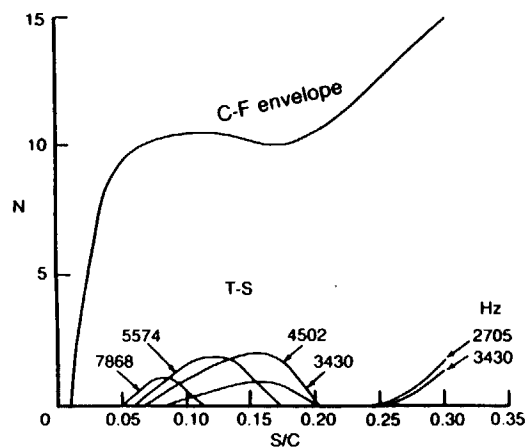


- Upper surface; WBL 308.5
- Flight 2, cond. 227 (inbd C_P)
- Flight 3, cond. 20 (outbd C_P)
- $M_\infty = 0.797$, alt = 40,449 ft
- $Re_C = 25.27 \times 10^6$
- $C_L = 0.537$
- $\beta = -4.0$ deg

Isobars and Transition Location



Boundary Layer Stability



Crossflow

- Compressible
- Irrotational
- $\omega^* = 0$
- $\Lambda = 20.1$ deg (0 to 0.08 x/c)
- $\Lambda = 38.1$ deg (0.09 to 0.30 x/c)

Tollmien-Schlichting

- Compressible
- $\psi = 42.5$ deg

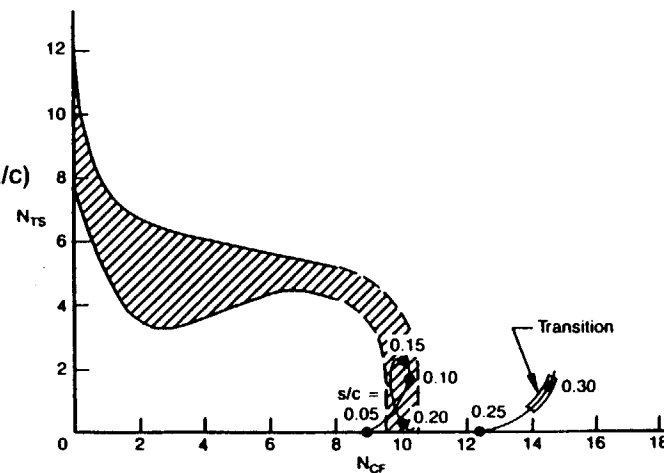
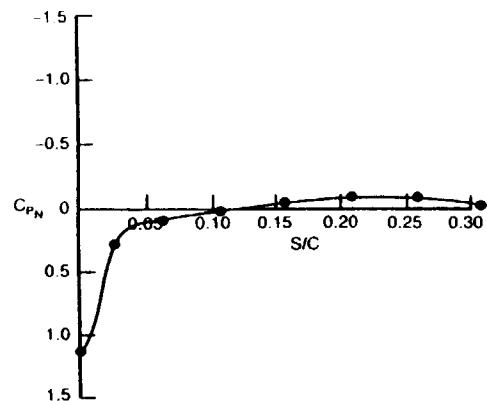


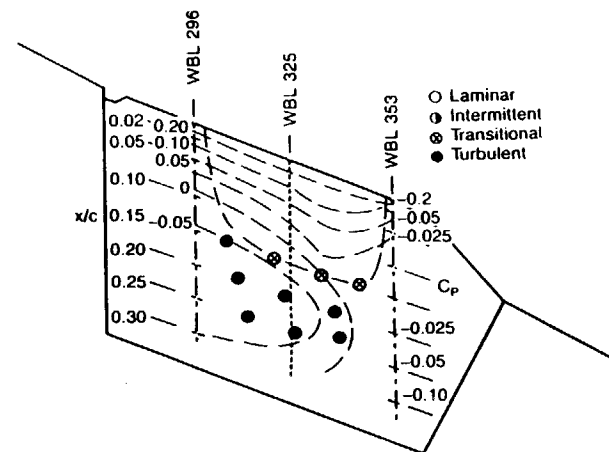
Figure 5-20. 757 NLF Glove: Case 15

Pressure Distribution

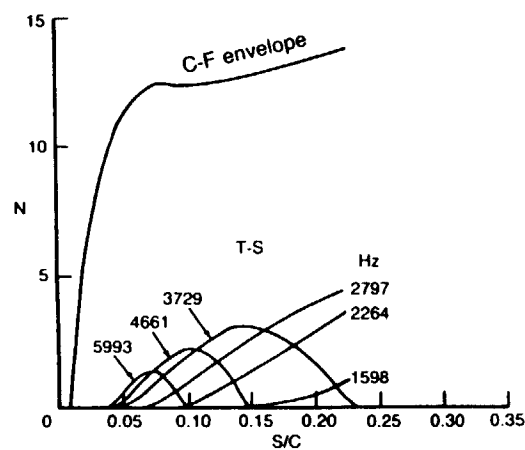


- Lower surface; WBL 325
- Flight 2, cond. 227 (inbd C_P)
- Flight 3, cond. 20 (outbd C_P)
- $M_\infty = 0.797$, alt = 40,449 ft
- $Re_C = 24.60 \times 10^6$
- $C_L = 0.537$
- $\beta = -4.0$ deg

Isobars and Transition Location



Boundary Layer Stability



Crossflow

- Compressible
- Irrotational
- $\omega^* = 0$
- $\Lambda = 31.1$ deg (0 to 0.08 x/c)
- $\Lambda = 41.6$ deg (0.09 to 0.25 x/c)

Tollmien-Schlichting

- Compressible
- $\psi = 42.5$ deg

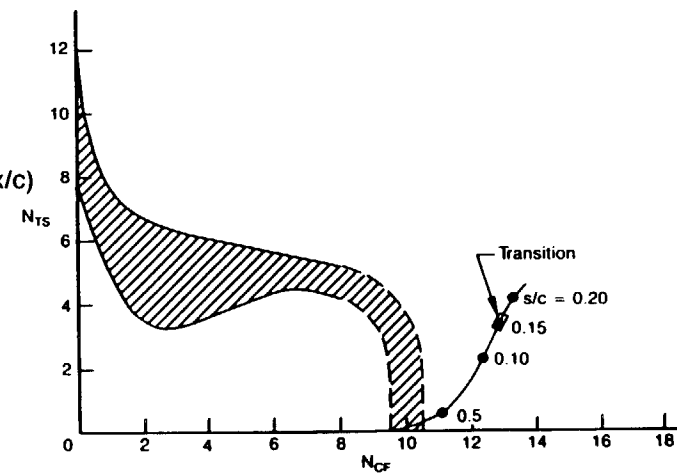
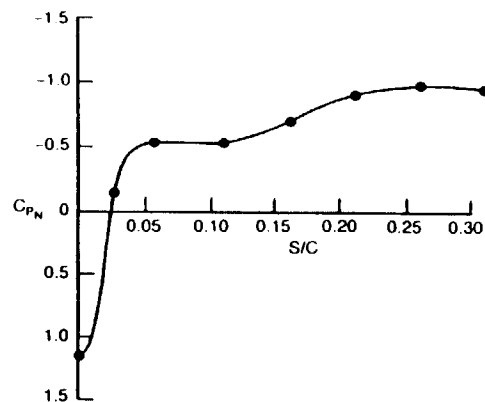


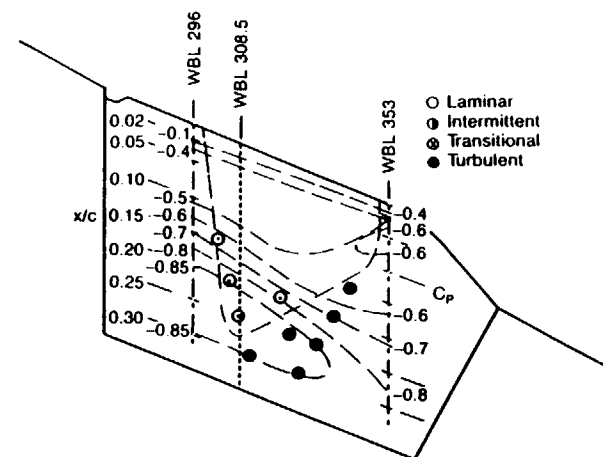
Figure 5-21. 757 NLF Glove: Case 16

Pressure Distribution

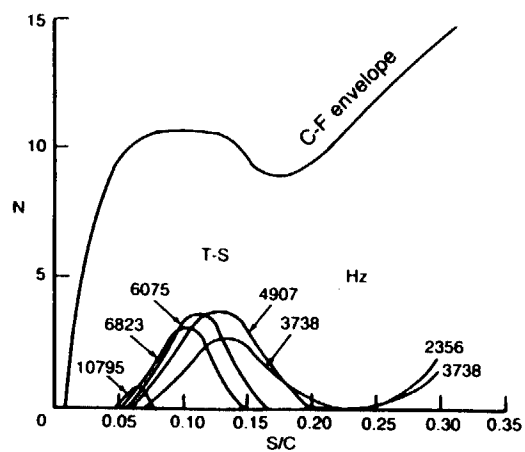


- Upper surface; WBL 308.5
- Flight 2, cond. 239 (inbd C_P)
- Flight 3, cond. 37 (outbd C_P)
- $M_\infty = 0.802$, alt = 37,999 ft
- $Re_C = 28.70 \times 10^6$
- $C_L = 0.460$

Isobars and Transition Location



Boundary Layer Stability



Crossflow

- Compressible
- Irrotational
- $\omega^* = 0$
- $\Lambda = 18.4$ deg (0 to 0.08 x/c)
- $\Lambda = 30.9$ deg (0.09 to 0.30 x/c)

Tollmien-Schlichting

- Compressible
- $\psi = 42.5$ deg

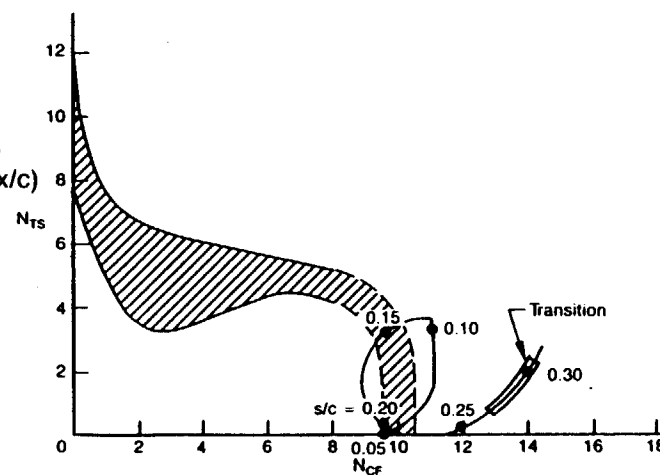
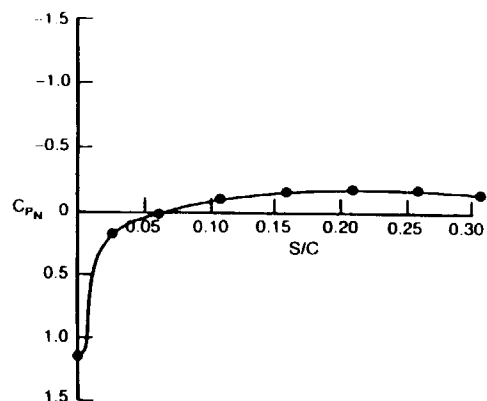


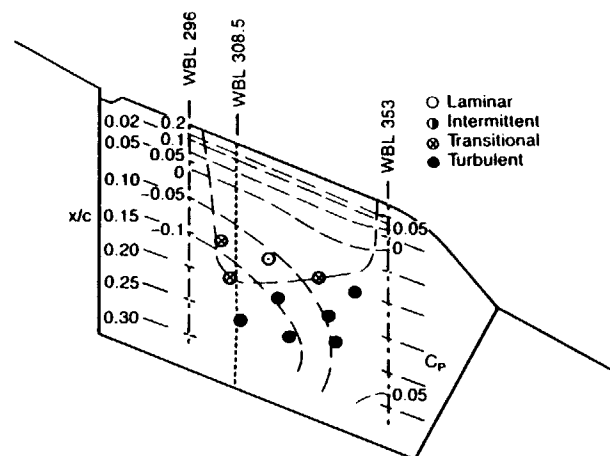
Figure 5-22. 757 NLF Glove: Case 17

Pressure Distribution

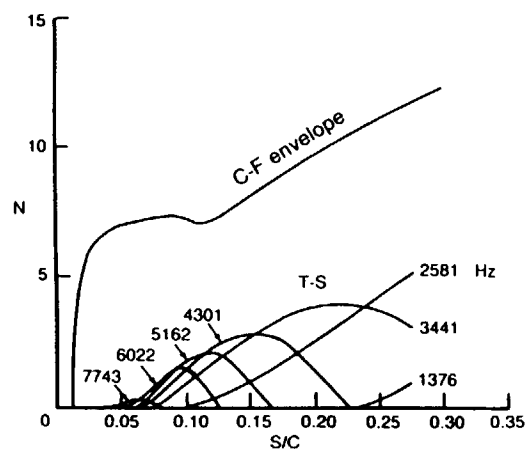


- Lower surface; WBL 308.5
- Flight 2, cond. 239 (inbd C_p)
- Flight 3, cond. 37 (outbd C_p)
- $M_\infty = 0.802$, alt = 37,999 ft
- $Re_C = 28.69 \times 10^6$
- $C_L = 0.460$

Isobars and Transition Location



Boundary Layer Stability



Crossflow

- Compressible
- Irrotational
- $\omega^* = 0$
- $\Lambda = 22.9$ deg (0 to 0.09 x/c)
- $\Lambda = 35.9$ deg (0.10 to 0.30 x/c)

Tollmien-Schlichting

- Compressible
- $\psi = 30$ deg

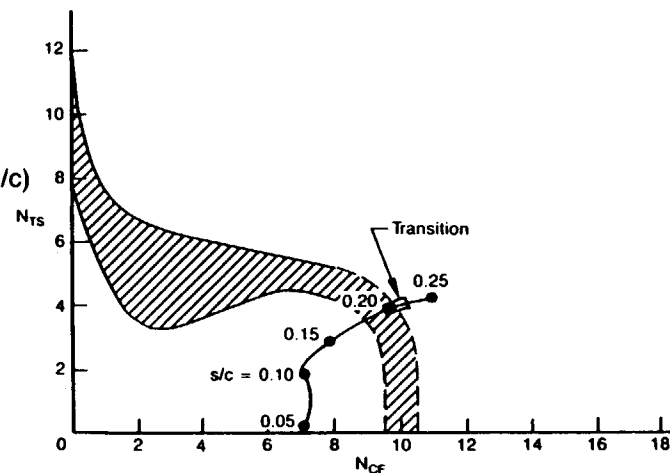
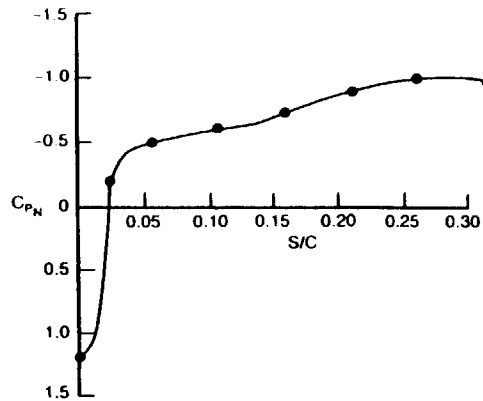


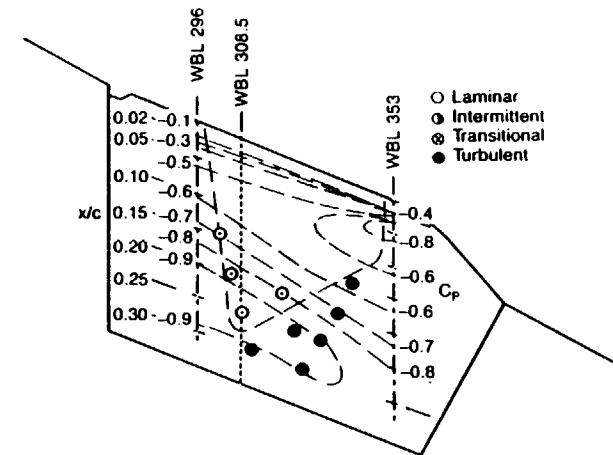
Figure 5-23. 757 NLF Glove: Case 18

Pressure Distribution

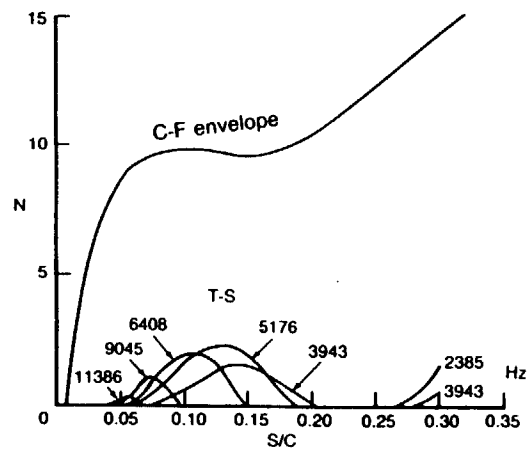


- Upper surface; WBL 308.5
- Flight 2, cond. 211 (inbd C_p)
- Flight 3, cond. 26 (outbd C_p)
- $M_\infty = 0.804$, alt = 37,994 ft
- $Re_C = 28.76 \times 10^6$
- $C_L = 0.498$

Isobars and Transition Location



Boundary Layer Stability



Crossflow

- Compressible
- Irrotational
- $\omega^* = 0$
- $\Lambda = 17.8$ deg (0 to 0.09 x/c)
- $\Lambda = 32.3$ deg (0.10 to 0.30 x/c)

Tollmien-Schlichting

- Compressible
- $\psi = 42.5$ deg

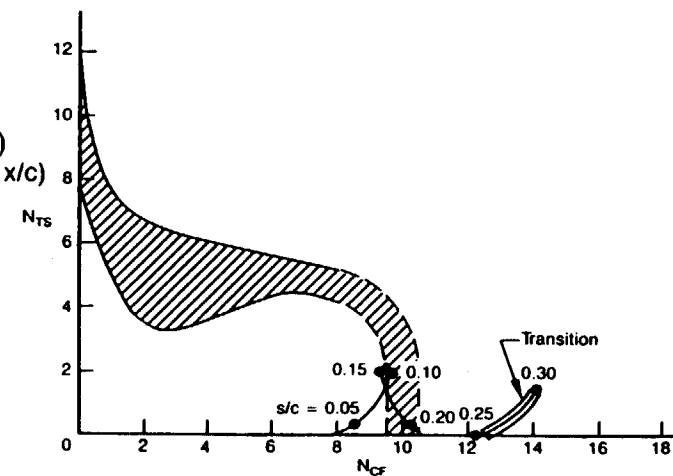
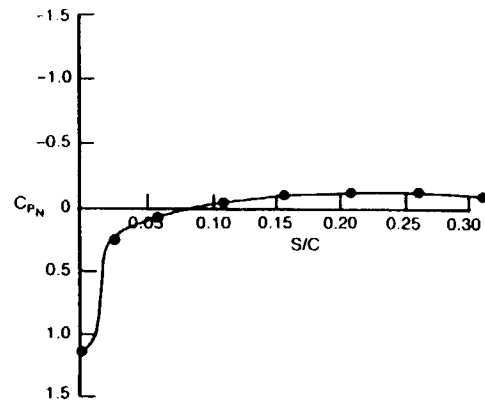


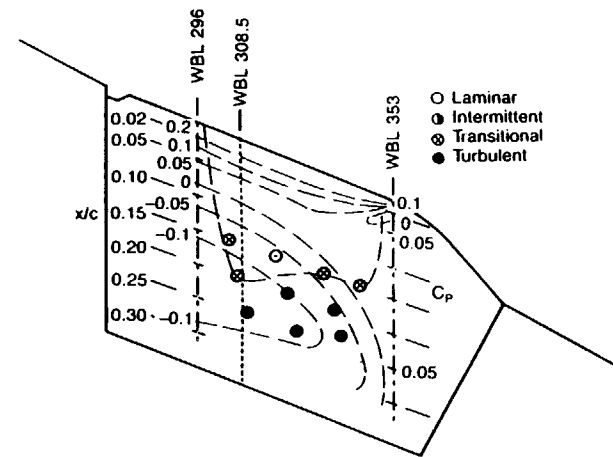
Figure 5-24. 757 NLF Glove: Case 19

Pressure Distribution

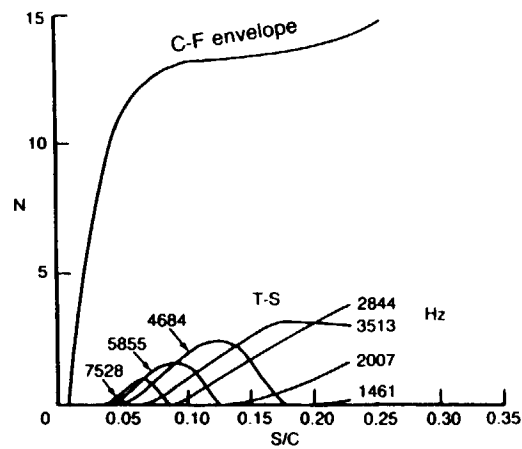


- Lower surface; WBL 308.5
- Flight 2, cond. 211 (inbd C_P)
- Flight 3, cond. 26 (outbd C_P)
- $M_\infty = 0.804$, alt = 37,994 ft
- $Re_C = 28.75 \times 10^6$
- $C_L = 0.498$

Isobars and Transition Location



Boundary Layer Stability



Crossflow

- Compressible
- Irrotational
- $\omega^* = 0$
- $\Lambda = 23.8$ deg (0 to 0.08 x/c)
- $\Lambda = 28.8$ deg (0.09 to 0.25 x/c)

Tollmien-Schlichting

- Compressible
- $\psi = 42.5$ deg

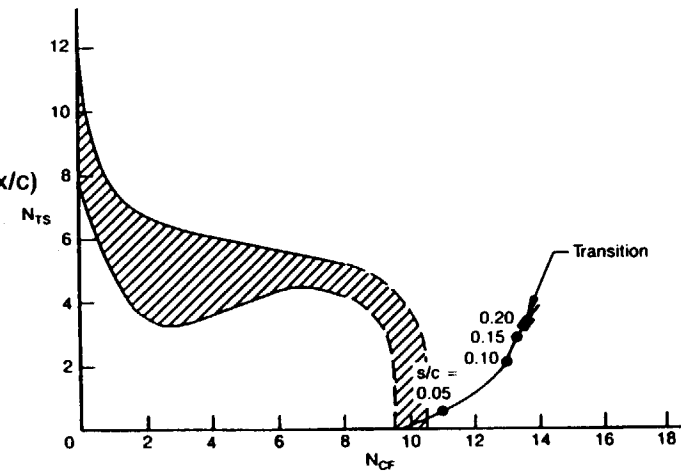
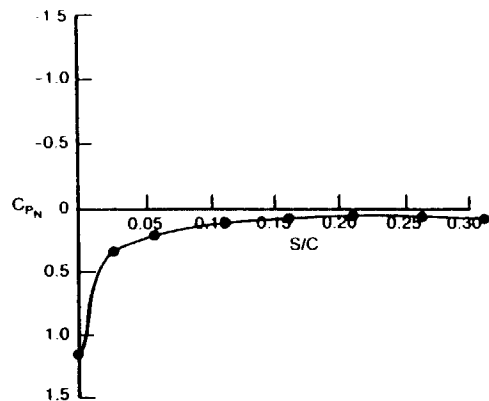


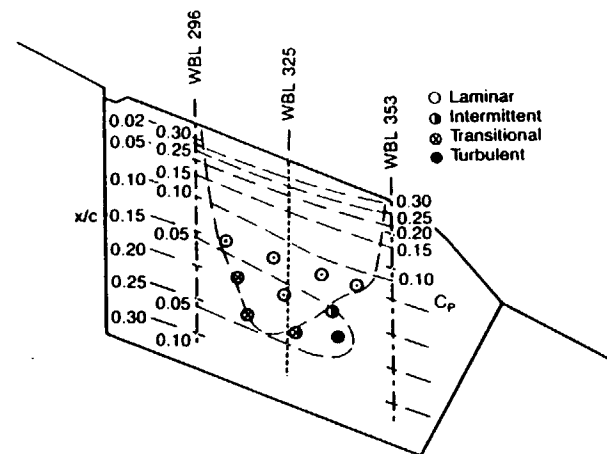
Figure 5-25. 757 NLF Glove: Case 20

Pressure Distribution

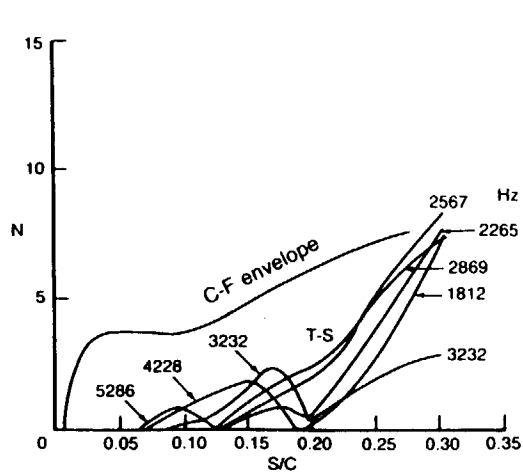


- Lower surface; WBL 325
- Flight 2, estimated (inbd C_P)
- Flight 4, cond. 40 (outbd C_P)
- $M_\infty = 0.700$, alt = 32,961 ft
- $Re_C = 30.08 \times 10^6$
- $C_L = 0.463$
- $\beta = 4.8$ deg

Isobars and Transition Location



Boundary Layer Stability



Crossflow

- Compressible
- Irrotational
- $\omega^* = 0$
- $\Lambda = 14.2$ deg (0 to 0.09 x/c)
- $\Lambda = 21.7$ deg (0.10 to 0.30 x/c)

Tollmien-Schlichting

- Compressible
- $\psi = 20$ deg

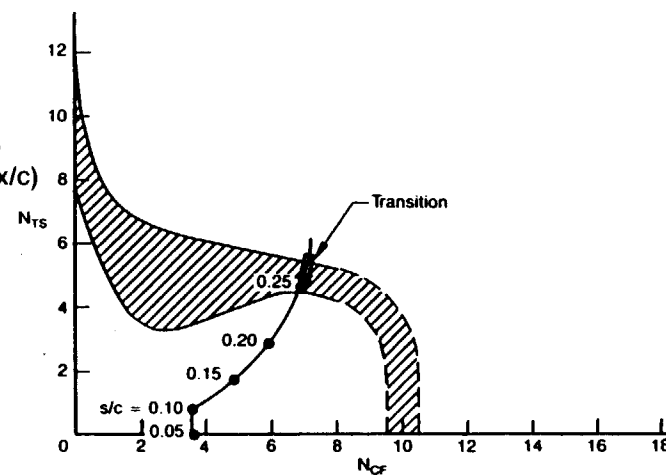


Figure 5-26. 757 NLF Glove: Case 21

Table 5-2. Summary of Boundary Layer Stability Results

Case	Surface	Mach no.	Altitude (ft)	C_L	β (deg)	α_B (deg)	N_{1E2}	Transition s/c	Re_C	$Re_{x_{TR}}$	N_{TS}	N_{CF}
1	Upper	0.804	40,483	0.537	+0.4	2.94	3934	0.29	25.57×10^6	7.42×10^6	0.8	12.4
2	Lower	0.804	40,483	0.537	+0.4	2.94	3934	0.18	25.54×10^6	4.60×10^6	2.7	12.1
3	Upper	0.830	40,968	0.488	0	2.45	3930	0.30	25.90×10^6	7.77×10^6	1.5	14.6
4	Upper	0.793	30,080	0.359	+3.5	1.82	3114	0.25	38.34×10^6	9.60×10^6	1.8	12.1
5	Lower	0.793	30,080	0.359	+3.5	1.82	3114	0.20	38.35×10^6	7.67×10^6	3.5	6.7
6	Lower	0.697	39,009	0.647	+0.4	4.59	3618	0.16	23.14×10^6	3.70×10^6	0.7	13.9
7	Lower	0.699	39,042	0.644	+7.0	5.30	3412	0.26	23.17×10^6	6.02×10^6	0	12.2
8	Lower	0.753	38,994	0.569	+0.2	3.59	3638	0.20	25.01×10^6	5.00×10^6	3.0	17.8
9	Upper	0.753	38,994	0.569	+0.2	3.59	3638	0.19	25.69×10^6	4.88×10^6	3.2	4.6
10	Upper	0.809	36,000	0.450	+0.1	2.31	3333	0.24	31.64×10^6	7.59×10^6	0.1	14.2
11	Upper	0.801	36,998	0.480	-0.1	2.61	3380	0.28	29.99×10^6	8.40×10^6	0.9	17.8
12	Upper	0.832	38,986	0.478	+0.1	2.40	3972	0.29	28.39×10^6	8.23×10^6	0.9	17.9
13	Upper	0.792	40,426	0.545	+4.0	3.54	3587	0.26	25.16×10^6	6.54×10^6	0	7.1
14	Lower	0.792	40,426	0.545	+4.0	3.54	3587	0.24	25.15×10^6	6.04×10^6	1.2	15.8
15	Upper	0.797	40,449	0.537	-4.1	3.58	3615	0.29	25.27×10^6	7.33×10^6	1.1	14.3
16	Lower	0.797	40,449	0.537	-4.1	3.58	3615	0.16	24.60×10^6	3.94×10^6	3.1	12.8
17	Upper	0.802	37,999	0.460	+0.1	2.41	3271	0.29	28.70×10^6	8.32×10^6	1.5	13.7
18	Lower	0.802	37,999	0.460	+0.1	2.41	3271	0.21	28.69×10^6	6.02×10^6	3.9	9.9
19	Upper	0.804	37,994	0.498	+0.2	2.67	3538	0.28	28.76×10^6	8.05×10^6	0.5	13.4
20	Lower	0.804	37,994	0.498	+0.2	2.67	3538	0.21	28.75×10^6	6.04×10^6	3.3	13.6
21	Lower	0.700	32,961	0.463	+4.8	3.14	2406	0.26	30.08×10^6	7.82×10^6	5.4	7.2

5.4 RECOMMENDATIONS FOR REVISED TRANSITION DATA BAND

One of the primary objectives in analyzing the boundary layer stability of the 757 NLF glove was to provide additional data points for the NTS versus NCF transition data band. The other objective was to determine the relative importance of T-S and C-F disturbances for a number of flight conditions to aid in the interpretation of the effects of noise on transition. For the latter purpose, knowing the exact NTS and NCF values is not as important as for the first objective. Because of this, some of the results may be acceptable only for use in interpreting noise effects and not in defining a new transition data band, because of higher uncertainty in the pressures or isobars. All cases have some uncertainty in the calculated N-factors. However, three cases have more uncertainty than the others. These three cases are 7, 13, and 15.

Case 7 had much more sideslip than any of the other cases analyzed. As explained in Section 5.2, program A488G was used to guide the fairing of the isobars between the measured pressures at the inboard and outboard glove location. However, A488G cannot be run with sideslip. Therefore, the higher the sideslip, the less useful are the A488G isobars as a guide. Therefore, Case 7 must be considered among the more uncertain of the cases analyzed.

Cases 13 and 15 are both based on outboard glove pressure data from Flight 4 at a high lift coefficient. Since the strip-a-tube was recessed back to a point between the Port 1 and Port 2 locations for Flight 4, the Port 1 pressure should be very good, since it was flush with the surface. However, the Port 2 pressures will show an increased strip-a-tube interference effect relative to the unrecessed configuration because the region of locally high curvature has been moved back closer to Port 2. The magnitude of this effect at low lift coefficients was shown previously in Figure 5-2. However, because of the pressure measurement problems during Flight 3 (as discussed in Section 6.2 of Volume II), no correction for this effect can be made at the high lift coefficients. Therefore, for Cases 13 and 15, it was necessary to use the Port 2 data from Flight 4 without any correction for the strip-a-tube interference effect. Therefore, Cases 13 and 15 must be considered to have more uncertainty than the other cases.

In defining a new transition data band, Cases 7, 13, and 15 have not been used. The band was defined by using the midpoints of the bands shown for each individual case in Figure 5-27, together with the previously calculated F-111 NLF glove data points. The resulting new transition data band is shown in Figure 5-28. One point was not included in the band simply because it falls outside of the region where the bulk of the points are. Neglecting this point may make the band slightly conservative.

In Figures 5-29, 5-30, and 5-31, the trajectory in the NTS versus NCF diagram is shown for each case, with the recommended transition data band. It can be seen that eight of the upper surface cases have loops in their trajectories. These are Cases 3, 4, 10, 11, 12, 15, 17, and 19. No lower surface cases have loops. The loops are caused by the flattening of the pressure distribution on the upper surface in the vicinity of 5% to 10% chord. This flattening causes an immediate increase in T-S disturbance growth and a slowing and eventual decay in C-F disturbance growth. When the pressure gradient begins to increase again near 15% chord, the T-S disturbances are damped, and the C-F disturbances stop decaying and slowly begin to grow. The end result is a loop in the N-factor trajectory. The loops remain below the transition data band for Cases 3, 5, and 15. However, five of the cases have loops that go up into the transition data band. Since the measured transition location for each of the five cases corresponds to a point on the trajectory beyond the loop, these cases illustrate that the proper way to use the transition data band is to assume—

1. There is a high probability of laminar flow for N-factor combinations below the band.
2. There is a high probability of turbulent flow for N-factor combinations above the band.
3. The band is an uncertainty zone in which the included N-factor combinations can result in either laminar or turbulent flow.

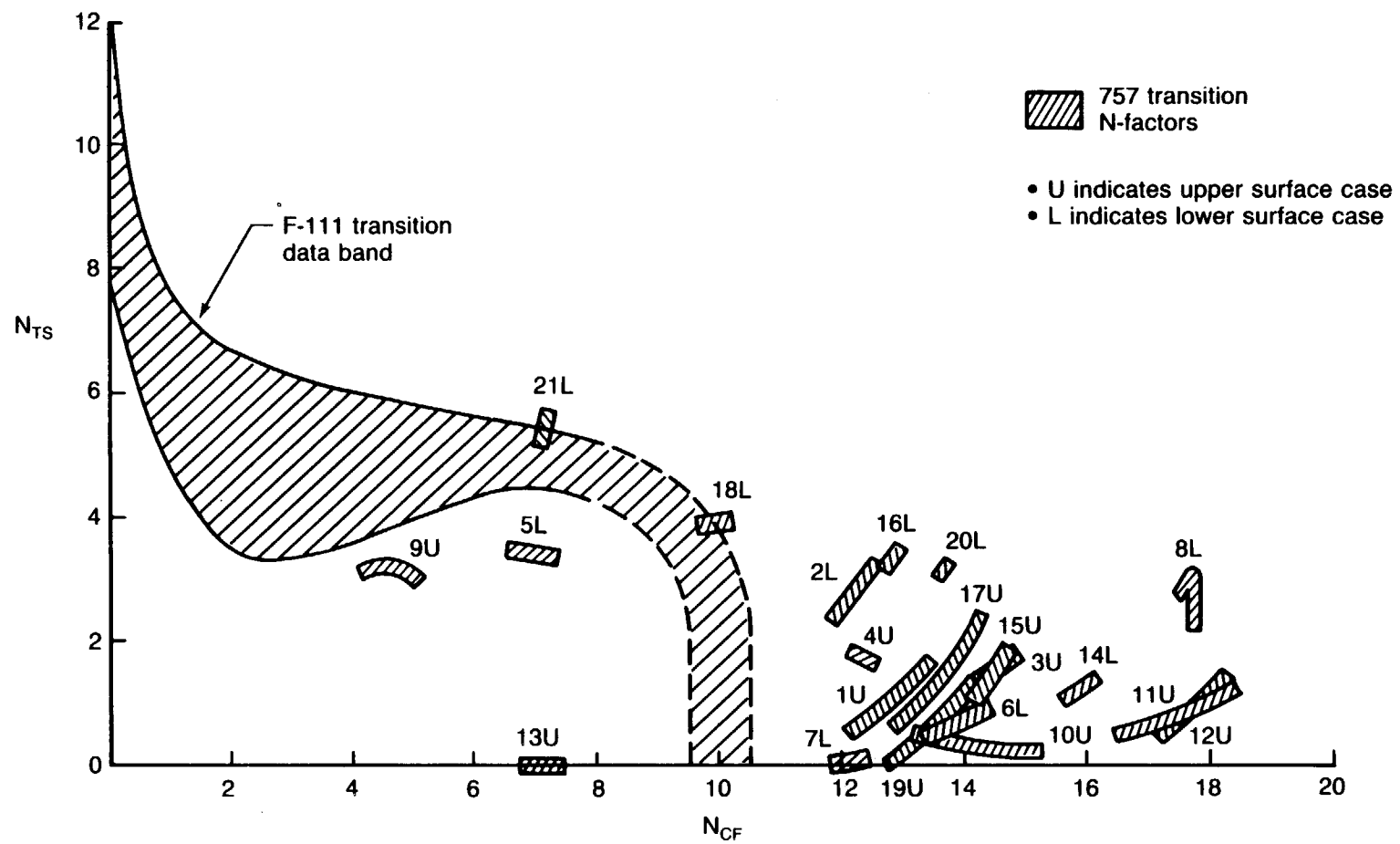


Figure 5-27. Transition N-Factors for 757 NLF Glove

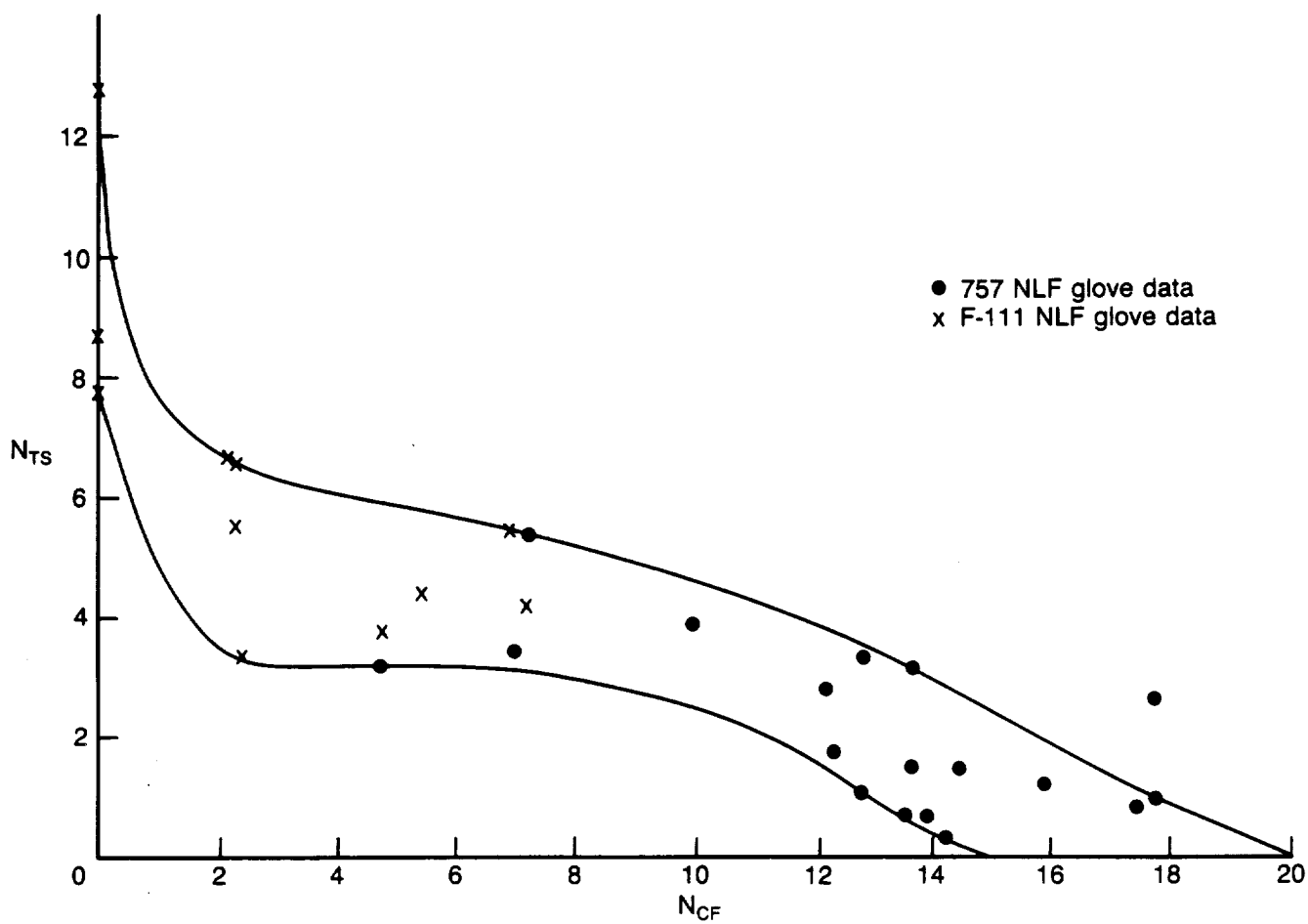


Figure 5-28. Transition N-Factors for 757 NLF Glove and F-111 NLF Glove

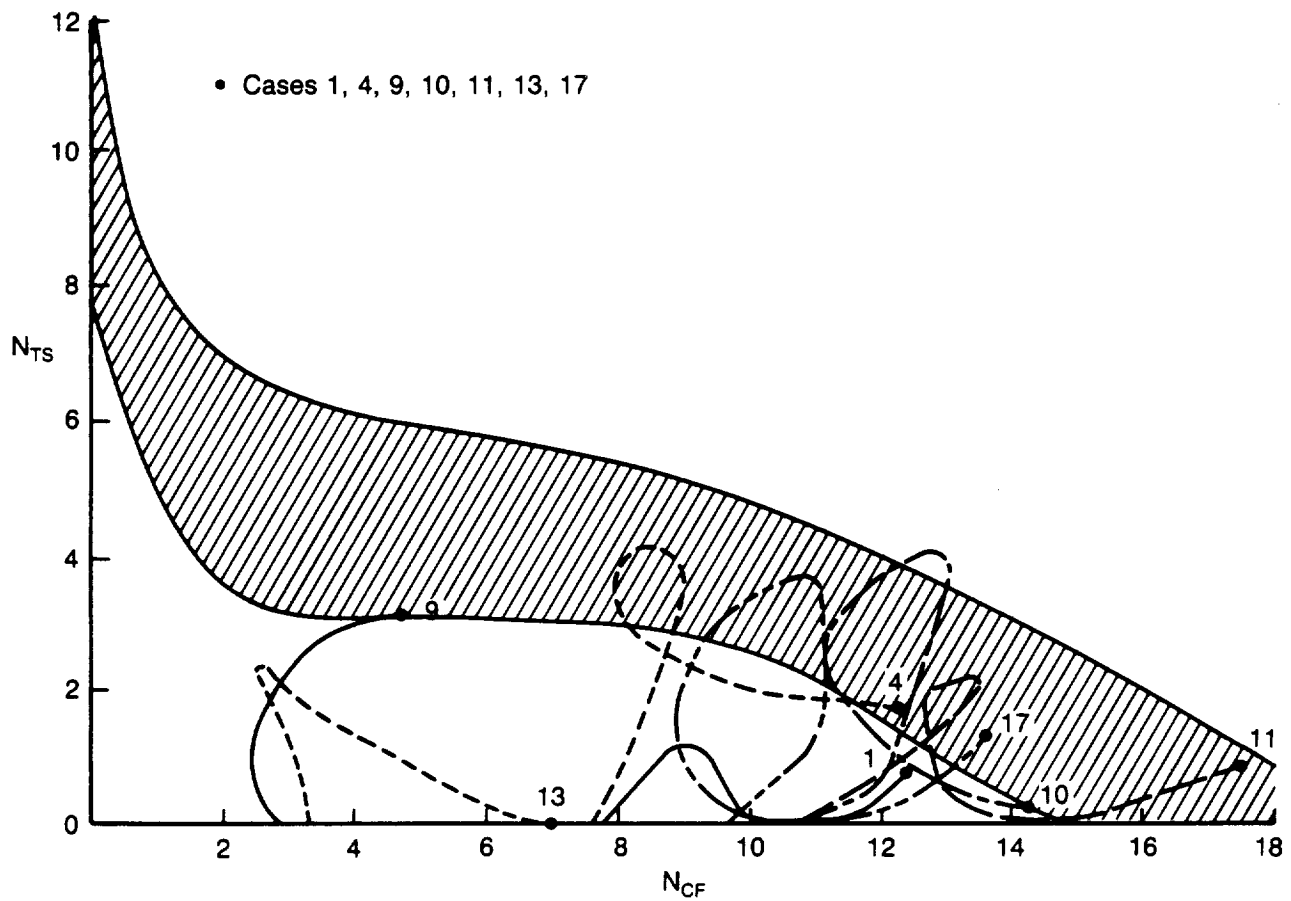


Figure 5-29. 757 NLF Glove: Upper Surface N-Factor Trajectories

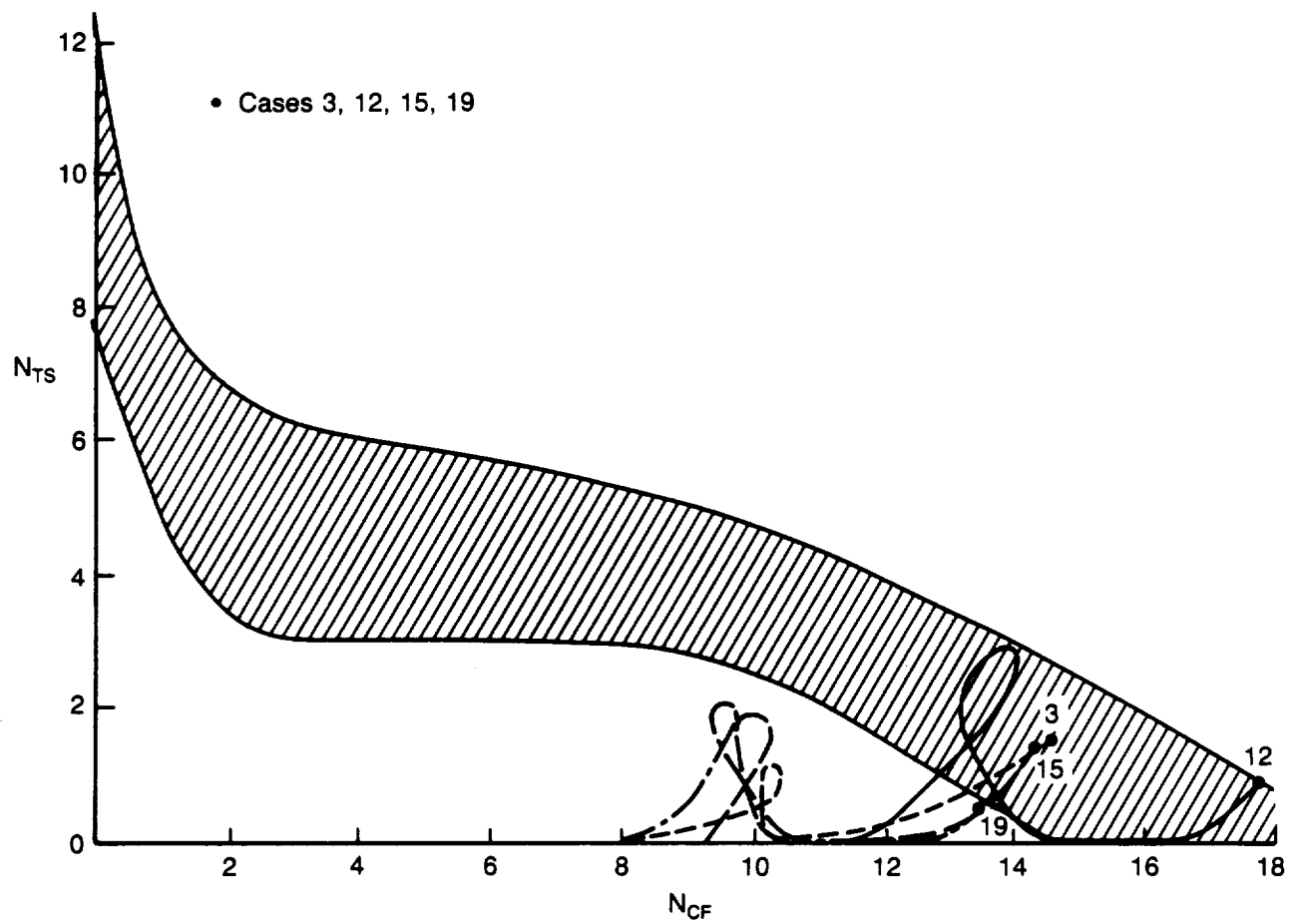


Figure 5-30. 757 NLF Glove: Upper Surface N-Factor Trajectories

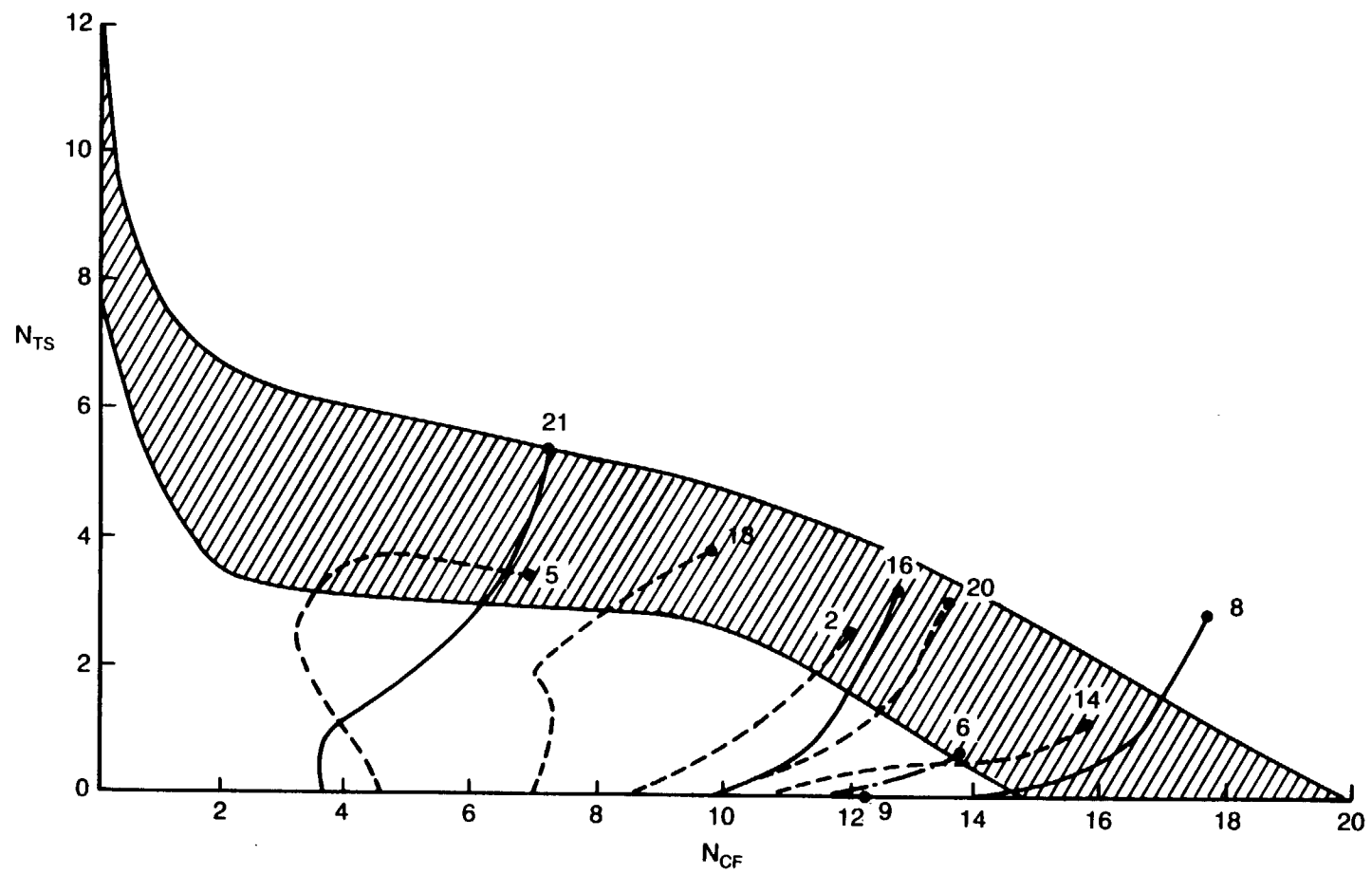


Figure 5-31. Lower Surface N-Factor Trajectories

5.5 UNCERTAINTY ANALYSIS

Because of the limited number of chordwise and spanwise stations at which pressures were measured on the glove, and because of the strip-a-tube interference effects, there is some uncertainty associated with the pressure distributions and isobars used in the stability analysis. To assess the magnitude of the effect of these uncertainties on the calculated transition N-factors, additional stability analyses were performed for one lower surface case (Case 8) and one upper surface case (Case 11) for various assumed pressure distributions and isobars.

The sources of uncertainty that were considered were:

1. **Fairing of Pressure Distribution**

The pressure distributions used in the original stability analysis for each case were interpolated at the appropriate spanwise station from the measured pressures at WBL 296 and WBL 353 based upon the estimated isobars. This interpolation combined with the limited number of pressure ports at WBL 296 and WBL 353 resulted in some uncertainty in the pressure fairing. Variations in the direction of both higher and lower pressures from the fairing used in the original analysis were analyzed.

2. **Isobar Sweep**

The sweep angles used in the infinite yawed wing boundary layer were chosen to best represent the isobars on the glove. Since the isobars on the glove do not have constant sweep angles, some uncertainty is introduced in trying to identify the most representative sweep. It should also be noted that the isobars used are not measured, but rather estimated ones based on pressure data measured at the inboard and outboard ends of the glove together with A488 isobars.

3. **Strip-a-Tube Effects**

The effect of the strip-a-tube correction was determined by removing it and analyzing the resulting pressure distribution.

4. **Attachment Line Location**

Results from the transonic viscous analysis program, A488G, were used to determine that the variation in the S/C location of the attachment line from $X/C = 0$ for the conditions of interest was likely to be less than 0.002. Therefore, a conservative change of 0.002 in the attachment line S/C location for Case 8 was made to assess the importance of this uncertainty.

Five different pressure distributions and isobar variations were analyzed for Case 8, as shown in Figure 5-32. Variation 1 assumed an isobar sweep angle of 30 deg from the leading edge to 30% chord, as compared to a sweep angle of 25 deg for the original analysis. The effect was to increase the crossflow N-factor, NCF, by 3.0. Variation 2 assumed an isobar sweep angle of 20 deg, causing a drop of 3.8 in the crossflow N-factor. The third modification considered an increase in the overall slope of the C_p distribution, by assuming an uncertainty of ± 0.04 in the C_p value at the given chordwise locations. It should be noted that the transducer C_p measurements are accurate to within less than ± 0.02 . Thus the ± 0.04 C_p uncertainty allows also for uncertainties in the isobar fairing and is probably a conservative value. The results showed a decrease of 1.8 in the Tollmien-Schlichting N-factor, NTS, and a small drop of 0.2 in the NCF. The fourth variation, consisted of decreasing the slope under the same assumptions made for variation 3. This time, a slight increase of 0.2 was observed for both NCF and NTS. Finally, variation 5, assumed a displacement toward the lower surface of 0.002 in the s/c location of the attachment line. The effect was a decrease of 0.4 in both NCF and NTS. The resulting estimated maximum uncertainty for all of these effects taken together is shown by the rectangle in Figure 5-32.

For Case 11, as shown in Figure 5-33, four alternative pressure distributions and isobar variations were analyzed. Variation 1 considered an isobar sweep angle of 38 deg, as opposed to 32.9 deg, in the region from $s/c = 0.08$ to $s/c = 0.30$. The results showed an increase of 0.9 in the crossflow N-factor. To determine the effect of lower isobar sweeps, a 25 deg sweep angle was used in variation 2. The effect was a drop of 3.2 in the NCF. The third modification consisted of increasing the slope of the C_p distribution curve near the leading edge. This region extended from $s/c = 0.015$ to $s/c = 0.035$, as shown in Figure 5-33. The influence on the transition NCF was a drop of 1.0. Variation 4 neglected the effects of the strip-a-tube correction and resulted in a decrease of 2.0 in NCF. All of the above analyses for Case 11 only considered the crossflow N-factors and did not account for the Tollmien-Schlichting N-factors.

Although it is difficult to draw firm quantitative conclusions with respect to the uncertainty of the transition N-factors calculated in this study, based on the above results the sensitivity of the N-factors to the various uncertainty sources is approximately as follows:

1. **Fairing of Pressure Distribution**
This source of uncertainty is less important than some of the others, with NCF probably not affected by more than ± 1 , and NTS by no more than +1 to -2.
2. **Isobar Sweep**
This is the most important source of uncertainty. An isobar sweep uncertainty of ± 5 deg results in an NCF uncertainty of about ± 3 . However, it is not likely that the actual isobar uncertainty is this large.
3. **Strip-a-Tube Effect**
It is important that this effect be accounted for properly, as indicated by an NCF difference of 2 between the corrected and uncorrected pressures.
4. **Attachment Line Location**
This is probably not a significant source of uncertainty, since the maximum estimated variation in the attachment line location changed both NTS and NCF by 0.4.

Since all of these uncertainty sources are not likely to be at a maximum in the same direction at the same time, a reasonable conclusion concerning the approximate overall uncertainty of the results might be: NCF +2 to -3 and NTS +1 to -2.

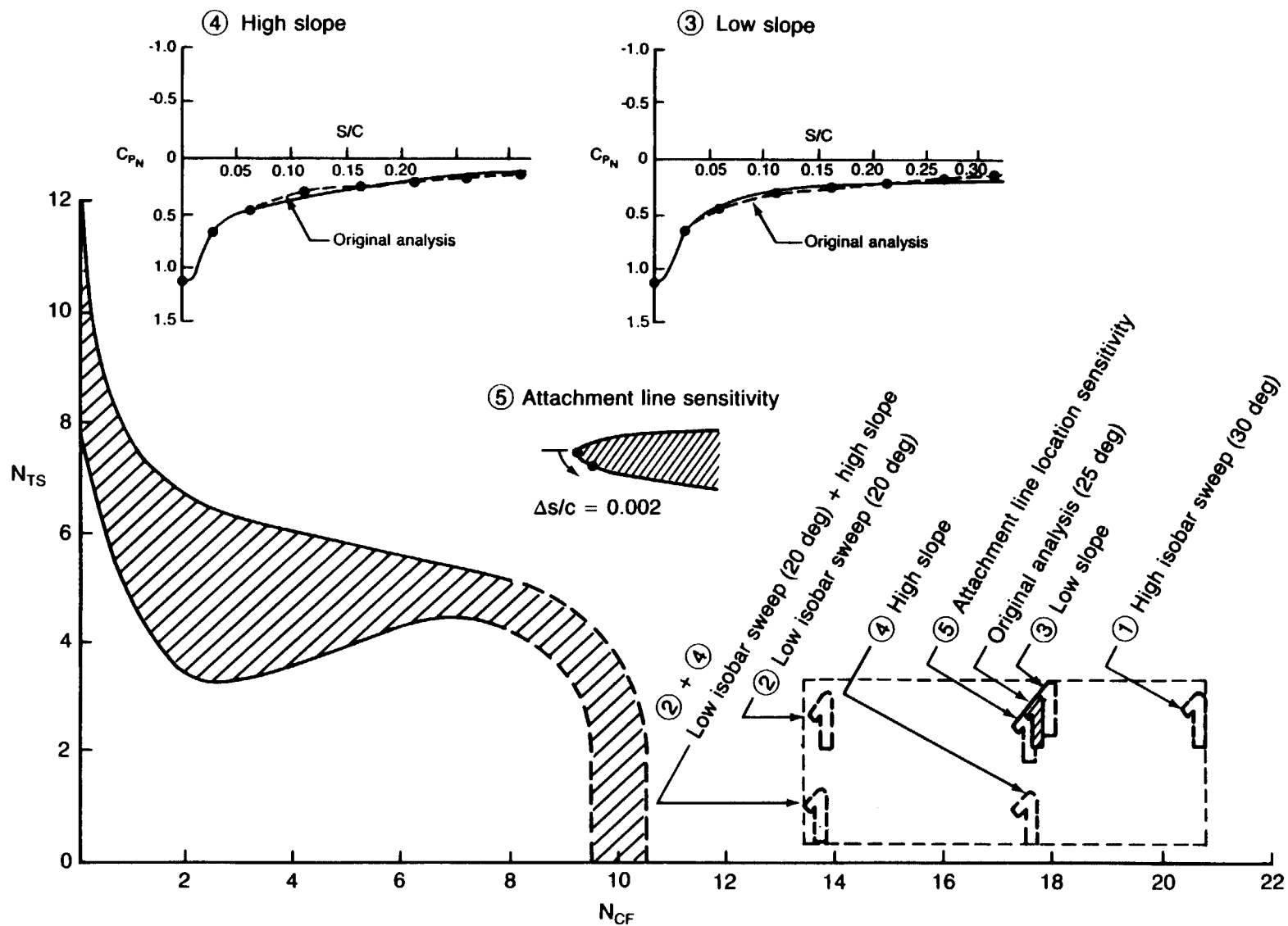


Figure 5-32. Uncertainty Analysis of Case 8

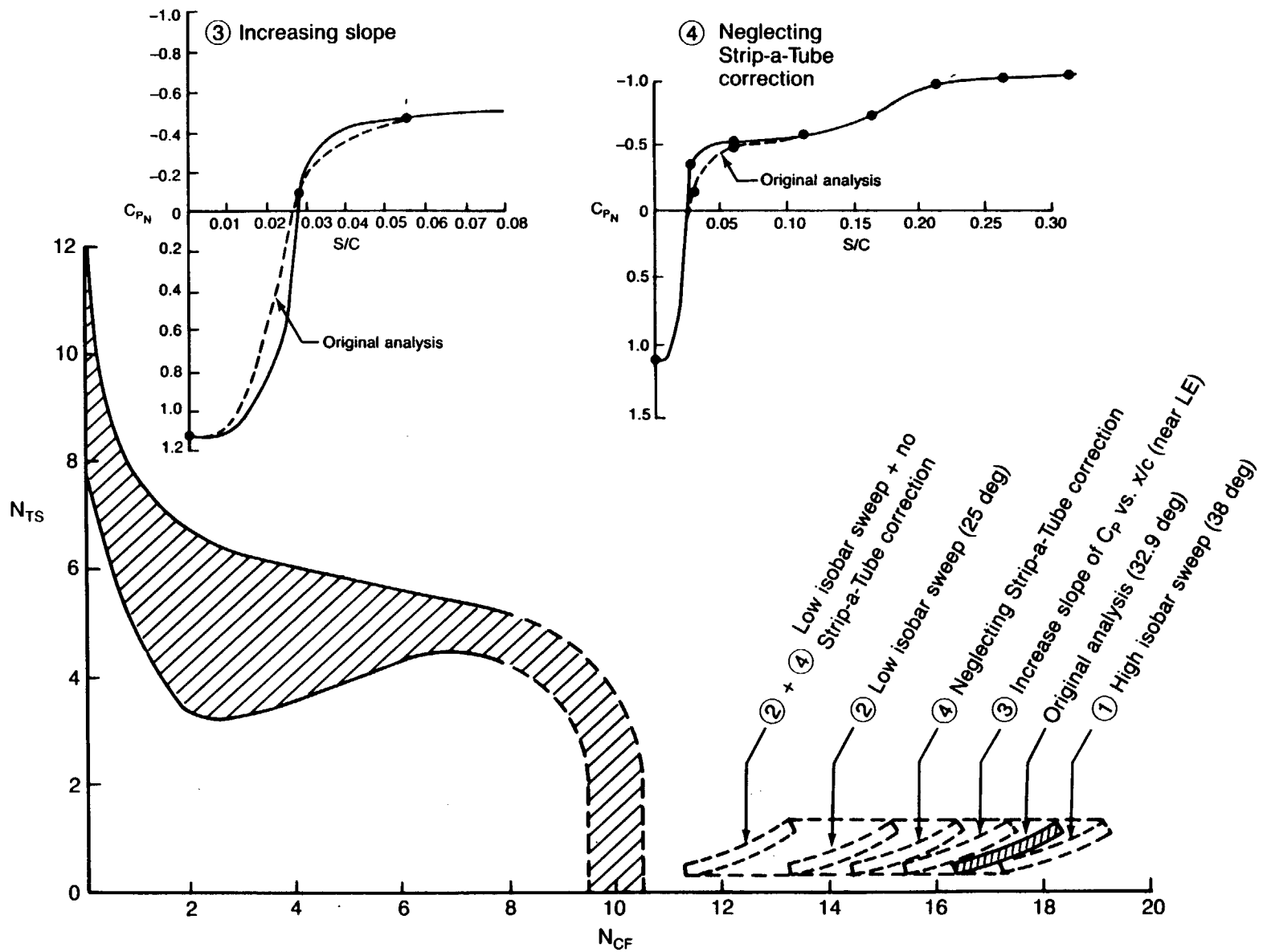


Figure 5-33. Uncertainty Analysis of Case 11

5.6 COMPARISON WITH USS STABILITY CODE

A new *automated* stability code known as the Unified Stability System (USS), being developed by Boeing under contract to NASA, was used to analyze three of the cases discussed previously to compare the results of this new approach (which was not available until the very late stages of the present study) with those of the method used in the present study. The USS is a system of programs that combines boundary layer calculation and stability calculation into a single run. It has a tapered wing boundary layer code, as compared to the infinite yawed wing boundary layer program used in the main part of the present study. A matrix of amplification rates for a range of wave angles and frequencies is computed and saved at each station in the downstream march. This matrix is then used to compute integrated N-factors based on the user-specified disturbance-following approach, of which there are a number of options available. Two of those disturbance-following approaches were used in the three cases to which it was applied in the current study. The first approach was identical to the standard one used on all 21 cases in the present study and will be called the *standard* Boeing approach. The second approach, which will be called the *maximum envelope* method, follows disturbances downstream keeping frequency fixed but letting wave angle vary to maximize the amplification rate at each station. A sufficient range of frequencies is analyzed to adequately define an envelope of disturbances. This approach will always give higher N-factors than the first approach. No differentiation is made between T-S and C-F disturbances in the *maximum envelope* method.

Cases 2, 11, and 13 were chosen for analysis using the USS, since they represented an assortment of flight conditions. The disturbance growth curves calculated using USS are shown in Figures 5-34 through 5-39. Figure 5-40 summarizes the results for all three cases and compares them to the results of the original analysis. The differences between the USS code results for the standard Boeing approach and the original analysis results are due primarily to the differences between the tapered wing boundary layer analysis and the *patched* infinite yawed wing solution used in the original analysis. The *maximum envelope* method gives N-factors at transition of 20.6, 32.0, and 17.4 for Cases 2, 11, and 13, respectively.

5.7 STABILITY ANALYSIS CONCLUSIONS

The boundary layer stability analysis of 21 757 NLF glove flight data cases shows the following:

1. For most of the cases, C-F disturbances are much more highly amplified at transition than T-S disturbances.
2. The results of the present study provide data in the high C-F, low T-S region of the N_{TS} versus N_{CF} diagram where none of the F-111 data points fell. These results indicate that the C-F N-factors are much higher than had been assumed in the original extrapolation of the F-111 data band. For 16 of the 21 cases analyzed, C-F N-factors were between 12 and 18.
3. Based on the combined F-111 and 757 NLF glove results, the recommended transition data band for laminar flow design applications is shown in Figure 5-41. Designs for which the combination of N-factors at the desired transition location falls below the lower part of the band will have a high probability of success. The probability of obtaining the desired extent of laminar flow decreases as the N-factor combination at transition moves into the band and toward the upper edge of it.
4. Because of the highly three-dimensional nature of the pressures and isobars on the glove, the limited number of locations at which pressure measurements were made, and the use of strip-tube to measure pressures, there is some uncertainty associated with the pressure distributions and isobar sweep angles used in the stability analysis. Those cases with the most uncertainty were not included in the recommended transition data band shown in Figure 5-41.
5. Based on an analysis of three cases, results from the USS stability code differed by no more than about 1 in N_{TS} and no more than about 2 in N_{CF} from the results of the stability method used in the present study. Use of the *maximum envelope* method of the USS for the same three cases resulted in N-factors as high as 32.

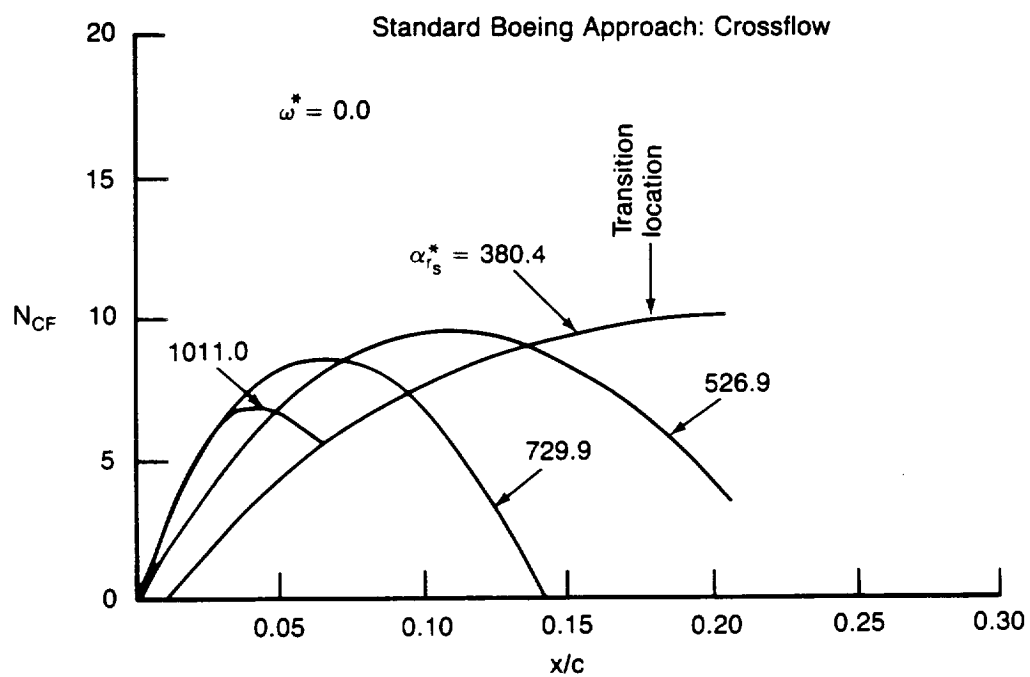
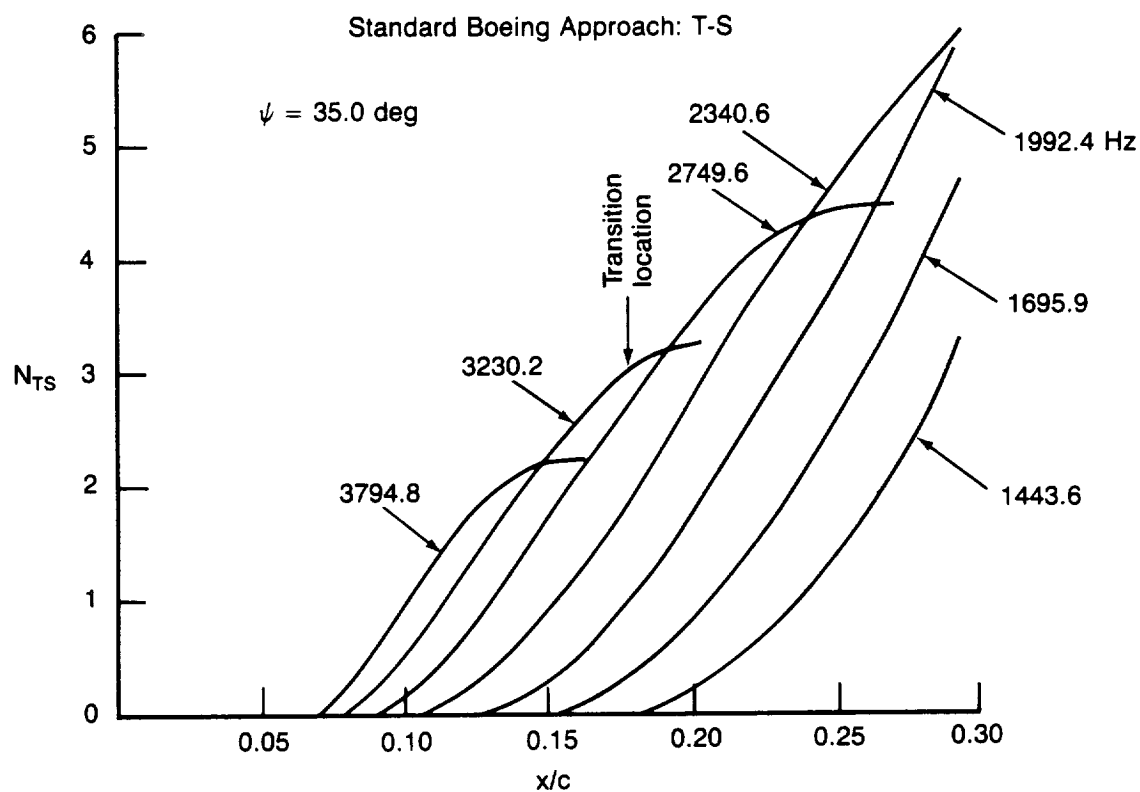


Figure 5-34. Case 2—Standard Boeing Approach, USS Results

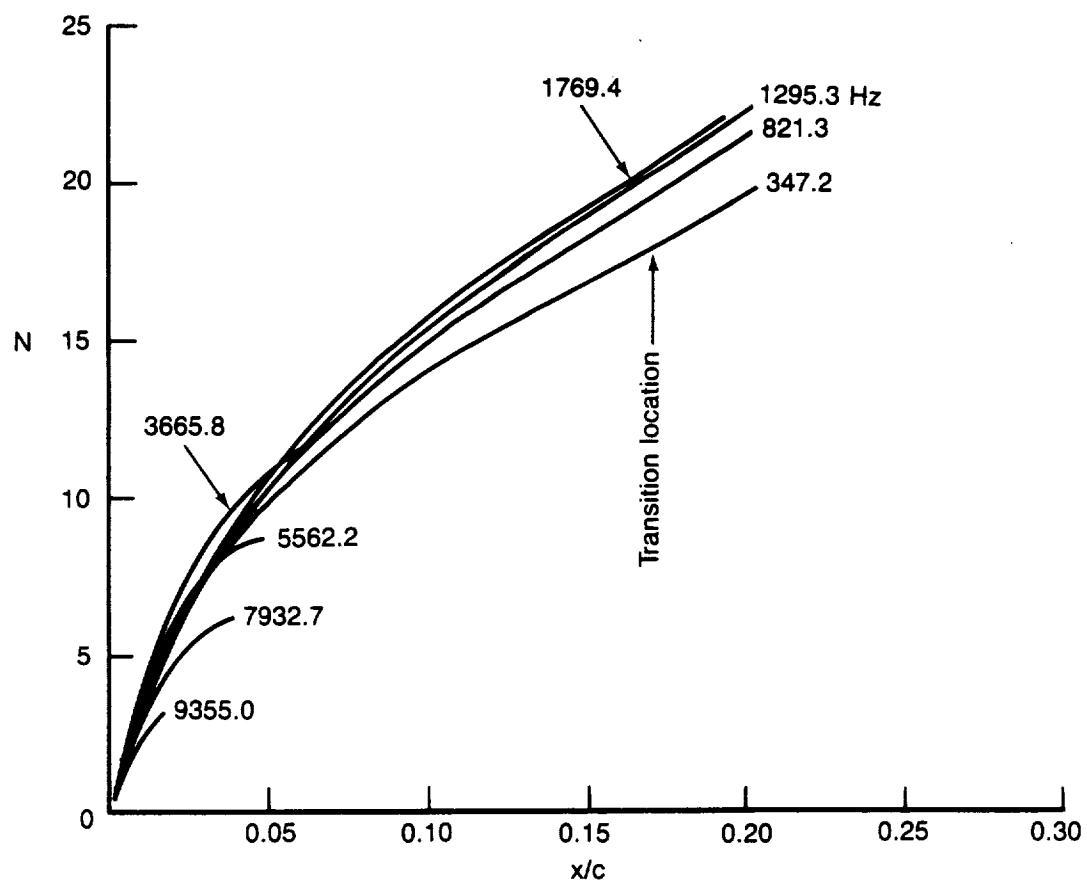


Figure 5-35. Case 2—Maximum Envelope Approach, USS Results

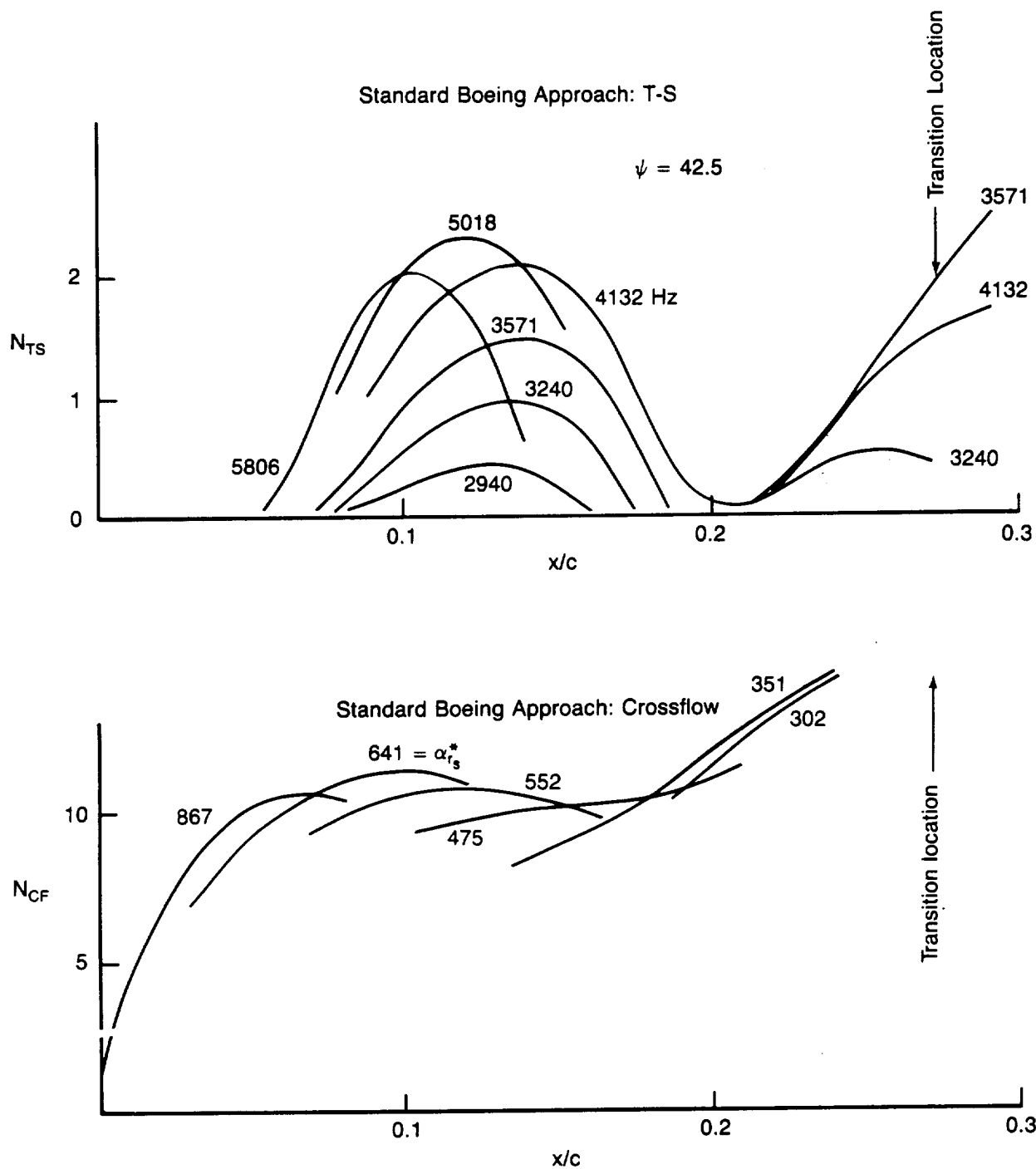


Figure 5-36. Case 11—Standard Boeing Approach, USS Results

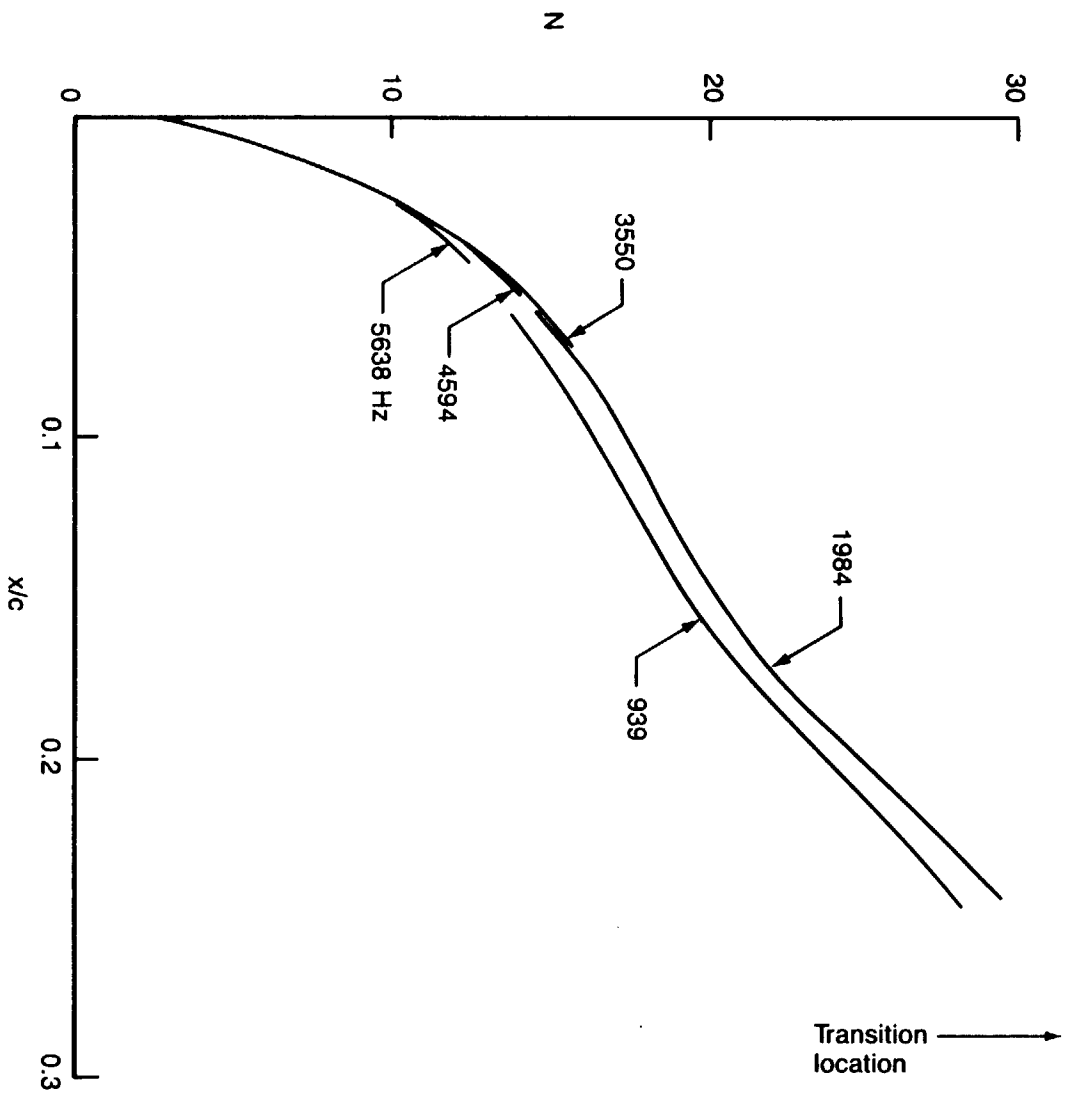


Figure 5-37. Case 11—Maximum Envelope Approach, USS Results

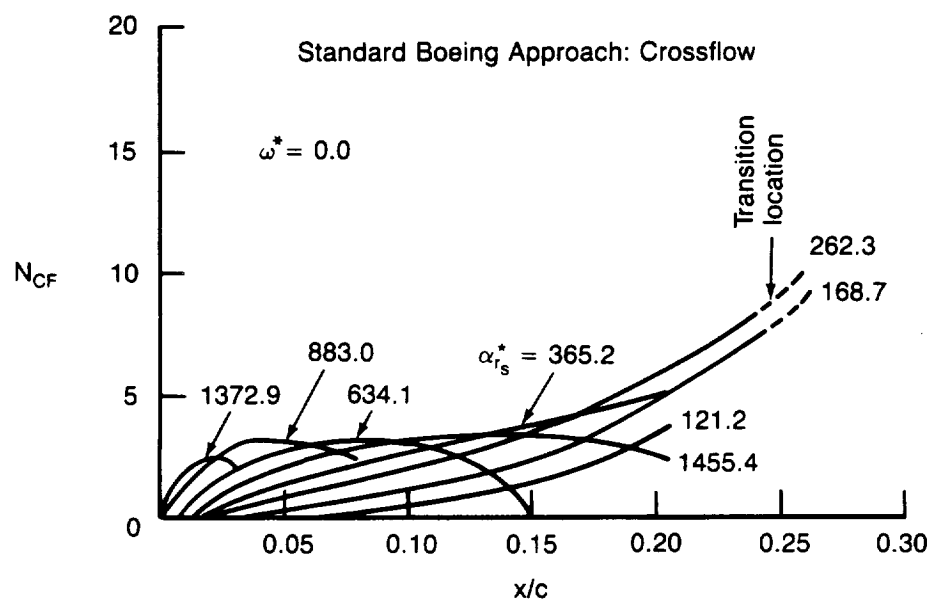
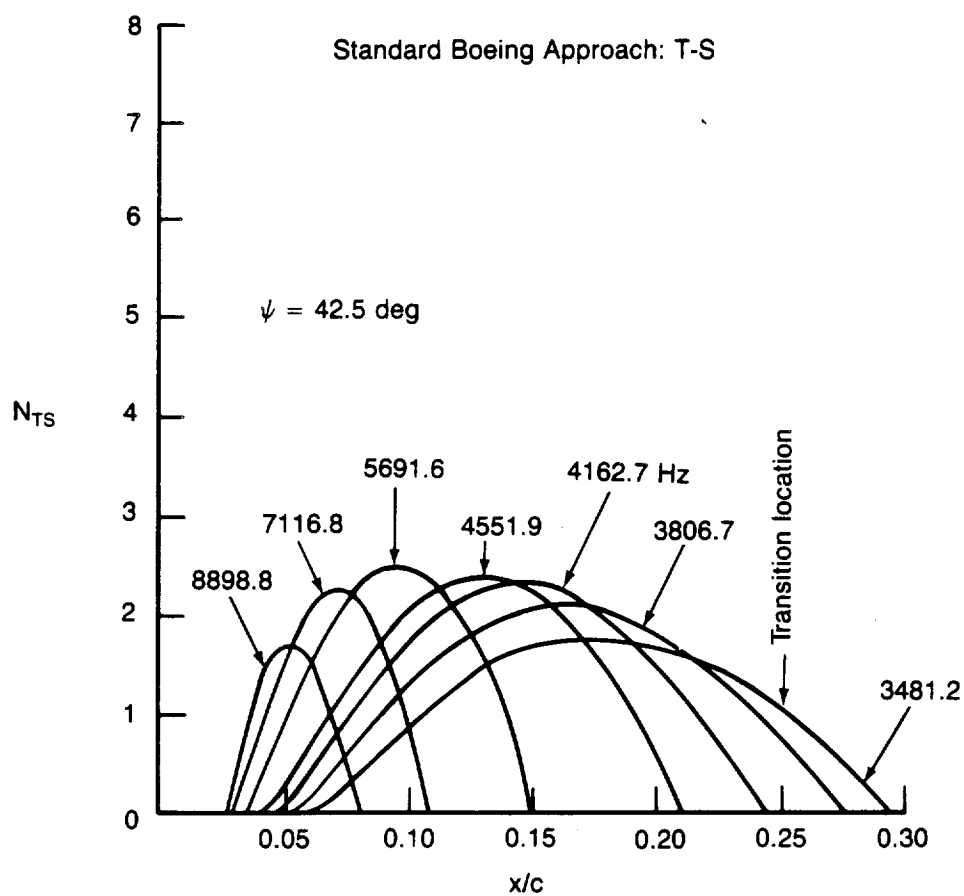


Figure 5-38. Case 13—Standard Boeing Approach, USS Results

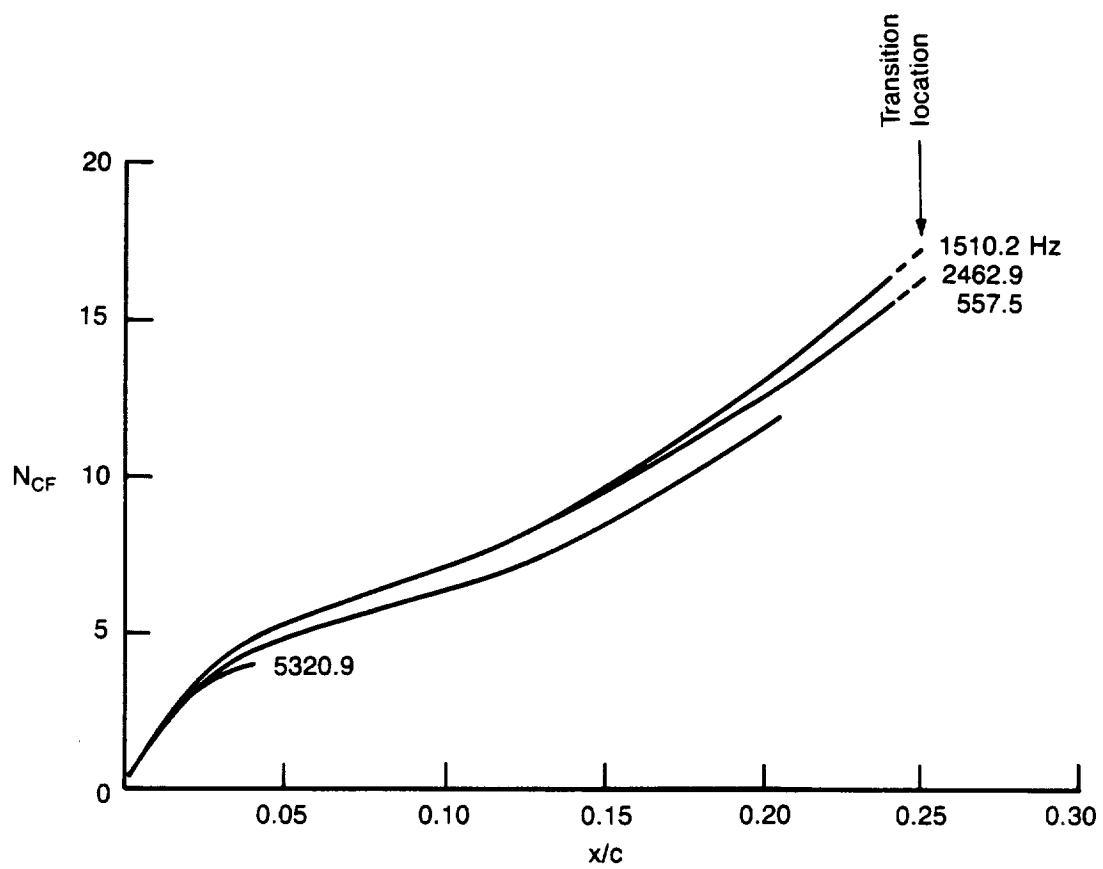


Figure 5-39. Case 13—Maximum Envelope Approach, USS Results

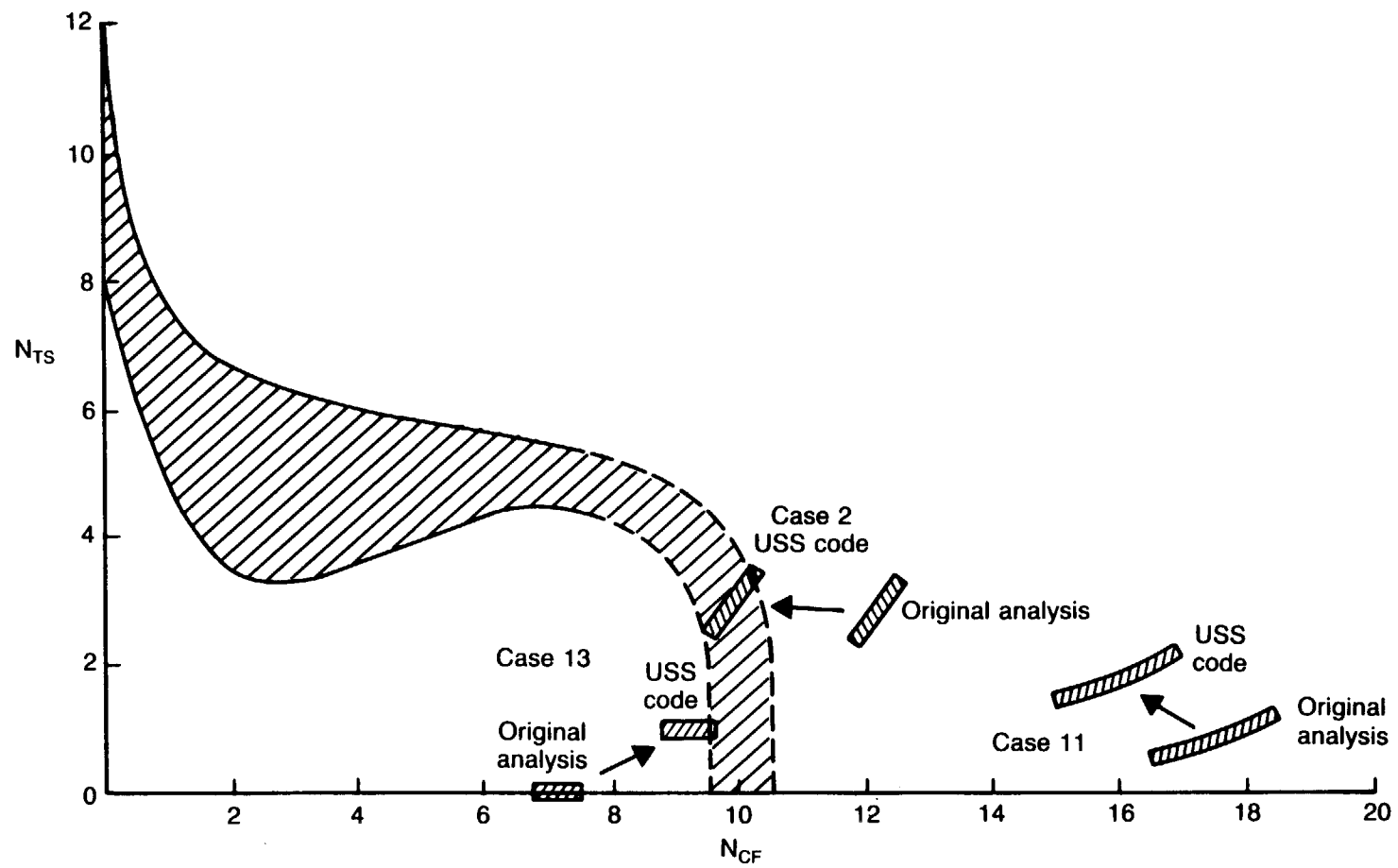


Figure 5-40. USS Code Results for Standard Boeing Approach Versus Original Analysis Results

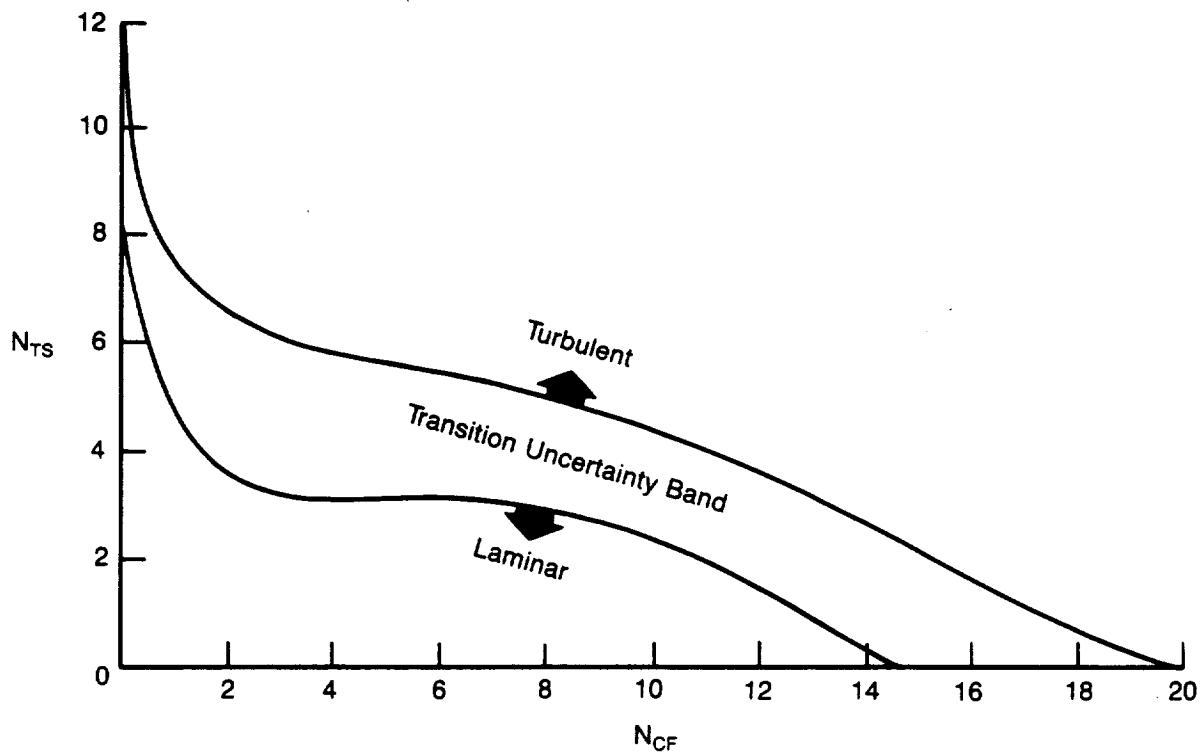


Figure 5-41. Recommended Transition Data Band

6.0 EFFECT OF NOISE ON BOUNDARY LAYER TRANSITION

6.1 EFFECT OF ENGINE NOISE ON EXTENT OF LAMINAR FLOW

The effect of the engine noise variation on the extent of laminar boundary layer flow on the lower surface of the glove is examined for three flight conditions in this section. For each case the measured noise data from microphone 8, which was the closest lower surface microphone to the hot films in the region of transition, is shown for a range of power settings. The measured hot film data on the glove at its midspan are also shown for the same conditions.

Case A (fig. 6-1) is for $M = .80$ and zero sideslip (nominally). The microphone 8 noise levels increase by 10 to 20 dB, depending on frequency, from the low power setting to the high power setting. The hot film data shows higher average rms output voltage levels between $x/c = 7.5\%$ and $x/c = 15\%$ for the higher noise level. The flow is still laminar in this region for both power settings, however. From $x/c = 25\%$ on aft, the boundary layer is turbulent for both engine noise levels. The low noise level case shows a peak that is characteristic of the transitional region at $x/c = 20\%$. The high noise level case shows an output level characteristic of turbulent flow at $x/c = 20\%$, indicating that the transitional peak is somewhere between $x/c = 15\%$ and $x/c = 20\%$. These results indicate that there is a forward shift of about 3% in the transition location at the high noise level.

The results of a boundary layer stability analysis for a flight condition similar to that of Case A are shown in Figure 6-2. The purpose of a boundary layer stability analysis is to calculate the growth of disturbances in the boundary layer. For the 757 NLF glove, these disturbances are of two types: cross-flow (C-F) disturbances and Tollmien-Schlichting (T-S) disturbances. For a discussion of boundary layer stability theory and the method used here, see Section 5.0. Here it will only be pointed out that the boundary layer stability analysis method used in the present study considers only stationary (zero-frequency) C-F vortices and a range of T-S disturbance frequencies.

The lower left part of Figure 6-2 shows the envelope of growth curves for stationary C-F disturbances and the growth curves for various T-S disturbance frequencies. For the low noise condition shown in Figure 6-1, measured transition occurred between $s/c = 0.15$ and $s/c = 0.20$. As shown in Figure 6-2, T-S disturbances of about 3000 Hz are the most highly amplified T-S frequencies in this region. The significance of this result is that it indicates that the T-S disturbances will be most sensitive to engine noise with a frequency of about 3000 Hz. Figure 6-1 shows that the noise levels were about 8 to 10 dB higher in this frequency range at the high power setting than at the low power setting. Thus, there is a significant variation in engine noise level in the critical T-S frequency range from low to high power setting.

The lower right hand part of Figure 6-2 shows the F-111 transition data band based on measured F-111 NLF glove flight data and calculated boundary layer stability (ref. 3). Also shown is the transition N-factor data band for the 757 glove, as discussed in Section 5.4. Superimposed on this plot is the trajectory of the calculated N_{TS} versus N_{CF} curve as a function of s/c location. It can be seen that in the 15% to 20% chord region, which is the measured transition location for low engine noise levels, the trajectory curve is inside the 757 data band. Since this band includes upper surface results, which do not appear to be affected by engine noise, this would indicate that the transition location for the low noise condition is probably not being affected significantly by the noise.

One final conclusion that can be drawn from the results shown in Figure 6-2 is that the stationary C-F disturbance N-factors in the vicinity of transition are much higher than the T-S N-factors. Thus, crossflow is probably the primary cause of transition at the low noise conditions. The small observed effect of the engine noise on extent of laminar flow may indicate that CF disturbances are not significantly affected by engine noise. The cause of the small shifts in transition location at the high noise levels may be due to slight increases in crossflow disturbances or sufficient increases in the TS disturbances to cause transition.

Case B is for $M = .70$ and zero sideslip (nominally). Figure 6-3 shows that the microphone 8 noise levels again increase by 10 to 20 dB, depending on frequency, from the low power setting to the high power setting. All of the hot film data falls within a narrow band at laminar flow output levels back to 10% chord. From 20% chord aft, all of the output data lies within a narrow band at levels characteristic of turbulent flow. At $x/c = 15\%$, all of the cases show elevated voltage levels characteristic of the transitional region. There is no consistent trend with noise level at $x/c = 15\%$. However, at $x/c = 12.5\%$ two of the higher noise level cases show elevated voltage levels, indicating that the voltage peak characteristic of the transitional region may be shifted forward slightly relative to the other cases. The highest noise level condition had an actual sideslip angle of 0.7 deg, whereas the lowest noise level condition had an actual sideslip angle of -0.8 deg. This results in an effective sweep angle 1.5 deg lower for the highest noise condition than for the lowest noise condition. This may be partially masking the noise effect for these two cases. Based on this data, no significant effect of engine noise on the extent of laminar flow is apparent.

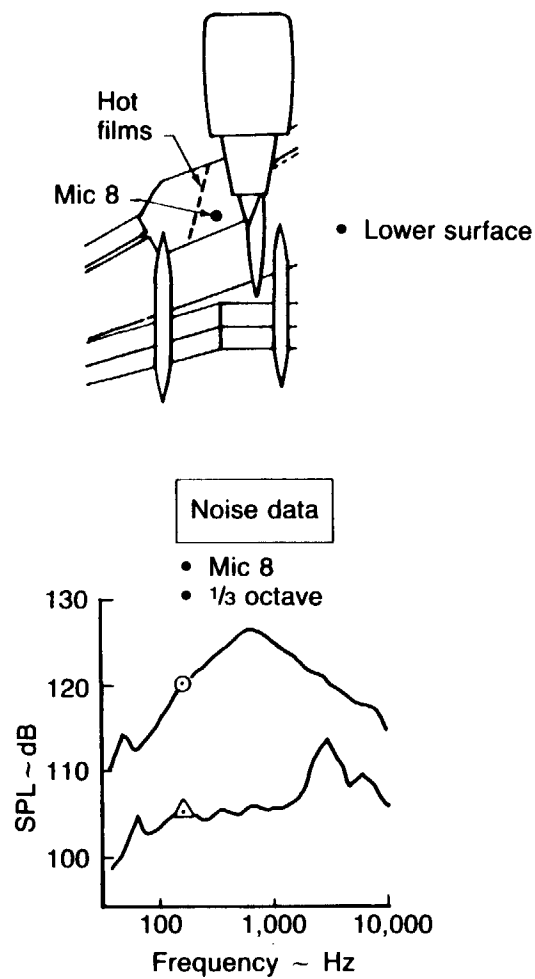
The boundary layer stability results for the Case B condition are shown in Figure 6-4. The most critical T-S disturbances are again at approximately 3000 Hz. It can be seen that C-F disturbances are again the dominant cause of transition, even more so than for Case A.

Case C, which is a high sideslip condition at $M = .70$, is shown in Figure 6-5. For the flight on which this data was taken, the hot films had been rearranged to provide better spanwise definition of the transition location. Therefore, at the midspan of the glove there were hot films only at $x/c = 15\%$, 20%, and 25%. The hot film output for the high noise level condition shows elevated voltage levels at $x/c = 15\%$ and 20% characteristic of a boundary layer that is intermittently laminar. The high noise level case shows a lower voltage level than the low noise level case at $x/c = 25\%$. This indicates that the location of the transitional peak is slightly further forward for the high noise case than for the low noise case.

Figure 6-6 shows the boundary layer stability analysis results for the Case C condition. It can be seen that the ratio of T-S to C-F disturbances in the vicinity of transition is much higher for this case than for the previous two cases. But, even though there appears to be a larger noise effect forward of the transitional peak for this case than for the previous two cases, the effect of noise on the location of the transitional peak does not appear to be any larger.

In summary, the three cases examined here indicate the following with respect to the effect of engine noise on the extent of laminar flow:

1. Two of the cases indicate a small forward shift of about 1% to 3% chord in the transition location for the highest noise levels relative to the lowest noise levels. The other case does not clearly show a noise effect.
2. Boundary layer stability analysis results indicate that the most critical T-S frequencies were in the 2500 to 3000 Hz range. The measured noise level ($1/3$ octave) in this frequency range varied from about 105 to 110 dB at the lowest power setting to about 120 dB at the highest power setting.
3. All three cases examined had combinations of T-S and C-F disturbance amplification factors at transition that were within the transition data band determined by all of the upper and lower surface 757 cases. This indicates that there was probably no significant effect of noise on the transition location at the low power setting.
4. Since C-F disturbances are the dominant cause of transition for all three cases, the small observed effect of variations in engine noise level on the transition location may indicate that engine noise does not have a significant effect on C-F disturbances.



Flight	Cond.	M_{AIRPLANE}	C_L	M_{FAN}	β (deg)	N_{1C}
⊙ 1	13	0.80	0.55	1.28	+0.2	4366
△ 2	228	0.79	0.57	0.94	-0.5	2645

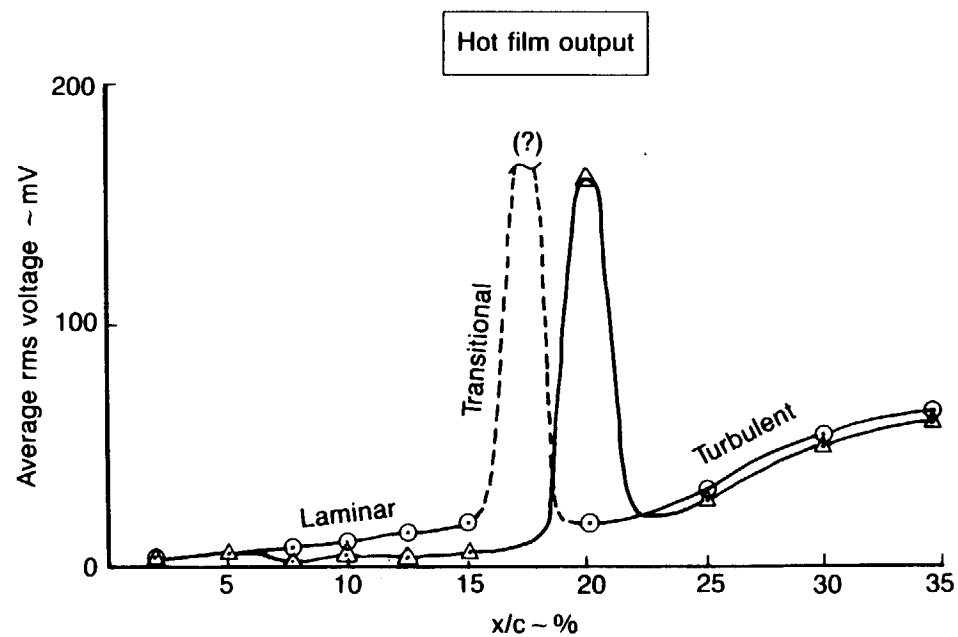
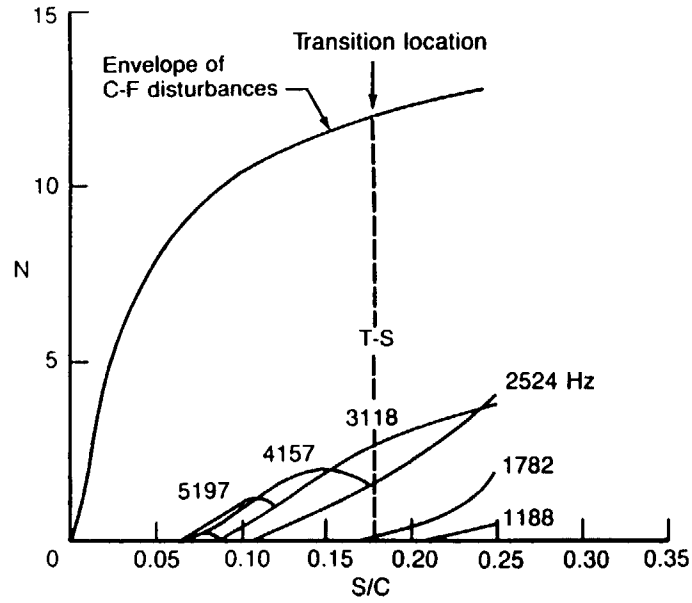


Figure 6-1. Effect of Engine Noise on Extent of Laminar Flow: Case A

- Lower surface; WBL 308.5
- Flight 3, cond. 16 (outbd C_p)
- Flight 2, cond. 223 (inbd C_p)
- $M_\infty = 0.804$, alt = 40,483 ft
- $Re_C = 25.5 \times 10^6$



Crossflow

- Compressible
- Irrotational
- $\omega^* = 0$
- $\Lambda = 22$ deg ($s/c = 0$ to 0.07)
- $\Lambda = 32$ deg ($s/c = 0.08$ to 0.25)

Tollmien-Schlichting

- Compressible
- $\psi = 35.0$ deg

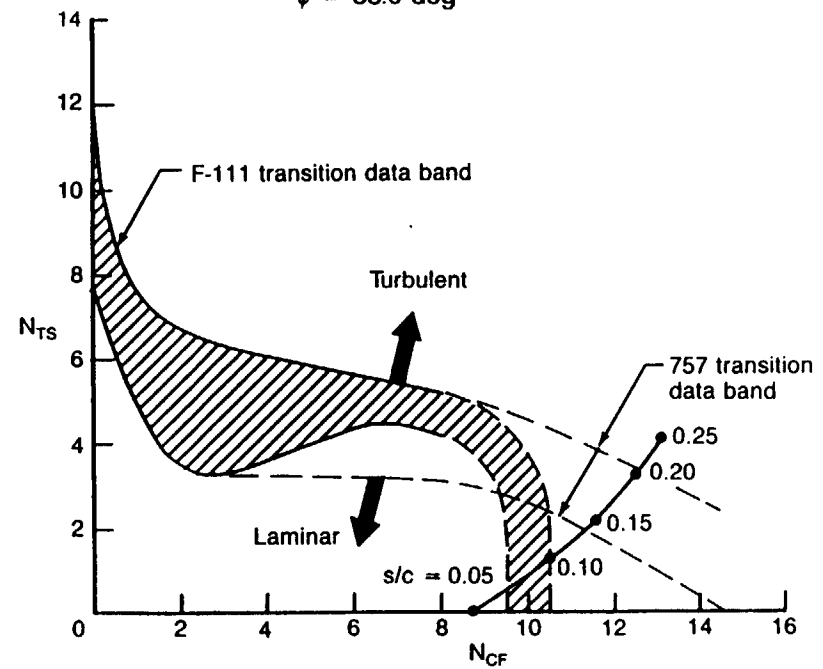


Figure 6-2. Boundary Layer Stability Analysis $M \approx 0.80$, $C_L \approx 0.53$, $\beta \approx 0$ deg

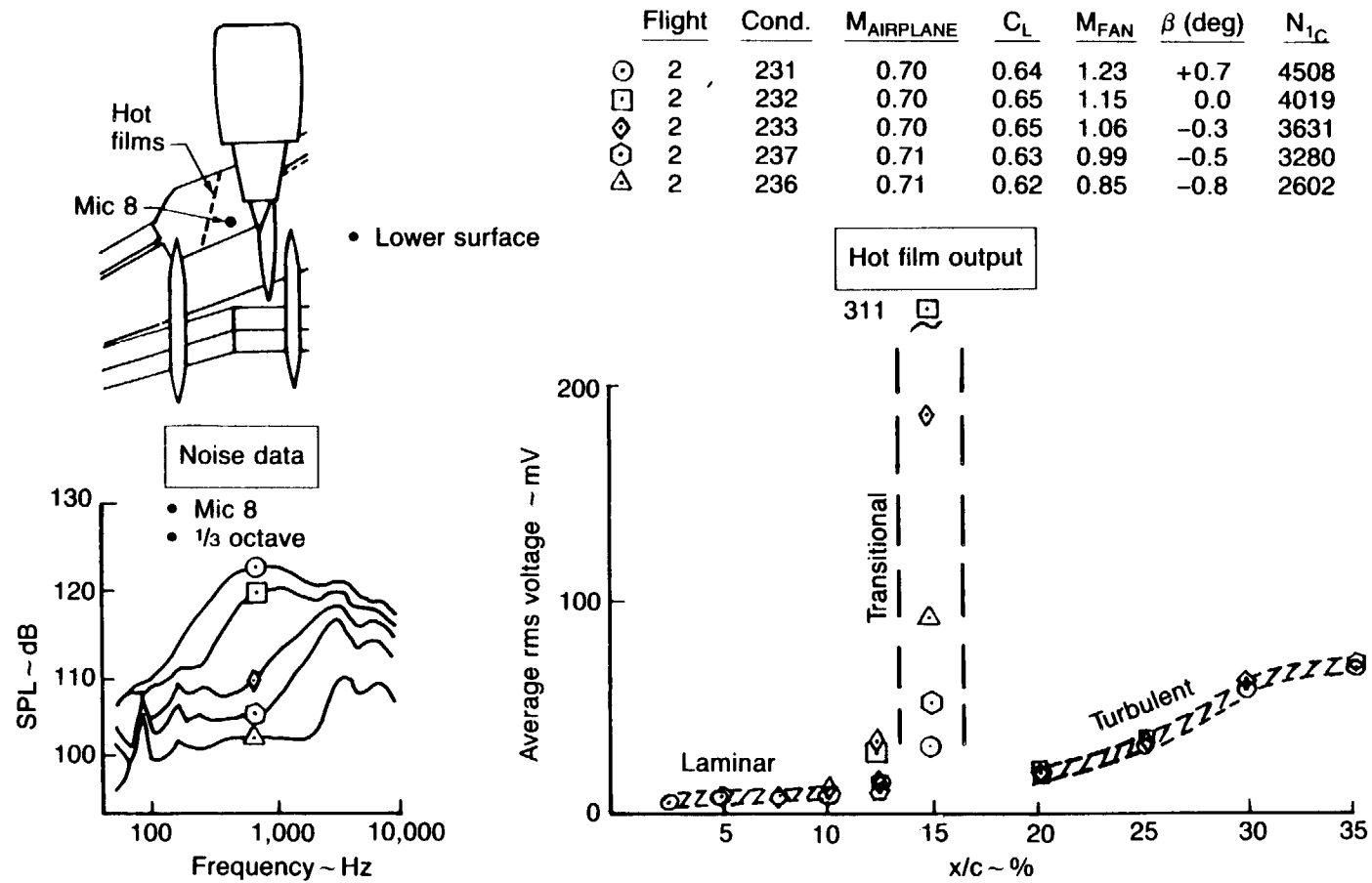


Figure 6-3. Effect of Engine Noise on Extent of Laminar Flow: Case B

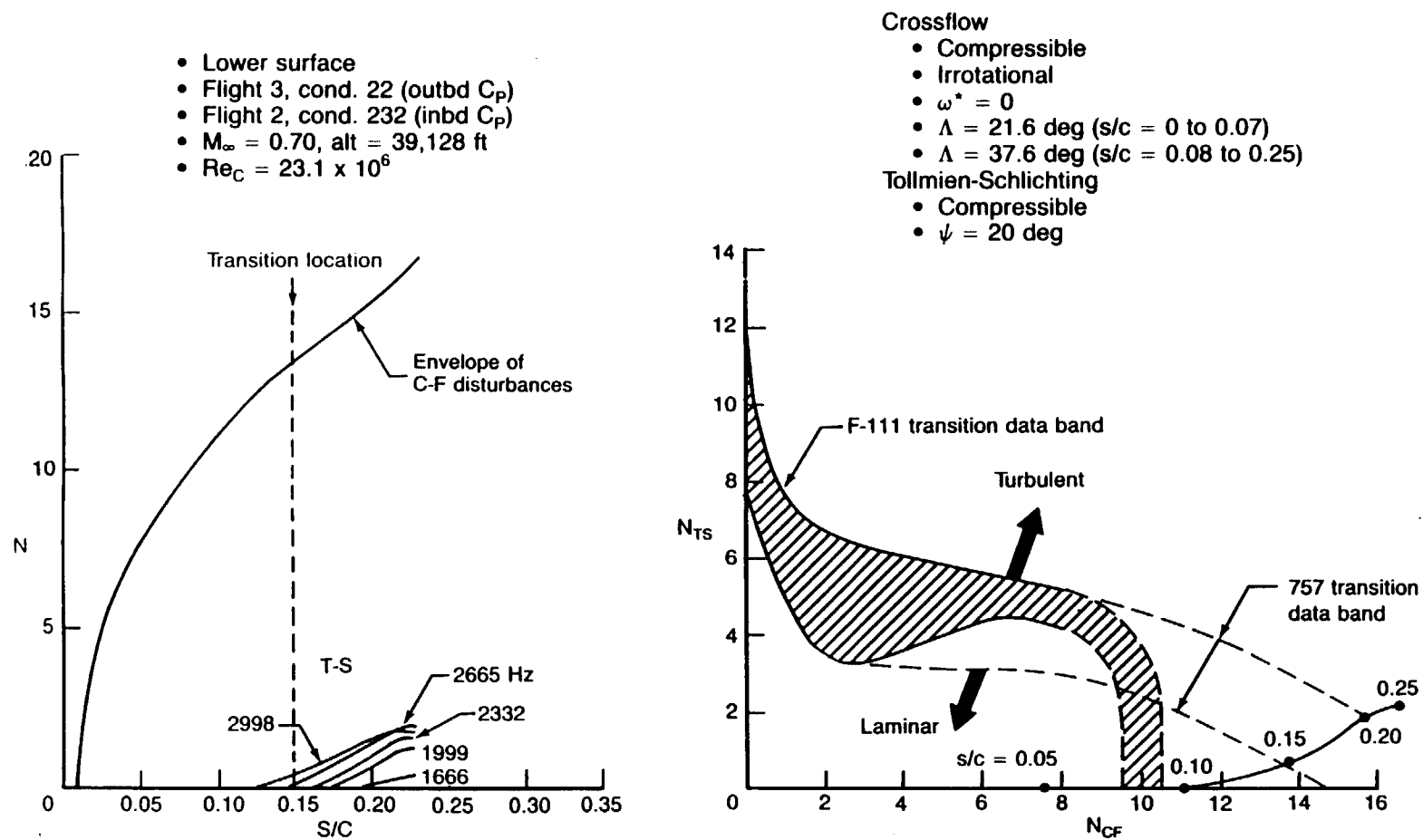


Figure 6-4. Boundary Layer Stability Analysis $M_\infty \approx 0.70$, $C_L \approx 0.64$, $\beta \approx 0$ deg

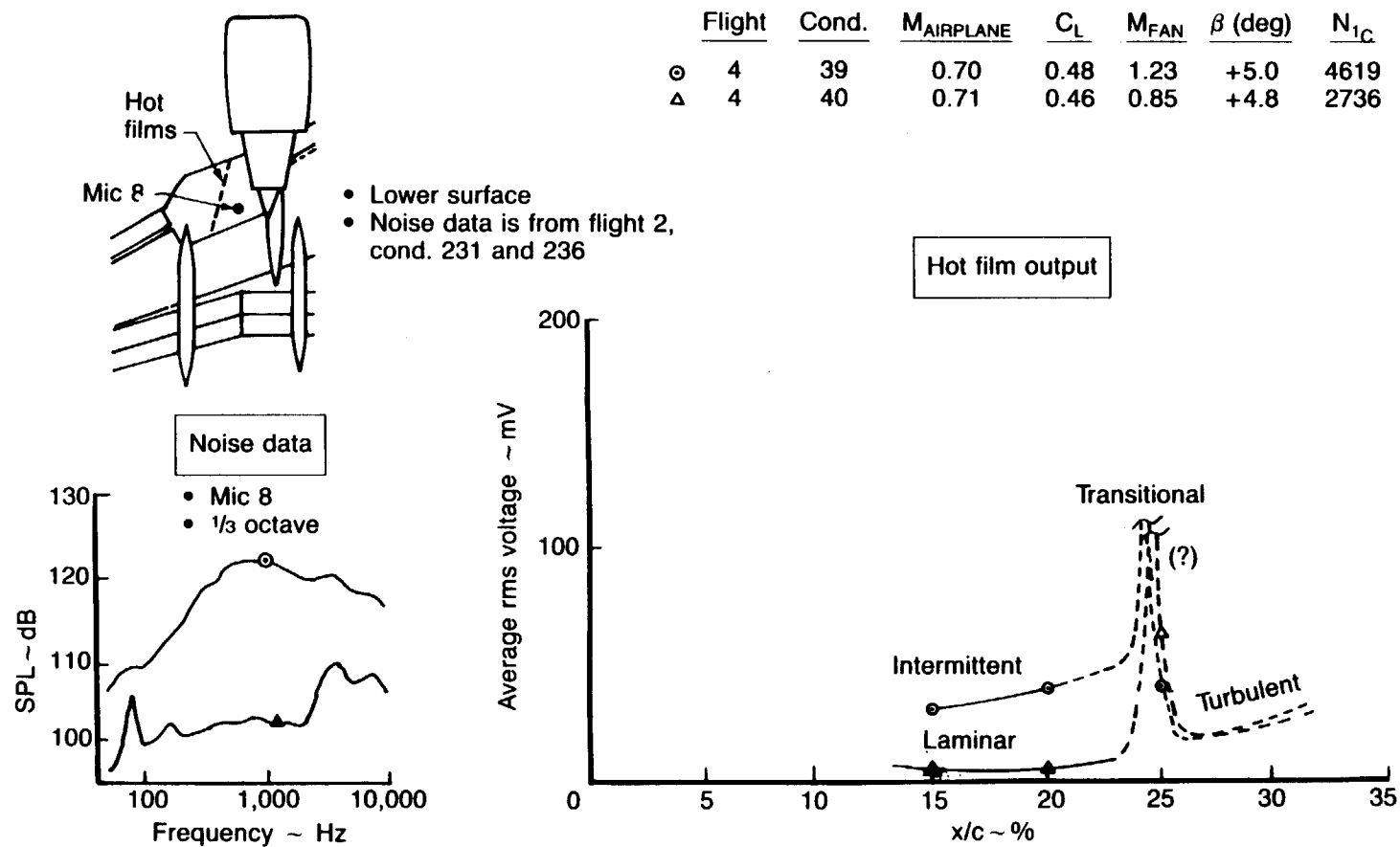
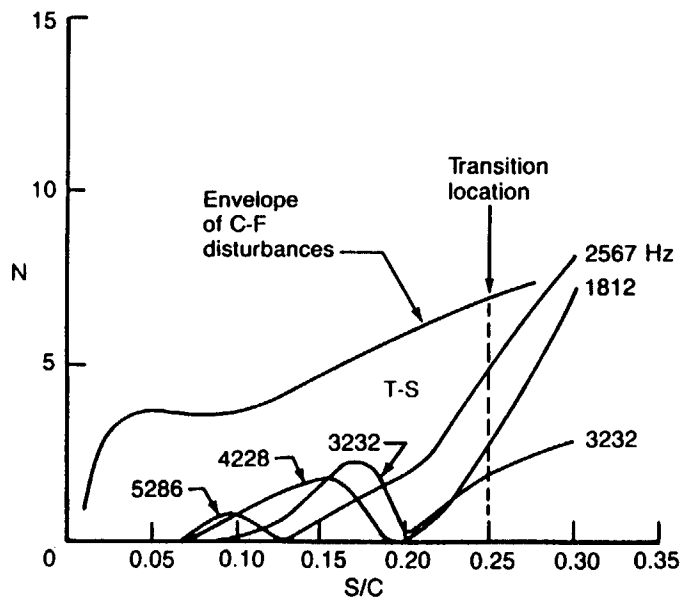


Figure 6-5. Effect of Engine Noise on Extent of Laminar Flow: Case C

- Lower surface; WBL 325
- Flight 4, cond. 40 (outbd C_p)
- Inbd C_p estimated from flight 2 data
- $M_\infty = 0.70$, alt = 32,961 ft
- $Re_C = 30.1 \times 10^6$



Crossflow

- Compressible
- Irrotational
- $\omega^* = 0$
- $\Lambda = 14.2$ deg ($s/c = 0$ to 0.09)
- $\Lambda = 21.7$ deg ($s/c = 0.10$ to 0.30)

Tollmien-Schlichting

- Compressible
- $\psi = 20$ deg

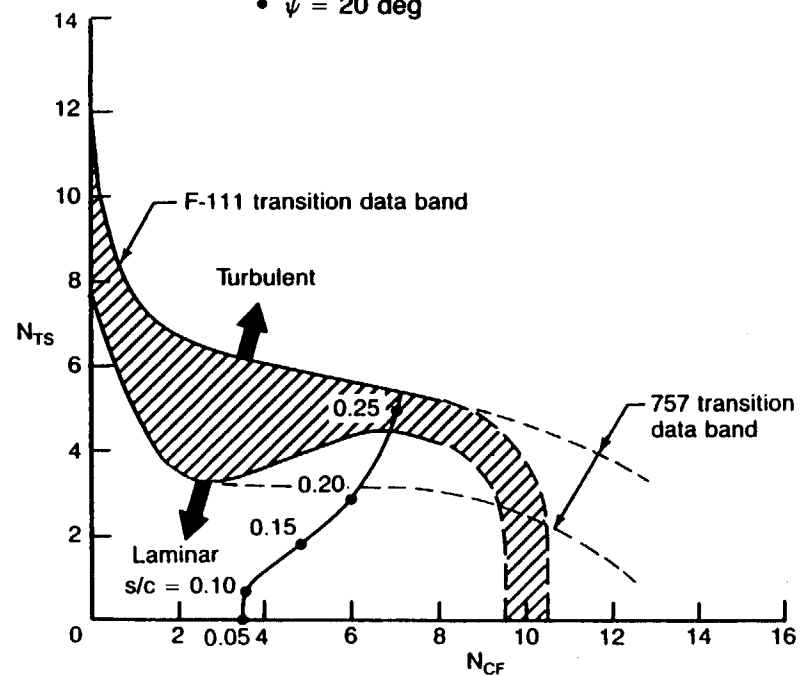


Figure 6-6. Boundary Layer Stability $M_\infty \approx 0.70$, $C_L \approx 0.47$, $\beta \approx +5$ deg

6.2 COMPARISON OF TRANSITION DATA WITH EXISTING CRITERIA

6.2.1 X-21A Criterion

The X21A LFC/Acoustic criterion (ref. 7) was developed in the early 1960s. This criterion relates transition Reynolds number to disturbance velocity ratio and was developed experimentally with wind tunnel data. Subsequent flight testing and wind tunnel testing supplied additional data. The original criterion is shown in Figure 6-7 with the later flight test data and wind tunnel data also indicated. The majority of the data were for configurations with boundary layer suction control. The disturbance velocity is determined primarily from wind tunnel turbulence measurements. For the Ames wind tunnel data and the X-21A flight test data, the disturbance velocity was calculated from the noise level measured away from the wing section assuming a plane wave. Many of the parameters considered important for laminar flow such as disturbance frequency spectrum, amount of suction, wing sweep, and angle of attack are not represented in the criterion.

One set of 757 data at $M = .80$ is shown in Figure 6-8, along with the X-21A data. The trend indicated by the X-21A flight test data leads to the expectation of increased laminar flow from the observed value of 17% chord (corresponding to $Re_{xTR} = 4.2 \times 10^6$) at maximum measured noise level to about 55% (corresponding to $Re_{xTR} = 13.5 \times 10^6$) at the minimum measured noise level. The observed transition location moved back only to 20% chord indicating, at first glance, that these results are not consistent with the trend of the X-21A flight test data.

The apparent discrepancy between the 757 results and the X-21A data is examined in more depth in Figure 6-9. This figure shows three 757 cases, together with the X-21A flight data. All three 757 cases show that the transition Reynolds number is flat with increasing sound particle velocity, except at the highest noise levels tested. One possible interpretation of the 757 results is that the region of constant transition Reynolds number corresponds to the background, low-disturbance, stability-limited transition location. In this region, transition is caused by amplified background disturbances. As discussed in Section 6, the dominant disturbance in this region for the 757 appears to be crossflow. This would not change with noise level as long as the disturbance due to the noise is significantly smaller than the amplified background disturbance level. The limiting transition Reynolds number is a function of the pressure distribution and flight condition, and is much lower for all three 757 cases than for the X-21A, which used boundary layer suction to reduce the disturbance growth. Only above a certain noise level does the amplified disturbance due to the noise begin to become significant relative to the amplified background disturbance level, resulting in a forward movement of the transition location. The trend line of premature transition due to noise appears to be fairly consistent between the X-21A data and the 757 data.

Thus, the 757 results for the effect of noise on the transition location are not inconsistent with the general trends shown by the X-21A flight data, when interpreted as explained above. This implies that, for wing designs where the low disturbance, stability-limited transition location is further aft than in the present test, such as might be expected for LFC or HLFC wing designs, engine noise effects on the extent of laminar flow may be significant.

Figure 6-10 shows what the potential loss in laminar area on the 757 lower wing surface is, based on the measured noise levels at cruise thrust, and based on the trend line of premature transition due to noise effects for the $M = .80$ data, as shown in Figure 6-9. It must again be stressed, however, that the trend line location is a function of the wing design, and a wing design that will allow laminar flow back to 60% chord in the absence of noise, (probably either an HLFC or LFC design) as assumed in Figure 6-10, will differ significantly from the NLF glove of the current test.

6.2.2 Mangiarotty Criterion

In Reference 8 Mangiarotty proposes a transition criterion based on the Tollmein-Schlichting (T-S) disturbance amplification rates resulting from stability calculations. No consideration of crossflow instabilities is given in the Mangiarotty procedure. In addition, the spatial character of the sound wave is not considered. The model assumes that the sound wave generates a T-S disturbance at the leading edge of the wing that grows until transition takes place. The *background* disturbance level, which can be due to airflow turbulence or surface irregularities, is not considered. The frequency dependent T-S amplifications calculated from stability theory are applied to the acoustic velocity that is calculated assuming a plane wave. If the resulting amplified disturbance velocity ratioed by the freestream velocity is greater than 0.01 to 0.05 (i.e., $\Delta U/U_\infty \geq 0.01$ to 0.05) transition is expected. In Reference 13 Mangiarotty considers a *transfer function* relating the calculated amplified acoustic velocity to the boundary layer disturbance velocity. Data is shown indicating that the disturbance velocity may be lower than the calculated amplified acoustic velocity by a factor of 0.37.

The amplified velocity ratios versus percent chord were calculated for the three 757 flight cases discussed in Section 6.1: $M_{AP} = 0.8, \beta = 0$ deg; $M_{AP} = 0.7, \beta = 0$ deg; and $M_{AP} = 0.7, \beta = 5$ deg. The lower wing surface stability calculation results shown in Figures 6-2, 6-4, and 6-6 supplied the T-S amplification values. The resulting curve for amplified acoustic velocity ratio versus chord position for the $M_{AP} = 0.8, \beta = 0$ -deg case is shown in Figure 6-11. Calculations were done for the low noise and high noise cases shown in Figure 6-1. If the 1% criterion is used with a *transfer function* of 0.37, transition is predicted at approximately 24.5% chord for the low noise condition and approximately 19.7% chord for the high noise condition. The 1% criterion used with a transfer function of 1 results in predicted transition at 20% for the low noise case and 13% for the high noise case. The measured transition was approximately 20% chord for the low noise case and 17% for the high noise case. This appears reasonably consistent with the prediction using a transfer function of 1. Figure 6-11 also shows the calculated amplified velocity disturbance versus chord for the $M_{AP} = 0.7, \beta = 0$ -deg condition. As seen in Figure 6-4, this case has higher crossflow and lower T-S amplification rates than the $M_{AP} = 0.8$ case. The 1% criterion with a transfer function of 1 results in a predicted transition at approximately 21.5% for the high noise condition and a point that appears to be well beyond the stability calculation range for the low noise condition. The measured data for this case showed transition somewhere between 13% and 18% for both conditions. This case is important because it points out one of the major deficiencies of the Mangiarotty procedure (i.e., no consideration of crossflow). As discussed in Section 6.1, it appears that for this flight condition the crossflow disturbance growth is primarily responsible for transition. Since Mangiarotty only considers the T-S disturbance, this procedure can only give useful results when the T-S amplification rates are high enough that the T-S disturbance would cause transition before the crossflow disturbance.

The $M_{AP} = 0.7, \beta = 5$ -deg case is seen in Figure 6-6 to result in the lowest crossflow amplification of the three cases studied. This is because of the effective 5-deg reduction of wing sweep resulting from the +5-deg sideslip. The calculated acoustic disturbance growth for the high and low noise cases are shown in Figure 6-12. A very rapid increase in u/U_∞ is seen at 20% chord for the high noise case and 20% to 25% chord for the low noise case. Using the 1% criterion and the unit transfer function results in predicted transition moving from approximately 22% to 16% for noise increasing from the low level to the high level. The 0.37 transfer function results in a 25% to 20.5% range. The measured data showed a small change of transition location from 25% to 24% associated with the noise level change of 120.8 to 136 dB. Again, when the crossflow amplification is more moderate, the Mangiarotty procedure, although still in need of a more precise definition of the required transfer function, gives results that are somewhat consistent with the 757 measured results.

The ability of the Mangiarotty procedure to possibly predict the T-S disturbance growth due to a sound wave but not account for background disturbances or crossflow suggests combining the F111/757 transition band criterion discussed in Section 5.4 with the Mangiarotty procedure. The N_{TS}/N_{CF} band appears to account for background disturbances and crossflow. A procedure for estimating transition

location may be to calculate transition location with both procedures. The smaller of the two predictions would then be the expected transition location. This procedure is appealing because it accounts for many of the physical aspects believed pertinent. These include: (1) the wing design (including suction) and the flight conditions through the stability curves (N_{TS} and N_{CF} versus X/C); (2) crossflow and background disturbances through the stability curves and the experimentally determined F-111/757, N_{TS}/N_{CF} curve; and (3) the noise level and spectrum shape through the TS stability curves. Physical aspects not accounted for in this approach are: (1) sound interaction with crossflow instabilities (assumed small); (2) interaction of the sound amplified TS disturbances with crossflow disturbances; (3) spatial character of the sound wave (disturbance at wing leading edge only considered); and (4) details of acoustic disturbance to boundary layer vorticity disturbance transfer function.

Items 3 and 4 above have been considered by Swift and Mungur in Reference 4. Mangiarotty's procedure appears to be very similar to their method for evaluating the effect of noise on laminar boundary layer transition.

6.2.3 Swift and Mungur Criterion

Swift and Mungur present a theoretical analysis showing their procedure for accounting for the influence of sound on laminar boundary layer transition to be a simplification of a general procedure that can account for the spatial character of the disturbing sound wave. They relate the sound field to vorticity generation and amplification in the boundary layer. They conclude that, because of interference effects, the spatial character of the sound wave actually can suppress the growth of the disturbance caused by the sound wave impinging on the boundary layer. Thus, considering only the leading edge disturbance results in somewhat of a conservative estimate of the transition location. They also show that the transfer function relating the boundary layer disturbance velocity to the amplified acoustic velocity is a function of the local Reynold's number, the directionality of the incident sound wave and other factors associated with the disturbance growth. They do not evaluate the transfer function directly but go to experimental data for an estimate. They relate the amplified disturbance velocity ratio to the incident sound wave through the following equation, which is essentially the same form used by Mangiarotty.

$$\frac{U}{U_{\infty}} = \frac{T(R_s \Phi) D(\theta_1, M_{\infty})}{U_{\infty}} \frac{P_i}{c \rho} A(f)$$

$P_i/\rho c$ is recognized as the particle velocity of an incident plane wave. $A(f)$ is the frequency dependent TS amplification. $(T(R_s \Phi) D(\theta_1, M_{\infty}))$ is similar to Mangiarotty's transfer function and depends on the sound wave directivity through $D(\theta_1, M_{\infty})$. If there is a particular U/U_{∞} at which a laminar boundary layer undergoes transition, the sound pressure that will cause transition is determined from:

$$\left(\frac{P_i}{\rho c} \right)_{crit} = \left(\frac{U}{U_{\infty}} \right)_{crit} \left(\frac{T D}{U_{\infty}} \right)^{-1} A(f)^{-1}$$

$$\begin{aligned} SPL_{crit} &= 20 \log \frac{P_{i,crit}}{P_{ref}} = 20 \log \left(\frac{U}{U_{\infty}} \right)_{crit} + 20 \log \frac{\rho c^2}{P_{ref}} \\ &\quad + 20 \log M_{\infty} - 20 \log T^* D - 20 \log A(f) \end{aligned}$$

At a constant altitude, flight Mach number and incidence angle

$$SPL_{crit} \approx \text{Constant} - 20 \log A(f)$$

Swift and Mungur estimate the constant to be 130 dB from wind tunnel data that appears to be at $M_\infty \approx 0.5$ and sea level density and sonic speed. They examine each sound frequency individually and do not consider the frequency integrated rms velocity or OASPL. Figure 6-13 compares the $-20 \log A(f)$ Tollmein-Schlichting amplification curves normalized to 128 dB (130 dB per Swift and Mungur corrected for airplane Mach number and altitude) with measured narrow band spectra (corrected to unit bandwidth) for the $M_{AP} = 0.8$, $\beta = 0$ case examined above. As was the case above, the noise data is taken from microphone 8. It is seen that the fan fundamental tone is predicted to cause transition at approximately 22% chord for the high noise case. The broadband noise would be expected to cause transition at approximately 30% chord for the low noise case. The corresponding curves for $M_{AP} = 0.7$, $\beta = 0$ deg and $M_{AP} = 0.7$, $\beta = +5$ deg are shown in Figures 6-13 and 6-14. Table 6-1 compares the estimated transition location resulting from these curves with the predictions using the Mangiarotty procedure (which uses the frequency integrated rms velocity rather than the per unit frequency value) and the 757 measured results. The Swift and Mungur procedure generally predicts larger percentage chord transition locations than the Mangiarotty method. This difference probably results from (1) uncertainty for transfer function and critical velocity ratio; and (2) consideration of the integrated spectrum in the Mangiarotty case versus consideration of unit frequencies individually in Swift and Mungur's case. Both procedures show very poor results when the crossflow disturbance amplification is large compared to the Tollmein-Schlichting disturbance amplification ($M_{AP} = 0.7$, $\beta = 0$ deg).

Swift and Mungur give a brief discussion of the effect of crossflow. They state that, if crossflow was the only flow component, the disturbance amplification calculation would be similar in principal to the Tollmein-Schlichting calculation for chordwise flow. When the two flows occur simultaneously, they point out that a three dimensional analysis may be required. At Boeing, the disturbance amplification for the zero Hz frequency limit is normally calculated for crossflow stability studies. Interaction of crossflow and TS disturbances are not analytically evaluated. The N_{CF} factors shown in curves such as in Figure 6-2 are for the zero frequency limit. The apparent low acoustic sensitivity of the 757 NLF glove seems to support this approach. It appears that the crossflow disturbance growth was not significantly affected by the presence of sound.

In summary, the Mangiarotty and the Swift and Mungur transition criterion procedures are in principal the same. Each requires more experimental data to more precisely understand the critical disturbance velocity ratio for transition and the transfer function relating amplified acoustic velocity to TS boundary layer disturbance velocity. Swift and Mungur limit their consideration to individual frequencies and do not consider the frequency integrated disturbance level. Both procedures only consider acoustic interaction with Tollmein-Schlichting instabilities. The introduction of crossflow instabilities by sound is considered by Swift and Mungur only generally and briefly. The present 757 data however suggest that the crossflow is not significantly influenced by sound. However, since the crossflow disturbance amplification of background disturbances can be quite large, its influence must be considered when predicting transition in the presence of sound. It is therefore suggested that a procedure combining the F-111/757, N_{TS}/N_{CF} criterion to account for crossflow and background disturbances with a procedure such as Mangiarotty's or Swift and Mungur's may be useful for laminar boundary layer analysis. The next section describes one such procedure.

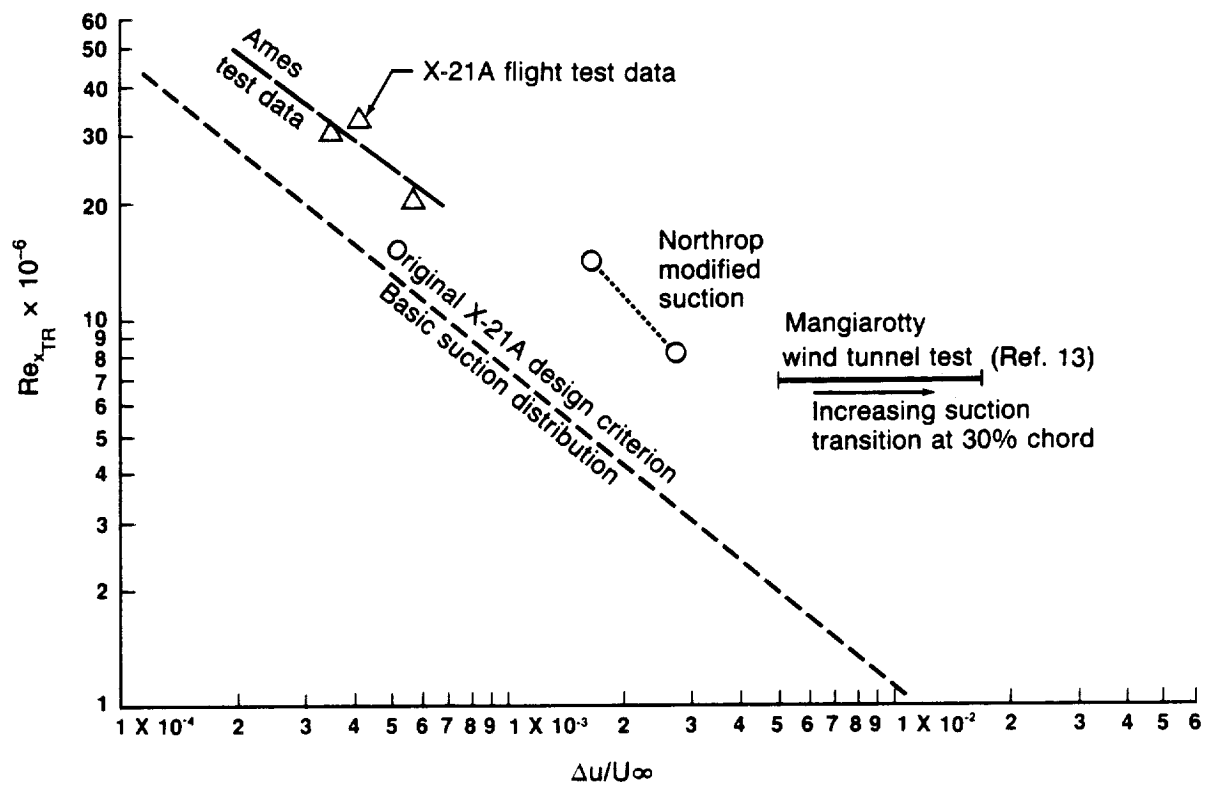


Figure 6-7. X-21A Acoustic Criterion

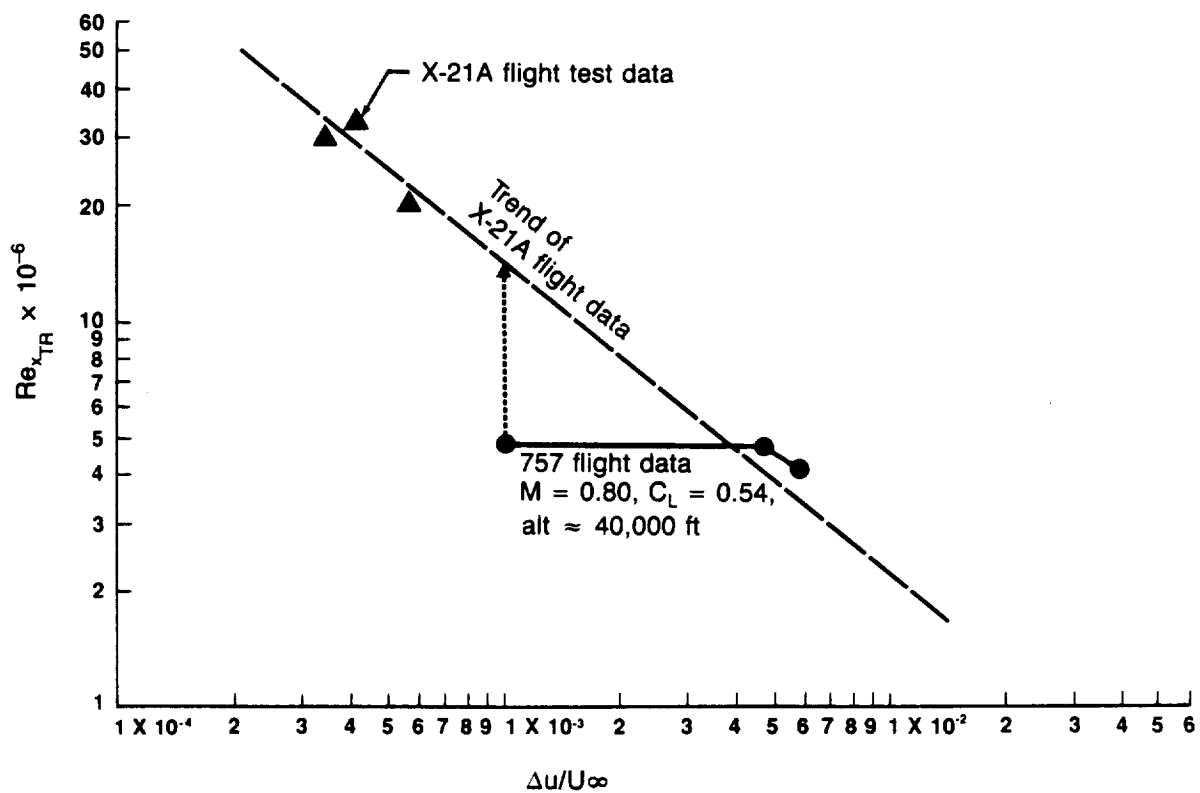


Figure 6-8. Comparison of X-21A and One 757 Flight Data Case

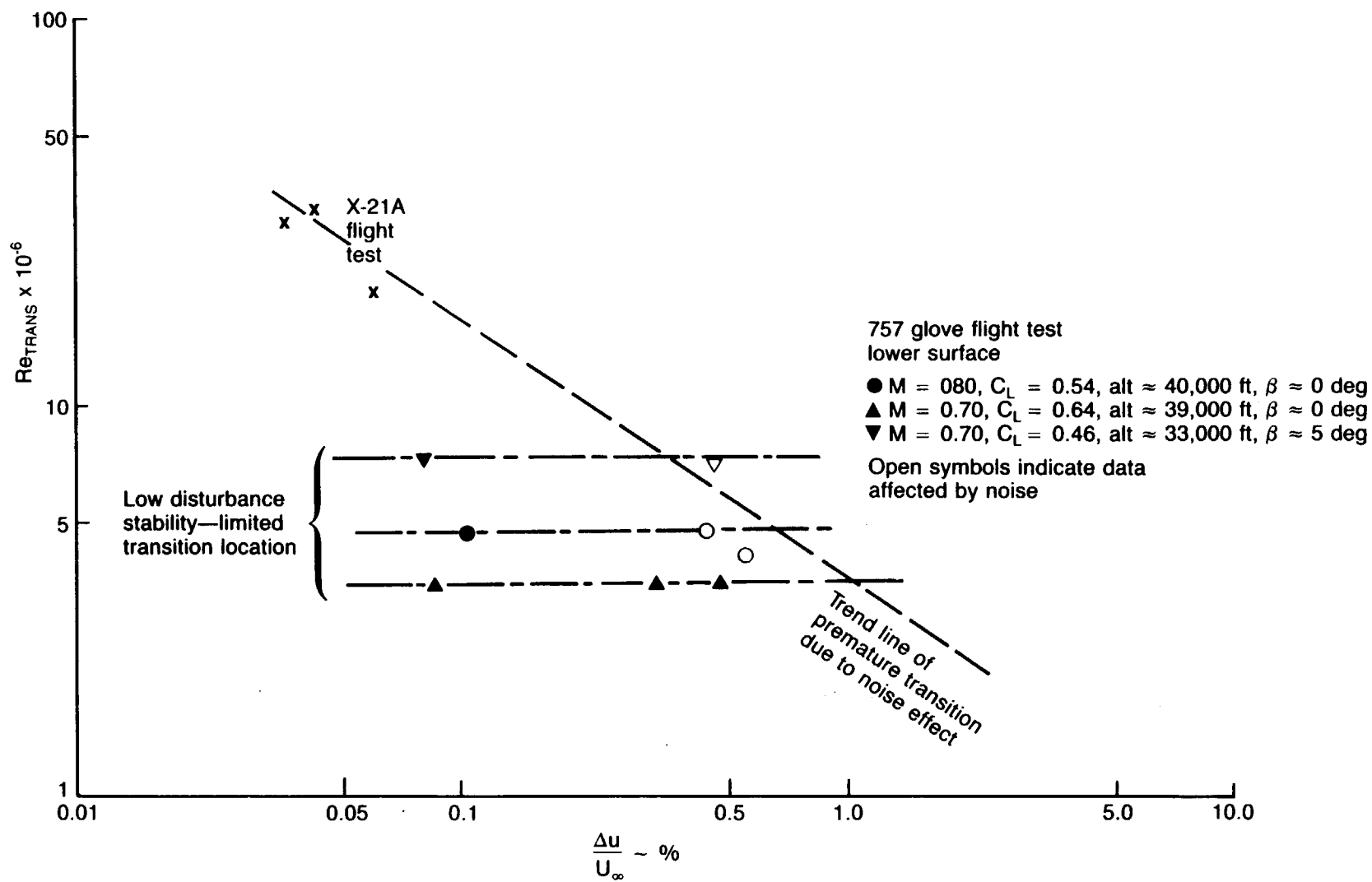


Figure 6-9. Interpretation of X-21A and 757 Flight Data Comparison

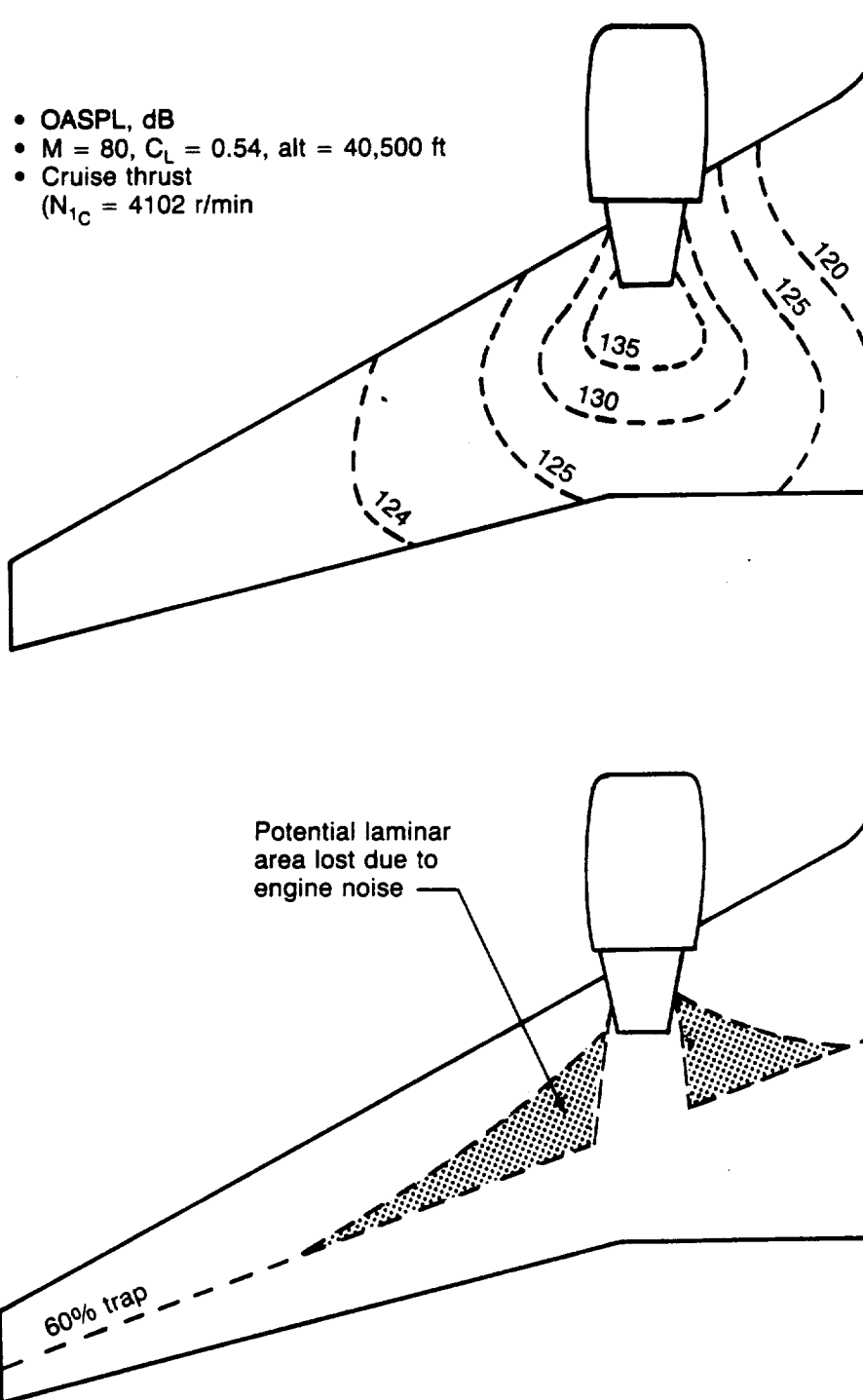


Figure 6-10. OASPL Distribution and Potential Loss of Laminar Area Due To Engine Noise
757 Lower Surface at Cruise

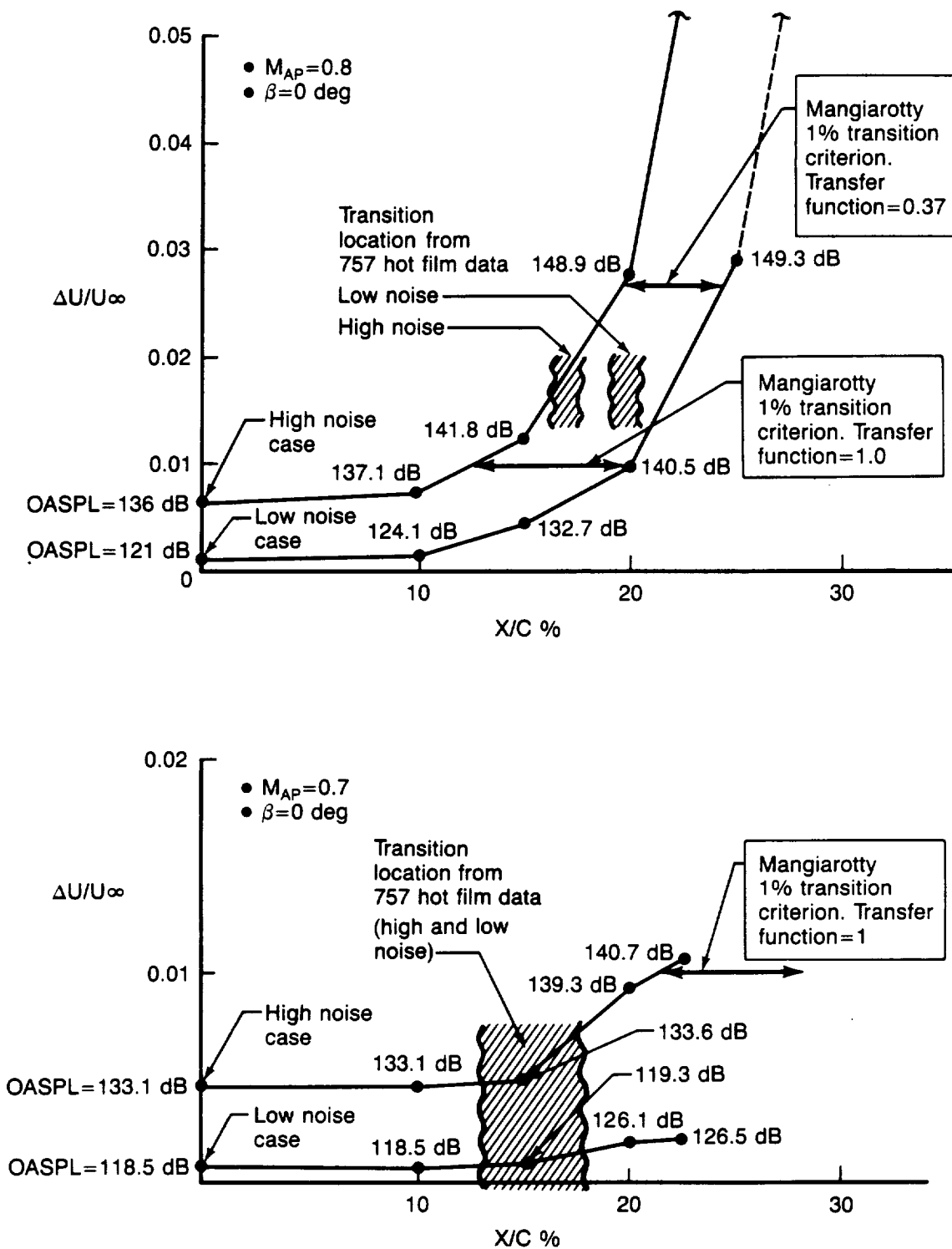


Figure 6-11. Amplified Boundary Layer Acoustic Disturbance Growth per Mangiarotti for $M_{AP}=0.8$ and $M_{AP}=0.7$

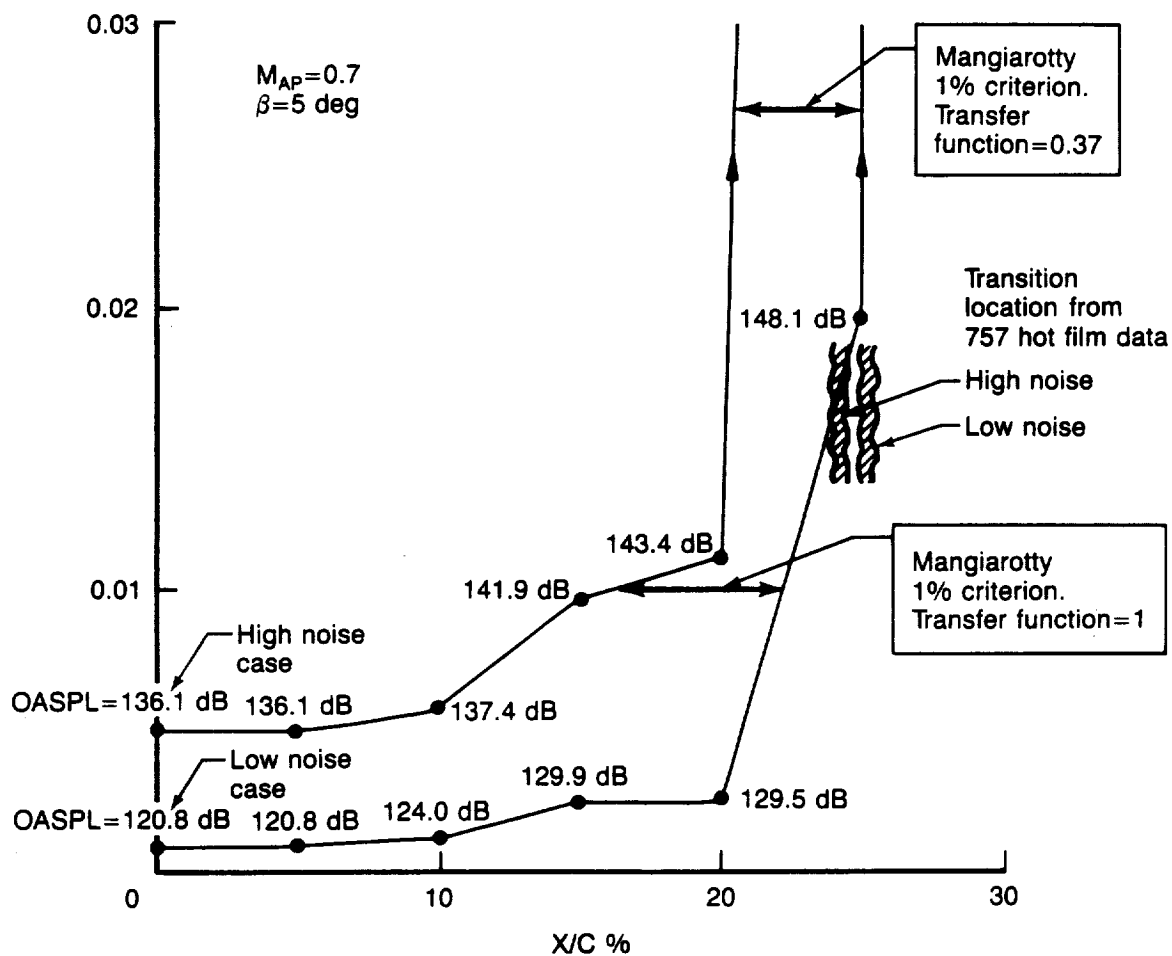


Figure 6-12. Amplified Boundary Layer Acoustic Disturbance Growth per Mangiarotty for $M_{AP}=0.7$, $\beta=5 \text{ deg}$

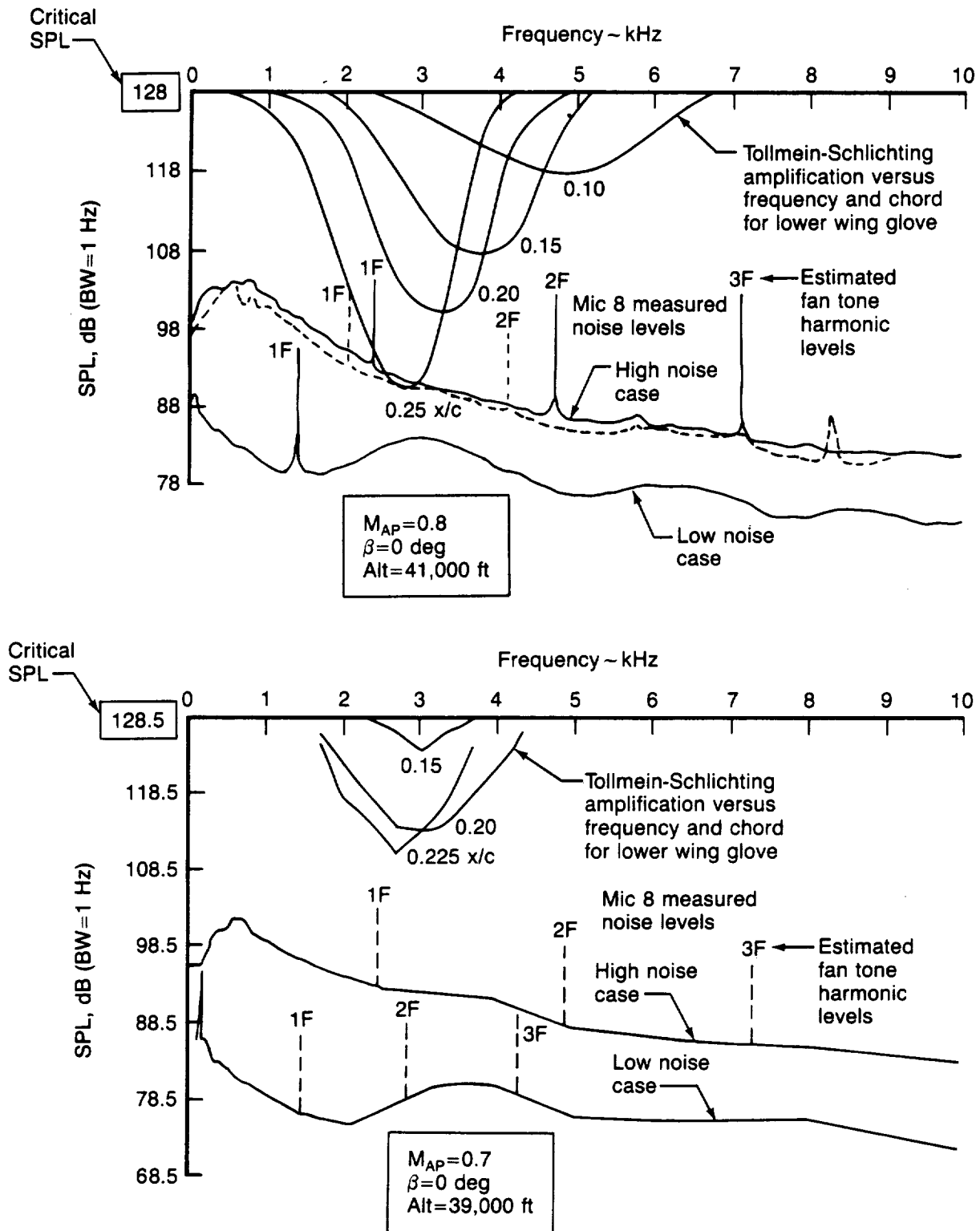


Figure 6-13. One Hz Bandwidth Measured Noise Versus Tollmein-Schlichting Amplification Curves Normalized to Critical SPL per Mungar, $M_{AP}=0.8$ and 0.7 , $\beta=0$ deg

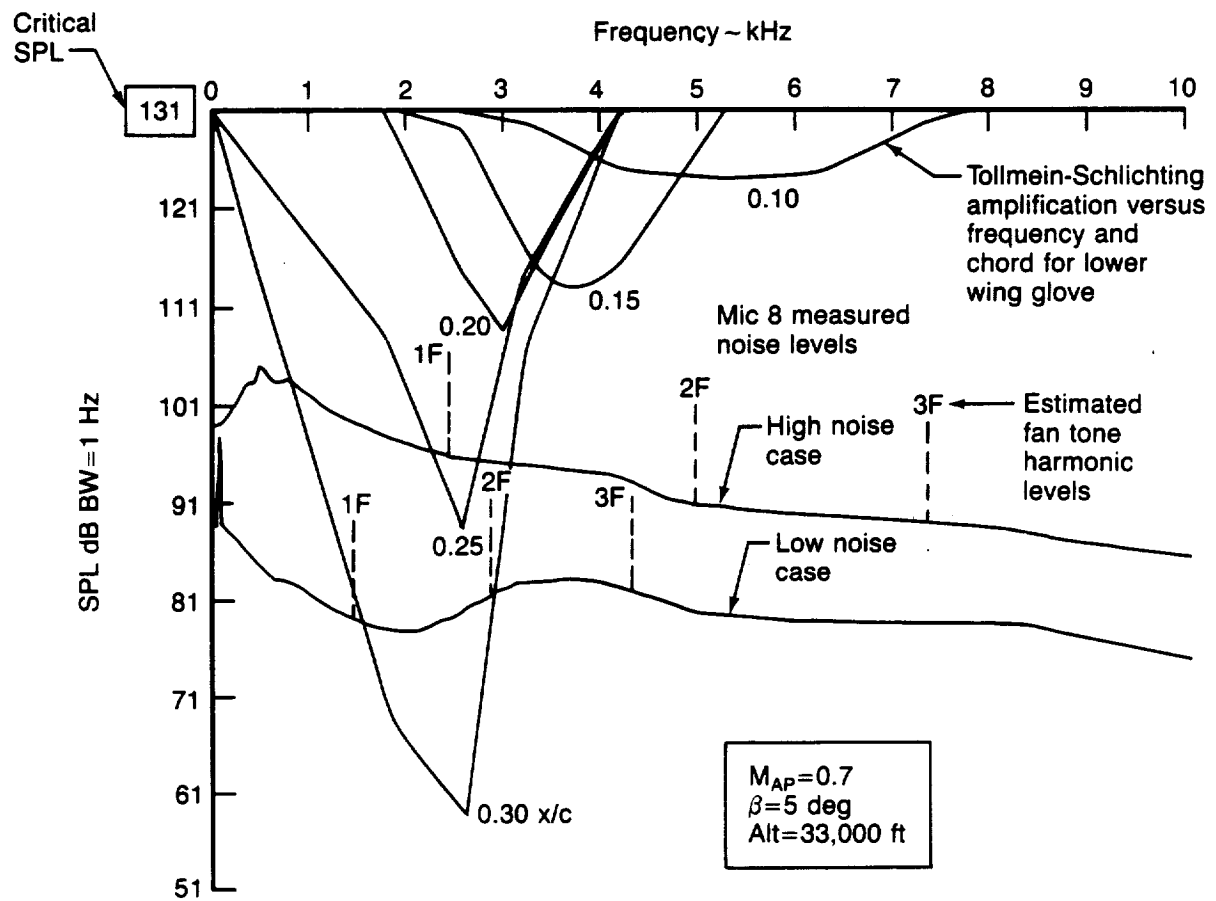


Figure 6-14. One Hz Bandwidth Measured Noise Versus Tollmein-Schlichting Amplification Curves Normalized to Critical SPL per Mungar, $M_{AP}=0.7$, $\beta=5$ deg

Table 6-1. Comparison of Transition x/c Percentage Predicted by Mangiarotty, Mungar, and Semiempirical Procedures With Measured 757 Data

Condition	Mangiarotty 1% criterion		Swift and Mungur 130 dB unit band- width criterion		757 hot film data lower wing glove		Semiempirical procedure	
	High noise level	Low noise level	High noise level	Low noise level	High noise level	Low noise level	High noise level	Low noise (background disturbance dominated)
$M_{AP}=0.8$ $\beta=0$ deg Alt=41K ft	Transfer function=1 13% 20% Transfer function=0.37 20% 24%		22%	30%	$\approx 17\%$	20%	14	17.5
$M_{AP}=0.7$ $\beta=0$ deg Alt=39K ft	Transfer function=1 21% > 30% Transfer function=0.37 > 30% > 30%		$\approx 30\%$	> 30%	13% to 18%	13% to 18%	16	18
$M_{AP}=0.7$ $\beta=5$ deg Alt=33K ft	Transfer function=1 $\approx 15\%$ $\approx 21\%$ Transfer function=0.37 21% 25%		$\approx 20\%$	$\approx 24\%$	24%	25%	21.5	23

6.3 SEMIEMPIRICAL PROCEDURE FOR PREDICTING THE ONSET OF LAMINAR BOUNDARY LAYER TRANSITION IN THE PRESENCE OF INTENSE SOUND

Combining the present N_{TS}/N_{CF} , F-111/757 criterion with the Mangiarotty (or Swift and Mungur) criterion directly to estimate the influence of noise on transition location would not consider any effect of crossflow on the sensitivity of the laminar boundary to noise. The empirical N_{TS}/N_{CF} , F-111/757 criterion used to evaluate *background* disturbance instability, as discussed in Section 6.1, however, implies an interaction of crossflow and TS disturbances. As seen in Figure 6-15, as the crossflow amplification factor increases the value of N_{TS} required for transition from laminar to turbulent, flow decreases. The combined F-111/757, Mangiarotty transition prediction method suggested in Section 6.2.2 uses the same TS transition criterion for all crossflow conditions.

A semiempirical procedure for predicting the onset of laminar boundary layer transition in the presence of sound that takes the interaction of crossflow and TS disturbances into account is now described. Figure 6-15 shows the F-111/757 transition data band with a mean line drawn through the band. This mean line is taken as the empirical transition criterion for boundary layer disturbances. Curves showing the 757 glove N_{TS}/N_{CF} trajectories taken from Section 6.1 are replotted on Figure 6-16. The effect of noise is considered as giving rise to an effective increase in N_{TS} for each point on the wing section trajectory. It is assumed, for the purposes of this method, that the crossflow disturbance is not affected by noise. Although there is no direct evidence of this, the discussion of Section 6.1 indicated that for the 757 glove the crossflow disturbance was not significantly influenced by noise. The increase in N_{TS} due to noise is evaluated as follows:

Suppose U_1 is the *background* disturbance velocity which when amplified according to TS stability calculations results in a disturbance of magnitude $U_{A1} = A.U_1$ where $A = e^{N_{TS}}$ is the amplification factor. If sound is added to the background disturbance the resulting amplified disturbance is

$$U_{A2} = A(U_1 + U_\alpha), \quad U_\alpha = \frac{P_{rms, acoustic}}{\rho c}$$

We now define a pseudo amplification

$$A' = \frac{U_{A2}}{U_1} = A (1 + U_\alpha/U_1)$$

and a pseudo N_{TS} factor

$$\begin{aligned} N_{TS}' &= \ln A' = \ln A + \ln(1 + U_\alpha/U_1) \\ &= N_{TS} + \ln(1 + U_\alpha/U_1) \\ \therefore (N' - N)_{TS} &= \ln(1 + U_\alpha/U_1) \end{aligned}$$

Therefore, the sound wave is viewed as causing an increase in the N_{TS} factor by $(N' - N) = \ln(1 + U_\alpha/U_1)$. This effectively shifts the wing section trajectory curve vertically resulting in a shift in the location where it crosses the transition criterion line.

The 757 NLF test data in Figures 6-1 to 6-6 was used to evaluate the above procedure. The observed results for the $M_{AP} = 0.8$, $\beta = 0$ -deg case were first used to determine U_1 . As shown in Figure 6-16, for this case the measured transition location for the low noise condition (121 dB) fell above the mean line of the band. Therefore, for purposes of this method, the mean line shape was maintained and it was shifted up locally to go through the measured transition location (20% chord). For the high noise condition (135.5 dB), the measured transition location moved forward by 3% chord to 17%. Figure 6-16 shows that an N_{TS} shift of 1 for the entire trajectory curve results in the required 3% forward movement of transition. Therefore, this is the ΔN_{TS} that the method assumes results from the high engine noise level. The initial disturbance velocity resulting from the high engine noise level is given by:

$$U_\alpha = \frac{P_{rms, acoustic}}{\rho c}$$

where

$$P_{rms} = P_{ref} * 10^{OASPL/20}$$

and

$$P_{ref} = 4.184 \times 10^{-7} \text{ psf}$$

For an OASPL of 135.5 dB, corresponding to the high noise condition, U_α is 4.6 ft/s.

If it is assumed that the 121 dB noise level gives a negligible contribution to the background disturbance, then the background noise level, U_1 , can be computed:

$$\Delta N_{TS} = 1n(1 + U_\alpha/U_1)$$

$$\Delta N_{TS} = 1.0; U_\alpha = 4.6 \text{ ft/s}$$

$$1.0 = 1n(1 + 4.6/U_1); U_1 = 2.7 \text{ ft/s}$$

This is a background disturbance intensity (U_1/U_∞ %) of 0.35%. Using this value of U_1 we can now calculate the ΔN_{TS} for the $M_{AP} = 0.7$, $\beta = 0$ -deg and $\beta = 5$ -deg cases.

$$M_{AP} = 0.7, \beta = 0 \text{ deg}$$

$$\text{Alt} = 39,000 \text{ ft}$$

$$OASPL_{MAX} = 133.5 \text{ dB}$$

$$U_\alpha = 3.32 \text{ fps}$$

$$\Delta N_{TS} = 0.80$$

$$M_{AP} = 0.7, \beta = 5 \text{ deg}$$

$$\text{Alt} = 33,000 \text{ ft}$$

$$OASPL_{MAX} = 135.9 \text{ dB}$$

$$U_\alpha = 3.37 \text{ fps}$$

$$\Delta N_{TS} = 0.81$$

From Figure 6-16 these ΔN_{TS} s result in estimated shifts of transition from $x/c = 0.23$ to $x/c \approx 0.215$ for the $M_{AP} = 0.7$, $\beta = 5$ -deg case and from $x/c = 0.18$ to $x/c = 0.16$ for the $M_{AP} = 0.7$, $\beta = 0$ -deg case. As seen in Table 6-1 these are reasonably close to the measured results.

Although the above procedure accounts for the interaction of T-S and crossflow disturbances, it does not consider the spectrum of the acoustic disturbances. The N_{TS} values associated with the N_{TS}/N_{CF} trajectory curves are the maximum spectral values. If the sound levels are very low at the frequencies of max N value the above calculations would probably be inaccurate. For the 757 data the narrow band spectra were very broad so that the calculations appear to be reasonably valid.

Summary

In summary, a method of using the F-111/757, N_{TS}/N_{CF} boundary layer transition criterion curve with acoustic disturbances is suggested which accounts for interaction of T-S and crossflow disturbances. The semiempirical method was presented to stimulate consideration of this type of an approach. As presented, this method does not consider the spectral details of the acoustic signal and is therefore, at best, only applicable to broadband noise. The method worked reasonably well with the 757 data when the assumption was made that the low noise levels (OASPLs of the order of 120 dB) resulted in disturbances that were small compared to the *background* disturbances. The background disturbance level was then estimated to be $U_1 \approx 2.7$ fps. Calculating the particle velocity of a plane wave with OASPL = 120 dB one obtains $U_a \approx 0.8$ fps (Alt = 40 Kft, $M_{AP} = 0.8$). While this is smaller than the calculated $U_1 = 2.3$ fps, it is not negligible in comparison.

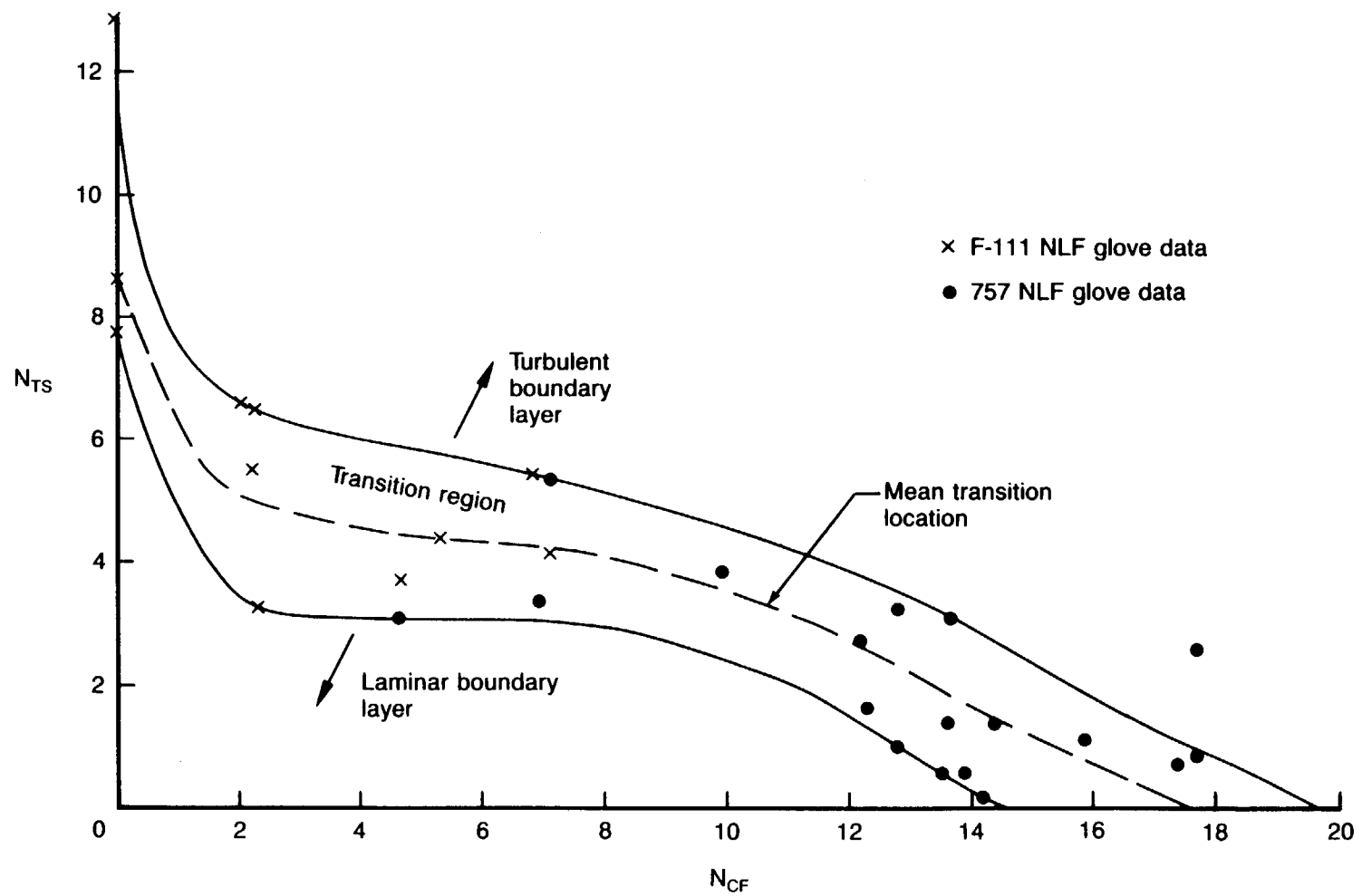


Figure 6-15. Tollmien-Schlichting Transition N-Factor Versus Crossflow Transition N-Factor

Figure 6-16. Illustration of Semiempirical NLF Transition Prediction Procedure

7.0 CONCLUSIONS AND RECOMMENDATIONS

CONCLUSIONS

The major conclusions resulting from the additional engineering analysis of the 757 NLF glove data are as follows:

1. For all 21 cases for which a boundary layer stability analysis was conducted, C-F disturbances were much more highly amplified than T-S disturbances. For 16 of the 21 cases, C-F N-factors were between 12 and 18.
2. The results of the boundary layer stability analysis, when combined with previous results based on F-111 NLF glove flight data (ref. 3) result in a new recommended transition data band for use in laminar flow design applications (see fig. 5-41).
3. Boundary layer stability analysis results indicate that the most critical T-S frequencies were in the 2500 to 3000 Hz range. The measured noise levels (1/3 octave) on the lower surface in this frequency range varied from about 105 to 110 dB at the lowest power setting to about 120 dB at the highest power setting. However, even though there was a significant variation in the measured noise level in the critical frequency range, the measured lower surface transition location showed only a small sensitivity to noise level.
4. Since C-F disturbances are the dominant cause of transition on the 757 NLF glove, the small observed effect of variations in engine noise level on the lower surface transition location may indicate that engine noise does not have a significant effect on C-F disturbances.
5. The 757 results for the effect of noise on the transition location, when interpreted in the light of boundary layer stability considerations, are not inconsistent with the general trends shown by the X-21A flight data. This implies that, for wing designs for which the low disturbance stability-limited transition location is further aft than in the present test, such as may be the case on an HLFC or LFC wing, engine noise effects on the extent of laminar flow may be significant.
6. On the lower wing surface, noise generated by the engine dominated the microphone measurements at higher engine power conditions.
7. The primary engine noise source at higher engine power conditions is broadband jet shock noise.
8. At moderate engine power conditions, many sources contribute to the noise floors, some of which were not identifiable. Those identified were cirrus clouds contamination, airflow disturbances from the outboard glove leading edge, engine bleed valve noise, and boundary layer turbulence generated by the surface microphone fairings.
9. Jet mixing noise was not evident in the measured noise data.
10. The upper wing surface noise measurements appear to be dominated by nonengine noise. The primary observation regarding the upper wing surface noise measurements is the apparent relation to the wing shock. It is not clear if the high noise levels are due to noise generated by the shock boundary layer interaction or to boundary layer pressure fluctuations directly when enhanced by the wing shock.
11. The upper surface noise levels may be influenced by wing trailing edge noise, secondary to shock boundary layer influence. However, the Lockheed prediction procedure was not helpful for evaluating the trailing edge noise. When *convective amplification* was included in the trailing edge predictions, large overprediction of the measured data resulted. When convective amplification was not included the trailing edge noise predictions were well below the measured data.

12. Use of convective amplification in the Lockheed predictions resulted in large overpredictions of the measured noise levels.
13. Both the Mangiarotty and Swift and Mungur methods for evaluating the effect of noise on laminar boundary layer transition resulted in predictions reasonably consistent with the measured results when the Tollmien-Schlichting disturbance amplifications were not small compared to the crossflow disturbance amplification. When the crossflow disturbance amplification was large compared to the T-S amplification, the Mangiarotty and Swift and Mungur procedures, which do not consider the crossflow, severely overpredicted the laminar flow range.
14. A semiempirical method of investigating the influence of noise on laminar boundary layer transition appears consistent with the 757 results, but needs further confirmation. This method uses the F-111/757 transition N-factor data band to account for the interaction of T-S and C-F disturbances in the presence of noise. It is probably only useful for evaluating the effect of broadband noise on laminar boundary layer transition because it does not explicitly consider the spectral details of the acoustic signal.

RECOMMENDATIONS

1. The influence of noise on the extent of laminar flow on an HLFC wing section should be investigated in a full-scale flight test. The results of the current study do not rule out the possibility of significant sensitivity to engine noise levels on the lower surface for such a configuration.
2. Whenever feasible, embedded pressure taps that are flush with the surface should be used rather than strip-a-tube to measure surface pressures. This would eliminate the need to correct the measured pressures for the strip-a-tube interference effect.
3. Microphones measuring noise in a laminar boundary layer should be flush mounted with the surface so they do not trip the boundary layer. When measuring noise near turbulent boundary layers, the microphone should be mounted on aerodynamic probes mounted outside the boundary layer.
4. Airframe flight noise measurements should not be made in the presence of cirrus clouds.
5. Further development of prediction methods is needed for jet broadband shock noise and wing trailing edge noise. Jet broadband shock noise was concluded to be the dominant engine noise source at normal airplane and engine cruise conditions affecting the lower wing boundary layer. The dominant noise source on the upper wing was due to the wing shock. If the shock is aft of the laminarized wing section, neither the wing shock noise nor the wing trailing edge noise should affect the boundary layer. If no shock is present however, trailing edge noise may be the dominant source affecting the upper wing surface.
6. The validity of the convective amplification corrections in the Lockheed prediction computer program is not supported by the 757 noise measurements. A switch should be incorporated into the computer program to remove this correction.
7. Carefully controlled experiments should be conducted to further develop the Swift and Mungur theory for sound/Tollmien-Schlichting instability interaction. The influence of crossflow on the sound/Tollmien-Schlichting interaction also needs to be investigated experimentally.
8. The F-111/757 based semiempirical procedure for predicting the onset of laminar boundary layer transition in the presence of intense broadband sound needs to be tested with data from other test situations to help establish its general usefulness.

8.0 REFERENCES

1. Boeing Commercial Airplane Co., "Flight Survey of the 757 Wing Noise Field and Its Effects on Laminar Boundary Layer Transition; Volume I - Program Description and Data Analysis," NASA CR-178216, March 1987.
2. Boeing Commercial Airplane Co., "Flight Survey of the 757 Wing Noise Field and Its Effects on Laminar Boundary Layer Transition; Volume II - Data Compilation," NASA CR-178217, March 1987.
3. Runyan, L. J., Navran, B. H., and Rozendaal, R. A., "F-111 Natural Laminar Flow Glove Flight Test Data Analysis and Boundary Layer Stability Analysis," NASA CR-166051, October 1983.
4. Swift, G. and Mungur, P., "A Study of the Prediction of Cruise Noise and Laminar Flow Control Noise Criteria for Subsonic Air Transports," NASA CR-159104, August 1979.
5. Butzel, L. M. Bohn, A. L., Armstrong, R. L., and Reed, J. B., "Noise Environment of Wing, Fuselage and Cabin Interior of a USB/STOL Airplane," NASA CR-159053, July 1979.
6. Lu, H. Y., "An Empirical Model for Prediction of Coaxial Jet Noise in Ambient Flow," AIAA 86-1912, AIAA 10th Aeroacoustics Conference, Seattle, WA, July 9-11, 1986.
7. "Laminar Flow Control Flight Test Results on the X-21A," USAF Contract AF33(657)-13930, Joint Report UAAF, Air Force Systems, 1964.
8. Mangiarotty, R. A., "Effects of Engine Noise on Aircraft Wing Laminar Boundary Layer Stability," *Journal Acoustical Society of America*, Vol. 70, No. 1, pp. 98-109, July 1981.
9. Carmichael, R. F., and Pelke, D. E., "In-Flight Noise Measurements Performed on the X-21A Laminar Flow Aircraft," Contract AF33(600)-42052, Document NOR-64-81, April 1964.
10. Tibbetts, J. G., "A Computer Program for the Prediction of Near-Field Noise of Aircraft in Cruising Flight—User's Guide," NASA CR-159274, June 1980.
11. Mack, L. M., "Computation of the Stability of the Laminar Compressible Boundary Layer," *Methods in Computational Physics*, edited by B. Adler, Academic Press, NY, pp. 247-299, 1965.
12. Mack, L. M., "On the Stability of the Boundary Layer on a Transonic Swept Wing," AIAA Paper 79-0164, AIAA 17th Aerospace Sciences Meeting, New Orleans, LA, January 15-17, 1979.
13. Mangiarotty, R. A., and Bohn, A. J. "Wind Tunnel Study of Acoustical Disturbance Effect on Controlled Laminar Flow," *AIAA Journal*, Vol. 18, No. 7, p. 801, July 1980.

9.0 APPENDIX: TABULATED PRESSURE DATA

This appendix contains tabulated pressure coefficient data for each of the 21 cases analyzed. As discussed in Section 5.2, two separate boundary layer analyses were made for each case using the infinite swept wing program, A552. This was necessitated by the variation in isobar sweep (typically from low to high) along the chord. Boundary layer data from the two solutions were then patched together using the low sweep results in the forward region and the high sweep results in the aft region. Thus, there are two tabulated pressure distributions for most cases and three for some cases where the isobar sweep variation was particularly large. The tabulations are in terms of C_{pN} versus s/c . In each case $s/c = 0$ corresponds to $x/c = 0$. This was a simplification justified by results for a number of cases from the Boeing transonic analysis code, A488. These results showed that the variation of the attachment line location from $s/c = 0$ is typically less than $\Delta x/c = 0.0002$, which corresponds to $\Delta s/c = 0.0001$. For each case, C_{pN} is based on the velocity component normal to an infinite sweptwing having the sweep angle used for that particular case. The attachment line C_{pN} also assumes that the leading edge sweep angle corresponds to that being used for the infinite sweptwing analysis, although in some cases it was necessary to make adjustments to the calculated C_{pN} at the attachment line to get the boundary layer program to run. For each tabulated pressure distribution, the corresponding sweep angle used in the infinite sweptwing analysis is noted.

PRECEDING PAGE BLANK NOT FILMED

$\Lambda = 20 \text{ deg}$		$\Lambda = 32 \text{ deg}$	
<u>s/c</u>	<u>C_{p_N}</u>	<u>s/c</u>	<u>C_{p_N}</u>
0	1.131	0	1.078
0.00107	1.128	0.00107	1.075
0.00214	1.117	0.00300	1.067
0.00378	1.083	0.00500	1.048
0.00480	1.055	0.00700	1.010
0.00598	1.017	0.00899	0.954
0.00734	0.972	0.01084	0.878
0.00899	0.908	0.01302	0.759
0.01084	0.807	0.01573	0.542
0.01302	0.653	0.01944	0.231
0.01573	0.441	0.02529	-0.133
0.01944	0.188	0.02798	-0.251
0.02529	-0.108	0.03328	-0.446
0.02798	-0.204	0.04000	-0.580
0.03328	-0.363	0.04821	-0.655
0.04000	-0.472	0.05919	-0.710
0.04821	-0.533	0.07245	-0.736
0.05919	-0.578	0.07970	-0.759
0.07245	-0.599	0.08989	-0.783
0.07970	-0.618	0.10008	-0.814
0.08989	-0.638	0.11024	-0.849
0.10008	-0.663	0.13559	-0.927
0.11024	-0.691	0.16086	-1.016
0.13559	-0.755	0.18610	-1.117
0.16086	-0.827	0.21128	-1.224
0.18610	-0.910	0.23644	-1.294
0.21128	-0.997	0.26149	-1.335
0.23644	-1.054	0.28655	-1.341
0.26149	-1.087	0.31158	-1.335
0.28655	-1.092		
0.31158	-1.087		

Table A-1. Input C_{p_N} Versus s/c for Case 1

$\Lambda = 22 \text{ deg}$		$\Lambda = 32 \text{ deg}$	
<u>s/c</u>	<u>C_{p_N}</u>	<u>s/c</u>	<u>C_{p_N}</u>
0	1.124	0	1.078
0.001	1.122	0.001	1.076
0.002	1.118	0.002	1.073
0.004	1.078	0.004	1.057
0.005	1.048	0.005	1.043
0.006	1.023	0.006	1.029
0.007	0.973	0.007	1.013
0.009	0.878	0.009	0.968
0.011	0.788	0.011	0.913
0.013	0.704	0.013	0.841
0.016	0.590	0.016	0.705
0.020	0.472	0.020	0.564
0.025	0.372	0.025	0.445
0.030	0.300	0.030	0.359
0.035	0.242	0.035	0.289
0.045	0.154	0.045	0.184
0.055	0.093	0.055	0.111
0.065	0.052	0.065	0.062
0.080	0.025	0.080	0.030
0.100	-0.002	0.100	-0.002
0.125	-0.030	0.125	-0.036
0.150	-0.060	0.150	-0.072
0.175	-0.083	0.175	-0.099
0.200	-0.103	0.200	-0.123
0.225	-0.120	0.225	-0.143
0.250	-0.117	0.250	-0.140

Table A-2. Input C_{p_N} Versus s/c for Case 2

$\Lambda = 20 \text{ deg}$		$\Lambda = 30 \text{ deg}$	
<u>s/c</u>	<u>C_{p_N}</u>	<u>s/c</u>	<u>C_{p_N}</u>
0	1.139	0	1.092
0.001	1.137	0.001	1.090
0.002	1.134	0.002	1.087
0.003	1.129	0.003	1.082
0.004	1.123	0.004	1.075
0.005	1.113	0.005	1.067
0.006	1.098	0.006	1.053
0.007	1.077	0.007	1.033
0.009	1.015	0.009	0.968
0.011	0.913	0.011	0.888
0.013	0.795	0.013	0.800
0.016	0.606	0.016	0.648
0.020	0.357	0.020	0.425
0.025	0.100	0.025	0.118
0.030	-0.067	0.030	-0.079
0.035	-0.163	0.035	-0.192
0.045	-0.295	0.045	-0.347
0.055	-0.363	0.055	-0.427
0.065	-0.404	0.065	-0.476
0.08	-0.442	0.08	-0.520
0.10	-0.488	0.10	-0.575
0.125	-0.538	0.125	-0.633
0.150	-0.600	0.150	-0.706
0.175	-0.719	0.175	-0.847
0.200	-0.838	0.200	-0.987
0.225	-0.885	0.225	-1.042
0.250	-0.918	0.250	-1.081
0.275	-0.940	0.275	-1.107
0.315	-0.957	0.315	-1.127

Table A-3. Input C_{p_N} Versus s/c for Case 3

$\Lambda = 16.5 \text{ deg}$		$\Lambda = 27.5 \text{ deg}$	
<u>s/c</u>	<u>C_{p_N}</u>	<u>s/c</u>	<u>C_{p_N}</u>
0	1.010	0	1.083
0.001	1.010	0.001	1.082
0.002	1.009	0.002	1.076
0.003	1.007	0.003	1.062
0.004	1.000	0.004	1.027
0.005	0.990	0.005	1.000
0.006	0.965	0.006	0.958
0.007	0.927	0.007	0.900
0.008	0.891	0.008	0.850
0.009	0.841	0.009	0.789
0.010	0.800	0.010	0.700
0.012	0.692	0.012	0.580
0.014	0.640	0.014	0.450
0.016	0.464	0.016	0.330
0.018	0.372	0.018	0.220
0.020	0.275	0.020	0.120
0.025	-0.017	0.025	-0.068
0.030	-0.234	0.030	-0.220
0.035	-0.348	0.035	-0.330
0.040	-0.432	0.040	-0.429
0.045	-0.498	0.045	-0.470
0.050	-0.555	0.050	-0.501
0.055	-0.594	0.055	-0.513
0.060	-0.614	0.060	-0.527
0.070	-0.622	0.070	-0.530
0.080	-0.609	0.080	-0.519
0.090	-0.592	0.090	-0.515
0.100	-0.585	0.100	-0.505
0.120	-0.620	0.120	-0.527
0.140	-0.725	0.140	-0.625
0.160	-0.858	0.160	-0.738
0.180	-0.930	0.180	-0.799
0.200	-0.980	0.200	-0.840
0.220	-1.015	0.220	-0.875
0.240	-1.045	0.240	-0.898
0.260	-1.063	0.260	-0.915
0.280	-1.080	0.280	-0.930
0.300	-1.090	0.300	-0.945

Table A-4. Input C_{p_N} Versus s/c for Case 4

$\Lambda = 14.5 \text{ deg}$		$\Lambda = 38.5 \text{ deg}$	
s/c	C_{p_N}	s/c	C_{p_N}
0	1.1458	0	1.0443
0.001	1.140	0.001	1.039
0.002	1.139	0.002	1.036
0.003	1.138	0.003	1.034
0.004	1.136	0.004	1.031
0.005	1.130	0.005	1.026
0.006	1.100	0.006	1.019
0.007	1.060	0.007	1.007
0.008	1.018	0.008	0.988
0.009	0.929	0.009	0.962
0.010	0.842	0.010	0.930
0.012	0.590	0.012	0.640
0.014	0.350	0.014	0.400
0.016	0.183	0.016	0.320
0.018	0.157	0.018	0.279
0.020	0.146	0.020	0.248
0.025	0.124	0.025	0.190
0.030	0.106	0.030	0.154
0.035	0.091	0.035	0.124
0.040	0.077	0.040	0.100
0.045	0.062	0.045	0.082
0.050	0.050	0.050	0.063
0.055	0.039	0.055	0.050
0.060	0.029	0.060	0.037
0.070	0.015	0.070	0.021
0.080	0.003	0.080	0.000
0.090	-0.005	0.090	-0.018
0.100	-0.019	0.100	-0.032
0.120	-0.038	0.120	-0.056
0.140	-0.047	0.140	-0.080
0.160	-0.072	0.160	-0.116
0.180	-0.107	0.180	-0.168
0.200	-0.134	0.200	-0.218
0.220	-0.167	0.220	-0.250
0.240	-0.185	0.240	-0.280
0.260	-0.198	0.260	-0.300
0.280	-0.205	0.280	-0.312
0.300	-0.210	0.300	-0.322
0.320	-0.219	0.320	-0.330

Table A-5. Input C_{p_N} Versus s/c for Case 5

$\Lambda = 21.6 \text{ deg}$

$\Lambda = 37.6 \text{ deg}$

<u>s/c</u>	<u>C_{pN}</u>	<u>s/c</u>	<u>C_{pN}</u>
0	1.0936	0	1.0382
0.001	1.093	0.001	1.038
0.002	1.092	0.002	1.037
0.003	1.090	0.003	1.036
0.004	1.088	0.004	1.035
0.005	1.080	0.005	1.034
0.006	1.075	0.006	1.033
0.007	1.063	0.007	1.032
0.008	1.048	0.008	1.029
0.009	1.026	0.009	1.021
0.010	0.990	0.010	1.015
0.012	0.867	0.012	1.000
0.014	0.783	0.014	0.980
0.016	0.728	0.016	0.957
0.018	0.680	0.018	0.924
0.020	0.643	0.020	0.892
0.025	0.578	0.025	0.800
0.030	0.522	0.030	0.716
0.035	0.473	0.035	0.640
0.040	0.429	0.040	0.580
0.045	0.382	0.045	0.527
0.050	0.344	0.050	0.479
0.055	0.310	0.055	0.433
0.060	0.281	0.060	0.393
0.070	0.241	0.070	0.334
0.080	0.204	0.080	0.294
0.090	0.180	0.090	0.255
0.100	0.160	0.100	0.225
0.120	0.132	0.120	0.177
0.140	0.100	0.140	0.132
0.160	0.068	0.160	0.101
0.180	0.059	0.180	0.080
0.200	0.040	0.200	0.060
0.220	0.024	0.220	0.042
0.240	0.010	0.240	0.027
0.260	0.001	0.260	0.000
0.280	-0.005	0.280	-0.002
0.300	-0.008	0.300	-0.005
0.320	-0.018	0.320	-0.010

Table A-6. Input C_{pN} Versus s/c for Case 6

$\Lambda = 16 \text{ deg}$		$\Lambda = 20 \text{ deg}$	
<u>s/c</u>	<u>C_{p_N}</u>	<u>s/c</u>	<u>C_{p_N}</u>
0	1.0986	0	1.0986
0.001	1.094	0.001	1.094
0.002	1.091	0.002	1.091
0.003	1.087	0.003	1.090
0.004	1.078	0.004	1.085
0.005	1.060	0.005	1.075
0.006	1.038	0.006	1.060
0.007	1.012	0.007	1.045
0.008	0.990	0.008	1.025
0.009	0.960	0.009	1.000
0.010	0.930	0.010	0.980
0.012	0.902	0.012	0.925
0.014	0.818	0.014	0.870
0.016	0.770	0.016	0.822
0.018	0.732	0.018	0.785
0.020	0.704	0.020	0.750
0.025	0.642	0.025	0.675
0.030	0.600	0.030	0.627
0.035	0.572	0.035	0.590
0.040	0.541	0.040	0.556
0.045	0.512	0.045	0.526
0.050	0.484	0.050	0.497
0.055	0.450	0.055	0.472
0.060	0.424	0.060	0.447
0.070	0.376	0.070	0.390
0.080	0.325	0.080	0.360
0.090	0.310	0.090	0.320
0.100	0.275	0.100	0.285
0.120	0.230	0.120	0.240
0.140	0.200	0.140	0.218
0.160	0.170	0.160	0.190
0.180	0.135	0.180	0.135
0.200	0.100	0.200	0.095
0.220	0.070	0.220	0.065
0.240	0.045	0.240	0.044
0.260	0.020	0.260	0.018
0.280	0.000	0.280	0.000
0.300	-0.010	0.300	-0.015
0.320	-0.020	0.320	-0.021

Table A-7. Input C_{p_N} Versus s/c for Case 7

$\Lambda = 25 \text{ deg}$

s/c	C_{p_N}
0	1.097
0.001	1.096
0.002	1.095
0.003	1.094
0.004	1.093
0.005	1.090
0.006	1.082
0.007	1.076
0.008	1.068
0.009	1.052
0.010	1.040
0.012	1.000
0.014	0.960
0.016	0.915
0.018	0.860
0.020	0.805
0.025	0.700
0.030	0.638
0.035	0.586
0.040	0.555
0.045	0.536
0.050	0.520
0.055	0.495
0.060	0.473
0.070	0.436
0.080	0.391
0.090	0.358
0.100	0.330
0.120	0.295
0.140	0.280
0.160	0.265
0.180	0.274
0.200	0.222
0.220	0.206
0.240	0.199
0.260	0.180
0.280	0.160
0.300	0.145
0.320	0.135

*Note: Only one
sweep angle was used for
this case.

Table A-8. Input C_{p_N} Versus s/c for Case 8

$\cdot\Lambda = 19.8 \text{ deg}$		$\cdot\Lambda = 42.8 \text{ deg}$	
<u>s/c</u>	<u>C_{p_N}</u>	<u>s/c</u>	<u>C_{p_N}</u>
0	1.116	0	1.0198
0.001	1.100	0.001	1.019
0.002	1.090	0.002	1.018
0.003	1.078	0.003	1.015
0.004	1.060	0.004	1.008
0.005	1.039	0.005	0.998
0.006	1.000	0.006	0.979
0.007	0.945	0.007	0.950
0.008	0.840	0.008	0.881
0.009	0.470	0.009	0.777
0.010	0.180	0.010	0.615
0.012	-0.200	0.012	0.092
0.014	-0.330	0.014	-0.475
0.016	-0.405	0.016	-0.623
0.018	-0.455	0.018	-0.710
0.020	-0.488	0.020	-0.762
0.025	-0.322	0.025	-0.847
0.030	-0.546	0.030	-0.904
0.035	-0.570	0.035	-0.943
0.040	-0.590	0.040	-0.972
0.045	-0.600	0.045	-0.994
0.050	-0.610	0.050	-1.017
0.055	-0.622	0.055	-1.031
0.060	-0.632	0.060	-1.048
0.070	-0.648	0.070	-1.067
0.080	-0.659	0.080	-1.080
0.090	-0.675	0.090	-1.107
0.100	-0.690	0.100	-1.128
0.120	-0.710	0.120	-1.160
0.140	-0.723	0.140	-1.198
0.160	-0.744	0.160	-1.227
0.180	-0.770	0.180	-1.272
0.200	-0.815	0.200	-1.340
0.220	-0.880	0.220	-1.445
0.240	-0.960	0.240	-1.578
0.260	-1.018	0.260	-1.670
0.280	-1.020	0.280	-1.681
0.300	-1.000	0.300	-1.623
0.320	-0.935	0.320	-1.540

Table A-9. Input C_{p_N} Versus s/c for Case 9

$\Lambda = 19.4 \text{ deg}$		$\Lambda = 32.4 \text{ deg}$	
<u>s/c</u>	<u>C_{p_N}</u>	<u>s/c</u>	<u>C_{p_N}</u>
0	1.1355	0	1.0772
0.001	1.134	0.001	1.077
0.002	1.132	0.002	1.076
0.003	1.130	0.003	1.075
0.004	1.128	0.004	1.072
0.005	1.125	0.005	1.069
0.006	1.120	0.006	1.060
0.007	1.110	0.007	1.048
0.008	1.100	0.008	1.033
0.009	1.090	0.009	1.020
0.010	1.079	0.010	0.993
0.012	1.039	0.012	0.930
0.014	0.985	0.014	0.840
0.016	0.905	0.016	0.728
0.018	0.790	0.018	0.590
0.020	0.660	0.020	0.450
0.025	0.230	0.025	0.110
0.030	-0.194	0.030	-0.170
0.035	-0.336	0.035	-0.365
0.040	-0.408	0.040	-0.480
0.045	-0.451	0.045	-0.544
0.050	-0.480	0.050	-0.587
0.055	-0.496	0.055	-0.615
0.060	-0.505	0.060	-0.630
0.070	-0.509	0.070	-0.637
0.080	-0.510	0.080	-0.638
0.090	-0.510	0.090	-0.639
0.100	-0.513	0.100	-0.640
0.120	-0.522	0.120	-0.659
0.140	-0.555	0.140	-0.710
0.160	-0.640	0.160	-0.810
0.180	-0.760	0.180	-0.934
0.200	-0.850	0.200	-1.058
0.220	-0.927	0.220	-1.170
0.240	-0.973	0.240	-1.222
0.260	-0.990	0.260	-1.240
0.280	-0.993	0.280	-1.238
0.300	-0.985	0.300	-1.226
0.320	-0.960	0.320	-1.210

Table A-10. Input C_{p_N} Versus s/c for Case 10

$\Lambda = 19.9 \text{ deg}$		$\Lambda = 32.9 \text{ deg}$	
<u>s/c</u>	<u>C_{p_N}</u>	<u>s/c</u>	<u>C_{p_N}</u>
0	1.1308	0	1.0731
0.001	1.130	0.001	1.071
0.002	1.129	0.002	1.070
0.003	1.127	0.003	1.069
0.004	1.125	0.004	1.068
0.005	1.120	0.005	1.066
0.006	1.114	0.006	1.062
0.007	1.109	0.007	1.050
0.008	1.100	0.008	1.040
0.009	1.081	0.009	1.022
0.010	1.064	0.010	0.996
0.012	1.000	0.012	0.872
0.014	0.920	0.014	0.740
0.016	0.832	0.016	0.589
0.018	0.700	0.018	0.448
0.020	0.530	0.020	0.320
0.025	0.109	0.025	0.0
0.030	-0.177	0.030	-0.200
0.035	-0.288	0.035	-0.310
0.040	-0.348	0.040	-0.395
0.045	-0.395	0.045	-0.465
0.050	-0.428	0.050	-0.518
0.055	-0.458	0.055	-0.569
0.060	-0.476	0.060	-0.613
0.070	-0.491	0.070	-0.660
0.080	-0.503	0.080	-0.680
0.090	-0.515	0.090	-0.690
0.100	-0.535	0.100	-0.693
0.120	-0.584	0.120	-0.715
0.140	-0.640	0.140	-0.784
0.160	-0.710	0.160	-0.890
0.180	-0.820	0.180	-1.042
0.200	-0.918	0.200	-1.155
0.220	-0.962	0.220	-1.210
0.240	-0.982	0.240	-1.230
0.260	-1.000	0.260	-1.245
0.280	-1.007	0.280	-1.262
0.300	-1.010	0.300	-1.278
0.320	-1.022	0.322	-1.290

Table A-11. Input C_{p_N} Versus s/c for Case 11

$\Lambda = 21.9 \text{ deg}$		$\Lambda = 27.9 \text{ deg}$	
<u>s/c</u>	<u>C_{p_N}</u>	<u>s/c</u>	<u>C_{p_N}</u>
0	1.1330	0	1.1047
0.001	1.132	0.001	1.104
0.002	1.131	0.002	1.102
0.003	1.127	0.003	1.100
0.004	1.120	0.004	1.097
0.005	1.110	0.005	1.090
0.006	1.102	0.006	1.084
0.007	1.090	0.007	1.076
0.008	1.080	0.008	1.070
0.009	1.065	0.009	1.060
0.010	1.050	0.010	1.050
0.012	1.009	0.012	1.029
0.014	0.955	0.014	0.998
0.016	0.896	0.016	0.960
0.018	0.829	0.018	0.910
0.020	0.755	0.020	0.840
0.025	0.440	0.025	0.399
0.030	-0.070	0.030	-0.050
0.035	-0.237	0.035	-0.226
0.040	-0.310	0.040	-0.315
0.045	-0.351	0.045	-0.368
0.050	-0.388	0.050	-0.409
0.055	-0.406	0.055	-0.431
0.060	-0.408	0.060	-0.450
0.070	-0.415	0.070	-0.451
0.080	-0.419	0.080	-0.452
0.090	-0.421	0.090	-0.458
0.100	-0.430	0.100	-0.465
0.120	-0.474	0.120	-0.520
0.140	-0.558	0.140	-0.610
0.160	-0.661	0.160	-0.730
0.180	-0.768	0.180	-0.840
0.200	-0.850	0.200	-0.940
0.220	-0.918	0.220	-1.008
0.240	-0.950	0.240	-1.019
0.260	-0.966	0.260	-1.058
0.280	-0.975	0.280	-1.060
0.300	-0.961	0.300	-1.050
0.320	-0.915	0.320	-1.020

Table A-12. Input C_{p_N} Versus s/c for Case 12

$\Lambda = 16 \text{ deg}$

$\Lambda = 30 \text{ deg}$

<u>s/c</u>	<u>C_{pN}</u>	<u>s/c</u>	<u>C_{pN}</u>
0	1.1410	0	1.0853
0.001	1.139	0.001	1.084
0.002	1.133	0.002	1.080
0.003	1.128	0.003	1.076
0.004	1.120	0.004	1.070
0.005	1.104	0.005	1.055
0.006	1.087	0.006	1.037
0.007	1.056	0.007	1.008
0.008	0.990	0.008	0.960
0.009	0.840	0.009	0.880
0.010	0.720	0.010	0.700
0.012	0.430	0.012	0.330
0.014	0.160	0.014	-0.030
0.016	-0.115	0.016	-0.390
0.018	-0.400	0.018	-0.568
0.020	-0.520	0.020	-0.636
0.025	-0.579	0.025	-0.708
0.030	-0.587	0.030	-0.718
0.035	-0.592	0.035	-0.724
0.040	-0.598	0.040	-0.732
0.045	-0.603	0.045	-0.740
0.050	-0.608	0.050	-0.747
0.055	-0.612	0.055	-0.753
0.060	-0.620	0.060	-0.761
0.070	-0.631	0.070	-0.780
0.080	-0.640	0.080	-0.790
0.090	-0.654	0.090	-0.812
0.100	-0.672	0.100	-0.840
0.120	-0.718	0.120	-0.888
0.140	-0.760	0.140	-0.940
0.160	-0.808	0.160	-0.999
0.180	-0.860	0.180	-1.055
0.200	-0.910	0.200	-1.124
0.220	-0.972	0.220	-1.204
0.240	-1.032	0.240	-1.280
0.260	-1.102	0.260	-1.360
0.280	-1.178	0.280	-1.460
0.300	-1.262	0.300	-1.564
0.320	-1.370	0.320	-1.678

Table A-13. Input C_{pN} Versus s/c for Case 13

$\Lambda = 20 \text{ deg}$		$\Lambda = 27.5 \text{ deg}$	
<u>s/c</u>	<u>C_{p_N}</u>	<u>s/c</u>	<u>C_{p_N}</u>
0	1.1275	0	1.0967
0.001	1.126	0.001	1.094
0.002	1.124	0.002	1.090
0.003	1.121	0.003	1.084
0.004	1.118	0.004	1.080
0.005	1.109	0.005	1.073
0.006	0.098	0.006	1.066
0.007	0.085	0.007	1.055
0.008	0.070	0.008	1.041
0.009	0.058	0.009	1.028
0.010	0.009	0.010	1.010
0.012	0.978	0.012	0.965
0.014	0.906	0.014	0.920
0.016	0.829	0.016	0.869
0.018	0.750	0.018	0.813
0.020	0.680	0.020	0.769
0.025	0.589	0.025	0.677
0.030	0.527	0.030	0.590
0.035	0.476	0.035	0.538
0.040	0.434	0.040	0.489
0.045	0.395	0.045	0.443
0.050	0.369	0.050	0.408
0.055	0.340	0.055	0.378
0.060	0.320	0.060	0.358
0.070	0.290	0.070	0.319
0.080	0.260	0.080	0.298
0.090	0.240	0.090	0.270
0.100	0.218	0.100	0.250
0.120	0.180	0.120	0.205
0.140	0.143	0.140	0.168
0.160	0.100	0.160	0.122
0.180	0.070	0.180	0.080
0.200	0.050	0.200	0.052
0.220	0.030	0.220	0.030
0.240	0.010	0.240	0.010
0.260	0.000	0.260	0.000
0.280	0.001	0.280	-0.001
0.300	-0.004	0.300	-0.004
0.320	-0.009	0.320	-0.010

Table A-14. Input C_{p_N} Versus s/c for Case 14

$\Lambda = 20.1 \text{ deg}$

$\Lambda = 38.1 \text{ deg}$

<u>s/c</u>	<u>C_{p_N}</u>	<u>s/c</u>	<u>C_{p_N}</u>
0	1.1288	0	1.0467
0.001	1.128	0.001	1.046
0.002	1.127	0.002	1.045
0.003	1.121	0.003	1.043
0.004	1.116	0.004	1.040
0.005	1.110	0.005	1.037
0.006	1.100	0.006	1.030
0.007	1.092	0.007	1.023
0.008	1.070	0.008	1.018
0.009	1.050	0.009	1.008
0.010	1.025	0.010	0.994
0.012	0.969	0.012	0.959
0.014	0.873	0.014	0.908
0.016	0.730	0.016	0.830
0.018	0.572	0.018	0.728
0.020	0.408	0.020	0.586
0.025	0.010	0.025	0.000
0.030	-0.330	0.030	-0.479
0.035	-0.449	0.035	-0.650
0.040	-0.498	0.040	-0.700
0.045	-0.522	0.045	-0.730
0.050	-0.540	0.050	-0.760
0.055	-0.554	0.055	-0.789
0.060	-0.568	0.060	-0.812
0.070	-0.584	0.070	-0.850
0.080	-0.600	0.080	-0.870
0.090	-0.620	0.090	-0.892
0.100	-0.638	0.100	-0.918
0.120	-0.674	0.120	-0.951
0.140	-0.716	0.140	-1.015
0.160	-0.760	0.160	-1.090
0.180	-0.840	0.180	-1.210
0.200	-0.925	0.200	-1.328
0.220	-1.004	0.220	-1.440
0.240	-1.048	0.240	-1.500
0.260	-1.072	0.260	-1.535
0.280	-1.068	0.280	-1.530
0.300	-1.050	0.300	-1.514
0.320	-1.020	0.320	-1.465

Table A-15. Input C_{p_N} Versus s/c for Case 15

$\Lambda = 31.1 \text{ deg}$		$\Lambda = 41.6 \text{ deg}$	
s/c	C_{p_N}	s/c	C_{p_N}
0	1.0811	0	1.0293
0.001	1.079	0.001	1.029
0.002	1.077	0.002	1.028
0.003	1.072	0.003	1.026
0.004	1.068	0.004	1.021
0.005	1.060	0.005	1.012
0.006	1.050	0.006	1.002
0.007	1.037	0.007	0.989
0.008	1.020	0.008	0.970
0.009	0.998	0.009	0.950
0.010	0.968	0.010	0.921
0.012	0.898	0.012	0.860
0.014	0.806	0.014	0.793
0.016	0.710	0.016	0.726
0.018	0.610	0.018	0.660
0.020	0.515	0.020	0.590
0.025	0.316	0.025	0.413
0.030	0.213	0.030	0.262
0.035	0.177	0.035	0.202
0.040	0.150	0.040	0.183
0.045	0.130	0.045	0.170
0.050	0.120	0.050	0.160
0.055	0.111	0.055	0.149
0.060	0.106	0.060	0.136
0.070	0.091	0.070	0.112
0.080	0.078	0.080	0.090
0.090	0.060	0.090	0.067
0.100	0.042	0.100	0.048
0.120	0.020	0.120	0.017
0.140	0.000	0.140	-0.015
0.160	-0.033	0.160	-0.048
0.180	-0.061	0.180	-0.080
0.200	-0.085	0.200	-0.110
0.220	-0.100	0.220	-0.127
0.240	-0.100	0.240	-0.120
0.260	-0.088	0.260	-0.110
0.280	-0.063	0.280	-0.080
0.300	-0.040	0.300	-0.042
0.320	-0.015	0.320	-0.006

Table A-16. Input C_{p_N} Versus s/c for Case 16

$\cdot\Lambda = 18.4 \text{ deg}$

$\cdot\Lambda = 30.9 \text{ deg}$

<u>s/c</u>	<u>C_{pN}</u>	<u>s/c</u>	<u>C_{pN}</u>
0	1.1366	0	1.0830
0.001	1.136	0.001	1.082
0.002	1.135	0.002	1.080
0.003	1.134	0.003	1.078
0.004	1.130	0.004	1.074
0.005	1.123	0.005	1.070
0.006	1.115	0.006	1.064
0.007	1.102	0.007	1.055
0.008	1.089	0.008	1.044
0.009	1.075	0.009	1.030
0.010	1.060	0.010	1.018
0.012	0.999	0.012	0.970
0.014	0.920	0.014	0.900
0.016	0.800	0.016	0.780
0.018	0.660	0.018	0.630
0.020	0.520	0.020	0.480
0.025	0.140	0.025	0.090
0.030	-0.230	0.030	-0.280
0.035	-0.380	0.035	-0.432
0.040	-0.450	0.040	-0.530
0.045	-0.491	0.045	-0.572
0.050	-0.507	0.050	-0.601
0.055	-0.509	0.055	-0.620
0.060	-0.510	0.060	-0.623
0.070	-0.511	0.070	-0.624
0.080	-0.512	0.080	-0.625
0.090	-0.513	0.090	-0.626
0.100	-0.514	0.100	-0.631
0.120	-0.534	0.120	-0.644
0.140	-0.592	0.140	-0.710
0.160	-0.698	0.160	-0.850
0.180	-0.798	0.180	-0.972
0.200	-0.872	0.200	-1.080
0.220	-0.940	0.220	-1.140
0.240	-0.965	0.240	-1.172
0.260	-0.979	0.260	-1.193
0.280	-0.971	0.280	-1.185
0.300	-0.960	0.300	-1.170
0.320	-0.930	0.320	-1.140

Table A-17. Input C_{pN} Versus s/c for Case 17

$\Lambda = 22.9 \text{ deg}$		$\Lambda = 35.9 \text{ deg}$	
<u>s/c</u>	<u>C_{p_N}</u>	<u>s/c</u>	<u>C_{p_N}</u>
0	1.1193	0	1.0584
0.001	1.119	0.001	1.058
0.002	1.118	0.002	1.057
0.003	1.117	0.003	1.054
0.004	1.110	0.004	1.048
0.005	1.100	0.005	1.038
0.006	1.081	0.006	1.027
0.007	1.058	0.007	1.013
0.008	1.010	0.008	0.999
0.009	0.910	0.009	0.970
0.010	0.785	0.010	0.940
0.012	0.530	0.012	0.830
0.014	0.400	0.014	0.700
0.016	0.333	0.016	0.570
0.018	0.290	0.018	0.470
0.020	0.257	0.020	0.390
0.025	0.195	0.025	0.255
0.030	0.149	0.030	0.180
0.035	0.118	0.035	0.140
0.040	0.090	0.040	0.110
0.045	0.070	0.045	0.087
0.050	0.050	0.050	0.070
0.055	0.037	0.055	0.054
0.060	0.025	0.060	0.040
0.070	0.000	0.070	0.018
0.080	-0.010	0.080	0.000
0.090	-0.022	0.090	-0.025
0.100	-0.034	0.100	-0.048
0.120	-0.060	0.120	-0.090
0.140	-0.085	0.140	-0.120
0.160	-0.101	0.160	-0.140
0.180	-0.119	0.180	-0.153
0.200	-0.132	0.200	-0.173
0.220	-0.150	0.220	-0.192
0.240	-0.160	0.240	-0.200
0.260	-0.165	0.260	-0.210
0.280	-0.163	0.280	-0.200
0.300	-0.142	0.300	-0.190
0.320	-0.125	0.320	-0.170

Table A-18. Input C_{p_N} Versus s/c for Case 18

$\Lambda = 17.8 \text{ deg}$

$\Lambda = 32.3 \text{ deg}$

<u>s/c</u>	<u>C_{pN}</u>	<u>s/c</u>	<u>C_{pN}</u>
0	1.1395	0	1.0766
0.001	1.139	0.001	1.075
0.002	1.137	0.002	1.073
0.003	1.134	0.003	1.070
0.004	1.131	0.004	1.068
0.005	1.129	0.005	1.061
0.006	1.121	0.006	1.052
0.007	1.117	0.007	1.041
0.008	1.110	0.008	1.032
0.009	1.099	0.009	1.020
0.010	1.088	0.010	1.005
0.012	1.046	0.012	0.953
0.014	0.989	0.014	0.888
0.016	0.900	0.016	0.810
0.018	0.755	0.018	0.690
0.020	0.550	0.020	0.500
0.025	0.055	0.025	0.010
0.030	-0.305	0.030	-0.376
0.035	-0.409	0.035	-0.500
0.040	-0.458	0.040	-0.570
0.045	-0.481	0.045	-0.610
0.050	-0.500	0.050	-0.641
0.055	-0.519	0.055	-0.660
0.060	-0.535	0.060	-0.671
0.070	-0.550	0.070	-0.683
0.080	-0.564	0.080	-0.699
0.090	-0.580	0.090	-0.726
0.100	-0.595	0.100	-0.745
0.120	-0.626	0.120	-0.800
0.140	-0.670	0.140	-0.860
0.160	-0.740	0.160	-0.947
0.180	-0.830	0.180	-1.033
0.200	-0.890	0.200	-1.125
0.220	-0.942	0.220	-1.200
0.240	-0.982	0.240	-1.262
0.260	-1.014	0.260	-1.286
0.280	-1.015	0.280	-1.285
0.300	-1.000	0.300	-1.265
0.320	-0.965	0.320	-1.230

Table A-19. Input C_{pN} Versus s/c for Case 19

$\Lambda = 23.8 \text{ deg}$

$\Lambda = 28.8 \text{ deg}$

<u>s/c</u>	<u>C_{pN}</u>	<u>s/c</u>	<u>C_{pN}</u>
0	1.1161	0	1.0935
0.001	1.114	0.001	1.093
0.002	1.110	0.002	1.092
0.003	1.107	0.003	1.090
0.004	1.102	0.004	1.088
0.005	1.099	0.005	1.084
0.006	1.090	0.006	1.080
0.007	1.080	0.007	1.070
0.008	1.073	0.008	1.060
0.009	1.062	0.009	1.044
0.010	1.050	0.010	1.025
0.012	1.010	0.012	0.969
0.014	0.950	0.014	0.896
0.016	0.855	0.016	0.803
0.018	0.725	0.018	0.708
0.020	0.620	0.020	0.610
0.025	0.350	0.025	0.363
0.030	0.180	0.030	0.183
0.035	0.125	0.035	0.128
0.040	0.100	0.040	0.110
0.045	0.086	0.045	0.090
0.050	0.076	0.050	0.080
0.055	0.066	0.055	0.070
0.060	0.057	0.060	0.060
0.070	0.040	0.070	0.040
0.080	0.020	0.080	0.020
0.090	0.005	0.090	0.010
0.100	-0.010	0.100	-0.007
0.120	-0.038	0.120	-0.038
0.140	-0.060	0.140	-0.060
0.160	-0.082	0.160	-0.090
0.180	-0.114	0.180	-0.120
0.200	-0.132	0.200	-0.140
0.220	-0.147	0.220	-0.162
0.240	-0.147	0.240	-0.162
0.260	-0.140	0.260	-0.158
0.280	-0.125	0.280	-0.140
0.300	-0.106	0.300	-0.112
0.320	-0.080	0.320	-0.085


Table A-20. Input C_{pN} Versus s/c for Case 20

$\Lambda = 14.2 \text{ deg}$

$\Lambda = 21.7 \text{ deg}$

<u>s/c</u>	<u>C_{pN}</u>	<u>s/c</u>	<u>C_{pN}</u>
0	1.1132	0	1.0941
0.001	1.110	0.001	1.092
0.002	1.107	0.002	1.089
0.003	1.100	0.003	1.081
0.004	1.090	0.004	1.070
0.005	1.070	0.005	1.050
0.006	1.036	0.006	1.012
0.007	1.000	0.007	0.940
0.008	0.954	0.008	0.840
0.009	0.900	0.009	0.750
0.010	0.849	0.010	0.689
0.012	0.707	0.012	0.580
0.014	0.580	0.014	0.505
0.016	0.470	0.016	0.457
0.018	0.413	0.018	0.423
0.020	0.382	0.020	0.400
0.025	0.331	0.025	0.360
0.030	0.300	0.030	0.330
0.035	0.277	0.035	0.310
0.040	0.258	0.040	0.290
0.045	0.244	0.045	0.269
0.050	0.230	0.050	0.250
0.055	0.215	0.055	0.237
0.060	0.200	0.060	0.225
0.070	0.180	0.070	0.203
0.080	0.165	0.080	0.180
0.090	0.150	0.090	0.160
0.100	0.136	0.100	0.140
0.120	0.105	0.120	0.115
0.140	0.087	0.140	0.090
0.160	0.078	0.160	0.080
0.180	0.050	0.180	0.060
0.200	0.040	0.200	0.040
0.220	0.030	0.220	0.035
0.240	0.040	0.240	0.040
0.260	0.045	0.260	0.045
0.280	0.052	0.280	0.057
0.300	0.062	0.300	0.067
0.320	0.080	0.320	0.092

Table A-21. Input C_{pN} Versus s/c for Case 21

1. Report No. NASA CR-178419		2. Government Accession No.		3. Recipient's Catalog No.	
4. Title and Subtitle Flight Survey of the 757 Wing Noise Field and Its Effects on Laminar Boundary Layer Transition; Volume III—Extended Data Analysis				5. Report Date March 1988	
				6. Performing Organization Code	
7. Author(s) New Product Development Organization Boeing Commercial Airplane Company (BCAC)				8. Performing Organization Report No. D6-53196-3	
9. Performing Organization Name and Address Boeing Commercial Airplane Company P.O. Box 3707 Seattle, WA 98124				10. Work Unit No. NAS1-15325	
				11. Contract or Grant No. Contractor Report	
12. Sponsoring Agency Name and Address National Aeronautics and Space Administration Washington, D.C. 20546				13. Type of Report and Period Covered	
				14. Sponsoring Agency Code	
15. Supplementary Notes Technical Monitors: D. W. Bartlett and D. B. Middleton NASA—Langley Research Center					
16. Abstract A flight program was completed in June of 1985 using the Boeing 757 flight research aircraft with an NLF glove installed on the right wing just outboard of the engine. The objectives of this program were to measure noise levels on the wing and to investigate the effect of engine noise on the extent of laminar flow on the glove. Details of the flight test program and results are contained in Volume I of this document. Tabulations and plots of the measured data are contained in Volume II. The present volume contains the results of additional engineering analysis of the data. The additional engineering analysis included analysis of the measured noise data, a comparison of predicted and measured noise data, a boundary layer stability analysis of 21 flight data cases, and an analysis of the effect of noise on boundary layer transition.					
17. Key Words (Suggested by Author(s)) Boundary Layer Transition Engine Noise Flight Pressure Data Flight Test Hot Film Sensors Natural Laminar Flow				18. Distribution Statement 	
19. Security Classif. (of this report) Unclassified		20. Security Classif. (of this page) Unclassified		21. No. of Pages 275	
				22. Price	

NA
FOR
REP

